Föhn winds on South Georgia and their impact on regional climate

A thesis submitted to the School of Environmental Sciences of the University of East Anglia in partial fulfilment of the requirements for the degree of Doctor of Philosophy

Daniel L. Bannister

October 2015

Abstract

South Georgia is a small and mountainous island, located in the remote Southern Ocean. The island's subantarctic climate is controlled by its location and steep orography; with 19 peaks over 2000m and situated within a belt of strong westerly winds South Georgia acts as an effective barrier to the winds that impinge upon it. Since the 1920s, average summer temperatures have risen by ~1^{o}C on South Georgia. Coupled with this has been an increase in the rate of glacial retreat throughout the last century, with glaciers on the northeast leeside of the island retreating at a faster rate than those on the southwest side. These asymmetrical changes are thought to be linked with the strengthening of the westerlies. If the strength of the westerlies is sufficient, downslope winds can develop on the leeside of the island causing significant temperature increases as the descending air warms adiabatically; this is known as the föhn effect. Therefore, the aim of this thesis is to investigate whether the observed asymmetric pattern of regional warming and glacier retreat are caused by the föhn warming process.

To explore the link between the föhn effect and its impact on the regional climate of South Georgia, a 10 year climatology (2003 – 2012) of föhn events is created. Using automatic weather station observations to identify abrupt changes in temperature, humidity and wind speed, it is found that föhn events are frequently observed (874 events are identified in total) with one event occurring every four days. Following this, sensitivity simulations with the Weather Research and Forecasting model for four föhn cases studies are presented, with the aim of deducing the optimal model setup for South Georgia. The model analysis is largely supported by observations, and föhn flow is well captured at high (< 3.3km) horizontal resolution. With the model optimised for South Georgia, a 21 month model run (at 0.9km resolution) produces the first ever detailed regional climatology of South Georgia. The results from this simulation illustrate the asymmetrical impact of föhn on the island's climate. During September 2011 – August 2012, modelled föhn events produced +2^{o}C air temperature anomalies and up to 3m water equivalent ablation at the termini of South Georgia's north-eastern glaciers. This supports the view that föhn is partly responsible for the asymmetrical retreat of glaciers, via enhanced leeside surface warming and melting. These results support the original hypothesis that an enhancement of the föhn warming process could have implications on future asymmetrical warming and melt.

Acknowledgements

None of this would have been possible if it were not for my supervisors; John King and Ian Renfrew. I would like to thank and gratefully acknowledge them for their guidance and assistance during this research. My gratitude goes especially to John, who offered invaluable advice on both academic and other issues during my time at the British Antarctic Survey (BAS). I also extend my thanks to other staff at BAS, in particular J. Scott Hosking, Tony Phillips, Andrew Orr and Steve Colwell, for their indispensable assistance, help and computing support. I would also like to thank my funders, the Natural Environment Research Council (NERC) for providing the financing to make this research possible. In the same vein, I also thank The Royal Meteorological Society and the University of East Anglia for additional funding so that I could visit South Georgia. My thanks also go to Barbara Brookes, Alan Gadian, Ralph Burton and James Groves who all made it a once in a lifetime trip, and one I shall never, ever forget. I would never have gained an appreciation for the complexity and meteorology of South Georgia without having visited the island.

My thanks also go to my family and friends, and especially my fiancée, who have always supported, encouraged and believed in me, in all my endeavours. I dedicate this to my son, Oscar Henry Bannister, who was such a wonderful surprise during my Ph.D.

I am, and always will be, indebted to you all.

"*May the wind under your wings*
bear you where the sun sails
and the moon walks"
– J. R. R. Tolkien

Contents

List of Figures

List of Tables

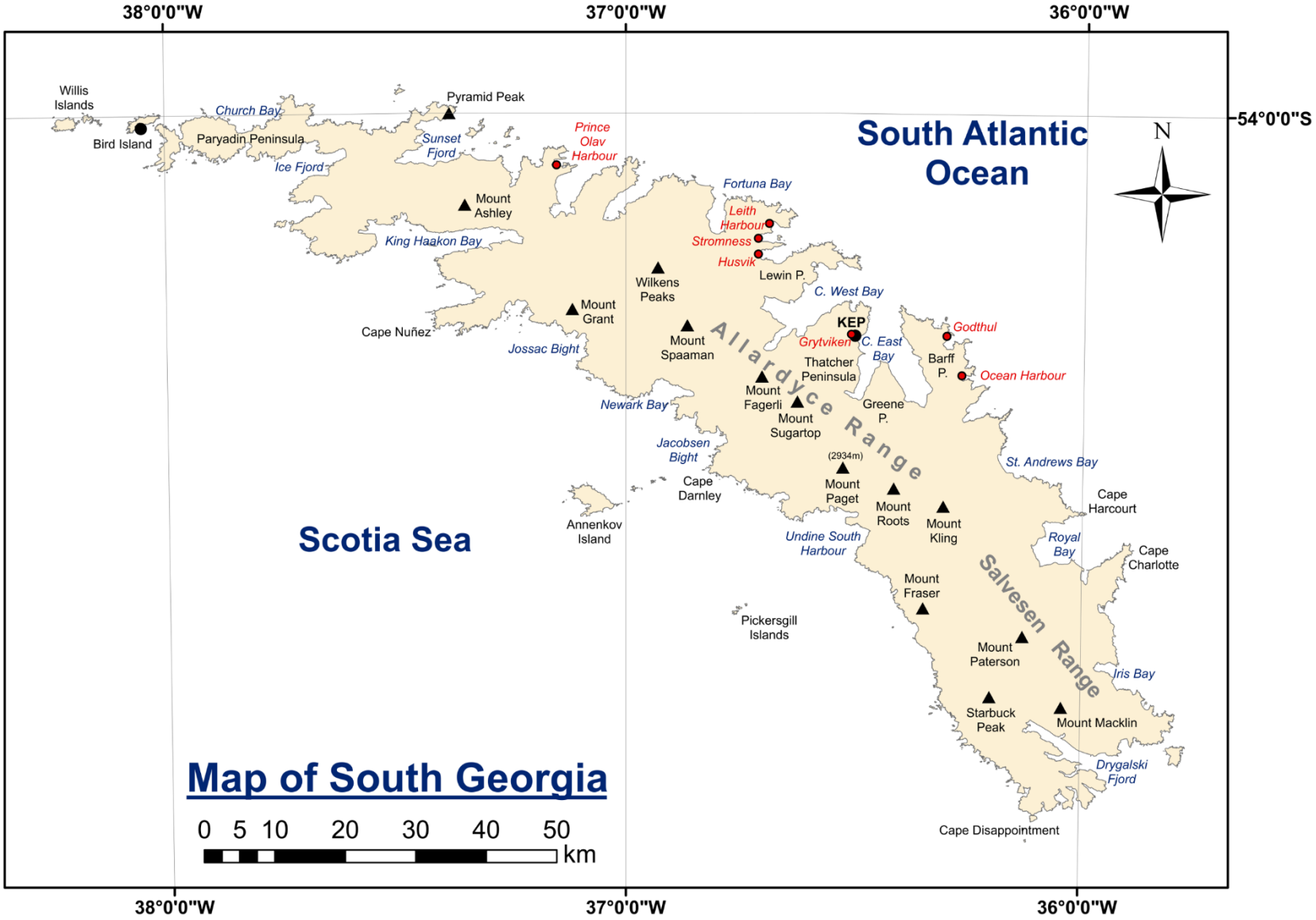
38°0'0"W
37°0'0"W
36°0'0"W
54°0'0"S
South Atlantic Ocean
Scotia Sea
N
Willis Islands
Bird Island
Church Bay
Paryadin Peninsula
Ice Fjord
Pyramid Peak
Sunset Fjord
Prince Olav Harbour
Mount Ashley
King Haakon Bay
Fortuna Bay
Leith Harbour
Stromness
Husvik
Lewin P.
Wilkens Peaks
C. West Bay
Mount Grant
Cape Nuñez
Jossac Bight
Mount Spaaman
KEP
Grytviken
C. East Bay
Godthul
Barff P.
Ocean Harbour
Thatcher Peninsula
Allardyce Range
Mount Fagerli
Mount Sugartop
Greene P.
Newark Bay
Jacobsen Bight
Cape Darnley
(2934m)
Mount Paget
Mount Roots
Mount Kling
St. Andrews Bay
Cape Harcourt
Annenkov Island
Undine South Harbour
Royal Bay
Cape Charlotte
Mount Fraser
Salvesen Range
Pickersgill Islands
Mount Paterson
Iris Bay
Starbuck Peak
Mount Macklin
Drygalski Fjord
Cape Disappointment
Map of South Georgia
0 5 10 20 30 40 50
km

Chapter One: Introduction

1.1 The Island of South Georgia

South Georgia and the South Sandwich Islands are a collection of small, remote subantarctic islands located in the Atlantic sector of the Southern Ocean. South Georgia (54° – 54°55'S, 35°50' – 38°W) is the largest of this group, measuring 3528km^2 in area, and situated 1500km east-southeast of the Falkland Islands, and some 520km northwest from the main group of South Sandwich Islands (Figure 1.1). Despite being the largest subantarctic island, South Georgia is still relatively small, measuring just 167km long and varying in width from 2 to 40km.

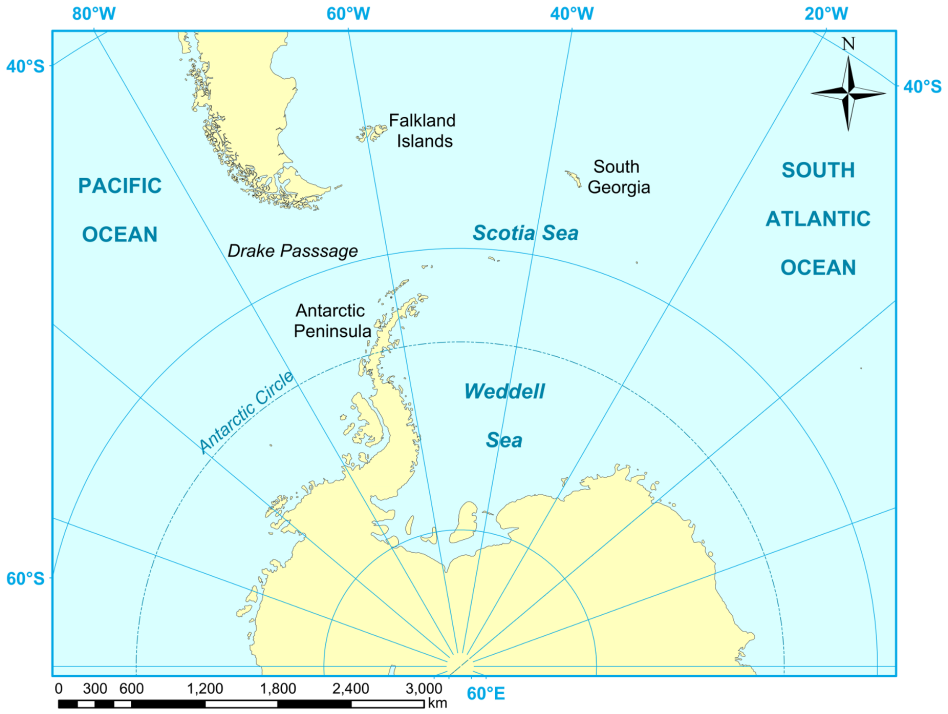

Figure 1.1 – *Geographic location of South Georgia in relation to the Falkland Islands and the West Antarctic Peninsula.*

The dominant physiographic feature of South Georgia is its axial mountain chain, composed predominantly by the Allardyce and Salvesen ridges, orientated in a crescent northwest to southeast direction, which extend over two-thirds of the total length of the island (Hayward, 1983). As such, South Georgia is a very mountainous island, having 19 peaks over 2000m, culminating in Mount Paget which rises 2934m above sea level (Figure 1.2). Approximately 13% of the island exceeds 1000m in elevation. It is hardly surprising that South Georgia is often described as *"the Alps in mid-ocean"* (Headland, 1992) or *"an isle of scenic grandeur"* (Turner, 1961).

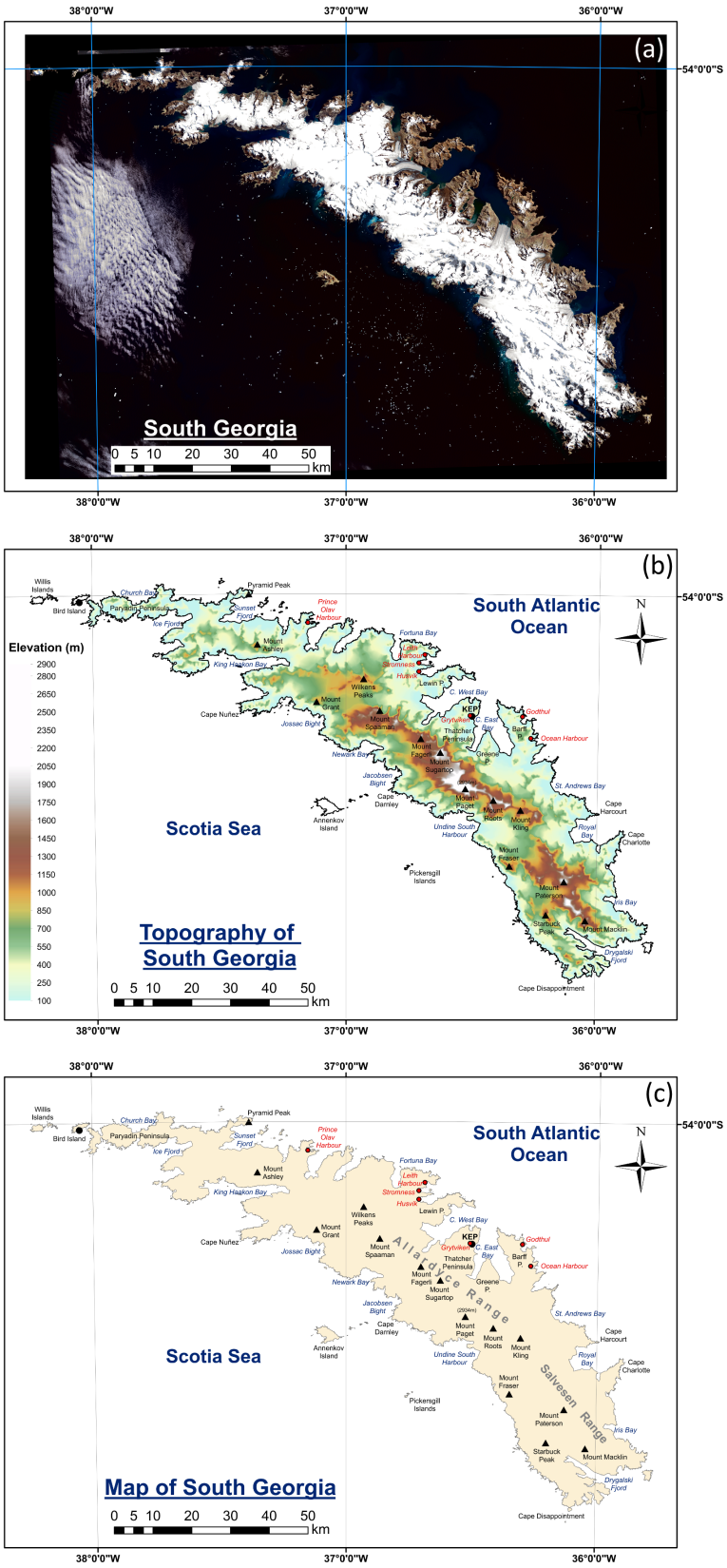

Figure 1.2 – *Panel (a) shows a satellite image of South Georgia. The glaciated and non-glaciated terrain is easily discernible. Panel (b) shows a topographic map of South Georgia. Panel (c) geographical map of South Georgia. A larger version of panel (c) is the shown in the frontispiece.*

The island has a broken coastline, which comprises of numerous small offshore islands (islets) and stacks, including a number of steep-sided and deep (>200 m) glacial bays and fjords (some of which extend a considerable way inland). The south-western side of South Georgia is more heavily glaciated due to its colder south-facing position and higher precipitation rates. The terrain here is also steeper and many of the glaciers descend to sea level (sea-calving and outlet glaciers), producing icefalls (Rosqvist & Schuber, 2003). In contrast, the mountains are at their lowest elevation along the north-eastern coast of the island, and here the glaciers are wider and less crevassed (Richards & Tickell, 1968). There are around 20 freshwater lakes on the north-eastern side of South Georgia (Trathan *et al*., 1996), as well as many smaller lakes and tarns elsewhere on the island.

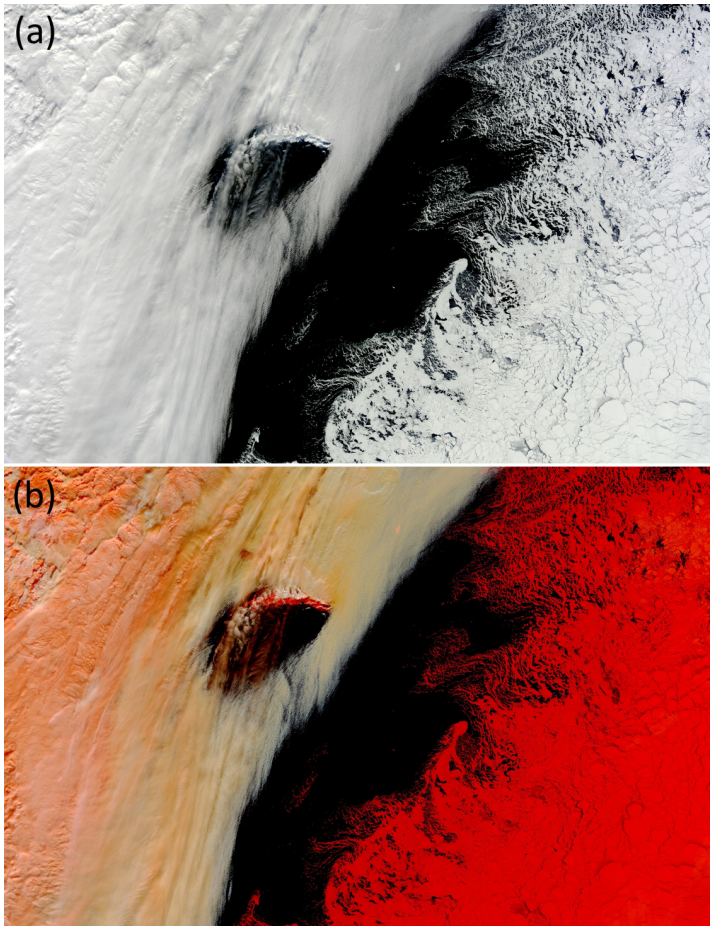

Figure 1.3 – *MODIS images over South Georgia on 6 September 2014, 13 days before the 2014 Antarctic maximum sea ice extent was observed. Panel (a) shows the visible image. Panel (b) shows a false colour image using, respectively, bands 3, 6 and 7 for red, green and blue. Snow and ice covered land and sea ice show up as red, cloud shows up as white, and the ocean shows up as black. The outline of the northern limit of the sea ice can be discerned. Both images are orientated on the 0º longitude. Images were taken from* https://earthdata.nasa.gov/labs/worldview/

Rivers and streams are widespread, particularly in summer when they are fed by snow and glacial meltwater. Approximately 56% of the total land surface of the island is covered by permanent snow and ice, 9% of the land area is vegetated, while the other 35% is too steep to permit permanent snow and ice (Headland, 1992). Despite being heavily glaciated, South Georgia is located 5^{o} north of the maximum winter Antarctic sea ice extent. The average northern limit of sea ice is ~160 km to the south of South Georgia in spring, and ~800 km to the south in autumn (Pepper, 1954). As a result, the northern limit of the winter drift ice is (almost) always south of South Georgia. Only during severe winters, such as in 1959 (Hydrographic Office, 2009), 1980 and 1987 (Comiso, 2010) has Antarctic sea ice been reported to have surrounded the south coast of the island. On 19 September 2014, the five-day average of Antarctic sea ice extent exceeded 20 million square kilometres for the first time since the long-term satellite observations began in 1979 (National Ice & Snow Data Center, 2014). Moderate Resolution Imaging Spectroradiometer (MODIS) images taken on 6 September 2014 (see Figure 1.3) show that the sea ice was approximately 150 – 250 km south of South Georgia.

1.2 The History of South Georgia

South Georgia was first landed on by Captain James Cook (on board HMS *Resolution*), who claimed it for the British Crown, on 17 January 1775. South Georgia was named after the monarch at the time, King George III. Prior to Captain Cook's exploration of South Georgia, the island had been spotted on at least two prior voyages. The first discovery of South Georgia was made in 1675 by Antoine de la Roché, and at the time, was the first land to be discovered south of the Antarctic Convergence. The second sighting of the island was in 1756 by Gregorio Jerez, a Spanish Commander of the *León* merchant vessel. From the discovery of the island to the beginning of the 20th century, South Georgia was intermittently occupied by English and American sealers. The island became permanently inhabited in 1904, when the first whaling station at Grytviken (Norwegian, '*gryte*' pot, '*viken*' cove) began operations. South Georgia subsequently became the world's largest whaling centre, with over 2000 residents at its height. The island was included in the British Empire in 1908 as part of the Falkland Islands Dependencies. By 1912, seven whaling stations had been established on South Georgia. These were located at Prince Olav Harbour, Leith Harbour, Stromness, Husvik, Grytviken, Godthul and Ocean Harbour

(Figure 1.2(c)). By the mid-1970s, hunting of large marine animals had ceased because of a collapse in the population of seals and whales. In 1985, the Falkland Islands Dependencies were renamed South Georgia and the South Sandwich Islands. The British Antarctic Survey occupied the buildings at King Edward Point from November 1969, until its closure by Argentine military forces in April 1982. There followed occupation by a small British garrison until March 2001. The British Antarctic Survey reoccupied the buildings, and since then have conducted scientific research with permanently staffed research stations (on rota) on Bird Island (north-western tip of the island) and at King Edward Point. There are now no permanent residents living on South Georgia. The Government of South Georgia and the South Sandwich Islands is based in Stanley, Falkland Islands. Government Officers and museum curators live on the island during the summer months, also on an overlapping rota basis.

1.3 The Regional Climate of South Georgia

The climate of South Georgia is maritime in nature; cool, moist and windy. Despite being located only 1½º south of the Falkland Islands, South Georgia is a bleaker and a substantially more glaciated island (Turner, 1961). This is because the climate of South Georgia is governed by two factors; its location in the Southern Ocean, and the island's dramatic topography.

Though only a narrow mountainous island, the central spine of South Georgia forms an effective barrier to air masses impinging upon it, as it is one of very few landmasses in the Southern Hemisphere at latitude of 54ºS. The island is effectively located within the centre of strong westerly winds (see section 1.6.3), commonly referred to as the 'roaring forties, furious fifties and screaming sixties'. This part of the Southern Ocean has a well-deserved reputation for having some of the strongest winds compared to the world's other oceans (Simmonds & King, 2004). Consequently, South Georgia acts as a formidable barrier to the mean westerly flow of the lower troposphere, and frequently experiences a wide range of hostile weather systems. The prevailing westerly winds mean that the western side of the island is particularly exposed to low cloud and severe weather conditions during the entire year. The south-western coastline and its extremities are also particularly exposed to eastward moving depressions that form in the circumpolar vortex, or which derive from the Drake Passage and/or generated off of the West Antarctic Peninsula. Such depressions travel

quickly across the Southern Ocean, accounting for the frequently rapid deterioration of the weather on South Georgia. In contrast, the north-eastern side of the island is more sheltered and often experiences clearer and quieter weather. Despite this, strong wind gusts (approaching $50ms^{-1}$) have been recorded at King Edward Point (Headland, 1992). Although being a comparatively protected area of the island, the cause of such extreme wind gusts is thought to be enhanced by orographic effects (see section 1.6). As such, the weather and climate of the island is greatly influenced by its own topography, leading to very different climate regimes over a short distance. The only study to quantify this was Richards & Tickell (1968), who recorded that Bird Island is considerably wetter, windier and on average 1.8°C colder than King Edward Point, therefore suggesting that Bird Island was more representative of the prevailing conditions over the ocean. The climate of South Georgia is also governed by its position within the Southern Ocean. The island is 350km south of the Antarctic Convergence (Headland, 1992) where Antarctic surface waters moving northward sink below subantarctic water, 5° north of the average maximum limit of Antarctic winter sea ice, and south of the present Polar Front Zone (Smith, 1960; Rosqvist & Schuber, 2003). This accounts for the island's cool (mean temperature of 2.5°C) and wet climate (annual average precipitation total of 2033 mm recorded at King Edward Point), and explains why more than half of South Georgia is locked up in snow and ice (Smith, 1960). Therefore, although South Georgia is located on the same latitude as the city of York (United Kingdom), the island has a subantarctic climate.

1.4 The Biogeography and Ecology of South Georgia

Though a small, remote and isolated island, South Georgia is incredibly rich in life and has high biogeographical importance in the high-latitude Southern Hemisphere. As discussed by Meredith *et al*. (2008) the ocean surrounding South Georgia is characterised by high levels of biological productivity, and plays a vital role in supporting vast colonies of both marine- and terrestrial-based animals. The island's importance in biological productivity has been attributed to the fact that it is outside the maximum Antarctic sea ice zone, and is, therefore, a perfect place for many terrestrial and marine animals to shelter, feed and reproduce away from the Antarctic frozen wilderness. For this reason, South Georgia is a vital refuge for Antarctic wildlife.

The Southern Ocean and the waters surrounding South Georgia are amongst the most productive regions of the world's oceans, because the conditions are particularly favourable for rich marine biodiversity (Comiso, 2010). South Georgia happens to be situated close to the convergence of cold dense surface water and warm nutrient rich waters. At this convergence zone (known as the Antarctic Convergence), the warmer, relatively less dense and nutrient rich water upwells, as the denser surface water converges and descends. At the same time, the melt of sea ice forms a stable layer of low density surface sea water, which allows plankton to readily grow (Comiso, 2010). The high abundance of plankton on the South Georgia shelf is thought to be responsible for sustaining an island with high biological productivity, since krill and other plankton are primary food sources (Trathan *et al*., 2012). This population is, however, not self-sustaining and is replenished by the transportation of krill and plankton from the Antarctic Peninsula, the South Orkney Islands and the Weddell Sea, via the Antarctic circumpolar current (Murphy *et al*., 2007).

South Georgia has long been recognised for its high biological productivity (Roux *et al*., 2002; Barnes, 2008; Barnes *et al*., 2006; 2010; among others), which has resulted in numerous scientific collaborations in biodiversity studies. For instance, De Broyer & Danis, 2010 (as part of the Scientific Committee on Antarctic Research – Marine Biodiversity Information Network project) concluded that South Georgia is a key source of regional biodiversity, which results in supporting anomalously high levels of endemic species, which are also at their thermal tolerance limits. Similarly, Hofman *et al*. (1998) have shown that the South Antarctic circumpolar current is responsible for the transport of nutrients and organisms (such as Antarctic krill [*Euphausia superba*]) from the Antarctic Peninsula towards the island, which enables it to support a diverse range of seabirds and marine mammals (including the humpback whale [*Megaptera novaeangliae*] and the southern right whale [*Eubalaena australis*]). This too is discussed by Hogg *et al*. (2011), who highlight that the island's geographical isolation and its proximity to nutrient rich currents are important catalysts in sustaining a biologically rich and distinct island. Arntz *et al*. (1997) and Hogg *et al*. (2011) also identify that the waters of South Georgia are the most speciose region of the Southern Ocean, with greater species richness than comparable northern latitudes. As a consequence, the ocean directly surrounding South Georgia has long been recognised as being commercially important, not only for fish and krill, but also for whales and

seals. South Georgia was a key economic centre for fisheries and sealers, and also sustained the world's largest whaling station in the early 20th century.

It is not just the surrounding sea shelf which has huge biological importance, but also the island itself. Although no terrestrial mammals (except for seals), reptiles or amphibians are indigenous to South Georgia (McIntosh & Walton, 2000), the island's location in the Southern Ocean makes it an important site of reproduction for many terrestrial-based animals. The most recent environmental assessment undertaken by the South Georgia Heritage Trust (hereafter SGHT (2014)) similarly highlights this rich biodiversity, listing: (introduced) Reindeer (*Rangifer tarandus*, population in 2011 ~3000; 2015 ~0); Southern elephant seals (*Mirounga leonina*, population 100,000); Antarctic fur seals (*Arctocephalus gazella*, population in the low millions); 100 million nesting birds, many of which are endangered (black-browed albatross [*Thalassarche melanophrys*]), vulnerable (white-chinned petrel [*Procellaria aequinoctialis*]) or near-threatened (South Georgia pipit [*Anthus antarcticus*]); four species of penguin (king [*Aptenodytes patagonicus*], gentoo [*Pygoscelis papua*], macaroni [*Eudyptes chrysolophus*] and chinstrap [*Pygoscelis antarcticus*]); and four species of albatross (wandering [*Diomedea exulans*], black-browed [*Thalassarche melanophrys*], grey-headed [*Thalassarche chrysostoma*] and light-mantled sooty [*Phoebetria palpebrata*]), as the most dominant species found on the island. Additionally, some 88 different bird species have been recorded, of which 30 breed on the island (Clarke *et al*., 2012; Black *et al*., 2013). South Georgia holds one of the world's most abundant and diverse seabird communities, which is why in February 2012 the South Georgia and South Sandwich Islands Marine Protected Area was created, which covers over 1 million km^2 of the highly productive waters around the island. South Georgia also suffers from an invasion of Norway rats (*Rattus norvegicus*) and house mice (*Mus musculus*), which are thought to have been introduced by early settlers and commercial operations in the 18th and 19th centuries (Poncet, 2000; Frenot *et al*., 2005; Cook *et al*., 2010).

Unlike the biological diversity of fauna on South Georgia, vegetation is generally more restricted to north-eastern coastal areas, low valleys and surrounding offshore islands. The southwest side of the island is permanently ice covered and, as a result, the dominant plant communities cover a large proportion of the non-glaciated coastal areas of South Georgia (Cook *et al*., 2010). Despite this, South Georgia has the most

extensive vegetation cover of any other island south of the Antarctic Convergence. Much of this vegetation is sparse or partial, and is characterised by a coastal band of dense tussac (*Poa flabellate)* and *festuca* grassland (Scott & Poncet, 2003; SGHT, 2014) along the less exposed north-eastern side of South Georgia. There are a limited number of flowering plants (such as Greater Burnet [*Sanguisorba officinalis*] and Antarctic hair grass [*Deschampsia antarctica*]), and no trees or shrubs (SGHT, 2014). Like many of the terrestrial animals, many plant species were introduced when the island was first colonised. Wavy bittercress (*Cardamine flexuosa)*, the dandelion (the *Taraxacum* genus)*,* yarrow *(Achillea millefolium),* and mouse-eared chickweed (*Cerastium vulgatum)*, are among the most widespread and well established invasive species across the island. There still remains a high proportion of indigenous and endemic onshore flora to the island, including 25 indigenous plant species (such as clubmoss [the *Lycopodiopsida* class]) and a number of endemic bryophytes and lichens. Despite the limited distribution of higher order flora on the island, the vegetation that is present provides important habitats for a whole host of non-native and native invertebrates, including arthropods, beetles, springtails and spiders. It is certainly clear that despite being a remote subantarctic island, South Georgia is an important sanctuary for many marine and terrestrial species as a refuge against the harsh and extreme Antarctic continent.

1.5 Recent Environmental Change on South Georgia

1.5.1 Regional Temperature Warming

The high latitude Southern Hemisphere is one of the most rapidly changing regions on the surface of the Earth. Attention has typically focused on to the warming trend experienced on the West Antarctic Peninsula (e.g. King, 1994; Kwok & Comiso, 2002a; 2002b; Cook *et al*., 2005; Meredith & King 2005). Such studies have shown an accelerated warming trend in annual air temperatures of around $3.7 \pm 1.6^{o}C$ over the last 100 years. While the temperature increase is well documented on the continent, it is less well explored across the subantarctic islands.

Only one long-term climate record exists for South Georgia (see Chapter 2 for further information). Based upon 110 years of discontinuous surface observations (1905 – present, but no data 1982 – 1999, from manual observations taken at Grytviken and the automatic weather station (AWS) at King Edward Point), the annual austral

summer (December, January, February) average surface temperatures on northeast South Georgia have risen by ~1°C since the 1920s ($r^2 = 0.20$, $p = 0.01$, Figure 1.4). In the early 1900s the summer temperatures were relatively high (a mean of 4.9°C), lower between 1920 and 1949 (a mean of 4.3°C), followed by higher temperatures during the 1950s and 1960s (a mean of 4.6°C), and have been progressively increasing since the 1970s to the present (a mean of 5.4°C). The warmest summer on record was 2002 (average 6.95°C), while the coldest summer on record was 1911 (average 2.00°C). The southwest coast of South Georgia, by contrast, is less accessible and hence there is no instrumental data available from this side of the island for comparison. Despite the lack of instrumental data, fluctuations in glacier extent can be used as proxy indicators of (local) climate change (Clapperton & Sugden, 1988; Clapperton *et al*., 1989a; 1989b; Gordon *et al*., 2008; Hodgson *et al*., 2014).

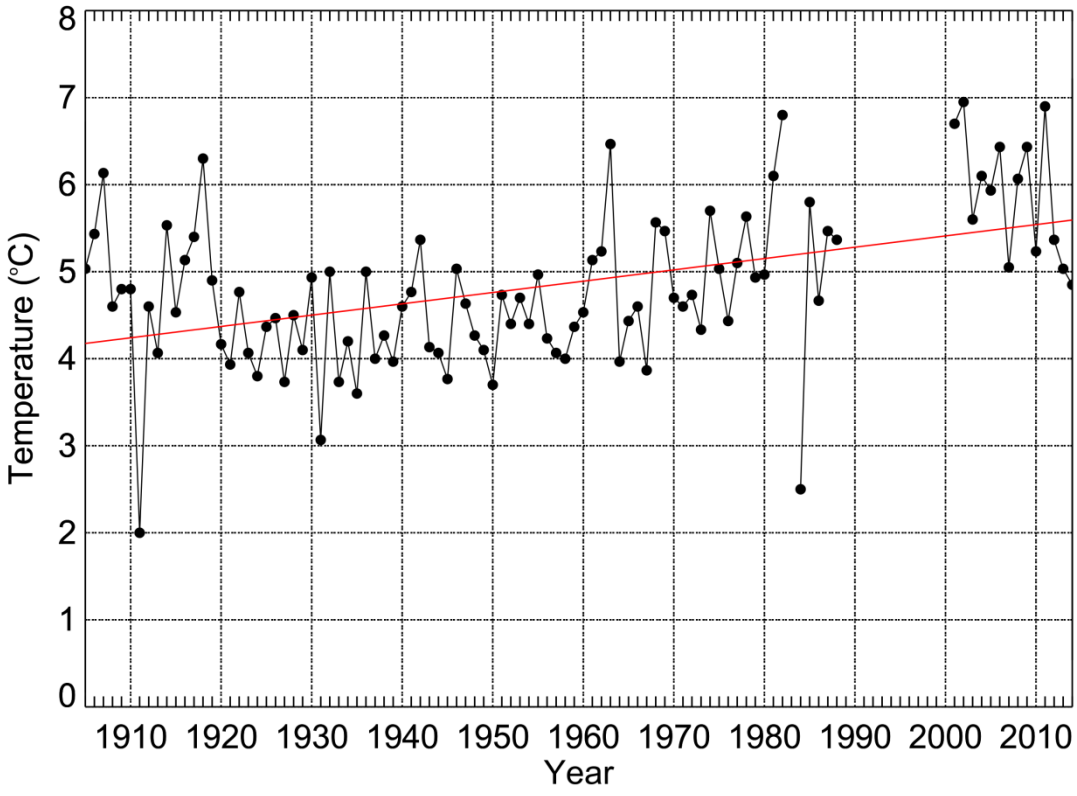

Figure 1.4 – *Annual average summer air temperatures at King Edward Point, 1905 – 2014. A linear least-squares fit to the data is shown by the red line (β = 0.01, r^2 = 0.20, correlation coefficient = 0.45, p = 0.01).*

1.5.2 Asymmetrical Glacial Retreat

There have also been signs of rapid ice-mass change across South Georgia since the 1950s. Gordon *et al*. (2008) have shown that 36 out of ~160 glaciers on the northeast

coast of the island have been receding in response to the sustained warming trend that began in the 1950s. Of these 36 glaciers, 26 were shown to have retreated, 6 were shown to be stable (i.e. show a negligible, complex, or ambiguous growth or decay), while only two of the total glaciers were shown to have advanced. Gordon *et al*. (2008) attribute the variable response to exposure, topography and weather. The two advancing glaciers were at higher altitudes where orographic precipitation is greater compared to lower elevations. In contrast, lower elevation glaciers were retreating faster, while southwest coast glaciers, where the climate is cooler and wetter, displayed complex responses. Gordon *et al*. (2008) thus concluded that *"from a process-oriented view, glacier hypsometry, surface slope and altitude range appear to have significant influence on glacier response and sensitivity to the climate warming at South Georgia"*. An earlier study by Gordon & Timmis (1992) also highlighted that glacial retreat has been sporadic, with different rates covering different periods for different glaciers. Despite observing different rates of change over a variety of glacier shapes and sizes, Gordon & Timmis (1992) concluded that the recession of glaciers was a response to a trend of climatic warming since 1950. They suggested that the background circulation patterns had induced variations in seasonal temperature that had been sustained sufficiently long enough for areal glacier responses across the island.

Cook *et al*. (2010) similarly shows significant coastal glacial retreat since the 1950s, with the most dramatic increases in the last decade. Using archival photography and satellite imagery, Cook *et al*. (2010) analysed the rates of advance and retreat of 103 coastal glaciers from the 1950s to the present (Figure 1.5). Of the 103 coastal glaciers investigated, 99 of them had retreated, with an average rate of retreat increasing from 8 m per year in the 1950s, to 35 m per year at present. In addition to this, Cook *et al*. (2010) also found that the glaciers on the northeast coast of the island were retreating at a faster rate than the glaciers on the southwest side of the island. Of the 41 north-facing glaciers investigated, 10 of them had retreated by over 1 km in the past 50 years, compared to just 4 out of the 62 south-facing glaciers. They also found that the average total change for north- and south-facing glaciers was -729.98 m (standard deviation (σ) = 629.83 m) and -355.64 m (σ = 370.72 m) respectively. Only four marine-terminating glaciers were found to have advanced on the island since the 1950s. Therefore, Cook *et al*. (2010) concluded that asymmetrical glacial retreat was

occurring on South Georgia, with the largest and fastest rates of retreat taking place along the northeast coastline of the island.

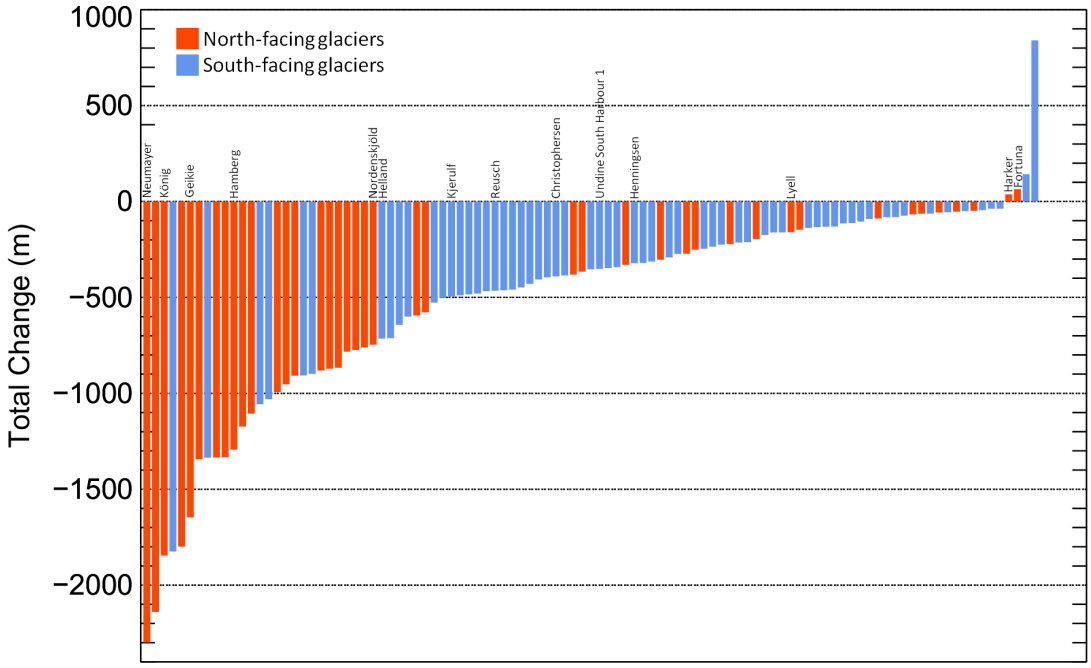

Figure 1.5 – *Total change in glacier length for 103 marine-terminating glaciers on South Georgia. Red bars – north-facing glaciers (northeast coastline), blue bars – south-facing glaciers (southwest coastline). The data is originally from Cook et al. (2010). The 14 glaciers labelled (left to right: Neumayer, König, Geikie, Hamberg, Nordenskjöld, Helland, Kjerulf, Reusch, Christophersen, Undine South Harbour 1, Henningsen, Lyell, Harker and Fortuna) are investigated further in Chapter 6.*

These studies indicate that although the pattern of change is broadly comparable with retreat driven by atmospheric warming, the rapidity and asymmetry of the migration suggests that this may not be the sole driver of glacier retreat in this region. The change in mass balance of glaciers is attributed to many other factors including topography, catchment area, and glacier width and flow dynamics. Besides the direct effect of a reduction in ice mass through enhanced melt, higher melt rates could trigger a speed-up of glacier flow through basal lubrication, accelerating the drainage of a number of the island's glaciers. Marine-terminating glaciers in particular, such as Neumayer and Nordenskjöld glaciers, are likely to show high sensitivity to local climatic conditions. Since 56% of South Georgia is permanently frozen, the consequences of warming on these glaciers could be extensive in a changing climate. This too will have further repercussions on the incredibly sensitive marine and terrestrial ecosystems of the island. Given the limited number of surface observations on the island, and since it is

one of only a few landmasses in the circumpolar Southern Ocean, the glaciers of South Georgia are an important proxy record of present and past climatic changes.

Broadly similar glacial retreat has also been observed across many subantarctic islands of the Southern Ocean. Glaciers at Kerguelen in the Southern Indian Ocean (Frenot *et al*., 1993; 1997) and in southern Patagonia have shown to be shrinking and retreating at accelerated rates (Aniya *et al*., 1997; Aniya, 1999; Rignot *et al*., 2003; Rivera & Casassa, 2004). Likewise, rapid glacier recession over the last decades, reflecting temperature rise since the 1950s and 1960s has been found in several locations, including Heard Island (Allison & Keage, 1986; Kiernan & McConnell, 1999; 2002; Budd, 2000), and the South Shetland Islands (Braun *et al*., 2001; Simões *et al*., 2004). Likewise, an earlier study by Cook *et al*. (2005) also found retreating glaciers on the Antarctica Peninsula. They found retreating trends in 87% of 244 glaciers on the Peninsula and adjacent islands over the past 61 years. Cook *et al*. (2005) concluded that the retreating pattern is likely driven by the recent atmospheric warming trend, but this may not be the only sole driving force for glacial retreat in this region. As a result, changes to glacial extent have been attributed to the trend towards slightly warmer, windier and wetter climate since the mid-20th century, across a variety of high latitude Southern Hemisphere locations (Clapperton *et al*., 1989b). These recent accelerated retreats may, as a result, reflect an anthropogenic contribution to increased global temperatures.

1.5.3 Species Reduction

At a local level, the regional warming of South Georgia has already brought about changes to terrestrial and marine ecology, bird distribution (Trathan *et al*., 2007; Forcada & Trathan, 2009; Convey *et al*., 2011; Richardson *et al*., 2012; Morley *et al*., 2014; among many others), and seasonal snow cover and glacier extent (Gordon & Timmis, 1992; Gordon *et al*., 2008; Cook *et al.,* 2010). Likewise, introduced flora and fauna (accidently and/or deliberately) has already profoundly damaged the natural ecosystem of the island (Frenot *et al*., 2005; SGHT, 2014). Early last century most of South Georgia's glaciers reached the sea, subdividing the coastline into a series of areas bounded by ice barriers, which were impassable to foreign species. In particular, these barriers protected large parts of the island from the colonisation by rats and reindeer. However, acceleration in retreat rates of glaciers on both sides of the island

have opened up new (ice-free) areas for such species to colonise. Signs of rats have been identified in several high mountain passes and offshore island which were free of rodents 20 years ago (SGHT, 2014). The invasion of rats has led to increased predation of seabirds and their eggs resulting in the increase of endangered species. The Norway rat has had a significant detrimental impact on South Georgia bird species, particularly South Georgia's blue petrels (*Halobaena caerulea*), Antarctic (*Pachyptila desolata*) and fairy prions (*Pachyptila turtur*), diving petrels (*Pelecanoides georgicus*) and the endemic Southern Georgia pipit (*Anthus antarcticus*) and pintail (*Anas georgica georgica*). These birds nest on open ground or in burrows, thus giving rats an easy access to their eggs and chicks (McIntosh & Walton, 2000; SHGT, 2014). The overgrazing of reindeer, particularly on native plants, seeds and seedlings, and tussac grass, has also profoundly impacted the habitat for ground- and burrow-nesting birds. As such, the introduction of foreign plant and animal species has ultimately altered the appearance and ecological function of the island (SGHT, 2014) in the last ~200 years.

Changes in the regional marine environment have also been observed. Whitehouse *et al*. (2008) have identified that near-surface waters around South Georgia are some of the fastest warming in the Southern Hemisphere. Orr *et al*. (2005) have similarly shown that projected increases in ocean wide acidification could put a great strain upon these waters, and the rest of the Southern Ocean. As a result, both Hogg *et al.* (2011) and Barnes *et al*. (2010) highlight that because many of these animal species are at their thermal tolerance limit (in combination with their high level of endemism), drastic changes in environmental conditions may have severe and irreversible impacts across the island's biodiversity. Coupled with this, is the fact that South Georgia's biota is Antarctic in character, and so consequently might find toleration to warmer climes, and thus adaptation, difficult (Peck, 2002; Barnes *et al*., 2006; Griffiths *et al*., 2009). Hogg *et al*. (2011) concluded that the ecological implications of environmental change to the island's ecosystems could be severe, i.e. it may result in the extinction of many of South Georgia's endemic species. Ecosystem variability on the island has also been linked with krill abundance (Thorpe *et al*., 2002). Krill on the South Georgia shelf are thought to be sustained by the oceanic transport of these crustaceans from the Antarctic Peninsula (Murphy *et al*., 1998). However, both the overturning circulation and the Antarctic circumpolar current are strongly driven by the circumpolar

westerlies. A consequence of this is a yearly variation in krill abundance, which in turn directly impacts higher predators that breed on South Georgia (Croxall *et al*., 1988; 1999; Boyd *et al*., 1994; Trathan *et al*., 2012). Therefore, future climate change is expected to have major physical and chemical changes in both the ocean and the atmosphere of this region (Dierssen *et al*., 2002; Vaughan *et al*., 2003; Meredith & King, 2005; Montes-Hugo *et al*., 2009; Costa *et al*., 2010; Schofield *et al*., 2010; Trivelpiece *et al*., 2011). This will have major consequences on the function and structure of the island's unique biological diversity (Murphy *et al*., 2012; 2013).

As explained by Frenot *et al*. (2005), therefore, further future climate change could have two potential impacts on South Georgia. First, a change in the climatic and environmental conditions of the island will result in changes to the climatic and environmental constraints which shape current biodiversity. This is because the island's geographical isolation coupled with current climatic constraints leads to high endemism of terrestrial species on South Georgia. As a result, many remain relatively defenceless against changing environmental conditions. Warming will directly affect terrestrial biota through shortening the winter period, through earlier spring thaws and later autumn freezing (Frenot *et al*., 2005). Likewise, changes in precipitation trends (and therefore water availability) related both to the local and microclimatic scale may result in changes to the distribution and numbers of many species. Coupled with this, and second, a change in conditions may result in increased biological invasions. Such environmental changes result in more habitable conditions in a previously hostile environment, therefore, providing more food and a better habitat for the colonisation of alien species (Cook *et al.*, 2010). As the SGHT (2014) concluded, glacial retreat as a result of climate change presents additional threats, because ice barriers that currently isolate rat- and reindeer-free areas become less effective each year. It is inevitable that continued retreat of South Georgia's glaciers, which has been accelerating, will allow the occupation of new species into areas that had previously been excluded. This will result in new regions of colonisation, and therefore, increased predation of important ground- and burrow-nesting birds found on the island (Cook *et al*., 2010). Though a very successful effort has been made at eradicating reindeer and rats from infested areas since February 2013, it will be some years before there is a noticeable recovery in vegetation, invertebrate populations, and, in particular, ground-nesting birds. South Georgia, therefore, remains particularly vulnerable to ecological

changes. The island's rich biodiversity is unique to the Southern Ocean and, therefore, has global importance. With a warmer climate and increased glacial retreat, South Georgia stands out as one of the most threatened islands to climate change, not only in the high latitude Southern Hemisphere, but also across the entire world.

1.6 The Cause of Climate Change on South Georgia

1.6.1 Orographic Processes

Air that impinges on a mountain can either rise over it ("unblocked" flow) and/or detour around it ("blocked" flow). From a dynamical viewpoint, which pathway the air takes, is dependent on several factors (Houze, 2012). The response of airflow to a barrier depends upon the strength of the cross barrier upstream airflow, the thermodynamic stability of the airflow, and the dimensions of the mountain barrier (Houze, 2012). These factors are combined into a non-dimensional ratio between inertial forces and buoyancy forces (Nicholls, 1973), known as the Froude number (Fr):

$$Fr = \frac{U}{Nh}$$

where U is a characteristic upstream wind speed, h is the mountain height, and N is the Brunt-Väisälä frequency, given by:

$$N^2 = \frac{-g}{\rho}\frac{d\rho}{dz}$$

where ρ is the fluid density, g is the acceleration due to gravity, and z is the vertical coordinate. Note: $N^2 > 0$ when the atmosphere is statically stable (since potential temperature increases with height). An air parcel will, as a result, perform an oscillatory motion when perturbed. In contrast, $N^2 < 0$ when the atmosphere is unstable, and no oscillatory motions will result. Therefore, $N^2 = 0$ when the atmosphere is statically neutral (in neutral equilibrium) with no forces acting on the parcel in a perturbed position.

Therefore, the Froude number represents the ratio of the kinetic energy of the impinging flow to the potential energy required to ascend the mountain. When the airflow is too weak to overcome the retarding effects of negative buoyancy (when the

Froude number < 1), and when the atmosphere is stably stratified and/or the barrier is relatively high, air will detour around the mountain. In this "blocked" flow regime, the low-level winds tend to lie parallel to contours of terrain height, rather than perpendicular to them. For this reason, wind speeds are generally lower on the upwind side of a mountain, and increase around the mountain edges (due to the Bernoulli Effect). Wind speeds may strengthen with height, either due to the ambient increase in wind speed with elevation and/or due to wave activity over the mountain crest. When the Froude number is small (i.e. < 1), then the flow can be described as nonlinear, and in such instances nonlinear phenomena (e.g. upstream flow blocking, wake generation and gravity-wave breaking) can be observed (Durran, 1990; Elvidge *et al*., 2014b). In contrast, when the Froude number > 1 the impinging flow possess enough momentum to overcome the negative buoyancy that it acquires over the upwind slope, which allows it to complete its ascent over the mountain. When the Froude number is large (i.e. > 1), then the flow can be described as linear. Therefore, the ability of an air parcel to ascend over a mountain is dependent on both the kinetic energy of the flow, and the height of the disturbance.

When air is forced over a barrier, disturbances are created in the wake and the energy associated with that disturbance is then typically propagated away from the mountain by mountain waves (also referred to as gravity waves) (Durran, 1990). As a result, the basic structure of a mountain wave is determined by the size and shape of the mountain and by the vertical profiles of wind speed and temperature. As explained by Fritts & Alexander (2003) mountain waves have received considerable attention in recent atmospheric research due to their importance in atmospheric circulation, structure and variability. Not only are large-amplitude mountain waves a severe hazard for aviation, but they are also responsible for strong lee slope winds and internal wave breaking. They also exert a significant drag on the upper-levels of the atmosphere. So much so, it is thought that the cumulative worldwide effect of mountain-wave drag influences the strength of the mean zonal circulation near the polar jet streams (Durran, 1990). They are also responsible for the formation of lenticular clouds in the presence of trapped lee waves. See Corby & Wallington (1956), Corby (1957), Scorer & Kleiforth (1959), Wallington (1960), Smith (1979) and Durran (1990) for further information regarding the generation of topographic gravity waves. While mountain waves are a common feature of airflow over a barrier, it has been identified that strong downslope

winds may accompany these mountain wave systems (see Long, 1953; Eliassen & Palm, 1960; Klemp & Lilly, 1975; Clark & Peltier, 1977; Peltier & Clark, 1979; Durran, 2003). Therefore, despite disturbing a small fraction of the atmospheric column, mountains cause significant excursions in the horizontal and vertical features of the wind profile of the atmosphere, thus leading to complex and dynamic wind regimes. Not only do mountains act as physical obstacles to airflow (which may lead to blocking and flow deflection), but they also act as important elevated heat and moisture storages, consequently impacting on exchanges of moisture and momentum between the land surface and the atmosphere (Raupach & Finnigan, 1997). The atmosphere is especially resistant to the vertical displacement of air parcels since buoyancy forces will act to restore a displaced air parcel back to its equilibrium level. In addition to this, the lower troposphere is generally rich in water vapour, so that any adiabatic ascent will bring the air to saturation, thus leading to condensation (Smith, 1979). Similarly, under favourable atmospheric and synoptic situations, orographic flows may lead to thermal and/or dynamical circulation patterns. One such meteorological process caused by the interaction of air flow with topography, is the föhn effect (caused by the so-called föhn wind). This process is thought to be responsible for, or partly responsible for, the observed change on South Georgia, and is at the heart of the research described in this thesis.

1.6.2 The Föhn Effect

A föhn is a small-scale (meso-γ) weather phenomenon found in the lee of mountainous regions (Barry, 2008), typically formed through the topographic modification of the gradient wind in the lee of a large mountain barrier. The World Meteorological Organization (1992) defines a föhn as a warm, dry, downslope wind, descending on the leeside of a mountain range as a result of synoptic-scale, cross-barrier flow.

Extensive research into föhn winds has been a focus of meteorological research spanning nearly 150 years. Hann (1866) very early on recognised the importance of adiabatic warming on descending air on the lee of mountain crests. Hann (1866) showed that adiabatic warming in the lee of the Alps was the main reason for the observed wind being warm and dry. This new theory subsequently allowed the scientific community to reject earlier hypotheses that suggested the föhn wind originated from the Sahara Desert (Hann, 1866; Kuhn, 1989). Hann (1866) further

recognised that the liberation of latent heat related to orographic precipitation was also an important contribution factor to the temperature difference observed between the windward and leeside of the Alps. This ultimately became the classic "thermodynamic föhn theory", which was later clarified by numerous föhn studies including Ficker (1931), Schweitzer (1953), Seibert (1990), and Zängl (2003) (among many others). This early work, therefore, led to the general definition of a föhn wind being described as a wind which is warmed and dried through descent on the lee of a mountain ridge. As such, "föhn" quickly became the generic locution for all descending, warm, dry winds regardless of the geographic and orographic setting. Likewise, while the thermodynamic theory was quickly accepted in explaining the warmth of the föhn, Seibert (2005) highlights that Hann's original definition became distorted during the early 20th century, with definitions claiming that latent heat release through orographic precipitation was the only relevant factor. Such definitions thus became the "textbook" explanations of describing this phenomenon, and therefore, excluded the huge variations possible and other important initiation mechanisms (Seibert, 2005; Richner & Hächler, 2008; 2013).

1.6.2.1 The Causes of Föhn Warming in the Lee of Mountains

Richner & Hächler (2008) note that *"[i]t is a little disturbing, that not only popular publications but also modern textbooks often present [the textbook case] without discussion alternate föhn schemes."* While the general definition of a föhn wind (a strong, warm and very dry wind observed descending from mountains toward the surface) roughly describes the phenomenon, it does not recognise that its spatial extension, intensity, frequency and effects depend strongly on the tropospheric characteristics and the regional atmospheric circulation. Today, therefore, it is widely accepted that there are two dominant mechanisms leading the warmth and dryness of a föhn wind. These are the thermodynamic (or the latent heating and precipitation) mechanism, and the dynamical (or isentropic drawdown) mechanism.

The Thermodynamic Mechanism

This classic mechanism, which was first recognised by Hann (1866), suggests that föhn warming occurs when moist air is forced to ascend over a mountain barrier (Figure 1.6 and Figure 1.7).

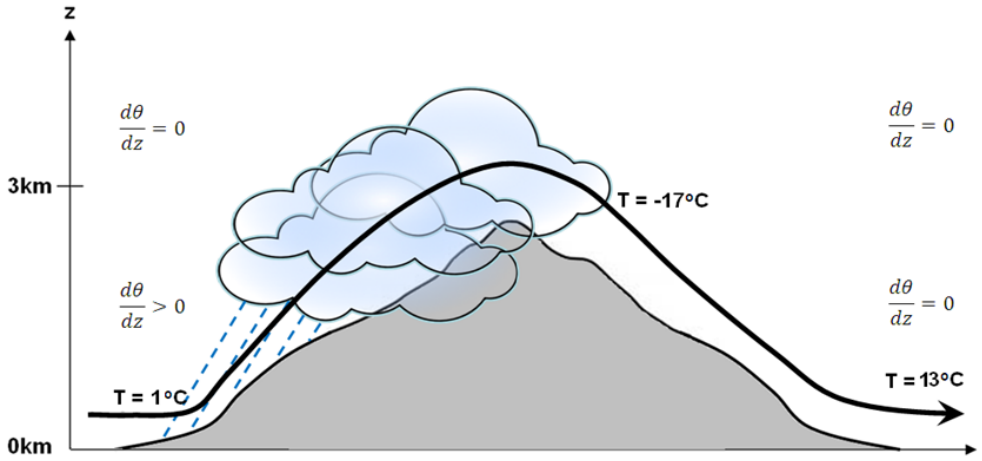

Figure 1.6 – *Schematic representation of the classical thermodynamic föhn mechanism, after Steinacker (2006).*

As a parcel of moist air approaches a mountain it will be forced to rise. As the ascending moist air continues to rise on the windward side, adiabatic cooling occurs resulting in condensation once the dew-point temperature is reached. Latent heat is subsequently released (condensational heating), allowing the air parcel to continue to cool at the saturated adiabatic lapse rate (~6ºC/km altitude). Precipitation may then occur on the windward side of the barrier, further lowering the humidity of the advected air parcel. As the parcel descends the leeward slope, the now unsaturated air is warmed due to adiabatic compression (~10ºC/km altitude) (Hann, 1866; Barry, 2008; Whiteman, 2000). This process results in a cross-barrier temperature gradient (ΔT, Figure 1.7), in which the leeside air temperatures are warmer than their windward counterpart at the same elevation. As highlighted by Richner & Hächler (2008), in reality, föhn winds often do not follow this classical textbook theory that is attributed to Hann (1866). While strong downpours on the upwind slope may be a result of orographic uplift and resultant föhn winds, it is also today widely accepted that föhn winds can occur without precipitation.

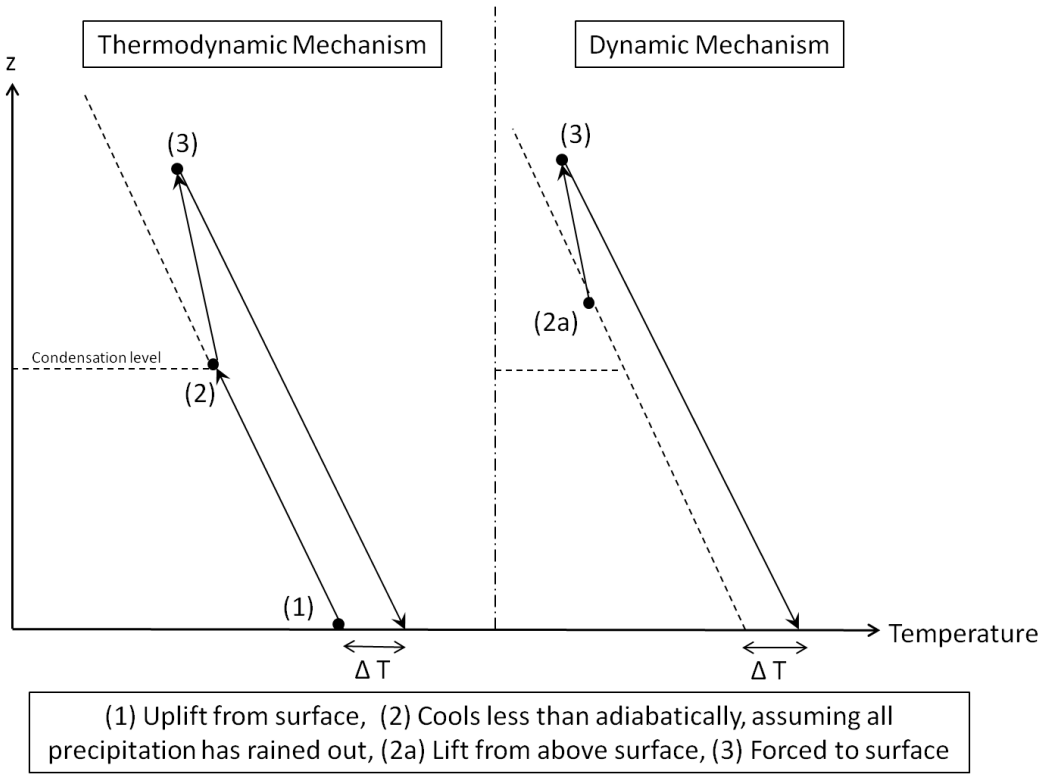

Figure 1.7 – *Schematic thermodynamic diagram, showing the path followed by an air parcel in (temperature, z) space for the thermodynamic mechanism (left) and the dynamical mechanism (right).*

The Dynamical Mechanism

The dynamical mechanism, or the isentropic drawdown mechanism, is the most prevalent variation on the classic theory, and does not require precipitation on the windward side of the mountain for föhn warming to occur (Scorer, 1978). Unlike the thermodynamic theory, blocked flow (caused by an upwind low level, stable layer) can also generate warming on the leeside by way of the descent of potentially warmer air sources above the mountain barrier (Figure 1.7 and Figure 1.8). This potentially warmer air is usually drier too, and will descend on the lee slopes, thus warming through adiabatic compression (~10ºC/km altitude). The lower the crest height, the more likely it is that advected air crosses the mountain ridge and, subsequently, descends (Richner & Hächler, 2008). Such a mechanism does not involve the ascent of air on the windward side, or the release of latent heat above the barrier. While this theory does require some degree of air flow toward the mountain barrier to incur the spill over of air from aloft, such a mechanism has been identified and studied, including those by Cook & Topil (1952), Lockwood (1962); Brinkmann (1973, 1974), Seibert (1990), Ustrnul (1992), and Elvidge *et al*., (2014a, 2014b).

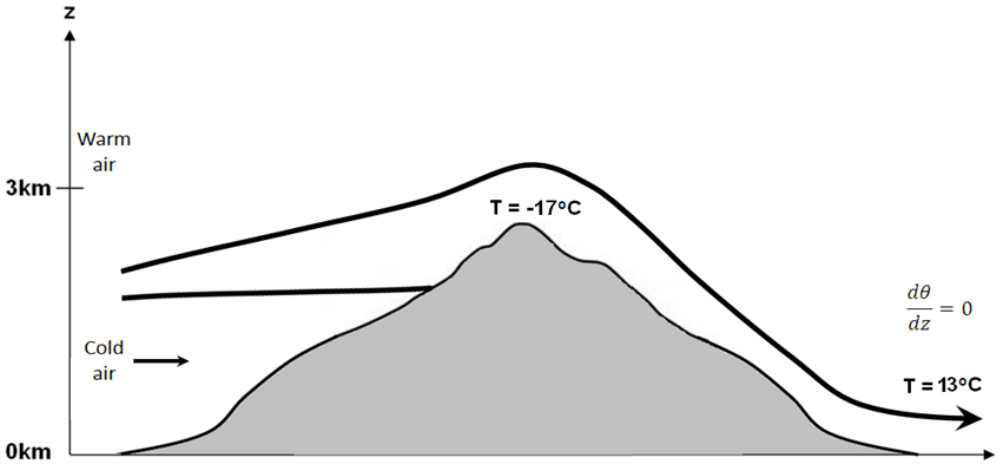

Figure 1.8 – *Schematic representation of the dynamical föhn mechanism, after Steinacker (2006).*

Clearly, therefore, a föhn wind can be initiated and maintained both dynamically and/or thermodynamically (and variations within the two) depending upon the local atmospheric conditions and orographic setting. Turbulent sensible heating caused by leeside mixing may also produce warm, dry winds as the flow passes over a mountain range (e.g. Scorer, 1978; Elvidge *et al*., 2014b; Elvidge & Renfrew, 2015). Regardless of the mechanism responsible for their warmth and dryness, the driving force behind a föhn wind is either through cross-mountain synoptic flow or by cross-mountain pressure gradient flow. Föhn can, therefore, be separated from winds that are diabatically heated from the ground surface, and/or through solar radiation, or winds forced by mountain slope temperature gradients, such as downslope katabatic winds.

1.6.2.2 Föhn Wind Classification Methods

Föhn winds have been extensively researched in a number of topographical settings. Recent research includes the documentation of föhn events in the Smoky Mountains (Gaffin, 2002), Japan (Takane & Kusaka, 2011), the Alps (Gohm & Mayr, 2004), the Appalachian Mountains (Gaffin, 2007; 2009), the American Rockies (Oard, 1993), the Antarctic Dry Valleys (Speirs *et al*., 2010; 2013; Steinhoff *et al*., 2013; 2014) and the Antarctic Peninsula (Elvidge *et al*., 2014a; 2014b; Grosvenor *et al*., 2014). Being found in such widely diverging geographical locations has resulted in a number of local names for the föhn wind, including the Chinook (American Rockies), the berg wind (South Africa), Santa Ana winds (California), the Zonda (Andes) and the Nor'wester (New Zealand) (among many others, see Richner & Hächler, 2013). While

such research has greatly improved our understanding of this phenomenon, our understanding is still incomplete. This is because föhn winds vary by region, by time of day, by geographical and orographic setting (such as mountain height, width and orientation), and atmospheric conditions. Föhn winds are intrinsically transient phenomena leading to different föhn diagnostics for different areas. As a consequence of this, it is inherently difficult to identify absolutely homogenous analogies of föhn from one geographical area to another. This has led to different föhn studies identifying various recognisable mechanisms and features, which have been used in diagnosing föhn conditions from non-föhn conditions. In other words, different locations require specific forecasting and identification methods.

The most common method for identifying a föhn wind is through a traditional föhn classification. The traditional method detects the onset of föhn from observational data at a single location (i.e. from an AWS) by abrupt temperature, humidity, and wind speed changes on the leeside with a surface wind from the direction of the mountain range. This is based on the theory that föhn will manifest itself near the leeside surface of a mountain range as a dry and warm wind due to adiabatic warming (see Figure 1.6 and Figure 1.8). Such a method has been used across the Northern Hemisphere to identify föhn in mountainous regions (see e.g. Conrad, 1936; Osmond, 1941; Obenland, 1956; among many others). Studies of föhn identification using a similar traditional method in the high latitudes of the Southern Hemisphere are, however, rarer (see e.g. Speirs *et al*., 2010; 2013; Steinhoff *et al*., 2014).

Often, arbitrary (numerical) thresholds and limits for temporal changes in temperature, relative humidity, and wind speed are used. For instance, Manuel & Keighton (2003) suggest that the wind gust must exceed 26ms^{-1}, while Longley (1967) classified a föhn if the maximum temperature records were greater than 4.4^{o}C. In Japan (Inaba *et al*., 2002) a föhn event is classified if the daily maximum temperature exceeds 35^{o}C, the daily maximum relative humidity is < 45%, and the daily mean wind speed is > 3ms^{-1} from across the mountain barrier. Since such criteria are case and location specific, they cannot be applied elsewhere. Gaffin (2007) reported that a föhn wind was determined to have occurred if a warming of at least 3^{o}C was recorded, during a period with wind speeds greater than 2.5ms^{-1} (with the wind in the appropriate downslope direction). Ungeheur (1952) similarly found that 2ms^{-1} was an adequate criteria for classifying föhn winds in the Alps. A number of different studies have also adopted

the same arbitrary thresholds. Speirs *et al*. (2010), Speirs *et al*. (2013), and Steinhoff *et al*. (2014) all identified a föhn wind by an increase of wind speed >5ms^{-1}, a warming of at least 1^{o}C and concurrent decrease in relative humidity by 5% per hour. A föhn day was defined as a day that has detected föhn onset and experiences 6 or more continuous hours of föhn conditions with wind speeds >5ms^{-1} from a consistent wind direction. Speirs *et al*. (2010) highlighted that (preliminary) validations showed that these criteria were 95% accurate in identifying föhn events. As a result, arbitrary limits are often set to ensure that the daily temperature rises observed are the result of adiabatic warming, instead of diabatic warming with height and/or variable winds (Gaffin, 2007). These thresholds also reduce misclassification and remove weak and brief periods that may not be of interest (Speirs *et al*. 2013).

While the studies described above have shown that changes in temperature, wind and relative humidity as useful indicators for föhn diagnosis and forecasting, such a method is subjective and is not always sufficient to identify föhn flow non-ambiguously from other strong winds. Distinguishing between föhn and non-föhn atmospheric phenomena (such as katabatic winds or convective outflows) is difficult. As discussed by Vergeiner (2004), this traditional method is inherently subjective, as it is based on the impact of föhn on the surface, rather than based on the underlying physical and dynamical processes which drive the föhn effect. Temperature, humidity and wind speed are not absolute criteria for distinguishing a dynamic phenomenon, and depend on the local atmospheric conditions before, during and after the wind (Brinkmann, 1971). As a result, such changes may be induced by other factors including air mass characteristics and the occurrence or absence of clouds (Gaffin, 2007). This means the surface föhn signal detected may or may not be absolutely associated with the föhn warming process. Despite the limitations of this method, such a classification scheme is typically the most appropriate since föhn is generally observed in isolated and remote regions of the Earth's mountain regions, where only a sparse network of measurements from AWS sites are available.

To address the issue of subjectivity, and in an attempt to provide a method for föhn identification which can be applied in any mountainous setting, several studies have further adapted this traditional method of classifying föhn events when more observational data has been available. Diagnostic accuracy increases with the availability of more observations, especially if the additional observations are either

upslope (i.e. at or near the crest of the mountain) or on the windward slopes of the mountain range. With more observational data available, the physical differences between föhn and other downslope winds can be investigated. For instance, Schuetz & Steinhauser (1955) suggested that during dynamical föhn (Figure 1.8) the potential temperature (θ) between two stations located near the crest of a mountain and near the valley floor should remain the same, whereby $\Delta\theta = \theta_{crest} - \theta_{valley} \approx 0$. Drechsel & Mayr (2008) also suggest that the "basic fingerprint" of a föhn can be identified through wind and the conservation of potential temperature in an adiabatic environment. Vergeiner (2004) determined a föhn wind using lapse rates and wind directions between a suitable mountain reference and a valley station. Vergeiner (2004) concluded that such a method is superior to the traditional subjective classification, since their approach utilised the physical mechanisms behind the föhn warming on the lee slope, which can, therefore, be applied to any other area around the world. Frey (1957) used additional criteria for borderline cases (such as weak föhn events). These included a pressure gradient across the mountain range, a lapse rate, and a horizontal temperature gradient between a station under the influence of the föhn wind's warmth and one outside of it. Other objective classification methods include that of McGowan & Sturman (1996) who used the usual traditional criteria to identify föhn, but also included the criteria whereby a trans-alpine pressure gradient (indicating that a lee trough was present) had to also be recorded. Norte (1998) used two categories for föhn winds (a high föhn and a surface föhn) depending on whether the föhn wind reached a station at a higher altitude on the eastern slopes of the Andes, compared to a surface station. Norte (1998) then further classified the events based on wind speeds, from light or moderate (< 30kt), severe (≥ 30kt) and very severe (≥ 50kt). Clearly, the availability of more observations both improves the manual classification accuracy and enables the formulation of an objective diagnostic method.

Another approach for the evaluation of föhn events is the consideration of pressure patterns, the upper air flow and cloud formation; diagnostics which are not typically measured at AWS sites. To overcome the issue of subjectivity, measuring and identifying empirically observable phenomena related to the dynamics of the föhn warming process is thought to be more appropriate. For instance, Hoinka (1985b) suggested that some föhn clearance can be clearly identified from satellite observations by broad gaps in cloud cover in the lee of a mountain. Ustrnul (1992)

also developed a classification based upon cloud formation. Ustrnul (1992) suggested that the observed wind must fulfil at least one of these criteria to be classified as a föhn: (assuming a cross-barrier wind flow) 1) a wind speed $\geq 5ms^{-1}$ with *Altocumulus lenticularis* clouds present; 2) a wind speed $\geq 5ms^{-1}$ and a relative humidity $\leq 70\%$; 3) a relative humidity $\leq 70\%$ and the presence of *Altocumulus lenticularis* clouds. Scanning Doppler lidar and other remote sensing observations (along with other surface observations) have also been used to identify downslope föhn winds (see e.g. Drobinski *et al*., 2001). More recently, statistical methods to estimate föhn frequencies have been developed. Plavcan *et al*. (2014) present an automatic classification scheme by using a statistical mixture model which separates föhn and non-föhn winds in a measured time series of wind. This method eliminates having to select threshold values individually for each location as required by previous traditional methods, and also includes information about the (un)certainty of the diagnosis. When applied and compared to the same time period as examined by Drechsel & Mayr (2008), Plavcan *et al*. (2014) found that their algorithm generally outperforms that the traditional classification method with just 7% of identified föhn events being misclassifications. They also suggest that since this method is able to diagnose föhn automatically and probabilistically, it is possible to compare föhn climatologies all over the world. The minimum that is required to undertake this is a wind dataset of one year.

Given the summary of different methods for föhn diagnosis in this section, it is clear that föhn presents a significant forecasting and identification challenge because of the breadth of their impact across the globe. The variety of dynamics responsible for föhn winds presents somewhat of a problem; the criteria adopted to determine the frequency of föhn conditions is particular for individual locations. There are numerous approaches for defining, classifying and predicting föhn occurrence, and yet none of them are universally appropriate. While the most commonly observed and recorded characteristics of a föhn wind in the lee of a mountain range are the large temperature and wind speed increases, and large decreases in relative humidity, these criteria cannot be applied to all föhn wind cases. One cannot apply an objective definition to all föhn winds, since surface characteristics, location and season have different degrees of importance both spatially and temporally. There is certainly a window of opportunity to use automated and statistical analyses (utilised along with satellite imagery and surface observations) for föhn identification, but this type of research is

still in its infancy. Likewise the short temporal and spatial extension of the phenomena, the sparse network of meteorological stations and the presence of a steep orographic barrier make creating a universal classification for a föhn near impossible. As such, a föhn wind classification method must be appropriate for the location and the topographical setting, and also depend on the amount and type of data available.

1.6.3 The Circumpolar Vortex and the Southern Annular Mode

The distribution of land, sea and ice, the pattern of sea-surface temperatures and ocean currents, and the topography of the continents in the Southern Hemisphere, all lead to a mean westerly flow around Antarctica and a vast circumpolar vortex poleward of 30°S (Figure 1.9). Although South Georgia is situated within the vast expanse of the Southern Ocean, it is also located within this centre of strong westerly winds, which, as a result, has huge implications for the climate and weather of the island.

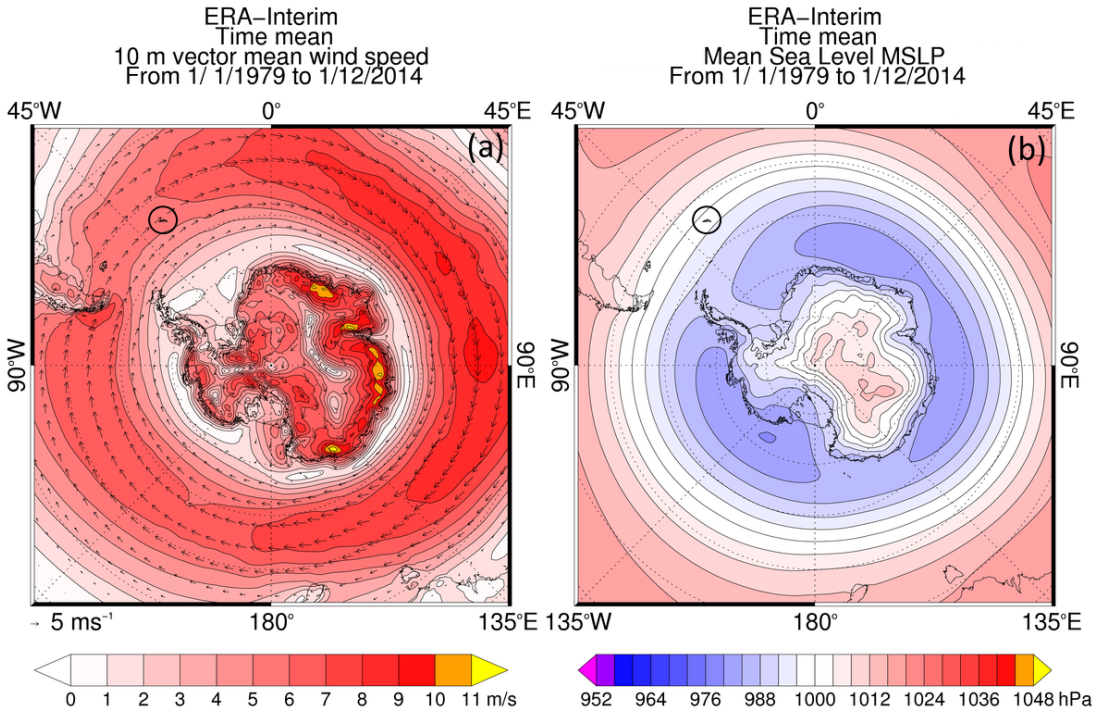

Figure 1.9 – *Panel (a) monthly mean (1979 – 2014) 10-m wind speed vectors (ms^{-1}) and filled contours over the Southern Ocean. Panel (b) monthly mean (1979 – 2014) sea level pressure contours (hPa). South Georgia is circled in black.*

Approximately 20% of the Southern Hemisphere is covered by land and ice caps, and there are relatively few landmasses and continental barriers in the latitudes between 50°S and 70°S. The consequence of this is a large (almost zonally symmetric) thermal gradient between the permanently frozen and domed continent of Antarctica, and the

surrounding oceans. This thermal contrast between the polar continent and the tropical ocean generates a steep pressure gradient over the Southern Hemisphere, and is thus responsible for producing a zone of mid-latitude westerlies (Figure 1.9). As a result, the mean atmospheric circulation of the mid-latitude Southern Hemisphere is dominated by a westerly circumpolar vortex that extends from the surface to the stratosphere, and has shown to be strongest during midwinter when polar temperatures are coldest (Thompson & Solomon, 2002).

Despite being a strong and climatologically persistent feature of the Southern Hemisphere, the circumpolar vortex exhibits considerable variability on month-to-month and year-to-year time scales. This was first recognised by Walker (1928) who noted the existence of a pressure opposition between Chile/Argentina and the Weddell and Bellingshausen Seas. This early work was further built upon in the late 20th century, when this mode of variability became known as the Southern Annular Mode (SAM) (Limpasuvan & Hartmann, 1999) (or also referred to as the Southern Hemisphere Annular Mode (SHAM, e.g. Thompson & Solomon, 2002), the Antarctic Oscillation (AAO, e.g. Gong & Wang, 1999), and the high-latitude mode (e.g. Rogers & van Loon, 1982)). Today, it is widely recognised that climate variability in the high latitude Southern Hemisphere is dominated by the SAM; a large-scale pattern of variability characterised by fluctuations in the strength of the circumpolar vortex (Thompson & Solomon, 2002). The SAM is the equivalent counterpart to the Northern Annular Mode (NAM) in the Northern Hemisphere.

The SAM index is commonly defined as the normalised difference in the zonal mean sea level pressure between 45ºS and 65ºS (Gong & Wang, 1999; Marshall, 2003), or the amplitude of the leading Empirical Orthogonal Function (EOF) of monthly mean 850hPa height, poleward of 20ºS (Thompson & Wallace, 2000). The sea level pressure pattern associated with SAM is a nearly annular pattern with a large low pressure anomaly centred on the geographic South Pole and a ring of high pressure anomalies at mid-latitudes. By geostrophy, this leads to a zonal wind anomaly in a broad band around ~55ºS with stronger circumpolar flow (westerlies), cold polar temperatures and low geopotential heights over the continent, when the SAM index is positive. In contrast, during a negative SAM index, the circumpolar flow weakens to produce weak westerlies, in addition to warmer polar temperatures and higher geopotential heights (Thompson & Solomon, 2002). Thompson & Wallace (2000) also highlight

that the SAM explains approximately 27% of the total hemispheric 850hPa geopotential height variance south of 20ºS. Unlike the NAM, the SAM exhibits relatively weak seasonal variability (Hartmann & Lo, 1998) as the thermal temperature gradient between the pole and equator also has relatively weak seasonality (Hall & Visbeck, 2002). A consequence of this is a persistent zonally symmetric mode of internal atmospheric variability that leads to an important co-variability between the ocean and the atmosphere (Hall & Visbeck, 2002). The SAM is, therefore, an important mechanism for controlling climate across the Southern Hemisphere.

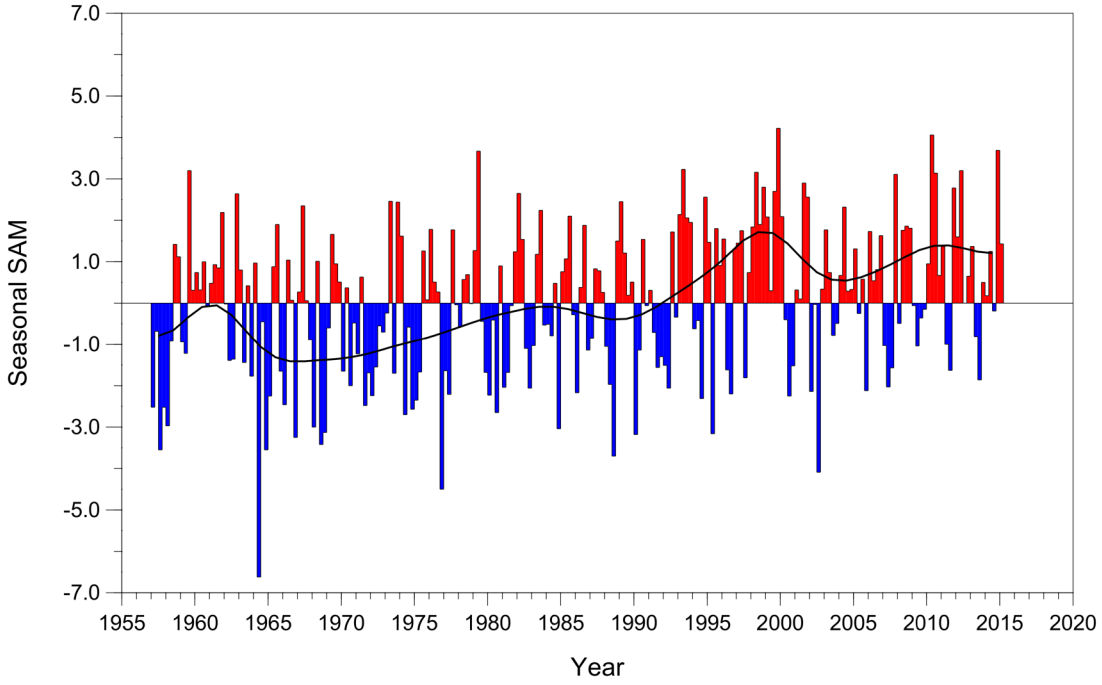

Figure 1.10 – *Seasonal values of the SAM index calculated from station data (updated from Marshall, 2003). The black curve shows decadal variations.*

The SAM index has exhibited a pronounced trend to more positive values over the past 50 years (since ~1965, see Figure 1.10), corresponding to a decrease in surface pressure over Antarctica and an increase over the southern mid-latitudes (Hegerl *et al*., 2007). Studies by Thompson *et al*. (2000), Marshall (2003) and Marshall *et al*. (2006) show this has occurred in all seasons, but a more pronounced positive trend has been observed over austral summer-autumn. To put these trends in a larger perspective, Jones and Widmann (2004) reconstructed the austral summer SAM index from 1878 onwards from a sparse network of instrumental sea level pressure measurements, Jones *et al*. (2009) produced analogous reconstructions for all seasons as far back as 1865, and Jones and Widmann (2003) used tree-ring records to estimate

the SAM index back to 1743. The seasonal reconstructions presented in Jones *et al*. (2009) show a stable SAM index between 1870 and 1960. Around 1960 a peak in the SAM index occurred which was followed by a sharp drop which is especially prominent in the austral summer reconstructions. Thereafter a significant trend in the index is visible (e.g. Figure 1.10). Jones and Widmann (2004) similarly noted an 'early peak' in their reconstructed December-January SAM index around 1960. These SAM reconstructions indicate that the trends in recent decades are not unprecedented, and thus natural climate forcings and internal climate variability can also strongly influence the SAM. It is important to note that the quantification and understanding of decadal and longer SAM variability is still limited due to the relatively short reconstructions and limited surface pressure observations from the early 20th century.

While it is clear the SAM has changed, the reasons and mechanisms behind the change are heavily contested. Along with internal climate variability, it is also thought that anthropogenic forcing may be a significant contributor (Marshall, 2002; Son *et al*., 2008). Marshall *et al*. (2004), for instance, highlight that the observed positive trend in SAM index is not consistent with simulated internal variability using the HadCM3 model, with fixed climate forcing. Their results, therefore, suggest an external cause of change. In contrast to this, Jones & Widmann (2004), developed a 95 year reconstruction of summer SAM indices (based on pressure measurements), and found that the SAM index during the 1960s was as high as it was in the 1990s, indicating no upward trend. Stratospheric ozone depletion is also thought to impact the polarity of the SAM index, as it cools and strengthens the Antarctic stratospheric vortex in austral spring (Randel & Wu, 1999; Hurrell & van Loon, 1994). A number of modelling and observational studies (Thompson & Solomon, 2002; Polvani & Kushner, 2002; Gillett & Thompson, 2003; Roscoe *et al*., 2006; Orr *et al*., 2012) confirm this process and also show that a strengthening of the stratospheric westerlies can be transmitted into the troposphere. However, and in addition to this, other model experiments indicate that circulation changes associated with increasing greenhouse gases also strongly influence the polarity of the SAM index (Fyfe *et al*., 1999; Kushner *et al*., 2001; Marshall *et al*., 2004; Shindell and Schmidt, 2004; Stone and Fyfe, 2005; Arblaster and Meehl, 2006). Despite such disagreements, it is widely accepted that the SAM index *has* become more positive in recent decades due to the *combined* effects of increasing greenhouse gases, and the development of the stratospheric ozone hole.

The positive trend in the SAM index has been attributed to the observed increase of approximately 3 ms^{-1} in the surface westerly winds over the Southern Ocean (Hegerl *et al*., 2007) and the current summer warming trends over the east side of the Antarctic Peninsula. This is because, during the positive phase of the SAM, the westerlies move poleward and strengthen (Marshall *et al*., 2004). Upon strengthening, the Antarctic continent cools due to anomalous ascent (due to a decrease in mean geopotential height over the Plateau) and associated adiabatic cooling (Karpechko *et al*., 2009). In contrast, the Peninsula warms due to a decrease in cold air outbreaks from the continent, leading to intensified advection of warm air from the ocean. Likewise, an increase in the strength of the westerlies also encourages enhanced air flow over the Peninsula, inducing strong lee-slope winds and adiabatic warming on the east side (the föhn effect). A number of laboratory and numerical modelling studies have further confirmed that under positive SAM conditions, flow-over regimes will result on the Antarctic Peninsula (see, for instance, Marshall *et al*., 2006; Orr *et al*., 2008; van Lipzig *et al*., 2008). As such, the increase in the annual mean velocity of the westerly flow around Antarctica of ~15-20% below the height of the Antarctic Peninsula (Marshall *et al*., 2002; Orr *et al*., 2004), is coupled with the trend towards the positive polarity in the SAM index since the 1960s. The eastern side of the Antarctic Peninsula is, therefore, thought to be warming due to an enhancement of the föhn effect. These föhn flows have recently been investigated as part of the Orographic Flows and Climate of the Antarctic Peninsula (OFCAP) project (Elvidge *et al*., 2014a; 2014b) and have been shown to have major implications on regional warming and near-surface energy and mass balances of ice sheets (Kuipers Munneke *et al*., 2012; Grosvenor *et al*., 2014; Luckman *et al*., 2014). The displacement of the circumpolar westerlies is also thought to be responsible for the recent cooling found on the interior of the Antarctic continent (Comiso, 2000). Consequently, changes to the SAM are currently thought to explain most of the summer surface cooling over the continent, and about one third to one half of the warming of the West Antarctic Peninsula (Thompson & Solomon, 2002; Carril *et al*., 2005; Marshall *et al*., 2006). There is, therefore, particularly strong evidence suggesting that changing atmospheric circulation may be interacting with the topography of the Peninsula, thus leading to a leeside warming trend.

While the observed summer warming of the Antarctic Peninsula may be connected to the strengthening of maritime surface westerlies (see Orr *et al*., 2004; Marshall *et al*., 2006; Thomas *et al*., 2008; Schneider *et al*., 2006), the impact of the SAM on climate extends beyond the Antarctic continent. The changing SAM has also been associated with observed changes in Southern Hemisphere rainfall (Brahmananda Rao *et al*., 2003), surface and sea surface temperatures (Mo 2000; Hall & Visbeck, 2002; Screen *et al*., 2009), Antarctic sea ice extent and concentration (Lefebvre *et al*., 2004; Liu *et al*., 2004), variability of storm tracks (Brahmananda Rao *et al*., 2003; Yin 2005; Lubin *et al*., 2008), oceanic circulation (Hall & Visbeck 2002; Sen Gupta & England 2006; Russell *et al*., 2006), and carbon dioxide (and heat) exchanges between the atmosphere and the ocean (Mignone *et al*., 2006). Gillet *et al*. (2006) have shown significant warming trends associated with a positive phase of the SAM between 40-60^{o}S, and even as far north as 20^{o}S. This is in agreement with other modelling studies (Watterson, 2000; Cai & Watterson, 2002; Sen Gupta & England, 2006) which have also shown significant warming trends (across the Southern Ocean) associated with the positive phase of the SAM. Therefore, the SAM is responsible for a number of regional-scale changes and variations to the physical environments of the high-latitude Southern Hemisphere.

Understanding the changes in the Southern Hemisphere westerlies and the interaction with climate variability is of high importance due to the large potential and diverse impacts that will continue to take place in a warming climate. In addition to this, the impacts connected with the changing SAM also cover the region of South Georgia. A strengthening SAM could potentially have a large impact upon the weather and climate of South Georgia. South Georgia is particularly vulnerable, since it lies in a region where the atmospheric and oceanic circulation patterns are prone to change (Figure 1.9). In addition to this, the island's own topography results in a strong dependence of local climate anomalies on regional atmospheric circulation. As such, understanding the role and importance of SAM to high-latitude Southern Hemisphere climates is important since changes to this dominant mode of atmospheric variability have the potential to impact the broad-scale and regional-scale climate and weather for many regions across the hemisphere. Therefore, South Georgia serves as a useful case study to illustrate the potential impact of regional climate change on both local and global scales, as well as the importance of mesoscale processes in shaping regional

climate. South Georgia is well situated for this since it lies in the region where the SAM and circumpolar vortex display the largest seasonality, and the climate of the island is largely dependent on the interaction of the broad-scale atmospheric circulation and its own orography.

1.7 Justification of Research

The investigation of orographic flow over the island of South Georgia has, in the past, been limited. This is not especially surprising, since there are very few long-term station records available across this small, remote and isolated island. In addition to this, it is only recently that numerical weather prediction and climate models have been able to accurately resolve such complex topography. The study of Wells *et al*. (2008) was undertaken to evaluate the performance of idealised numerical simulations and the effects of wind direction on orographic drag (over an elongated mountain ridge based on the topography of South Georgia). When using the real orography of South Georgia the study found that the island is an important source of lee vortices and gravity wave production. Wells *et al*. (2008) also highlight that their study was not to provide a detailed analysis of orographic flow round South Georgia, but the island is important since it is an example of complex, high orography that is not currently accurately resolved in typical global weather prediction models. In recent years, it has also become apparent that that stratospheric wind biases in global and climate models in the Southern Hemisphere may result from insufficient orographic wave drag, particularly over the Southern Ocean in the latitude belt centred near 60^{o}S. Alexander & Grimsdell (2013) and Jiang *et al*. (2014) have demonstrated that South Georgia could generate deep propagating waves, which potentially contribute to the stratospheric wave drag. Similarly, Alexander *et al*. (2009) used the Atmospheric Infrared Sounder (AIRS) instrument on NASA's Aqua satellite to explore mountain wave activity above South Georgia. By exploring the wave patterns as detected by temperature anomalies in the AIRS instrument, Alexander *et al*. (2009) found that mountain waves in the stratosphere commonly occur above the island. Conducting high-resolution (1.5km horizontal resolution) simulations using the Met Office Unified Model, Vosper (2015) has also shown the significant flow modification by South Georgia which is responsible for large amplitude mountain waves in austral winter months along with a significant wake region which extends hundreds of kilometres from the island. The frequency of such events suggests that South Georgia

is a significant source of mountain wave momentum flux and is a climatologically significant source of drag on the circulation of the stratosphere and of the mesosphere. Hosking *et al*. (2015) similarly showed that high-resolution simulations (3.3km) over South Georgia are required to accurately capture surface disturbances in wind speed around the island. This study found that fine-scale structure in winds, forced by South Georgia's steep orography, contribute to the generation of important surface forcing of the surrounding shelf seas. When compared to Quick Scatterometer (QuikSCAT) observations, the modelled wind field was shown to be in good agreement with the satellite-derived winds. Such fine-scale wind effects and their subsequent surface forcing were entirely missing from global atmospheric reanalyses, therefore highlighting the need to use high spatial resolution wind forcing in a regional ocean model. South Georgia is also the location of a new observing programme (which begun in early 2015): the South Georgia-Wave Experiment (SG-WEX), which involves prolonged radiosonde and mesospheric-sensing meteor radar measurements of gravity waves on the island for the first time. The aim of the project is to combine measurements from a variety of satellite instruments and analyses from a global climate model to produce the first detailed temporal and spatial climatology of wave fluxes in this region of the Southern Ocean.

It has also long been known that the orographic effect of the island's central mountain ranges greatly influences the regional precipitation and weather, as well as producing localised föhn warming and downslope katabatic winds (Mansfield & Glassey, 1957). However, there has been no thorough nor quantitative investigation into föhn winds in the lee of South Georgia. While the föhn warming process has been measured and investigated across many regions of the earth's mountain regions, the föhn wind of South Georgia remains unexplored. The earliest meteorological record of a föhn event on South Georgia appears to date back to 1 May 1883 at Royal Bay, during a German expedition of the island during the First International Polar Year (von Danckelman, 1884). Although first described over 130 years ago, the physical characteristics and features of föhn events experienced across South Georgia have not been studied or investigated in any great detail. Understanding the structure and characteristics of föhn flow has great practical importance, due to its strong and damaging behaviour (Brinkmann, 1974; Sharples, 2009; Sharples *et al*., 2010), its ability to quickly melt (and sublimate) surface snow and ice (Grosvenor *et al*., 2014), and other impacts upon

atmospheric structure and composition (Nkemdirim & Leggat, 1978; Hoinka & Rösler, 1987). Therefore, South Georgia provides a unique environment to investigate the characteristics and mechanisms leading to föhn winds on this small, remote island. Ultimately, large temperature rises (and consequent repercussions) may occur on South Georgia due to the adiabatic compression associated with föhn winds, especially because of the island's high relief and steep slopes. South Georgia is in a climatically sensitive region, an enhanced understanding of small scale meteorological processes and their interaction with larger scale phenomena is required in order to better predict potentially significant regional changes.

Given the dramatic changes in atmospheric conditions at the West Antarctic Peninsula, and due to similarity in barrier height, the potential for changes in adjacent South Georgia is clear. The glaciers of South Georgia have been undergoing extensive and widespread retreat in recent years, as shown from satellite and surface observations. Geomorphological evidence generally indicates that the majority of glaciers have, at present, reached their minimum extent during the entire Holocene (Clapperton & Sugden, 1988; Clapperton *et al*., 1989a; 1989b). In addition to this, the largest retreats have all taken place along the north-eastern coast (i.e. north-facing glaciers), where retreat rates have accelerated to an average of 60 meters per year, but those on the south-western coast (i.e. south-facing glaciers) have been retreating more slowly since the 1950s (Gordon & Timmis, 1992; Gordon *et al*., 2008; Cook *et al*., 2010). Concurrently, surface temperatures at King Edward Point have risen since the start of the meteorological record. The annual mean temperature has shown a statistically significant increase of 1^{o}C since the 1920s. Combining this evidence together, it suggests that South Georgia is undergoing an asymmetric pattern of regional warming (similar to the observed summer warming on the east side of the Antarctic Peninsula), where the interaction of strengthening summer westerlies (resulting from stratospheric ozone depletion and increased greenhouse gases) with steep orography has led to amplified warming on the north-eastern (lee) side of the mountain barrier.

1.8 Aims and Objectives

The main motivation of the research described in this thesis is to explain whether the recent rapid asymmetrical glacial retreat and near-surface warming of South Georgia is a result of the föhn warming process. Strong föhn events have the potential to have

a significant impact on the near-surface meteorology and energy balance on glaciers on the island. The potential impact of regional climate change has importance on both local and global scales. This work provides a unique and enhanced understanding of the small scale meteorological processes and their role in regional climatic changes, which has never been explored in great detail on South Georgia. As such, this investigation into synoptic-scale processes and the resulting meteorological influences has significance in terms of understanding regional and local effects of global climate variability and change.

Therefore, the aims of this study are to present the first in-depth analysis of the climatology of föhn events at King Edward Point, to understand the large-scale meteorological conditions which cause föhn events, and to explore their impact on the regional climate of South Georgia. The methods and data utilised to achieve the research aims are presented and discussed in Chapter 2, with results presented in Chapter 3 through Chapter 6. The research questions which will be explored, investigated, and answered in the preceding chapters are as follows:

- *How frequent are föhn events and what synoptic conditions are associated with föhn at King Edward Point?* Chapter 3 explores the climatology of föhn events at King Edward Point using 10 years of automatic weather station (AWS) data, and a föhn detection method appropriate for this location is developed and applied. This provides an insight into whether föhn events have been increasing in frequency or intensity since the start of the AWS record. The physical and temporal characteristics of föhn are also described. The dominant driving synoptic forces behind strong, weak and non-föhn conditions are also investigated.

- *Can we accurately simulate weak and strong föhn flow using a state-of-the-art atmospheric model?* Chapter 4 makes use of radiosonde and lidar observations from a small field campaign in January 2013 to supplement surface (AWS) observations and provide the most comprehensive observations of föhn events obtained for South Georgia. A series of föhn case are simulated using the Weather Research and Forecasting (WRF) model. The model is validated against the observations. For these case studies, various sensitivity studies are conducted, including varying the model's horizontal and vertical resolution as

well as physics schemes. The results are used to determine the optimal model setup to capture the regional climate (and surface föhn effect) of South Georgia.

- *How does the orography of the island control the regional climate of South Georgia, what is the best method for detecting föhn in the model, and how well does the model capture föhn events?* Having defined the optimal model setup in Chapter 4, Chapter 5 details a 21 month high-resolution (<1km) WRF model simulation which is used to explore the regional climate of South Georgia. Using this model data as proxy observations, three föhn detection methods are developed and applied, and are used to produce a WRF climatology of föhn events between June 2011 and February 2013. The model climatology is then compared to the AWS föhn climatology, and the reasons for discrepancies are evaluated. The most accurate föhn detection method is then used to select events to investigate the impact of föhn on the glaciers of South Georgia in Chapter 6.

- *What impact do föhn winds have on the regional climate of South Georgia and, in particular, on the surface mass and energy balance of its glaciers?* The thesis culminates with Chapter 6, which explores the extent to which föhn winds are responsible for the observed asymmetrical rates of retreat on 14 glacier basins on central South Georgia. The first ever glacier catchment map of South Georgia is also presented. The impact of föhn on the regional climate of South Georgia, on surface energy and mass balances, as well as on melt rates, are evaluated for the eight north- and six south-facing glaciers. The impact of föhn on precipitation and ablation rates is quantified in order to link the föhn warming process to the recently observed asymmetrical glacier retreat across South Georgia.

The main findings of the research presented in this thesis and a synthesis of the conclusions are summarised in Chapter 7. Natural extensions and potential areas of future work to enhance our understanding of the dynamics and climate variability of the region, and how this relates to larger-scale climatic changes, are also suggested. The end result of the research proposed here is a better understanding of the föhn warming process at King Edward Point and of the regional climate of South Georgia.

Chapter Two: Methods and Observations

2.1 Introduction

Following on from the aims and objectives in section 1.8, this chapter outlines the key observations and methods used in this thesis. The primary observational dataset used throughout this work is that from the automatic weather station (AWS) observations from the King Edward Point Research Station on South Georgia. Information pertaining to the station location, observations used, and processing methods is provided. Details of a small field campaign in January and February 2013 are also given, outlining the radiosonde and lidar observations taken. Following this the Weather Research and Forecasting (WRF) model, the numerical weather prediction model used in this thesis (Chapter 4 and onwards), is introduced. Detailed descriptions of the model and modifications, as well as details regarding the sensitivity simulations in Chapter 4, are also given here. The chapter concludes with a brief summary of other data sources (a geographical information system database and satellite observations) which are also utilised in the research presented in this thesis.

2.2 Observational Data

Manual observations of the weather at Grytviken whaling station began in 1905, shortly after the station began operations. Only monthly means are available between January 1905 and December 1958. In 1970, 6-hourly manual observations commenced, and from 1971, 3-hourly manual observations were taken (Shanklin *et al*., 2009). These observations ended in 1982 with the outbreak of the Falklands conflict. Observations using an AWS recommenced in March 2001 at King Edward Point (approximately 700m east of Grytviken) by the British Antarctic Survey, which also coincided with the withdrawal of the small British garrison that had remained on the island. An AWS was also installed at Bird Island Research Station in 2000. Covering 110 years, the meteorological observations from South Georgia are the second longest in the high-latitude Southern Hemisphere, exceeded only be Orcadas Base (South Orkney Islands, Argentina). Local time on South Georgia is two hours behind Greenwich Mean Time (GMT-2), and does not operate Daylight Saving Time. Unless specified, the timing convention used throughout this thesis is Coordinated Universal Time (UTC).

2.2.1 The AWS at King Edward Point

Meteorological data presented here was obtained from the AWS operated by the British Antarctic Survey at King Edward Point (World Meteorological Organization station number: 88903; 54°17′S, 36°29′W). It is the primary source of observations for South Georgia. The AWS is the longest running station on the island. The Milos 500 AWS was installed at King Edward Point in March 2001, and recorded data at hourly intervals. This was subsequently replaced in March 2006, with a Milos 530 AWS, and one-minute observations were then available. An optical rain gauge was also installed in February 2010 and records daily precipitation totals at King Edward Point.

Description	**Measurement Period**		**Instrument**	**Accuracy**	**Measurement Range**
	Hourly	*Minute*			
	March 2001 – March 2006	**March 2006 – onwards**			
2-m Air Temperature (°C)	✓	✓	Platinum Resistance Thermometer probe	±0.2°C	-40 – +60 °C
2-m Relative Humidity (%)	✘	✓	Vaisala HMP45D	±2%	0.8 – 100%
10-m Wind Speed (ms^{-1})	✓	✓	Vaisala WS425 sonic anemometer	±0.1 ms^{-1}	0 – 65 ms^{-1}
10-m Wind Direction (°)	✓	✓	Vaisala WS425 sonic anemometer	±2°	0 – 360°
Sea Level Pressure (hPa)	✓	✓	Vaisala DPA503	±0.1 hPa	500 – 1100 hPa

Table 2.1 – *Summary of the instrumentation used on the AWS at King Edward Point Research Station. All observations (hourly and every minute) are instantaneous values.*

Of the 110 years of meteorological observations available at King Edward Point, the AWS period from 2003 onwards was selected for this research. This period is the most continuous and the least patchy of all the available time periods. Specifications for the main meteorological fields used throughout this study (2-m air temperature, 2-m relative humidity, sea level pressure, and 10-m wind components) are shown in Table

2.1. These variables are used to detect and define föhn events at King Edward Point (see Chapter 3). Although the data has already been quality controlled, there were still some erroneous peaks and values. These were checked by hand, and removed if deemed appropriate to do so. Data from the AWS at Bird Island Research Station, roughly 100km northwest of King Edward Point (see Figure 1.2(c)), are not used in this research. With a shorter temporal history, and located outside the main influence of the Allardyce and Salvesen Ranges, Bird Island is neither upstream of King Edward Point nor within the influence of westerly föhn events.

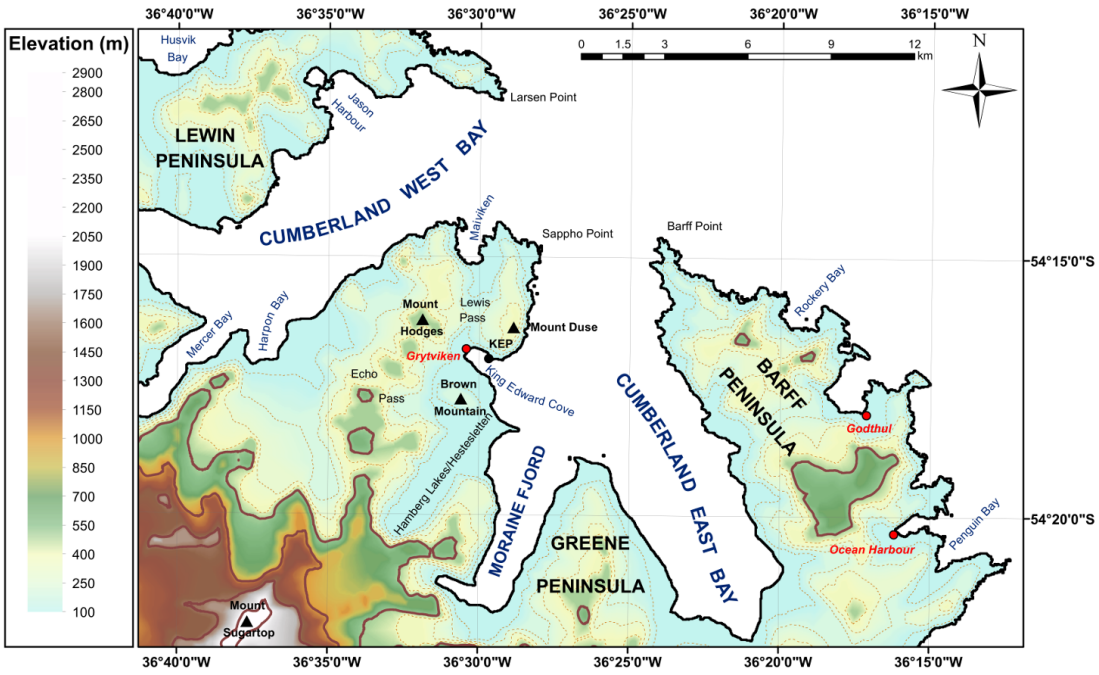

Figure 2.1 – *The topography of Thatcher Peninsula and surrounding areas. Three of the seven whaling stations on South Georgia are marked in red (Grytviken, Godthul and Ocean Harbour). Brown dotted lines – 100 – 400 m elevation contours, solid brown – 500, 1000, 1500, 2000 and 2500 m elevation contours.*

Figure 2.1 provides a topographical view of the central northeast coast of South Georgia. Figure 2.2 also provides a view of King Edward Cove, as well as the AWS. The AWS is located on King Edward Point, which is a low-lying shingle spit, which extends roughly 400m into King Edward Cove. The majority of King Edward Point is covered with grass and tussac grass, which extends from the beach edge up to the surrounding hills. Mount Hodges (633m) lies just over 1km to the west-northwest, with Mount Duse (507m) just less than 500m to the northeast. Both these peaks are part of two separate chains that block most of King Edward Point from northeast to northwest, and are separated by the Bore Valley/Lewis Pass which runs roughly north

by east towards Maiviken. To the south of the AWS site (across King Edward Cove) exposed cliffs rise 15 – 30m from the shore, and then rise to a 332m ridge (Brown Mountain). As a result, the east and southeast of the site are the most exposed sides of the Cove. Although the station is relatively sheltered within King Edward Cove, the complex surrounding topography means that the area is still affected by strong downslope winds (Mansfield & Glassey, 1957). During the winter, the Thatcher Peninsula and surrounding areas are snow covered. Pack ice does not normally reach the station, even during winter. However ice does form in the bay (both in summer and in winter), and large icebergs, either calved from local glaciers and/or the Antarctic ice sheet, are common within Cumberland Bay.

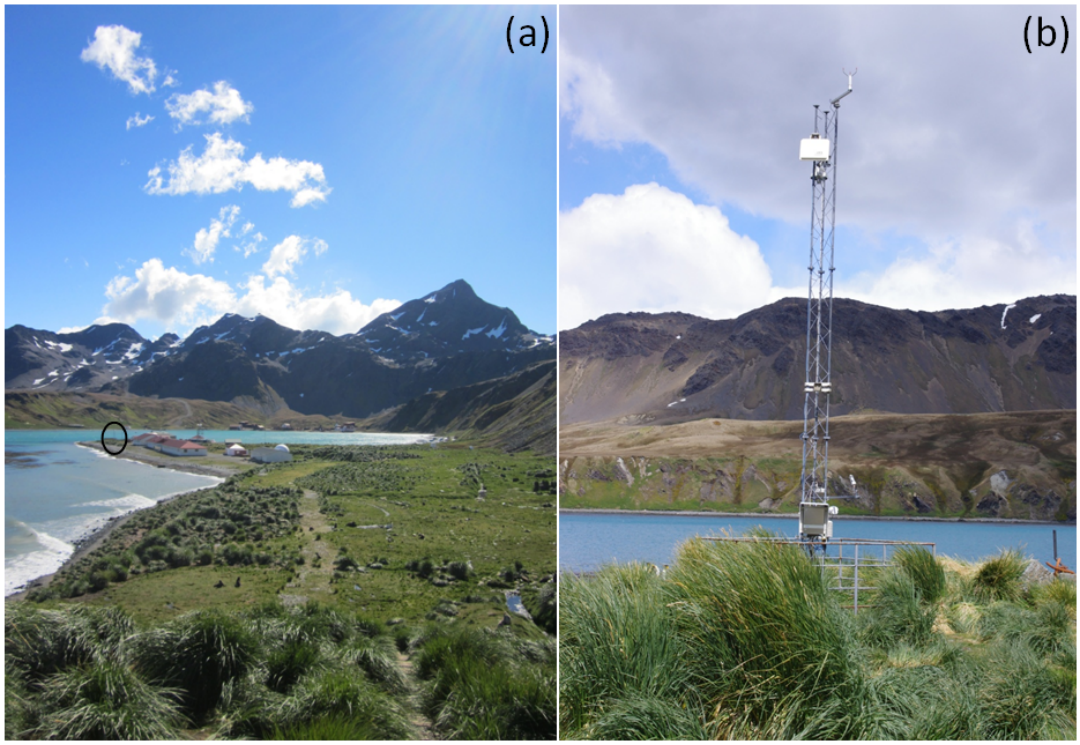

Figure 2.2 – *View overlooking King Edward Cove (photograph (a)), showing Hope Point (foreground), King Edward Point Research Station (midground), and Grytviken whaling station (background), taken from Hope Point looking due west towards Mount Hodges. The AWS site is circled in black. Photograph (b) is of the AWS at King Edward Point, taken looking south towards Brown Mountain (background).*

From the 1-hour instantaneous surface AWS observations, the mean annual temperature at King Edward Point between January 2003 and December 2012 was 2.5°C (σ = 4.4). The mean austral winter (June, July, August) temperature was -0.8°C (σ = 3.7), while the mean austral summer (December, January, February) temperature was 5.9°C (σ = 3.5) (Figure 2.3). The maximum and minimum temperatures recorded

during this period were 23.5°C and -11.1°C respectively. The mean relative humidity during this period was 70.0% (σ = 15.4), and reached a minimum of 7.0%. The wind regime of King Edward Point is strongly influenced by local topographically adjusted flow (see Figure 3.1), but is dominated by the prevailing westerlies (see Figure 1.9). The mean wind direction recorded was 308°. The mean wind speed during January 2003 – December 2012 was 8.8ms^{-1} (σ = 6.9). The maximum wind speed to have been recorded at King Edward Point was a remarkable 43.8ms^{-1}.

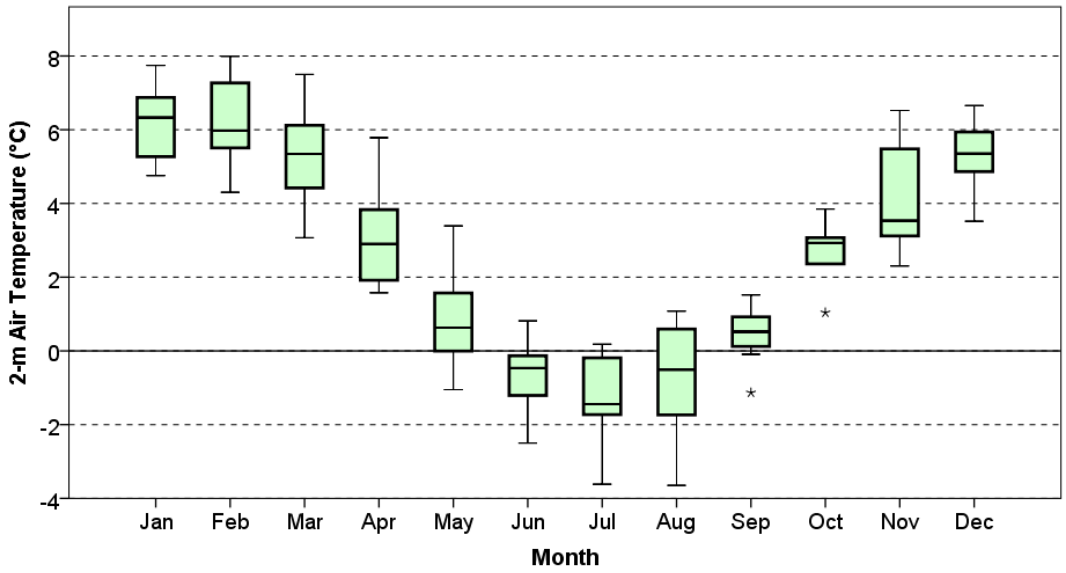

Figure 2.3 – *Box plot of mean monthly 2-m air temperature as recorded by the surface AWS observations at King Edward Point (January 2003 – December 2012). Thick horizontal line is the median, box indicates first and third quartiles, bars extend to 1.5 interquartile ranges outside of the quartiles. Outliers (✶) are defined as being >1.5 interquartile ranges outside of the quartiles.*

2.2.2 The January 2013 Field Campaign

Based at the King Edward Point Research Station, a number of additional measurements were made to complement the permanent AWS during a small field campaign between 23 January and 6 February 2013. The campaign was led by a team from the National Centre for Atmospheric Science (NCAS). The main aim of this project was to produce a local area forecast model for King Edward Cove, and the South Georgia region using the Weather Research and Forecasting (WRF) model. In addition to this, the project also aimed to provide a unique dataset, promoting greater understanding of gravity wave propagation and breaking, the dynamics of the circulation at King Edward Point, and the regional features and characteristics of föhn events.

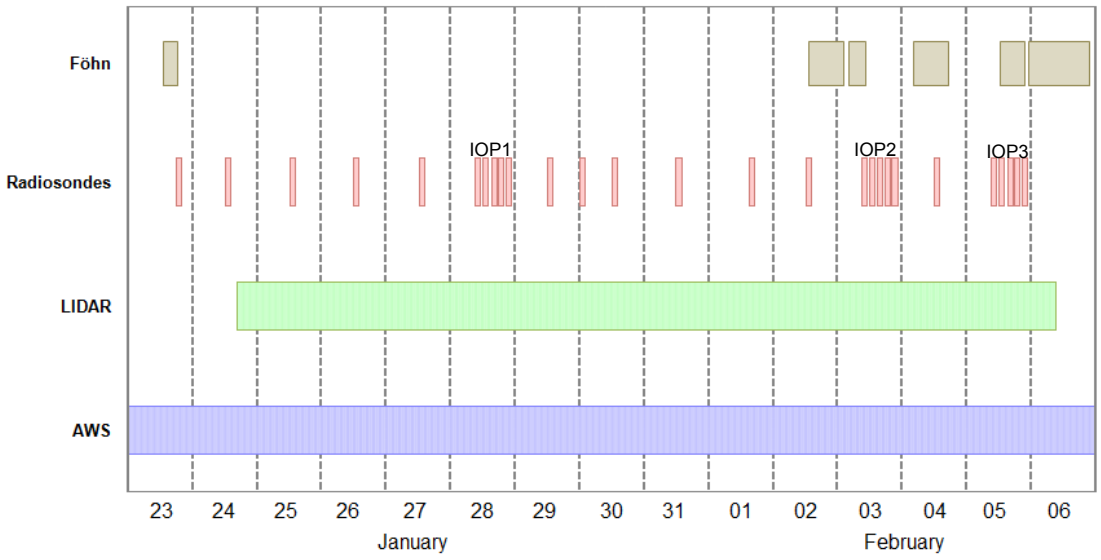

Figure 2.4 – *Timeline showing timing and duration of radiosonde, lidar and AWS observations during 23 January – 6 February 2013 field campaign. The three IOPs are labelled. The six föhn events detected are also represented in the top row.*

Upper air measurements were made during 27 radiosonde flights, launched from the beach at King Edward Point. The radiosondes were attached to 1200g latex weather balloons, filled with ~3m^3 helium to achieve an ascent rate of ~4ms^{-1} (≈ 787 ft min^{-1}) and a 26 km bursting altitude. Vaisala radiosonde system sondes (RS92) were attached, and these measured temperature, pressure and humidity at a rate of 2 Hz. Wind speed and wind direction were calculated from the GPS position of the package and its position relative to the ground station. The data was transmitted to a fixed receiver at the surface. These 27 balloons were released over a period of 14 science days, three of which were declared to be intensive observation periods (IOPs). A sonde was released at 1200 UTC every day (synoptic sounding), irrespective of the conditions. During the IOPs, an enhanced sounding programme was carried out. Two föhn events, as detected by the AWS observations (see Chapter 4), occurred during two of the IOPs. Six föhn events in total occurred during the field campaign. The event on 5 February 2013 is used as a case study in Chapter 4. A timeline showing the periods covered by all observations during the campaign is shown in Figure 2.4.

In addition to the upper-air soundings, a Halo Photonics Streamline Light Detection and Ranging (LIDAR) instrument was also setup alongside the beach at King Edward Point. The lidar system measured all three components of the wind (u, v, w) through the evaluation of the Doppler shift undergone by a laser beam emitted into the

atmosphere and back-scattered due to the presence of aerosol. The instrument operated at a wavelength of 1.55 μm, and is therefore insensitive to molecular scattering. The lidar system setup and location with respect to the AWS can be seen in Figure 2.5.

Figure 2.5 – *Photograph of the lidar instrument located behind the beach at King Edward Point during the 2013 field campaign. The AWS can be seen in the background, approximately 30m from the lidar instrument, behind the tussac grass.*

The additional observational data made during this field campaign are valuable resources of information for the documentation of föhn event case studies and for model validation purposes. A number of föhn events were observed during the January 2013 campaign, making this dataset ideal for verifying the performance of the atmospheric model used in this study.

2.3 The Weather Research and Forecasting (WRF) Model

Much of the research in this thesis is carried out with the Weather Research and Forecasting (WRF) model. With recent advances in computing power and numerical model development for both complex terrain and polar environments, a realistic representation of South Georgia in numerical models is now possible. This research aims to provide a better understanding of South Georgia's meteorology and climate through a series of model simulations using the WRF model. Therefore, the purpose of this section is to give an introduction and description of WRF, the mesoscale

numerical weather prediction model used in this study. A more detailed description of WRF, including details of atmospheric forcing, topography and land surface type datasets, nested domain configurations, and model physics parameterisations for the sensitivity simulations (see Chapter 4) is also presented here.

The Advanced Research Weather Research and Forecasting Model (WRF-ARW) is a fully compressible (volume of an air parcel changes with time), non-hydrostatic model that solves for the Euler equations (horizontal and vertical momentum, mass continuity, thermodynamic energy, equation of state, conservation of water vapour, and an equation for geopotential) in perturbation and flux form, using a terrain-following pressure coordinate in the vertical. Details of the model formulation can be found in the WRF-ARW technical notes (Skamarock *et al.*, 2008). Released in August 2012, version 3.4.1 of the WRF model was utilised in this thesis. The model is developed at the National Center for Atmospheric Research (NCAR), and is intended for both meteorological forecasts and idealised research. WRF has been chosen for this research primarily for the model's ability to simulate at very high spatial and temporal resolutions, and its dynamics allow for a precise representation of processes strongly forced by orography, such as precipitation and near-surface winds. Additionally, WRF has a large and active research community, and it is updated on a regular basis.

For all simulations presented in the following chapters, the initial and lateral boundary conditions for the outermost WRF domain were derived from the ERA-Interim pressure-level re-analysis, which is European Centre for Medium-Range Weather Forecasts' (ECMWF) most recent global reanalysis product (Simmons *et al*., 2007; Dee *et al*., 2011). The lateral boundary conditions were updated every six hours from ERA-Interim. It has a N128 (nominally 0.7º, ~45km × ~80km near South Georgia) spatial resolution. ERA-Interim features several improvements upon ERA-40, including 12 hour 4D-Var data assimilation, T255 (~0.7°) horizontal resolution, improved humidity analysis, variational bias correction of satellite radiance data, more extensive use of satellite radiances, and additional observations. Important data sources for high-latitude regions that are ingested into the ECMWF analyses used in ERA-Interim from 2001 onwards include Moderate Resolution Imaging Spectroradiometer (MODIS) winds, Atmospheric Infrared Sounder (AIRS) radiances, and Constellation Observing System for Meteorology, Ionosphere, and Climate

(COSMIC) GPS radio occultation soundings (Andersson, 2007). ERA-Interim is widely regarded as the most reliable at reproducing mean sea level pressure patterns, low-frequency variability, temperature trends, and the surface radiative budget (see e.g. Dee *et al*., 2011; Screen & Simmonds, 2011; Cornes & Jones 2013; Simmons *et al*., 2014), along with the best representation of precipitation among global reanalyses for Antarctica (Bromwich *et al*., 2011). Evaluating several reanalysis data sets, Bracegirdle & Marshall (2012) also found that in Antarctica the ERA-Interim data set was the most reliable at reproducing mean sea level pressure and geopotential height at 500hPa. As such, ERA-Interim is better regarded than other available reanalysis products. It should also be noted that the island of South Georgia is not resolved by ERA-Interim. The reanalysis dataset treats all the grid cells containing South Georgia as ocean and therefore completely fails to represent the island's orography and land-sea distribution.

A series of nested domains is used in this study. Nesting allows an area of interest to be viewed at significantly higher resolution, taking the boundary conditions from the coarser mother domain. This strategy is used so that the initial and boundary conditions from ERA-Interim can be properly scaled down to high-resolution around South Georgia. In the WRF model, the downscaling is dynamic as it takes place during the simulation as a nested structure, whilst the full model physics are being implemented (Skamarock & Klemp, 2008). In the current implementation of the nesting algorithm, only horizontal nesting is available (i.e. all domains have to use the same vertical grid). The nested grids use a 3:1 ratio between the resolution of the coarse and fine grids. This allows the finer resolution domains to feed data back to the coarser domains. A description of the two different WRF model configurations is given in section 2.3.1.2.

WRF also offers a whole host of ways of combining the different physics and parameterisation schemes on top of the horizontal, vertical and topographical resolution and nesting options. The suite of WRF physic schemes is extensive, and includes numerous options for, planetary boundary layer, land-surface model, radiation and diffusion schemes, microphysics, and cumulus parameterisation. It is important that these parameterisation schemes, which represent sub-grid scale physical processes that are not explicitly represented, are effectively utilised in WRF simulations. Only the alterations, schemes and parameterisations used in this study are

briefly detailed here; see Skamarock *et al*. (2008) for a description of all the options available in the WRF model. A description of WRF for the sensitivity simulations (see Chapter 4) will now be given.

2.3.1 Description of WRF Sensitivity Analyses

In Chapter 4, a sensitivity case study approach was adopted to assess the model's performance in capturing föhn events. A number of model simulations were conducted for a series of föhn case studies to evaluate the accuracy of the model against available observations. The sensitivity of the model to topography height, vertical and horizontal resolution and boundary layer and physics schemes were tested. These key areas were tested since it is expected that different resolutions and schemes to impact the model's performance at simulating föhn events. The model is likely to respond to these changes through changes in short and longwave radiation, as well as wind speed, and the small-scale thermodynamic processes responsible for, and associated with, föhn events. Details of all the sensitivity simulations conducted can be found in Table 2.2. The baseline (also referred to as the standard/default) model setup is denoted with the number 1 for all the WRF namelist options. Based upon the performance of the model at simulating the föhn flow, a best configuration was chosen. Computational efficiency and cost was a leading decision.

A detailed description of all föhn case studies are given in Chapter 4. Since all the case studies were relatively short runs, the sea surface temperature and sea ice fields were not updated during the simulation. The sea surface temperature and sea ice fields at the initial time were constant fields for all time periods. The cumulus scheme (Kain-Fritsch cumulus scheme (Kain, 2004)) was only switched on in the outer domains of the baseline and high-resolution domain configurations (30km and 8.1km resolution respectively). It is assumed that convection is explicitly resolved in the finer-scale domains. Due to the steeply sloping terrain and high horizontal and vertical resolution, an adaptive time step (rather than fixed) was required in order to rectify computational instability. As with the domain nesting ratio, the time step also follows the 3:1 ratio. After the coarse grid is advanced, the lateral boundaries for the fine grid are computed, the fine grid is advanced three time steps, and then the fine grid is fed back to the coarse grid. Unless specified, forcing between domains was two way.

	WRF Namelist Options
Topographical Resolution & Land Surface Type	1. Standard WRF topography (30 arc seconds, ~0.9km) and land surface type datasets A. Improved topography (4 arc seconds, ~0.1km) dataset B. Improved land surface type dataset
Horizontal Resolution	1. Nested domain (30km – 10km – 3.3km) C. Nested domain (8.1km – 2.7km – 0.9km)
Vertical Resolution	1. 30 vertical levels D. 70 vertical levels E. 140 vertical levels
Model Top	1. 50 hPa (30 vertical levels) F. 70 hPa (30 vertical levels) G. 10 hPa (70 vertical levels)
Planetary Boundary Layer Physics	1. Yonsei University scheme (YSU) H. Mellor-Yamada-Janjic scheme (MYJ) I. Mellor-Yamada Nakanishi and Niino Level 2.5 scheme (MYNN) J. Quasi-Normal Scale Elimination scheme (QNSE)
Microphysics Options	1. WRF Single-Moment 3-class scheme (WSM3) K. Lin *et al*. scheme L. WRF Single-Moment 5-class scheme (WSM5) M. Eta microphysics N. WRF Single-Moment 6-class scheme (WSM6)
Longwave and Shortwave Radiation Physics	1. Rapid Radiative Transfer Model (RRTM) and Dudhia schemes O. New Goddard scheme
Land Surface Physics	1. Noah Land Surface model P. RUC Land Surface model
Slope and Shading Effects	1. All switches off Q. topo_shading switched on R. slope_rad switched on S. topo_wind switched on

Table 2.2 – *Description of WRF namelist options used in the sensitivity studies. The standard model setup (also referred to as the default baseline simulation) is denoted with the number 1 for all the namelist options. The individual sensitivity simulations are indicated by letters. Including the baseline simulation, a total of 20 sensitivity simulations were conducted for each case study. See text for further information and relevant references. See Skamarock et al. (2008) for a full list of available options, schemes and parameterisations available for use in the WRF model.*

Nudging was switched off for these simulations. Nudging is a method of data assimilation designed to force a numerical simulation towards observations. Grid nudging forces the model to a gridded analysis point-by-point and can be used to keep a model simulation in line with the forcing dataset (Skamarock *et al*., 2008). The domains are not nudged because it can have a detrimental effect if relatively coarse-resolution forcing (i.e. ERA-Interim analysis) is applied to much finer grid scales, especially over small areas of complex terrain (Stauffer & Seaman, 1994). There was no evidence of model drift in the simulations, and since the resolution of the ERA-Interim analysis is too coarse to resolve the topography of South Georgia, flow over the island, and the föhn effect, there is no justification to adopt this approach. An important requirement for modelling the surface energy balance is that the radiation parameterisation accounts for both self-shading and topographic shading in order to reproduce the asymmetric irradiation effects correctly. Therefore, slope effects, such as shadowing and varying incident solar radiation were accounted for with the shortwave parameterisation in WRF (Garnier and Ohmura, 1968). The topographic correction for surface winds to represent extra drag from sub-grid topography and enhanced flow at hill tops was also used (Jiménez and Dudhia, 2012) in the sensitivity simulations (see Table 2.2).

To account for the elevation inconsistencies of the model equivalent grid cell for King Edward Point (27m above sea level), WRF model data was also extracted from a grid cell more representative of King Edward Point. This was done instead of vertically interpolating the King Edward Point model timeseries. This location was also a water body-bordering grid cell, with an elevation of 4m above sea level (the same as the height of the surface AWS at King Edward Point) and less than 2km south of King Edward Point. Hereafter, this will be referred to as Hestesletten. See Figure 2.1 or Figure 3.1 for a geographical reference to Hestesletten.

The different alterations, schemes and parameterisations used in this study will now be described sequentially.

2.3.1.1 WRF Static Data Fields: Terrain Height and Land Surface Type

For an accurate high-resolution simulation it is important that the model represents the island's terrain height, terrain slope and land surface type (surface land use) characteristics realistically at model resolution. Due to the complex terrain of South

Georgia, terrain height can change rapidly between adjacent gridpoints leading to potentially wide-ranging conditions between contiguous model grid cells. Consequently, two specific modifications were made to the static data fields in WRF to improve the representation of the island's topography and land surface type. Comparisons of WRF standard topography height and land surface type to the improved model topography height and land surface type are shown in Figure 2.6 and Figure 2.7.

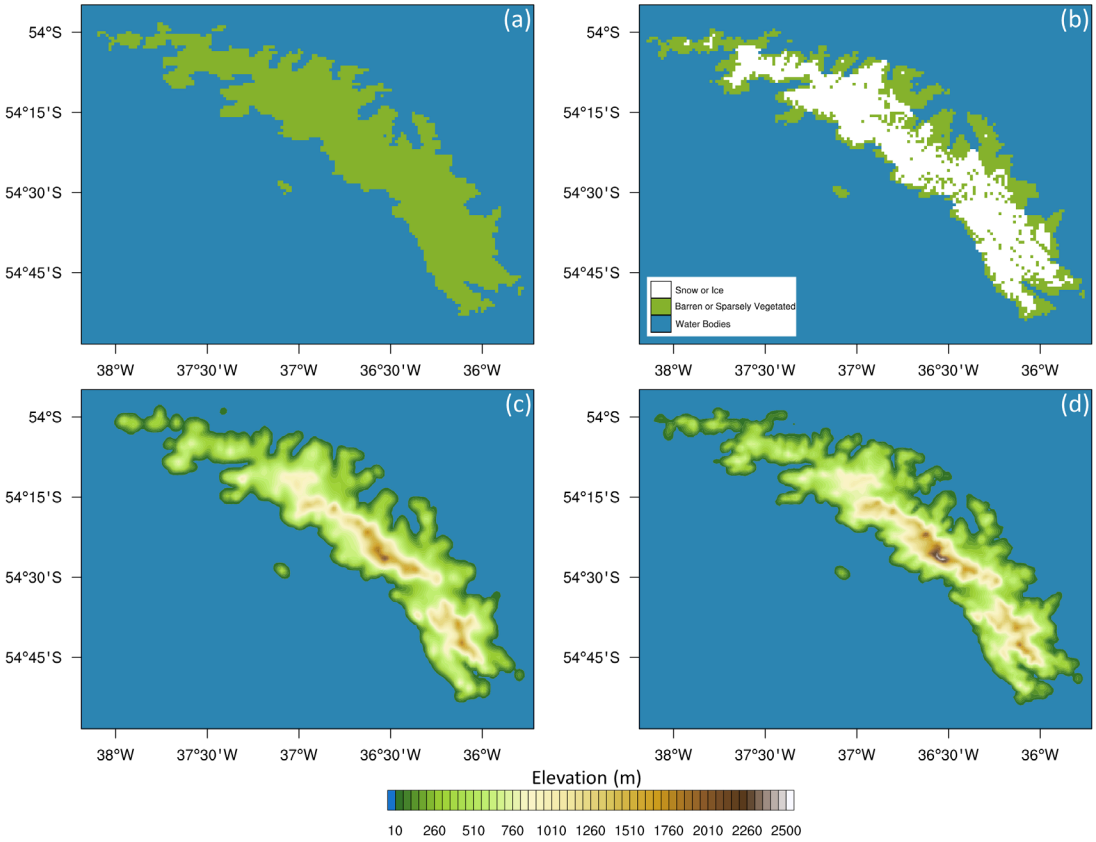

Figure 2.6 – *Comparison of the default WRF land surface type dataset (panel (a)) with the improved dataset (panel (b)), in a domain with a horizontal resolution of 1km. Panels (c) and (d) as above, but for the default WRF topography dataset set (30 arc seconds, ~0.9km), and the improved topography dataset (4 arc seconds, ~0.1km).*

To deal with the complex terrain and the potentially wide-ranging conditions between adjacent grid cells, the topography of South Georgia was increased from the highest resolution standard WRF topography of 30 arc seconds (~1km resolution), to 4 arc seconds (~0.1km resolution). This dataset was originally derived from 90m Shuttle Radar Topography Mission dataset (Jarvis *et al.*, 2008; see section 2.4.1 for more details). At a horizontal resolution of 1km, the standard topography in the model is sufficient to represent the island overall (Figure 2.6(c)). It captures the main peaks of

the Allardyce and Salvesen Ranges, as well as many other features of the island's complex topography and coastline. However, the original data does not fully resolve many of the topographic features that may have important consequences on the interaction between airflow and topography. The standard data set does not resolve all of the island's highest peaks, many of which are half of their true height (Figure 2.7(c)). Similarly, much of the low-lying areas of South Georgia are submerged below sea level. This is most noticeable in the north-west of the island, including Paryadin Peninsula which, as a consequence of the coarse-resolution, forms its own group of separate small islands. In comparison, the new dataset (with a resolution of ~0.1km) better represents the complexity and scale of South Georgia's topography and ragged coastline. One of the most noticeable improvements is that the heights of the major peaks are now represented much more realistically. Increasing the resolution increases the height of Mount Paget (with a true height of 2934m) in the 1km resolution domain from 2188m to 2408m (Figure 2.7). Similarly, the average height of the island in the model increases from 60.5m to 61.8m. In addition to this, the elevations of many of the low-lying areas of South Georgia increase. This includes Paryadin Peninsula, Pyramid Peak and surrounding the peninsula in north-east South Georgia, Cape Charlotte, and around Jossac Bight.

In the area of interest, Thatcher Peninsula is also better represented (Figure 2.7). Mount Paget is no longer an (almost) isolated peak in the middle of the island, with elevation decreasing radially around it. The Henriksen Buttress is now resolved, which forms a ridge (~1500m in elevation) connecting Mount Paget to Mount Sugartop, south of Thatcher Peninsula. The model also now somewhat captures Mercer Bay and Hamberg Lakes (along the Hestesletten glacial plain), which are completely absent in the standard dataset. The same is true for other areas, including glacial bays such as Drygalski Fjord on the south coast of the island. Therefore, the new topography used in WRF is much more representative to the real terrain height of South Georgia. It is able to resolve the low-lying areas to the north end of the island, and other fine-scale orographic features on South Georgia are more apparent at the higher resolution.

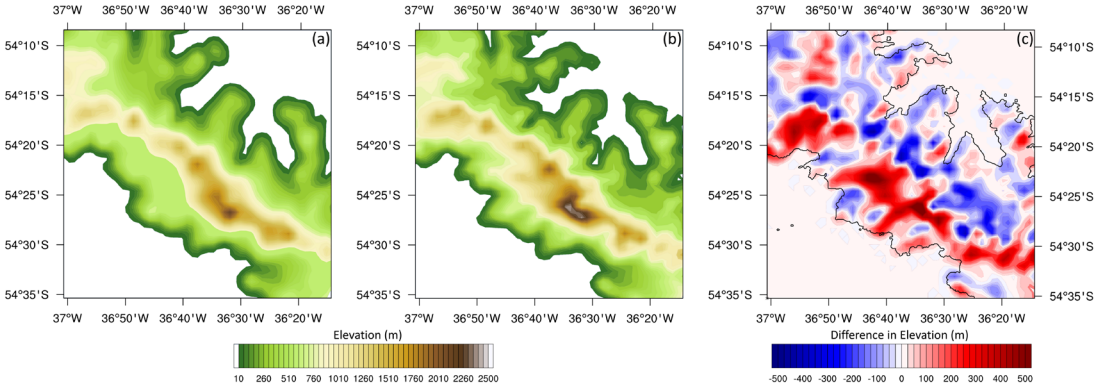

Figure 2.7 – *Detailed comparison of the default topography dataset set (30 arc seconds, ~0.9km), panel (a), with the new topography data set (4 arc seconds, ~0.1km), panel (b), in a domain with horizontal resolution of 1km. Panel (c) shows the difference between the improved and default topography datasets. The domain is roughly centred over Mount Paget and central South Georgia.*

The land surface type of South Georgia was also altered. By default, the entire land surface of South Georgia in WRF is treated as barren or sparsely vegetated. Although true for much of the coastal extremities of the island, 56% of the island remains permanently frozen throughout the year. Using a 90m resolution data set derived from Landsat data using a Normalized Difference Vegetation Index analysis (www.sggis.gov.gs; see section 2.4.1 for more detail), the land surface classification was changed to include permanent snow cover. Alterations to the land surface type were necessitated so that the model accurately resolved the ice surface across South Georgia, in turn allowing for a more accurate representation of glacier catchments in the model. As such, the improved land surface type also leads to more realistic modelled surface energy and mass balance components (including the surface turbulent heat fluxes, radiation, and precipitation) which are required in later chapters. Despite improving the representation of permanent snow and ice in the WRF model (see Figure 2.6(b)), the representation of the land surface type is still an oversimplification of South Georgia's biomes. There is currently no dataset which separates barren or sparsely vegetated areas from tundra, rangeland and bog/wet ground, which also characterise the land surface of South Georgia. Despite this, at a horizontal resolution of 1km, South Georgia is 60.7% permanent snow and ice (Figure 2.6(b)), and is a vast improvement on the default dataset in the WRF model (Figure 2.6(a)).

Both the high-resolution topography and the land surface type datasets are available to download from The South Georgia Geographic Information System website (see section 2.4.1 for more details).

2.3.1.2 Horizontal and Vertical Resolution of WRF Domains

To test the sensitivity of the model to the vertical resolution and placement of vertical levels, simulations were conducted using 30, 70 and 140 full-eta levels. The WRF model by default arranges the vertical grid so that there are 7 vertical levels below 1km, and then subsequently places levels at constant δz. This is equivalent to levels every ~1000m, ~325m, and ~150m when using 30, 70 and 140 vertical levels, respectively. In all three arrangements, the lowest model level is approximately 26.5m above the surface. The computational efficiency of the model degrades rapidly with increasingly vertical resolution. For the high-resolution configuration, the simulation time increased fivefold when simulating with 140 vertical levels. The model top was also varied between 10hPa, 50hPa and 70hPa.

Two different nested domain configurations were used in this study. These are referred to as the baseline simulation and the high-resolution simulation. A description of the two different WRF model configurations is given below (also see Table 4.1).

The baseline simulation is defined as the standard model setup, with no changes to the default settings in WRF. The configuration of the three nested domains used is illustrated in Figure 2.8. The outer domain has 75 × 45 grid points at a horizontal grid-spacing of 30 km, covering a relatively large ocean area in order to better resolve the prevailing westerly winds of the Southern Ocean, and particularly the representation of small mesocyclones (scales of a few hundred kilometres) which are also inadequately represented by reanalysis (Condron *et al.*, 2006). The intermediate domain has 115 × 91 grid points and a horizontal grid-spacing of 10 km. The innermost domain has 151 × 151 grid points at a horizontal grid-spacing of 3.3 km, covering South Georgia and the surrounding shelf sea. This configuration was subsequently used by Hosking *et al*. (2015) to simulate orographic disturbances of surface winds in the lee of South Georgia.

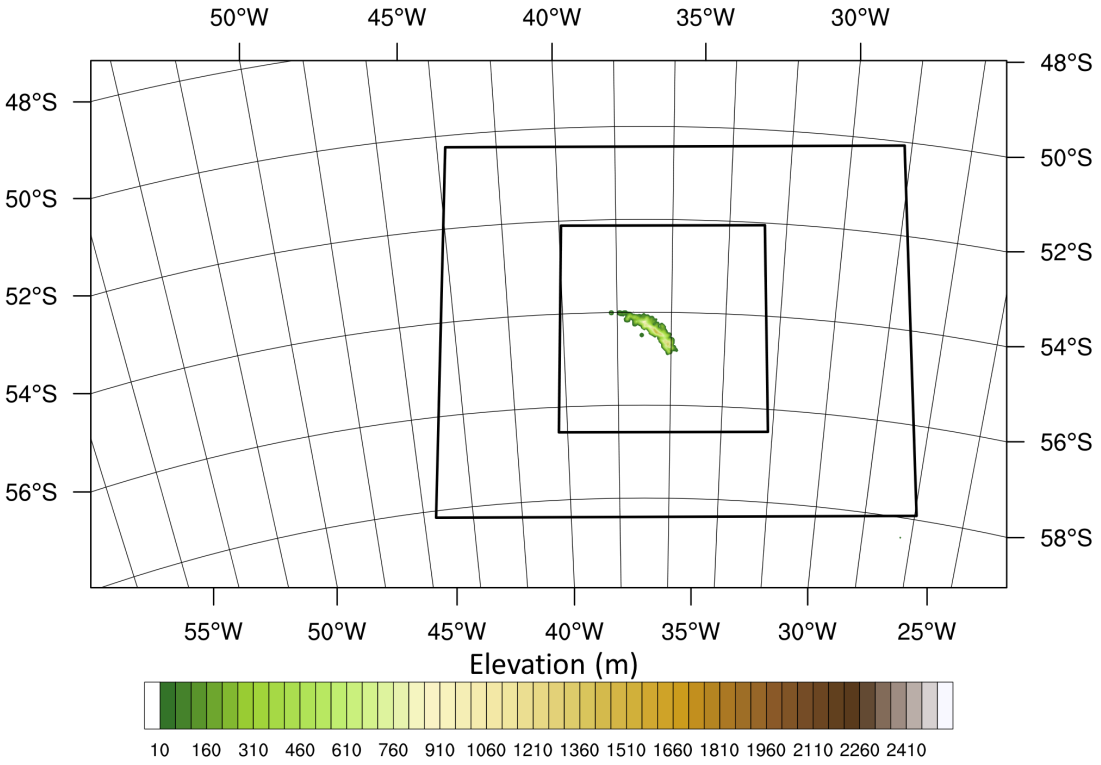

Figure 2.8 – *The WRF model configuration for the baseline simulations. The horizontal boundaries are shown by the black line boxes. The outer domain has a horizontal resolution of 30km, the intermediate domain has a horizontal resolution of 10km, and the innermost domain has a horizontal resolution of 3.3km. Elevation is plotted from the inner domain using the default topography dataset.*

To improve the representation of the South Georgia's complex terrain, a high-resolution nested domain configuration is also used (Figure 2.9). As with the baseline simulation, the outer domain covers a large area of ocean, with 94 × 54 grid points at a horizontal grid-spacing of 8.1km. The intermediate domain has 85 × 73 grid points at a horizontal grid spacing of 2.7km. The innermost domain has 52 × 52 grid points at a horizontal grid spacing of 0.9km, and is centred over Mount Paget and the central section of South Georgia. Although it is advised not to have boundary edges running through steep topography, the model fails through Courant-Friedrichs-Lewy (CFL) violations if the size of the domain (Figure 2.9) or the horizontal grid spacing is any larger. This is because WRF solves the governing equations in the three dimensional space using explicit finite difference schemes. These schemes remain conditionally stable when the computational time step of the model is smaller than the horizontal grid size (known as the CFL condition). In the case of the WRF model, a time step (in seconds) should be less than six multiplied by the horizontal grid size (in kilometres) (i.e. 6 × dx). This means that for the 8.1km – 2.7km – 0.9km configuration (Figure

2.9), the computational time step for each domain should be ~49 – 16 – 5 seconds. If, however, the model becomes unstable (CFL errors are generally caused when grid nesting is applied in regions of complex terrain, causing numerical errors arising from grid skewness of the terrain-following coordinates, since the vertical dimensions of the model are much shorter compared to the model's horizontal dimension), then reducing the resolution or increasing the computational time step should rectify the instability. Therefore, this model configuration was the highest horizontal resolution which could be achieved without violating the CFL condition. Although these simulations are more computationally intensive than the baseline simulation, it is hoped that resolving the island at such high-resolution will allow for a view into the fine features of atmospheric flow over South Georgia.

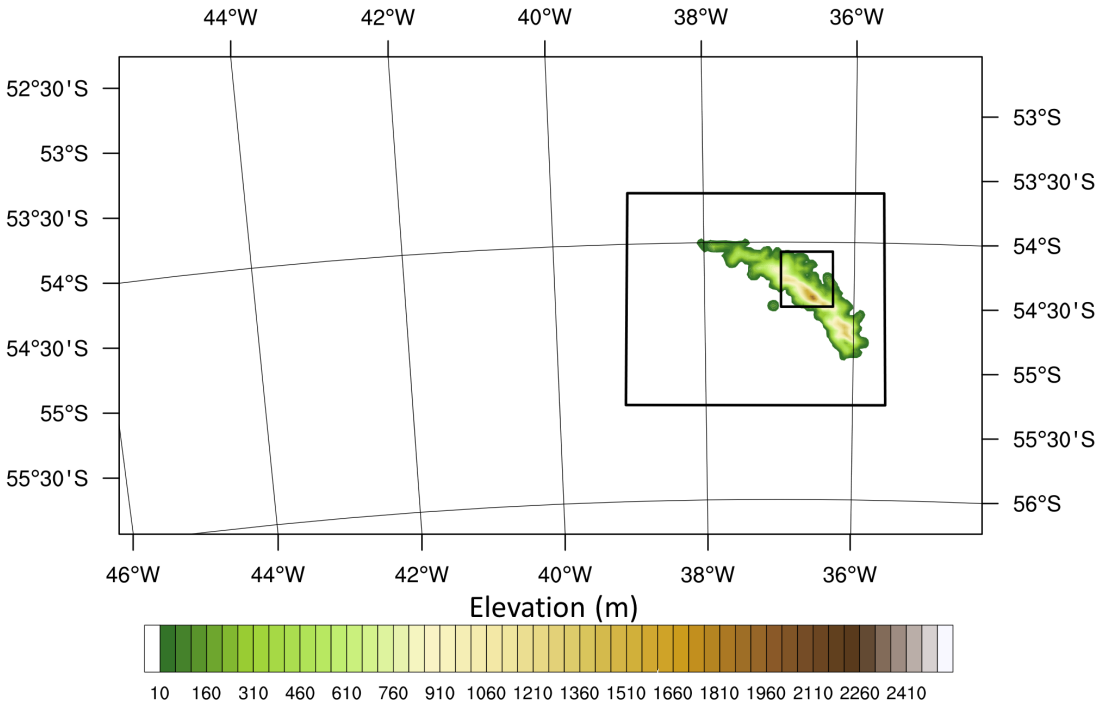

Figure 2.9 – *The WRF model configuration for the high-resolution simulations. The horizontal boundaries are shown by the black line boxes. The outer domain has a horizontal resolution of 8.1km, the intermediate domain has a horizontal resolution of 2.7km, and the innermost domain has a horizontal resolution of 0.9km. Elevation is plotted from the 2.7km domain using the improved topography dataset.*

2.3.1.3 Planetary Boundary Layer Schemes

The planetary boundary layer parameterisation schemes are responsible for representing the effects of vertical sub-grid-scale turbulent fluxes of momentum, heat and moisture. For the purposes of this study, the Yonsei State University (Hong *et al*.,

2006), Mellor-Yamada Janjic (Janjić, 1994), the Mellor-Yamada Nakanishi and Niino (Nakanishi, 2001; Nakanishi & Niino, 2004; 2006) and the Quasi-Normal Scale Elimination (Sukoriansky *et al*., 2006) planetary boundary layer schemes (hereafter YSU, MYJ, MYNN and QNSE, respectively) are used. These particular schemes are chosen for the sensitivity simulations as they include different types of turbulence closure models, and the MYNN and QNSE schemes are generally more complex than the YSU and MYJ schemes.

The YSU scheme is a 1st-order non-local scheme, where turbulent mixing is carried out over the whole of the boundary layer depth in order to represent mixing by large scale eddies. The YSU scheme is also based on the local K profile approach, in which the degree of mixing over time is directly proportional to the second derivative of a model variable with respect to height. In contrast, in the MYJ 1.5 order Turbulent Kinetic Energy (TKE) local scheme, turbulence is closed using the TKE equation. Therefore, eddy diffusivities are a function of TKE rather than just wind shear and stability (Stensrud, 2007). The 1.5 order MYNN TKE scheme is somewhat similar to the MYJ scheme; however, it accounts for surface, turbulent and buoyancy length scales, and as result, gives a more explicit treatment of the stability of the planetary boundary layer. These changes help the MYNN scheme alleviate underestimation of mixed-layer depth and TKE magnitude and better resolve Kelvin-Helmholtz instability compared to the MYJ scheme. The MYNN 2nd-order scheme (Nakanishi and Niino, 2004) is not tested as it is more computationally expensive than the MYNN scheme. The QNSE scheme is also a TKE-prediction parameterisation in the WRF model and accommodates the stratification-induced disparity between the transport processes in the horizontal and vertical directions and accounts for the combined effect of turbulence and waves.

In WRF, surface schemes are paired with a corresponding planetary boundary layer scheme. The surface layer scheme provides exchange coefficients and friction velocities for surface fluxes and surface stress. Therefore, the MM5 similarity scheme is used with the YSU scheme, the Eta similarity is used in conjunction with the MYJ and MYNN schemes, and the corresponding QNSE surface layer scheme is used with the QNSE planetary boundary layer scheme. Details on surface scheme formulation in WRF can be found in Skamarock *et al*. (2008).

2.3.1.4 Microphysics Schemes

The microphysics scheme handles the explicitly resolved water vapour, cloud, and precipitation processes. In this study, 5 different microphysics schemes are tested. These include the WRF Single-Moment 3- (Hong *et al*., 2004), 5- (Hong *et al*., 2004), and 6-class schemes (Hong and Lim, 2006) (hereafter WSM3, WSM5, and WSM6, respectively), the Lin scheme (Lin *et al*., 1983) and the Eta microphysics schemes (Rogers *et al*., 2001). The WSM5 and WSM6 schemes differ from the WSM3 scheme as they feature more realistic melting and freezing processes, which occur over a deeper layer than in the WSM3 scheme (where such processes are instantaneous at the freezing level). The WSM6 scheme also includes a predictive equation for graupel. Both the WSM6 and Lin schemes are particularly good for high-resolution simulations at high latitudes due to their sophistication.

2.3.1.5 Shortwave and Longwave Radiation Schemes

Radiation schemes provide both the total radiative flux at the surface and the vertical radiative flux divergence in the free atmosphere (Stensrud, 2007). The longwave Rapid Radiative Transfer Model (RRTM, Mlawer *et al*., 1997) scheme in conjunction with the shortwave Dudhia scheme (Dudhia, 1989), and the New Goddard radiation scheme (Chou and Suarez, 1999) were tested. Since the shortwave and longwave portions of the electromagnetic spectrum are distinct, they are calculated separately.

2.3.1.6 Land Surface Model

The primary function of the land-surface model is to provide surface heat and moisture fluxes over land and sea-ice points. The model uses atmospheric information (e.g. radiative forcings and the surface energy balance) as input to represent heat and moisture fluxes within the soil layers, and the evapotranspiration, runoff, and canopy layer processes. In the WRF model, the soil of South Georgia is set to the default silty clay loam category (10% sand, 56% salt, and 34% clay). Soil category is largely irrelevant for the glacierized areas of South Georgia. There are four principal type of soil across South Georgia: organic soils, meadow tundra soils, brown soils, and raw mineral soils (Headland, 1992). However, there is no island-wide geographical dataset to improve the representation of soil type in WRF, and as such, the default category is deemed satisfactory. The sensitivity of the model to the Noah land surface model

(Chen & Dudhia, 2001) and the Rapid Update Cycle (RUC) land surface model (Smirnova *et al*., 2000) is tested. Both models dynamically predict water and energy fluxes and states at the land surface, although their parameterisations and/or structures representing various processes are different. For instance, the Noah land surface model has 4 soil layers with thicknesses (top to bottom) of 10, 30, 60 and 100cm; whereas the RUC model has 6 soil layers with thicknesses of (5, 10, 20, 40, 160 and 300cm). Snow is treated as a single bulk layer in both land surface models.

This concludes the description of WRF and the information pertaining to the sensitivity simulations. A summary of the WRF sensitivity analyses procedure and all case studies is given again in Chapter 4, and details of the best domain configuration used for the climatological simulation is also given in Chapter 5.

2.4 Additional Sources of Data

2.4.1 The South Georgia Geographic Information System

The South Georgia Geographic Information System (SGGIS, available from www.sggis.gov.gs), created by the British Antarctic Survey for the Government of South Georgia and South Sandwich Islands, contains data about the wildlife of South Georgia, its human history and its changing physical environment. Many of the layers included in the GIS were from datasets compiled from a recent 1:200 000 scale map of the island, including topographic features, bathymetry and toponymy (see British Antarctic Survey, 2004). The database also contains the frontal positions for 103 coastal glaciers (i.e. those that terminate on or near the coast) on South Georgia. It does not signify the total number of glaciers on the island, but it is a comprehensive resource of all glaciers on South Georgia for which there is source material available. The web-based database has previously been used to aid effective environmental management of the island and for analysing the combined datasets for patterns of change (SGHT, 2014). The SGGIS database was also used by Cook *et al*. (2010) to investigate the rates of advance and retreat of the 103 coastal glaciers from the 1950s to the present (see section 1.5.2). The land surface type, topography (see Chapter 2), and glacier fronts (see Chapter 6) from the SGGIS database are used throughout this thesis.

2.4.2 Satellite Observations

Another important source of data and information on the regional conditions over South Georgia and the surrounding ocean is that from satellite observations. In the absence of island-wide measurements, high-resolution satellite observations have previously been used to explore the impact of South Georgia's steep orography on the regional atmospheric circulation (as discussed in section 1.7). In particular, satellite observations have commonly been used to compute the wave momentum fluxes (e.g. Alexander *et al*., 2009; Alexander & Grimsdell, 2013; Jiang *et al*., 2014) and the surface winds over the island and surrounding sea shelf (e.g. Hosking *et al*., 2015) during occasions of strong westerly flow. Such studies have shown that South Georgia is an important source of drag on the atmosphere in global climate models, and that satellite-derived winds compare well with high-resolution regional climate simulations. Studies such as these have been prompted by the fact that small island orography (like South Georgia) is generally neglected in mountain wave parameterisations used in global climate models because limited model resolution treats the grid cell containing the island as ocean rather than land. As a consequence, satellite data allows us to explore the impact of the island on the atmospheric circulation in an otherwise data sparse region.

It is clear that satellite data is a good source of information (both vertically and horizontally) on regional wind patterns in this area of the Southern Ocean, and such observations could be used to quantify the föhn wind process by identifying föhn gaps (see e.g. Hoinka, 1985b) and/or mountain wave activity and other regional scale orographic disturbances on surface winds. However, it would be challenging to use such data as an automated method for systematic föhn identification since very little is known on the dynamics of air flow over South Georgia. It is beyond the scope of this study to explore this. In spite of this, satellite data will be used to qualitatively describe the larger-scale pattern during identified föhn periods. When available, satellite images from https://earthdata.nasa.gov/labs/worldview/ are utilised. Unfortunately, due to a hardware failure at NASA, Moderate Resolution Imaging Spectroradiometer (MODIS) satellite images are only available from May 2012 onwards. Therefore, this dataset only covers a very small portion of the period examined throughout the work presented in this thesis. In addition to this, the orbital track of the Aqua/MODIS satellite typically passes over South Georgia between 1615

– 1745 UTC. This further reduces the number of beneficial satellite images. A limited number of images are also available from the Advanced Very High Resolution Radiometer (AVHRR) data set from Rothera Research Station (from February 1993 to data, collected by the British Antarctic Survey), which covers the Southern Ocean, the Antarctic Peninsula and the coast of West Antarctica. These have not been used in this thesis.

Chapter Three: A Climatology of Föhn Events at King Edward Point

3.1 Introduction

It has long been known that the interaction between the westerlies and South Georgia's steep orography can produce föhn winds on the north-eastern (lee) side of the island. Despite the fact that some knowledge about the occurrence of föhn winds on South Georgia does exist, it is severely limited. The earliest record of the föhn effect being measured on South Georgia appears to be in 1883, during the First International Polar Year (von Danckelman, 1884; Headland 1982). At midnight on 1 May 1883, a maximum temperature of 9ºC during strong westerly winds was recorded at the German site at Royal Bay (southeast South Georgia, see Figure 1.2(c)). Föhn events on the island have since not been widely explored, and no detailed scientific studies have ever been conducted. The occurrence of föhn at Grytviken and King Edward Point was later noted by Pepper (1954), Mansfield & Glassey (1957), Richards & Tickell (1968), and Headland (1992), but there have been virtually no studies to quantify the föhn effect on South Georgia. Mansfield & Glassey (1957) recorded (via thermograph traces) a temperature rise of 10.5ºC in 30 minutes on 19 January 1951 at King Edward Point, followed by a second event with an increase in temperature of 12.2ºC in 10 minutes on 17 April 1951. The author is unaware of any research which has quantified föhn on South Georgia in the last 40 years. In addition to this, föhn has never been recorded or noted elsewhere on the island. Therefore, the atmospheric processes which control the regional climate of South Georgia, specifically the föhn effect, are not well understood. This is primarily due to being an isolated island in a remote location.

Föhn research has been equally limited on similarly isolated and mountainous subantarctic islands (see e.g. Loewe, 1950 (Balleny Islands); Kruszewski, 2000 (King Georgia Island); Ruddell, 2001 (Heard Island)) in spite of huge advancements in our knowledge of the föhn warming process worldwide. See Richner & Hächler (2013) for a detailed history of worldwide föhn research. Since the meteorological record on South Georgia is the second longest in the high-latitude Southern Hemisphere, it could provide valuable insights on regional-scale atmospheric variability, and how this relates to global climate change. Likewise, understanding the occurrence, characteristics, variability and predictability of föhn winds also has significance due

to the recently observed environmental, glaciological and ecological changes across South Georgia (see section 1.5). Therefore, the aim of the work described in this chapter is to provide the very first climatological analysis of föhn events at King Edward Point, South Georgia.

In this chapter, the climatology of föhn events at King Edward Point will be examined and interpreted. The method for föhn detection using 10 years of observational automatic weather station (AWS) data is described at length, with supporting examples of strong, weak and ambiguous föhn events. Using this definition of föhn, a summary of their occurrence and characteristics from 2003 through 2012 is presented. The large scale flow related to strong and non-föhn conditions are then evaluated in order to discern the large-scale atmospheric circulations that produce such events. The inter-annual variability in the frequency and intensity of föhn events in response to the Southern Annular Mode (SAM) is also discussed. The AWS climatology of föhn events at King Edward Point is revisited in Chapter 5, where it is used as a validation tool for the Weather Research and Forecasting (WRF) model data.

3.2 The Definition of a Föhn Event

As highlighted in section 1.6.2.2, various criteria, indices and/or algorithms are commonly used in föhn identification methodologies, since the flow characteristics of the föhn effect are highly dependent on local topography and are thus unique to each mountainous region. As such, regional and temporal differences in the characteristics and dynamics of the föhn warming process make it inherently difficult to form a universal definition of a föhn event. This is further complicated by the fact that föhn generally occurs in remote and isolated mountain regions. Therefore, they are usually sporadically measured and observed by limited near-surface observations (e.g. AWS stations). As a consequence of this, the definitions of föhn, and the subsequent methodologies used to identify, forecast and detect them, only hold true for a particular physical setting and the local character of föhn. This has resulted in numerous different föhn identification and detection schemes being used to separate föhn events from non-föhn events.

Since the föhn effect on South Georgia has never before been quantified in any great detail, the method for föhn detection described here strives to be the most objective it can be given the type and amount of data and observations available on the island. The

föhn detection method used for the research presented in this thesis is appropriate for this location, and it is also a variation of the traditional föhn classification method (as previously detailed in section 1.6.2.2). Using observations at 1-hour (January 2003 – March 2006) and 1-minute (March 2006 – December 2012) frequency, a selection of criteria were developed to identify föhn events in the King Edward Point AWS observations, similar to studies of Alpine (e.g. Ungeheaur, 1952), Appalachian (e.g. Gaffin, 2007) and Antarctic föhn (e.g. Speirs *et al*., 2013), among many others (e.g. Conrad, 1936; Osmond, 1941; Obenland, 1956; Inaba *et al*., 2002). The method employed here relies on the impact of föhn on 2-m air temperature, 2-m relative humidity, and 10-m wind speed and wind direction as recorded by the AWS at King Edward Point. Although there are more rigorous methods that can be applied, the lack of long-term island-wide meteorological data on South Georgia restricts this study to a simple method. Since there is currently only one AWS station on South Georgia downstream of the island's main mountain range, detecting föhn winds from surface observations is reliant upon this single dataset. To investigate such a transient phenomenon like föhn, it is also necessary to generalise the properties of individual cases to those of the whole class. Therefore, the simplicity of the method used here is based upon the basic detectable surface föhn signature in the available surface AWS observations. The identification method used to detect föhn in the AWS observations at King Edward Point will now be described.

For a wind to be classified as a föhn event, it must first meet the primary criterion:

(1) An increase of air temperature, greater than 2^{o}C within 1 hour of föhn onset

This threshold is set to remove detections of any gradual changes in temperature, which may be associated with diurnal changes, solar and cloud effects, or other downslope wind effects (see e.g. Mansfield & Glassey, 1957). If an event meets this criterion, then it must also meet *each* of the following secondary criteria:

(2) A decrease in relative humidity, during the specified event, and;

(3) An increase in wind speed, during the specified event, and;

(4) Wind from the direction of the barrier.

Considering the orientation of the island's main mountain chain, winds with a direction 150^{o} – 330^{o} were deemed as having potential for generating leeside föhn at

King Edward Point and thus being indicative of cross-barrier flow-over conditions. The AWS observations at King Edward Point indicate that between 2003 and 2012, 60.8% of winds blew from a direction between 150° and 330°. The annual mean wind rose (2003 – 2012) is shown over the topography of Thatcher Peninsula in Figure 3.1. It is important to note that the gradient wind is markedly modified by the complex topography surrounding King Edward Point. In addition to this, thresholds are not given for criteria (2) and (3) because the signals in near-surface wind speed and relative humidity were often more muted, variable or inconsistent compared to the temperature signal (see Case C, for instance).

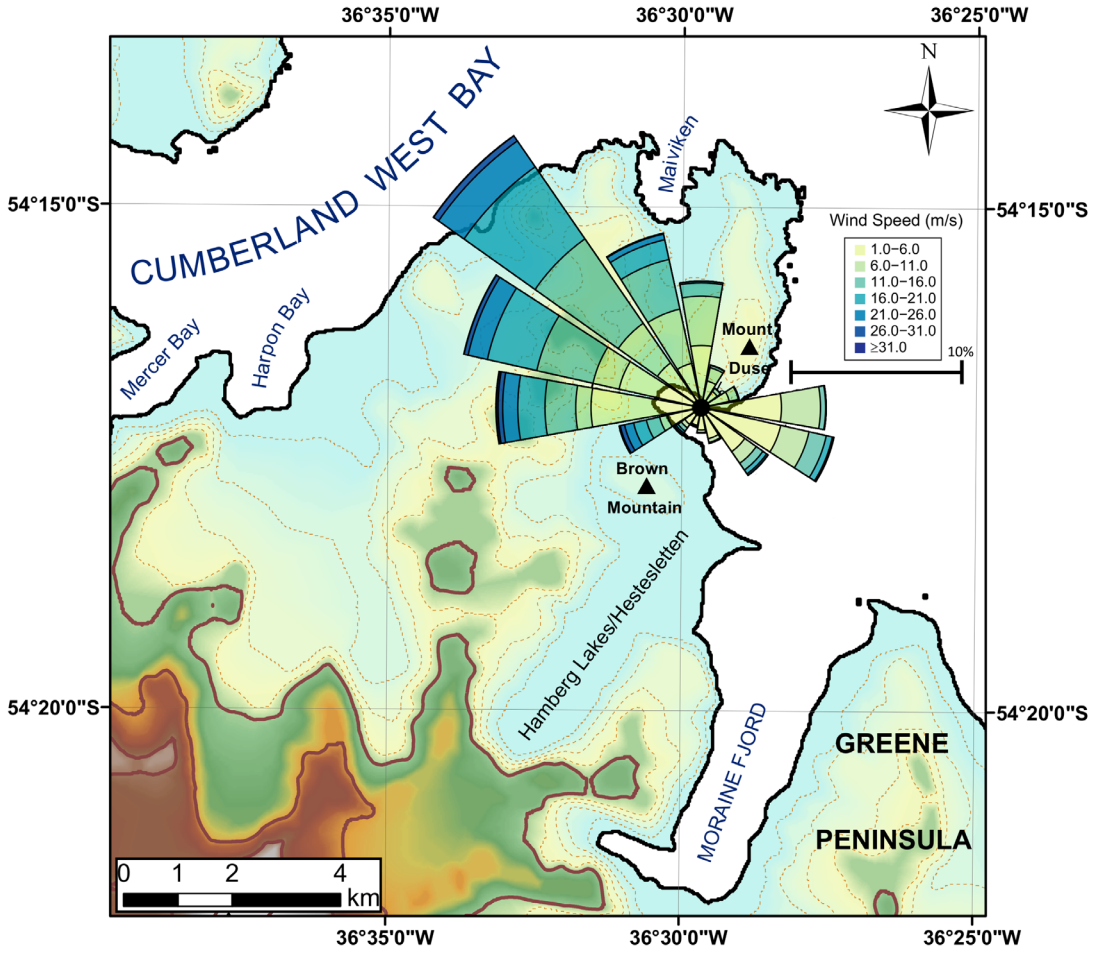

Figure 3.1 – *Wind rose from King Edward Point AWS (using hourly instantaneous values) over the period January 2003 – December 2012, overlaid onto the topography of the surrounding area (see Figure 2.1).*

The end of the event was defined and set when a sudden change in temperature was observed (the end taken to be the largest change in temperature over the shortest period of time, e.g. Case A), akin to the beginning of the event, which may or may not have coincided with concurrent changes in wind speed, wind direction and/or relative

humidity. This was the primary criterion for föhn cessation. If there was no discernible drop in temperature (see e.g. Case D) and the observed wind direction was still within the $150^{o} – 330^{o}$ range, then a sudden decrease in wind speed or a sudden increase in relative humidity (whichever change occurred first) over the shortest period of time defined the end of the föhn event. As with the start of a föhn event, wind speed was not given a specific threshold to mark the end of event because it is topographically controlled and can easily obscure onset and cessation of föhn events (see e.g. the end of Case A and Figure 3.1). In the same vein, the change in relative humidity was not given a specific threshold, and of only secondary importance, because it was found that the warming conditions as a result of the föhn process often remained established despite the increase in relative humidity compared to its pre-föhn value (see e.g. Case C). Based on the AWS observations at King Edward Point, neither wind speed nor relative humidity provided consistent föhn onset and cessation signals and, therefore, were only occasionally used to define the end of an event; for the majority of events a significant drop in temperature was evident. If there was no discernible end to an event (i.e. no sudden changes in any of the variables) despite having apparently started, then the event was not recorded as föhn.

For clarity, a 'föhn event' refers to an individual episode which has been classified and catalogued as föhn. In contrast, a 'föhn day' at King Edward Point is defined as a day that experiences 6 or more hours of continuous föhn conditions which meet the above criteria. A föhn day is not constrained to a calendar day. These terms are used throughout the text.

It is important to note that the classification of föhn onset and cessation was undertaken manually, making the collection of the results time-consuming and somewhat subjective. Diagnostic accuracy decreased when distinguishing weaker föhn flows since concurrent temporal changes of temperature, relative humidity and wind became difficult to manually identify. Because of the subjective nature of the föhn classification method employed here, it is possible that some events are included in the analyses which have been falsely classified as föhn. Since there are no other windward or leeward observations for comparison, it is assumed that the surface föhn signal (i.e. warming and drying, and increased wind speeds) in the surface AWS observations at King Edward Point is only associated with föhn. As previously highlighted, wind direction and wind speed within King Edward Cove vary

considerably over relatively short distances because of the surrounding complex topography (see Figure 2.1 and Figure 3.1). As such, it may be possible that some events recorded may have been disturbed and/or influenced by (non-föhn) local and/or larger scale flows. Due to local topographic modification, the recorded wind direction at King Edward Point AWS is not indicative of the synoptic wind pattern. For instance, wind channelling from different valleys and basins in the surrounding topography are common across the Cove (Mansfield & Glassey, 1957; Headland, 1992). This may result in local sudden shifts in wind direction and/or wind speed at the AWS site, which may lead to an increase or a decrease in temperature. Easterly intrusions can occur at King Edward Point, and these winds (which are cool and moist maritime winds) have the potential to interrupt föhn conditions at King Edward Point. The AWS observations at King Edward Point indicate that between 2003 and 2012, 19.0% of winds blew from a direction between 45^{o} and 135^{o} (Figure 3.1). Intermissions may also be down to larger-scale process, such as frontal systems moving over the island and/or competing air masses. Therefore, although these processes may cause an intermission during a föhn event at King Edward Point, it is likely it may still be the same large-scale wind event. Short breaks should not be a reason to count a föhn period as two separate events. As such, short breaks of less than two hours were ignored when defining separate föhn events.

Missing data was also a problem in the classification process, and is largely responsible for the low occurrence of föhn events in 2007 (see section 3.3.2). An event was not classified as a föhn if data from the beginning or the end of the event was missing. In addition to this, föhn events were not catalogued if there were one or more hours of continuous missing data during the event. Because of the change in the temporal resolution of the data (as described in section 2.2.1), minor allowances were made in the detection method; criterion (2) was only used from March 2006 onwards. This too may have led to the misclassification of some föhn events before March 2006.

3.2.1 Examples of Föhn Events at King Edward Point

To provide a general overview of what is known about the general characteristics of föhn at King Edward Point, four föhn case studies of different intensities which have been identified from the surface AWS observations are described in this section. These are presented to demonstrate how the detection method is applied to the surface AWS

observations in order to distinguish a föhn event. These examples also show the wide variety of föhn characteristics at King Edward Point, illustrating that the development of föhn generation and cessation is complex, and that they can occur under very different forms and circumstances. In some of these cases it is not clear in the AWS data whether föhn is present, whether a föhn has begun, or whether a föhn has ceased. Therefore, the reasons for their inclusion or omission in the AWS föhn climatology are given. The aim of detailing these examples is to illustrate how föhn manifests itself and evolves at King Edward Point, and how the detection method performs in selecting (omitting) föhn (non-föhn) events from the AWS data.

Case A is an example of an event with a rapid rise in temperature, the onset of high winds, and constant wind direction throughout the event, but with missing relative humidity data. The onset of this event can easily be determined, but the cessation of the event is more subjective. To contrast this, Cases B and C are ambiguous events, though both do meet a different combination of the criteria. Case B is not included as a föhn as the event does not meet the temperature criterion, while Case C is considered as a föhn event but only just meets the temperature criterion. Case C also illustrates how föhn-like conditions can remain established at King Edward Point despite a change in relative humidity to its pre-föhn level. Case D is an example of two intense föhn events which occur in close succession. The onset of föhn is easily discernible for both of these events. It is important to note that Cases C and D are later revisited in Chapter 4. These events are simulated using a high-resolution atmospheric model to explore the characteristics and dynamics of föhn further. Each of the four case studies are presented separately, detailing why they were included (or excluded) from the 2003 – 2012 föhn climatology. The synoptic situation from ERA-Interim reanalysis before and after each of the four events is presented in Figure 3.2.

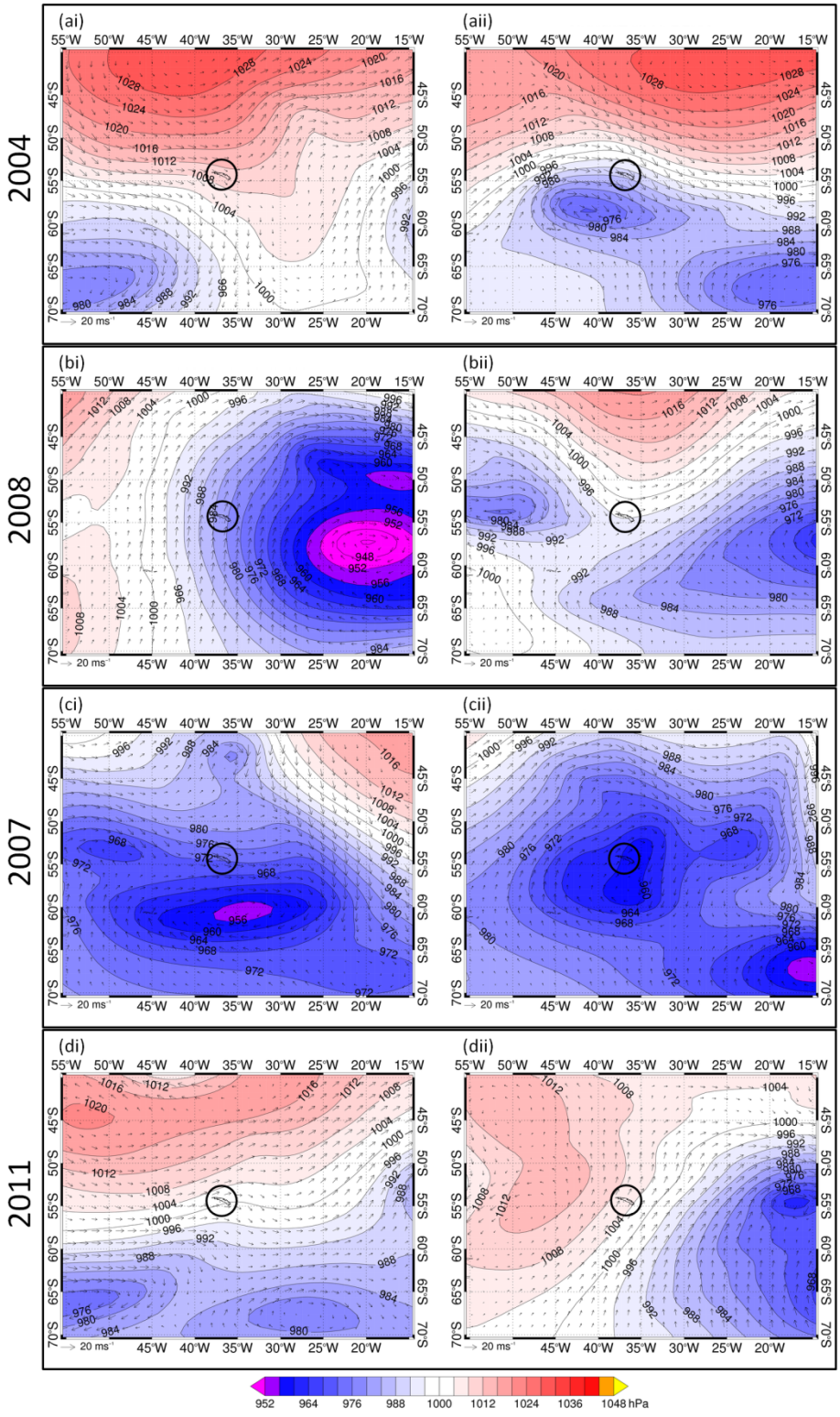

Figure 3.2 – *ERA-Interim sea level pressure (hPa) and 10-m wind vector plots for before and after respective föhn events. Panels (ai) and (aii) – Case A at 0600 UTC 9 February and 0000 UTC 11 February 2004, panels (bi) and (bii) – Case B at 0600 UTC 16 May and 1800 UTC 17 May 2008, panels (ci) and (cii) – Case C at 1200 UTC 1 November and 1200 UTC 2 November 2007, panels (di) and (dii) – Case D at 1800 UTC 10 February and 0000 UTC 13 February 2011. South Georgia is circled in black.*

Case A: 9 – 10 February 2004

Before Case A had formally begun, the ERA-Interim reanalysis plots of sea level pressure at 0600 UTC 9 February show that South Georgia was dominated by a ridge of high pressure which extended south from a high pressure system (1028 hPa) situated in the Argentine Basin region of the South Atlantic Ocean (Figure 3.2(ai)). During 9 February 2004, this ridge of high pressure was pushed northwards and eastwards as an area of low pressure deepened in the Drake Passage. Through 9 – 10 February, this system moved eastwards and remained south of South Georgia. Therefore, this föhn event was caused by the presence of a low pressure system, which generated a strong westerly cross-barrier pressure gradient across the island. The system continued to deepen after Case A had ceased, and through 11 February 2004 (Figure 3.2(aii)).

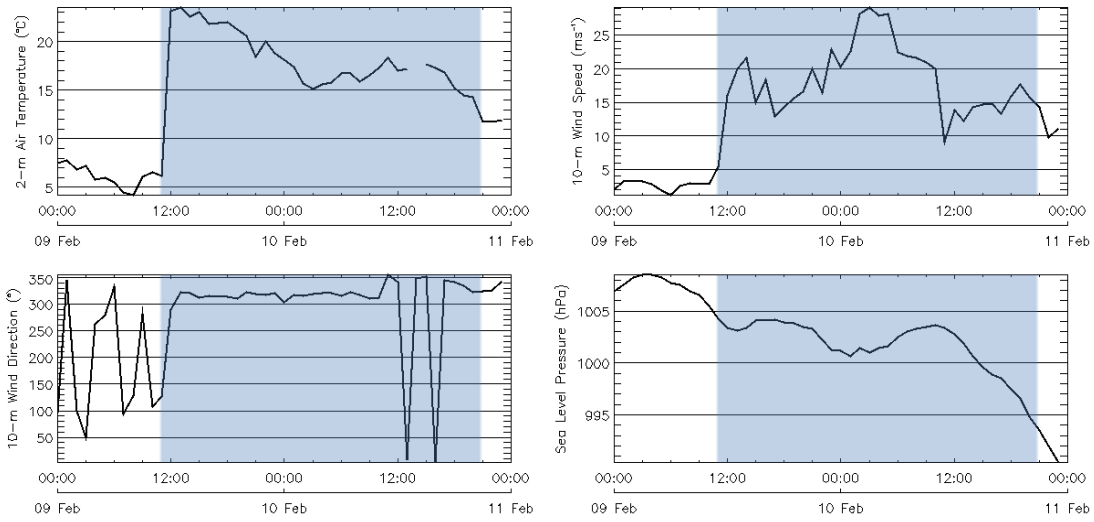

Figure 3.3 – *Meteorological conditions (2-m air temperature, 10-m wind speed, 10-m wind direction and sea level pressure) during 9 – 10 February 2004. Blue shading highlights föhn event as defined and detected by the AWS föhn classification method.*

Of all the föhn events detected in the King Edward Point AWS observations, Case A is the most intense event in terms of having the highest total temperature rise (Figure 3.3). Within 4 hours of föhn onset, the temperature had risen from 4.2ºC to 23.5ºC; a 19.3ºC rise in 2-m air temperature. This sudden rise in temperature and a coincident jump in wind speed from near-calm to over 20ms^{-1} clearly mark the beginning of the föhn event. The wind speed, although variable, remained above 10ms^{-1} for much of the event (peaking at 29.3ms^{-1}), with a strong north-westerly flow (average observed wind direction of 306º). Although the start of Case A is obvious, the cessation of this event is more ambiguous. In this instance, the largest temperature drop over the

shortest time period was used to define the end of the event (2100 UTC). Though the surface temperature dropped at 2100 UTC, wind speeds exceeded 10ms^{-1} for another 24 hours, and the pressure continued to fall as the low pressure system continued its passage south of the island. It appears that the event may have ended in several phases with stepped drops in temperature. Since the end of the event is also associated with a deepening low pressure, the breakdown of this event may have been a result of competing air masses in the vicinity of King Edward Cove. Therefore, Case A is a classic example of a föhn event, and one which can be easily diagnosed as föhn using the identification method. Case A is characterised by the surface föhn signature, and the event is easily distinguished by abrupt and sudden temperature and wind speed changes, and a surface wind from the direction of the mountain range. In spite of this, Case A is also an example of a föhn with an ambiguous and indistinct end, highlighting that föhn cessation (as well as föhn onset) can be misinterpreted when only limited near-surface observations are available.

Case B: 16 – 17 May 2008

Case B developed in the prescence of a very deep and large area of low pressure (946 hPa) east of South Georgia, which generated strong southerly winds (Figure 3.2(bi)). During 16 – 17 May 2008, this area of low pressure remained almost stationary but it also began to fill. At the same time, another smaller area of low pressure system moved eastwards from Argentina towards South Georgia. By the end of the detected event, this low pressure system remained west of South Georgia (Figure 3.2(bii)), restoring north-westerly winds to the island.

Case B is a substantially different event; it is classified as a strong wind event, but not a föhn event. Case B meets each of the secondary föhn classification criteria, but there is no sudden rise in temperature greater than 2^{o}C during the event (Figure 3.4). At 0600 UTC there are abrupt and obvious changes in wind speed and relative humidity (following similar, but less extreme, changes three hours previously). The wind speed reached a maximum of 25.4ms^{-1} (compared to 2.7ms^{-1} at the beginning of the event), while relative humidity dropped to 34% (compared to 85% at the beginning of the event). Wind direction also sustained a dominant and strong south-westerly component for the entire period, due to the position of the large low pressure system in the Southern Ocean (Figure 3.2(bi)). Despite the conditions being favourable for

föhn, there was no abrupt change in temperature ≥ 2ºC. Within the first hour of the event, the temperature had only risen by 1.2ºC, and continued to hover below -3ºC for 24 hours. From 0200 UTC 17 May onwards, temperature began to gradually rise, reaching a maximum of 0.2ºC, just as the wind event ended. Given that this event does not meet all of the criteria described earlier, it is not included in the föhn climatology. Since the wind direction is indicative of, and favourable for, flow-over conditions, and since significant near-surface drying and strong winds were experienced at the AWS site, this suggests that the surface föhn warming signal may have occurred outside of King Edward Cove. Clearly, more observations in the lee of the island would be beneficial for the exploration of föhn variability across South Georgia. Therefore, this event can only be described and labelled as a strong wind event.

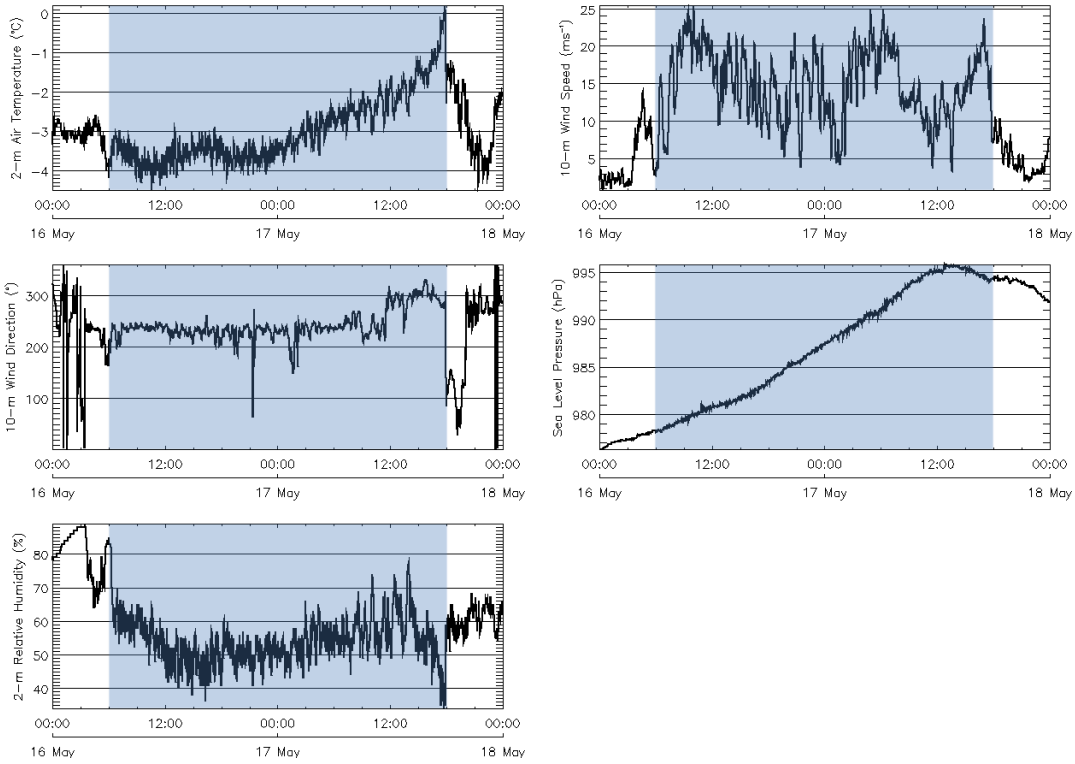

Figure 3.4 – *Meteorological conditions (2-m air temperature, 10-m wind speed, 10-m wind direction, sea level pressure, and 2-m relative humidity) during 16 – 17 May 2008. Blue shading highlights a strong wind event.*

Case C: 1 – 2 November 2007

Case C was also generated by a low pressure system situated to the south of South Georgia (Figure 3.2(ci)). During 1 – 2 November 2007, an almost stationary deepening low pressure generated strong cross-barrier westerly winds. During the detected event,

the system had deepened by 11.4 hPa and by 1200 UTC 2 November it had deepened by a total of 14.5 hPa within 24 hours. During 2 November, the system gradually moved northwards over South Georgia, leading to more variable wind direction and lower wind speeds (Figure 3.2(cii)).

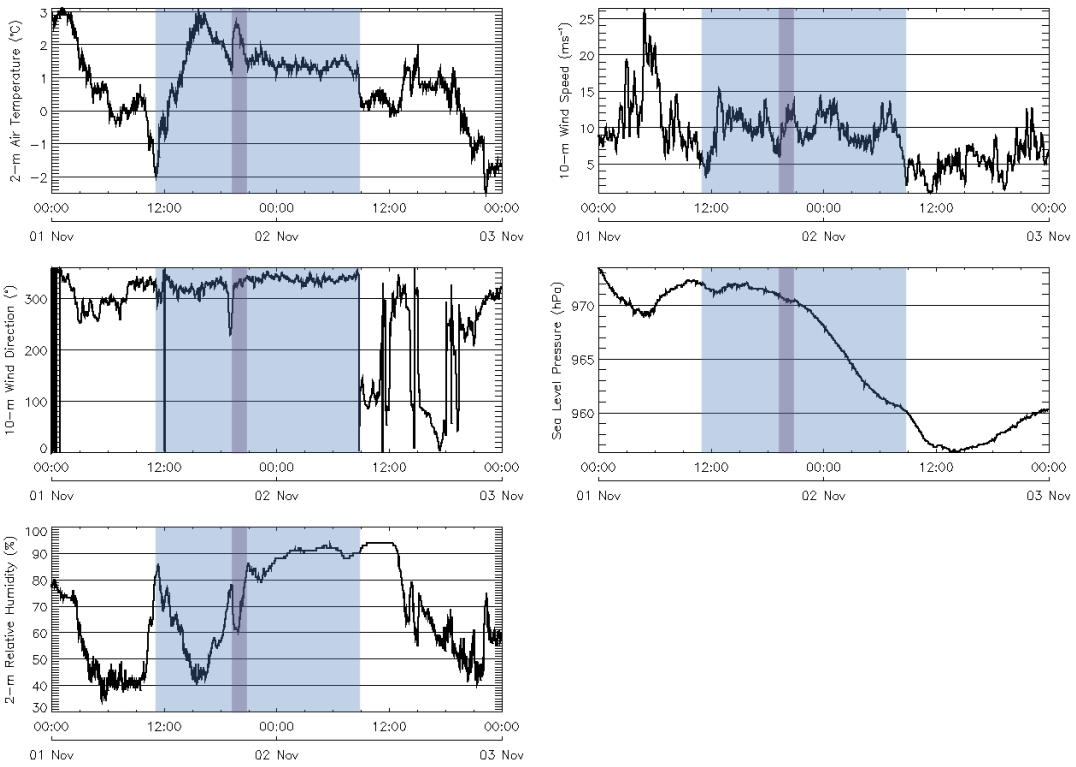

Figure 3.5 – *Meteorological conditions (2-m air temperature, 10-m wind speed, 10-m wind direction, sea level pressure, and 2-m relative humidity) during 1 – 2 November 2007. Blue shading highlights föhn event as defined and detected by the AWS föhn classification method. Purple shading highlights secondary warm event.*

Case C (Figure 3.5) is another example of an ambiguous föhn event, but one that has been included as a positive detection in the AWS föhn climatology as the föhn criteria were met. At 1120 UTC, the temperature increased by 2ºC within 1 hour, and, therefore, only just met the temperature criterion. For another 4.5 hours, the temperature continued to rise, reaching a maximum of 3.1ºC at 1541 UTC. Over the same period the relative humidity had fallen to 40%, with a concurrent gradual but small increase in wind speed. Until the end of the event, wind speeds varied between 15ms^{-1} and 5ms^{-1}. After 1541 UTC, the AWS detected a cooling and a moistening, followed by a secondary warm event at 1919 UTC (purple shading, Figure 3.5) though this does not met the temperature criterion as the increase in temperature was less than 2ºC within one hour. After this warm event, the relative humidity returned to 80 – 90%

with a mean temperature of 1.4ºC. At 0847 UTC the rapid drop in temperature marked the end of the föhn event, which is similarly marked by a turning and calming of the wind. Although this event was included as a positive detection, it clearly has a weak surface föhn-like signature, especially when compared to Case A and Case D. Diurnal changes or other wind effects may have been responsible for the initial increase in temperature at 1120 UTC. With such a weak surface signal, this may not be a föhn event. Though the end of the event is abrupt, the deepening low pressure (like Case A) may have resulted in competing air masses in the vicinity, thus resulting in a sudden drop in temperature below the monthly average. The end of the event was set at 0847 UTC 2 November due to the concurrent decrease in temperature and wind speed, along with a sudden change in wind direction. The end of this event could also have been set to 2057 UTC after the increase in relative humidity following the second warm event. This was not done because it is clear the near-surface warming remained established despite the increase in relative humidity to its pre-föhn value. The end of this occasion is clearly marked by a turning of the wind and a subsequent drop in temperature and wind speed. As highlighted in section 3.2, relative humidity was rarely used to mark the end of an event since its variability often obscured the cessation of föhn events whilst warming was still occurring.

Case D: 10 – 12 February 2011

As shown by the ERA-Interim reanalysis plots (Figure 3.2(di)), there already existed a strong pressure gradient over South Georgia before the first event was detected. The variable and easterly direction of the wind during 10 February may have been localised (via localised topographic modification) rather than a result of the synoptic-scale flow. A sudden localised shift in wind direction may have generated the föhn event, since there is no change in the synoptic situation during this time. In contrast, the second föhn event was generated by a small area of low pressure (988 hPa) tracking eastwards, south of South Georgia. The föhn event ended as the low pressure moved out of the vicinity of South Georgia, which resulted in the high pressure system moving southwards (Figure 3.2(dii)).

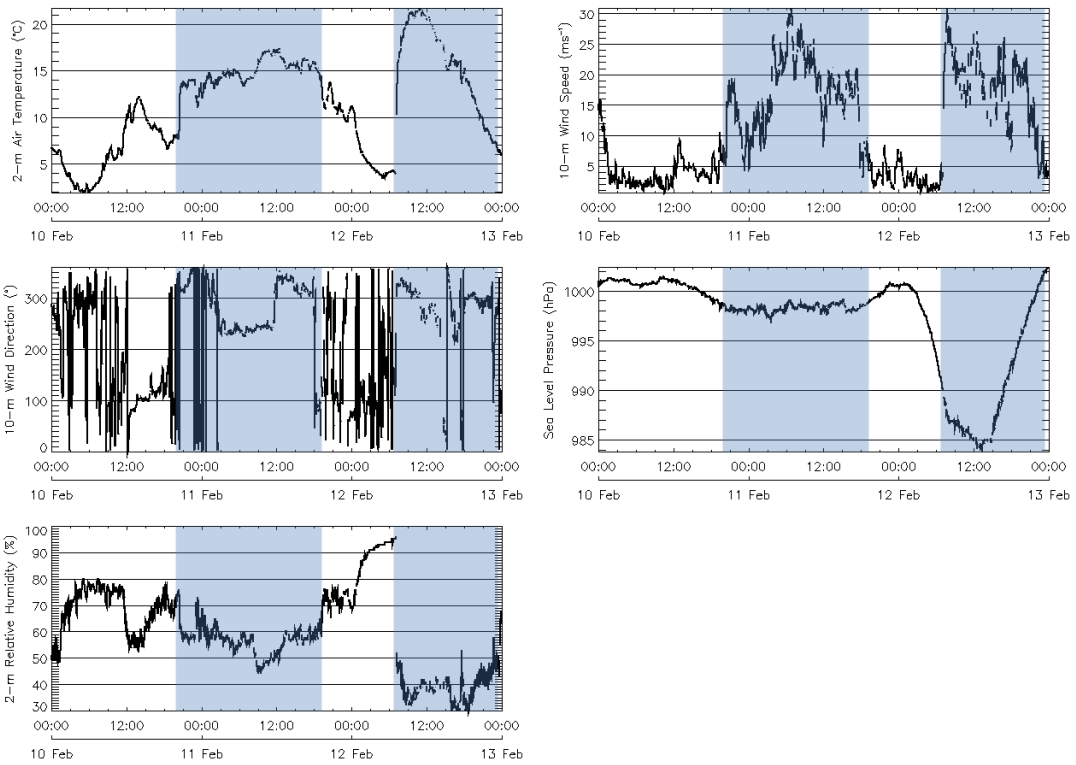

Figure 3.6 – *Meteorological conditions (2-m air temperature, 10-m wind speed, 10-m wind direction, sea level pressure, and 2-m relative humidity) during 10 – 12 February 2011. Blue shading highlights föhn event as defined and detected by the AWS föhn classification method.*

In the period of 10 – 12 February 2011, two föhn events were observed at King Edward Point, which occurred within 15 hours of each other (Figure 3.6). In both instances, the onset of föhn happened suddenly, with abrupt changes in temperature, wind speed, relative humidity and wind direction (as with Case A). The first föhn event, which had a duration lasting just less than one day (23 hours 30 minutes), was not particularly intense in terms of changes in temperature, wind speed, and relative humidity. It developed in response to a shift from easterly winds in the afternoon, to north-westerly winds, and therefore, just meets the wind direction criterion. While the wind direction varied considerably during the first hours of föhn warming, by 0300 UTC the wind had shifted to a more typical westerly/north-westerly direction, resulting in a maximum temperature of 17.3ºC. Temperatures were already elevated, due to the diurnal temperature cycle at King Edward Point. This föhn event terminated with a sudden shift to (variable) easterly winds, and was also marked by a sudden drop in temperature and wind speed, and a coincident rise in relative humidity.

While the first föhn event was not particularly intense, the second föhn event experienced a jump in temperature of 17.8°C, reaching a maximum temperature of 21.7°C, within just 3 hours of föhn onset. Of all föhn events which occurred between 2003 and 2012, this was the fifth absolute warmest event, and was also characterised with the second largest change in temperature (after Case A). This föhn event is also the tenth driest, and reached a minimum relative humidity of 27%. There is 5 minutes worth of missing data at the beginning of this event. In comparison to the start of the event, the cessation is obscure, as the temperature response appears to lag behind the drop in wind speed (similar to Cases A and C). Similarly, there is no clear abrupt drop in temperature at the end of the event. Instead, the cessation of this event was decided by the abrupt rise and fall in relative humidity and wind speed, respectively. Like Case A, both of the events which occurred during 10 – 12 February clearly fit the detection criteria and can be objectively classified as föhn events.

3.2.2 Summary

Four very different occasions characterised by surface föhn-like signatures have been shown to illustrate the variety of events experienced at King Edward Point. Each of the events described occur with abrupt temperature, humidity, and wind speed changes; though these signals do not always occur in tandem. Sometimes the surface signature is clearly föhn driven (Figure 3.3 and Figure 3.6), other times the signal is ambiguous (Figure 3.5), while sometimes the signal is unlikely to be associated with föhn at all (Figure 3.4). Although the method for föhn detection is subjective, it is clear that it is possible to use the surface AWS observations from King Edward Point to select föhn (from non-föhn) occasions. It is also clear that föhn manifests itself in a variety of ways. While the characteristics of föhn identified here are specific to King Edward Point, it is these same abrupt changes in temperature, humidity and wind speed which meant föhn could be identified at Royal Bay over 130 years ago (von Danckelman, 1884), and elsewhere across the world (Osmond, 1941; Longley, 1967; Inaba *et al*., 2002; Gaffin, 2007; Speirs *et al*., 2010; 2013; Steinhoff *et al*., 2014; among many others). Therefore, the föhn detection method described here is believed to be the most appropriate for this research, because of the type of data that is available.

3.3 Climatology of Föhn Events at King Edward Point

3.3.1 Annual Distribution and Characteristics

Using the classification of föhn events on South Georgia described earlier, a total number of 874 föhn events that produced temperature rises in excess of 2ºC at King Edward Point were found to have occurred between January 2003 and December 2012. This translates into a frequency of 7.3 events per month, or one event approximately every four days. The 874 föhn events experienced at the AWS site between 2003 and 2012 have a total duration of approximately 2 years and 356 days. With such a high frequency of föhn events, it means that King Edward Point is under föhn warming (and drying) for approximately 30% of the total time. Of all the months between 2003 and 2012, January 2004 is found to have the highest total duration of föhn conditions, whereby 70.2% (≈ 522 hours) of the month was identified as föhn. It is interesting to note that January 2004 is the equal warmest month (along with January 2009) between 2003 and 2012, as well as being the equal third warmest month since 1905, with a mean temperature of 7.7ºC.

To visualise the inter- and intra-annual frequency of föhn, Appendix 3A.1 (Figure 3.15) indicates all the days between 2003 and 2012 in which föhn was found to occur. Figure 3.15 highlights significant temporal variability and complexity in the onset and duration of föhn events at King Edward Point. May 2009 had the highest total number of events (17 events), while May 2007 had the fewest recorded events (0 events). The total number of föhn events in each month at King Edward Point for the period 2003 – 2012 is also given in Figure 3.7. This figure shows that föhn events occur throughout the year, and they exhibit little to no seasonality. March has the greatest total number of events (95 events in total), compared to April which has the fewest recorded number of events (58 events in total). The mean frequency of occurrence of föhn in any particular month is not significantly different to the annual mean frequency of 72.8 events ($p > 0.05$ for all months). Therefore, while the frequency of föhn events at other locations often exhibits a seasonal cycle (e.g. the McMurdo Dry Valleys, Speirs *et al*., 2013; and the Alps, Weber & Prévôt, 2002), there is no statistically significant annual cycle in the number of föhn events at King Edward Point.

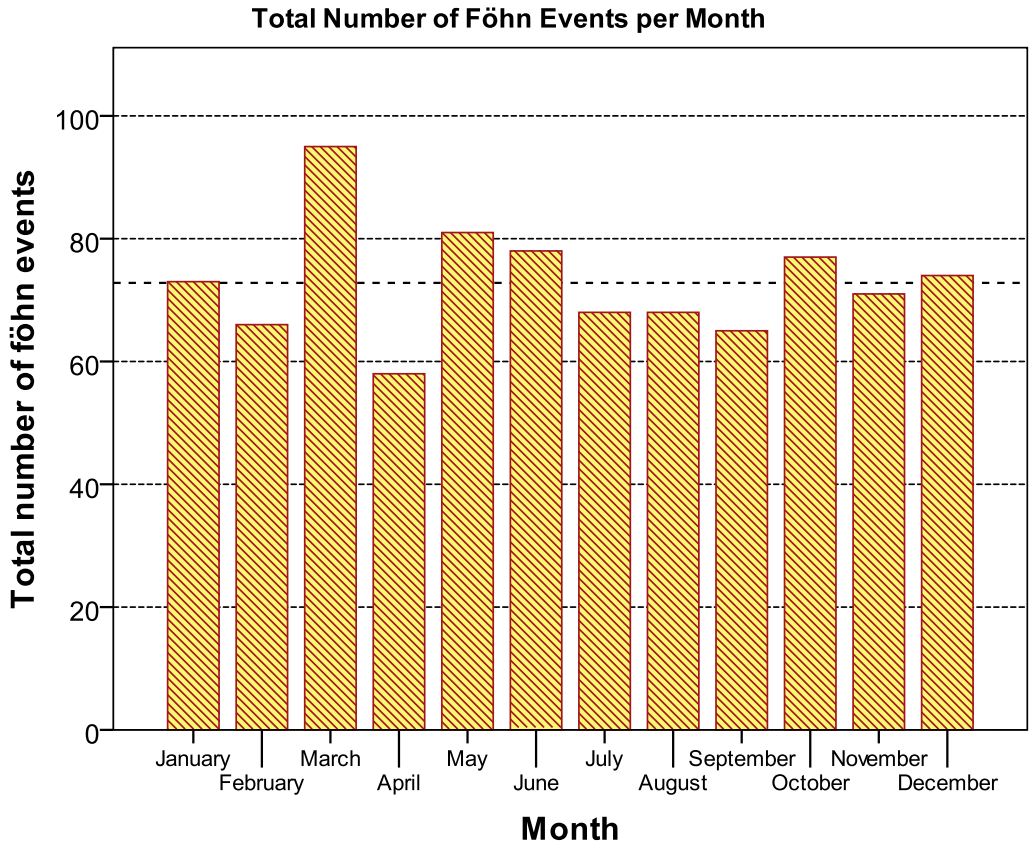

Figure 3.7 – *Total number of föhn events per month, 2003 – 2012. Dotted line represents monthly average of föhn events, at 72.8 per month.*

One might expect fewer föhn events during the winter, when the winter air over South Georgia becomes more stably-stratified. This is because deep temperature inversions in a stable air mass over King Edward Point and South Georgia will limit a descending föhn wind from reaching the leeside surface. This has similarly been found by Speirs *et al*. (2010) in the McMurdo Dry Valleys of Antarctica. At King Edward Point, however, near-surface wind speeds tend to be stronger in the austral summer. The mean wind speed recorded at King Edward Point between 2003 and 2012 was 8.9ms^{-1} (standard deviation (σ) = 6.9). During austral summer, this increases to 9.7ms^{-1}, and in winter this decreases to 8.0ms^{-1}. Since the p value is less than 0.05, the difference in the summer and winter wind speed means at King Edward Point is statistically significant at the 95% confidence level. In spite of a small change in the strength of wind speed throughout the year, King Edward Cove is not enclosed, nor is King Edward Point sheltered from the extreme weather conditions which dominate South Georgia. The prevailing winds are from the west during the entire year, meaning that the synoptic conditions are almost always favourable for the generation of föhn winds, regardless of the season.

In all seasons, föhn events can raise the 2-m air temperature above freezing. In winter this is especially important as these events have potential implications on South Georgia's mountain hydrology via increased surface melt of snow and ice. Of the 214 föhn events found to occur during austral winter, 198 of them (92.5% of cases) have a maximum observed 2-m air temperature greater than 0°C. In contrast, of the 213 föhn events found to occur during austral summer months, all 213 of them (100% of cases) have a maximum observed 2-m air temperature greater than 0°C. For the transitional seasons (austral spring and austral autumn), 213 and 234 föhn events occurred, of which 98.6% and 99.6% have a maximum observed 2-m air temperature greater than 0°C, respectively. Of all the 874 föhn events catalogued between 2003 and 2012, only 20 events do not reach (nor exceed) the freezing point of water. The mean maximum temperature reached during all 874 föhn events, during all austral summer events, and during all austral winter events was 8.9°C (Table 3.1), 12.6°C, and 4.9°C, respectively. Since strong winds over the main mountain chain of South Georgia can produce temperatures higher than 0°C at King Edward Point throughout the year, then such temperatures could promote melting of glacier surfaces elsewhere along the leeside of the island. It is likely that föhn is (at least partly) responsible for the recent observed asymmetrical retreat of glaciers across South Georgia (Gordon & Timmis, 1992; Gordon *et al*., 2008; Cook *et al*., 2010). The impact of föhn on the surface energy and mass balances on the glaciers of South Georgia is explored in Chapter 6.

	Duration (hh mm)	Max. Temperature (°C)	Temperature Change (°C)	Max. Wind Speed (ms^{-1})	Wind Speed Change (ms^{-1})	Min. Relative Humidity (%)	Relative Humidity Change (%)
Mean	29h 49m	8.9°C	7.2°C	11.9ms^{-1}	10.3ms^{-1}	40.7%	41.1%
Standard Deviation	27h 42m	4.7°C	3.1°C	6.1ms^{-1}	6.2ms^{-1}	14.1%	15.5%
Max.	192hr 0m	23.5°C	19.3°C	42.3ms^{-1}	39.6ms^{-1}	7.0%	85.0%
Min.	0hr 32m	-6.7°C	2.0°C	7.4ms^{-1}	1.9ms^{-1}	84.0%	3.0%

Table 3.1 – *Mean meteorological conditions (along with maximum and minimum values, and standard deviations) during the 874 observed föhn events which occurred between January 2003 and December 2012 at King Edward Point.*

The average characteristics, along with maximum, minimum and standard deviations (σ), of the 874 events are presented in Table 3.1. On average, the föhn events which occur at King Edward Point are 29 hours and 49 minutes in duration, and are characterised by a mean change in temperature, wind speed and relative humidity of 7.2ºC, 10.3 ms^{-1}, and 41.1% respectively. There are also occasions of very extreme and intense föhn (see Table 3.1). Föhn winds in the vicinity of King Edward Point can be characterised by anomalously high temperatures and wind speeds, and/or anomalously low relative humidity. The highest maximum temperature reached during a single event was 23.5ºC (Case A). This equated to a total temperature rise of 19.3ºC, with the event lasting 66 hours in total. The absolute driest föhn event was recorded on 16 December 2011, when the relative humidity dropped to 7% (a total drop of 85%), while the windiest föhn occurred on 30 August 2006, which reached a remarkable 42.3ms^{-1}. Föhn events were also found to occur for extended periods of time. Of the 874 events, 7% of them had a duration lasting 72 hours or more. The longest event was 192 hours (25 November – 3 October 2003, see section 3.3.2 for the reasons why such a long event may be classified). These long events are not typically characterised with especially large temperature and wind speed changes. For instance, the event that lasted 192 hours experienced a 7.4ºC warming over the entire duration of the event. This compares to a mean change in temperature of 7.2ºC ($\sigma = 3.1$) for all 874 föhn events. As detailed more in section 3.3.2, this event is likely to be a misclassification since only hourly observations were available during this event. It is very likely that the end of the event was simply not detected sooner. Of the 63 events with a duration lasting greater than 72 hours detected between January 2003 and March 2006, 46 of them (73%) were detected with the hourly AWS observations at King Edward Point. There may also be other possible forcing mechanisms that can sustain such long föhn events. For instance, alterations between westerly föhn winds and other wind regimes (e.g. competing air masses, advection etc.) may be a factor leading to the misclassification of extremely long föhn events.

While there is no observable seasonality in terms of the number of föhn events, there is a statistically significant seasonal cycle in the average duration of föhn events and the temperature, relative humidity and wind speed changes associated with them. On average, austral summer föhn events tend to be longer, with larger temperature and wind speed increases, and relative humidity drops, compared to austral winter föhn

events. The average duration of events, and the fraction of events exceeding certain temperature (11.3ºC), wind speed (24.0ms^{-1}) and relative humidity (46%) values are plotted in Figure 3.8. These values were selected since they are 1 standard deviation away from their respective mean value.

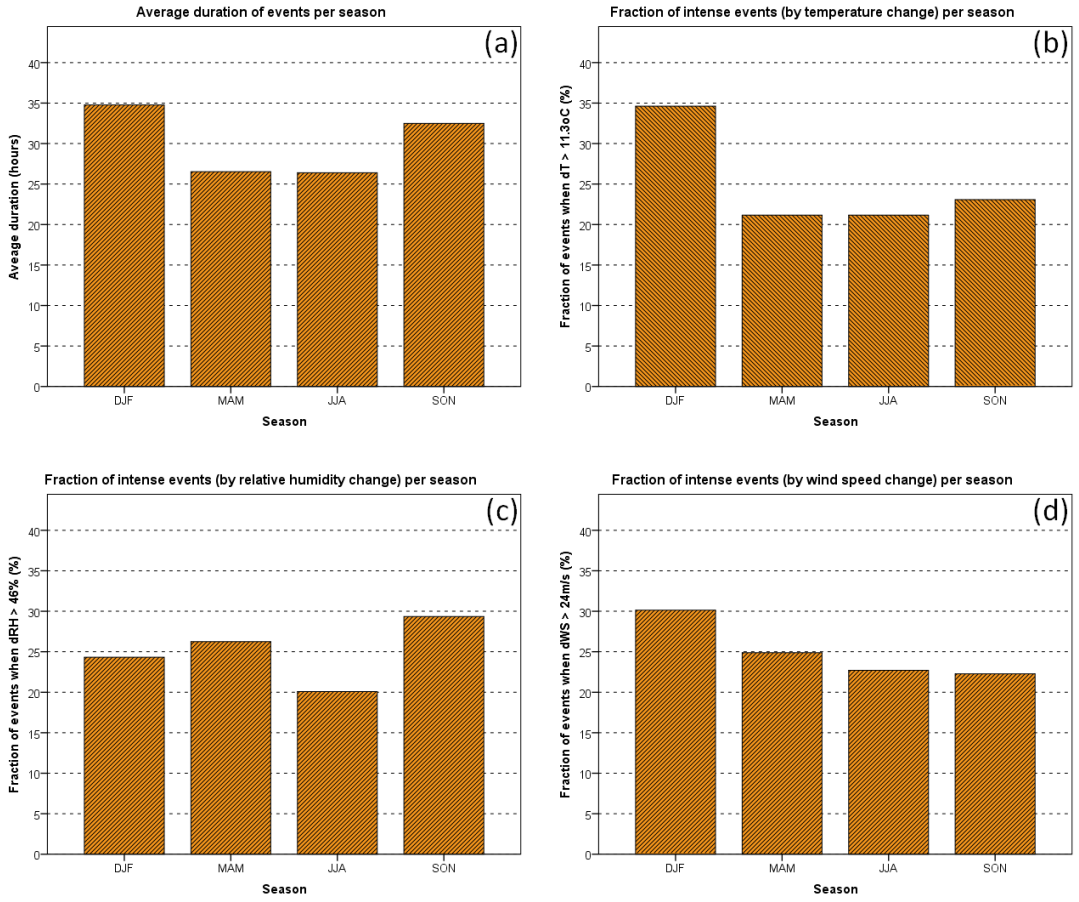

Figure 3.8 – *Panel (a) average duration of föhn events per season. Panel (b) the fraction of extreme events with a change in temperature ≥ 11.3ºC per season. Panel (c) the fraction of extreme events with a change in relative humidity ≥ 46%. Panel (d) the fraction of extreme events with a change in wind speed ≥ 24ms^{-1}.*

Figure 3.8(a) shows that föhn events are, on average, just over 8 hours longer during the summer months, than in the winter months. Variability in föhn duration is largest in austral autumn (σ = 16.3), followed by spring (σ = 15.3) and summer (σ = 15.1). Austral winter shows the least variability in frequency of föhn days compared to the other seasons (σ = 11.4). This also corresponds to a greater fraction of events with a change in temperature greater than or equal to 11.3ºC in summer (34.6%) than winter (22.2%) (Figure 3.8(b)). Similarly, 24.3% of föhn events which occur in summer have a change in relative humidity greater than or equal to 46%, compared to 20.1% in winter (Figure 3.8(c)). There are also a greater fraction of events with a change in wind

speed greater than or equal to 24ms^{-1} in summer (30.1%) than winter (22.7%) (Figure 3.8(d)). Therefore, although föhn events do not appear to be more common during the summer (Figure 3.7) they are certainly longer and more intense than they are in the winter (Figure 3.8).

This seasonality in the intensity of events may be driven by the seasonal variation in prevailing wind direction and speeds, and the larger scale atmospheric variations between winter and summer. Though, in general, the circumpolar westerlies in this region of the Southern Ocean are stronger during the austral winter season (Thompson & Solomon, 2002), it has already been shown that at King Edward Point wind speeds tend to be stronger in the summer. The gradient wind is markedly enhanced over the island from November through February (see section 5.4.3), and as such local topographic modification of the airflow within Cumberland Bay results in stronger wind speeds at King Edward Point. Since dynamical arguments suggest that stronger wind speeds promote more flow-over conditions (see section 1.6.1 for more details), it is unsurprising that austral summer föhn events at King Edward Point are more intense, compared to austral winter föhn events. For comparison, the intensification of the westerlies associated with the summer trend in the Southern Annular Mode index has been linked with an increase in the föhn effect on the eastern side of the Antarctic Peninsula (Marshall *et al*., 2006; Orr *et al*., 2008). The impact of the Southern Annular Mode index (one of the leading modes of variability which control the strength of the westerly winds in this area of the Southern Ocean, see section 1.6.3) on föhn frequency and intensity at King Edward Point is examined further in section 3.3.3.

Föhn events are also responsible for the majority of the warmest days at King Edward Point, since (potentially) warmer air brought to the surface from upper levels and adiabatically warmed will significantly influence the temperature regime of South Georgia's north-eastern slopes and coastline. Over the record examined here 85% of days with a mean temperature greater than 10^{o}C are classified as föhn days. To further illustrate the important of föhn warming on the weather at King Edward Point, Figure 3.9 presents the standardised monthly föhn anomaly against 2-m air temperature anomalies for King Edward Point. Monthly data is standardised by subtracting the 2003 – 2012 mean and dividing by the standard deviation, whereby:

$$Standardised\ Föhn\ Anomaly = \frac{(Monthly\ Mean\ Föhn\ Temperature) - (2003 - 2012\ Monthly\ Mean\ Temperature)}{Standard\ Deviation}$$

$$Standardised\ Air\ Temperature\ Anomaly = \frac{(Monthly\ Mean\ Air\ Temperature) - (2003 - 2012\ Monthly\ Mean\ Air\ Temperature)}{Standard\ Deviation}$$

The monthly mean föhn temperature is defined as the average 2-m air temperature during föhn occasions only for a specific month. This compares to the monthly mean air temperature which is defined as the average 2-m air temperature for the entire month (including föhn and non-föhn occasions) at King Edward Point. Figure 3.9 presents the monthly standardised föhn and monthly standardised air temperature anomalies.

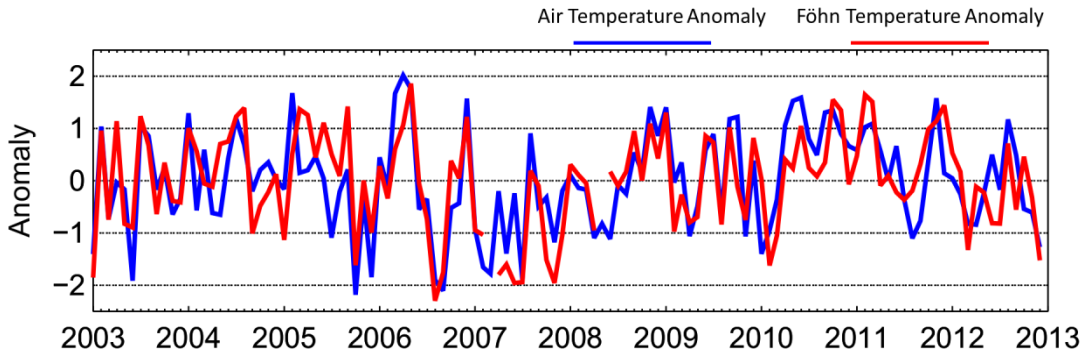

Figure 3.9 – *Monthly standardised föhn anomaly compared with the standardised air temperature anomaly (January 2003 – December 2012).*

The relationship between these anomalies quantifies the extent to which föhn warming is responsible for monthly temperatures at King Edward Point. The stronger the relationship between the föhn anomaly and the air temperature anomaly, then more of the variability in monthly temperatures can be explained by the föhn effect. The relationship between the standardised monthly föhn anomaly and air temperature anomalies for King Edward Point is statistically significant ($r^2 = 0.52$, $p < 0.05$), which is not surprising, given the persistence of föhn events at King Edward Point. The relationship is strongest during austral summer ($r^2 = 0.58$, $p < 0.05$) and weakest in austral autumn ($r^2 = 0.45$, $p < 0.05$). Since it has already been shown that föhn events tend to be more intense in summer, one would expect föhn to also have a more significant impact on air temperature at King Edward Point during this season. Therefore, it can be seen that föhn is largely responsible for temperature variations at

King Edward Point between January 2003 and December 2012. Figure 3.9 also illustrates the significant yearly variability in the föhn and temperature records.

Although there is a statistically significant relationship between monthly air temperature and monthly föhn temperature, longer föhn events do not necessarily lead to higher temperatures and winds speeds, or lower relative humidity (as is the case for the November/October 2003 event which lasted for 192 hours in total). Duration does have a highly statistically significant ($p < 0.01$) relationship with maximum/minimum temperature, wind speed and relative humidity, as well as mean change in temperature, wind speed and relative humidity, but there is overall a weak correlation, with r^2 values less than 0.24 (see Table 3.2).

Relationship with Föhn Duration	r^2 Value	Statistical Significance
Maximum Temperature	0.18	$p < 0.01$
Temperature Change	0.12	$p < 0.01$
Maximum Wind Speed	0.22	$p < 0.01$
Wind Speed Change	0.24	$p < 0.01$
Minimum Relative Humidity	0.18	$p < 0.01$
Relative Humidity Change	0.17	$p < 0.01$

Table 3.2 – *The relationship between föhn duration and observed föhn 2-m air temperature, 10-m wind speed, and 2-m relative humidity.*

Therefore, föhn duration alone cannot explain much of the variability in föhn intensity. Maximum wind speed and overall change in wind speed have the strongest relationship with föhn duration ($r^2 = 0.22$ and $r^2 = 0.24$ respectively). As such, longer events may lead to more intense events, but this is not necessarily always the case. The change in temperature and change in wind speed have a very significant but weak positive correlation ($r^2 = 0.20$, $p < 0.01$). This may be a result of stronger winds causing more turbulent mixing, with drier air from higher layers entraining into the föhn air stream and acting to increase surface temperature at King Edward Point. This relationship is stronger for winter föhn events ($r^2 = 0.60$, $p < 0.01$) than it is for summer föhn events ($r^2 = 0.20$, $p < 0.01$). Similarly, although föhn events tend to be 8 hours longer in summer than in winter, there are still a similar number of events in each season. Therefore, there is no statistically significant relationship between seasonal mean air temperature and föhn frequency in any season, in any year. It is found that the effect of föhn warming on mean temperature is consistent throughout the year.

Föhn winds are also the predominant source of strong winds at King Edward Point. Over the period of record studied here they account for 65% of days with mean wind speed $\geq 5 ms^{-1}$, and 65% of days with mean wind speed $\geq 10 ms^{-1}$. Therefore, föhn events play a significant role in controlling the overall wind and temperature regime of King Edward Point.

It should also be noted that föhn events do not always start or end in a certain part of the day. There are a large portion of events (399 events) which have a duration lasting greater than 24 hours, which are, therefore, not primarily influenced by small-scale daily variability within King Edward Cove. However, those events with a duration lasting less than 24 hours (475 events) tend to start before midday, with 56.63% events starting before 1200 UTC.

3.3.2 Inter-annual Distribution and Characteristics

Table 3.3 shows the total number of föhn events which were recorded each year between 2003 and 2012 with the surface AWS observations at King Edward Point. Clearly, the frequency of föhn events shows sporadic variation with alternating years (similarly shown in Figure 3.15). The highest number of föhn events was recorded in 2006 (103 in total), compared to 2007 which had the fewest (54 in total). On average, there are 87.4 föhn events per year ($\sigma = 25.4$). A linear least-squares fit to the data indicates a small positive trend of 2 events per year that is not statistically significant ($r^2 = 0.11$, $p = 0.36$).

	Hourly Data			**Minute Data**						
Year	**2003**	**2004**	**2005**	**2006**	**2007**	**2008**	**2009**	**2010**	**2011**	**2012**
Number of Events	75	99	73	103	54	88	95	97	99	91

Table 3.3 – *The total number of föhn events recorded each year, 2003 – 2012.*

Although it has been established that föhn events are very frequent, the short period covered by the AWS observations at King Edward Point (10 years), as well as the changes in temporal resolution of the dataset through time (see section 2.2.1), means that assessing the inter-annual variability and characteristics of föhn events is severely restricted. Figure 3.10(a) shows the total number of föhn events between 2003 and 2012 from the minute surface AWS observations at King Edward Point. Since these observations began in March 2006, there are no recorded events prior to this date. A

linear least-squares fit to the number of events during the 2006 – 2012 period indicates a small positive trend of 2 events per year that is not statistically significant ($r^2 = 0.09$, $p = 0.50$). Therefore, since 2006 there has been no significant change in the annual frequency of föhn events at King Edward Point.

To investigate the sensitivity of the detection rate of föhn events to the temporal resolution of the data further, the years with minute data (2006 – 2012) were transformed to hourly averages to reflect the data available for the 2003 – 2005 period. Föhn events were then re-classified using the original föhn identification method. The total number of föhn events between 2003 and 2012 from the hourly surface AWS observations at King Edward Point are presented in Figure 3.10(b). In this adjusted föhn climatology, 2007 still has the fewest föhn events (with a total of 42 events), while 2004 has the most föhn events (with a total of 99 events). By classifying föhn events with the same temporal dataset, it is found that the 2003 – 2005 events which have been catalogued may be longer and warmer than recorded had minute AWS observations been available for that period (see Table 3.4).

	Minute Data	**Hourly Data**
Number of Cases	874	725
Average Duration (hh/mm)	29h 49m	40h 01m
Average Maximum Temperature (°C)	8.90°C	9.29°C
Average Maximum Wind Speed (ms^{-1})	11.90ms^{-1}	10.44ms^{-1}
Average Minimum Relative Humidity (%)	40.7%	42.93%

Table 3.4 – *A comparison of the average föhn conditions during the 2006 – 2012 period using the minute (left) and hourly (right) surface AWS data at King Edward Point.*

Re-classifying föhn events using a coarser temporal resolution leads to clear and significant differences in the climatology of föhn events at King Edward Point. As shown in Table 3.4, the minute data classifies 17% more föhn events, which are on average, cooler, drier and windier than if hourly data had been used. Both the frequency and the intensity of föhn events are affected by the coarser temporal resolution of the earlier observations. As a consequence, it appears that a number of events between 2003 and 2005 may have been misclassified and/or merged into

longer, single föhn events. Given these results, the overall number of events recorded in 2003 – 2005 is approximately what one would expect given the lower temporal resolution of that part of the dataset. This explains why 73% of events with a duration lasting greater than 72 hours occur between January 2003 and March 2006. A linear least-squares fit to the number of events (using hourly data) during the 2003 – 2012 period indicates a small negative trend of 1 event per year that is not statistically significant ($r^2 = 0.04$, $p = 0.60$).

In addition to the temporal resolution of the data, it also appears that missing surface AWS observations also impact the 2003 – 2012 föhn climatology at King Edward Point. For instance, a lower than average number of föhn events were recorded in 2007. This can be attributed to the fact that during 2007 approximately 19.2% (the equivalent of ~70.1 days) of the AWS data is missing. This compares, for instance, to just 2% missing for 2012. This can be corrected for, by assuming that one föhn event occurs every four days at King Edward Point. Within the 70.1 days missing in 2007, one would expect an additional 18 events to occur. This correction suggests that 72 events would be observed in 2007 if all the data was available. Therefore, the number of events recorded in 2007 is approximately consistent with what one would expect given the amount of missing data. Missing data has been accounted for in all years between 2006 and 2012, and the expected number of föhn events during this period (along with the total number of events detected using minute observations) is shown in Figure 3.10(c) (blue shading). There is a negligible amount of missing data in the instantaneous hourly AWS observations and so no corrections regarding this have been made prior to 2006. However, the AWS föhn catalogue prior to 2006 does not contain föhn events with durations of less than one hour. For comparison, 20 föhn events occurred which had a duration of one hour or less (the average duration of all these 20 events being 46 minutes long) between 2006 and 2012. Therefore, this has also been roughly accounted for by assuming that 3 events per year occur with a duration lasting less than one hour (red shading). Figure 3.10(c) accounts for all these adjustments. Between 2006 and 2012, all föhn events detected with minute observations (i.e. Figure 3.10(a)) along with the expected number of föhn events due to missing data (blue shading) are shown. Between 2003 and 2005, all föhn events detected with the hourly surface observations (i.e. Figure 3.10(b)) along with the expected number of föhn events with a duration lasting less than hour (red shading)

are shown. A linear least-squares fit to the number of events during the 2003 – 2012 period indicates a small positive trend of 1 event per year that is not statistically significant ($r^2 = 0.12$, $p = 0.30$).

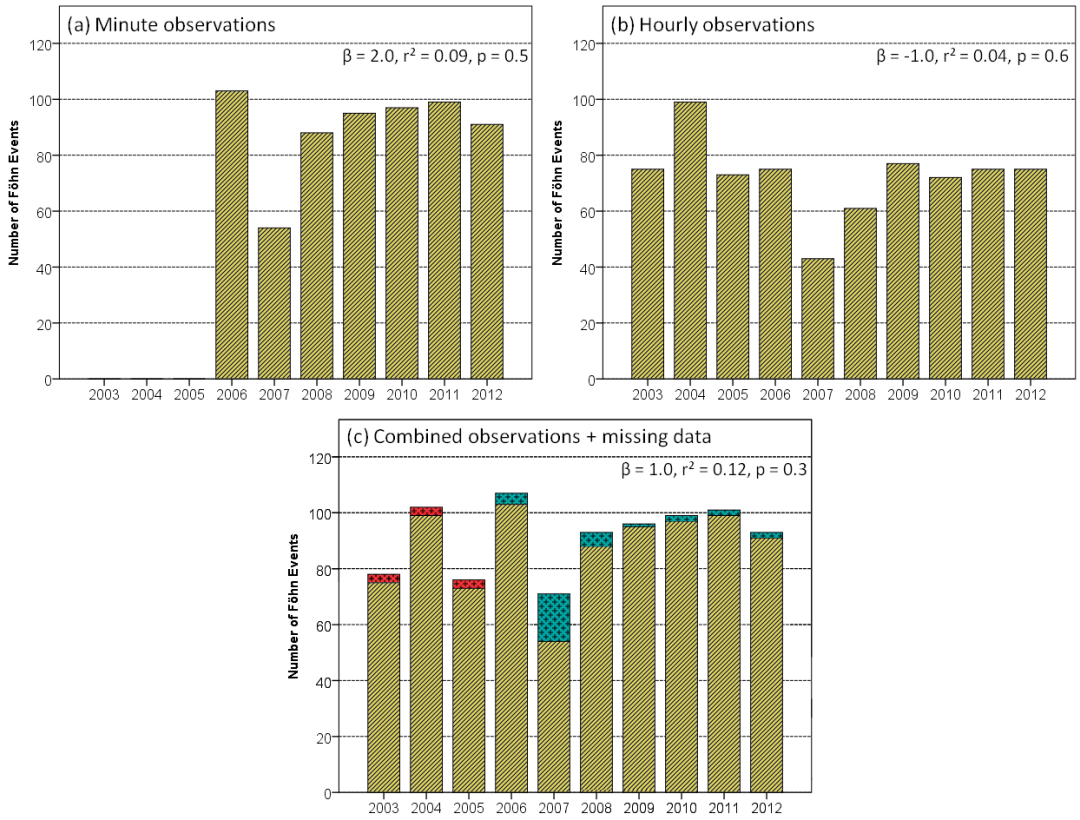

Figure 3.10 – *The annual total number of föhn events, 2003 – 2012. Panel (a), the total number of föhn events between 2003 and 2012 using minute surface AWS observations (there is no minute data prior to 2006). Panel (b), the total number of föhn events between 2003 and 2012 using hourly surface AWS observations. Panel (c), the total number of föhn events between 2003 and 2012 using both temporal (minute and hourly) surface AWS observations. Between 2003 and 2005, missing events with a duration lasting less than an hour (approximately 3 per year) are accounted for (red shading). Between 2006 and 2012, missing events due to missing data are accounted for (blue shading). The results of a linear least-squares fit to each of föhn occurrences is also given.*

While there has been no significant change in the number of föhn events since 2003 (Figure 3.10), it also appears that föhn events are not becoming significantly more intense either. The total number of föhn events exceeding certain temperature, wind speed and relative humidity values each year are plotted in Figure 3.11. Data prior to January 2006 has been discounted. As with Figure 3.8, these values were selected since they are 1 standard deviation away from their respective mean value. Relative humidity has undergone the largest change since 2006. There has been an increase of

2.5 events every year which exceed a change in relative humidity by 46% (or more). In contrast, the frequency of intense temperature events has undergone no change since 2006. None of the linear relationships are significant ($p > 0.1$ in all cases). This is not surprising, given the short observational record. Therefore, whether or not föhn events are becoming more or less is intense is difficult to quantify since variability between years is so great and because of the short record. It is an inherent problem with a short dataset which is in a remote location.

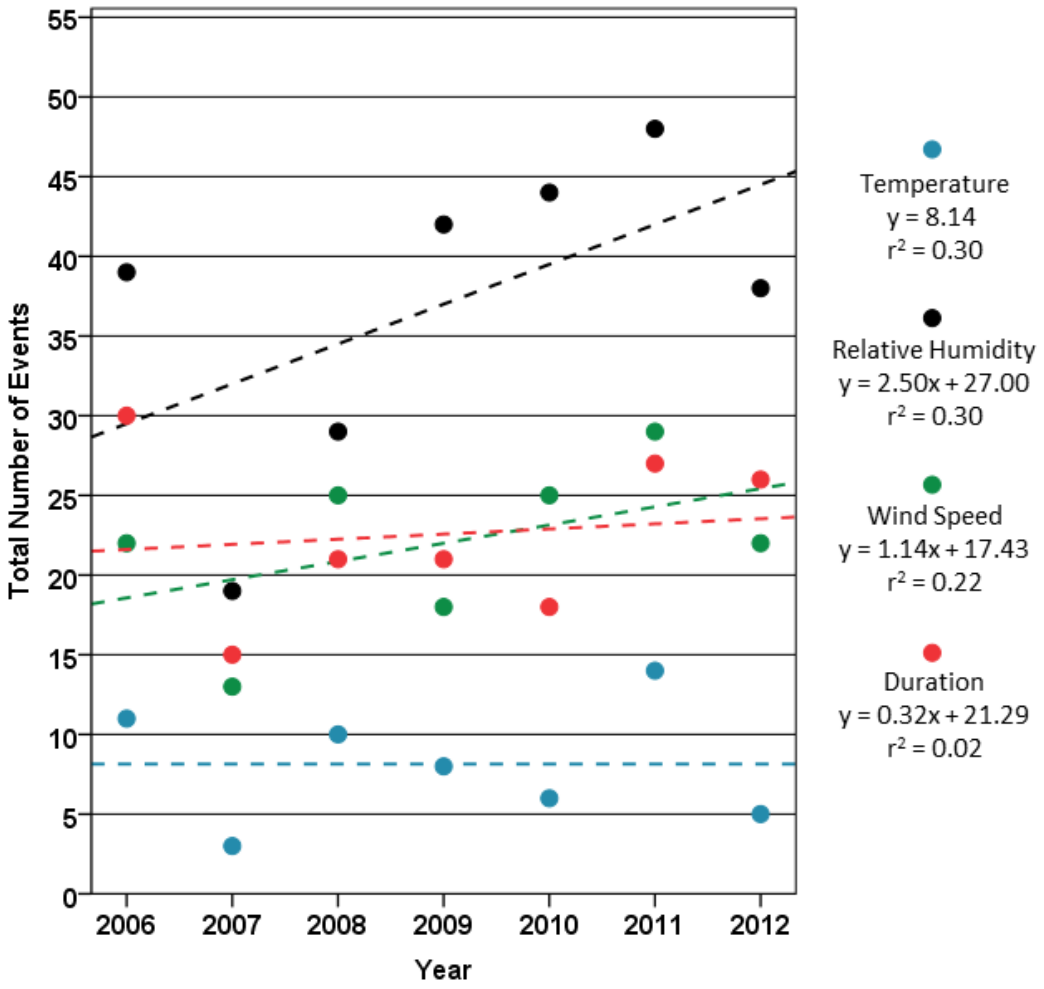

Figure 3.11 – *The number of intense föhn events per year with a change in temperature ≥ 11.3°C (blue), a change in relative humidity ≥ 46% (black), a change in wind speed ≥ 24ms^{-1} (green), and a total duration ≥ 34 hours (red).*

Although a combination of monthly and daily means, along with 3- and 6-hourly meteorological observations and data are available from Grytviken and King Edward Point since 1905, it is too discontinuous and patchy to accurately quantify the total number of föhn events before 2003. It has already been shown that high temporal

resolution datasets (i.e. minute observations) from King Edward Point are required to accurately diagnose föhn conditions, since diagnostic accuracy decreases using the coarser resolution temporal dataset. Although this data cannot be used to reliably identify föhn frequency since the beginning of the record, it can be used to identify anomalously warm and high wind speed events. Using 6-hour observations from 1959 – 1981, there were 17 instances when the 2-m air temperature was ≥20°C. Assuming each of these instances in the 22 year period was in fact a föhn event, then this frequency is consistent with the catalogued 10 föhn events (also with a maximum temperature ≥20°C) which occurred in the 10 year föhn climatology between 2003 and 2012. There were also 73 occasions when the air temperature in the record increased by greater than 10°C within 6 hours. These events could also be potentially marked as intense föhn events. As such, the lack of homogeneity in the dataset, together with its rather short duration makes it impossible to say with any certainty whether or not föhn events have become more or less frequent in the last century. However, there is a clear avenue for future work. With 110 years of meteorological data, along with other sporadic data sources (meteorological logs, AWS data and ship cruises), anomalously warm and high wind speed days could be examined in more detail. This may give an indication of how the 2003 – 2012 föhn climatology at King Edward Point relates to anomalously warm days since 1905.

3.3.3 Characteristic Large-Scale Synoptic Patterns

South Georgia is located in the Scotia Sea between the temperate climate of the South Atlantic Ocean, and the polar climate of the Southern Ocean. The region is dominated by intense westerly circulations (Figure 1.9) and is located within the main Southern Hemisphere storm track, meaning that the island continually experiences rapidly changing weather conditions (Mansfield & Glassey, 1957). Therefore, the climate of South Georgia is strongly influenced by variations in large-scale circulation over the surrounding Southern Ocean. Composite charts of mean sea level pressure can be used to look at the large-scale synoptic variations associated with strong, weak and non-föhn conditions. The European Centre for Medium-Range Weather Forecasts (ECMWF) ERA-Interim reanalysis data has been used to illustrate synoptic conditions during föhn events and hence, to examine the impact of circulation variability on the inter-annual variability in the frequency and intensity of events.

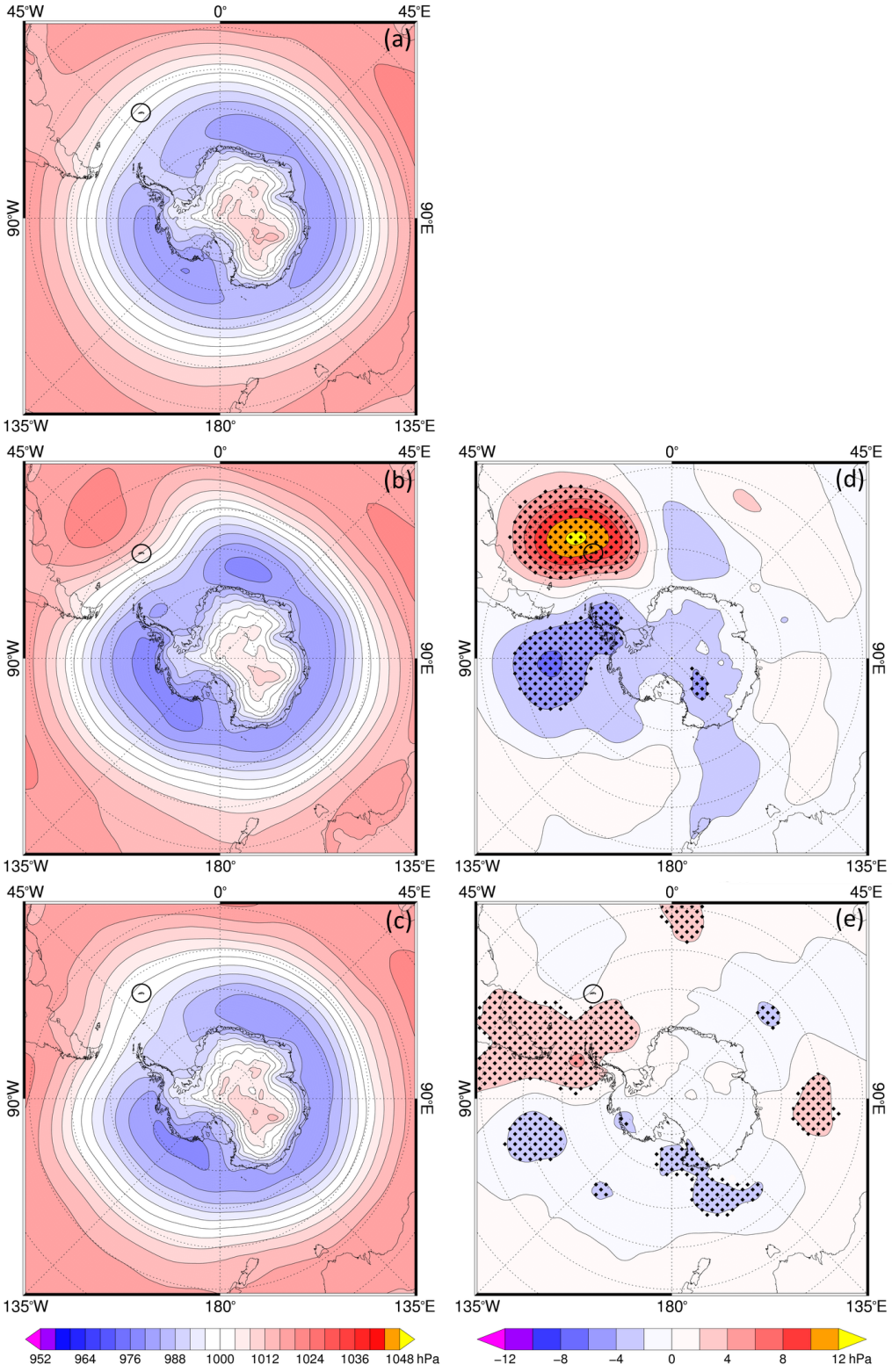

Figure 3.12 – *Panel (a) ERA-Interim composite monthly mean sea level pressure (hPa) chart (January 1979 – January 2013). Panel (b), as (a) but for 100 strong (by absolute temperature change/increase) föhn days. Panel (c), as (a) but for 100 randomly selected non-föhn days. Panel (d) difference between the climatological average and 100 föhn days. Panel (e) difference between the climatological average and 100 non-föhn days. Stippling indicates statistical significance at the 95% confidence level. South Georgia is circled in black.*

To explore the difference in the large-scale synoptic conditions between strong and non-föhn conditions, a random selection of strong föhn days was taken. As detailed previously in section 3.2, a föhn day at King Edward Point is defined as a day that experiences 6 or more hours of continuous föhn conditions. From the AWS climatology of föhn events, 100 föhn days were selected. These were the 100 strongest events which had the highest absolute temperature jumps observed in the surface AWS observations. The change in temperature of all these events is $\geq 11.3^{o}C$, with a mean of $13.2^{o}C$ (σ of mean temperature for all 100 events = 1.2). To contrast this, 100 random (roughly 8 from each month to discount any seasonal biases) non-föhn days were also selected. These days have zero hours of föhn conditions as defined by the AWS föhn classification method.

To begin with, composite maps using ERA-Interim reanalysis data for the 100 strongest (by temperature) föhn event days and the long-term climatological (January 1979 – January 2013) average field reveal the synoptic situation favourable for strong föhn events (Figure 3.12). Immediately apparent is the well-defined ridge of high pressure, roughly centred at ~40ºS 40ºW, during strong föhn conditions (Figure 3.12(b) and (d)). This feature is absent in the climatological mean (Figure 3.12(a)). Sea level pressure in the strong föhn composite is also generally lower than the climatological mean over most of the South Pacific Ocean, including the Drake Passage, the Bellingshausen Sea, and the Weddell Sea, resulting in an enhanced meridional pressure gradient over the Scotia Sea. As a consequence of this, isobars are more closely spaced in the föhn composite, implying stronger incident winds approaching the island, which one might expect to be associated with increased leeside föhn warming. However, the direction of geostrophic wind is more parallel to the main mountain chain of South Georgia for the strong föhn mean composite (Figure 3.12(b)). In comparison, the climatological and non-föhn composites show that the geostrophic wind is more perpendicular over the island (Figure 3.12(a) and (c)). This implies less cross-barrier flow over conditions during the 100 strongest föhn events, compared to the climatological mean, and this is counterintuitive. However, by definition, the AWS föhn classification method detects occasions when there are large temperature rises in the air temperature (at King Edward Point). Since the composite charts indicate parallel isobars with air coming from the direction of the South Atlantic Ocean and

Argentina, rather than the Weddell Sea, this is a strong indication that (warm air) advection events may also be detected by this method.

It has already been established that this method detects föhn events based upon their impact on the near-surface meteorological fields. Therefore, the surface föhn-like signature (i.e. increased temperature and wind speed and decreased relative humidity) may not always be solely a result of the föhn warming process. To explore this further, Figure 3.13 shows mean climatological, föhn and non-föhn vertical profiles of the wind components and potential temperature from a point (-54.492ºS, -39.496ºW) approximately 250km upwind of South Georgia (from ERA-Interim reanalysis). These profiles confirm that for the strongest föhn days, the airflow below 3km is more northerly (268º) than it is when compared to the climatological mean (260º) and the non-föhn days (253º). The vertical wind speed profiles also confirm an enhanced meridional pressure gradient over the Scotia Sea during the strong föhn days. The mean upstream Froude number (between 0.2km and 2km, see section 1.6.1 for the calculation) for the climatological mean, the 100 strong föhn days and the non-föhn days are 2.1, 2.5 and 1.3 respectively. Unsurprisingly, for the 100 strong föhn days, the potential temperature profile is 4.4K and 5.4K warmer (below 3km) than the climatological and non-föhn means respectively. Given these results, it is likely that a number of the 874 föhn events observed at King Edward Point between 2003 and 2012 are not true föhn events. We can postulate that the föhn-like signature which is frequently observed at King Edward Point is not solely due to adiabatic warming of a descending air parcel in the lee of South Georgia. It is unsurprising that a method which detects occasions of föhn by rapid surface warming also detects occasions of warm air advection, since both processes will result in observable changes in near-surface temperature and relative humidity at King Edward Point. Therefore, there are three distinct possibilities relating to the AWS föhn climatology at King Edward Point. Firstly, we could assume that all of the events detected are instances of cross-barrier flow over conditions as a result of the closely spaced isobars over South Georgia, leading to leeside surface warming. The second possibility is that, given the limited amount of observations available, an unknown number of detected events are a result of warm air advection from the north. These events should be classified as (rapid, strong or weak) warming events, and not föhn events. The third possibility is that an unknown number of the events detected are föhn events, and the surface warming

detected by the AWS observations at King Edward Point is also enhanced by warm air advection from the north. In order to improve our knowledge of the dynamics of airflow over the island and the resulting leeside föhn warming, high-resolution atmospheric modelling over a South Georgia domain would be required.

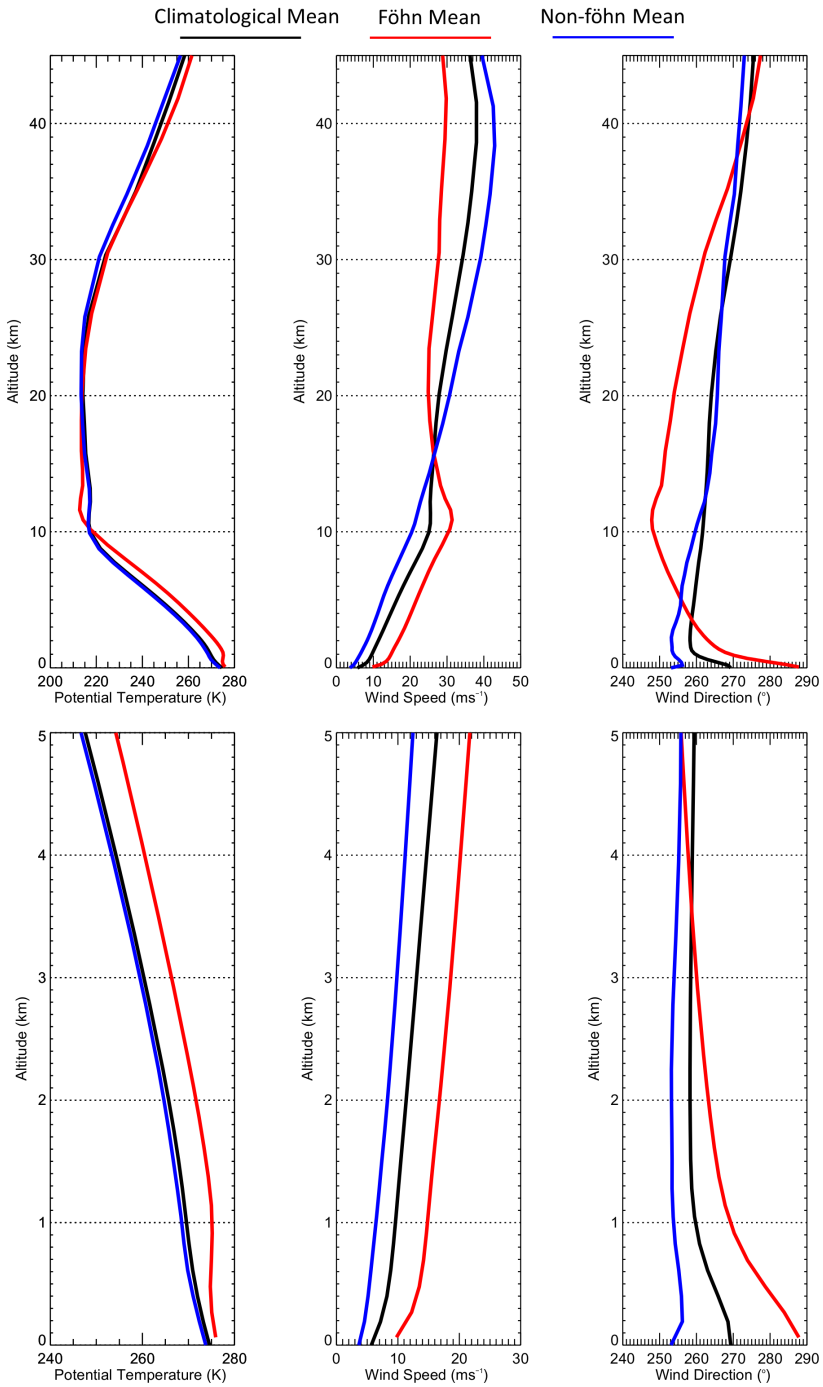

Figure 3.13 – *Vertical profiles of mean potential temperature (left), mean wind speed (middle), and mean wind direction (right) from a point upstream of South Georgia. Black line – climatological mean (1979 – 2013), red line – 100 strongest (by absolute temperature change/increase) observed föhn days, blue line – 100 random non-föhn days. Data are interpolated from 6-hourly ERA-Interim reanalysis.*

In spite of this, similar synoptic configurations (i.e. an anomalous area of high pressure in the South Atlantic Ocean, and an anomalous area of low pressure in the Weddell Sea and Pacific Ocean) are also apparent when looking at 100 strongest föhn days by an absolute increase in wind speed and an absolute decrease in relative humidity (these are not shown). There are slight differences in the positioning, extent and depth of the pressure systems, between wind speed, relative humidity and temperature anomalous charts. This is hardly surprising, since a stronger pressure gradient in the Southern Ocean will be characteristic of föhn days with higher wind speeds in the lower troposphere. Therefore, the large-scale synoptic pattern is broadly similar for all types of intense föhn days, but slight variations in the positioning and depth of the systems leads to variations in the warmth, windiness and dryness of the föhn events observed at King Edward Point. In all instances, the high pressure anomaly is roughly barotropic, while the low pressure appears to be a surface feature (not shown). In addition to this, the differences in the synoptic-scale situation are largely independent of season, and the anomalous features are persistent throughout the year (also not shown). Therefore, the characteristic synoptic flow pattern during intense föhn events is markedly different compared to non-föhn conditions. Since similar anomalous pressure patterns are responsible for intense temperature, low relative humidity and high wind speed föhn days, this gives confidence that these extreme occasions are synoptically and meteorologically related (i.e. a stronger pressure gradient over this region results in stronger wind speeds, higher temperatures, and lower relative humidities in the lee of South Georgia). Therefore, the föhn warming process is likely to be the major phenomena responsible for these near-surface signals at King Edward Point during such synoptic conditions.

To investigate whether these anomalous features have changed (i.e. whether the anomalous low and high pressure centres have weakened or strengthened) over the same period (2003 – 2012) as the AWS observations at King Edward Point, and whether such changes explain monthly and annual variations in föhn characteristics, time series of the de-seasonalised mean sea level pressure were taken from roughly the centre of the high and low pressure anomalies (~45^{o}S 45^{o}W and ~67^{o}S 45^{o}W respectively). For simplicity, the de-seasonalised pressure difference index will be referred to hereafter as the 'ABSO index', after the proximity of the respective anomaly centres to the Argentine Basin and the South Orkney Islands.

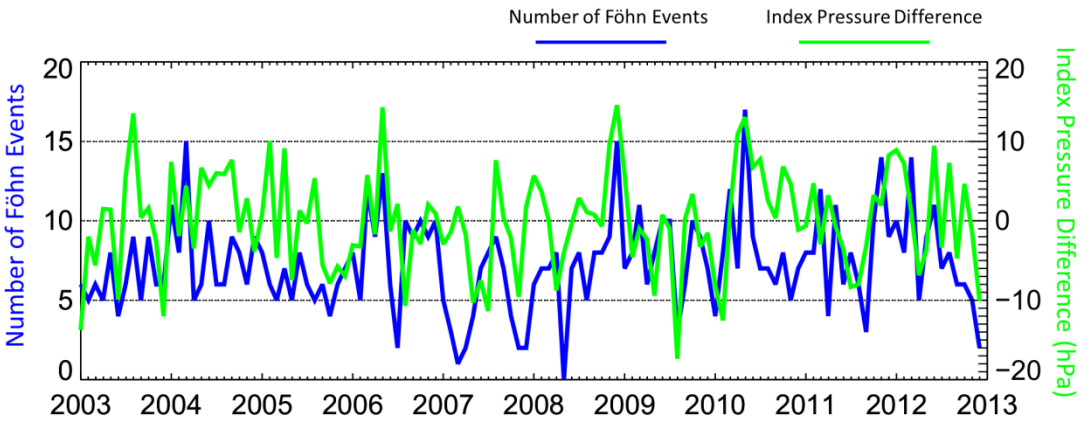

Figure 3.14 – *Monthly mean ABSO (Argentine Basin – South Orkney) pressure difference index (green line), and monthly total number of föhn events (blue line), for the period January 2003 – December 2012.*

The ABSO index indicates that there has been no significant trend in the difference in pressure between the high and low pressure anomaly centres from 2003 onwards (β = 0.007, r^2 = 0.002, p = 0.66, Figure 3.14). However, there are statistically significant correlations between monthly values of the ABSO index and föhn frequency on South Georgia. A higher pressure difference between the centres (i.e. a stronger pressure gradient over the Scotia Sea) generally leads to an increase in the number of events (Figure 3.14). This is particularly noticeable in December 2008 and May 2010, for example. Similarly, a low pressure difference between the centres (i.e. a weaker pressure gradient over the Scotia Sea) generally leads to a decrease in the number of events (i.e. August 2009 and December 2012). A linear least-squares fit of the number of events during the 2003 – 2012 period to the ABSO index indicates a small positive trend of 0.2 event per 1 hPa pressure difference that is statistically significant (see Table 3.5, r^2 = 0.17, $p < 0.01$). A high pressure difference is also is statistically correlated to a number of other föhn characteristics (Table 3.5). Therefore, a strengthening of the pressure difference across this area of the Southern Ocean could lead to more frequent and more intense föhn events on South Georgia.

Considering that the Southern Annular Mode (SAM) is known to affect synoptic circulation in this area of the Southern Ocean (see e.g. Marshall *et al*., 2004; 2006; Orr *et al*., 2008; van Lipzig *et al*., 2008), and within the latitudinal range of the ABSO index, it is also important to investigate the relationship of this teleconnection on föhn frequency and intensity at King Edward Point (see section 1.6.3 for background on the

SAM). Data pertaining to the SAM index can be found at http://www.nerc-bas.ac.uk/icd/gjma/sam.html.

	ABSO Index			SAM Index		
	r^2 Value	Corr. Coef.	p Value	r^2 Value	Corr. Coef.	p Value
Number of Events	0.17	0.41	<0.01	0.02	0.15	0.11
Mean Duration	0.00	0.00	0.95	0.01	-0.04	0.67
Mean Maximum Temperature	0.07	0.27	<0.01	0.02	0.17	0.07
Mean Temperature Change	0.07	0.27	<0.01	0.00	0.17	0.86
Mean Maximum Wind Speed	0.04	0.20	0.03	0.00	0.04	0.68
Mean Wind Speed Change	0.02	0.16	0.09	0.00	-0.01	0.83
Mean Minimum Relative Humidity	0.12	-0.34	0.02	-0.02	-0.13	0.26
Mean Relative Humidity Change	0.05	0.22	0.04	0.02	0.07	0.52

Table 3.5 – *The relationship (r^2 values, correlation coefficients, and statistical significance) between the ABSO and SAM indices and several föhn characteristics.*

In the time periods examined here (2003 – 2012), there is a weak positive correlation between the ABSO index and monthly SAM index ($r^2 = 0.35$, $p < 0.05$). However, there is a stronger positive correlation in winter months ($r^2 = 0.52$, $p < 0.05$), followed by summer ($r^2 = 0.37$, $p < 0.05$) and autumn ($r^2 = 0.30$, $p < 0.05$). The weakest relationship between the ABSO index and SAM polarity is during spring ($r^2 = 0.15$, $p < 0.05$) when compared to other months. Unsurprisingly therefore, a positive SAM index, which leads to a greater meridional pressure gradient across the Scotia Sea, is also connected with the enhancement of the ABSO index. This synoptic pattern thus *potentially* increases the frequency of föhn events experienced on the northeast side of South Georgia (e.g. Figure 3.14). During positive SAM summers, summer föhn events are seven hours shorter compared to föhn events during negative SAM summers. The opposite is true for positive SAM winters. Föhn events are, on average, five hours longer during positive SAM winters, compared to negative SAM winters. Therefore, from a process orientated view, during summer at King Edward Point, a positive SAM (and a positive ABSO index) *potentially* leads to increased frequency but decreased duration of föhn events. In contrast, in winter at King Edward Point, a

negative SAM (and a reduced ABSO index) *potentially* leads to decreased frequency but increased duration of föhn events.

Consequently, an increase in the SAM index could *potentially* lead to increased frequency and/or intensity in föhn events on South Georgia through stronger pressure gradients and stronger winds over the Southern Ocean. Already, the strength of the circumpolar westerly winds in this region of the Southern Ocean has increased. From a point upstream of South Georgia (-54.492ºS, -39.496ºW) from ERA-Interim reanalysis fields, during the period examined here (2003 – 2012), the average mountain height wind speed (~2000m) has increased by $1.2ms^{-1}$ (a linear least-squares fit to the data indicates $r^2 = 0.01$, $p = 0.30$). Therefore, on inter-annual timescales, a positive SAM, along with stronger westerly winds, would be expected to be favourable for föhn on South Georgia. However, there is no significant correlation directly between the SAM and number of föhn events directly ($r^2 = 0.02$, $p = 0.11$), nor duration ($r^2 = 0.01$, $p = 0.67$) and any of the other key föhn characteristics (see Table 3.5). Therefore, any relationship between the SAM and föhn frequency and intensity appears to be nonlinear. It is also likely that the King Edward Point AWS record is too short to examine significant trends. The Southern Hemisphere atmospheric circulation is characteristic of variations in high-frequency (synoptic and monthly) and low-frequency (inter-annual to geological) circulation patterns between the extratropics and the high latitudes. As a consequence of this, it is unsurprising that the ABSO and SAM indices cannot alone primarily explain the inter-annual variations in föhn event frequency and intensity at King Edward Point. Despite this, these results support the original hypothesis that a strengthening of the westerlies winds could enhance the föhn warming process, and this could have implications on the associated leeside warming which extends down to near-surface levels on the northeast coastline of South Georgia. If a positive SAM trend continues into the future, South Georgia could experience increased föhn frequency and/or intensity. Therefore, these results are similar to that found in other areas also affected by the SAM; see e.g. the Antarctic Peninsula (Marshall *et al*., 2006; Orr *et al*., 2008), and the McMurdo Dry Valleys of Antarctica (Speirs *et al*., 2012).

There are a number of other important patterns of variability in the atmospheric circulation of the Southern Hemisphere (e.g. the El Niño-Southern Oscillation, the Antarctic Dipole, and the Pacific-South American Pattern) which also have centres of

action surrounding the area of South Georgia (see e.g. Kwok & Comiso, 2002a; 2002b; Yuan, 2004; van den Broeke 1998a; 1998b; 2000a; 2000b; 2000c). In particular, the semi-annual oscillation (SAO) consists of a twice-yearly contraction and expansion of the circumpolar pressure trough. The amplitude and phases of the SAO is a consequence of the seasonal differences in the storage of energy between Antarctica and the surrounding ocean. The strength of the SAO shows significant variability on inter-annual to decadal time scales (van Loon *et al*., 1993; Hurrell & van Loon, 1994; Simmonds & Jones, 1998), and has also been shown to influence near-surface wind speed and temperature patterns across the high-latitude Southern Hemisphere, notably at Halley and Faraday stations (van den Broeke, 2000a), via the alteration of baroclinicity and storm activity and tracks. For South Georgia, the synoptic activity in this region of the Southern Ocean is strongly associated with the phase of the SAO (Meehl, 1991). Unfortunately, it is beyond the scope of this study to examine the influence of all these teleconnections on the inter-annual variability on föhn frequency and intensity. Therefore, this a clear area for future work; to link South Georgia's regional climate variability and changes to the variety of teleconnection effects on temperature, pressure, wind speed, precipitation and sea ice extent anomalies in this area of the Southern Ocean.

3.4 Conclusion

The föhn wind of South Georgia has been known to occur at Grytviken (Pepper, 1954; Headland, 1992), and has also been sporadically measured at King Edward Point (Mansfield & Glassey, 1957) and Royal Bay (von Danckelman, 1884). This is the first study to quantify the frequency of föhn events at King Edward Point over a 10 year period. This study has examined the typical characteristics and synoptic conditions that produced föhn events with large temperature, wind speed and relative humidity differences which were detected in surface AWS observations at King Edward Point. It should be reiterated that this study did not find all föhn events for a complete climatology, and an unknown number of events may have been missed and/or misclassified using the identification method adopted. This work adds to the body of research which has explored the föhn effect across the world's mountain regions (Richner & Hächler, 2013).

Few previous studies have investigated the occurrence and characteristics of föhn events on South Georgia, and almost nothing is known of the fundamental meteorological and synoptic processes which drive the climate and weather of this small, isolated island. Using 10 years of surface AWS observations (January 2003 – December 2012), a climatology of föhn events at King Edward Point was explored in detail for the very first time. Generally, föhn events at King Edward Point are characterised by abrupt and sudden near-surface temperature, wind speed and relative humidity changes. Föhn events are also frequently experienced at King Edward Point, with one event occurring every four days. A total of 874 events were recorded in the period of this study. As a consequence of this, King Edward Point is under föhn influence for approximately 30% of the total time. Therefore, föhn events are a major part of South Georgia's climate system. These events frequently raise the winter air temperature above freezing, and they also constitute the majority of the warmest and windiest days experienced at King Edward Point. The föhn events observed by Mansfield & Glassey (1957) at King Edward Point are consistent with the events characterised here. There is no significant trend in seasonal number of föhn events, but föhn events tend to be longer and more intense in austral summer months. Strong föhn events are statistically correlated with strong synoptic forcing associated with high pressure in the South Atlantic, and low pressure systems in the Weddell and Scotia Seas. The results indicate that these atmospheric features cause strong pressure gradients and synoptically forced westerly winds across the Salvesen and Allardyce Ranges, causing strong downslope and adiabatically-warmed föhn winds. Being situated in an area of strong westerly winds, therefore, (and in an area climatologically favourable for such synoptic systems to develop), high föhn event frequency is correlated to such activity. Due to the short record, it is impossible to conclude whether föhn events are becoming more or less frequent and/or intense. In spite of this the results support the hypothesis that, with an increase in the SAM index and westerly wind speeds, King Edward Point could experience more frequent and intense föhn events in the future. Despite the limitations of this method, the föhn detection method described here is believed to be the most appropriate for this research, because of the amount and type of data that is available. While it is purely dependent on the surface conditions and changes that may or may not be directly associated with föhn warming, such a classification system is currently the only way to construct a climatology of föhn events at King Edward Point.

Owing to the lack of meteorological data in this region, it is clear that future work is required to understand how the drivers of variability could impact föhn event frequency. Future observational and modelling studies combined with longer meteorological records will provide more detail on the dynamics of föhn winds in this area. It also remains to be seen whether föhn events are experienced along the entire length of the lee coast of South Georgia. While it has been shown that föhn winds are frequent at King Edward Point, it is unknown what role they play in the overall wind and temperature regime of the entire island. It would be of great interest to determine whether the recent observed asymmetrical retreat of glaciers across South Georgia is linked to the föhn warming process. To understand this, high-resolution atmospheric modelling over the South Georgia is needed as a proxy for observations.

3A.1 South Georgia's Föhn Barcode

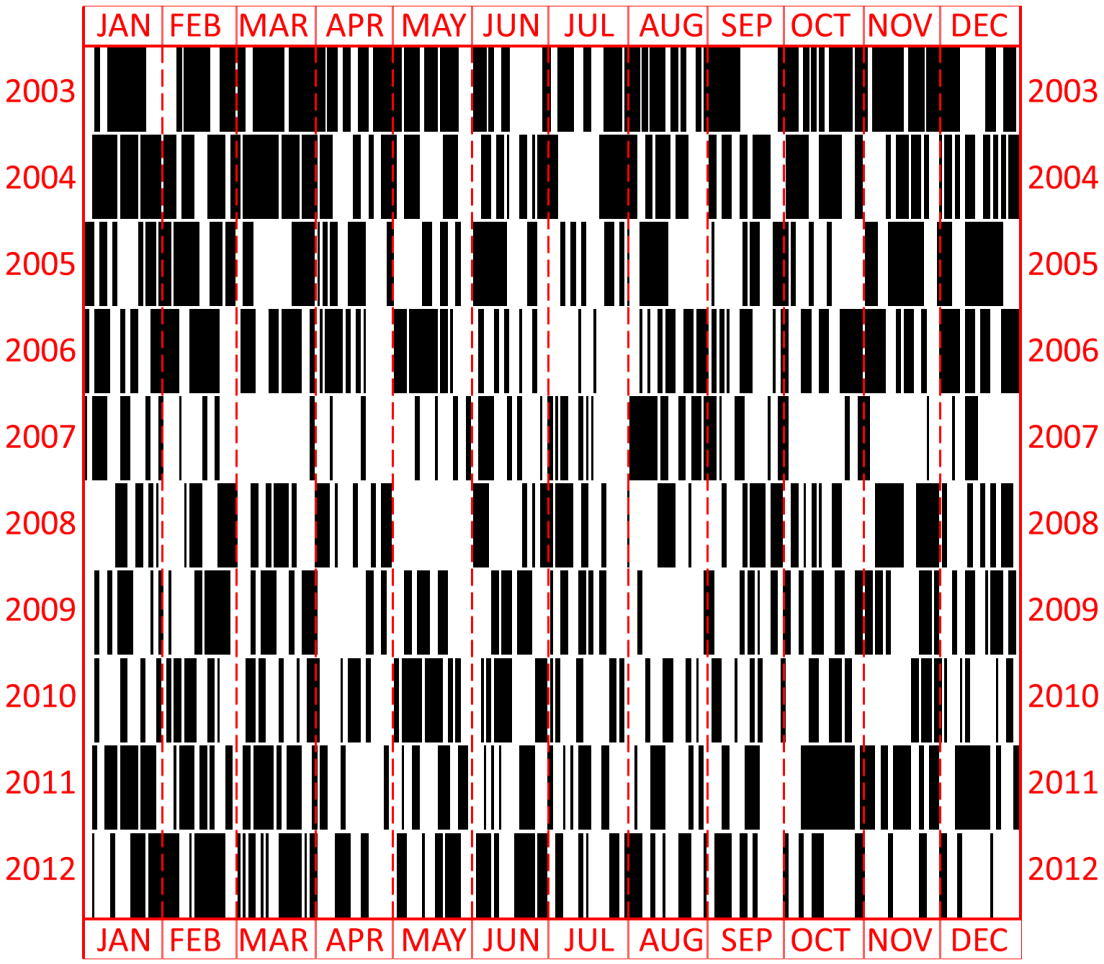

Figure 3.15 – *The days in each month in which föhn occurs at King Edward Point, from 2003 – 2012. Note: all the days in which föhn occurred (whether that was for 1 minute or 24 hours in duration) are marked by a black bar. The black bars do not indicate the previously defined 'föhn day' in section 3.2. The number of black bars does not equate to 874 föhn events.*

Chapter Four: High-resolution Weather Research and Forecasting Model (WRF) Simulations of Föhn Events at King Edward Point

4.1 Introduction

Atmospheric modelling has long been used to understand föhn flow features, structure and dynamics in the absence of *in situ* meteorological data (see e.g. Zängl, 2002; Jaubert & Stein, 2003; Lothon *et al*., 2003; Drechsel & Mayr, 2008; Speirs *et al*., 2010; Steinhoff *et al*., 2013; 2014; Elvidge *et al*., 2014a, 2014b; Grosvenor *et al*., 2014; among many others). Since the results from Chapter 3 were specific to King Edward Point, atmospheric model simulations are needed to explore the characteristics, features and dynamics of South Georgia's föhn events more extensively. Therefore, the main aim of this chapter is to present a verification of high-resolution föhn simulations with the Weather Research and Forecasting (WRF) model over a South Georgia domain, and to validate the skill of the simulations with automatic weather station (AWS) observations, and when possible, radiosonde profiles and lidar measurements. WRF is an advanced mesoscale atmospheric model and is capable of simulating atmospheric processes with very high spatial and temporal resolution. Numerous sensitivity studies were conducted for four different föhn case studies. The model's sensitivity was tested by changing the horizontal and vertical resolution, as well as improving the model topography and land surface type, in addition to changing the model's physics and planetary boundary layer schemes. The key aim of this chapter is to obtain the most realistic interpretation of föhn on South Georgia through optimising the WRF model for King Edward Point.

The chapter begins with an overview of the data and methods employed, including information pertaining to the WRF sensitivity simulations, the AWS at King Edward Point and the January 2013 field campaign. The results of the sensitivity simulations for each case study are then presented individually, and some of the key large- and small-scale features associated with föhn flow over South Georgia are discussed. Based on the results, the optimal model setup which gives the most realistic interpretation of föhn at King Edward Point is then selected.

4.2 Data and Methods

4.2.1 The WRF Model

A detailed description of WRF, the mesoscale numerical weather prediction model used in this study, including datasets, domains, model physics parameterisations, and modifications to the topography and land surface datasets, has previously been given in Chapter 2 (see section 2.3). A very brief summary of this will be given here.

A sensitivity case study approach was adopted to assess the model's performance in capturing föhn events. A number of model simulations were conducted for a series of föhn case studies to evaluate the accuracy of the model against available observations. The sensitivity of the model to topographic height and land surface type (section 2.3.1.1), vertical and horizontal resolution (section 2.3.1.2), planetary boundary layer scheme (section 2.3.1.3), microphysics scheme (section 2.3.1.4), longwave and shortwave radiation scheme (section 2.3.1.5) and land surface model (section 2.3.1.6) were all tested. All simulations were given a spin-up time of 24 hours. Details of all the sensitivity simulations conducted can be found in Table 2.2.

Domain Configuration	**Baseline Simulation (coarse-resolution)**			**High-resolution Simulation**			
Horizontal Resolution	*Outer*	*Middle*	*Inner*	*Outer*	*Middle*	*Inner*	
	30km	10km	3.3km	8.1km	2.7km	0.9km	
Location of Model Timeseries	King Edward Point			King Edward Point			Hestesletten

Table 4.1 – *A summary of the baseline and high-resolution domain setups.*

To summarise (see Table 4.1), the baseline simulation (see section 2.3.1.2, Figure 2.8) refers to the coarse-resolution domain configuration (30km – 10km – 3.3km), with the default WRF namelist model setup. All sensitivity simulations are relative to the baseline simulation. The high-resolution simulation (see section 2.3.1.2, Figure 2.9) refers to the 8.1km – 2.7km – 0.9km nested domain configuration, with the default WRF namelist model setup. The 3.3km and 0.9km domains are the innermost domains for each configuration. As previously highlighted in section 2.3.1, the model is also validated using data extracted from a grid cell representative of Hestesletten (extracted from the 0.9km resolution domain only). This grid cell was selected instead of vertically interpolating the King Edward Point model timeseries to the height of the

AWS. Hestesletten is also a water-bordering grid cell, with an elevation of 4m above sea level (the same as the height of the surface AWS at King Edward Point), and 2 grid cells directly south of King Edward Point in the WRF model. See Figure 2.1 or Figure 3.1 for a geographical reference to Hestesletten.

4.2.2 Surface and Vertical Observations and Measurements

Additional detail of the AWS at King Edward Point and of the radiosonde and lidar observations made during the 2013 field campaign can be found in Chapter 2. The AWS fields (2-m temperature, 2-m relative humidity, 10-m wind speed and direction) are validated against the model equivalent, and are interpolated to a location representative of King Edward Point (and when stated, Hestesletten). Since the WRF model output is every 1 hour, the hourly instantaneous values from the AWS observations are used in the validation process.

In addition to the 874 föhn events found to occur between 2003 and 2012, a further 12 föhn events were observed and detected in the King Edward Point AWS observations during January and February 2013. Of these events, only 6 occurred during the radiosonde and lidar deployment, and the event on 5 February 2013 (Case 1) is the only event to be fully observed by three different measuring systems (the surface AWS observations, the radiosonde profiles, and the lidar system). Case 1 was also the absolute warmest, windiest and driest of these 6 events. The 5 February 2013 event was declared to be an intensive observation period (IOP) due to the strong south-westerly flow over the island, and as a result, radiosondes were released approximately every 3 hours (0857, 1200, 1515, 1754, 2044 UTC) from King Edward Point Research Station. One sonde was launched prior to the event starting and an additional 4 others were launched during the event (see Figure 2.4). The trajectories of all 5 radiosondes are presented in Figure 4.1. Each of the radiosondes had a horizontal range of approximately 80km, and a bursting altitude of 30 – 35 km. The mean ascent rate for the five radiosonde launches was 5.2ms^{-1} (≈ 1024 ft min^{-1}). The lidar was collecting data continuously through the event. See section 2.2.2 for full details on the field campaign.

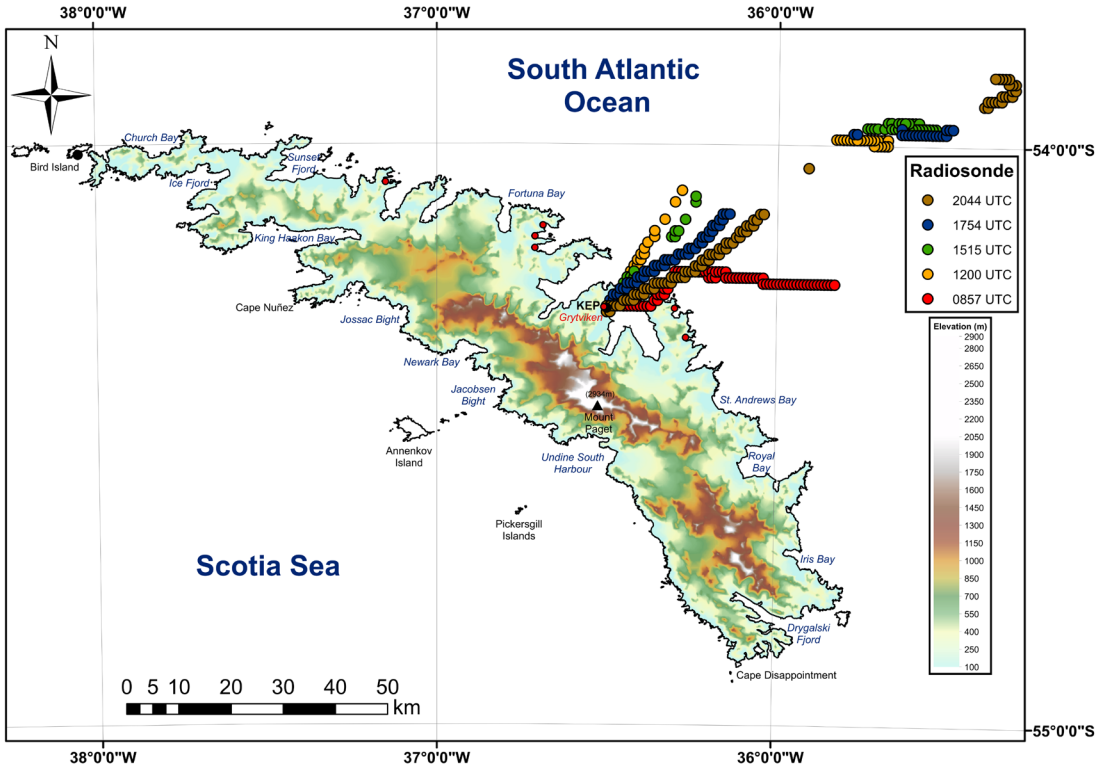

Figure 4.1 – *Ascent trajectories of the 0857 (red), 1200 (orange), 1515 (green), 1754 (blue), and 2044 (brown) UTC radiosondes on 5 February 2013. There is missing data between ~8 and ~20km for 4 of the sondes due to the balloons being in the shadow of Mount Duse which resulted in the loss of telemetry with the ground station.*

To assess how well the WRF model represents the vertical structure of the atmosphere, comparisons with radiosonde and lidar observation were conducted. To account for horizontal drift of the radiosonde, data from the WRF model were temporally and spatially interpolated to the sonde location. Although the 12 events which occurred during January and February 2013 were not included in the climatological analysis of föhn winds in Chapter 3, the 5 February event has been selected as a case study since it occurred during the January 2013 field campaign at King Edward Point when additional validation data were available.

4.2.3 Föhn Event Case Studies

In addition to Case 1 (5 February 2013), an additional three contrasting cases have been selected from the catalogue of 874 events (January 2003 – December 2012) for further investigation and validation with the WRF model. These case studies were chosen to determine the optimal model setup for a 21 month simulation (see Chapter 5). The four cases provide a representative selection of strong and weak instances of föhn at King Edward Point. They all have a duration of less than 24 hours, which

makes these events well suited for short, high-resolution WRF simulations. The case studies selected for investigation are as follows:

- Case 1: 5 February 2013
- Case 2: 9 – 10 August 2012
- Case 3: 1 – 2 November 2007 (also Case C, Chapter 3, see section 3.2.1)
- Case 4: 10 – 12 February 2011 (also Case D, Chapter 3, see section 3.2.1)

It is important to note that Case 3 and Case 4 in this chapter are the same föhn events described in Chapter 3 as Case C and Case D (respectively). Note Chapter 3's Case A was not selected for this study due to no relative humidity data. Case B was also not selected since it is not defined as a föhn event using the föhn identification criteria of Chapter 3.

Therefore, the four case studies which have been selected here (Cases 1 to 4) are fully captured in the AWS observations at King Edward Point, and they also provide a good range of föhn characteristics to optimise and test the model with. In particular, each of the four case studies display varying degrees of temperature, wind speed and relative humidity intensities (e.g. typical, weak or intense), and therefore, are a good sample of all the events found to occur at King Edward Point. Each of the four case studies is explored and investigated separately. Comparisons between observed and modelled key diagnostic fields (2-m air temperature, 10-m wind speed, 10-m wind direction, and 2-m relative humidity) are presented for each case study in an effort to determine the best model setup which gives the most realistic interpretation of the föhn event. Details of the fine- and large-scale flow structure and the dynamics of the events are also explored through vertical cross-sections and plan views of South Georgia.

4.3 Case 1: 5 February 2013

4.3.1 The Evolution of Case 1: Observations and Measurements

On 5 February 2013, a föhn event was recorded in the AWS observations at King Edward Point (Figure 4.2). The leeside warmth and dryness associated with the föhn effect was also observed in the radiosonde profiles (Figure 4.3), while increased vertical wind speeds (directed towards the surface) were measured by the lidar system (Figure 4.4). This case study is a typical example of föhn at King Edward Point, with

the characteristic signature of surface warming, increased wind speeds and surface drying. In the context of all the föhn events which were observed between January 2003 and February 2013 (i.e. all 874 catalogued events plus those which occurred in early 2013; 886 events in total), Case 1 is the 131st absolute warmest event, the 165th driest event, and the 338th absolute windiest event. The progression of the event as seen in the observations will now be described.

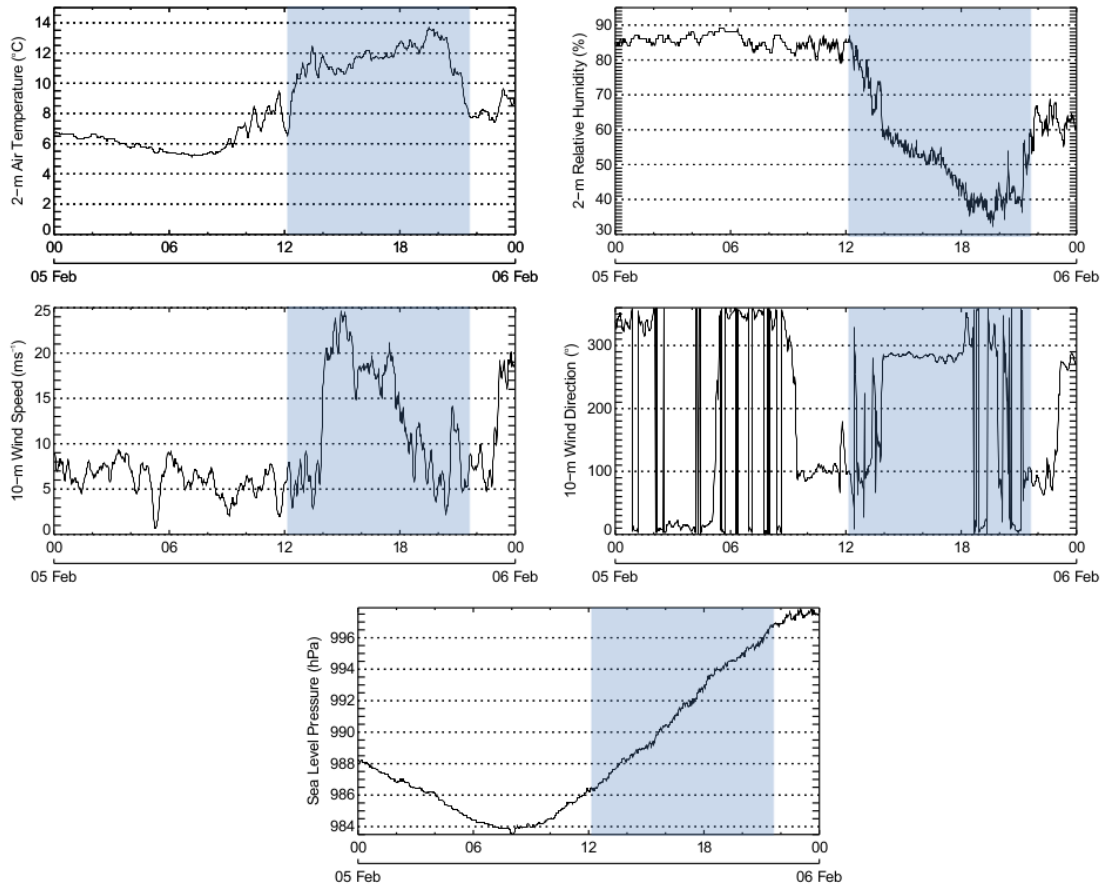

Figure 4.2 – *Meteorological conditions (2-m air temperature, 2-m relative humidity, 10-m wind speed, 10-m wind direction, and sea level pressure) during 5 February 2013. Blue shading highlights föhn event as defined and detected by the AWS föhn classification method.*

The morning of 5 February 2013 was calm and relatively mild (Figure 4.2). There was a moderate breeze with a mean wind speed of 6.1ms^{-1} until 1200 UTC. The air temperature remained around 6ºC up until 0900 UTC, when it slowly began to increase due to the diurnal variation of incoming solar radiation. Up until 0900 UTC, the mean wind direction recorded by the AWS was 359º, before becoming easterly for 3 hours. The first radiosonde (0857 UTC) was launched before the event was detected in the AWS observations, and shows a stable (morning) inversion layer at ~925 hPa (at the

height of Mount Hodges), very low wind speeds at the surface (<2ms^{-1}) and a strong north-westerly wind direction below 5km (Figure 4.3). The lidar system also detected weak negative vertical velocities below 1000m during the morning of 5 February (Figure 4.4), reaching -2.1ms^{-1} between 0600 and 0700 UTC. This may be evidence of a morning downslope valley wind into King Edward Cove, which developed under the clear and calm conditions on the morning of 5 February. Morning valley winds in King Edward Cove have not previously been measured or observed in great detail (Mansfield & Glassey, 1957; Headland, 1992).

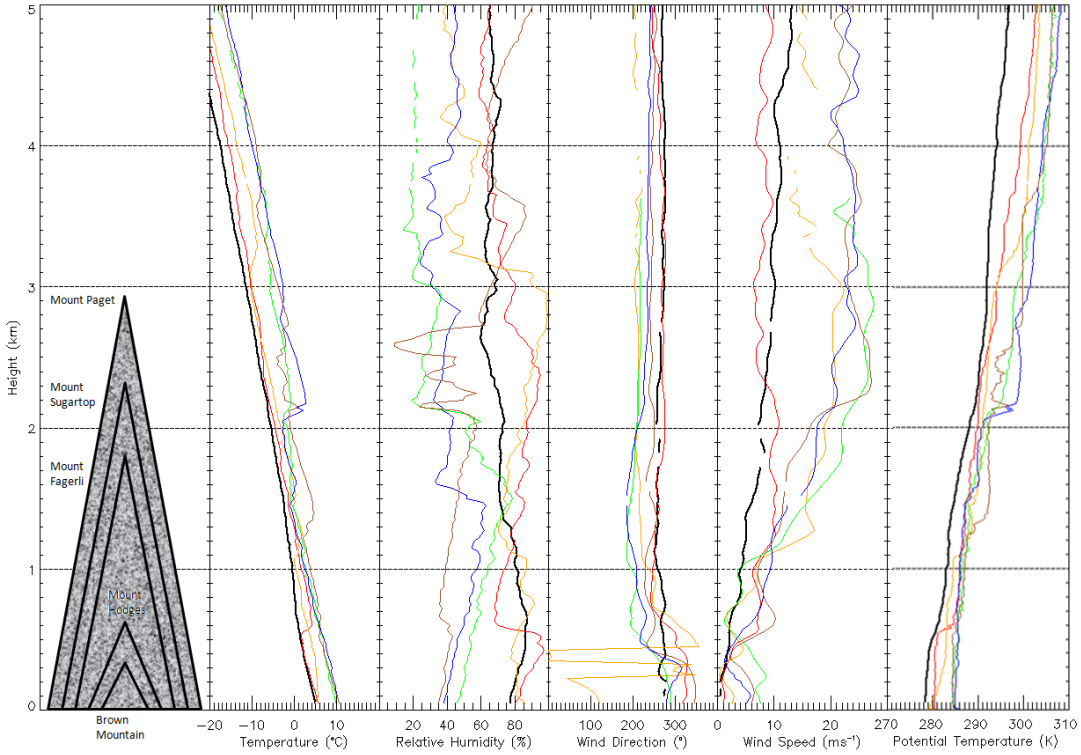

Figure 4.3 – *Vertical air temperature, relative humidity, wind direction, wind speed, and potential temperature profiles of the 0857 (red), 1200 (orange), 1515 (green), 1754 (blue), and 2044 (brown) UTC radiosondes launched during 5 February 2013. The solid black line is the mean synoptic sounding of radiosondes during non-föhn episodes between 23 January and 3 February 2013 (21 sondes in total). For vertical reference, the peak heights for Mount Paget (2934m), Mount Sugartop (2323m), Mount Fagerli (1880m), Mount Hodges (633m) and Brown Mountain (332m) are also plotted.*

The start of the föhn event was detected at 1210 UTC in the surface AWS observations (blue shading, Figure 4.2). Within 1 hour of föhn onset, the air temperature at King Edward Point had increased by 4.9ºC. The start of the event was also marked by a simultaneous decrease in relative humidity (a fall of 16% in 1 hour), and a (albeit delayed) increase in wind speed (of just ~6ms^{-1} in 1 hour). The average wind direction

at King Edward Point during the event was 297°, though it was somewhat variable during the start and end of 5 February. This was likely a result of small-scale local topographic modification of the air flow within King Edward Cove. This also accounts for the variable and weak surface wind speeds at the beginning and at the end of this event. The second sounding was launched at 1200 UTC. Since this sonde was launched right at the start of the event, the föhn signature is not discernible in this sounding when compared to the next three profiles (Figure 4.3). The 1200 UTC sounding shows that the morning inversion layer had lifted and weakened to ~870 hPa. Although the wind speed profile shows that air flowing over the island had now increased in the order of 5 – 10ms^{-1}, the air was still cool and humid. The low-level wind direction varied greatly and is consistent with the surface AWS observations at the same time. The lidar system also detected the start of the event, and confirms that descending föhn flow from mountain height towards the surface (i.e. King Edward Point) had commenced. This is shown by the large area of negative vertical velocity from (approximately) 1200 UTC onwards (Figure 4.4).

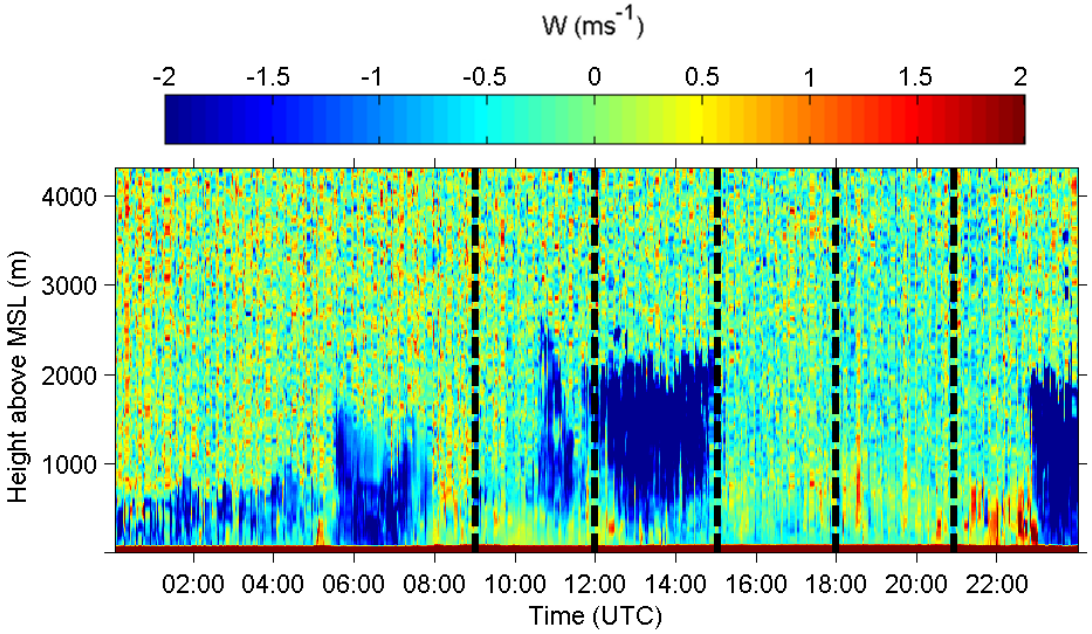

Figure 4.4 –*Vertical velocity signal at King Edward Point as measured by the lidar system during 5 February 2013. Negative values indicate air moving towards the surface, and positive values indicate air moving upwards from the surface. Black dashed lines indicate time of 0857, 1200, 1515, 1754 and 2044 UTC radiosonde launches.*

The lidar system shows continued descending flow from mountain height towards the surface (i.e. King Edward Point) during the event, which reached speeds in excess of

-8ms^{-1} at ~1500m above sea level at the height of the event (Figure 4.4). The ability of the lidar system to provide measurements is dependent on the amount of particulates and aerosols in the atmosphere. The decrease in atmospheric backscatter which occurs at approximately 1400 UTC (not shown), which also coincided with the end of the negative vertical velocity signal (Figure 4.4), does not necessarily mark the end of the descending föhn air. This is also associated with a concurrent change in wind direction as shown in the AWS observations. It may be that the change in wind direction indicates cleaner air from this direction which does not contain enough aerosols to backscatter the lidar signal. Generally, particulates are contained within the boundary layer and the air above is usually cleaner. It does not mean that the strong downdraughts were no longer observed (or taking place) at King Edward Point, nor that föhn had ceased.

The maximum temperature and wind speed recorded by the surface AWS observations during the event were 13.7^{o}C and 24.7ms^{-1} respectively (the highest measurements of the day), while relative humidity reached a minimum of 32%. Figure 4.5(a) shows a Moderate Resolution Imaging Spectroradiometer (MODIS) image over South Georgia during the middle of the event, at 1645 UTC on 5 February 2013. A corresponding photograph taken at 1730 UTC looking towards Mount Paget from Hope Point (~300m east from King Edward Point Research Station) is also presented in Figure 4.5(b). The satellite image clearly shows an extensive cloud free region, which extends from the mountain tops to ~200km downwind of South Georgia. This cloud free region is a direct result of the descending warm, dry and unsaturated föhn air in the lee of South Georgia, and is commonly referred to as a föhn gap (Richner & Hächler, 2013). The impact of föhn many kilometres downstream of a mountain barrier has also been found by Hoinka (1985b), Elvidge *et al*., (2014a), and Bannister & King (2015). Figure 4.5(a) also shows a train of mountain waves propagating north-eastwards from the island as a result of the cross-barrier flow. Alexander *et al*. (2009) and Vosper (2015) have previously found that mountain waves are very frequent above South Georgia in the presence of strong westerly winds. The area surrounding and upstream of the island is clearly masked in cloud.

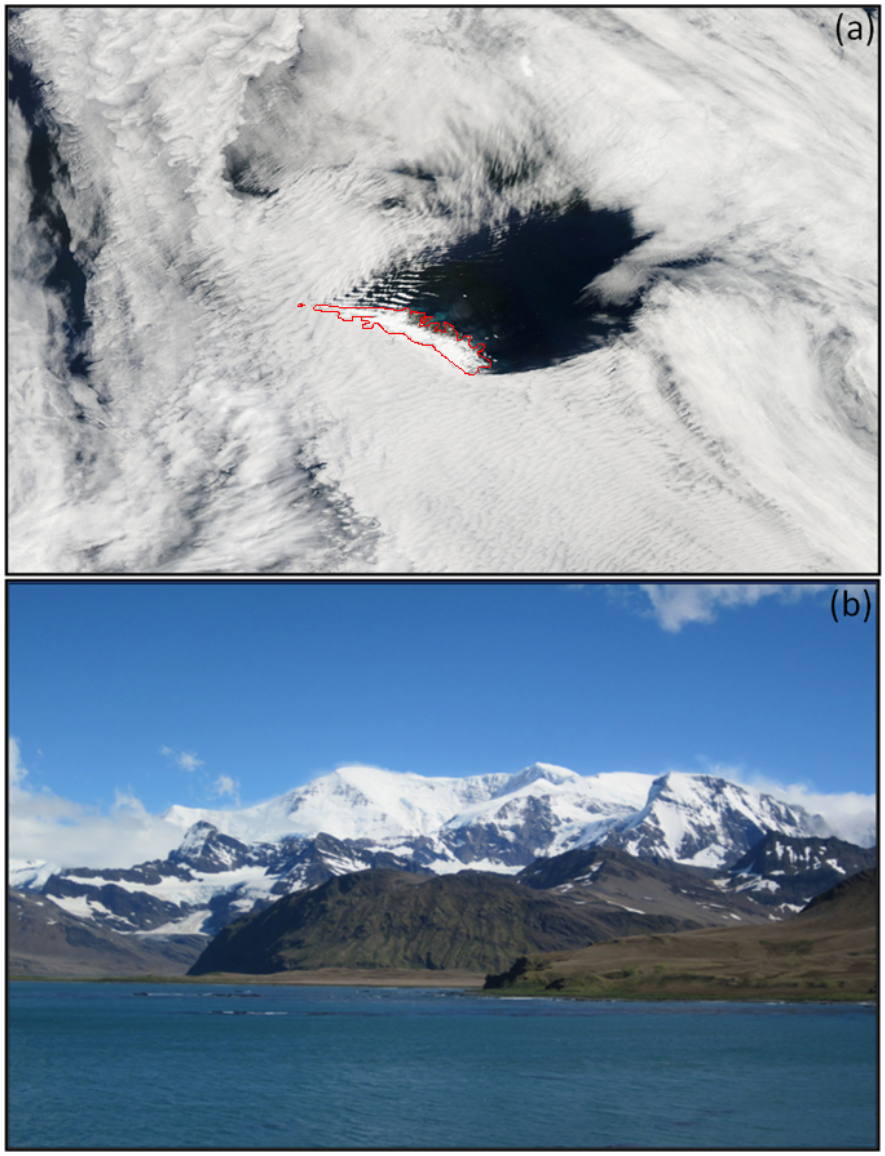

Figure 4.5 – *Panel (a) Aqua/MODIS (true colour, visible) image over South Georgia (the island is outlined in red) at 1645 UTC on 5 February 2013. This image was taken from: https://earthdata.nasa.gov/labs/worldview. Panel (b) a photograph of Mount Paget (the central peak in the background), taken looking south from Hope Point, at 1730 UTC on 5 February 2013. Hestesletten is hidden by Susa Point (right midground).*

Using a geographic information system package, the cloud free region has an estimated area of 34000km^2 (nine times the area of South Georgia itself) which extends approximately 230km northeast of King Edward Point. Clearly, the föhn effect extends many kilometres downstream of the island. This is evidence of the extent to which orographic forcing has on the wind fields downstream of South Georgia, which was also explored by Wells *et al*. (2008), Hosking *et al*. (2015) and Vosper (2015). Unfortunately, satellite imagery is not available for the three other case

studies (see section 2.4.2). Perusing MODIS satellite images (May 2012 onwards) that are available for the strongest events as defined by the AWS föhn catalogue (not shown), this clearance in the cloud is a common feature during intense föhn events, and is typically three times the size of South Georgia.

Radiosonde (hhmm UTC)	Mean Temperature (°C)	Maximum Temperature (°C)	Minimum Temperature (°C)	Standard Deviation (σ)
0857	1.0	6.1	-4.5	2.8
1200	2.0	6.1	-3.2	5.4
1515	4.3	12.1	-1.7	3.7
1754	3.8	12.1	-3.0	4.2
2044	5.1	11.6	-1.0	2.8

Radiosonde (hhmm UTC)	Mean Relative Humidity (%)	Maximum Relative Humidity (%)	Minimum Relative Humidity (%)	Standard Deviation (σ)
0857	81.5	97.0	68.0	8.1
1200	80.4	92.0	70.0	5.2
1515	58.5	79.0	44.0	8.7
1754	48.1	63.0	33.0	8.1
2044	41.3	57.0	34.0	5.1

Radiosonde (hhmm UTC)	Mean Wind Speed (ms^{-1})	Maximum Wind Speed (ms^{-1})	Minimum Wind Speed (ms^{-1})	Standard Deviation (σ)
0857	6.84	10.7	0.7	3.2
1200	8.48	19.2	0.3	6.6
1515	9.10	22.0	1.1	6.5
1754	8.87	17.6	1.2	5.1
2044	8.47	16.2	2	3.3

Table 4.2 – *The mean, maximum, minimum, and standard deviation (of all values between the surface and 2000m; approximately mountain height) of air temperature (top), relative humidity (middle), and wind speed (bottom) as recorded by each of the 5 radiosondes launched on 5 February 2013.*

The radiosonde observations also clearly show the warm and dry föhn as a result of the föhn warming process (Figure 4.3). The next three sondes launched show that the leeside temperatures in the vicinity of King Edward Point were noticeably warmer during the föhn event. Table 4.2 summarises the radiosonde statistics which illustrate the progression of the event and the extent of warming, drying and increased wind speeds. Taking the surrounding mountain height as 2000m, then at the height of the

föhn event (1515 UTC sounding) the mean temperature below mountain height was 3.3ºC warmer, the relative humidity was 23.0% drier, and the wind speed was 2.3 ms^{-1} stronger, compared to the 0857 UTC atmospheric sounding (Table 4.2).

The end of the event was marked at 2135 UTC by a drop in temperature of 5.0ºC within an hour, and a concurrent increase in relative humidity in the surface AWS observations (Figure 4.2). As previously stated, surface wind speeds had already decreased, and this is attributed to the variable northerly winds from 1800 UTC onwards. The event lasted 9 hours and 24 minutes in total, making it the 669th longest föhn event of all 886 events which occurred between January 2003 and February 2013. All the observational evidence strongly suggests that a cross-barrier flow on 5 February 2013 generated a föhn event that produced strong winds (in excess of 20ms^{-1}) and temperatures higher than 10ºC in the vicinity of King Edward Point.

4.3.2 Synoptic Background

The movement of a low pressure system across the Scotia Sea, south of South Georgia, during 5 February 2013 appears to have generated the observed föhn event (Figure 4.6). The track of the low pressure system in to, and out of, the vicinity of South Georgia can also be seen in the sea level timeseries as recorded by the AWS station (Figure 4.2). During the morning of 5 February, the low pressure system (998 hPa) was situated to the southwest of South Georgia, which generated northwest wind flow over the island. ERA-Interim reanalysis fields have been used to calculate the wind speed (20.1ms^{-1} at 0600 UTC) and wind direction (319º) at mountain top height (2000m) for a point upstream of South Georgia (-54.492ºS, -39.496ºW). This north-westerly flow was also measured in the surface AWS observations (Figure 4.2) which shows before 0900 UTC, the mean wind direction at King Edward Point was 359º. By 1200 UTC the low pressure system had tracked to the southeast of South Georgia, and this induced south-westerly flow (from 218º). At this time, föhn was detected in the AWS observations. The synoptic configuration in Figure 4.6 clearly shows cross-barrier, perpendicular flow over South Georgia from 1200 UTC onwards. The föhn event ceased in the AWS observations at 2135 UTC, and this coincides with the low pressure system tracking eastwards throughout the evening, restoring a westerly air flow by 0000 UTC 6 February 2013. How well this föhn event is replicated in the

WRF model, along with the large-scale spatial characteristics and features of the event, will now be examined.

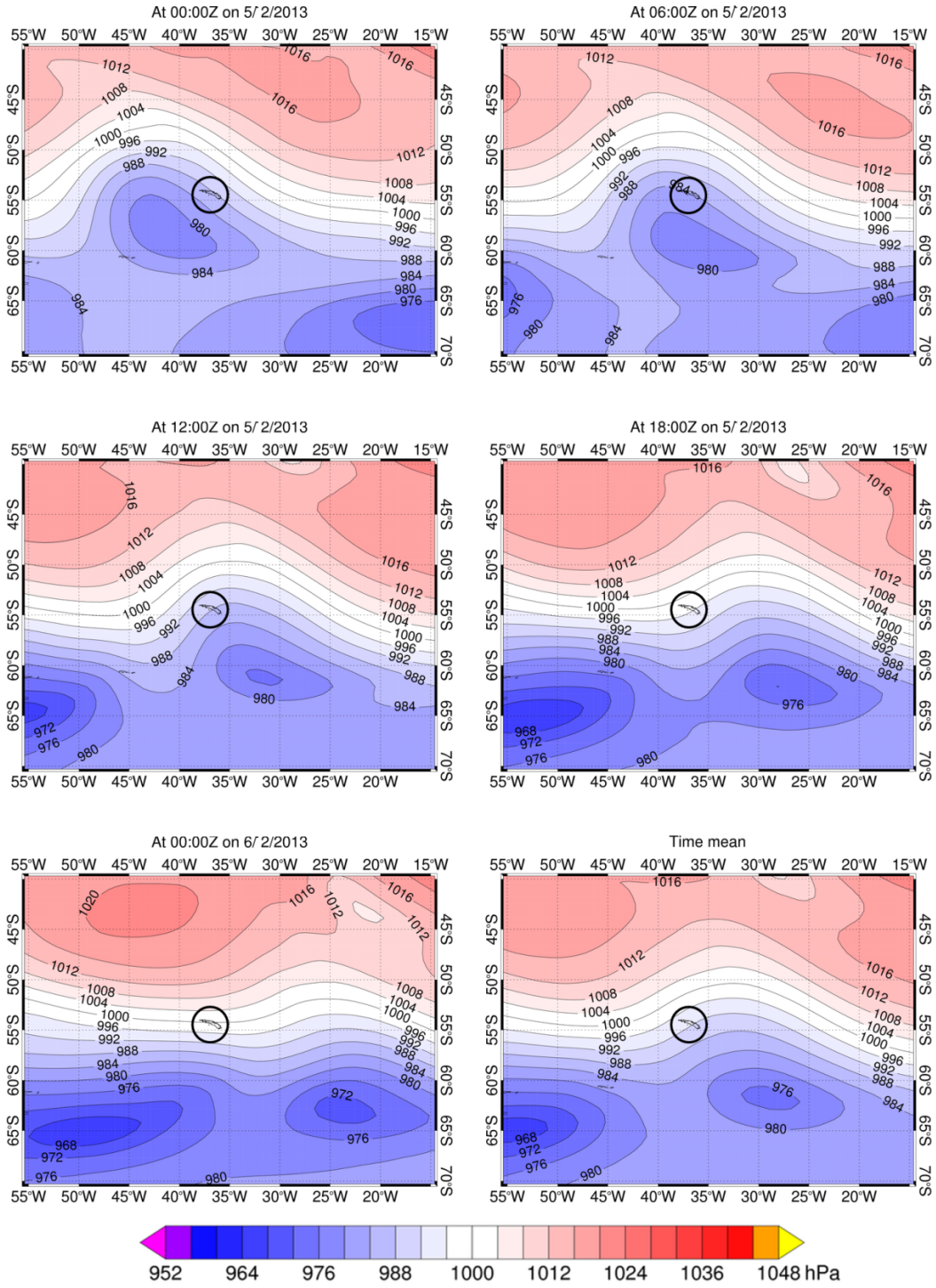

Figure 4.6 – *6-hourly ERA-Interim sea level pressure plots for 0000, 0600, 1200, 1800 UTC 5 February, and 0000 UTC 6 February 2013. The bottom right panel shows the mean sea level pressure pattern for 1200 – 1800 UTC 5 February 2013 (i.e. during the observed föhn event at King Edward Point). South Georgia is circled in black.*

4.3.3 WRF Simulations

Only the results of the sensitivity of the model to the horizontal resolution for Case 1 are presented here (Figure 4.7). This is because the results from the WRF simulations show that the model is most sensitive to the horizontal resolution. Plots of all the sensitivity simulations are shown in Appendix 4A.1. Similarly, error statistics (mean biases, root-mean-square (RMS) errors, and correlation coefficients) for 2-m air temperature, 2-m relative humidity and 10-m wind speed are given in Appendix 4A.5. The sensitivity of the modelled near-surface meteorology to all model options is discussed here, and also in greater detail in section 4.7.

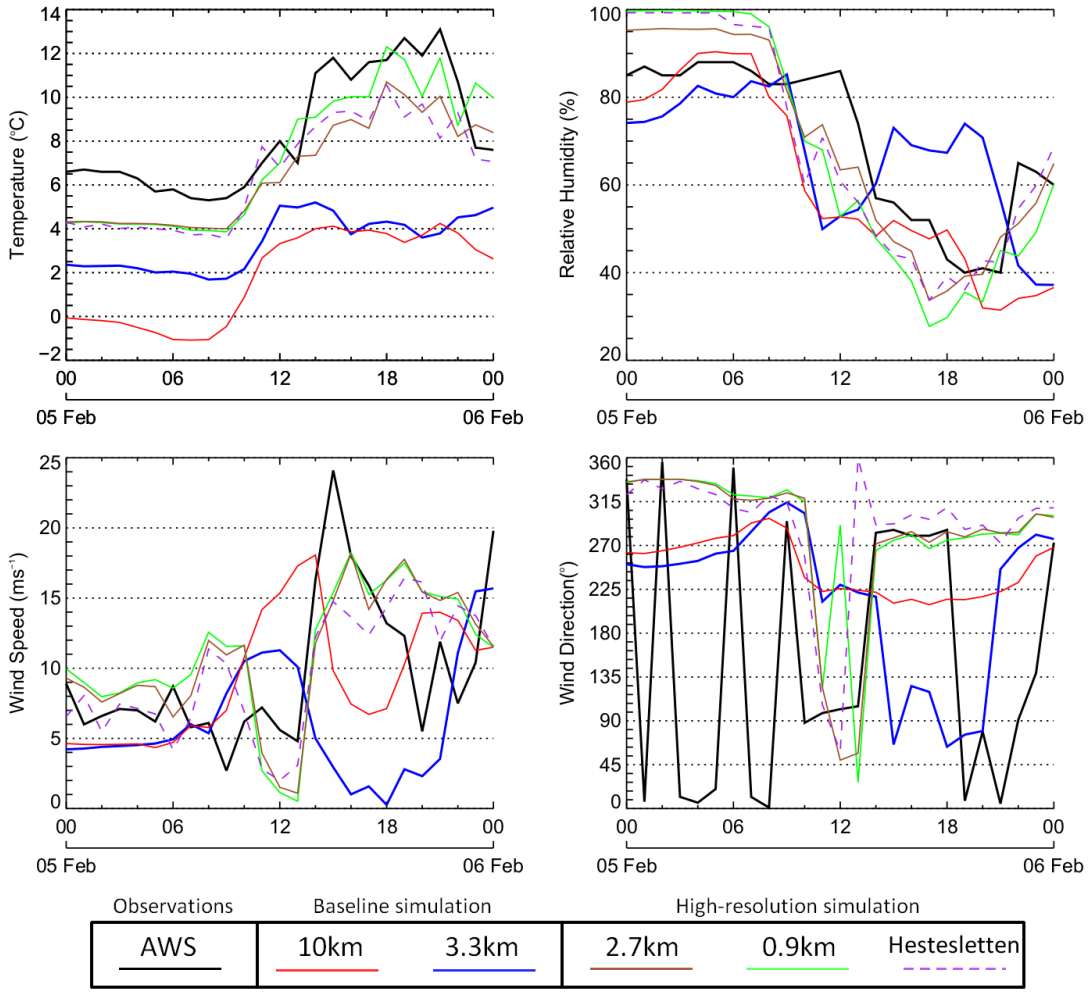

Figure 4.7 – *Observed and simulated 2-m air temperature, 2-m relative humidity, 10-m wind speed, and 10-m wind direction during 5 February 2013 (Case 1). The lines show the AWS observations (black), the simulated values at different horizontal resolutions of 10km, 3.3km, 2.7km and 0.9km (see legend), and the model timeseries at Hestesletten (purple dashed line).*

Figure 4.7 illustrates how extremely sensitive the model is to changes in the model configuration. It appears that at coarse-resolution (the baseline simulation), the surface warming, drying and increased wind speeds associated with the föhn flow are not well captured by the WRF model. There is a clear systematic cold bias which dominates the model at coarse-resolution. In the 3.3km domain, the modelled 2-m air temperature is 5.0^{o}C cooler than observed by the surface AWS observations during this period. While there is an increase in the model temperature at 1100 UTC of about 2.5^{o}C, this is significantly smaller than the 7.0^{o}C warming measured by the AWS. During the event, the maximum temperature measured by the AWS and WRF were 13.1^{o}C and 5.2^{o}C respectively. There is also an increase in relative humidity in the 3.3km domain, which contrasts with the decrease in the observations. The model also indicates a drop in wind speed to calm conditions (< 5ms^{-1}) during the föhn event, and this can be attributed to the easterly winds it also simulates during the event. The AWS observations show almost the opposite situation, with winds peaking at 24.1ms^{-1}, from a westerly direction. Clearly, at this coarse-resolution, the model does not perform adequately, and the observed meteorological fields are not replicated.

In contrast to the baseline simulation, there is generally very good agreement between the modelled and observed near-surface meteorological conditions at King Edward Point in the high horizontal resolution domain configuration. By increasing the resolution of the model to less than 3km, all meteorological fields are much better resolved by the model. The temperature bias (Table 4.3, Appendix 4A.5) is reduced from a mean of -5.0^{o}C to -1.0^{o}C. Similarly, in the 0.9km configuration, the maximum temperature reached is 12.3^{o}C at 1800 UTC, matching the peak temperature observed by the AWS of 12.7^{o}C at 1900 UTC. The model also captures the fall in relative humidity at the start of the event, which was missing in the 3.3km domain. The timing of the simultaneous increase in wind speed agrees with the observations, though, as with the temperature response, the modelled peak wind speed (18.3ms^{-1}) is not as great as that observed (24.1ms^{-1}). The modelled distribution of wind speed has a correlation coefficient of 0.54 and a RMS error of 4.9ms^{-1} (Table 4.5, Appendix 4A.5) when compared to the AWS observations. The modelled wind speeds also stay too high for too long at King Edward Point, and this may be an artefact of the wind direction staying westerly at the end of the event. It appears that the horizontal resolution of both domain configurations are just too coarse to simulate intrusions into the area

which may be responsible for the short and rapid changes in wind speed and wind direction seen in the observations (e.g. at 1900 UTC). This, along with poor physical parameterisations, may also account for the inaccurate wind and other meteorological fields at King Edward Point in the baseline simulation. Unsurprisingly, the model timeseries at Hestesletten (purple dashed line, Figure 4.7) is not remarkably different from the model timeseries at King Edward Point (green solid line). However, there is a more rapid increase in temperature at 1000 UTC at Hestesletten. Based upon the WRF model simulations, and using the föhn identification method described in Chapter 3, föhn would be declared at Hestesletten in the 0.9km domain at 1000 UTC on 5 February 2013, and at 1200 UTC at King Edward Point. Therefore, by the AWS definition, the model is producing a föhn event.

Compared to the baseline simulation, some modifications to the model's parameterisations do lead to improved results (see Appendix 4A.1 and Appendix 4A.5). Of all the variables, wind direction appears to be the most sensitive to changes in the model setup. There are negligible changes to the model output when altering the model top, but the model is sensitive to the number of vertical levels. By increasing the number of levels from 30 (baseline) to 70 and 140 vertical levels, the model more accurately captures the westerly flow during the defined event. Similarly, both the MYJ and MYNN boundary layer parameterisations along with the WSM6 and Lin physics schemes also lead to an improvement in the modelled wind direction. At 3.3km resolution, the model does appear to be somewhat sensitive to the improved topographical resolution, along with being very sensitive to the surface wind correction option (topo_wind). When the option is switched on in a domain with horizontal resolution of 3.3km, the wind fields within King Edward Cove are remarkably more accurate than they are in the baseline simulation (when the option is switched off; see Table 4.5, Appendix 4A.5). Similarly, the subgrid-scale orography scheme also improves the representation of relative humidity in Case 1. The drop in relative humidity at 3.3km resolution is captured when this scheme is used, and this results in a higher mean correlation (0.80) and lower RMS error (12.1%) compared to when the scheme is not used (0.37 and 19.0%, respectively). Despite this, the temperature at King Edward Point remains unrealistic at this resolution. At coarse-resolution, difficulties arise from the resolution of essential topographic structures, and subsequent adjustments to wind and pressure fields within King Edward Cove. It

is unsurprising, therefore, that increasing the horizontal resolution of the model remarkably improves the representation of the föhn event in the model compared to any other namelist option.

To assess the model's performance in the vertical, Figure 4.8 presents vertical air temperature, wind speed, and wind direction profiles from the radiosonde launches (0857, 1200, 1515, 1754, and 2044 UTC), the WRF model and the lidar measurements. Since it has already been established that the model performs better at higher resolution, only vertical profiles from the innermost domains of the baseline (3.3km) and high-resolution (0.9km) simulations are shown. The black dotted lines indicate the range (minimum and maximum values) of all 20 sensitivity simulations. Although there is good agreement between the sonde and lidar observations during 5 February föhn event, Figure 4.8 shows that the WRF model does not perform adequately in the vertical. Wind speed is especially poorly reproduced, and there are large disagreements between simulations. Modelled and observed vertical velocity over King Edward Point also show large disagreements (not shown). Vertical grid spacing is likely to be important here. The model in the vertical and at the near-surface shows negligible sensitivity to increasing vertical resolution, and there is no benefit of increasing the number of levels. However and as previously highlighted in section 2.3.1.2, the WRF model by default arranges the vertical grid so that there are 7 levels below 1km, and then distributes the levels at constant δz above 1km. Therefore, adding vertical levels does not increase the vertical resolution of the model at, and below, mountain height. This effectively explains why increasing the vertical resolution of the model does not lead to drastically improved results in the vertical or near the surface. Furthermore, the largest ranges are below mountain height (< 2000m), implying that the variation in the simulations is primarily due to topographic modification of the air flow and coarse vertical resolution. Above 3km, the model and the observations are in good agreement across all radiosondes. The mean RMS error of air temperature across all five sondes in the 3.3km (coarse-resolution) and 0.9km (high-resolution) WRF simulations is 3.6^{o}C and 2.4^{o}C respectively. Therefore, considering the RMS error, the high-resolution domain performed best in the vertical for simulating air temperature. In contrast, the mean RMS error for wind speed in the coarse- and high-resolution domains is 6.2ms^{-1} and 8.2ms^{-1} respectively. Therefore, the coarse-resolution domain performed better at capturing the observed wind speeds.

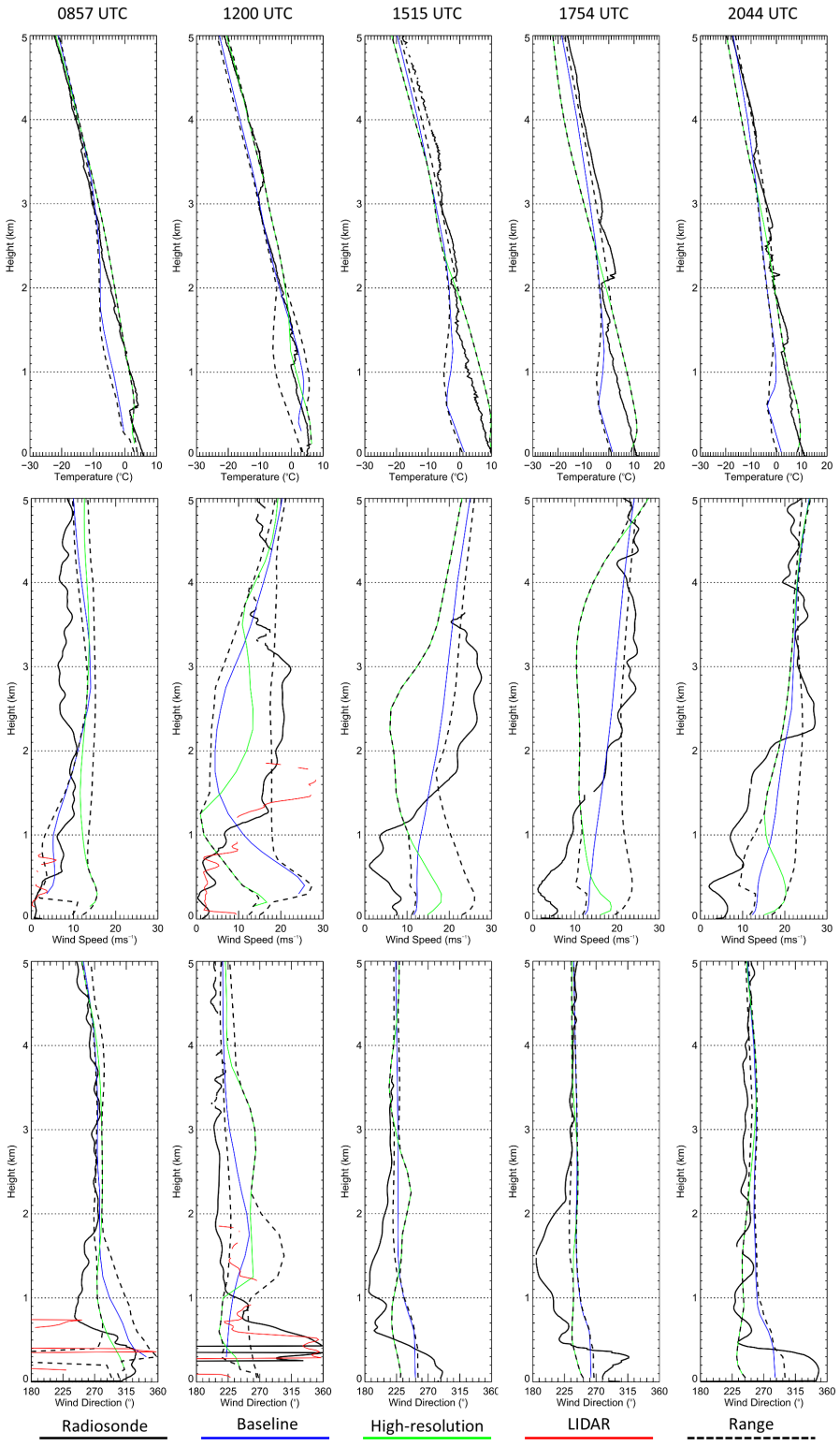

Figure 4.8 – *Vertical profiles of air temperature (top), wind speed (middle), and wind direction (bottom) as measured by the 0857, 1200, 1515, 1754, and 2044 UTC radiosonde launches during 5 February 2013. Black and red solid lines are the sonde and lidar profiles, respectively. The blue and green solid lines are WRF model output from the 3.3km (baseline) and 0.9km (high-resolution) simulations. The black dotted lines indicate the range (maximum and minimum values) for all 20 sensitivity simulations.*

Although the results indicate that increasing the horizontal resolution of the model to 0.9km does lead to improved vertical representation of air temperature and wind direction, especially in the 1515, 1754 and 2044 UTC sondes, wind speed remains poorly reproduced. This is the same across all sensitivity simulations; the RMS error for all of the meteorological fields is not drastically reduced by any sensitivity simulation. There does not appear to be one parameterisation or scheme which is better across all vertical profiles and heights than any other parameterisation or scheme.

While there are inconsistencies (even at high-resolution) at the surface and in the vertical, this is an inherent problem with limited observations for verification and a result of the limitations with the WRF model. It seems that further testing with the model, both in horizontal and vertical resolution and parameterisation, could improve the representation of föhn at King Edward Point. Overall, the WRF model replicates the near-surface föhn variability of Case 1 adequately, and the model at high-resolution clearly replicates a leeside surface warming and drying as a result of strong westerly cross-barrier flow.

4.3.4 The Spatial Characteristics and Dynamics of Case 1

Since the observations suggest that the föhn effect was observed at King Edward Point, and since there is relatively good agreement between the model and observations, the WRF model can also be used to explore the flow characteristics, features, dynamics and physical mechanisms responsible for the 5 February 2013 föhn event. Figure 4.9(b) shows the mean 2-m air temperature of the WRF model during the föhn event (1200 UTC – 2100 UTC), and this figure illustrates the regional asymmetry of temperature across South Georgia, which can be attributed to the föhn effect.

During the event, there is a mean temperature gradient between Cape Darnley (-54.4580ºS, -36.8186ºW; 29km southwest of King Edward Point) and King Edward Point of +10.6ºC. The warmest temperatures generally occur in the vicinity of King Edward Cove, as well as along Hestesletten and Moraine Fjord. Therefore, the model indicates that the warmest regions were in the immediate lee of the mountains, on relatively low and flat terrain, in the wake region of the föhn gap, during 5 February 2013. Figure 4.9(a) also highlights the large-scale features of the near-surface wind speed during this period. The structure of the wind fields is clearly forced by South Georgia's steep orography, and these important surface features have previously been

explored by Hosking *et al*. (2015) and Vosper (2015). The upstream flow shows deceleration due to flow stagnation, and this appears to incur flow splitting, so that flow navigates around rather than over South Georgia. As a consequence of this, there is an apparent wake region in the lee of the island with strong tip jets (~14ms^{-1}) either side. This decelerated flow extends into the föhn gap, observed in Figure 4.5(a). It appears that the tip jet to the north end of South Georgia may also be responsible for the wave trains previously seen in Figure 4.5(a). Downwind of the wake region, near-surface westerly winds gradually strengthen once more (~9ms^{-1}). These large-scale features are further discussed in Case 2 and Case 4, as they are also apparent during these föhn events.

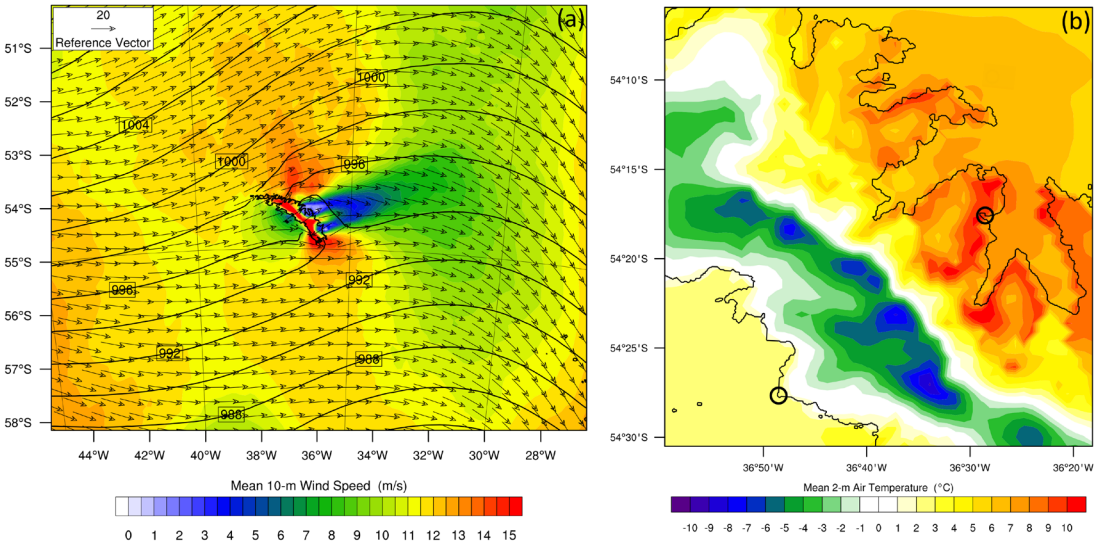

Figure 4.9 – *The mean modelled conditions during the 5 February 2013 föhn event. The mean is calculated from the model's hourly output from 1200 – 2100 UTC. Panel (a) mean 10-m wind speed (filled contours), mean 10-m wind vectors and mean sea level pressure (hPa, black contours). This is plotted from the 10km baseline WRF simulation. Panel (b) mean 2-m air temperature. This is plotted from the 0.9km high-resolution WRF simulation. Cape Darnley and King Edward Point are circled in black. Both locations are approximately at the same elevation.*

Figure 4.10 shows three different vertical cross-sections of potential temperature and wind speed through the island. These cross-sections were aligned roughly parallel to the island's mountain chain (a), roughly perpendicular to the island (b), and roughly north-south (c). Immediately apparent in (b) and (c) are the mountain waves over South Georgia. These cross-sections appear to suggest that the flow is nonlinear (see Elvidge *et al*., 2014a; 2014b), as evidenced by the large wave amplitudes and strong leeside acceleration. Strongly-stratified, slow moving flow approaching a high

mountain usually leads to these non-linear phenomena (see Durran, 1990; Elvidge *et al*., 2014b).

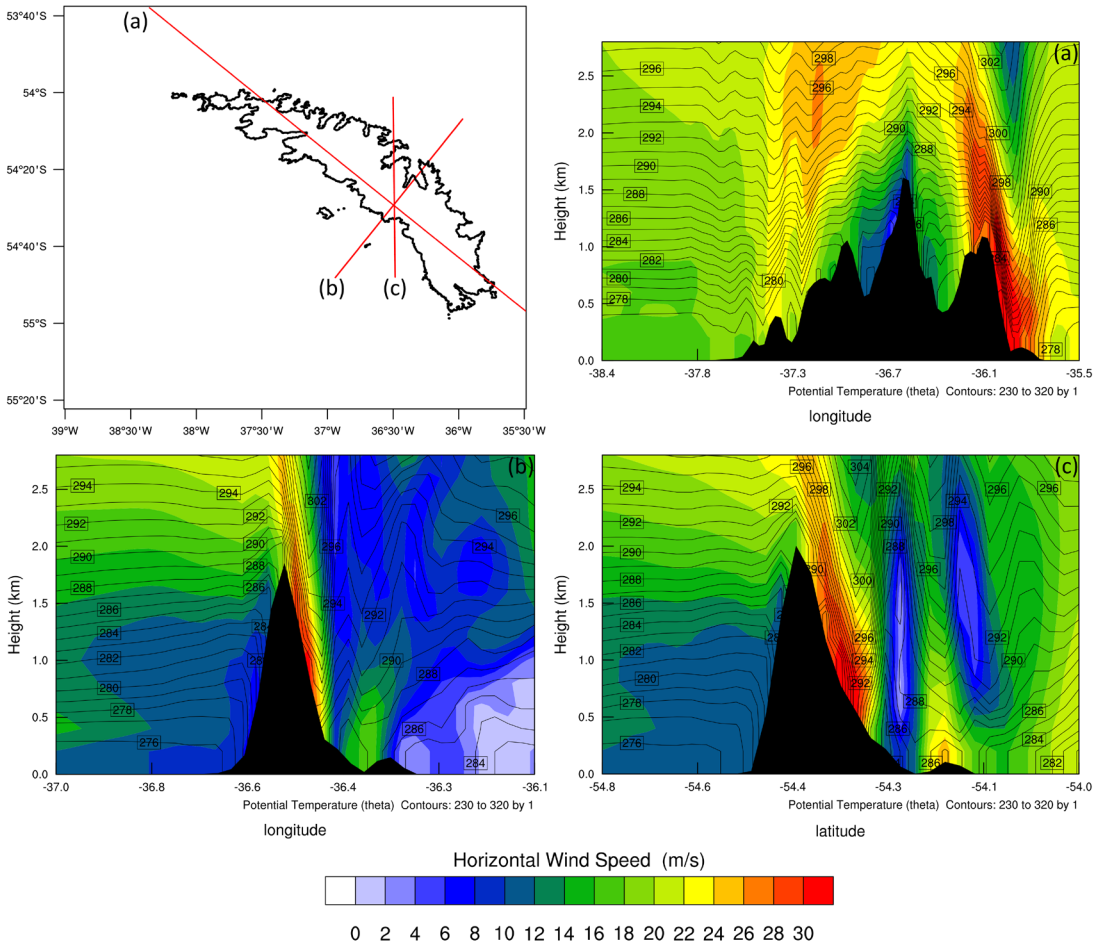

Figure 4.10 – *Vertical potential temperature (K, black contours) and wind speed (ms^{-1}, filled contours) cross-sections through lines (a), (b) and (c), for 1700 UTC 5 February 2013. This is plotted from the 2.7km high-resolution WRF simulation.*

Cross-section (a) penetrates the tip jet at the south end of South Georgia, showing that wind speeds are in excess of 30ms^{-1} from the surface to ~2km. Cross-section (b) penetrates the wake region (where wind speeds < 4ms^{-1}) and the föhn gap over the surrounding shelf-sea, and shows strong isentropic drawdown leading to a relatively strong potential temperature gradient across the island. Cross-section (c) runs north-south over South Georgia, and also shows evidence of strong isentropic drawdown and mountain wave activity over the northeast coast of South Georgia, with stronger wind speeds (>28ms^{-1}) in the immediate lee of Mount Paget. The upstream Froude number was calculated from the intermediate (2.7km) domain, ~250km upstream of South Georgia (-54.492°S, -39.496°W) between 0.2km and 2km throughout this event. The Froude number is defined as:

$$Fr = \frac{U}{Nh}$$

where U is a characteristic upstream wind speed, h is the typical mountain height, and N is the upstream Brunt-Vaisala frequency. Fr ≥ 1 is satisfied when U = 24.0ms^{-1}, N = 0.012 s^{-1} (characteristic values for approaching flow) and h = 2000m. See section 1.6.1 for more details.

For a nonlinear flow regime the Froude number becomes small. This happens when the mountain becomes very high, the incident flow becomes very slow, and/or the stratification of the air becomes very strong. Perturbations generated by the mountain become larger in nonlinear flow. For a linear flow regime, the opposite is true, and such flows are characterised with high Froude numbers (Durran, 1990; Elvidge *et al*., 2014b). An upwind Froude number of 1.1 is found at 1700 UTC 5 February 2013 suggesting that this is a more linear case despite the nonlinear wave response over South Georgia. The drawdown of air from aloft appears to be the major driver of föhn warming and drying in this case (i.e. this is a dynamic föhn). Under these conditions, the föhn signature is observed at King Edward Point. This case study provides the very first look at the fine- and large-scale features and physical mechanisms associated with föhn on the northeast of South Georgia.

4.3.5 Summary

In summary, although the intensity of the event is somewhat underestimated even at high-resolution, there is a good comparison between the WRF model and the AWS observations. The results show that the flow structure in the model is similar to that of reality, though with reservations regarding the vertical structure. Previous modelling work which has used WRF to represent föhn flow has come to similar conclusions. For instance, Steinhoff *et al*. (2013) have looked at föhn flow in the McMurdo Dry Valleys of Antarctica and have shown significant relative humidity biases in the WRF model, as well as unrealistic near-surface wind fields (also see Grosvenor *et al*., 2014). Despite the limitations, the WRF model does capture much of the variability in near-surface and vertical meteorological fields at King Edward Point, and therefore the model is suitable for this analysis. The observations indicate strong downslope winds and a leeside surface warming during the event, and the model (at high-resolution) also replicates this. Of all the föhn events detected in the surface AWS observations,

this event is covered by the most observational data. Therefore, this event allows us to interpret some of the large- and small-scale features which give rise to föhn events at King Edward Point, and also provides the first basic insight into the dynamics and features of föhn flow on South Georgia. It is possible to make several generalisations about föhn events on South Georgia, specifically the large-scale processes and features, based on this case. A föhn gap associated with isentropic drawdown and stronger winds appear to result in relatively warmer regions in the immediate lee of the island. Tip jets off of the extremities of South Georgia are also associated with wave effects, and upstream blocking/stagnation drives flow splitting. Elvidge *et al*. (2014b) have shown that wind effects such as these are consistent with nonlinear flow regimes, yet this particular case study is rather linear. Hosking *et al*., (2015) have shown that these orographically-induced disturbances in the wind fields are responsible for strong wind stress curl and enhanced heat fluxes over the surrounding continental shelf waters of South Georgia. The modification of the regional wind field by the orography during strong westerly föhn flow could impact the ocean system through modification of local circulation currents, and this could also influence the variability in marine ecosystems (Young *et al*., 2012; 2014). Since the results presented here show that the impact of föhn extends many kilometres downstream of South Georgia, changing patterns in the intensity or the frequency of these warm and dry winds could also feedback into the ocean system.

4.4 Case 2: 9 – 10 August 2012

4.4.1 The Evolution of Case 2: Observations and Measurements

The 9 – 10 August 2012 case study was also selected for the sensitivity simulations as it is another example of a typical föhn event at King Edward Point. Like Case 1, this event is characterised by rapid changes in near-surface air temperature, wind speed and relative humidity (Figure 4.11). In the context of föhn events which were observed between January 2003 and February 2013, Case 2 is the 287th absolute warmest event, the 487th absolute windiest event, and the 309th driest event (from 886 events in total).

The morning of 9 August 2012 was cold and calm, with relatively low humidity values (Figure 4.11). The mean temperature, relative humidity, wind speed and wind direction at King Edward Point (up until 0600 UTC) was -0.9ºC, 60%, 1.6ms^{-1} and 317^{o} respectively. Throughout the morning of 9 August, the air temperature and

humidity began to slowly increase. At 0910 UTC, a warming event was recorded in the AWS observations, with a 1.9ºC rise in temperature within 1 hour, which also coincided with a rapid increase in wind speed (reaching 11.5ms^{-1}) and a small drop in relative humidity (reaching a minimum of 76%). Since this did not meet the AWS föhn criteria as described in Chapter 3, this was not declared as a föhn event.

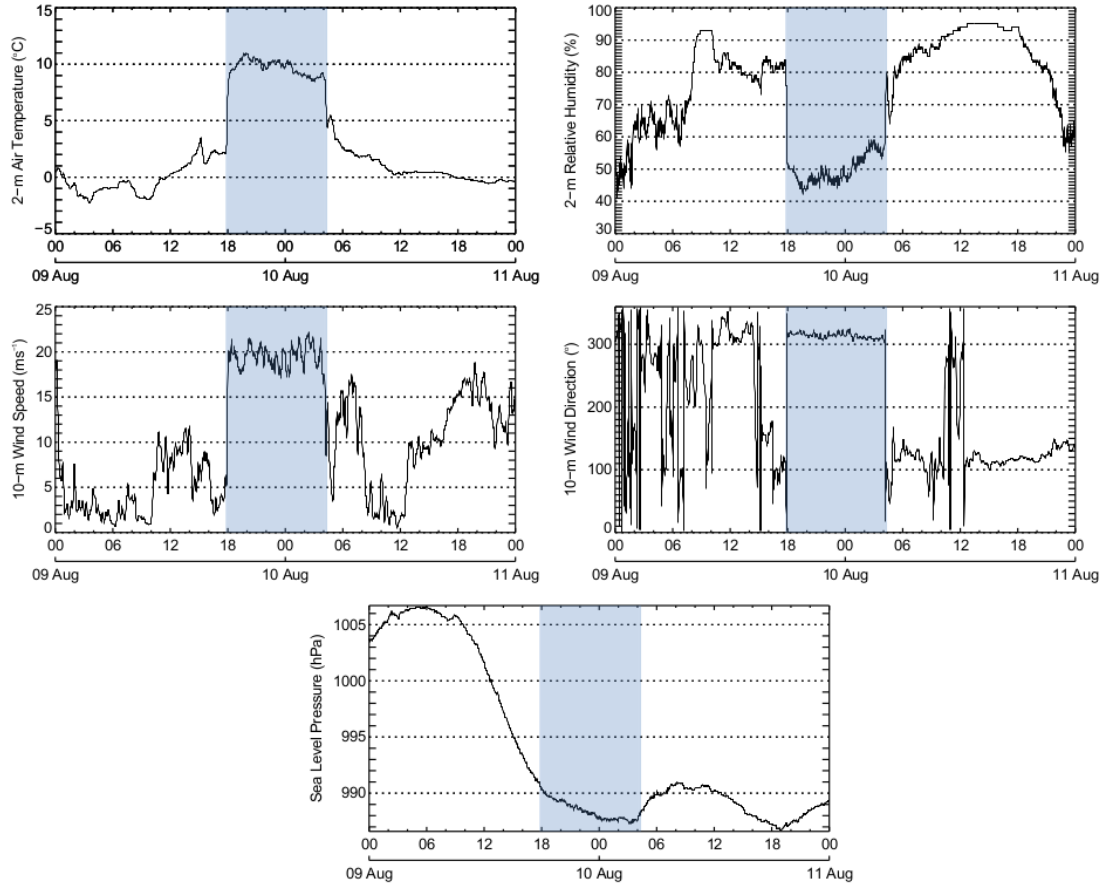

Figure 4.11 – *Meteorological conditions (2-m air temperature, 2-m relative humidity, 10-m wind speed, 10-m wind direction, and sea level pressure) during 9 – 10 August 2012. Blue shading highlights föhn event as defined and detected by the AWS föhn classification method.*

At 1749 UTC 9 August 2012, there was a distinct föhn signature detected in the surface AWS observations, with a rapid increase in temperature and wind speed, along with a simultaneous decrease in relative humidity (blue shading, Figure 4.11). Within 1 hour of föhn onset, the air temperature at King Edward Point had increased by 7.9ºC. The maximum temperature and wind speed recorded was 11.0ºC and 22.2ms^{-1} respectively (the highest measurements of the day), while relative humidity reached a minimum of 41%. The average wind direction during the event was 316º. These conditions were sustained for 10 hours and 25 minutes in total, and the föhn event ended at 0424 UTC

10 August. The end of the event was marked by a drop in temperature of 4.9ºC within an hour, and a concurrent increase in relative humidity, a decrease in wind speed and a turning of winds from the east. Throughout 10 August, the temperature continued to drop to below 0ºC and the relative humidity increased to 95%. For the rest of the day, the wind came from the east (from a direction of ~120º) and this was characterised by high winds of greater than $10ms^{-1}$. This was briefly interrupted at 1100 UTC by variable northerly winds at King Edward Point. Given that such a clear föhn signature was detected in the AWS observations, this is a good case study to explore further with the WRF model.

4.4.2 Synoptic Background

Figure 4.12 shows 6-hourly ERA-Interim sea level pressure plots from 0000 UTC 9 August to 1800 UTC 10 August 2012. It is clear that this föhn event, like Case 1, was generated by an eastward moving small low-pressure system across the Scotia Sea. Prior to the event (9 August 0000 UTC), a high pressure ridge, associated with a significant high pressure system over the Argentine Basin (1032 hPa), dominated the conditions at South Georgia. Throughout 9 August, this ridge of high pressure was gradually pushed eastwards and northwards as a small area of low pressure (984 hPa) developed and tracked eastwards from the Drake Passage. As this system passed south of South Georgia, it generated strong westerly airflow over the island, which coincided with the appearance of a föhn signature in the AWS observations. The ERA-Interim reanalysis fields show that at 0000 UTC 10 August, the upstream wind direction at mountain top height was 277º. By midday 10 August, the system had quickly moved out of the vicinity of South Georgia. Another area of deepening low pressure (988 hPa) had also moved in from the west, but this passed to the north of South Georgia, and generated easterly winds. At 1800 UTC 10 August, the upstream wind direction at mountain top height was 112º. The passage of these systems can also clearly be seen in the sea level pressure timeseries as recorded by the AWS at King Edward Point during this period (Figure 4.11). How well this föhn event is replicated in the WRF model, as well as the spatial characteristics and features of this event, will now be examined.

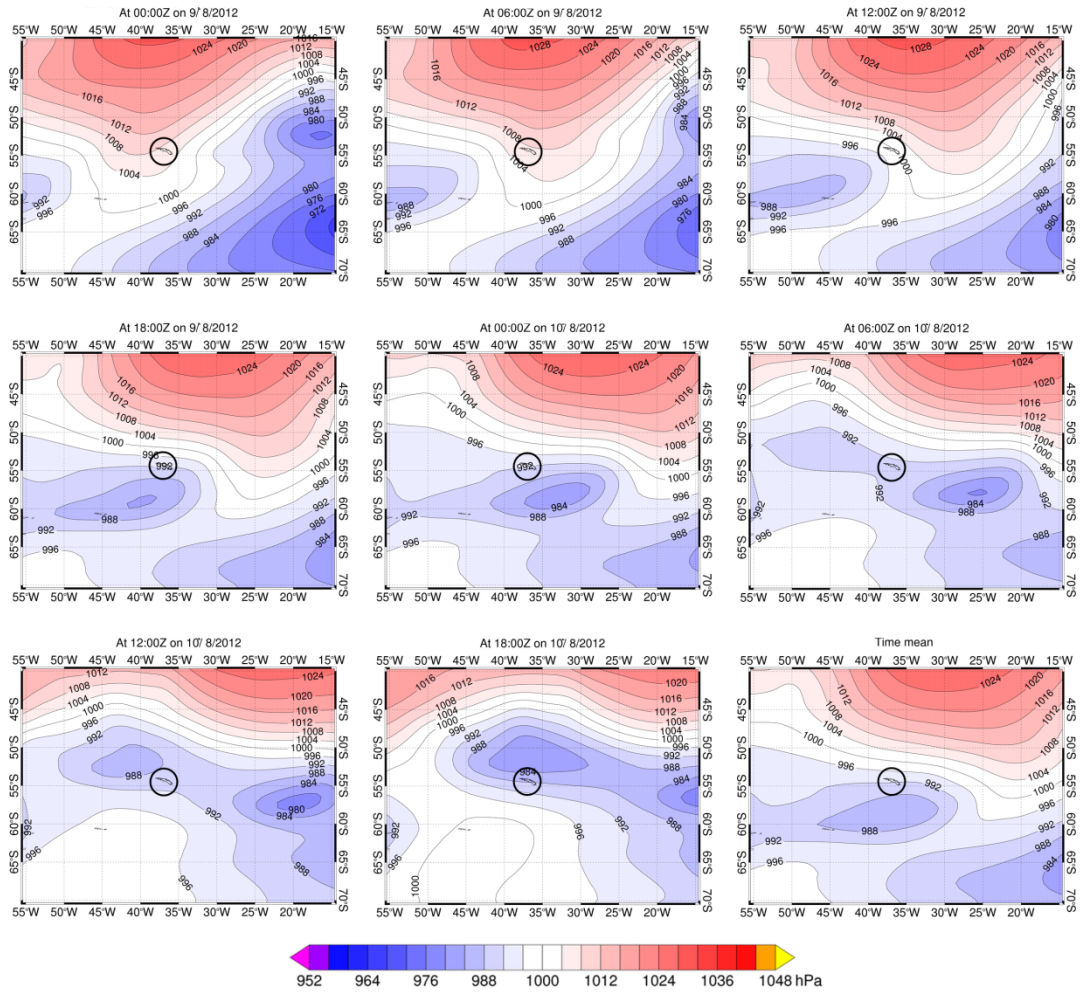

Figure 4.12 – *6-hourly ERA-Interim sea level pressure plots from 0000 UTC 9 August to 1800 UTC 10 August 2012. The bottom right panel shows the mean sea level pressure pattern for 1800 – 0000 UTC 10 August 2012 (i.e. during the observed föhn event at King Edward Point). South Georgia is circled in black.*

4.4.3 WRF Simulations

The results from the sensitivity simulations of this case study show that the model is largely insensitive to altering the vertical resolution and different planetary boundary layer and physics (see Appendix 4A.5). As such, plots of all the sensitivity simulations for this case study are shown in Appendix 4A.2. Only the horizontal sensitivity simulations for Case 2 are presented here (Figure 4.13).

Once again, there is a clear cold temperature bias throughout all the simulations. On average, the 3.3km resolution bias is 3.4ºC colder the surface AWS observations, and this cold bias is more apparent during the föhn event itself (> -6ºC). In marked contrast to Case 1, altering the vertical resolution or changing the boundary layer and physics schemes does not lead to improved results (see Appendix 4A.2 and Appendix 4A.5).

The horizontal resolution of the model has the largest sensitivity, and the results degrade rapidly for simulations with 3.3km grid resolution or higher. Since no other sensitivity simulation vastly improves the modelled near-surface meteorology, this föhn warming signal at King Edward Point is simply not captured in the model at this resolution. The results are substantially improved in the high-resolution simulation, and this implies that the föhn signature in the AWS observations is a (small-scale) local feature, within a broad-scale leeside föhn flow. Even in the 0.9km domain, there is still a clear temperature bias in the model during the height of the föhn event, but the mean bias for the entire period is just -0.1°C (Table 4.3, Appendix 4A.5). The maximum air temperature observed at the AWS site was 10.9°C, which compares to 6.8°C as modelled by WRF.

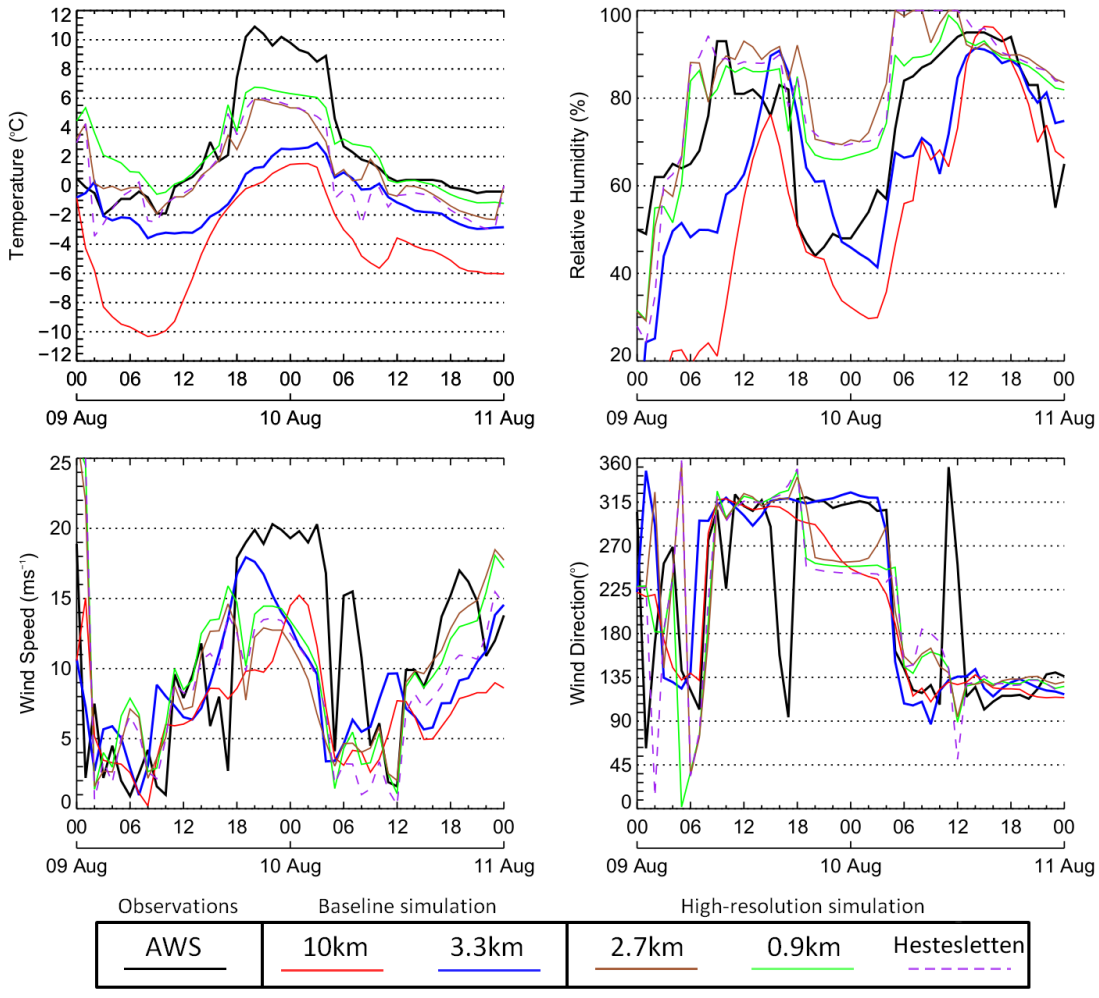

Figure 4.13 – *Observed and simulated 2-m air temperature, 2-m relative humidity, 10-m wind speed, and 10-m wind direction during 9 – 10 August 2012 (Case 2). The lines show the AWS observations (black), the simulated values at different horizontal resolutions of 10km, 3.3km, 2.7km and 0.9km (see legend), and the model timeseries at Hestesletten (purple dashed line).*

Despite not reaching the intensity of the observations, the WRF model does replicate the sustained warming and drying between 1900 UTC and 0500 UTC. Therefore, in terms of the near-surface temperature at King Edward Point, although the range of extreme temperatures is not captured, the temperature signal associated with the föhn event is well captured at high-resolution.

The relative humidity timeseries suggest a timing discrepancy between the model and the observations for this event at resolutions coarser than 3.3km. The overall change of relative humidity during this period is well captured, and the model and AWS observation have similar maximum and minimum values. However, there is a clear offset by approximately six hours in the relative humidity response to the föhn warming. Since there are no timing discrepancies in the simulated sea level pressure (not shown), this is unlikely to be a forcing error. None of the sensitivity simulations rectify this discrepancy, apart from increasing the horizontal resolution of the model. The model results from the high-resolution domains (2.7km and 0.9km) more accurately capture the change in relative humidity during this föhn, but under-represent the magnitude of the drying event. This is evidenced by a mean positive bias of 5.7% and 9.6% at 0.9km and 2.7km resolution, which compares to -8.4% at 3.3km resolution (Table 4.4, Appendix 4A.5). As with temperature, this implies that the meteorological conditions observed by the AWS are unique to a very small area, despite being part of a large-scale leeside föhn effect.

The simulated wind speeds for this föhn event are generally weaker than the observed wind speeds. In the 3.3km domain, the wind speed peaks at ~17 ms^{-1} at 1900 UTC 9 August, compared to ~20ms^{-1} at 2100 UTC 9 August in the AWS observations. The modelled wind speeds before the event are in relatively good agreement, and the rapid increase matches the start of the event as detected in the observations. The modelled wind speed peaks too early at the beginning of the event, whereas it remains strong at ~20ms^{-1} throughout the observed event. After the event, wind speeds are generally too low and are not in good agreement with the observations. In terms of wind speed, the model appears to be insensitive to the horizontal resolution of the domain. The results from the high-resolution domains are not drastically different from the coarse-resolution domains.

There is a good match between the modelled and observed wind direction. The wind direction changes from southerly to strong west-northwesterly, which appears to generate the cross-barrier flow over the island. There is a brief turning of the wind in the observations which is not replicated in any of the simulations, although the high-resolution domains do simulate a change in direction from 1800 UTC 9 August until the end of the event. After the event ended (0500 UTC onwards), the observations indicate that the wind direction turned easterly, and the model captures this well. As with the sudden and brief turning of the wind on 9 August, the model does not capture the sudden turning of winds from the north at 1200 UTC 10 August. In Case 1, this was attributed to the fact that both domain configurations appear to be too coarse to replicate sudden and brief intrusions into King Edward Cove which are likely to be responsible for the short and rapid changes in wind speed and wind direction seen in the observations. Despite this, overall, the WRF model appears to be producing a realistic föhn in terms of wind speed and wind direction structure at King Edward Point.

Therefore, based upon the WRF model simulations, and using the föhn identification method described in Chapter 3, föhn would be declared at King Edward Point and at Hestesletten in the 0.9km domain at 1700 UTC on 9 August 2012. In addition to this, föhn would also be declared slightly later at 2000 UTC at King Edward Point in the 2.7km high-resolution domain. Therefore, by the AWS definition, the model is producing a föhn event at King Edward Point, and this is replicated well in the high-resolution simulation.

4.4.4 The Spatial Characteristics and Dynamics of Case 2

Plan views of the average 2-m air temperature from the WRF model output during the event (1800 UTC – 0400 UTC) are shown in Figure 4.14. Figure 4.14(b) indicates that the warmest leeside temperatures during the föhn event were not experienced at King Edward Point, but rather in Moraine Fjord and across Cumberland West Bay. For instance, the mean modelled maximum temperature during the event reached 7.9^{o}C in Moraine Fjord; 3^{o}C lower than the maximum observed temperature at King Edward Point during the event. Figure 4.14(b) also illustrates the asymmetry of the föhn warming across South Georgia, similar to Case 1 (Figure 4.9(b)). Figure 4.14(a) also shows similar, yet distinct, structure of near-surface winds to Case 1 (Figure 4.9(a)).

Figure 4.14(a) shows that there is a smaller and less intense (~4ms^{-1}) wake region to the east of the south end of the island, along with less distinct and weaker tip jets compared to Case 1. The differences in the near-surface wind structures between Case 1 and Case 2 are a result of the positioning of the low pressure system driving each of the events. In Case 2, the low pressure system drives a mean west-northwesterly flow over South Georgia, compared to a mean west-southwesterly flow in Case 1 (Figure 4.9(a)). This appears to alter the positioning and the intensity of the wake and tip jet regions.

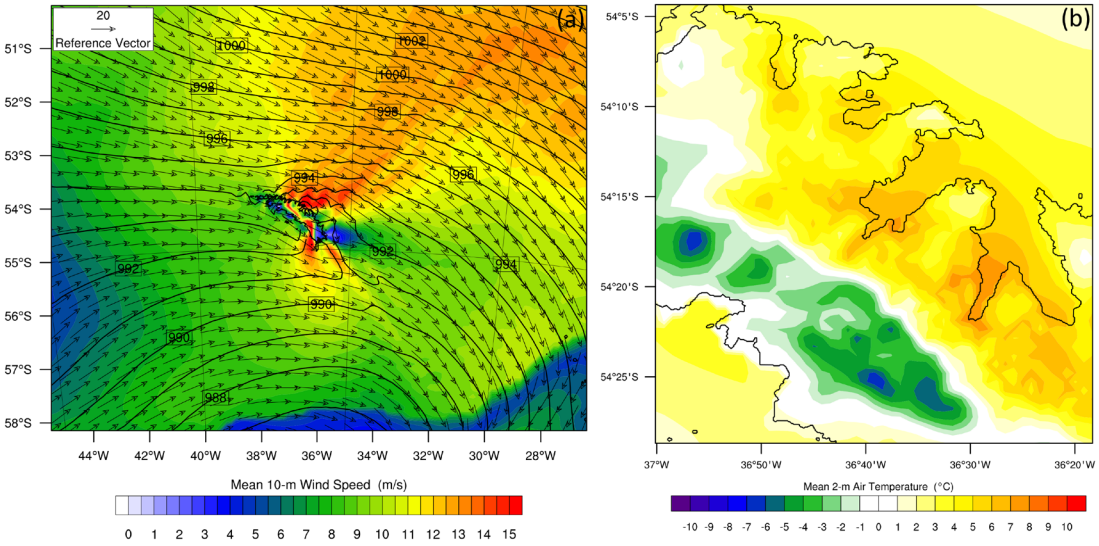

Figure 4.14 – *The mean modelled conditions during the 9 – 10 August 2012 föhn event. The mean is calculated from the model's hourly output from 1800 – 0400 UTC. Panel (a) mean 10-m wind speed (filled contours), mean 10-m wind vectors and mean sea level pressure (hPa, black contours). This is plotted from the 10km baseline WRF simulation. Panel (b) mean 2-m air temperature. This is plotted from the 0.9km high-resolution WRF simulation.*

As it has already been established that the timing of föhn onset in WRF is good, the large-scale structure of the föhn flow at the height of the event (taken to be at 0000 UTC 10 August 2012) can also be explored to examine this event further. Figure 4.15 shows three different vertical cross-sections of potential temperature and wind speed through South Georgia from the intermediate (2.7km) high-resolution WRF simulation. Immediately apparent are the large amplitude wave disturbances to the lee of South Georgia. Lower near-surface wind speeds upstream are likely to be associated with the blocking phenomena (Durran, 1990; Zängl, 2002). Flow accelerates in the lee of the main mountain chain, underneath the region of the steeply-descending isentropes, which then suddenly increase in height. This behaviour is best explained

by the hydraulic theory (e.g. Houghton & Kasahara, 1968; Durran, 1990). There is clear evidence that air is descending from height towards the leeside surface, which causes the apparent rise in temperature (as the air has been warmed adiabatically) and wind speed in the surface AWS observations at King Edward Point. As with Case 1, Case 2 also appears to be a dynamic föhn. To quantify this, the calculated Froude number for a volume upstream of South Georgia at 0000 UTC on 10 August is 1.1. This is consistent with the observation of upwind blocking, the wave response, the leeside warming and flow acceleration observed in Figure 4.15. For comparison, the Froude number at 0600 UTC 09 August 2012 was 0.5. From a dynamical viewpoint, the föhn events presented in Case 1 and Case 2 are very similar.

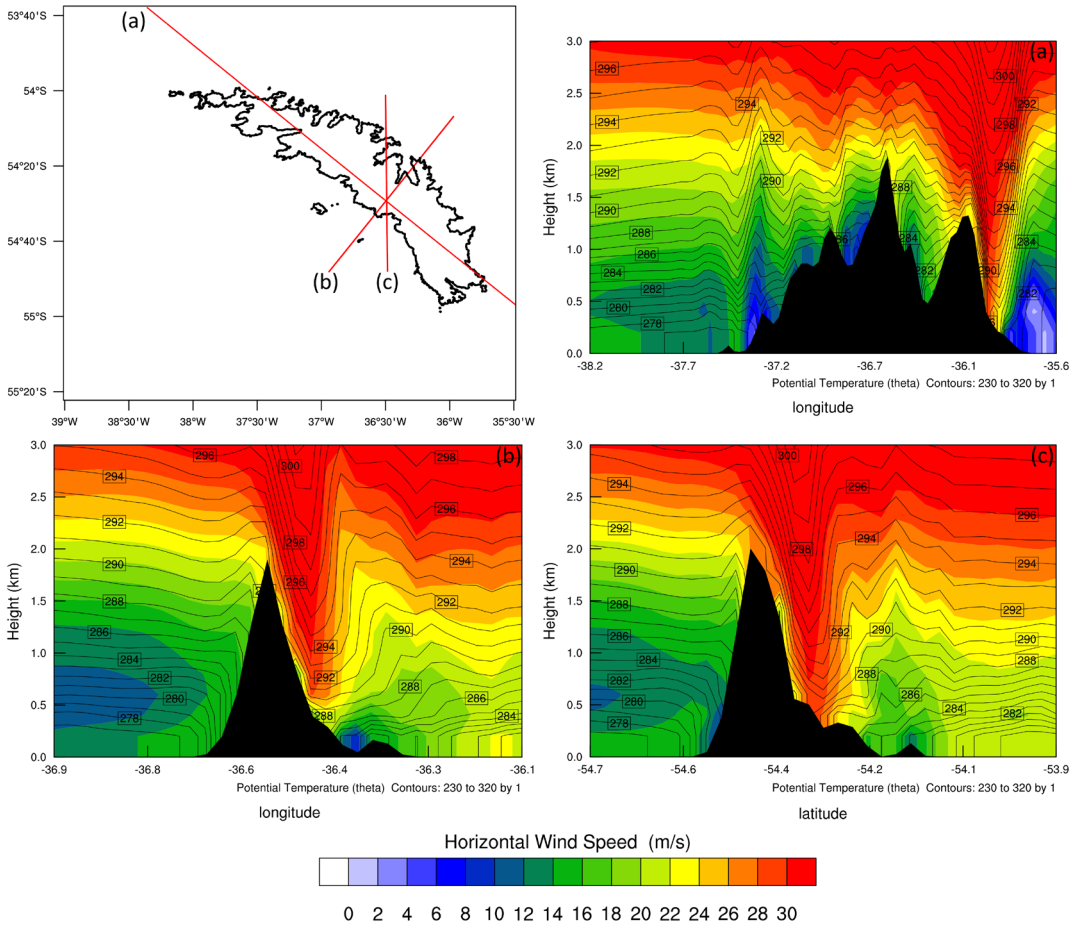

Figure 4.15 – *Vertical potential temperature (K, black contours) and wind speed (ms^{-1}, filled contours) cross-sections through lines (a), (b) and (c), for 0000 UTC 10 August 2012. This is plotted from the 2.7km high-resolution WRF simulation.*

4.4.5 Summary

In summary, the WRF model simulates a strong downslope wind in the presence of strong westerly cross-barrier flow and isentropic drawdown, causing warming in the

immediate lee of the mountains of South Georgia. This process results in a föhn signature being detected at King Edward Point during 9 – 10 August 2012, and this event would be declared using the surface AWS criteria (see Chapter 3). Overall, the WRF model at coarse-resolution fails to replicate the variability and intensity of the warming, drying and increased wind speeds during this event. Despite a temperature bias, the model performs much better at high-resolution, and the 0.9km domain and the observations are largely in good agreement (see section 4.7 for more discussion). Of all the case studies presented here, the WRF model gives the most realistic interpretation of the surface föhn warming signature at King Edward Point during this event, and this is evidenced by the lowest magnitude bias and highest correlation for 2-m temperature (Table 4.3, Appendix 4A.5) at a horizontal resolution of 0.9km. Cross-sections and plan views exploring the spatial pattern of warming and near-surface wind fields of this event are qualitatively similar to that of Case 1. In addition to this, both cases have similar surface föhn signatures and both events were driven by an eastward moving low pressure system over the Scotia Sea. This gives confidence that these fine-scale signals in the near-surface meteorology and the characteristics in the large-scale flow dynamics are directly indicative of flow-over föhn conditions. Therefore, it is possible to start developing our understanding of the fine- and large-scale features which occur and can be observed across South Georgia, and which are associated with strong westerly föhn flow, through these WRF simulations.

4.5 Case 3: 1 – 2 November 2007

4.5.1 The Evolution of Case 3: Observations and Measurements

In Chapter 3 (see section 3.2.1), Case 3 (named Case C in Chapter 3) was identified as an ambiguous föhn event because of its weak surface föhn signature. It was subsequently included as a positive detection in the AWS föhn climatology as the AWS criteria were met. In the context of föhn events which were observed between January 2003 and February 2013, Case 3 is the 797th absolute warmest and windiest event, and the 294th driest event. This event has been selected for the sensitivity simulations with the WRF model because it is a clear example of a weak föhn event; it has a weak surface föhn-like signature compared to the other case studies presented here. The only way to confirm that events with weak surface föhn-like signatures are a direct result of the föhn warming process is through atmospheric modelling.

The meteorological conditions as recorded by the AWS at King Edward Point, during 1 – 2 November 2007, are show in Figure 4.16. During the entire period, the temperature at King Edward Point remained within a 5.6°C range. The morning of 1 November 2007 was cold, and the air temperature dropped below freezing at 0600 UTC. Before 0600 UTC, the mean temperature, relative humidity, wind speed and wind direction were 1.2°C, 60%, 11.0ms^{-1} and 294° respectively. At 1120 UTC, the air temperature increased by 2°C within 1 hour. This marked the beginning of the föhn event (blue shading, Figure 4.16).

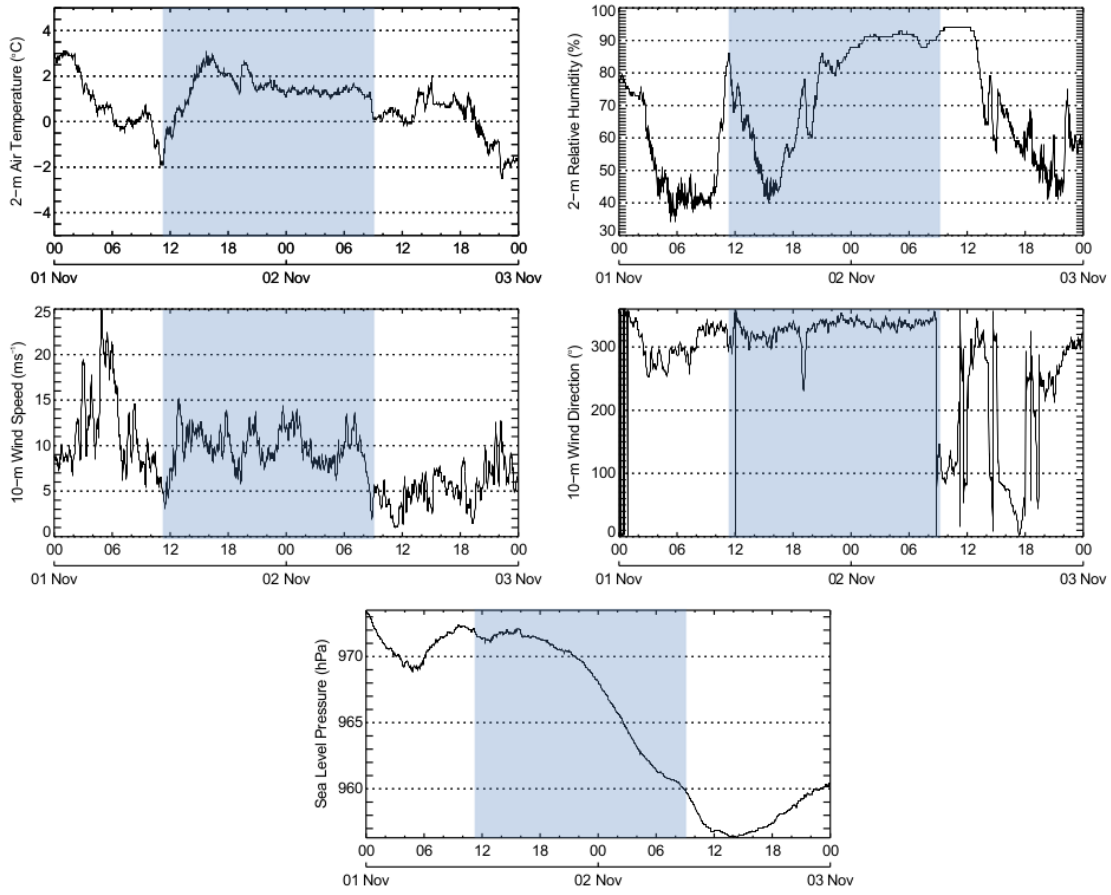

Figure 4.16 – *Meteorological conditions (2-m air temperature, 2-m relative humidity, 10-m wind speed, 10-m wind direction, and sea level pressure) during 1 – 2 November 2007. Blue shading highlights föhn event as defined and detected by the AWS föhn classification method.*

For another four hours, the temperature continued to increase, gradually reaching a maximum of 3.1°C at 1541 UTC. Over the same period the relative humidity had fallen to 40%, with a concurrent gradual, but small, increase in wind speed (reaching a maximum of 14.9ms^{-1}). Until the end of the event, wind speeds varied between 15ms^{-1} and 5ms^{-1}. After 1541 UTC, the AWS detected a cooling and a moistening, and the

temperature very gradually began to decrease. Relative humidity had increased to 90% by 0000 UTC 2 November. As such, the humidity signal associated with föhn was not maintained throughout this event. At 0847 UTC a drop in temperature of 1.2°C in less than 30 minutes marked the end of the föhn event, which was similarly marked by a turning and calming of the wind. The föhn event had a total duration of 21 hours 31 minutes. Compared to Case 1 (Figure 4.2) and Case 2 (Figure 4.11), Case 3 clearly has a weak föhn-like signature in the surface AWS observations at King Edward Point.

4.5.2 Synoptic Background

Figure 4.17 shows 6-hourly ERA-interim sea level pressure plots from 0000 UTC 1 November to 1800 UTC 2 November 2007.

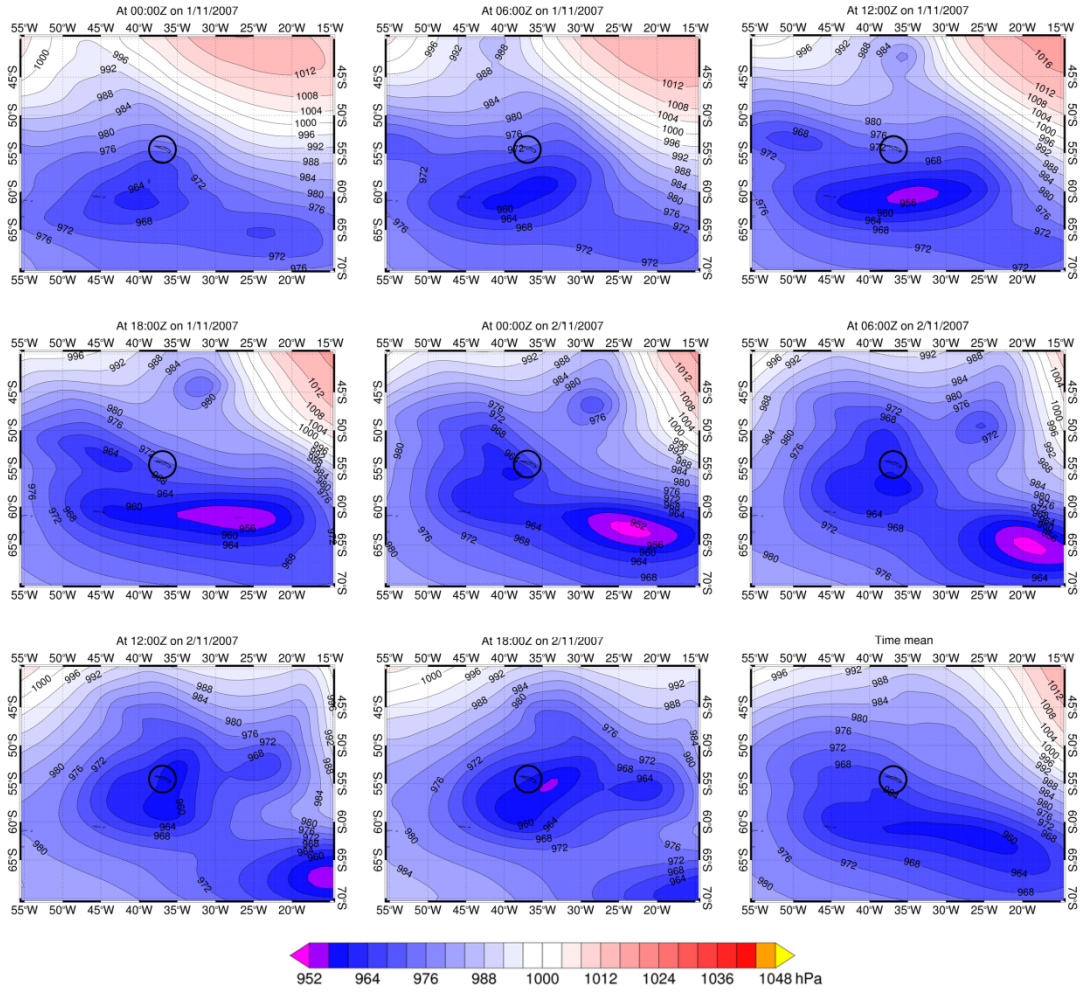

Figure 4.17 – *6-hourly ERA-Interim sea level pressure plots from 0000 UTC 1 November to 1800 UTC 2 November 2007. The bottom right panel shows the mean sea level pressure pattern for 1200 – 0600 UTC 2 November 2007 (i.e. during the observed föhn event at King Edward Point). South Georgia is circled in black.*

Like the previous case studies of föhn events at King Edward Point, this event was also generated by a low pressure system situated to the south of South Georgia (Figure 4.17). However, during this case study, the low pressure was an almost stationary deepening system, situated directly south of South Georgia, which was generating strong cross-barrier westerly winds throughout the 9 November. The ERA-Interim reanalysis fields show that at 1800 UTC 1 November, the upstream wind direction at mountain top height was 272^{o}. The low pressure system continued to deepen into 2 November. During the föhn event, the sea level pressure at King Edward Point had decreased 11.4 hPa and by 1200 UTC 2 November it had deepened by a total of 14.5 hPa within 24 hours (Figure 4.16). During 2 November, the system very gradually moved northwards, leading to more variable wind direction as it passed over South Georgia. This also coincided with the end of the event in the surface AWS observations.

4.5.3 WRF Simulations

As with the previous case studies, only the horizontal sensitivity simulations for Case 3 are shown here (Figure 4.18). Plots of all the sensitivity simulations for this case study are shown in Appendix 4A.3, and the error statistics can be found in Appendix 4A.5. Overall, there is generally a poor match between the modelled and observed near-surface meteorological conditions at King Edward Point during the 1 – 2 November 2007 föhn event.

The WRF simulation of the near-surface meteorology of this event is much poorer than that of the two events described previously. Across all 20 sensitivity simulations for Case 3, the range in 2-m air temperature is not fully realised in the WRF model, and this was also seen with the two previous case studies. The increase in temperature of 2^{o}C at 1100 UTC in the surface AWS observations (which marked the beginning of the event) is somewhat replicated, to varying degrees, across all sensitivity simulations. The timeseries from Hestesletten, as well as the timeseries from King Edward Point in both the 2.7km and 10km domains, show very large diurnal temperature variations. This results in very low correlation coefficients (< 0.26) and high RMS errors (> 4.4^{o}C) when compared to the AWS observations (Table 4.3, Appendix 4A.5). Therefore, the temperature pattern at Hestesletten at high-resolution and at King Edward Point at coarse-resolution is unrealistic, and thus does not appear

to be föhn driven. The sustained föhn warming for a further 22 hours in the observations is also not replicated by WRF, and all the simulations model a reduction in air temperature (to below -2°C) from 2300 UTC 1 November onwards. While increasing the spatial resolution of the model does improve the results (e.g. the RMS error and bias decreases by 0.3°C and 0.4°C, respectively; see Table 4.3, Appendix 4A.5), the 2-m air temperature is still very unrealistic compared to the surface AWS observations. Föhn would not be declared at King Edward Point in the 0.9km domain. Since the temperature in the Hestesletten model timeseries varies rapidly over this period, two föhn events would be declared based upon the AWS föhn criteria.

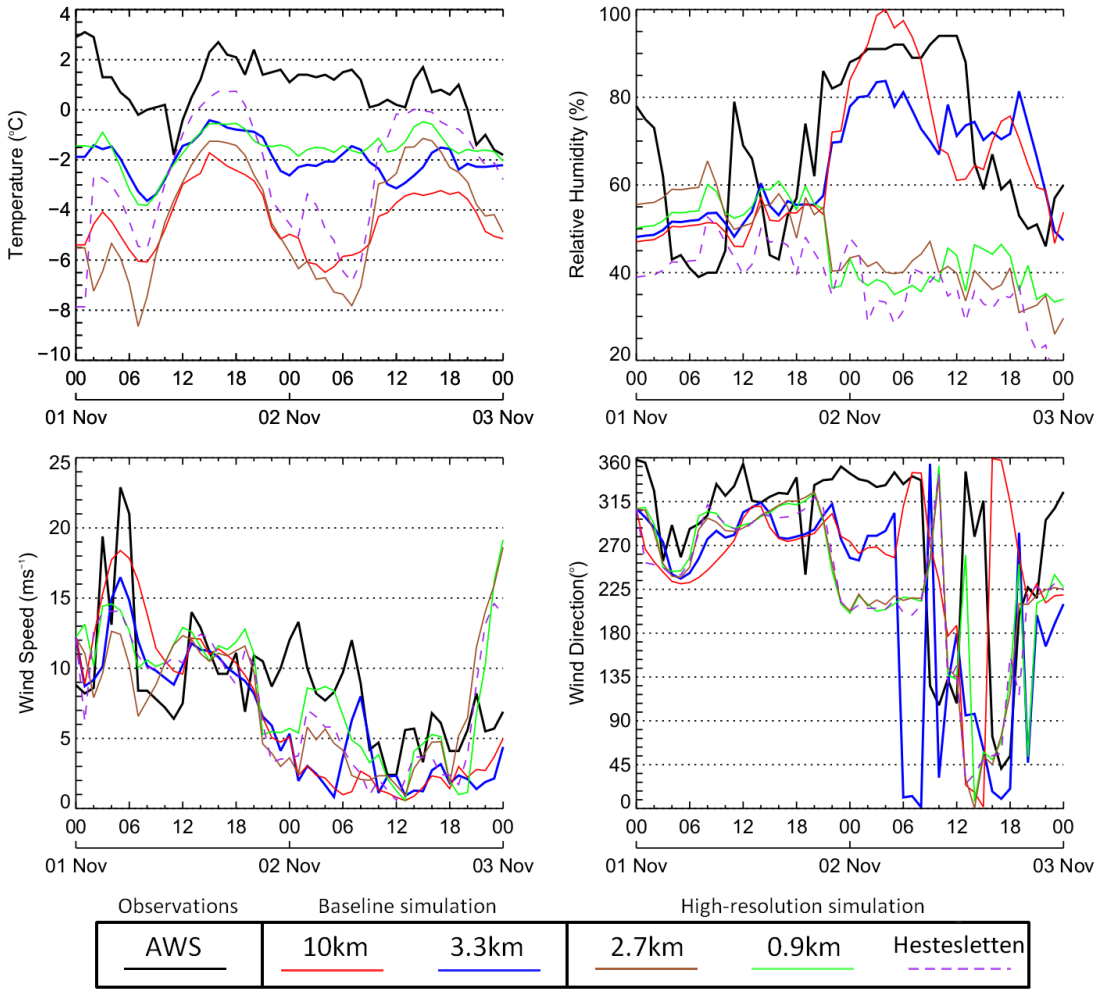

Figure 4.18 – *Observed and simulated 2-m air temperature, 2-m relative humidity, 10-m wind speed, and 10-m wind direction during 1 – 2 November 2007 (Case 3). The lines show the AWS observations (black), the simulated values at different horizontal resolutions of 10km, 3.3km, 2.7km and 0.9km (see legend), and the model timeseries at Hestesletten (purple dashed line).*

The observations of relative humidity at King Edward Point agree more with the modelled humidity in the coarse-resolution domains (10km and 3.3km), than in the high-resolution domains (2.7km and 0.9km). In the 0.9km domain, the relative humidity is much drier for the entire simulation, and is very unrealistic compared to the observations. At a resolution of 0.9km, the model has a negative correlation coefficient (-0.53), and a high RMS error (32.7%) and bias (-21.8%). This compares to a positive correlation of 0.51, a RMS error of 15.7%, and a bias of -4.6% in the 3.3km configuration (see Table 4.4, Appendix 4A.5). Therefore, for Case 3, the higher horizontal resolution model setup does not improve the representation of relative humidity at King Edward Point.

In spite of this, WRF does a good job of capturing the wind field within King Edward Cove during this period, and this is evidenced by relatively low wind speed RMS errors and biases (see Table 4.5, Appendix 4A.5) compared to the other case studies. All the simulations include a sudden rise in wind speed at 0200 UTC 1 November. The AWS peaked at 22.9ms^{-1}, whereas the 10km domain simulates the highest speed of all the simulations at 18.4ms^{-1}. The model also captures the increase in wind speed at 1100 UTC at the beginning of the event. The intensity of the wind speed in the model matches the observations, however, the winds calm (to below 5ms^{-1}) too quickly, and remain so for the rest of the simulation. This can be attributed to the inaccurate representation of wind direction during the end of the event. At coarse-resolution, the wind direction is too northerly and very variable. In the 0.9km domain, wind direction appears to be more realistic during the morning of 1 November and during the evening of 2 November. In the high-resolution domains, the model simulates a turning of the wind to ~210^{o} for 10 hours at 2100 UTC 1 November. In contrast, the observations show that the wind was continually blowing from ~350^{o}. The turning of the wind in the high-resolution domains also coincides with the drop in relative humidity. Therefore, it is possible that at high-resolution, WRF is completely capturing the incorrect air mass in King Edward Cove during the event, resulting in diverging agreement between the modelled and observed near-surface meteorology.

Overall, the sensitivity simulations in the baseline simulations agree better with the AWS observations. Unlike Cases 1 and 2, there are no vast improvements by using the results from the high-resolution simulation. For this case study, it appears that the general characteristics of the föhn event are captured (i.e. a near-surface warming

event at 1100 UTC on 1 November), however, the intensity of the event at King Edward Point is not captured.

4.5.4 The Spatial Characteristics and Dynamics of Case 3

Compared to the other cases, the föhn warming signal on the northeast coast of South Georgia is indistinguishable in this case (Figure 4.19). As shown by Figure 4.19(b), there is no distinguishable cross-barrier surface temperature gradient between the southwest and northeast coasts of South Georgia. The 2-m air temperature at King Edward Point (AWS observations) remains below 3ºC (with a mean temperature of 0.9ºC, σ = 1.1) for the entire period, while the 2-m air temperature at Cape Darnley (WRF model) also remains below 2ºC (with a mean temperature of -1.3ºC, σ = 1.2). In addition to this, the synoptic conditions which appear to drive this warming event are significantly different compared to Cases 1 and 2. Figure 4.19(a) shows that this event developed in relatively weak north-westerly air flow, with the upstream air parallel to the island, rather than perpendicular to it. None of the orographically-induced features seen in Case 1 (Figure 4.9(a)) and Case 2 (Figure 4.14(a)) can be seen in this case study.

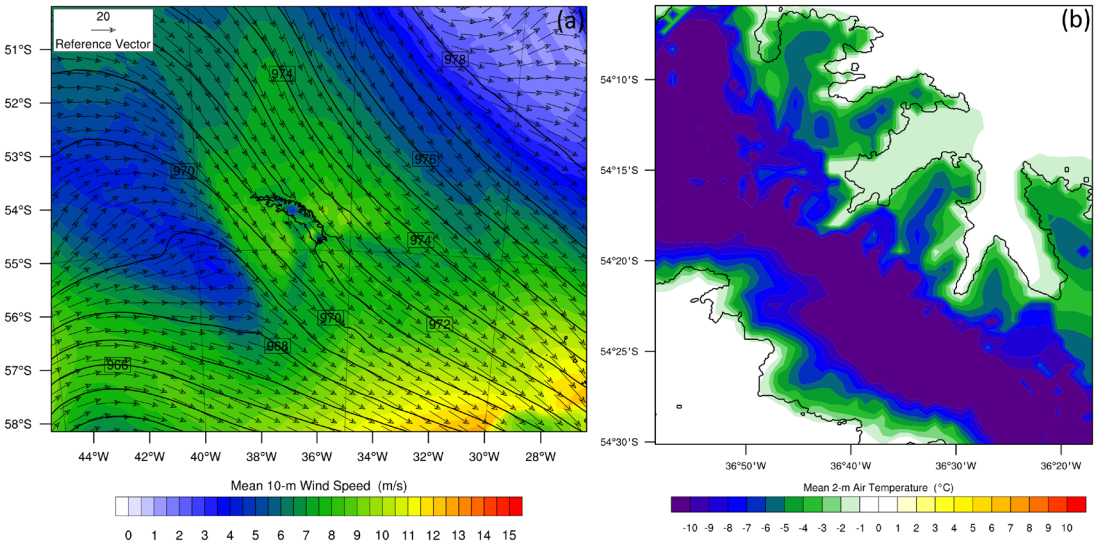

Figure 4.19 – *The mean modelled conditions during the 1 – 2 November 2007 föhn event. The mean is calculated from the model's hourly output from 1200 – 0800 UTC. Panel (a) mean 10-m wind speed (filled contours), mean 10-m wind vectors and mean sea level pressure (hPa, black contours). This is plotted from the 10km baseline WRF simulation. Panel (b) mean 2-m air temperature. This is plotted from the 0.9km high-resolution WRF simulation.*

Figure 4.20 shows three different vertical cross-sections of potential temperature and wind speed through the island. Cases 1 and 2 have shown that during strong föhn conditions, there are large amplitude wave disturbances to the northeast of the South Georgia, along with leeside flow acceleration and isentropic drawdown. Immediately apparent in Figure 4.20 are the significant differences of the flow dynamics and characteristics of this event, compared to Case 1 (Figure 4.10) and Case 2 (Figure 4.15).

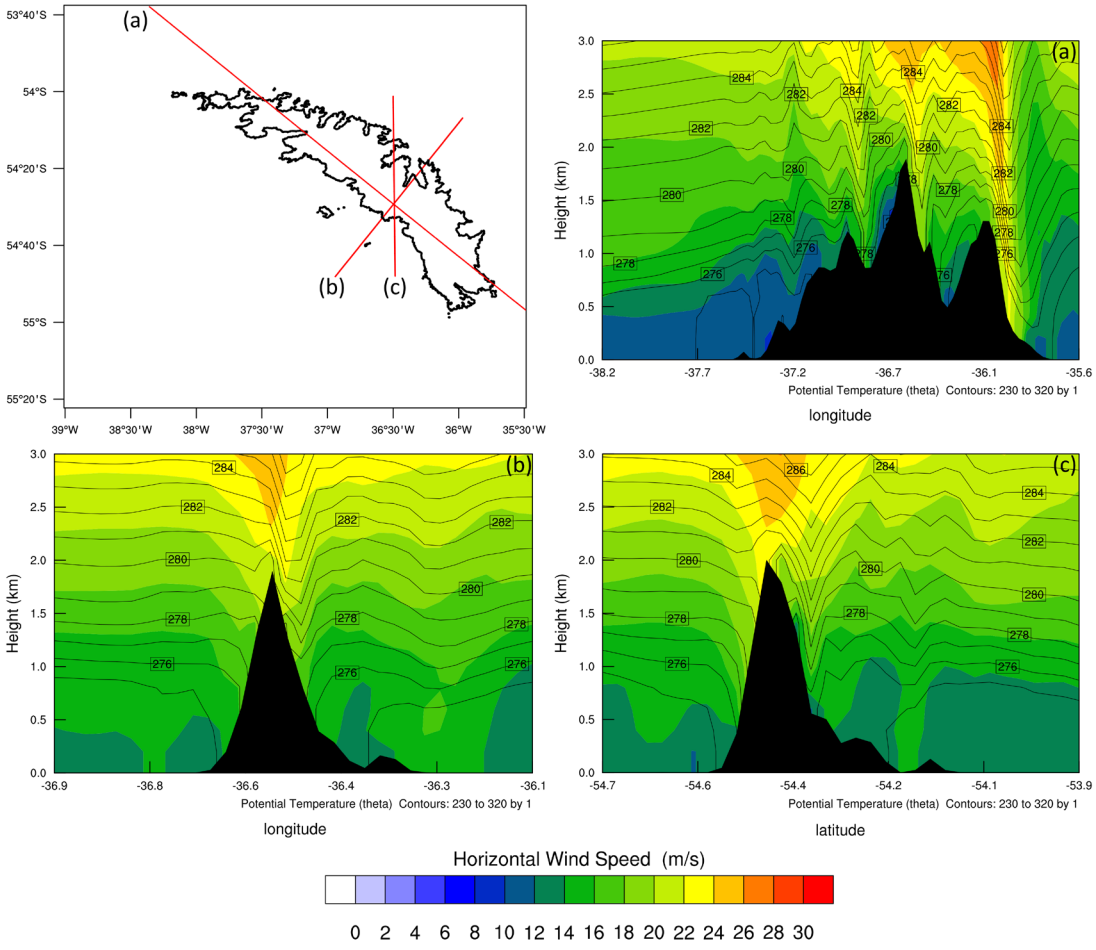

Figure 4.20 – *Vertical potential temperature (K, black contours) and wind speed (ms^{-1}, filled contours) cross-sections through lines (a), (b) and (c), for 1600 UTC 1 November 2007. This is plotted from the 2.7km high-resolution WRF simulation.*

There is very little wave activity in the lee of the island, and as such, wind speeds are not increased in the lee (see cross-sections (b) and (c)). There is no evidence of strong downslope winds as a result of cross-barrier flow, and there is no potential temperature gradient between the southwest and northeast coastlines. The potential temperature contours below 1km west and east of South Georgia reveal that the atmosphere is neutral. Therefore, vertical motion over the island is not being enhanced in these

conditions. Likewise, there is neither any evidence of a wake region at the south end of South Georgia (cross-section (b)) nor of tip jets at either end of the island (cross-section (a)).

4.5.5 Summary

Case 3 and the results of the WRF sensitivity simulations are interesting for two reasons. Firstly, WRF does not reproduce the föhn-like event at King Edward Point during this period adequately, regardless of the domain configuration and of the physics and boundary layer schemes and parameterisations used. Even at high horizontal resolution, the model fails to replicate the variability and intensity of the near-surface meteorological fields within King Edward Cove. Secondly, and assuming that the larger-scale features are consistent with reality, then Case 3 should not be declared to be a westerly föhn event. The large-scale features of the flow suggest that föhn is not occurring at King Edward Point during this time. Strong downslope winds and a leeside surface warming are not observed in the WRF model. Although föhn would be detected by the AWS criteria, it is likely that the 2^{o}C warming (and subsequent small surface drying and increased wind speeds) at King Edward Point are not related to the föhn flow over the main mountain chain of South Georgia. The weak surface föhn-like signature may have been a result of weak föhn warming associated with flow over Thatcher Peninsula and surrounding topography and/or due to warm air advection from the north. This case study not only shows that WRF fails to reproduce the meteorological conditions at King Edward Point during this period, but this case study also illustrates that some of the events detected in the AWS catalogue may actually be instances of (rapid, but weak) warming events (i.e. an increase in temperature by 2 – 3^{o}C in 1 hour at King Edward Point) which are not a result of westerly flow over conditions. The only way to refine the detection of föhn across South Georgia is by using high-resolution atmospheric models which give a much greater spatial and temporal coverage of the entire island. In the absence of the flow features previously seen in Cases 1 and 2, the WRF model adds credence that this event is a non-föhn event altogether.

4.6 Case 4: 10 – 12 February 2011

4.6.1 The Evolution of Case 4: Observations and Measurements

Case 4 was also examined in Chapter 3 (see Figure 3.6 or Figure 4.21) (named Case D in the previous chapter). In the period of 10 to 12 February 2011, two föhn events were observed at King Edward Point within quick succession. In both instances, the onset of föhn happened suddenly, with abrupt changes in temperature, wind speed, relative humidity and wind direction. In the context of föhn events which were observed between January 2003 and February 2013, the first föhn is the 39th absolute warmest event, and the 92nd absolute windiest and driest event. Then second föhn event during this period is the 6th absolute warmest event, the 101st absolute windiest event, and the 98th absolute driest event. This period was chosen for the WRF sensitivity simulations to explore how faithfully the model reproduces two intense föhn events, as well as their characteristics, features and dynamics. Therefore, the intense föhn events of Case 4 are simulated with the WRF model to contrast the weak event of Case 3. The meteorological conditions as recorded by the AWS at King Edward Point, during 10 – 12 February 2011, are show in Figure 4.21.

The morning of 10 February 2011 was calm and cool. Throughout the morning, there was a light breeze of < 5ms^{-1} from a variable north-westerly direction. The air temperature slowly increased through the morning and early afternoon, as a result of the diurnal cycle of incoming solar radiation. This too coincided with an increase in relative humidity. From 1200 UTC, the AWS recorded a turning of the winds from the east. By late afternoon, the air temperature slowly began to decrease. The start of the first föhn event was detected at 2020 UTC 10 February (blue shading, Figure 4.21). Within 1 hour of föhn onset, the air temperature at King Edward Point had increased by 6.2^{o}C. The start of the event was also marked by a simultaneous decrease in relative humidity of 20% in 1 hour, and rapid increase in 10-m wind speed. As with Case 1, the wind direction during the beginning and the end of this event was variable, and this again appears to drive the delayed and muted wind speed increase also at the beginning and at the end of this event. The maximum temperature, and wind speed reached during the föhn was 17.3^{o}C and 30.9ms^{-1}. The minimum relative humidity recorded by the AWS was 44%. The föhn event lasted 23 hours and 30 minutes in duration. The end of the event (at 1950 UTC 11 February) was marked by a drop in

temperature and a simultaneously increase in humidity. The winds at King Edward Point once again became very variable.

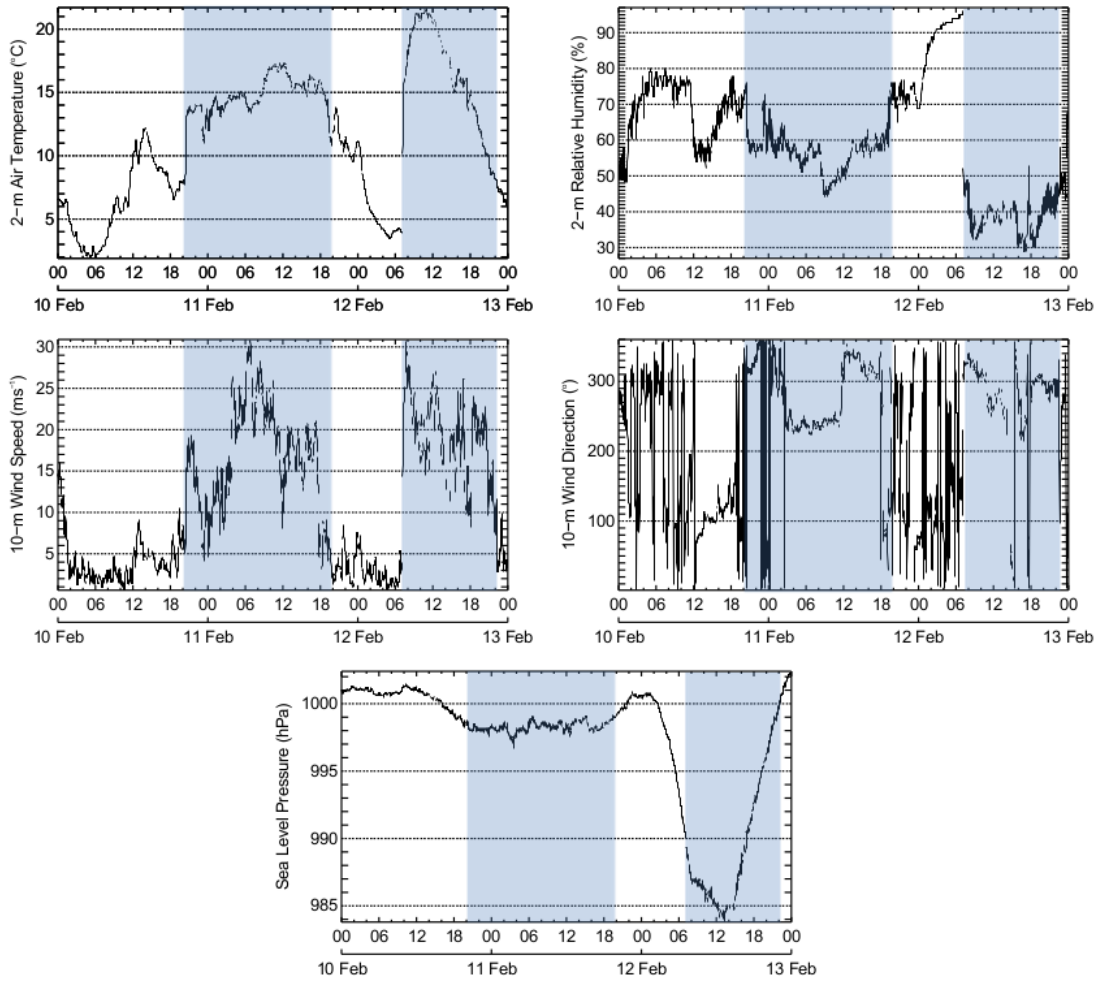

Figure 4.21 – *Meteorological conditions (2-m air temperature, 2-m relative humidity, 10-m wind speed, 10-m wind direction, and sea level pressure) during 10 – 12 February 2011. Blue shading highlights föhn event as defined and detected by the AWS föhn classification method.*

For the rest of 11 February, the temperature at King Edward Point continued to cool, reaching a minimum of 1ºC, with winds speeds <8ms^{-1}. The start of the second föhn event was detected at 0705 UTC 12 February (blue shading, Figure 4.21). While the first föhn event was not particularly intense, the second föhn event experienced a jump in temperature of 17.8ºC, reaching a maximum temperature of 21.7ºC, within just 3 hours of föhn onset. Of all föhn events which occurred between 2003 and 2013, this was the second highest absolute increase in temperature during a föhn event. There was also a simultaneous increase in wind speed reaching a maximum of 30.7ms^{-1}, along with a simultaneous decrease in relative humidity reaching a minimum of 27%.

This föhn warming was not sustained, and throughout the evening of 12 February, the temperature and wind speed gradually decreased. There is no abrupt end to this event, and so it was set at 2355 UTC (see section 3.2.1). This föhn event had a total duration of 16 hours and 50 minutes.

4.6.2 Synoptic Background

Figure 4.22 shows 6-hourly ERA-Interim sea level pressure plots from 1800 UTC 10 February to 1800 UTC 12 February 2011. As shown by Figure 4.22, a strong west-southwesterly flow across South Georgia was observed for the entire period. The ERA-Interim reanalysis fields show that the mean upstream wind direction at mountain top height for the entire period was 241^{o}. Up until 12 February, the synoptic situation did not change, and this is also reflected in the sea level pressure timeseries from the King Edward Point AWS (Figure 4.21) which did not change considerably during 10 – 11 February 2011. In the surface AWS observations, the first föhn event (10 – 11 February 2011) was generated after the wind direction at King Edward Point had turned from an easterly direction to a north-westerly wind direction. The variable and easterly direction of the surface wind at King Edward Point AWS during 10 February may have been localised (via localised topographic modification) rather than a result of the synoptic-scale flow. The synoptic features during the first event maintain a strong west-southwesterly flow across the island during this time. In contrast, the second föhn event (12 February 2011) was generated by a small area of low pressure (988 hPa) which tracked eastwards, south of South Georgia. The passage of this system was also measured at the AWS site, which shows that the pressure dropped by 15.7 hPa within 12 hours. This system continued to move south and north of South Georgia and by 1800 UTC, its position in the Southern Ocean resulted in strong south-westerly flow over the island. The föhn event appears to have ended as the low pressure moved out of the vicinity of the island, which resulted in the high pressure system moving southwards, west of South Georgia. This was seen by an increase in sea level pressure in the surface AWS observations at King Edward Point (Figure 4.21), bringing a strong south-westerly (211^{o}) flow over South Georgia.

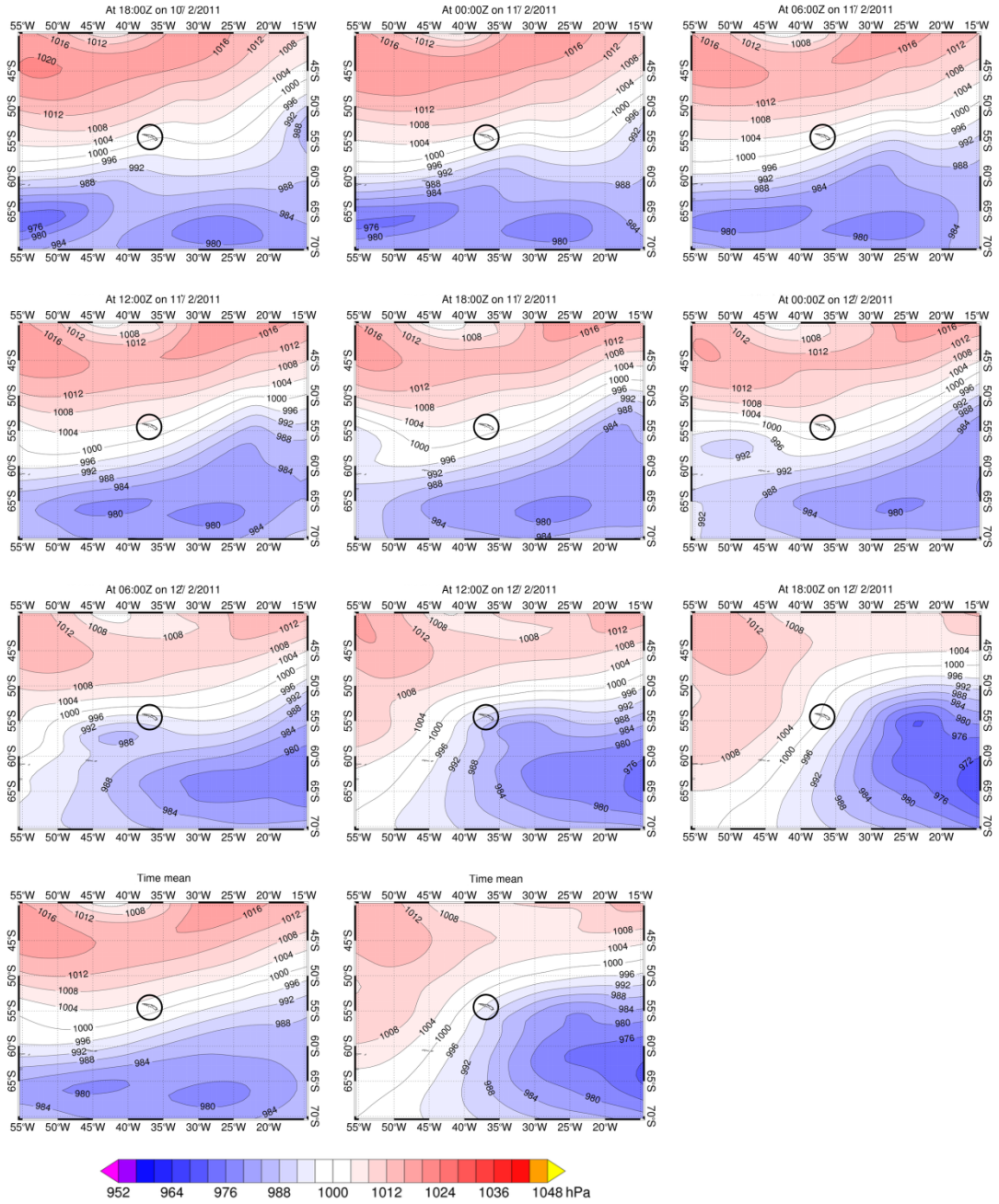

Figure 4.22 – *6-hourly ERA-Interim sea level pressure plots from 1800 UTC 10 February to 1800 UTC 12 February 2011. The bottom panels show the mean sea level pressure pattern for 0000 – 1800 UTC 11 February 2011 (i.e. during the first observed föhn event at King Edward Point) and 1200 – 1800 UTC 12 February 2011 (i.e. during the second observed föhn event at King Edward Point). South Georgia is circled in black.*

4.6.3 WRF Simulations

There is generally a very good match between the modelled and observed near-surface meteorological conditions at King Edward Point during the 10 – 12 February 2011

(Figure 4.23). Plots of all the sensitivity simulations for Case 4 are shown in Appendix 4A.4, and the error statistics are given in Appendix 4A.5.

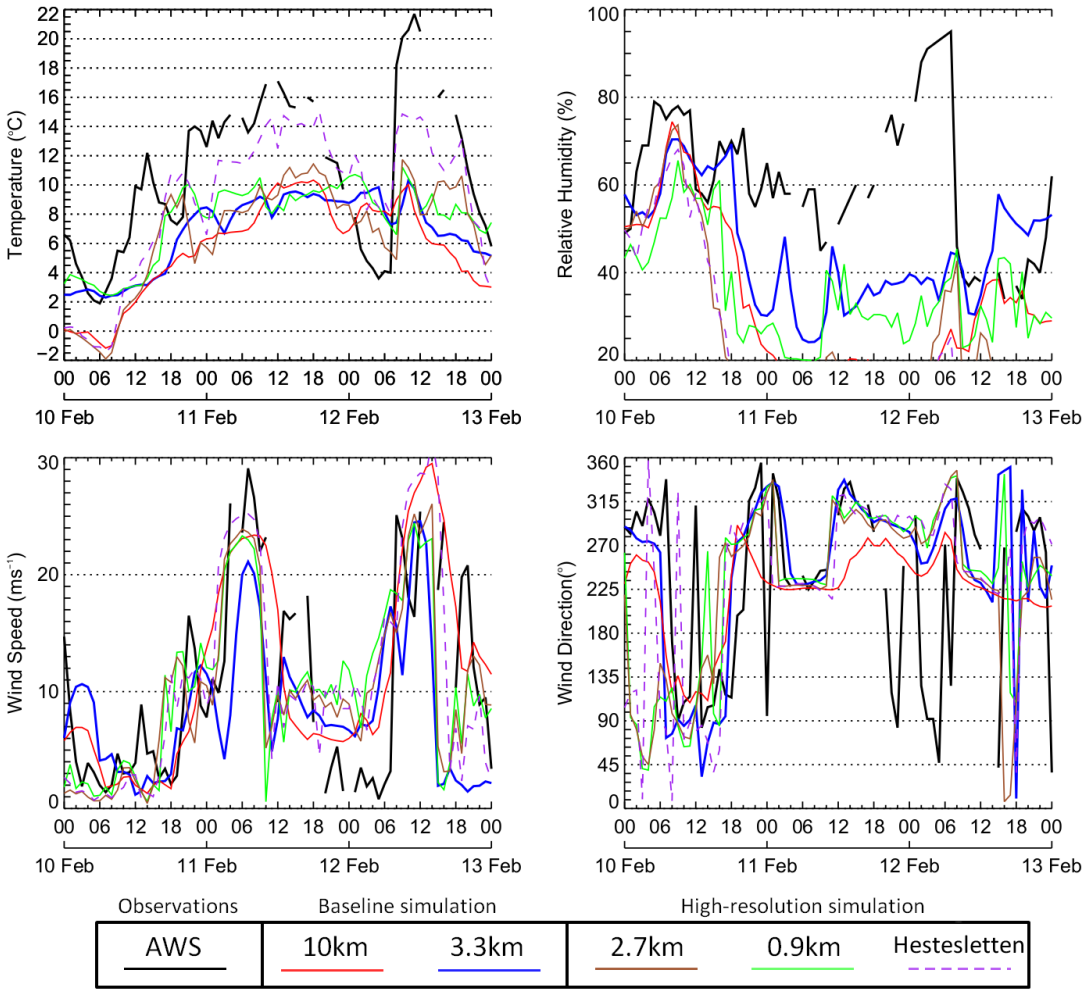

Figure 4.23 – *Observed and simulated 2-m air temperature, 2-m relative humidity, 10-m wind speed, and 10-m wind direction during 10 – 12 February 2011 (Case 4). The lines show the AWS observations (black), the simulated values at different horizontal resolutions of 10km, 3.3km, 2.7km and 0.9km (see legend), and the model timeseries at Hestesletten (purple dashed line).*

Both of the events observed during 10 – 12 February 2011 are cases of classic föhn winds; they are associated with rapid responses in temperature, wind speed and wind direction. Overall, WRF captures these changes, and the variability of this period, realistically. As previously found in Cases 1 and 2, increasing the horizontal resolution of the WRF simulations has the biggest impact on the model's accuracy of simulating föhn flow at King Edward Point. This is because the model is more adequately able to resolve the complex topography of South Georgia, which has important consequences on the thermodynamic processes associated with such events. In the 3.3km and 0.9km

domains, both modelled föhn events at King Edward are somewhat muted, and this is consistent with the previous case studies. There is a clear cold temperature bias in the model, and neither the 3.3km nor the 0.9km horizontal resolution domains simulate the cooling between the events (at 0100 UTC 12 February). Despite this, the model timeseries from Hestesletten (from the high-resolution domain) does capture the intensity of both föhn events. The temperature distribution at Hestesletten has a higher correlation (0.88) and a lower bias (-2.1^{o}C) compared to the modelled temperature at King Edward Point (0.78 and -3.3^{o}C, respectively; see Table 4.3, Appendix 4A.5) at the same resolution. The maximum temperature observed at King Edward Point and modelled in Hestesletten during the first föhn event are 17.1^{o}C and 15.1^{o}C respectively. During the second event, they are 21.7^{o}C and 15.0^{o}C respectively. Although no assumptions can be made about the real impact of föhn on Hestesletten during this period, the modelled intensity and variability of the near-surface temperature at Hestesletten matches the observed near-surface temperature observed at King Edward Point. This suggests that the modelled föhn warming did not extend far enough into King Edward Cove. Inspection of Figure 4.24(b) and (d) show that the warmest 2-m air temperatures (>10^{o}C) during both events did terminate over Hestesletten. Therefore, had the warming extended slightly more north (by <1km) in the model, then the observed and modelled temperatures at King Edward Point may have agreed more.

Unlike temperature, the relative humidity throughout the 10 – 12 February period is poorly reproduced by the model (as with Case 3). All sensitivity simulations have a low correlation coefficient (< 0.52), and very high RMS errors (> 22%) and biases (> -11%; see Table 4.4, Appendix 4A.5). Following a decrease in humidity in all sensitivity simulations from approximately 1100 UTC 10 February onwards, the relative humidity at King Edward Point stays below 50%. These low values are very unrealistic compared to the observations. Steinhoff *et al*. (2013) also noted a significant negative relative humidity bias in their WRF simulations, and this was subsequently attributed to a negative moisture bias over Antarctica in ERA-Interim. The cause of negative relative humidity biases at King Edward Point during föhn needs further investigation. Since the other fields are well replicated compared to the observations, it may be a moisture and/or mixing problem with the WRF model and/or the reanalysis forcing dataset. There are no simulations which rectify the modelled

relative humidity bias, and horizontal resolution appears to have the biggest sensitivity on this field (see Appendix 4A.4 and Appendix 4A.5).

Despite the disagreements regarding the modelled relative humidity, the variability of wind speed and wind direction at King Edward Point (during both events) is well captured by the WRF model. Across all the simulations, the peaks in wind speed match that of the observations, and increasing the horizontal resolution also improves this. The peak wind speed during the first föhn event in the observations and in the 0.9km resolution domain are 29.1ms^{-1} and 23.3ms^{-1} respectively. During the second event, the peak wind speeds are 25.4ms^{-1} and 24.4ms^{-1} respectively. Between the föhn events (i.e. ~0100 UTC 12 February) the modelled wind speed stays too strong (5 – 10ms^{-1}), and this may be an artefact of the winds also staying too north-westerly during this period. As with wind speed, the quick variability in the wind direction field is captured across all simulations, and there are few differences between the 3.3km and 0.9km domain.

Despite reservations over the modelled relative humidity during this case study period, the model does capture much of the variability in wind direction along with the intensity in air temperature and near-surface wind speed fields. Based upon the WRF model simulations, and using the föhn identification method described in Chapter 3, föhn would be declared at King Edward Point and at Hestesletten in the 0.9km domain at 1700 UTC on 10 February 2011. In addition to this, föhn would also be declared at 0800 UTC and 0900 UTC at Hestesletten and King Edward Point (respectively) on 12 February 2011. Therefore, by the AWS definition, the model is producing two föhn events during this period. Clearly, WRF is able to model the föhn effect at King Edward Point during this period.

4.6.4 The Spatial Characteristics and Dynamics of Case 4

The high-resolution simulation produces significant fine-scale spatial variability as a result of the strong cross-barrier conditions (Figure 4.24). Immediately apparent is the generation of important surface features, which were also observed, but to a lesser extent, in Cases 1 and 2. During the first föhn event (Figure 4.24(a)), there again is evidence of deceleration of the upstream incident flow, along with flow splitting around the island (diverting more to the right when looking downwind as a result of Coriolis force, see Ólafsson & Bougeault, 1996).

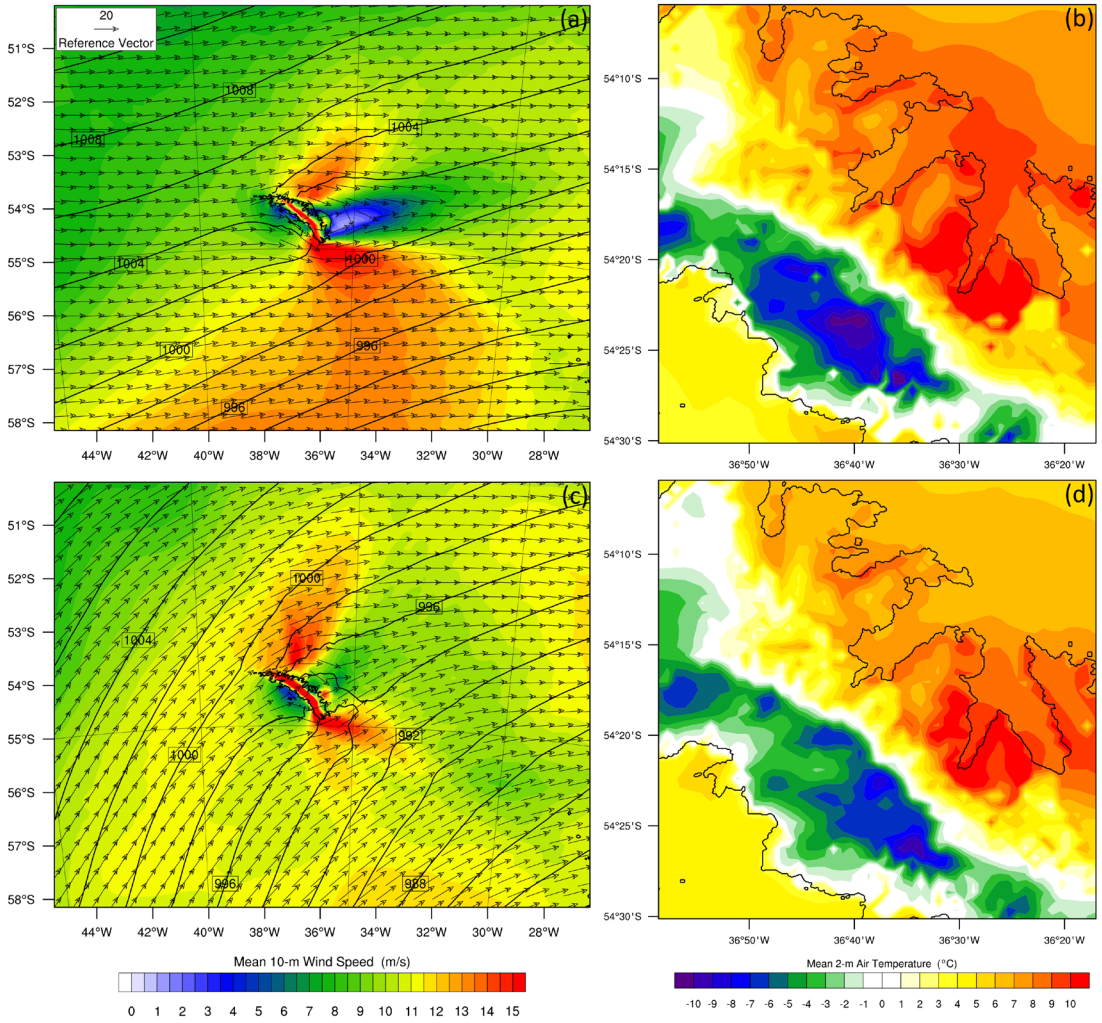

Figure 4.24 – *The mean modelled conditions during the 10 – 11 February and 12 February 2011 föhn events. The means are calculated from the model's hourly output from 2000 UTC 10 February – 1900 UTC 11 February, and from 0700 – 2300 UTC 12 February, respectively. Panel (a) mean 10-m wind speed (filled contours), mean 10-m wind vectors and mean sea level pressure (hPa, black contours) during the 10 – 11 February föhn event. Panel (b) mean 2-m air temperature during the 10 – 11 February föhn event. Panel (c) as (a) but for the 12 February föhn event. Panel (d) as (b) but for the 12 February föhn event. Panels (a) and (c) are plotted from the 10km baseline simulation. Panels (b) and (d) are plotted from the 0.9km high-resolution simulation.*

There is also a wake region of relatively weak winds (<6ms^{-1}) which extends many tens of kilometres downstream of South Georgia (Figure 4.24(a)). There are also two jets of up to 16ms^{-1} either side of the wake region. All these features are also observed 24 hours later, during the second föhn event (Figure 4.24(c)). As previously highlighted, the leeside orographically-driven wind disturbances observed here are also similar to those observed by Hosking *et al.* (2015). They found that such disturbances are responsible for strong wind stress curl and enhanced heat flux over

the continental shelf waters surrounding South Georgia. Hosking *et al*. (2015) concluded that these features have important implications on the surrounding marine environments.

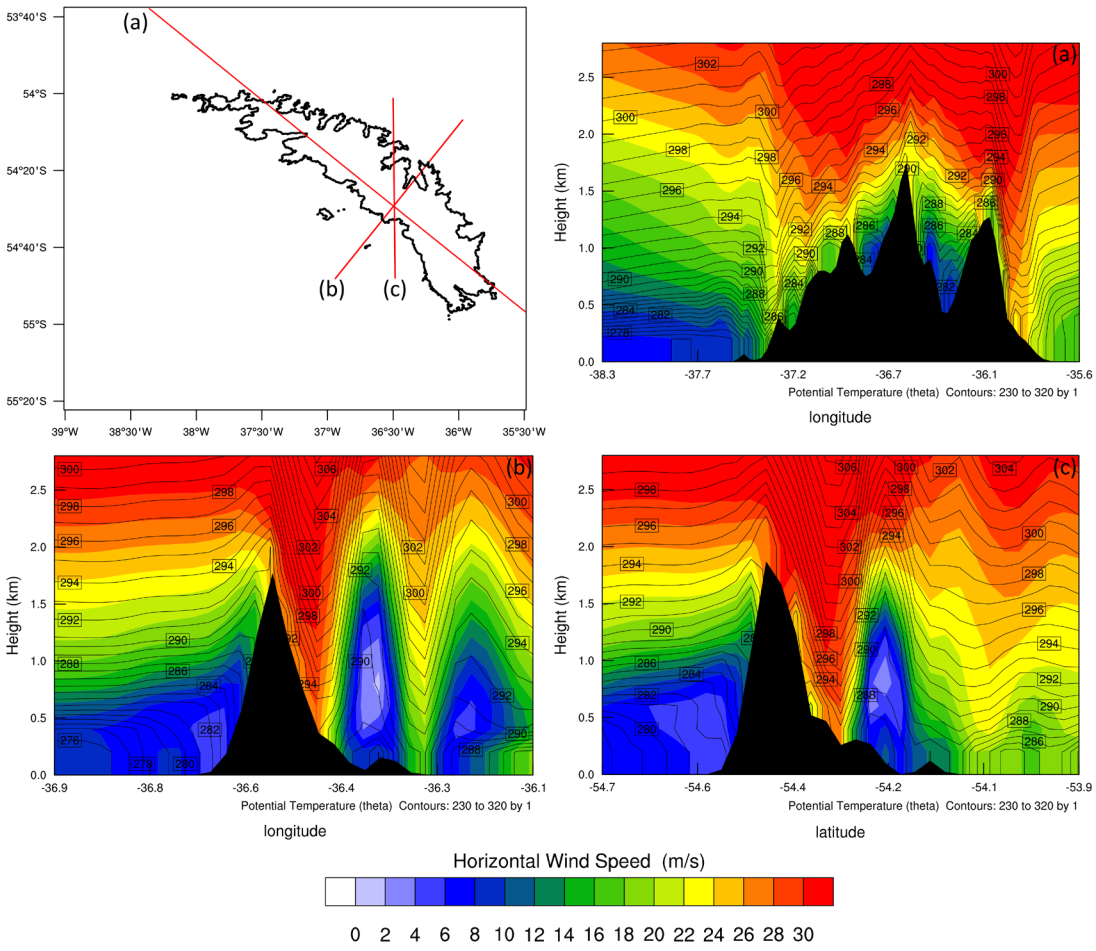

Figure 4.25 – *Vertical potential temperature (K, black contours) and wind speed (ms^{-1}, filled contours) cross-sections through lines (a), (b) and (c), for 1200 UTC 11 February 2011. This is plotted from the 2.7km high-resolution WRF simulation.*

In addition to this, the asymmetrical pattern of warming during both these föhn events can also be seen in Figure 4.24(b) and Figure 4.24(d), with the north-eastern coastline much warmer than the south-western coastline. The WRF model reveals that 2-m air temperatures are particularly high along the exposed and non-ice covered regions along the northeast coast of South Georgia. The highest temperatures are experienced to the south of King Edward Point along Hestesletten glacial plain, as well as across Moraine Fjord and Greene Peninsula. This was also seen with Case 2 (Figure 4.14(b)). Since the model indicates that high temperatures were also experienced along the north-facing coasts of Lewin and Barff Peninsulas (see Figure 1.2(c)), both of these

föhn events may have been detectable had observations also been available from Husvik and Godthul whaling stations.

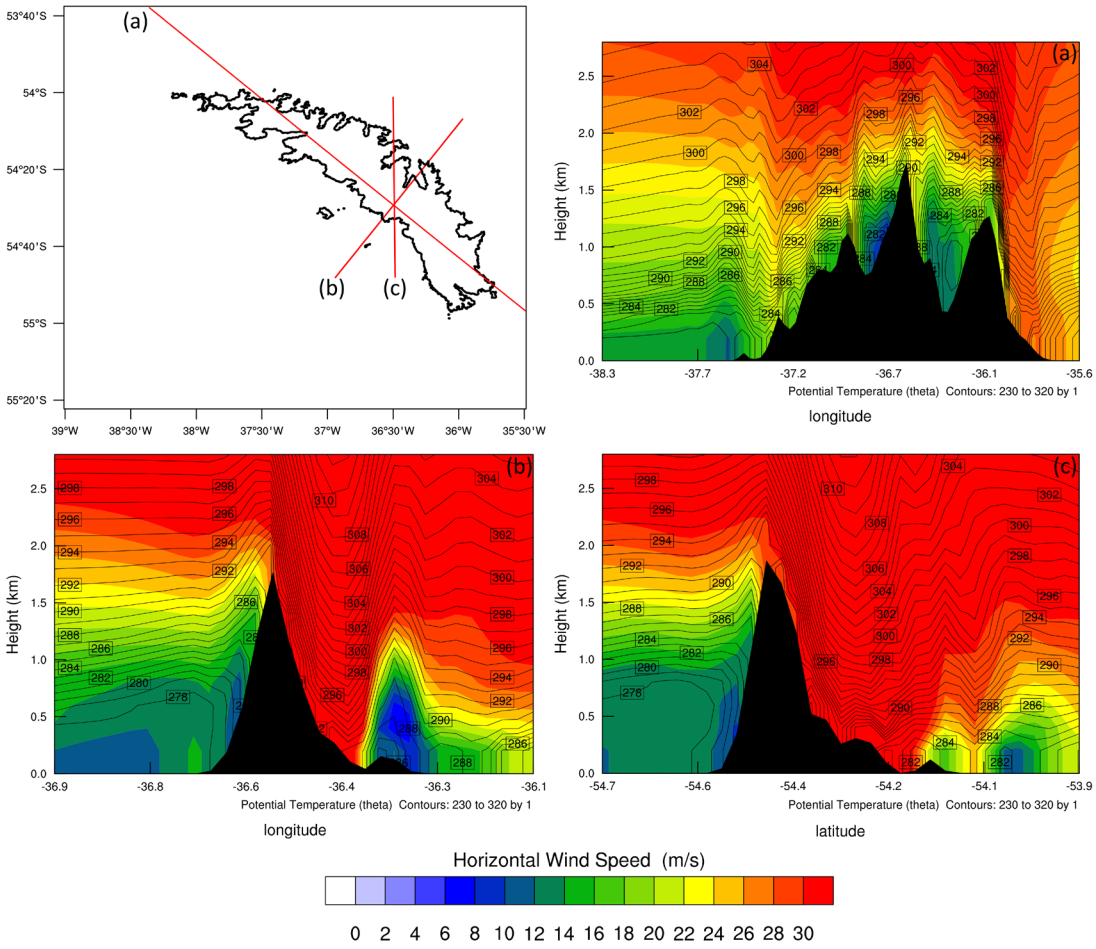

Figure 4.26 – *Vertical potential temperature (K, black contours) and wind speed (ms^{-1}, filled contours) cross-sections through lines (a), (b) and (c), for 1200 UTC 12 February 2011. This is plotted from the 2.7km high-resolution WRF simulation.*

Since it has already been established that these case studies are instances of strong föhn conditions, and that the model is able to sufficiently model the conditions, it is unsurprising that the dynamics responsible for the events are easily discernible. Figure 4.25 and Figure 4.26 show different vertical cross-sections of potential temperature and wind speed through South Georgia, for both föhn events. As with Cases 1 and 2, the most striking feature of these cross-sections are the large amplitude wave disturbances in the lee of South Georgia, along with particularly strong winds directed down the lee slopes, underneath a region of tightly-packed isentropes (Figure 4.25(b) and 4.26(b)). The upstream mountain height Froude number for both föhn events was 2.5 (at 1200 UTC 11 February 2011) and 2.8 (at 1200 UTC 12 February 2011) respectively, much higher than Case 1 and Case 2. These high Froude numbers are

consistent with linear flow regime and should be contrasted with the Froude number of 1.1 during the morning of 9 February 2011 (before the first event commenced). There is clear evidence that during this event, air is descending from height towards the surface on the north-eastern slopes of South Georgia, which is responsible for the rapid rise in 2-m air temperature (which has been warmed adiabatically) and 10-m wind speed in the surface AWS observations at King Edward Point. Therefore, both föhn events during 10 – 12 February 2011 appear to have been dynamic föhn, where leeside isentropic drawdown caused large warm temperature and dry humidity anomalies close to the base of the lee slopes.

4.6.5 Summary

Consistent with the previous case studies, increasing the horizontal resolution of the model has the biggest impact of the model's ability to reproduce the observations. By doing so, the model correctly captures the complex terrain and geometry of South Georgia. From the analysis of flow dynamics, leeside isentropic drawdown again is the likely driver of leeside warming and drying (indicating that these are dynamic föhn events). The large-scale features associated with strong upstream westerly flow, lead to an amplified response in near-surface warming in the low-lying north-eastern coastline of South Georgia. These features are consistent with Cases 1 and 2.

4.7 Evaluation of WRF Simulation Quality: A Comparison between Case Studies

In order to evaluate the performance of the WRF model and to compare its performance between case studies, Appendix 4A.5 summarises the mean bias, RMS errors, and correlation coefficients for modelled versus observed 2-m air temperature (Table 4.3), 2-m relative humidity (Table 4.4) and 10-m wind speed (Table 4.5) for all four case studies. The error statistics are compiled from hourly instantaneous data from the AWS at King Edward Point and the corresponding location in the WRF model. The sensitivity of WRF at replicating the observed föhn case studies with the different model setups will now be evaluated (see Table 2.2 for a full description of all the sensitivity studies).

It is important to note that while temperature, relative humidity and wind speed are evaluated in more detail, high correlations (correlations near unity) and low biases are characteristic of the surface pressure across all four case studies (not shown), and

across all sensitivity simulations, indicating that the model is capturing the surface pressure with high skill. Minor pressure biases can be attributed to the small differences in the elevation of King Edward Point and the surrounding topography in the model.

4.7.1 Sensitivity of the Model to Horizontal Resolution

For each of the four cases, the sensitivity of the model to the horizontal resolution was tested by using two domain configurations; one at 30 – 10 – 3.3km resolution (baseline simulation, see Figure 2.8) and another at 8.1 – 2.7 – 0.9km resolution (see Figure 2.9).

It is clear from the results that have been presented that increasing the horizontal resolution of the model had the best improvement on the results for temperature, wind speed and relative humidity. This is illustrated by the low biases and RMS errors and high correlations between the observed versus modelled temperature (Table 4.3), relative humidity (Table 4.4), and wind speed (Table 4.5) in the 0.9km configuration. At 3.3km resolution, there is a systematic cold bias (typically -3 – -5^{o}C) which dominates the whole temperature range for all four cases. This bias is reduced to an average of -1.7^{o}C in the 0.9km domain for the four events. Likewise, the RMS error decreases from an average of 4.5^{o}C at 3.3km resolution to 3.3^{o}C at 0.9km resolution, while the mean correlation coefficient increases from 0.71 to 0.76. Wind speed also shows strong dependency on the horizontal resolution of the model, and biases in this field are likely related to the steep, complex topography of Thatcher Peninsula. The magnitude of the correlation coefficients (0.35 – 0.64) and biases (-0.8 – 1.3ms^{-1}) tend to be higher and lower (respectively) at high horizontal resolution compared to coarse-resolution (-0.18 – 0.57, -3.5 – -2.0ms^{-1}, respectively). It is important to note that increasing the horizontal resolution of the model did not always give better results, which is likely due to important unresolved topographic and heterogenic effects even for the 0.9km resolution. This is particularly true for the modelled relative humidity in Cases 2, 3 and 4 which show higher RMS errors (typically 11% greater) and biases (typically 4% greater) than the 3.3km simulation. In contrast to these cases however, the relative humidity RMS error (19.0%) and bias (-4.9%) for Case 1 is significantly reduced (14.7% and -1.4%, respectively) at high-resolution. The poorly simulated

relative humidity field, which is persistent throughout all the sensitivity simulations, is discussed more in section 4.7.7.

Therefore, the results clearly demonstrate the important role of horizontal resolution in simulating the meteorological conditions at King Edward Point. The step from 3.3km to 0.9km significantly improves model performance. This is in agreement with previous atmospheric modelling studies which have also looked at föhn events and other strong downslope wind events (see e.g. Valkonen *et al*., 2010; Steinhoff *et al*., 2013; Orr *et al*., 2014; Elvidge *et al*., 2014; Gómez-Navarro *et al*., 2015). Since the events are better captured in domains with higher horizontal resolution, this implies that the horizontal resolution of the model is a key constraint for capturing sufficient small-scale detail of the föhn flow at King Edward Point. There may be a minimum required spatial resolution to simulate föhn winds at this location due to the significant reduction in the model's skill at horizontal resolutions coarser than 3.3km. Since biases in the temperature, humidity and wind speed fields become exacerbated at coarse-resolution, this also suggests that the main source of error in the model is due to unresolved orography. This is because the complex terrain of South Georgia is better resolved at higher spatial resolutions.

4.7.2 Sensitivity of the Model to Vertical Resolution and Model Top

Three different vertical configurations were tested, using 30 (baseline simulation), 70 and 140 vertical levels. In addition to this, the model top was also varied from 50hPa (baseline simulation) to 70hPa and 10hPa.

The results indicate that the WRF model is somewhat sensitive to the number of vertical levels. Table 4.3 shows that for the modelled near-surface temperature at King Edward Point, the vertical resolution does not lead to significantly different results. While Cases 1, 2 and 4 have higher correlation coefficients (0.70, 0.87, and 0.84, respectively) when simulated with 70 vertical levels compared to the baseline simulation with 30 vertical levels (0.68, 0.86, and 0.77, respectively), the RMS errors and biases for each of the case studies are not drastically different. In contrast to temperature, increasing the number of vertical levels does lead to improvements in the wind field at King Edward Point, and this is reflected in (generally) lower magnitude biases, RMS errors and higher correlations. For instance, the mean correlation coefficient for all four case studies using 30, 70 and 140 vertical levels is 0.31, 0.41

and 0.44 respectively. Improvements in the modelled wind speed are particularly noticeable for Case 3, whereby the model setup using 140 vertical levels significantly improves the near-surface wind field, increasing the correlation coefficient from 0.42 to 0.68 (which is also the joint highest correlation coefficient for wind speed for all the Case 3 sensitivity simulations). As with wind speed, increasing the vertical resolution also has small improvements in the modelled relative humidity (see e.g. Case 1).

In summary, therefore, increasing the vertical resolution of the WRF model generally reduces the model bias and RMS errors. As such, the modelled temperature, wind speed and relative humidity are closer to the AWS observations with higher vertical grid spacing. However, it is important to note that this advantage is most noticeable between 30 to 70 vertical levels, rather than between 70 to 140 vertical levels; there does not appear to be much gained from using 140 vertical levels compared to 70 vertical levels. As previously highlighted, this is a likely result of how the WRF model (by default) arranges the vertical grid below 1km; adding vertical levels does not increase the vertical resolution of the model at, and below, mountain height. Not only are there few improvements (i.e. there is little difference between the RMS errors, biases and correlation statistics between 70 and 140 vertical levels for each of the case studies), but such a high-resolution vertical grid spacing is also computationally very expensive. The computational efficiency of the model degrades rapidly with increasing vertical resolution, and it was found that the simulation time increased fivefold when simulating with 140 vertical levels. As such, the longer simulation time with this vertical setup may not be advantageous in relation to model performance. It is also important to note that the model remains largely insensitive to model top. There does not appear to be any advantage from increasing or decreasing the height of the model top relative to 50hPa.

4.7.3 Sensitivity of the Model to Planetary Boundary Layer and Microphysics Schemes

The tested planetary boundary layer parameterisation schemes are the Yonsei University (YSU, baseline simulation) scheme, the Mellor-Yamada-Janjic (MYJ) scheme, the Mellor-Yamada Nakanishi and Niino Level 2.5 (MYNN) scheme and the Quasi-Normal Scale Elimination (QNSE) scheme. Additionally, five different

microphysics schemes were also tested. These included the WRF Single-Moment 3-, 5- and 6-class (WSM3 [baseline simulation], WSM5 and WSM6, respectively) schemes, the Lin scheme and the Eta microphysics scheme. The statistical evaluation of the different planetary boundary layer and microphysics schemes for temperature, relative humidity and wind speed are given in Table 4.3, Table 4.4 and Table 4.5, respectively.

It is evident from the WRF results that the model is also comparatively insensitive to the choice of microphysics and boundary layer schemes. For temperature (Table 4.3) it is clear that the RMS errors and biases using the YSU scheme (the baseline simulation) are not remarkably changed when using either the MYJ, MYNN or QNSE schemes. The RMS errors for the four different boundary layer schemes for all four case studies vary between 2.9 – 5.9^{o}C. While the correlation coefficients for temperature show the largest variability for the different schemes (e.g. the MYJ scheme rather considerably reduces the correlation coefficient from 0.54 to 0.28 for Case 3), it is clear the modelled near-surface temperature at King Edward Point is consistently insensitive to the planetary boundary layer schemes. Figure 4.27, Figure 4.28, Figure 4.29 and Figure 4.30 have also show that the modelled temperature at King Edward Point remains underestimated in WRF. As such, Table 4.3 indicates that the YSU boundary layer scheme typically provides the best temperature distribution throughout all case studies. The same is also true for the five different microphysics schemes tested; for the modelled temperature there is no scheme which performs any better than the others. For wind speed, the choice of microphysics is also of minor importance (Table 4.5), while the different boundary layer schemes improve the wind speed error statistics for some of the case studies, but also worsen for others. Most notably, the QNSE scheme results in a very low correlation (-0.08) for Case 1 (worse than the baseline simulation, -0.18) but a very high correlation (0.71) for Case 4 (better than the baseline simulation, 0.41). In spite of this, the wind distribution remains typically too low in the model, and there is no clear scheme that outperforms the others across the case studies. Relative humidity is, perhaps as expected, most affected by the microphysics and boundary layer schemes due to these schemes influencing the processes which determine moisture in the atmosphere. The more sophisticated MYNN scheme generally outperforms the other schemes at capturing the relative humidity field for the four case studies. The mean correlation coefficient, RMS error

and bias for the MYNN scheme across all four case studies are 0.48, 17.9% and -4.5%, respectively. This compares to the baseline simulation (which utilises the YSU scheme) with mean error statistics of 0.48, 19.1% and -8.4%, respectively.

Therefore, the modelled föhn events remain largely insensitive to the choice of planetary boundary layer and microphysics schemes, especially when compared to the sensitivity of the model to the horizontal resolution. Unsurprisingly, there is very little difference between the WSM3, WSM5 and WSM6 schemes since the physics which drive these choices are so similar (Hong *et al*., 2004; Hong & Lim, 2006). In addition to this, the simpler microphysics schemes (e.g. WSM3, baseline simulation) do not generally do worse than the more advanced schemes (e.g. the Eta scheme). Similarly, the results do not indicate that the more sophisticated QNSE and MYNN turbulent schemes outperform the YSU and MYJ planetary boundary layer schemes. We might expect the different schemes to produce very different planetary boundary layer cycles and to therefore have a strong influence on the winds and temperature at King Edward Point. However, the model performances for each of the parameterisations are similar to one another. It is also important to note that some of these differences in the performance of these schemes may be due to seasonal and diurnal differences in how well the parameterisations perform in summer (e.g. Case 1 and Case 4) and winter (e.g. Case 2) months, and during the night (e.g. Case 2 and Case 3) and during the day (e.g. Case 1). Finding the best of them may require further testing since each of the options appears to be satisfactory for replicating the observed föhn effect at King Edward Point.

In summary, for all four föhn case studies, the WRF model is capable of reproducing the surface parameters to some degree of accuracy without large differences between the planetary boundary layer schemes. Temperature and wind speed are in good agreement with the observations for all the schemes. As such, there is no scheme which matches the observations from the AWS at King Edward Point better than the others in a consistent way. The tendency here is that the YSU and WSM5 scheme work better across the four case studies. The added advantage of the YSU scheme is that the subgrid-scale orography parameterisation scheme (the topo_wind switch, see Jiménez & Dudhia, 2012) is only compatible with this planetary boundary layer scheme (see section 4.7.5).

4.7.4 Sensitivity of the Model to Longwave and Shortwave Parameterisations and Land Surface Model

The schemes tested for the föhn sensitivity simulations were the Rapid Radiative Transfer Model (RRTM) and Dudhia schemes (baseline simulation), and the New Goddard scheme. Two different land surface models were also tested; these were the Noah (baseline simulation) and RUC land surface models.

Neither the longwave and shortwave parameterisations nor the land surface model appear to consistently improve the modelled case studies, compared to their respective baseline counterparts. They do not appear to outperform the other baseline options, and the correlation coefficients, RMS errors and biases are consistent throughout all case studies. For instance, the RUC land surface model improves the modelled wind speed during Case 3 (correlation coefficient = 0.68, RMS error = 4.1ms^{-1}, bias = -2.5ms^{-1}) compared to the baseline simulation (0.42, 4.3ms^{-1}, -2.4ms^{-1}, respectively), but also results in worse modelled relative humidity during Case 3 (0.33, 22.4%, -9.2%, respectively) compared to the baseline simulation (0.51, 15.7%, -4.6%, respectively). This is similarly found for all four case studies. As such, the modelled conditions at King Edward Point do not appear to be sensitive to the longwave and shortwave parameterisation nor the land surface model. The differences between the schemes are so small that an identification of a setup which significantly outperforms the others is not possible when considering the modelled temperature, wind speed and relative humidity fields.

4.7.5 Sensitivity of the Model to Topographical Resolution, Land Surface Type, and Slope and Shading Effects

In addition to the default datasets for topography and land surface type (baseline simulation), high-resolution datasets of these static data fields were also tested (see section 2.3.1.1). The models performance with the slope (slope_rad), topography (topo_wind) and shading (topo_sha) switches turned on were also tested.

Using the high-resolution topography dataset results in small reductions in RMS errors, as well as increases in correlation coefficients, across the modelled temperature, wind speed and relative humidity fields for all four case studies. This is particularly noticeable for Case 4 in which the correlation coefficients for temperature,

wind speed and relative humidity increase from 0.77, 0.41 and 0.41 (respectively) to 0.84, 0.64 and 0.50 (respectively). The relative humidity field also shows a reduction in bias (from a mean of -8.4% to -6.2% across the four case studies). Such improvements in the modelled föhn events can be attributed to a better representation of the complex surrounding topography. As with the results of varying the horizontal resolution (see section 4.7.1), these results strongly indicate that the main source of error in the model is due to unresolved orography. Deb *et al*. (2015) have similarly shown that for detailed modelling of near-surface variables over complex (Antarctic) terrain requires a high-resolution representation of topography. The new land surface of South Georgia has similarly important impacts on the modelled föhn events, and this is a likely consequence of altering the surface energy balance which is otherwise unrealistic without permanent snow and ice resolved in the model (see section. 2.3.1.1 for more details). Nearly every temperature and wind speed error statistic is improved (see e.g. Case 4), while correlations and RMS error values for relative humidity show low sensitivity to the land surface type. Interestingly, the new land surface data set decreases the performance of capturing the relative humidity field for Case 3; the RMS error and bias are 4.3% and 2.3% greater compared to the baseline simulation. In spite of this, numerous studies using WRF across for regional climate analysis across complex terrain have previously shown that accurate representation of the land surface is important, and such data sets do produce more accurate temperature, precipitation and energy balance patterns (see e.g. Sertel *et al*., 2009; Tao *et al*., 2013; de Meij *et al*., 2014).

The results also show that the topographic adjustment of wind (topo_wind) switch leads to more representative surface winds at King Edward Point (especially in Cases 1 and 4). For nearly every case study statistic (most notably wind speed), the topo_wind scheme improves the representation of these model fields when compared to when this is switched off in the 3.3km domain. Such improvements to the modelled fields are unsurprising, since this scheme accounts for unresolved topographic features which are not explicitly resolved at coarse-resolution by introducing a correction term in the moment equation (Jiménez & Dudhia, 2012). Therefore, this scheme aims to correct the general tendency of WRF to overestimate wind speed (see e.g. Cheng & Steenburgh, 2005), and has subsequently been shown to be more suited for reproducing wind speed over complex terrain (Jiménez & Dudhia, 2012; Lee *et al*.,

2014; Gómez-Navarro et al., 2015; Gonçalves-Ageitos *et al*. 2015). In contrast to this switch, accounting for topographical and shading effects (slope_rad and topo_sha; these switches account for shadows induced by nearby topography, self-shading and land surface inclination, which subsequently affect incoming radiation) have minimal impact on the surface meteorology during these föhn case studies. While these parameterisations are expected to have greater control on the modelled surface energy balance (i.e. net shortwave and longwave radiation) across the island, there are no surface radiation measurements available for validation during this period. Despite this, it is reassuring that the inclusion of these parameters in the model setup does not lead to any erroneous influences on the modelled conditions at King Edward Point.

In summary, therefore, these results further highlight that the unresolved topography of South Georgia leads to relatively large biases of temperature, wind speed and relative humidity at 3.3km resolution. However, these biases, particularly for temperature and wind speed, can be substantially reduced by using high-resolution topographical and land surface type data sets, as well as by using a planetary boundary layer scheme that explicitly considers the effects of non-resolved topography. These sensitivity simulations thus demonstrate that the WRF model has greater quantitative skill (i.e. the systematic errors are reduced) at reproducing the föhn effect at King Edward Point when optimising the model's orography boundary conditions in a number of ways.

4.7.6 The Optimal WRF Model Setup for King Edward Point

It is clear that the WRF föhn simulations for the four different case studies differ greatly in how faithfully the model reproduces the available observations. To summarise, there is no major difference in the near-surface meteorology at King Edward Point from using different planetary boundary layer parameterisations, microphysics schemes, nor varying the model top, or using different radiation and land surface schemes. However, the results do show that increasing the model resolution vastly improves the modelled wind, relative humidity and temperature when compared to observations. In the same manner, high-resolution topographical and land surface data sets also lead to more realistic interpretations of föhn. Further improvements in the model's skill can also be achieved by using the subgrid-scale orography parameterisation scheme.

Given the results presented in this chapter, it is possible to deduce a suitable model configuration. This setup will subsequently be used for a climatological simulation over a South Georgia domain. Therefore, in Chapter 5 a high-resolution nested domain model run with a horizontal resolution of 8.1 – 2.7 – 0.9km, a vertical resolution of 70 vertical levels in all three domains with the lowest level being placed at approximately 2m, the YSU planetary boundary layer scheme (Hong *et al*., 2006), the WSM5 microphysics (Hong *et al*., 2004) and New Goddard radiation schemes (Chou and Suarez, 1999), the Kain-Fritsch cumulus parameterisation (Kain, 2004), the Noah land surface model (Chen & Dudhia, 2001), all slope shading and topographic effects switches turned on (Garnier and Ohmura, 1968; Jiménez and Dudhia, 2012), and the new land surface type and improved topographic dataset is used. These are the optimal model settings which give the most realistic interpretation of the climate and föhn warming process at King Edward Point.

4.7.7 Discussion

It is important to recognise that the model has been tested and optimised for King Edward Point. It is unlikely that the choice of parameterisations will work for other mountain regions or even for other locations on South Georgia at different resolution. As such, modelling studies such as this would benefit greatly from the kind of detailed local measurements obtained in field campaigns. Such measurements for South Georgia are currently severely lacking. Future model simulations along with more extensive observational programmes will provide further insight in to the regional climate of South Georgia.

In addition to this, while this model setup is believed to be the most appropriate it is also important to recognise that these simulations have highlighted a systematic cold bias in the modelled air temperature at King Edward Point along with poorly resolved near-surface relative humidity values. It may be the case that some of these events (particularly Case 3) are poorly simulated events (as with the föhn case studies of Steinhoff *et al*., 2013), and that other observed föhn events between 2003 and 2012 may be modelled more successfully. This would require further testing. From the four case studies that are presented here, it appears that WRF performs better when the surface föhn signature is prominent (e.g. Case 2), and therefore, the model is likely to perform better for intense case studies. In particular, relative humidity at King Edward

Point and wind speeds at height are particularly poorly reproduced in the WRF model. Looking at föhn jets over the Larsen Ice Shelf, Grosvenor *et al*., (2014) have also found an underrepresentation of the intensity of föhn wind speeds with the WRF model. The representation of föhn flow with other atmospheric models compared to observations has also been met with mixed success (see Zängl *et al*., 2004; Gohm *et al*., 2004; Elvidge *et al*., 2014a; 2014b). The temperature and relative humidity biases are a strong indication of problems related to the modelled radiative fluxes, resulting from differences with the simulation of clouds (Valkonen *et al*., 2014; King *et al*., 2015). Therefore, future improvements and sensitivity studies could be conducted to further improve the representation of the climate of South Georgia. Given current computing constraints, it would be interesting to see how the model performs if a domain of ~1km covered the entire island, and another domain of approximately ~400m resolution covered Mount Paget and Thatcher Peninsula. Since the upstream flow patterns are quite diverse for the different case studies, trajectory analysis would also be an interesting area for future research for the exploration of the regional climate of South Georgia and of the dynamics of föhn flow. It is important to keep in mind how topographically complex South Georgia is. Even over King Edward Cove and the Thatcher Peninsula there are very large variations over very short distances (see Figure 2.1). King Edward Cove has an area of approximately 0.8km^2, and is, therefore, only resolved with one grid cell in the 0.9km nested high-resolution WRF simulations. While WRF is able to capture the broad scale features of föhn and local flow, it would be naive to expect the model to validate perfectly against the single point limited observations which are available. Despite these limitations, the WRF model does capture much of the variability in near-surface meteorological fields during föhn, and therefore the model is suitable for this analysis.

The results in this chapter have also extended our understanding of föhn on South Georgia beyond what could be established solely from the surface AWS observations at King Edward Point. During cases of intense föhn (Cases 1, 2 and 4), föhn warming (and associated drying and increased wind speeds) is observed at King Edward Point, and elsewhere on the northeast coast of South Georgia, especially in low-lying exposed coastal regions of the Thatcher and Greene Peninsulas (see e.g. Figure 4.24(b)). The highest temperatures during these cases are not experienced at King Edward Point. Given the results from the different case studies presented here,

generalisations regarding the large-scale features and mechanisms of föhn events on South Georgia can be made. In terms of large-scale synoptic features, isentropic drawdown and nonlinear wave effects, strong accelerated flow above and immediately downwind of the lee slopes, as well as topographic modification of surface winds around South Georgia are common features of strong westerly air flow. As such, the drawdown of air from aloft appears to be the major driver of föhn warming and drying. Under these conditions, the föhn effect is observed at King Edward Point. These features are shown to be robust across many events, and these modelled characteristics of föhn flow over South Georgia carry on throughout Chapter 5. These characteristics and signals of föhn over the island are also consistent with other observational and modelling work which have looked at föhn flow over the Antarctic Peninsula (e.g. Elvidge *et al*., 2014a; 2014b), the Alps (e.g. Hoinka, 1985a) and the McMurdo Dry Valleys (e.g. Speirs *et al*., 2010; 2013; Steinhoff *et al*., 2013; 2014). These studies have also found similar fine- and large-scale features during föhn flows. Verification of the large-scale features across all föhn events found to occur over South Georgia is still necessary, as the limited surface observations are not sufficient. Clearly, the January 2013 field campaign provides valuable information of the characteristics of föhn flow and dynamics of Case 1. As previously highlighted, a future temporally limited field program with vertical wind profiling across South Georgia could aid in our understanding of föhn flow considerably.

4.8 Conclusion

In this chapter, the performance of the WRF model at simulating four instances of föhn at King Edward Point was tested, and this has given us a greater insight into the characteristics of föhn on South Georgia. Numerous sensitivity simulations were conducted to assess the model's performance of capturing föhn flow, including changing the horizontal and vertical resolution, improving the model topography and land surface type, and varying the boundary layer parameterisations and physics schemes. The aim of this was to identify a suitable model setup which realistically captured the complex weather conditions at King Edward Point. The WRF model output was examined via the analysis of time series, vertical transects and plan view plots of the near-surface meteorology for each of the föhn case studies. To assess the accuracy of the model in the vertical, comparisons with radiosonde and lidar observation were conducted, when available. By validating the model with available

observations, the results indicate that high-resolution simulations can be used to accurately simulate föhn flow, and the best model configuration for South Georgia has subsequently been identified. Generally, the model performance in reproducing föhn events exhibits little sensitivity to the majority of the evaluated model configurations. However, it is clear that the model performance is dominated by the horizontal and topographical resolution of the model, thus indicating that the main source of error in the WRF model is due to unresolved orography. In the absence of meteorological observations, the high-resolution simulations have also provided a means of exploring the characteristics, dynamics and features of föhn flow which would otherwise not be possible. This study has demonstrated that WRF is an effective tool to assist understanding large-scale circulations, regional airflow and local-scale atmospheric dynamics in this region of the Southern Ocean where few observations exist. In particular, the model brings to light interesting fine- and large-scale features associated with westerly föhn flow over South Georgia. During föhn at King Edward Point, significant leeside isentropic drawdown, tip jets and nonlinear wave effects are also observed across the island. It appears that strong föhn events are also caused by the presence of eastward moving low pressure systems to the south of South Georgia, and this is consistent with the results presented in Chapter 3 (section 3.3.3). All of these features are absent during the weak föhn case study. By identifying such features, it is possible to develop a more accurate and less subjective method for distinguishing between föhn and non-föhn events, and this carries on through to Chapters 5 and 6. In conclusion, the results of the high-resolution model simulations provide a new insight into the nature and dynamics of föhn events on South Georgia. The results provide the first in-depth analysis of föhn over the island, with a particular focus on the spatial distribution of warming and the structure and dynamics of föhn flow.

Appendix 4A.1 Sensitivity Simulations of Case 1

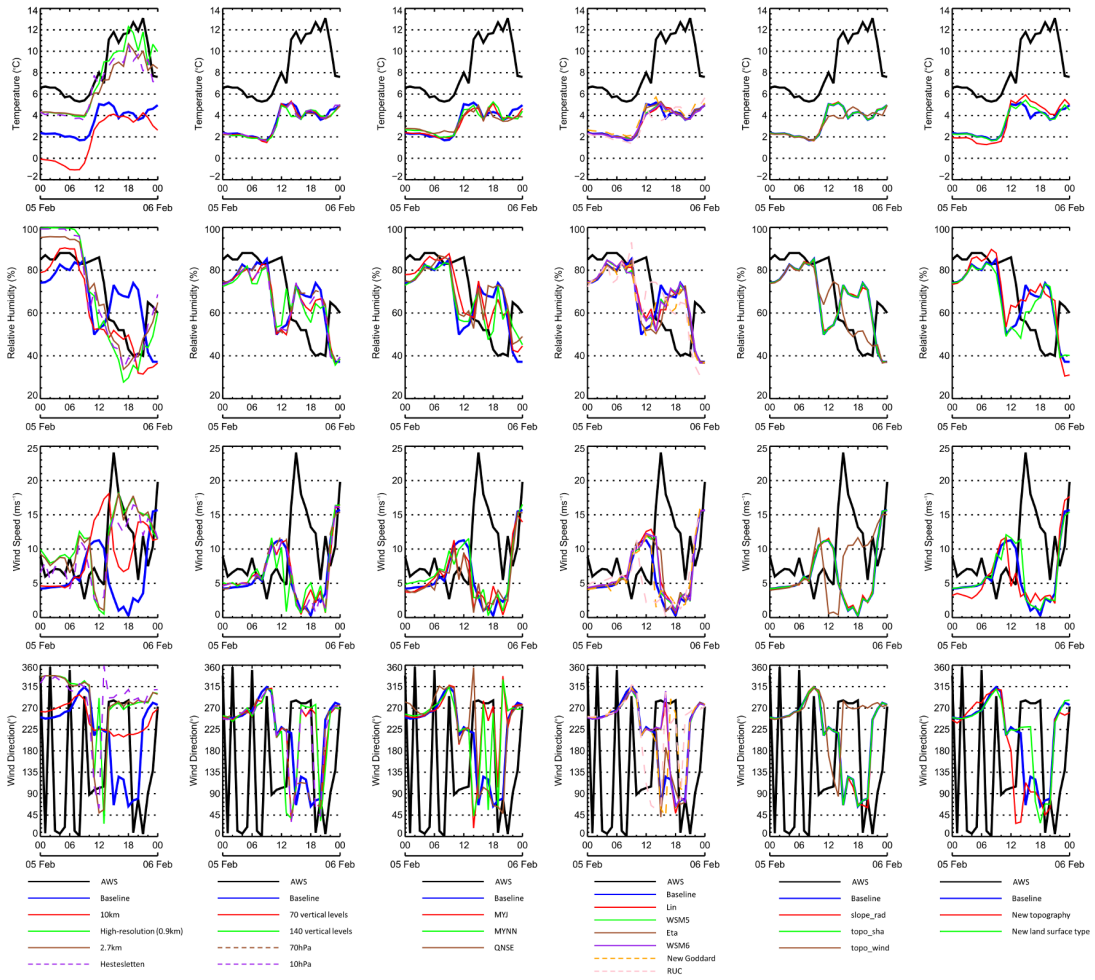

Figure 4.27 – *Observed and simulated 2-m air temperature, 2-m relative humidity, 10-m wind speed, and 10-m wind direction during 5 February 2013 (Case 1). The lines show the AWS observations (black) and the 20 different sensitivity simulations (see legend). See section 2.3 for details of all the WRF namelist options.*

Appendix 4A.2 Sensitivity Simulations of Case 2

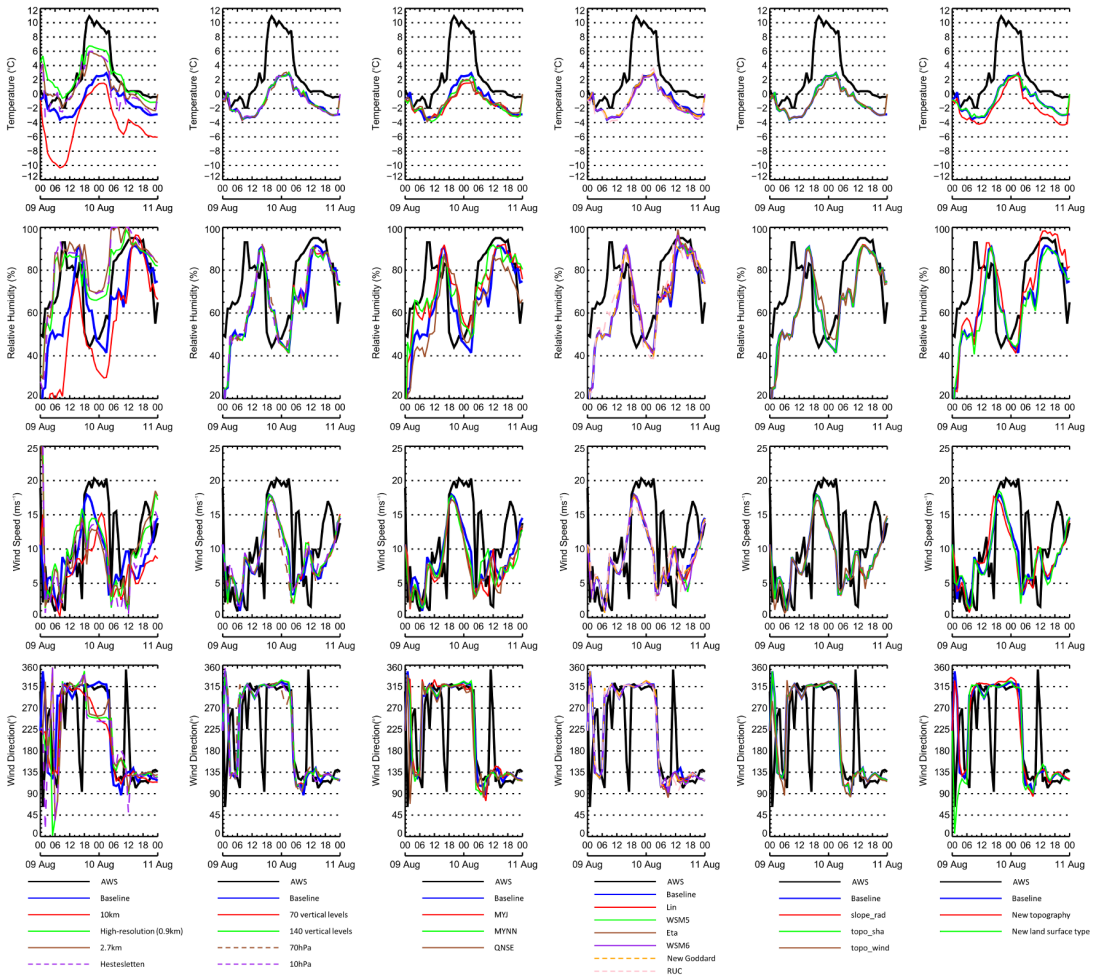

Figure 4.28 – *Observed and simulated 2-m air temperature, 2-m relative humidity, 10-m wind speed, and 10-m wind direction during 9 – 10 August 2012 (Case 2). The lines show the AWS observations (black) and the 20 different sensitivity simulations (see legend). See section 2.3 for details of all the WRF namelist options.*

Appendix 4A.3 Sensitivity Simulations of Case 3

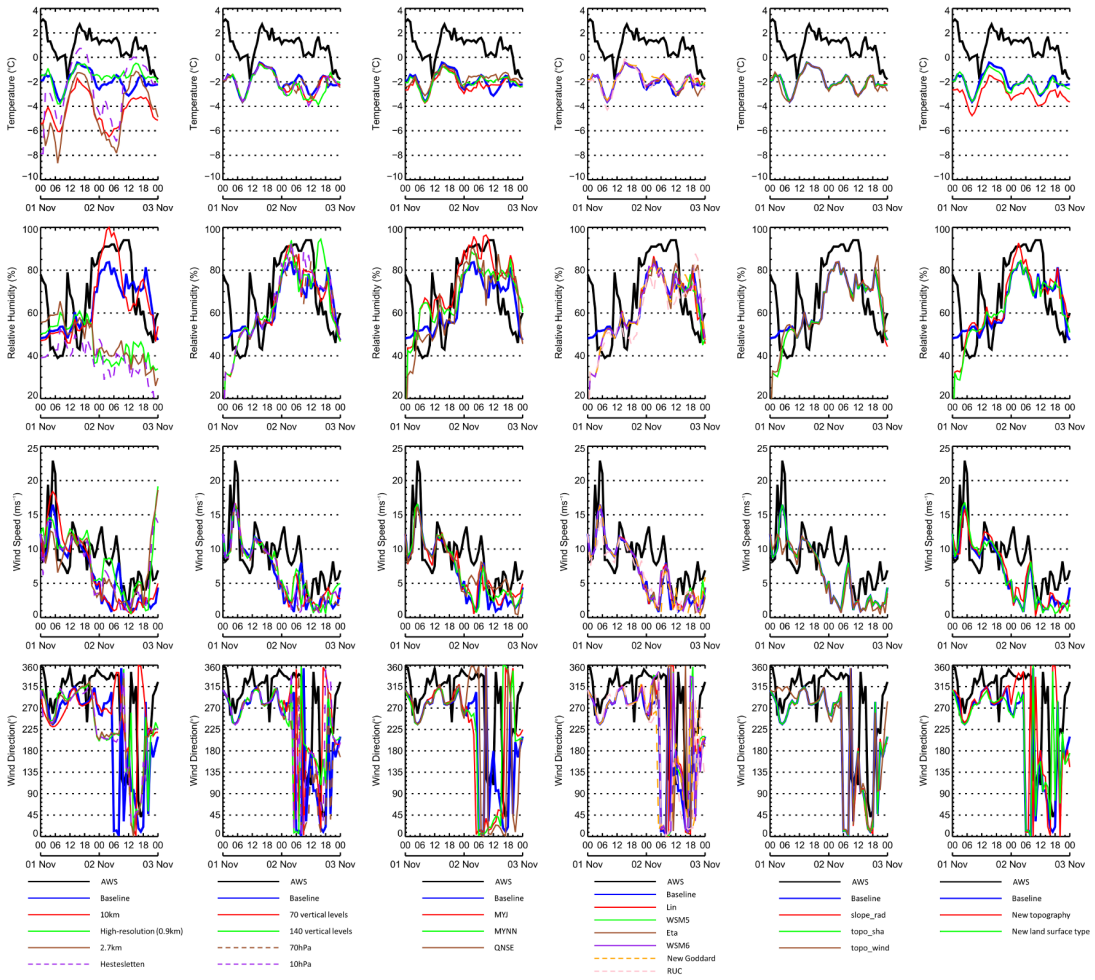

Figure 4.29 – *Observed and simulated 2-m air temperature, 2-m relative humidity, 10-m wind speed, and 10-m wind direction during 1 – 2 November 2007 (Case 3). The lines show the AWS observations (black) and the 20 different sensitivity simulations (see legend). See section 2.3 for details of all the WRF namelist options.*

Appendix 4A.4 Sensitivity Simulations of Case 4

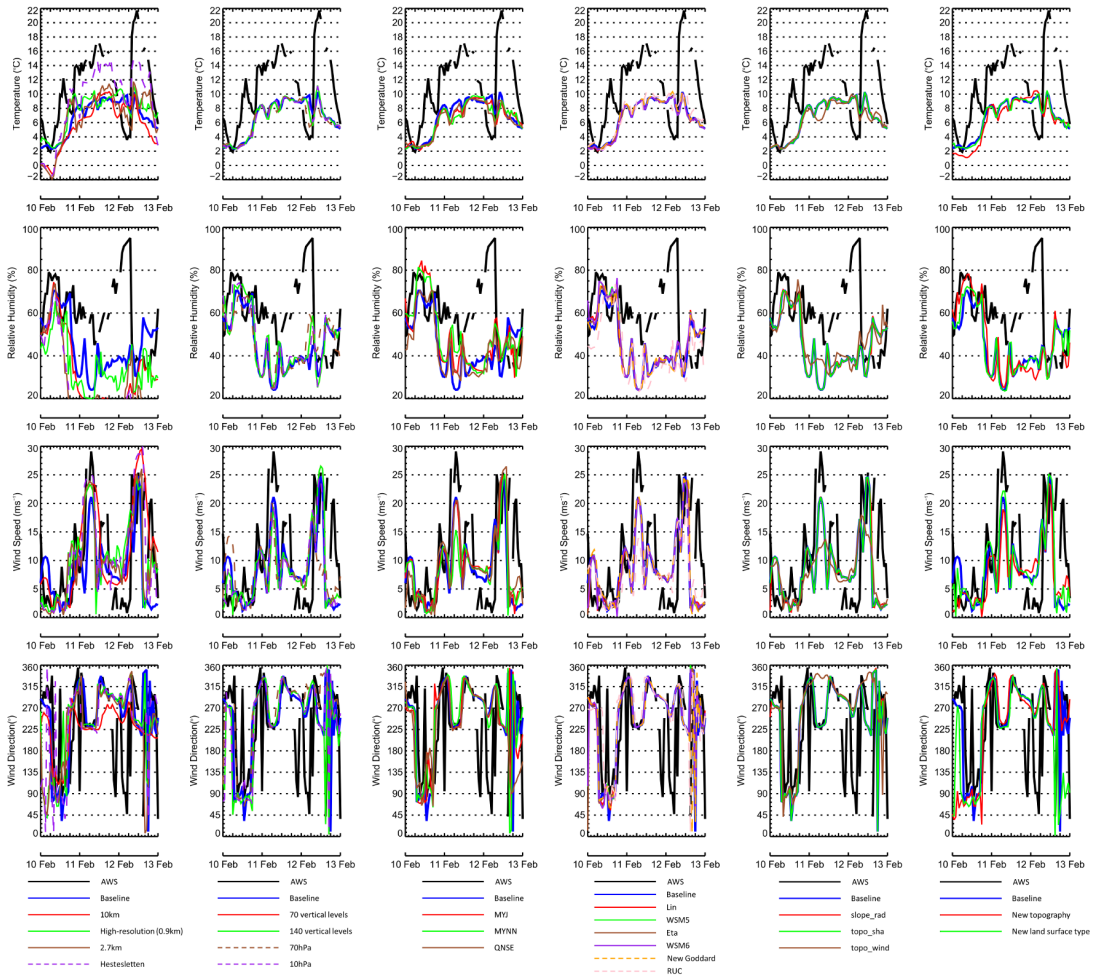

Figure 4.30 – *Observed and simulated 2-m air temperature, 2-m relative humidity, 10-m wind speed, and 10-m wind direction during 10 – 12 February 2011 (Case 4). The lines show the AWS observations (black) and the 20 different sensitivity simulations (see legend). See section 2.3 for details of all the WRF namelist options.*

Appendix 4A.5 Error Statistics for Modelled versus Observed Temperature, Relative Humidity and Wind Speed

Simulation		Case 1			Case 2			Case 3			Case 4		
		Corr. Coef.	RMS error (°C)	Bias (°C)	Corr. Coef.	RMS error (°C)	Bias (°C)	Corr. Coef.	RMS error (°C)	Bias (°C)	Corr. Coef.	RMS error (°C)	Bias (°C)
Horizontal Resolution	10km	**0.85**	6.7	-6.6	**0.86**	7.0	-6.7	0.26	5.4	-5.2	**0.87**	6.3	-5.3
	3.3km	**0.68**	5.3	-5.0	**0.86**	4.2	-3.4	**0.54**	3.0	-2.8	**0.77**	5.6	-4.1
	2.7km	**0.90**	2.1	-1.7	**0.91**	3.3	-1.4	0.01	5.7	-5.1	**0.82**	6.0	-4.3
	0.9km	**0.88**	1.8	-1.0	**0.93**	3.3	-0.1	**0.45**	2.7	-2.4	**0.78**	5.3	-3.3
	Hestesletten	**0.89**	2.2	-1.8	**0.91**	3.3	-1.8	-0.10	4.4	-3.5	**0.88**	5.5	-2.1
Vertical Resolution and Model Top	70 vertical levels	**0.70**	5.4	-5.0	**0.87**	4.2	-3.4	**0.38**	3.2	-3.0	**0.84**	5.6	-4.3
	140 vertical levels	**0.70**	5.5	-5.1	**0.86**	4.2	-3.4	**0.29**	3.4	-3.1	**0.84**	5.6	-4.3
	70hPa model top	**0.66**	5.4	-5.0	**0.84**	4.4	-3.5	**0.44**	3.1	-2.9	**0.82**	5.7	-4.4
	10hPa model top	**0.68**	5.4	-5.0	**0.86**	4.3	-3.4	**0.38**	3.3	-3.0	**0.86**	5.6	-4.3
Planetary Boundary Layer Scheme	MYJ	**0.78**	5.4	-5.1	**0.81**	4.8	-3.8	0.28	3.3	-3.1	**0.79**	5.9	-4.5
	MYNN	**0.77**	5.3	-5.0	**0.84**	4.6	-3.7	**0.46**	3.0	-2.8	**0.79**	5.9	-4.5
	QNSE	**0.70**	5.5	-5.0	**0.82**	4.6	-3.6	0.25	2.9	-2.6	**0.81**	5.9	-4.6
Microphysics, Radiation and Land Surface Schemes	Lin	**0.73**	5.3	-5.0	**0.86**	4.4	-3.6	**0.47**	2.9	-2.8	**0.86**	5.6	-4.3
	WSM5	**0.71**	5.3	-5.0	**0.85**	4.5	-3.6	**0.51**	2.9	-2.8	**0.86**	5.7	-4.3
	Eta	**0.71**	5.3	-4.9	**0.87**	4.3	-3.5	**0.58**	3.0	-2.8	**0.86**	5.6	-4.2
	WSM6	**0.72**	5.4	-5.0	**0.85**	4.5	-3.6	**0.53**	2.9	-2.8	**0.86**	5.7	-4.3
	New Goddard	**0.69**	5.1	-4.7	**0.88**	4.2	-3.4	**0.50**	2.8	-2.6	**0.85**	5.5	-4.0
	RUC	**0.71**	5.4	-5.1	**0.90**	4.3	-3.6	**0.54**	3.1	-2.9	**0.84**	5.5	-3.8
Slope and Shading Effects	slope_rad	**0.67**	5.3	-4.9	**0.86**	4.2	-3.4	**0.49**	3.0	-2.8	**0.86**	5.6	-4.1
	topo_sha	**0.68**	5.3	-5.0	**0.86**	4.2	-3.4	**0.50**	3.0	-2.8	**0.86**	5.6	-4.1
	topo_wind	**0.78**	5.4	-5.1	**0.90**	4.3	-3.5	**0.56**	3.1	-2.9	**0.85**	5.8	-4.5
Topographical Resolution and Land Surface type	New topography	**0.76**	5.2	-4.9	**0.86**	4.2	-4.3	**0.58**	4.0	-2.9	**0.84**	6.0	-4.5
	New land surface type	**0.72**	5.3	-4.9	**0.86**	4.2	-3.3	**0.52**	3.1	-3.0	**0.84**	5.6	-4.1

Table 4.3 – *Mean bias, root-mean-square (RMS) errors and correlation coefficients (Corr. Coef.) for modelled (versus observed) 2-m air temperature for each of the 4 föhn events. The statistics are based on instantaneous hourly values from the WRF model and King Edward Point AWS. For each of the events, underlining highlights values with lowest magnitude bias, RMS error and highest correlation. Correlations that are significantly different from zero at the 95% confidence level are indicated in bold type. A negative bias indicates that the model underestimates the observations. See section 2.3 for details of the WRF namelist options.*

Simulation		Case 1			Case 2			Case 3			Case 4		
		Corr. Coef.	RMS error (%)	Bias (%)	Corr. Coef.	RMS error (%)	Bias (%)	Corr. Coef.	RMS error (%)	Bias (%)	Corr. Coef.	RMS error (%)	Bias (%)
Horizontal Resolution	10km	**0.80**	15.6	-9.5	**0.66**	28.4	-20.7	**0.52**	15.5	-4.0	**0.50**	30.1	-27.9
	3.3km	0.37	19.0	-4.9	**0.63**	18.1	-8.4	**0.51**	15.7	-4.6	**0.41**	23.5	-15.8
	2.7km	**0.87**	10.0	-3.2	**0.76**	28.5	9.6	**-0.34**	32.2	-21.8	**0.41**	36.8	-35.4
	0.9km	**0.81**	14.7	-1.4	**0.69**	29.5	5.7	**-0.53**	32.7	-21.8	**0.37**	29.2	-25.7
	Hestesletten	**0.87**	12.6	-1.3	**0.64**	31.3	9.0	-0.17	37.0	-30.1	**0.42**	40.4	-40.9
Vertical Resolution and Model Top	70 vertical levels	0.38	18.3	-4.6	**0.66**	17.7	-8.4	**0.55**	18.7	-6.5	**0.37**	23.6	-13.8
	140 vertical levels	**0.45**	17.1	-4.9	**0.64**	17.9	-8.6	**0.44**	20.7	-5.0	**0.37**	23.6	-13.8
	70hPa model top	0.30	19.1	-3.1	**0.61**	18.0	-7.4	**0.47**	19.8	-6.7	**0.36**	23.4	-14.8
	10hPa model top	0.35	18.7	-4.7	**0.66**	17.5	-8.0	**0.54**	18.7	-5.6	**0.47**	22.6	-13.8
Planetary Boundary Layer Scheme	MYJ	**0.64**	14.0	-1.4	**0.58**	15.7	-2.0	**0.46**	19.2	3.8	**0.35**	22.8	-11.8
	MYNN	**0.58**	15.0	-3.7	**0.65**	14.5	-2.5	**0.33**	19.9	-0.7	**0.36**	22.0	-11.0
	QNSE	**0.41**	16.9	-1.0	**0.48**	21.5	-10.7	**0.43**	20.4	-4.2	**0.45**	24.0	-16.9
Microphysics, Radiation and Land Surface Schemes	Lin	**0.45**	17.2	-2.7	**0.63**	18.1	-7.7	**0.46**	20.0	-7.7	**0.49**	23.1	-14.5
	WSM5	**0.41**	17.7	-2.9	**0.62**	18.2	-7.0	**0.45**	20.2	-7.9	**0.47**	23.1	-14.0
	Eta	**0.40**	18.3	-4.4	**0.65**	17.8	-7.7	**0.36**	21.3	-6.5	**0.50**	23.1	-14.9
	WSM6	**0.41**	17.7	-2.9	**0.62**	18.3	-7.0	**0.42**	20.3	-7.5	**0.48**	23.1	-14.1
	New Goddard	**0.43**	17.9	-4.9	**0.66**	17.6	-8.0	**0.41**	20.6	-7.6	**0.49**	23.7	-16.0
	RUC	**0.52**	16.9	-3.5	**0.71**	16.0	-6.8	**0.33**	22.4	-9.2	**0.41**	25.1	-18.7
Slope and Shading Effects	slope_rad	0.34	18.7	-3.2	**0.63**	18.1	-8.3	**0.43**	20.5	-7.5	**0.52**	23.2	-15.7
	topo_sha	0.33	19.0	-3.1	**0.63**	18.1	-8.4	**0.43**	20.3	-7.4	**0.50**	23.5	-15.8
	topo_wind	**0.80**	12.1	-5.6	**0.71**	16.0	-7.9	**0.36**	20.9	-6.2	**0.49**	21.3	-13.3
Topographical Resolution and Land Surface type	New topography	0.38	18.7	-1.4	**0.63**	18.1	-3.2	**0.43**	19.8	-5.0	**0.50**	22.9	-15.0
	New land surface type	0.37	18.7	-4.9	**0.63**	18.1	-9.2	**0.43**	20.0	-6.9	**0.50**	23.7	-15.8

Table 4.4 – *Mean bias, root-mean-square (RMS) errors and correlation coefficients (Corr. Coef.) for modelled (versus observed) 2-m relative humidity for each of the 4 föhn events. The statistics are based on instantaneous hourly values from the WRF model and King Edward Point AWS. For each of the events, underlining highlights values with lowest magnitude bias, RMS error and highest correlation. Correlations that are significantly different from zero at the 95% confidence level are indicated in bold type. A negative bias indicates that the model underestimates the observations. See section 2.3 for details of the WRF namelist options.*

Simulation		Case 1			Case 2			Case 3			Case 4		
		Corr. Coef.	RMS error (ms^{-1})	Bias (ms^{-1})	Corr. Coef.	RMS error (ms^{-1})	Bias (ms^{-1})	Corr. Coef.	RMS error (ms^{-1})	Bias (ms^{-1})	Corr. Coef.	RMS error (ms^{-1})	Bias (ms^{-1})
Horizontal Resolution	10km	0.14	6.4	-0.5	**0.62**	6.3	-3.6	**0.46**	4.6	-2.1	**0.52**	6.6	0.5
	3.3km	-0.18	8.1	-3.5	**0.57**	5.7	-2.0	**0.42**	4.3	-2.4	**0.41**	6.2	-2.1
	2.7km	**0.54**	4.9	1.1	**0.43**	7.6	-1.3	**0.31**	5.2	-1.4	**0.68**	7.1	-0.7
	0.9km	**0.54**	4.9	1.3	**0.35**	7.6	-0.8	**0.49**	4.4	-0.4	**0.64**	7.4	-0.4
	Hestesletten	**0.54**	4.7	-0.1	**0.46**	7.7	-2.1	**0.51**	4.5	-1.3	**0.76**	6.5	0.2
Vertical Resolution and Model Top	70 vertical levels	-0.18	7.9	-3.2	**0.53**	5.8	-1.9	**0.67**	4.0	-2.1	**0.62**	6.9	-2.4
	140 vertical levels	-0.08	7.8	-3.5	**0.53**	5.8	-1.8	**0.68**	3.9	-2.0	**0.62**	6.9	-2.4
	70hPa model top	-0.23	8.2	-3.3	**0.45**	6.3	-2.3	**0.62**	4.5	-2.6	**0.37**	7.9	-2.2
	10hPa model top	-0.19	8.1	-3.5	**0.51**	5.9	-1.9	**0.66**	4.2	-2.4	**0.71**	6.5	-2.6
Planetary Boundary Layer Scheme	MYJ	-0.15	8.0	-3.9	**0.53**	6.3	-3.0	**0.66**	3.9	-1.9	**0.68**	6.5	-1.7
	MYNN	-0.19	7.9	-3.2	**0.59**	5.9	-2.6	**0.65**	4.0	-2.0	**0.54**	7.2	-2.3
	QNSE	-0.08	7.9	-4.1	**0.53**	6.2	-2.9	**0.64**	3.7	-1.6	**0.71**	6.3	-1.6
Microphysics, Radiation and Land Surface Schemes	Lin	-0.07	7.5	-2.7	**0.56**	5.8	-2.0	**0.65**	4.1	-2.2	**0.68**	6.5	-2.4
	WSM5	-0.10	7.6	-2.9	**0.55**	5.9	-2.1	**0.64**	4.1	-2.1	**0.70**	6.4	-2.4
	Eta	0.03	7.2	-2.8	**0.57**	5.7	-2.0	**0.64**	4.3	-2.3	**0.68**	6.5	-2.2
	WSM6	-0.09	7.6	-2.8	**0.55**	5.9	-2.1	**0.65**	4.2	-2.2	**0.70**	6.4	-2.4
	New Goddard	-0.15	7.9	-3.4	**0.57**	5.7	-2.0	**0.63**	4.4	-2.5	**0.73**	6.2	-1.8
	RUC	-0.11	8.0	-4.1	**0.54**	5.8	-2.0	**0.68**	4.1	-2.5	**0.51**	7.5	-3.1
Slope and Shading Effects	slope_rad	-0.18	8.0	-3.4	**0.57**	5.7	-2.0	**0.66**	4.3	-2.4	**0.69**	6.4	-2.2
	topo_sha	-0.18	8.1	-3.5	**0.57**	5.7	-2.0	**0.66**	4.3	-2.4	**0.72**	6.2	-2.1
	topo_wind	**0.35**	5.9	-2.1	**0.54**	5.8	-2.3	**0.54**	4.9	-2.9	**0.71**	6.8	-2.6
Topographical Resolution and Land Surface type	New topography	-0.02	7.9	-3.8	**0.57**	5.7	-2.0	**0.65**	4.2	-2.1	**0.64**	6.9	-2.7
	New land surface type	-0.13	7.9	-3.2	**0.57**	5.7	-2.0	**0.68**	4.3	-2.4	**0.79**	5.8	-1.9

Table 4.5 – *Mean bias, root-mean-square (RMS) errors and correlation coefficients (Corr. Coef.) for modelled (versus observed) 10-m wind speed for each of the 4 föhn events. The statistics are based on instantaneous hourly values from the WRF model and King Edward Point AWS. For each of the events, underlining highlights values with lowest magnitude bias, RMS error and highest correlation. Correlations that are significantly different from zero at the 95% confidence level are indicated in bold type. A negative bias indicates that the model underestimates the observations. See section 2.3 for details of the WRF namelist options.*

Chapter Five: Exploring the Regional and Föhn Climatology of South Georgia with the Weather Research and Forecasting (WRF) Model

5.1 Introduction

The climate and weather of South Georgia has been measured and observed ever since the island was first discovered (Headland, 1992). Meteorological observations for periods longer than a year have been made at the Bay of Isles, Bird Island, King Edward Point, Maiviken, and the seven whaling stations, throughout the last century (see e.g. von Danckelman, 1884; Pepper, 1954; Mansfield & Glassey, 1957; Richards & Tickell, 1968; Headland, 1982; Shanklin, 1985; Craig & Gordon, 1990; Shanklin *et al*., 2009; among many others). Sporadic observations have also been recorded elsewhere on the northeast coast of the island during various expeditions (see e.g. Tickell & Cordall, 1960; Tickell, 1962; Tickell *et al*., 1965; among many others). Many of these observations have demonstrated the cold, wet and windy nature of the climate of South Georgia. However, having been taken in sheltered areas along the northeast coast, such observations do not fully represent the severity and wide variety of conditions across the island. There have also been limited studies which have compared the climate of areas on the island to elsewhere on South Georgia (e.g. Richards & Tickell, 1968; Craig & Gordon, 1990). Despite this, the observations which have been made are limited, discontinuous and patchy. The southwest coast of South Georgia is less accessible than elsewhere, and hence there is no instrumental data available from this side of the island for comparison. As such, there remains a considerable amount that we do not know about the weather and climate of South Georgia.

Since there has never been a detailed regional climatology of South Georgia, one of the aims of this research is to fill this gap in our knowledge. This began in Chapter 3, where a detailed climatology of föhn events as detected and defined by 10 years of surface automatic weather station (AWS) observations at King Edward Point was presented. From this study, it was found that föhn events are very frequent there, with approximately one event occurring every four days. It was also found that föhn events play a significant role in the regional wind and temperature regime of King Edward Point. However, given the sparse meteorological datasets available across South Georgia, it remains unknown how frequent föhn events are elsewhere on the island.

Therefore, Chapter 4 showed that high-resolution atmospheric model simulations over South Georgia are required to better understand the large- and fine-scale features of the climate of the island. High-resolution model simulations over South Georgia allow us to explore the regional climate and conditions across the island, far beyond the region of where observations currently allow us to look. Such data can act as proxy observations, and inform us of the impact of föhn warming on the regional climate of South Georgia. Since the föhn effect has been shown to be an important process in controlling the localised climate of Thatcher Peninsula, one would expect that cases of intense föhn to cause significant leeside melt along the island's north-eastern glaciers via an enhanced surface warming. Such effects have also been similarly observed and modelled on the leeside of the Antarctic Peninsula, with a particular focus on the Larsen Ice Shelf melt (e.g. Kuipers Munneke *et al*., 2012; Elvidge *et al*., 2014a; 2014b; Grosvenor *et al*., 2014). The degree of warming föhn is likely to provide to the surface of glaciers across South Georgia is unknown. Nothing is known of the impact of föhn flow on glacial melt, or on the regional climate of South Georgia. Since there is currently a lack of data in this region, model output from a high-resolution atmospheric model is vital for high temporal and spatial sampling across the entire island which would otherwise not be possible.

This chapter begins with a brief overview of the Weather Research and Forecasting (WRF) model setup and a validation of surface observations with output from 0.9km grid-spacing simulations. Having extensively validated WRF on a case study basis in Chapter 4, presented here is a validation of the model output with the AWS observations for a 21 month model simulation (June 2011 – February 2013). Since there are no *in situ* climatological observations or studies currently available, this validation is accompanied with annual and seasonal mean maps for the entire island. The regional climate of South Georgia is explored, with a particular focus on near-surface temperature, relative humidity, wind speed, and precipitation patterns. This data is subsequently used to identify areas which may frequently experience the föhn effect, based upon surface warming, drying and increased wind speeds. Following this, using the model data as proxy observations, three different model-appropriate föhn identification methods are then used to define föhn and non-föhn conditions on the leeside of South Georgia. The results from Chapter 3 and Chapter 4 have shown that the current method for föhn detection using surface AWS observations does not ensure

that only föhn warming events are exclusively identified. Therefore, a more appropriate method must be deduced in order to explore the impact of föhn on the regional climate of South Georgia in the absence of island-wide meteorological observations and measurements. These methods are presented and evaluated, and identified föhn events in the WRF model are then compared against the King Edward Point AWS föhn climatology (which was previously presented in Chapter 3). Finally, a decision on the best method for föhn identification using the WRF model is made. As a result of this, a representative set of föhn events are selected and these are used to investigate the role that strong föhn events have on the near-surface energy and mass balance conditions between north- and south-facing glaciers on South Georgia, which is then presented in Chapter 6. By creating a climatology of föhn events from WRF model output, model data is subsequently used to investigate whether there is a link between upwind flow characteristics and asymmetrical glacial retreat on South Georgia.

5.2 Method

The purpose of this section is to provide a description of WRF, the mesoscale numerical weather prediction model used in this study, including datasets, domains, model physics parameterisations, and modifications specifically made to South Georgia for the climatological simulation. The three different methods for föhn identification using the model as proxy observations for föhn occurrence are also briefly introduced here. Further details pertaining to the three different föhn identification methods and their development are given later (see section 5.6).

5.2.1 WRF Model Setup

Version 3.4.1 of the Advanced Research Weather Research and Forecasting (WRF) model was used for the simulations. See Chapter 2 for more information regarding the WRF model. In Chapter 4, the WRF model was validated extensively against available observations, and the model's sensitivity was tested by changing the horizontal and vertical resolution, as well as improving the model topography and land surface type, in addition to changing the model's physics and planetary boundary layer schemes. Through optimising the WRF model for King Edward Point, the results were subsequently used to identify the best model setup which gave the most realistic interpretation of föhn on South Georgia (see section 4.7.6). Therefore, the results from

Chapter 4 suggested the following model setup as the optimum for a regional-scale analysis of föhn flow across South Georgia. The configuration of the three nested domains (two-way interaction) used in this study is illustrated in Figure 5.1.

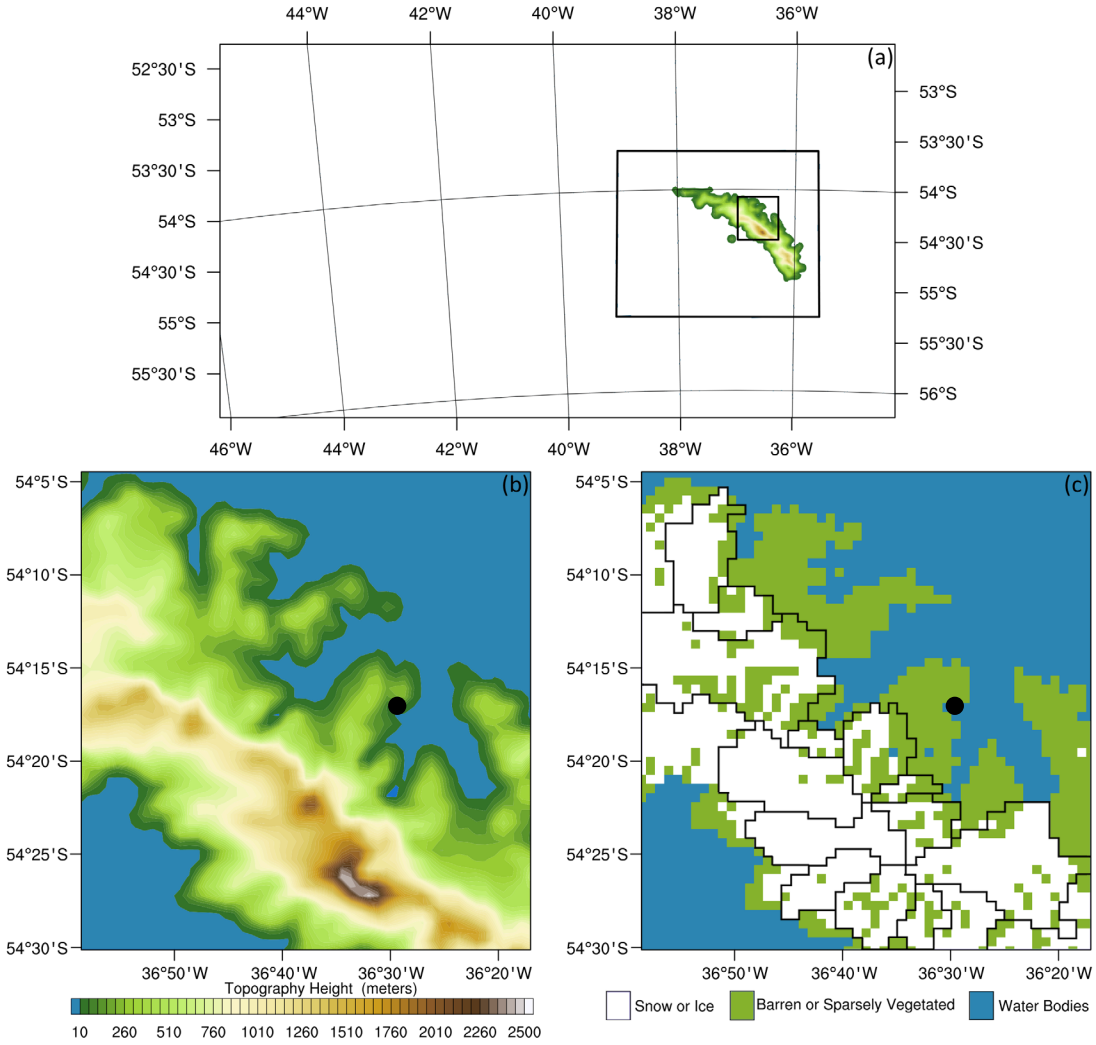

Figure 5.1 – *WRF model configuration for the South Georgia simulation. Panel (a) illustrates the horizontal boundaries for the three nested domains, including the 8.1km outer domain, the 2.7km intermediate domain, and the 0.9km inner domain (black line boxes). Elevation is plotted from the 2.7km domain. The innermost domain is also illustrated in panel (b), along with the island's orographic elevation (green-brown shading) at 0.9km resolution. Panel (c) shows the land surface type with 14 glacier catchments (see Chapter 6 for more detail regarding glacier catchments). King Edward Point is located by the filled black circle.*

Domain 1, the coarsest domain of the three, has 94 x 54 grid points at a horizontal resolution of 8.1km. Domain 2 was nested with 85 x 73 grid points at 2.7km grid spacing. And domain 3, the finest domain of the three, has 52 x 52 grid points at a horizontal resolution of 0.9km, centred over King Edward Point. The outermost domain was designed to cover a relatively large ocean area in order to better resolve

the prevailing westerly winds of the Southern Ocean. All three domains had 70 vertical levels between the surface and the model top at 50hPa. These were arranged according to terrain-following hydrostatic pressure vertical coordinates, and were manually selected. Of the 70 vertical levels, 17 of these spanned the lowest 2km of the atmosphere, with the lowest level (on average) 5.5m above terrain level. The initial and lateral boundary conditions were derived from the ERA-Interim pressure-level re-analysis (Dee *et al.*, 2011). The lateral boundary conditions, sea surface temperature and sea ice fields were updated every six hours from ERA-Interim.

To avoid computational instability and improve computational efficiency over the steeply sloping terrain, an adaptive timestep was used for all domains. Implicit Rayleigh damping of vertical velocity was used, to prevent unphysical downward reflection of gravity waves from the model top (Klemp *et al.*, 2008). Slope effects, such as shadowing and varying incident solar radiation were also accounted for with the shortwave parameterisation in WRF (Garnier and Ohmura, 1968). Given the results of Chapter 4, the subgrid-scale orography scheme (Jiménez and Dudhia, 2012) was also utilised. Briefly, the other physics parameterisation options selected include: the New Goddard scheme for longwave and shortwave radiation (Chou and Suarez, 1999), the Yonsei State University planetary boundary layer scheme (Hong *et al*., 2006), the WRF Single-Moment 5-class microphysics scheme (Hong *et al*., 2004), the Noah land-surface model (Chen & Dudhia, 2001), and the Kain-Fritsch cumulus parameterisation (Kain, 2004). The simulations also used the improved high-resolution topography and land surface type datasets (see Chapter 2, section 2.3.1.1, for more detail).

Using this model set-up, the WRF run started at 0000 UTC 1 June 2011 and ended 0000 UTC 1 March 2013. The model was restarted every three months. This period was chosen as a representative full melt year, covering one melt and two accumulation seasons, with an additional nine months to cover the observations collected in 2013 field campaign. Only model output from the innermost and intermediate (0.9km and 2.7km resolution) domains is discussed here. During this period, the AWS recorded 159 föhn events of varying intensities (see Table 5.8, Appendix 5A.2, for a list of all 159 observed föhn events). This gives a satisfactory sample of all föhn events documented between January 2003 and February 2013.

5.2.2 Detecting and Identifying Föhn Events with the WRF model

To explore the impact of the föhn effect on climate variability across the island of South Georgia, a representative set of events must be identified first. The föhn climatology from Chapter 3 is specific to King Edward Point, and the results do not identify föhn conditions elsewhere on the island. The results from Chapters 3 and 4 also highlight the limitations of identifying föhn conditions based upon their impact on the near-surface meteorology. Therefore, an objective model-appropriate föhn identification method must be developed and accurately used to identify and categorise föhn conditions from non-föhn conditions. Three different classification methods were developed to build a model climatology of föhn events using properties and characteristics which are dynamically, theoretically, and empirically observable and associated with föhn flow over the main mountain chain of South Georgia. These methods are briefly introduced below.

Method 1 focuses on the associated surface warming at the model's surface (King Edward Point) during föhn events. This method is analogous to the system used to identify the occurrence of föhn from AWS observations in Chapter 3. Variations of this method have been applied all over the world (see Conrad, 1936; Osmand, 1941; Obenland, 1956; Inaba *et al*., 2002; Speirs *et al*., 2013; and many others). This method is based on the assumption that the air has been warmed either by descent from heights upstream above the mountain range or by release of latent heat and fallout of precipitation on the windward slopes, leading to a warm and dry air mass descending the lee slopes. Therefore, there must also be a near-surface leeside warming, drying and a rise in wind speed for föhn to be declared at the grid cell representative of King Edward Point. Method 1 classifies events based purely on surface characteristics, and it does not say anything about the situation aloft or upstream of South Georgia. See section 5.6.1 for more details regarding this method.

Method 2 considers the upstream conditions, which have the potential to determine the temporal, horizontal and vertical extent of the föhn warming across South Georgia. In this method, the change in isentrope height across the main mountain chain is calculated. This is based on the assumption that cross-barrier isentropic drawdown is sufficient to cause föhn in the lee of the island, since air from aloft is brought down to the surface through lee wave effects which is drier and potentially warmer. This driver

of surface warming and drying was observed in Chapter 4, and has also been shown to be responsible for the föhn effect elsewhere (see e.g. Elvidge *et al*., 2014a; Grosvenor *et al*., 2014). See section 5.6.2 for the details and results of this method.

Method 3 also considers the upstream conditions, and the occurrence of föhn is detected when dynamical arguments (upstream Froude number) suggest the conditions should be associated with föhn in the lee of the island (Smith, 1980; Durran 1990). This is based on the assumption that the magnitude of the Froude number determines whether an approaching air mass has the potential to flow over the main mountain chain, therefore generating a föhn in the lee of South Georgia. See section 5.6.3 for this method.

It is important to note that Method 1 uses the model output from the innermost WRF domain (0.9km resolution). Since Methods 2 and 3 require upstream and cross-island profiles to identify föhn events, these methods use the model output from the intermediate WRF domain (2.7km resolution). Each of these methodologies, along with their respective föhn climatologies, is discussed separately in more detail in section 5.6.

5.3 Validation of the WRF Model with AWS Observations

To facilitate comparison with AWS observations, WRF output data was interpolated to the AWS observation location (King Edward Point) to create a model timeseries at hourly intervals. Mean and seasonal averages for all near-surface variables, as well as statistical significance are shown in Appendix 5A.1 (Table 5.7). While WRF does not validate perfectly with observations, overall, the model represents well the mean annual and seasonal conditions. A comparison of the hourly annual and seasonal 2-m air temperatures recorded at the AWS site and as modelled at the equivalent WRF location is presented in Figure 5.2. The determination coefficient (r^2) of the annual relationship between all 1-hour temperature observations and model temperature values is 0.71 ($p < 0.05$).

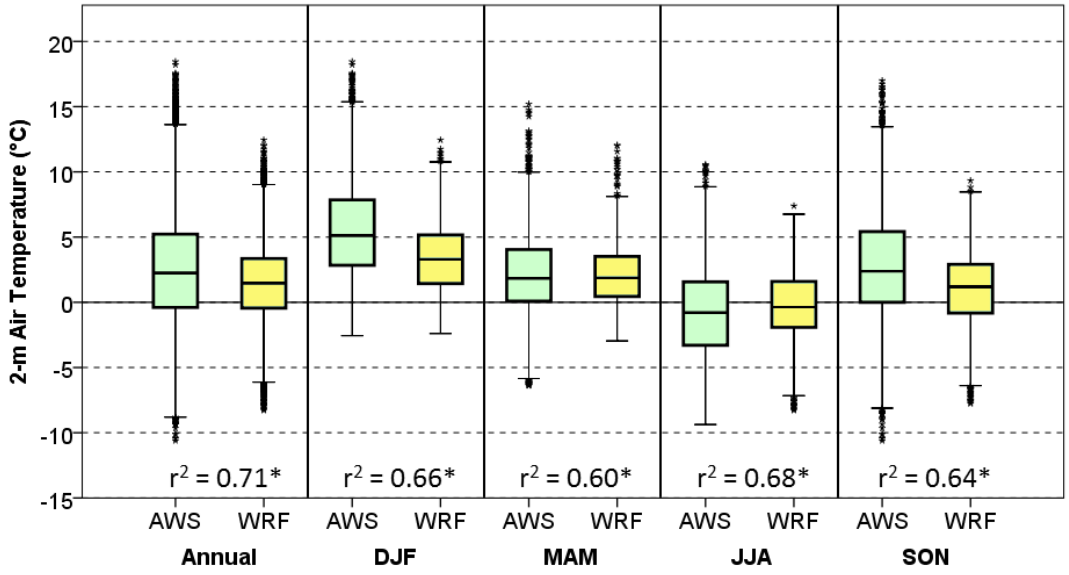

Figure 5.2 – *Box plot of hourly annual and seasonal 2-m air temperature, as recorded by the AWS observations at King Edward Point and at the equivalent location in the WRF model (0.9km domain). Thick horizontal line is the median, box indicates first and third quartiles, bars extend to 1.5 interquartile ranges outside of the quartiles. Outliers (✶) are defined as being >1.5 interquartile ranges outside of the quartiles. Stars indicate determination coefficients are significant at the 95% confidence level.*

Figure 5.2 shows that the WRF model exhibits less variability in 2-m air temperature than the observations. In the observations, the temperature ranges from -10.6ºC to 18.5ºC, with a mean of 2.4ºC (σ of all 1-hour observations = 4.5). This is normally distributed, with skewness of 0.17 (standard error of 0.02) and kurtosis of 0.10 (standard error of 0.04). These values are considered acceptable in order to prove normal distribution. In contrast, the temperature ranges in the WRF model from -8.3ºC to 12.4ºC, with a mean and 1.5ºC (σ of all 1-hour modelled values = 3.0). This too is normally distributed, with skewness of 0.04 (standard error of 0.02) and kurtosis of 0.14 (standard error of 0.04). Therefore, the annual distributions of temperature in the model and the observations are similar, although the range in temperature is somewhat larger in the observations. A one-way ANOVA F-test indicates that the difference of variance between the annual modelled and observed air temperature is statistically significant ($F = 3.9$, $p < 0.05$). The model also exhibits less variability than the observations throughout the year. Figure 5.2 clearly shows that the model systematically underrepresents the occurrence of warm and cold temperatures at King Edward Point throughout the year. As with the results from Chapter 4 and the specific WRF föhn case studies, it is likely that the reduced frequency of high temperatures in WRF is partly a result the systematic cold bias, overall resulting in a muted surface

temperature response to föhn in WRF. The mean RMS error, bias, and correlation coefficient for the entire period (June 2011 – February 2013) are 2.7°C, -0.9°C, and 0.84, respectively. December 2011 is the warmest month both in observations and the model (mean of 6.7°C and 4.4°C respectively), while August 2011 is the coolest month (mean of -2.4°C and -2.1°C respectively). The season with the highest mean standard deviation in both the observations and in the model is austral spring ($\sigma = 3.8$ and $\sigma = 2.5$ respectively), while the season with the lowest mean standard deviation in both the observations and in the model is austral autumn ($\sigma = 3.1$ and $\sigma = 2.2$ respectively).

Modelled relative humidity is poorly represented compared to the AWS observations. The determination coefficient (r^2) of the annual relationship between all 1-hour relative humidity observations and model relative humidity values is 0.42 ($p < 0.05$). For the entire period, the mean RMS error, bias, and correlation coefficient are 14.0%, 2.0%, and 0.65, respectively. The mean annual model relative humidity in WRF is 72.5 ± 17.4%, compared to 70.3 ± 15.2% as measured at the AWS site. The model only slightly underestimates occurrences of very low humidity, with 0.1% occurrences below 20%, compared to 0.2% in the observations. In contrast, the model overestimates occurrences of high humidity, with 19.1% occurrences above 90%, compared to 12.1% in the observations. The minimum relative humidity reached during the June 2011 – February 2013 period in the AWS observations was 10.5%. This compares to a minimum of 16.0% in the model. As with air temperature, the model overestimates 2-m relative humidity throughout the year (Table 5.7, Appendix 5A.1). A one-way ANOVA F-test indicates that the difference of variance between the annual modelled and observed 2-m relative humidity is statistically significant ($F = 5.6$, $p < 0.05$). Biases in the modelled relative humidity (compared to the observations) are a likely result of small localised processes not being fully realised and captured within the model. Steinhoff *et al*., (2013) have also noted significant relative humidity biases with the WRF model when simulating over the McMurdo Dry Valleys of Antarctica. This was attributed to a negative moisture bias over Antarctica in ERA-Interim (also see Nicholas & Bromwich, 2011) and the horizontal diffusion scheme used in the WRF simulations, resulting in the diffusion of moisture at higher elevations than in reality. Given that King Edward Cove is only just resolved at 0.9km horizontal resolution, unresolved topographic features is likely to be a leading cause of the model not capturing the variability of humidity at King Edward Point.

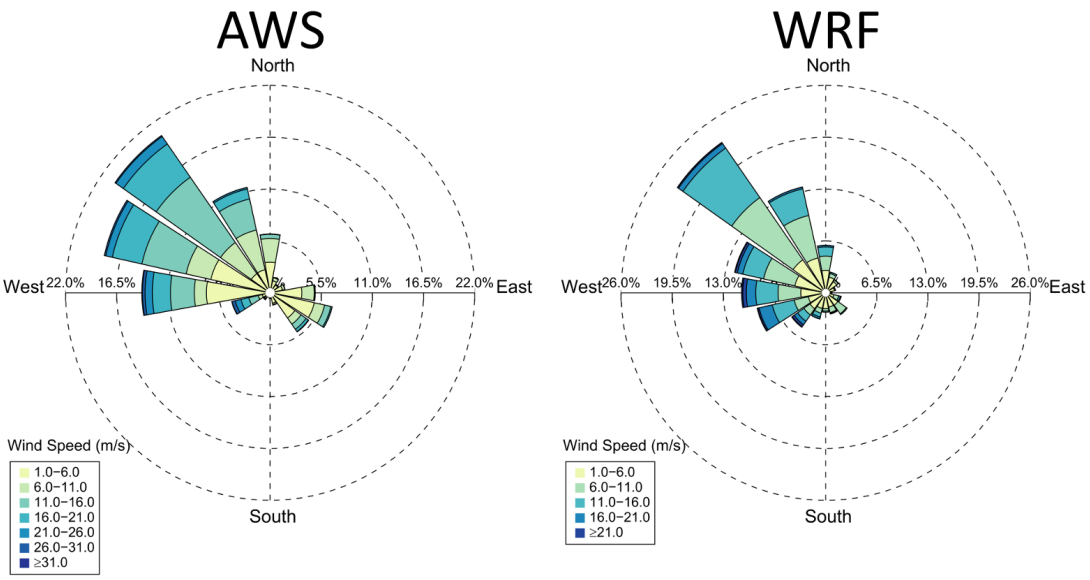

Figure 5.3 – *Wind roses representing the frequency and strength of winds blowing from a particular direction for King Edward Point for the period June 2011 – February 2013, based on hourly instantaneous 10-m wind data from the AWS observations (left) and 10-m wind data from the WRF model (right).*

The model accurately captures varying flow orientations throughout the year, as well as the dominant north-westerly flow (Figure 5.3). Since topography plays a large part in determining local conditions at King Edward Point, marked funnelling of the true westerly winds creates these north-westerly winds (Mansfield & Glassey, 1957). Compared to the AWS observations, the model produces wind that is too south-westerly. In WRF, 24.5% of winds occur within the 180 – 70° quadrant, compared to 12.3% in the observations. Strong winds are only slightly underrepresented in the WRF model; 0.6% of winds exceed 26ms^{-1}, compared to 1% in the observations. Although the determination coefficient (r^2) of the annual relationship between all 1-hour wind speed observations and model wind speed values is only 0.36 ($p < 0.05$), there is no statistically significant difference in the variance between the modelled and the observed wind speeds. The mean, maximum and standard deviation of all 1-hour wind speeds recorded by the AWS were 8.3ms^{-1}, 36.0ms^{-1} and 6.7 respectively. This compares to a mean of 7.7ms^{-1}, a maximum of 34.0ms^{-1} and a standard deviation of 5.6 in the WRF model. For the entire period, the mean RMS error, bias and correlation coefficient are 5.6ms^{-1}, -0.6ms^{-1}, and 0.60, respectively. Biases in wind speed and wind direction may be a result of the smoothed topography and any unresolved topographic features. King Edward Cove is topographically very complex (see Figure 2.1), and it

is only just resolved in the model and so will not capture the precise wind fields within the Cove.

The measured sea level pressure, in particular, is in excellent agreement with the modelled pressure, 996.9 ± 12.5hPa and 996.4 ± 12.4hPa respectively ($r^2 = 0.99$, $p < 0.01$). This is true for all seasons (see Table 5.7, Appendix 5A.1). The mean RMS error, bias and correlation coefficient for the entire period are 1.2hPa, -0.4hPa and 0.99, respectively.

5.3.1 Summary

Overall, there is a clear degree of unreliability in reproducing the observed climate of South Georgia, and this is primarily due to restrictions in the model's horizontal and vertical resolution, as well as limitations with the representation of the island's topography. The mountains of South Georgia have a large altitudinal range and this orographic divide is orientated almost perpendicular to the prevailing air flow, forming a clear boundary between the northeast and southwest sides of the island. These characteristics lead to great climatic heterogeneity over short distances. This restricts a realistic representation of the climatic complexity of the region within an atmospheric model. Despite these limitations, the results suggest we can be moderately optimistic that WRF is able to capture the regional climate of South Georgia. The lack of meteorological records restricts the use of more common and more exhaustive validation approaches. Though WRF is able to accurately reproduce the main patterns, large deviances and noticeable differences compared to the observations should be considered with caution. In summary, the model's performance at the surface is good. WRF is able to capture the broad scale seasonal changes in temperature and the other surface variables, but it does not capture the full magnitude of extremes at King Edward Point.

5.4 The Regional Climate of South Georgia

The weather and climate of South Georgia has long been measured, observed and described (see section 5.1). We know that the cold climate of the island is predominately a result of its location, as it is situated in the Scotia Sea between the temperate climate of the South Atlantic Ocean and the polar climate of the Southern Ocean. The region is also dominated by intense westerly circulations (Figure 1.9) and

is located within the main Southern Hemisphere storm track, meaning that the island continually experiences rapidly changing weather conditions (Mansfield & Glassey, 1957). The high mountains of the island run almost perpendicular to the prevailing winds, and this also leads to very different climatic conditions across the mountain range.

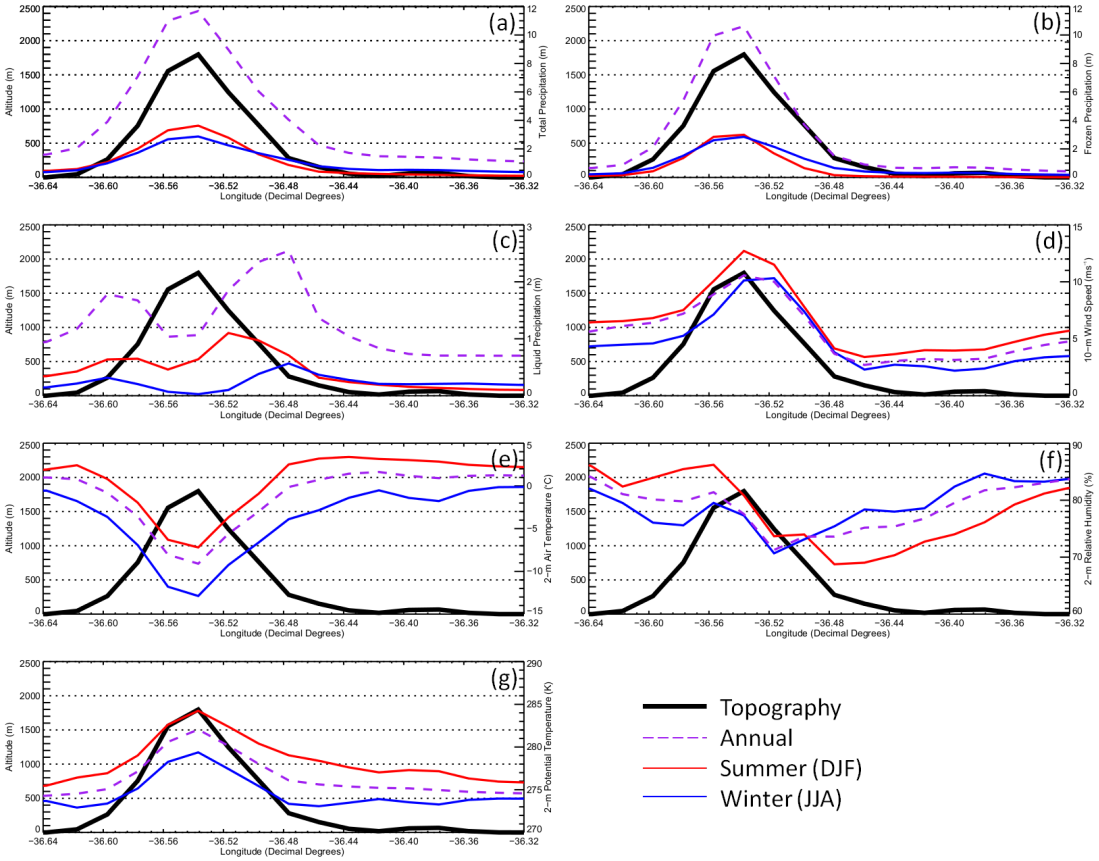

Figure 5.4 – *Horizontal cross-sections of panel (a) total precipitation accumulation (mm), panel (b) total frozen precipitation accumulation (mm), panel (c) total liquid precipitation accumulation (mm), panel (d) 10-m wind speed (ms^{-1}), panel (e) 2-m air temperature (^{o}C), panel (f) 2-m relative humidity (%), panel (g) 2-m potential temperature (K). Black solid line – topography cross-section, purple dashed line – annual mean, red solid line – austral summer (DJF) mean, blue solid line – austral winter (JJA) mean. Note: precipitation accumulations (panels (a), (b) and (c)) are expressed as annual and seasonal totals. See Figure 5.5 for geographic reference of cross-section through South Georgia.*

Despite this, the meteorological observations which have made across South Georgia, typically in low-lying areas along the northeast coastline, are patchy, discontinuous and temporally limited. It is near impossible to gauge a climatological perspective of climatic conditions across the entire island given the current datasets. Therefore, the high-resolution WRF simulation can be used to produce the first ever regional

climatology of South Georgia. Mean annual and seasonal cross-sections through South Georgia (Figure 5.4), along with regional maps of 2-m air temperature (Figure 5.5), 2-m relative humidity (Figure 5.6), 10-m wind speed and wind vectors (Figure 5.7), and precipitation (frozen and liquid) accumulation (Figure 5.8), using model output data from the intermediate (2.7km) WRF domain, are presented in the following sections. These figures will now be used to explore the regional climate of South Georgia.

5.4.1 Temperature

Topography plays a major role in determining the regional climate of South Georgia. The mean annual and seasonal temperature maps (Figure 5.5) reveal that the south end of the island is significantly colder compared to the north end of South Georgia, which can be attributed to slope aspect and orientation. Furthermore, the north-eastern coastline is comparatively warmer than elsewhere on the island since this region is largely modified by föhn and rain shadow effects. The predominance of the föhn effect can be observed in both the mean annual maps of temperature (Figure 5.5) and humidity (Figure 5.6), with relatively higher near-surface temperatures and drier conditions in the immediate lee (north-eastern slopes) of South Georgia throughout the year. The horizontal cross-sections through South Georgia (Figure 5.4) reveal that the mean annual 2-m temperature at sea level upwind and downwind of Mount Paget is 0.4^{o}C and 1.1^{o}C respectively. Throughout the year, Barff, Greene, Thatcher, and Lewin Peninsulas are warmer than elsewhere on the island, as they lie directly in the lee of Mount Paget (2934m) and are only seasonally snow-covered (Figure 5.8). Likewise, on the south-eastern side of the island, Cape Harcourt and Cape Charlotte (both of which form the north and south side of the entrance to Royal Bay (see Figure 1.2(c)) are generally warmer since also being in the lee of the Mount Paterson (2196m) and other major peaks, and are also only seasonally snow-covered (Figure 5.8). Regardless of the föhn effect, much of the island remains frozen throughout the year (< -5^{o}C). The winter and summer seasons of air temperature are clearly defined, and the annual temperature is within a 10^{o}C range. This is largely owing to the maritime nature of the climate. The warmest location is Hestesletten glacial plain, which, in austral summer, has an average temperature of 4.1^{o}C. Unsurprisingly, the coldest location on the island is Mount Paget, which reaches an average temperature of -13.3^{o}C during the winter.

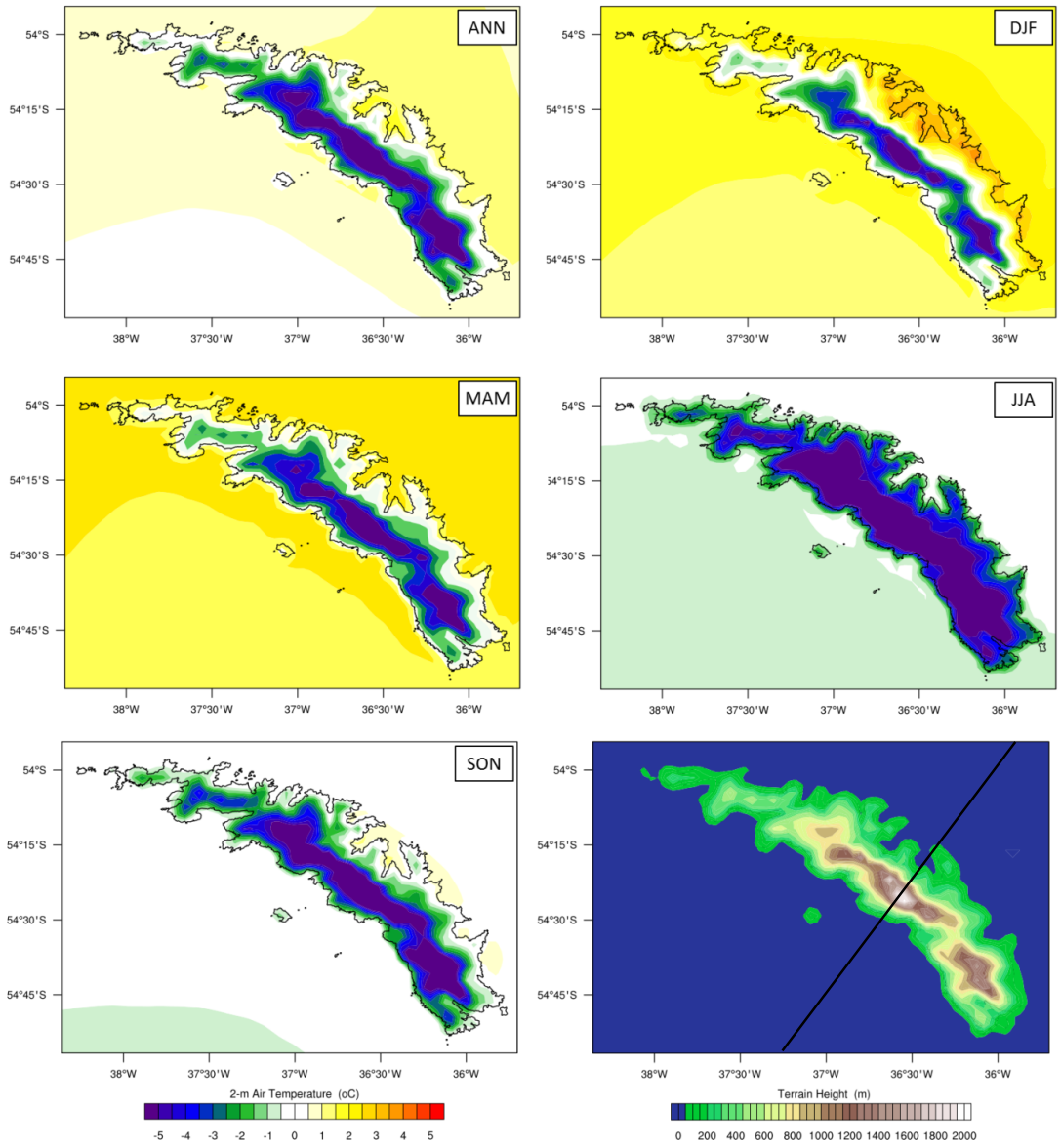

Figure 5.5 – *Mean (annual, summer (DJF), autumn (MAM), winter (JJA), and spring (SON)) maps of 2-m air temperature, along with terrain height for reference. The black solid line indicates the cross-section used for the profiles shown in Figure 5.4.*

5.4.2 Humidity

Figure 5.6 shows that the near-surface relative humidity is also largely topographically dependent, with lower humidity in the lee of the island (consistent with the föhn effect), and at higher elevations. There is a very clear and discernible cross-barrier gradient in humidity (Figure 5.4). This gradient is highest in summer, with the mean summer 2-m relative humidity at sea level upwind and downwind of Mount Paget at 90% and 86% respectively.

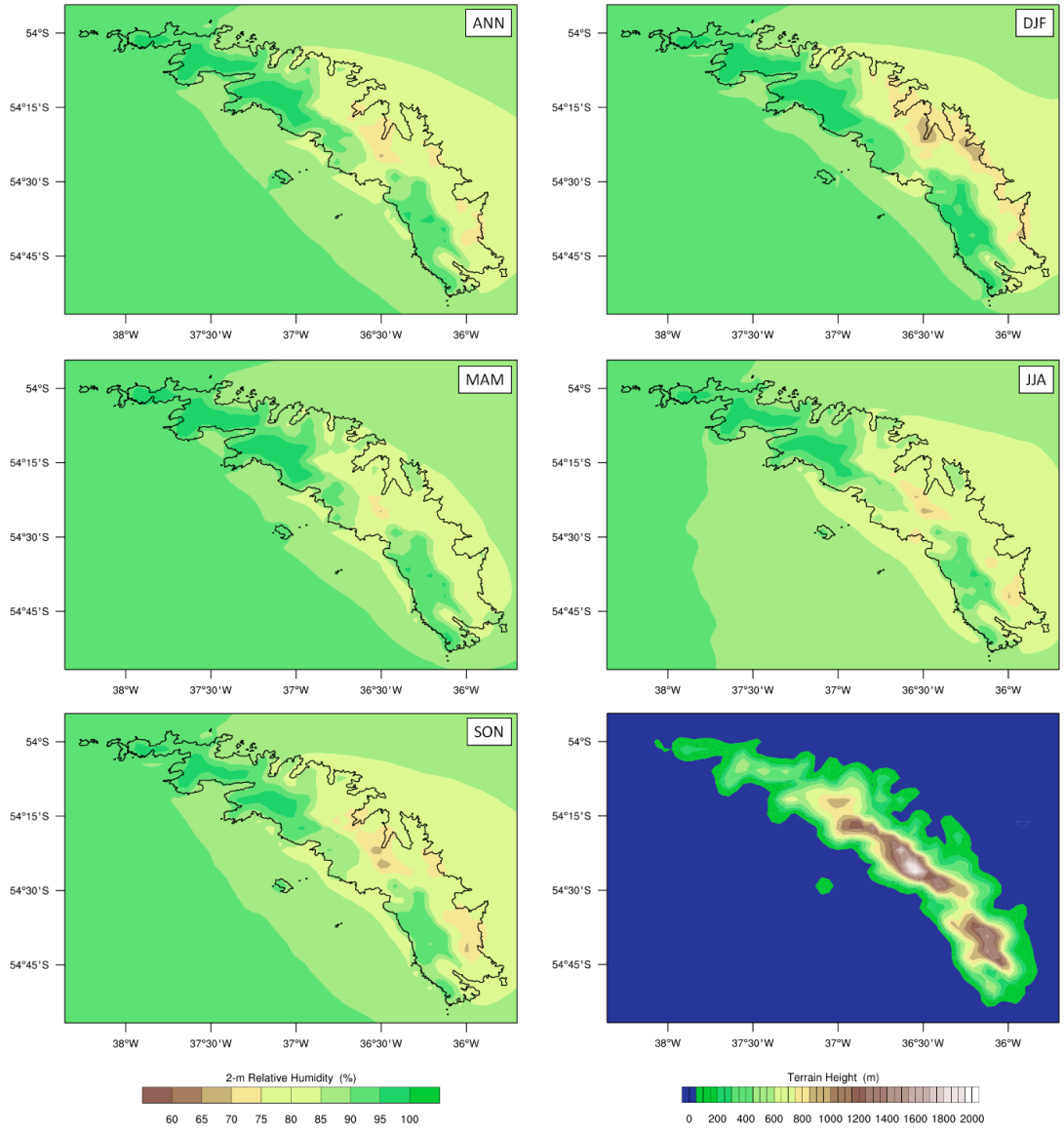

Figure 5.6 – *Mean (annual, summer (DJF), autumn (MAM), winter (JJA), and spring (SON)) maps of 2-m relative humidity, along with terrain height for reference.*

The north end of South Georgia is the most moist, where the temperatures are also generally higher throughout the year (Figure 5.5). The majority of southwest coast is also more humid than the northeast coast of South Georgia. Relative humidity is generally lower along the exposed regions of the island, along the north-eastern coastline, and in areas which are only seasonally covered in snow and ice. The relative humidity pattern shows large variability throughout the year in the immediate lee of Mount Paget, and this variability extends over Thatcher, Greene and Barff Peninsulas. Since the relative humidity pattern shows large variability over short distances, this may account for the model not accurately capturing the humidity field within King Edward Cove (see Chapter 4 and section 5.3). There is little variation of the spatial

humidity pattern throughout the year, but the intensity of the drier and humid areas does change. Based upon the mean annual relative humidity across South Georgia, the driest location on the island is in the immediate lee of Mount Paget, with a mean annual relative humidity of 68.2%. In contrast, the most moist location on the island is over the northern most peninsula of South Georgia (~12km east of Bird Island), with a mean annual relative humidity of 98.8%.

5.4.3 Wind Speed and Wind Direction

The predominance of westerly flow in this region of the Southern Ocean results in a clear west-east asymmetry in the wind pattern (Figure 5.4). Since South Georgia is in the path of continuous atmospheric depressions and frontal systems which originate and are generated in the Drake Passage and off the Antarctic Peninsula, wind speeds are in excess of $10ms^{-1}$ across most of the interior of the island throughout the year. As such, the prevailing westerly winds make South Georgia generally a very windy island (Figure 5.7). The strength of the winds is also clearly enhanced by local orographic effects. Wind speeds are highest (exceeding $12ms^{-1}$) over the Salvesen mountains, since they are comparatively more north-south trending than the Allardyce mountains. There are also areas of comparatively low wind speed on South Georgia. Due to increased surface roughness, there is a deceleration of airflow as it collides with the south-western side of the island, and this is most noticeable over some of the major peninsulas of South Georgia. This is indicative of low-level upwind flow blocking (i.e. low upstream wind speeds and/or high upstream static stability). Flow blocking has also been found to occur upwind of the Antarctic Peninsula (Orr *et al*., 2008; Elvidge *et al*., 2014a; Grosvenor *et al*., 2014) and upstream of other isolated and complex topographies (Drobinski *et al*., 2001; Gohm *et al*., 2004; Moore & Renfrew, 2005; Steinhoff *et al*., 2013). There is also evidence of flow splitting around South Georgia (diverting more to the right when looking downwind as a result of Coriolis force; see Ólafsson & Bougeault, 1996) throughout the year. This creates a jet off of the southern tip of South Georgia, with an average annual speed of $10ms^{-1}$. These tip jets have previously been found to occur during intense föhn events at King Edward Point (see Chapter 4) and were also modelled by Wells *et al*. (2008), Hosking *et al*. (2015) and Vosper (2015). Corresponding to the strong westerly flow, there is also a wake region ($<5ms^{-1}$) to the northeast (lee) of the island which extends several kilometres downstream of South Georgia. Over the island itself, this area of

decelerated flow is most noticeable over Greene Peninsula and Neumayer glacier, where wind speeds are <5ms^{-1} throughout the year. As a result, there is a clear cross-barrier gradient of wind speed (Figure 5.4). The mean annual 10-m wind speed at sea level upwind and downwind of Mount Paget is 6.4ms^{-1} and 4.5ms^{-1} respectively.

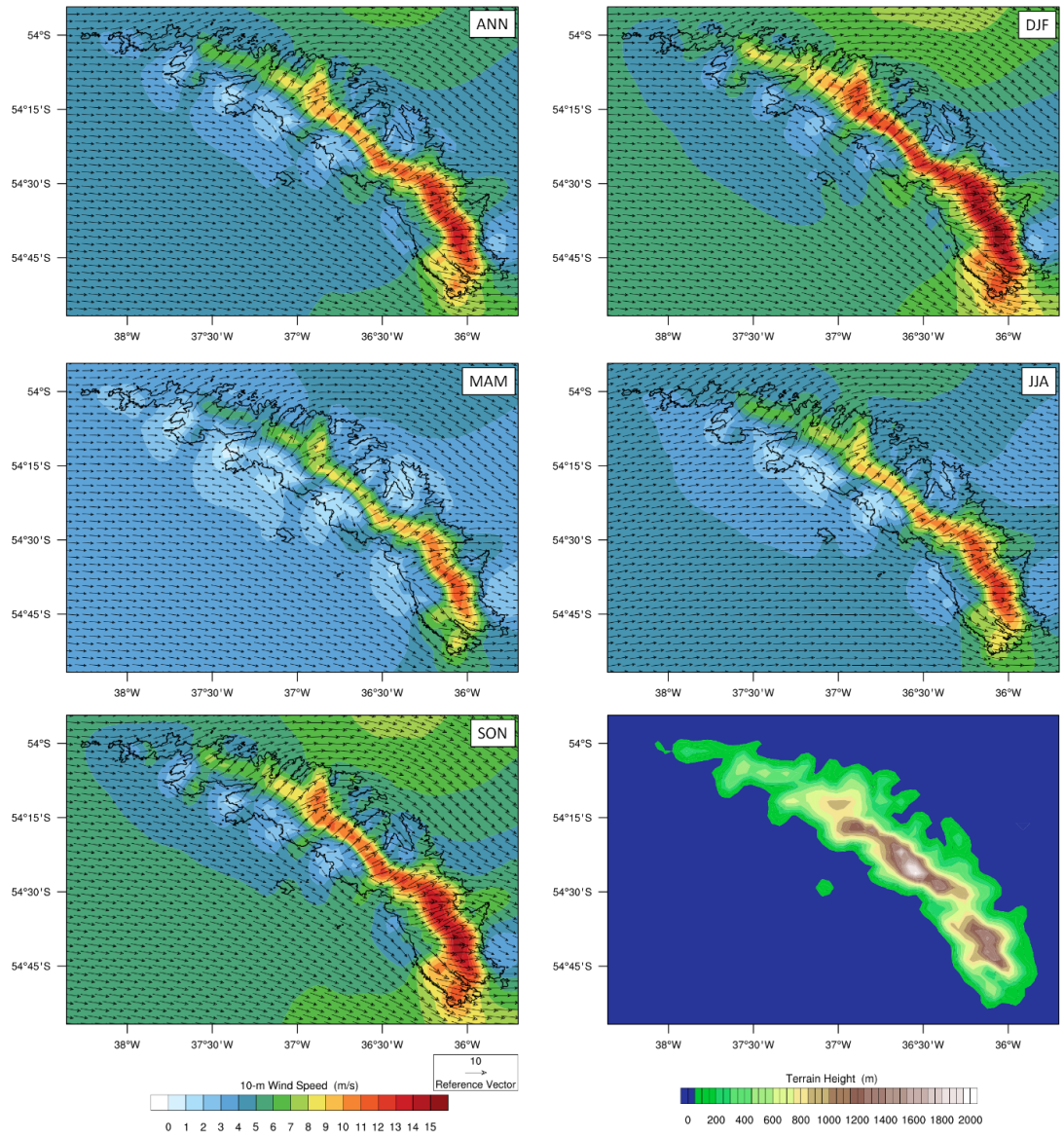

Figure 5.7 – *Mean (annual, summer (DJF), autumn (MAM), winter (JJA), and spring (SON)) maps of 10-m wind speed and 10-m wind vectors, along with terrain height for reference.*

The windiest location on the island is Mount Paterson, where the maximum mean annual wind speed reaches 14.0ms^{-1}. The least windy location is to the south of King Haakon Bay (northern end of South Georgia, see Figure 1.2(c)), where the minimum mean annual wind speeds reaches 1.1ms^{-1}. Wind speeds are strongest over South Georgia from November through February. There is little to no seasonal variation in

wind direction, with strong westerlies prevailing throughout the year. On shorter timescales, this prevailing pattern does vary significantly (see, for instance, Figure 5.18).

5.4.4 Precipitation

South Georgia is a very wet island (Figure 5.8). Precipitation (both in its liquid and solid form) occurs throughout the year, with substantial seasonal variations. Total precipitation is generally high (>2500mm) inland of South Georgia throughout the year, which is unsurprising given that precipitation is positively correlated with elevation (Figure 5.8). Total precipitation is generally greatest in austral summer over the highest mountains, especially on the south-facing side of South Georgia (Figure 5.4), which is also colder (Figure 5.5) and more humid (Figure 5.6) than the north-facing side of the island. Total precipitation is also noticeably lower in the northern region, more exposed and relatively flatter areas, as well as in the lee (since being in the rain shadow of the mountains) of South Georgia. This is consistent with the description of the regional climate of South Georgia, as provided by Richards & Tickell (1968). The annual total precipitation accumulation at King Edward Point in the WRF model is comparable to observations. The annual average precipitation total (January 2011 – January 2014) recorded at King Edward Point is 2033 mm, compared to 2262 mm in the WRF model. The daily precipitation totals at King Edward Point were measured by an optical rain gauge, which was installed at the station in February 2010. Liquid precipitation shows very large seasonal variations. As would be expected, the interior of the island is relatively free of rain (liquid precipitation) for much of the year, while the north-eastern coastline is relatively free of snow (frozen precipitation). The model indicates that the highest annual total precipitation accumulation occurs over Mount Paterson (14569.2mm), while the least amount of total precipitation accumulation occurs over the Willis Islands (1018.0mm, the northern most islands of South Georgia). The highest liquid precipitation accumulations are directly upwind and downwind of the major peaks. There is a band of rain in the lee of Mount Paget, Mount Sugartop and Mount Fagerli, extending over Thatcher Peninsula. The smoothed, unresolved and relatively coarse resolution of South Georgia's topography at this horizontal resolution is likely to cause an overestimation of rain at high elevation during austral summer months. The annual total precipitation plot (see Figure 5.9) from the high-resolution WRF domain (0.9km)

gives a greater indication of precipitation accumulations over the mountains of South Georgia, and these maps also show the level of detail available at this resolution.

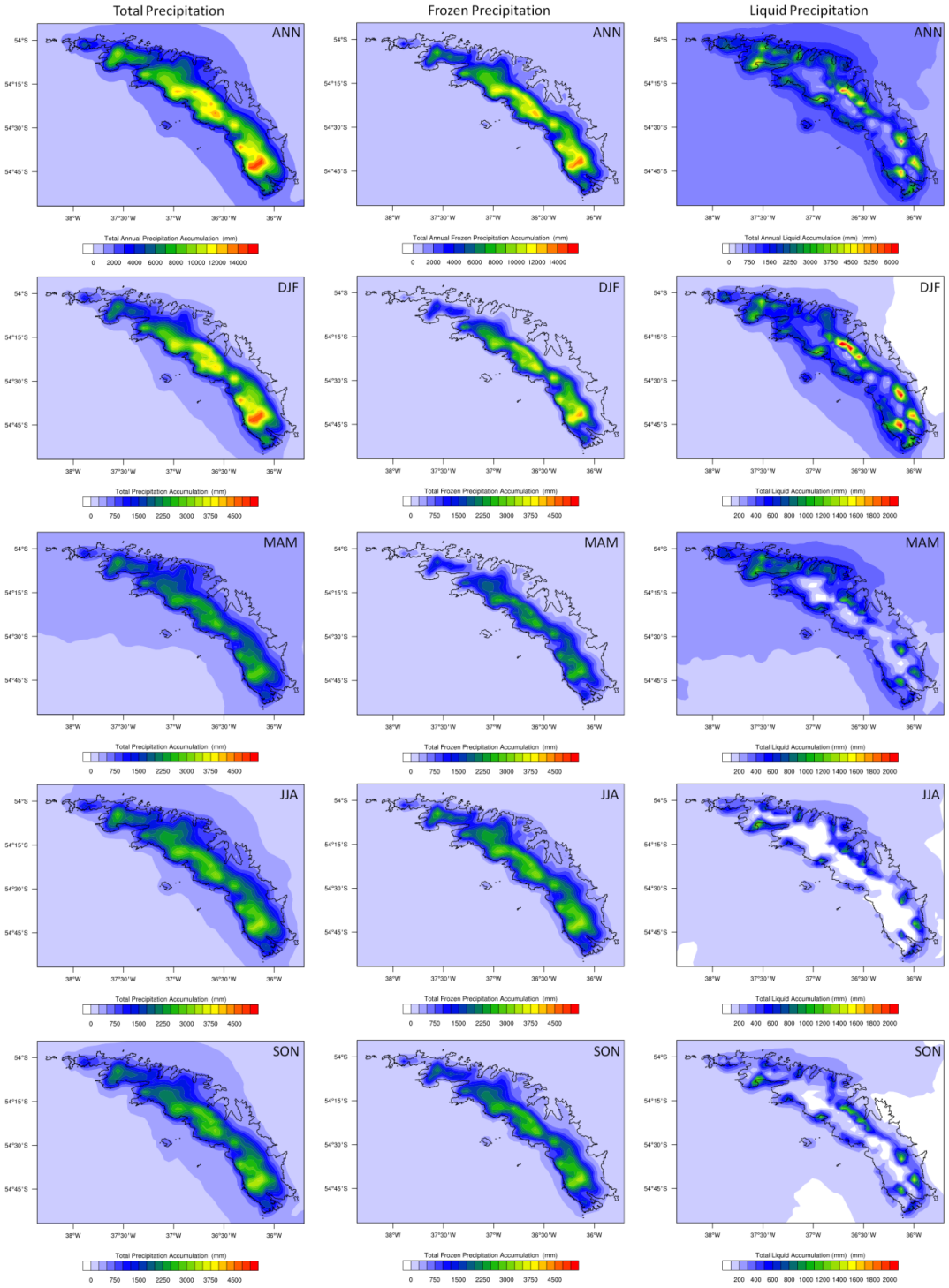

Figure 5.8 – *Annual, summer (DJF), autumn (MAM), winter (JJA), and spring (SON)) maps of total (frozen + liquid) precipitation (left), total frozen precipitation (middle), and total liquid precipitation (right). Frozen precipitation includes snow, graupel and hail accumulations.*

5.4.5 Summary

This data provides the very first indication of the regional climate of South Georgia, in the absence of island-wide *in situ* meteorological data. Throughout the year, the southwest side of South Georgia is wetter, colder, more humid and windier, than the north-eastern coastline. This is primarily due to the orographic divide and the predominance of the föhn effect. Likewise, throughout the year, the north end of South Georgia is warmer and more humid than the south end. This is primarily due to exposure, and topographic aspect and slope orientation. For a regional comparison, Table 5.1 shows the mean annual model climatology for 4 locations across South Georgia; King Edward Point (northeast coastline), Cape Darnley/Jacobsen Bight area (southwest coastline), Bird Island (north end), and Iris Bay area (south end). See Figure 1.2(c) for geographic reference of these locations. All these locations are approximately at the same elevation (~10 – 20m above sea level) in the WRF model.

Location	Mean Annual Temperature (°C)	Mean Annual Relative Humidity (%)	Mean Annual Wind Speed (ms^{-1})	Total Annual Precipitation Accumulation (mm)
Northeast: King Edward Point	1.5 °C	78%	3.9 ms^{-1}	2261mm
Southwest: Cape Darnley	0.6 °C	85%	5.7 ms^{-1}	2817mm
North end: Bird Island	0.7 °C	93%	3.3 ms^{-1}	1367mm
South end: Iris Bay	0.1 °C	75%	5.9 ms^{-1}	5007mm

Table 5.1 – *A summary of the mean meteorological conditions at King Edward Point, Cape Darnley/Jacobsen Bight area, Bird Island, and Iris Bay area.*

Though there are no high-resolution observations for quantitative comparison, overall, WRF is able to reproduce the seasonal distribution of precipitation, wind, temperature and humidity across South Georgia with qualitative accuracy. The model climatology of South Georgia is consistent with what we would expect from our current limited understanding of the regional broad-scale climate and of the associated topographic impacts of South Georgia (e.g. Mansfield & Glassey, 1957; Smith, 1960; Richards & Tickell, 1968; Headland, 1992; Rosqvist & Schuber, 2003). The same regional maps

using the innermost 0.9km WRF also domain show a much more detailed representation of the seasonal means, and the level of detail available, over the central portion of South Georgia.

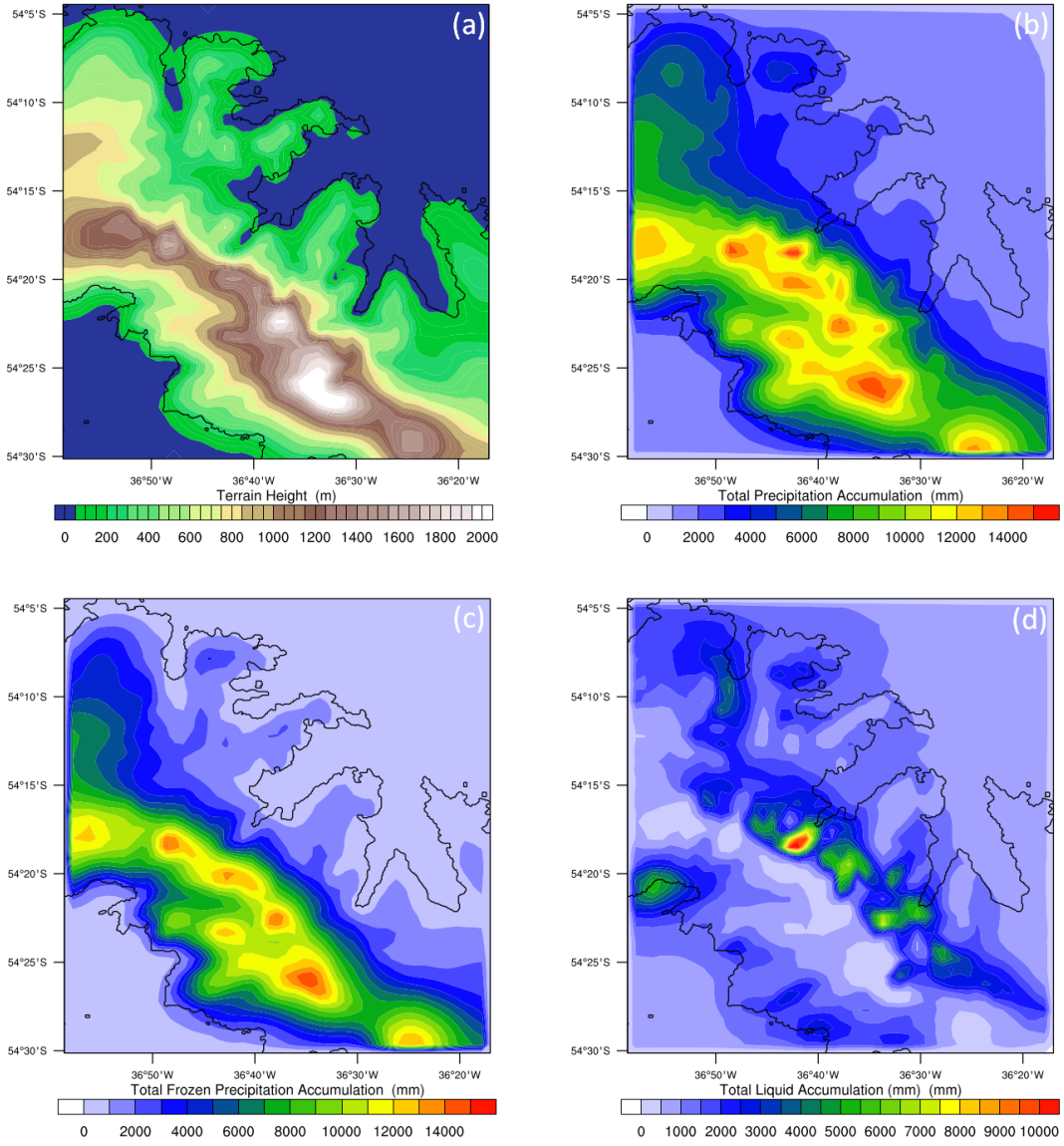

Figure 5.9 – *Annual total (frozen + liquid) precipitation accumulation (panel (b)), total annual frozen precipitation (panel (c)), and total annual liquid precipitation (panel (d)). Terrain height (panel (a)) is also shown for reference. This output is from the innermost 0.9km horizontal resolution WRF domain.*

In Figure 5.9, maps of the annual total precipitation accumulation are shown as examples of this. Figure 5.9 clearly shows that the highest frozen precipitation accumulations correspond with some of the highest peaks of the Allardyce range (e.g. Mount Paget and Mount Sugartop), while the highest liquid precipitation accumulations can be seen over Mercer Bay, the upper reaches of Lyell, Hamberg and

Harker glaciers (see Figure 6.3), as well as over the Hamberg Lakes and Hestesletten glacial plan. Since this chapter focuses on the regional climate of South Georgia, see Chapter 6 for a discussion of the impact of föhn on the climate using the model output from this domain.

Clearly, WRF is able to represent and reproduce the geographical distribution of seasonal near-surface climate of the island, as well as the fast variability of weather extremes on South Georgia. These maps provide a new insight into the nature of the regional climate and weather of South Georgia, with a particular focus on the spatial patterns of air temperature, relative humidity, wind speed, and precipitation accumulation. The author is unaware of any such climatological maps (either derived from observations or model simulations) existing for the entire island of South Georgia.

5.5 Where is the Föhn Effect Most Frequent on South Georgia?

Before identifying and detecting individual föhn events for a climatological analysis with the WRF model, the model climatology described above has been used to identify the areas of South Georgia that are most likely to experience the föhn effect. The only two locations on the island which the author is aware that föhn has previously been measured are at King Edward Point (Mansfield & Glassey, 1957) and Royal Bay (von Danckelman, 1884). Therefore, the WRF model output can be used to identify other areas which frequently experience surface warming, drying and increased wind speeds. The fraction of time the mean daily temperature and wind speed are in excess of 5.1^{o}C and 17.8ms^{-1}, and relative humidity below 61.5%, are shown in Figure 5.10. These thresholds were chosen as the criteria indicative of the föhn effect, as these are the mean daily temperature, wind speed and relative humidity experienced at King Edward Point during the 159 föhn events that were detected by the AWS climatology between June 2011 and February 2013. The values are also statistically significantly different ($p < 0.05$) to the observed non-föhn climatological (June 2011 – February 2013) means of 1.4^{o}C, 12.5ms^{-1} and 73.7%. Figure 5.10 effectively provides a guide to where the föhn effect is likely to be felt most frequently across South Georgia.

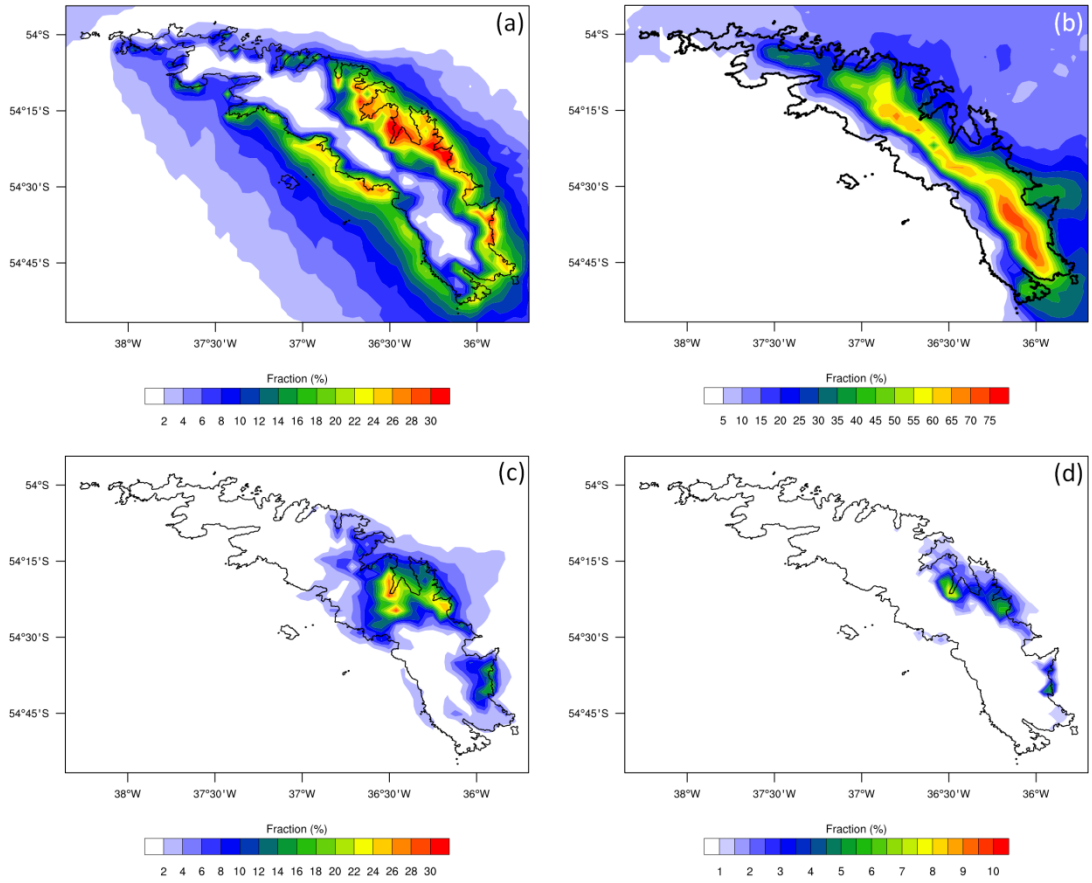

Figure 5.10 – *Fraction of time (with respect to 21 months) when the mean daily 2-m air temperature (panel (a)), 10-m wind speed (panel (b)), and 2-m relative humidity (panel (c)), are in excess of 5.1°C and 17.8ms^{-1} and below 61.5%, respectively. Panel (d) shows the fraction of time when all three conditions are met.*

The fraction of time the 2-m temperature exceeds 5.1°C shows that warmest temperatures occur along the exposed, intermittently snow-covered, low-lying areas of South Georgia (Figure 5.10(a)). As expected, the warmest temperatures are especially persistent along the north-eastern coastline. This is most noticeable over Moraine Fjord, Hestesletten, Hound Bay and St. Andrews Bay, and the fringes of Cumberland West Bay, where the temperature exceeds 5.1°C for ≥25% of the time. At King Edward Point and the surrounding area, 28 – 32% of the time is dominated by temperatures in excess of 5.1°C. Across South Georgia, the altitudinal limit at which 5.1°C is exceeded is approximately 1500m. The fraction of time the near-surface winds exceed 17.8ms^{-1} (Figure 5.10(b)) indicates that strong wind events are virtually non-existent on the windward side of South Georgia, and this is a consequence of the predominance of westerly flow and subsequent orographic enhancement in the lee of the island. As with Figure 5.7, Figure 5.10(b) shows that the strongest wind speeds at this level are most frequent over the main mountain chain, running parallel with South

Georgia's axis. The winds are frequently stronger over the Salvesen mountain range (exceeding 17.8ms^{-1} 75% of the time at Mount Paterson), than they are over the Allardyce mountain range (exceeding 17.8ms^{-1} 66% of the time at Mount Paget). There are three core areas on the lee slopes of South Georgia where the relative humidity is frequently less than 61.5% (Figure 5.10(c)). These are Hestesletten and Moraine Fjord, St. Andrews Bay, and Cape Charlotte, Gold Harbour and Iris Bay. Therefore, this provides the first indication of areas which are mostly likely to experience the föhn effect at the surface. Areas which are frequently warmer, windier and drier than the climatological (June 2011 – February 2013) mean are indicative of being under the influence of the föhn effect (Figure 5.10(d)).

This information is useful for planning future placements of AWS stations on South Georgia to detect föhn flow. While Figure 5.10 shows that the location of the AWS at King Edward Point is suitable for detecting the föhn effect at the surface, it also illustrates that there are more appropriate locations for this. On the north-eastern side of South Georgia, AWS stations located at the disused whaling stations sites of Husvik, Godthul and Ocean Harbour, as well at Hestesletten and St. Andrews Bay would be an advantage for future föhn research. Given the results of Figure 5.10, it seems that these locations may also regularly be under the influence of the föhn effect. Since there are no meteorological observations available for the southwest side of South, AWS stations located directly upwind of King Edward Point (i.e. on Annenkov Island and/or in the Cape Darnley and Jacobsen Bight vicinity) would also be beneficial for future climate research.

5.6 WRF Föhn Climatology

One of the aims of this chapter is to deduce the best method for detecting occasions of föhn on South Georgia with the WRF model. This is because the results presented in Chapter 3 are specific to King Edward Point. In the absence of island-wide near-surface meteorological observations, it is impossible to determine if the föhn effect observed in the King Edward Point observations also impacts the rest of South Georgia. By ascertaining how frequent föhn events are across the entire island, then the difference in the near-surface meteorological fields between föhn and non-föhn conditions can be explored further. Therefore, the purpose of this section is to detail the best method possible for föhn detection with the WRF model. These methods were

briefly introduced in section 5.2.2. The impact of föhn warming on climate variability on South Georgia is then explored in Chapter 6, after a representative set of events have been identified using the most appropriate method.

The three different methods for detecting the occurrence of föhn in the WRF simulation were used to generate climatologies of föhn events. Each method uses properties and characteristics which are dynamically, theoretically, and empirically observable and associated with föhn flow. Each of the three methods is presented and evaluated separately. The model climatologies are compared with that obtained from the AWS observations. If a modelled föhn event occurs within ±6 hours of an observed (AWS) event, the modelled event is declared to be a "hit". If the model generates an event but there is no corresponding event in the observations, the modelled event is labelled a "false positive". Similarly, if the model indicates non-föhn conditions at a time when the observations indicate a föhn event, a "false negative" model event is recorded (see Table 5.2).

		WRF Model	
		Föhn	Non-föhn
AWS Observations	Föhn	"Hit"	"False negative
	Non-föhn	"False positive"	

Table 5.2 – *Schematic table describing a "hit", a "false negative", and a "false positive". These terms are used when comparing the modelled föhn climatology with the observed AWS föhn climatology.*

The hit rate is defined as the ratio between the total number of "hits" to the total number of observed föhn events (159 in total), expressed as a percentage. Validation statistics are recorded for the 21 months of the WRF simulation and are compared to the AWS climatology of föhn events during the same period. A total of 159 föhn events that produced large temperature differences were found to have occurred at King Edward Point between June 2011 and February 2013. A summary of the modelled föhn climatologies for each of the three methods is given in Table 5.6, after

each of the methods have been described and evaluated separately. A list of all the "hits" for each of the methods tested is shown in Table 5.8 (Appendix 5A.2).

5.6.1 Method 1: Identification Using Surface Data

This method is analogous to the method used to identify the occurrence of föhn from King Edward Point AWS observations, and the simplicity of this method is based upon the detectable near-surface föhn signature as previously described in detail in Chapter 3 (see section 3.2). For a wind to be classified as a föhn event in the model, it must first meet the primary criterion:

(1) An increase of air temperature, greater than 2^{o}C within 1 hour of föhn onset

As in the AWS classification method, this threshold is set to remove detections of any gradual changes in temperature, which may be associated with other meteorological phenomena. If an event meets this criterion, then it must also meet *each* of the following secondary criteria:

(2) A decrease in relative humidity, during the specified event, and;

(3) An increase in wind speed, during the specified event, and;

(4) Wind from the direction of the barrier.

Considering the orientation of South Georgia, winds with a direction 150^{o} – 330^{o} were deemed as having potential for generating leeside föhn at King Edward Point and thus being indicative of cross-barrier flow-over conditions in the model. For a modelled föhn event to be declared a "hit", the above criteria had to be met within ±6 hours of the observed AWS föhn event. This was to account for timing errors in the forcing data, and the muted signal in föhn warming as shown in previous case studies (Chapter 4). As with the AWS classification method (Chapter 3), there are no thresholds for changes in relative humidity and wind speed due to their intermittent signature. This method does not account for, nor consider, föhn cessation in the identification process. This is Method 1A.

The sensitivity of the WRF föhn detection hit rate to the above thresholds was also tested. This is because poorly resolved mesoscale and subgrid-scale effects may have large impacts on föhn conditions, which can result in fewer events being captured. Similarly, föhn conditions may develop slower in the model as a result of the smoothed

terrain. In order to account for differences between the observed and modelled data, the above temperature and timing thresholds were altered to account for these potential discrepancies. Therefore, criterion (1) was changed so that a föhn was detected when there was "*an increase in temperature, greater than 1.5^{o}C within 2 hours of föhn onset*". All other criteria remained the same. This is Method 1B. To account for the fact that King Edward Cove is poorly resolved in the WRF model, a different grid cell was also chosen which was deemed to be topographically more representative of King Edward Point. In Chapter 4, and throughout Chapter 5, this is referred to as Hestesletten. For a föhn to be declared at Hestesletten, the same criteria as Method 1A had to be met. The modelled föhn climatology at Hestesletten also provides a spatial window (similar to the temporal window used in Method 1B) to account for the fact that föhn may not always develop at King Edward Point in the model. The climatology of föhn events detected with the model at Hestesletten is Method 1C.

The validation statistics comparing the number of modelled föhn events against the number of observed föhn events for Methods 1A, 1B and 1C is summarised in Table 5.3. See Table 5.6 for a full summary of all modelled föhn climatologies using all three methods. Table 5.8 (Appendix 5A.2) provides a full list of all the föhn "hits" for Methods 1A, 1B and 1C. While the AWS recorded 159 föhn events between June 2011 and February 2013, Method 1A detects 73 events at King Edward Point in the model. Of these 73 events, 49 are "hits", 24 are "false positives", and 110 events are "false negatives". Therefore, Method 1A has a hit rate of 30.8% when compared to the observed AWS föhn climatology. While the original AWS method (presented in Chapter 3) was efficient at identifying föhn conditions in the surface observations, it is clearly not suitable for identifying observed events from WRF model surface output data. When the same criteria are applied to the modelled timeseries at King Edward Point, only 49 of the observed föhn events are detected. Clearly, the föhn climatology declared by Method 1A struggles to match with the observed AWS föhn climatology during this period. Method 1A has the lowest hit rate of all the methods tested (see Table 5.6). Fewer modelled föhn events compared those observed is a likely consequence of the muted modelled variability in the near-surface air temperatures at King Edward Point (see Figure 5.2), since Method 1 relies solely on the impact of the föhn warming process on the surface to detect such occasions.

Method	Total number of events detected	"Hit"	"False Positive"	"False Negative"	Hit Rate
AWS (surface observations, Chapter 3)					
	159	/	/	/	/
Method 1 (surface observations)					
Method 1A King Edward Point	73	49	24	110	30.8%
Method 1B Reduced thresholds	163	103	60	56	64.8%
Method 1C Hestesletten	296	59	237	100	37.1%

Table 5.3 – *The number of föhn events detected in the WRF model using Method 1 compared to the AWS föhn climatology. See Table 5.2 for a description of "hit", "false positive" and "false negative".*

To account for the poorly resolved topographic features which may influence the modelled föhn climatology at King Edward Point, the number of föhn events detected at Hestesletten was also calculated. When using Method 1C for föhn detection, overall there is larger hit rate of 37.1%. Method 1C identifies 296 events in total, 59 are "hits" and 237 are "false positives". This shows that >2ºC rises in temperature in the model are more frequent at Hestesletten than they are at King Edward Point since more "hits" are declared. Although there are no observations at Hestesletten for verification, it is interesting to note that the model föhn climatology from this grid cell agrees more with the observed AWS föhn climatology, than the model föhn climatology from the King Edward Point grid cell.

To account for timing errors and muted föhn warming in the model, Method 1B identified föhn events by reducing the threshold of the föhn criteria. In doing so, over twice as many (103 events) are declared using Method 1B than Method 1A. The hit rate for Method 1B is 64.8%. It is unsurprising that reducing the threshold to *an increase in temperature, greater than 1.5ºC within 2 hours of föhn onset* leads to 90 more events being declared at King Edward Point than with the default thresholds of Method 1A. This is consistent with the previous results of section 5.3 and Chapter 4, which have shown that the modelled föhn events have a muted surface temperature response compared to the observations. This appears to be a systematic error in the model during föhn and non-föhn conditions.

By considering all "hits" detected across Methods 1A, 1B, and 1C, 55 observed föhn events in the AWS föhn climatology (of 159 in total) are declared "false negatives" (see Table 5.8, Appendix 5A.2). The majority of these 55 "false negative" föhn events can be considered weak föhn events, as the majority fall within the lowest 50% of events when categorised by temperature change. In all 55 cases, WRF is unable to capture these events because the model does not meet the temperature criterion. Across these 55 events, 91% and 65% of them meet the wind direction and wind speed criteria (respectively), with 52% matching the relative humidity criterion. Wind speed and wind direction criteria are less of a problem, implying that the winds remain correct, but an event is not recorded at the exact location.

Generally, it seems that the föhn climatology of Method 1, specifically Method 1B, is comparable to the observed AWS föhn climatology. However, due to the inherent ambiguity with this method, there are a number of limitations that must also be recognised. Increases in temperature of >2^{o}C that do not occur during föhn flow are very common in the model and in the observations. These changes in temperature may be a result of any number of synoptic, regional and local meteorological processes, including the diurnal change in temperature, solar and cloud effects, or other downslope/valley winds such as the katabatic effect (Mansfield & Glassey, 1957). In Chapter 4, it was shown that a weak surface warming of 2^{o}C (section 4.5) may not be indicative of föhn at all, and this event was later classed as a rapid warming event. Similarly, in Chapter 3, it was shown that intense increases in temperature at King Edward Point may be related to synoptically driven warm air advection and island-wide warming. Although Method 1B has a hit rate of 64.8%, it is an indirect method of detection as it is evaluating the impact of föhn (i.e. surface warming etc.) at the surface. Therefore, the föhn-like surface signal may not always be a result of the föhn effect. Consequently, it is inherently difficult to develop an accurate method of föhn detection based on surface conditions alone. Method 1 also only identifies föhn events affecting an area within the immediate vicinity of King Edward Point. Just because a föhn event is not picked up at the AWS location or equivalent WRF grid cell does not necessarily mean there is not one occurring elsewhere on the lee of the island (and vice versa). This also means that a föhn observed in the AWS or model may not necessarily have ended, but it is just no longer observed at King Edward Point. This method also assumes that all föhn events on the leeside extend to the surface. For

instance, cold air pooling within King Edward Cove or outflow from other valleys could prevent the föhn from reaching the surface (Mansfield & Glassey, 1957). To overcome some of these limitations and improve the hit rate, two other methods were developed based upon the broad-scale flow conditions to give a greater measure of the occurrence of föhn conditions in the lee of the island.

5.6.2 Method 2: Leeside Isentropic Drawdown

As the previous case studies have shown (Chapter 4), isentropic drawdown on the leeside of the island is a significant characteristic of föhn events on South Georgia. The drawdown of air from aloft appears to be a major driver of föhn warming and drying. Relatively warm regions are found in the immediate lee of the mountains, under the steepest isentropes and strongest winds. This has also been observed during föhn flow over the Antarctic Peninsula (see e.g. Elvidge *et al*., 2014a; Grosvenor *et al*., 2014) and over the McMurdo Dry Valleys (see e.g. Speirs *et al*., 2010; Steinhoff *et al*., 2013). Therefore, isentropic drawdown is often sufficient to bring about leeside warming. It is a valid assumption that a larger drawdown in the isentropes generates, and is more indicative of, a stronger föhn event.

In this classification scheme, a west-east cross-section (transect A, Method 2A) through South Georgia is taken (see Figure 5.11 and Figure 5.12). For each model output time an isentrope is chosen at 2200m (Z_1, i.e. just above mountain height), approximately 140km upstream of the island. The point at which Z_1 is taken is in undisturbed flow, and is slightly less than the Rossby Radius of deformation (Hunt *et al*., 2001), λ_R, for this latitude. This is so that Z_1 is not taken close to the boundary edges of the domain. λ_R is given by:

$$\lambda_R = \frac{Nh}{f}$$

where N is the upstream Brunt-Vaisala frequency (typically $0.01s^{-1}$), h is the typical mountain height (2000m) and $f = 2\Omega\sin\theta$ is the local Coriolis parameter ($-1.2x10^{-4}$ s^{-1}). Using these typical values gives a Rossby Radius of deformation of 167km at South Georgia.

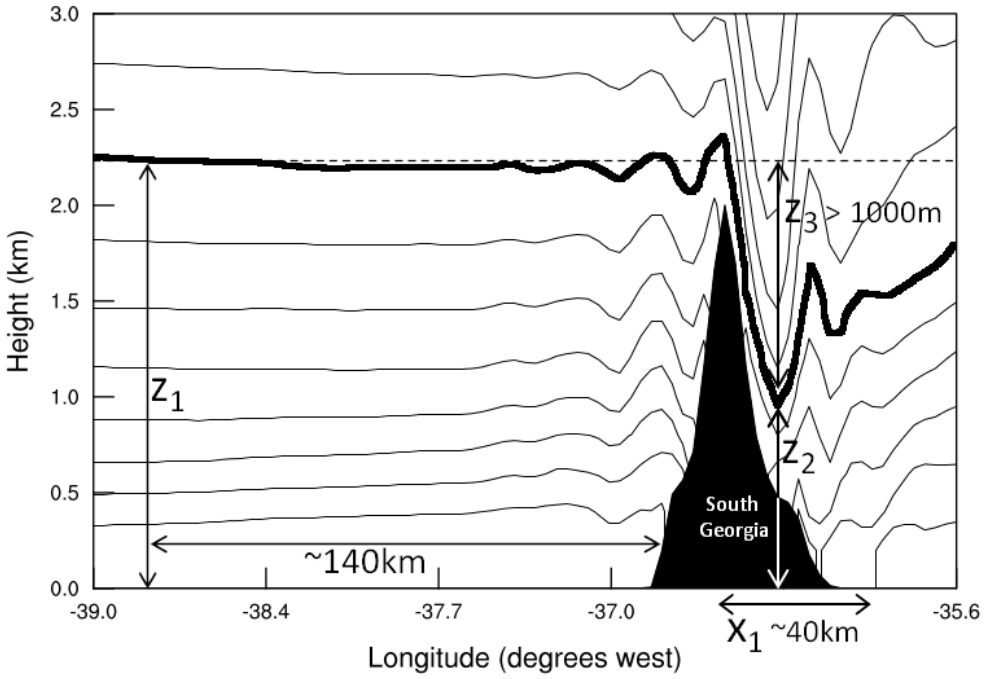

Figure 5.11 – *Schematic diagram of calculating the extent of isentropic drawdown across South Georgia for Method 2.*

The minimum height, Z_2, of that isentrope is then found downstream of the island within a 40km transect (X_1). Due to the large number of positive detections, it was required that the change in isentrope height ($Z_3 = Z_1 - Z_2$) must exceed 1000m for 6 or more continuous hours for a föhn event to be declared. The only other criterion was that the average mountain height wind direction had to be between 225° – 315°. The transect of Method 2A intersects King Edward Point.

To account for the fact Method 2A intersects west-east through the WRF domain and over King Edward Point, Method 2B was also created so that its transect (transect B, Figure 5.12) intersected Mount Paget (the highest mountain on South Georgia). The downstream transect (X_1) of Method 2B intersects St. Andrews Bay. Methods 2A and 2B both assume that the steepest cross-barrier isentropic profiles are orientated west-east through South Georgia due to the alignment of their transects (Figure 5.12). Since the incident airflow is not truly west-east trending, Method 2C was also created, and this transect (transect C, Figure 5.12) is perpendicular to South Georgia (at an angle of ~217°). Therefore, Method 2 calculates the change in isentrope height along three different transects over South Georgia. Transect A (Method 2A) intersects King Edward Point, transect B (Method 2B) intersects St. Andrews Bay, and transect C

(Method 2C) runs roughly perpendicular to the island (see Figure 5.12). Unlike Method 1, which detects occasions of föhn only at King Edward Point, Method 2 is directly connected to föhn dynamics, and therefore, ought to identify conditions when the föhn warming process is taking place anywhere in the lee of South Georgia.

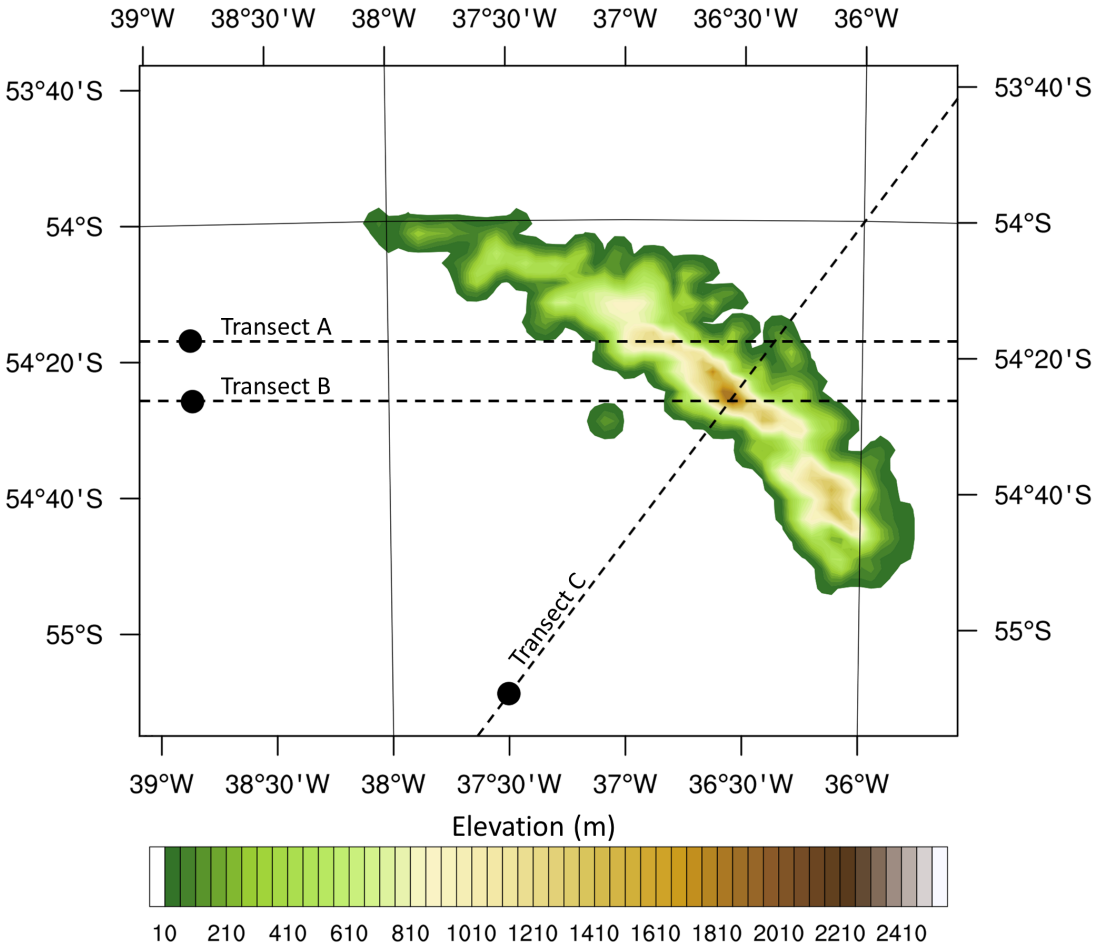

Figure 5.12 – *The three isentrope cross-sections through South Georgia: transect A intersects King Edward Point, transect B intersects St. Andrews Bay, and transect C intersects Mount Paget and South Georgia at an angle of ~217°. The black filled circles indicate the location of Z_I for each of the three methods: Method 2A: -54.284°S, -38.833°W, Method 2B: -54.433°S, -38.833°W, Method 2C: -55.155°S,-37.500°W.*

Methods 2A, 2B and 2C were developed to give a broader scale validation of indicative föhn conditions upstream and across the lee of South Georgia. The validation statistics comparing the number of modelled föhn events against the number of observed föhn events for Methods 2A, 2B and 2C is summarised in Table 5.4. The results of Method 2 are presented alongside the results of the two other methods in Table 5.6. Table 5.8 (Appendix 5A.2) provides a full list of all the föhn "hits" for Methods 2A, 2B and 2C.

Method	Total number of events detected	"Hit"	"False Positive"	"False Negative"	Hit Rate
AWS (surface observations, Chapter 3)					
	159	/	/	/	/
Method 2 (isentropic drawdown)					
Method 2A Transect A	143	55	88	104	34.6%
Method 2B Transect B	209	120	89	39	75.5%
Method 2C Transect C	209	55	154	104	34.6%

Table 5.4 – *The number of föhn events detected in the WRF model using Method 2 compared to the AWS föhn climatology. See Table 5.2 for a description of "hit", "false positive" and "false negative".*

Overall, Method 2 performs more accurately than Method 1, and Method 2B has the highest hit rate (75.5%) of all föhn detection methods (see Table 5.6). Of the 209 föhn events which are detected by Method 2B, 120 are "hits" and 89 are "false positives". Of the observed 159 events, just 39 are "false negatives". It is also important to note that one would not expect Method 2 to detect all 159 events, since it only detects events with a duration lasting more than 6 hours. In the AWS climatology of föhn events, there are 27 events with a duration lasting less than 6 hours. Of these 27 events, Method 2B declares 4 of these events to be "hits". The hit rate of Method 2B increases to 87.9% when accounting for these 27 events. Therefore, by accounting for this arbitrary threshold in duration, Method 2B is quantitatively comparable to the surface AWS observations when detecting individual föhn events. Although Methods 2A and 2C detect a large number of föhn events (143 and 209 respectively), the hit rate for these methods (34.6% for both methods) are much smaller than Method 2B. Clearly, different transects across South Georgia lead to drastically different hit rates, and these results also further highlight the complexity of flow over the island.

Despite the large hit rate with Method 2B, it is also important to note that (like Method 1) just because a föhn event is declared with Method 2 does not necessarily mean that it will have an impact on surface conditions at King Edward Point. Regardless of this, Method 2 removes the subjectivity of identifying potentially erroneous changes in the near-surface conditions which Method 1 is based upon. Of the three methods tested, it

is the only method which dynamically ensures that föhn warming and drying is occurring (somewhere) on the lee of South Georgia when the criteria are met.

5.6.3 Method 3: Upstream Froude Number

The vertical atmospheric structure upstream of South Georgia must also be considered when detecting föhn events. This method is based upon the assumption that strong flow over conditions are met when the Froude number ≥ 1 (see section 1.6.1 for more detail). When this condition is met, a föhn event on the leeside of South Georgia will occur.

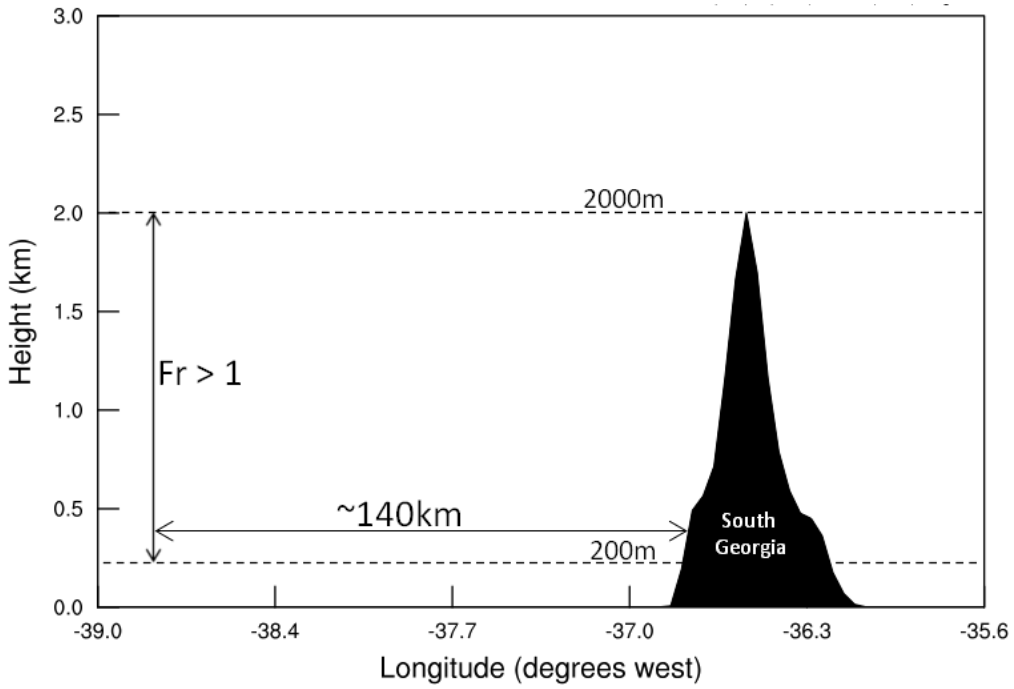

Figure 5.13 – *Schematic diagram of calculating the upstream Froude number for Method 3. The average Froude number between 0.2 – 2km was calculated at -54.433°S, -38.833°W for Method 3A and 3B, and at -55.155°S,-37.500°W for Method 3C.*

An average upstream Froude number was calculated 140km upstream of the island, between 0.2km and 2km (Figure 5.13). For a föhn to be detected, the Froude number,

$$Fr = \frac{U}{Nh}$$

where U is a characteristic upstream wind speed, h is the typical mountain height, and N is the upstream Brunt-Vaisala frequency, had to exceed 0.9 for 6 or more continuous hours. For example, if N = 0.012 s^{-1} (characteristic value for approaching flow) and h = 2000m respectively, then Fr ≥ 0.9 is satisfied when U = 21.6ms^{-1}. The detected

events were also limited by wind direction, whereby the average mountain height wind direction had to be between 225º-315º. This is Method 3A. A Froude value of 0.9 was specifically chosen so that upstream flow dynamics were statistically different to that of the climatological (June 2011 – February 2013) mean. The average Froude number during non-föhn times (the climatological non-föhn mean) was found to be 0.64 ± 0.38, whilst the average during föhn times as defined in the AWS observations was found to be 0.76 ± 0.29. These values are statistically significantly different ($p < 0.05$). Values of Froude larger than 0.9 should, therefore, represent strong flow-over conditions along with a strong föhn signal in the lee.

In addition to Method 3A, Method 3B further assumes that South Georgia is roughly north-south trending, and that the prevailing winds are west-east orientated. Therefore, Method 3B calculates an upstream Froude number using the zonal (u) wind component in place of the average (non-directional) wind speed component. Since this is a generalisation, a third upstream Froude number was also calculated along a transect (at an angle of 217º) perpendicular to the average axis of South Georgia (~127º) (see Figure 5.14). This is Method 3C. In this instance, the characteristic upstream wind speed perpendicular to the island (U_T) was calculated by:

$$U_T = vsin\theta + usin(\frac{\pi}{2} - \theta)$$

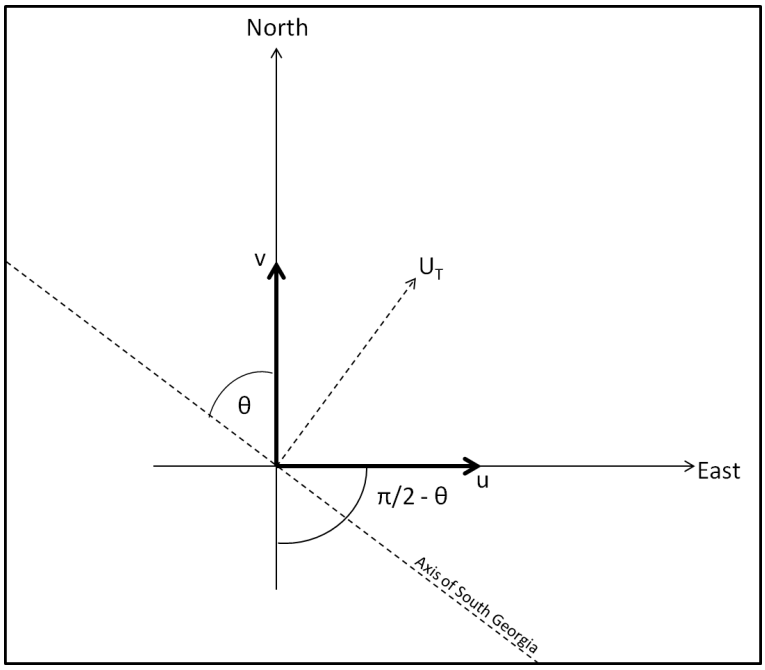

Figure 5.14 – *Schematic diagram showing how the wind component perpendicular to South Georgia (U_T) is calculated.*

The results of using the directional (u) wind speed (Method 3B), and the perpendicular wind speed (U_T) (Method 3C), in the Froude number calculation are presented alongside the default method for identifying föhn (using the mean (non-directional) wind speed) (Method 3A) in Table 5.5. The results of Method 2 are presented alongside the results of the two other methods in Table 5.6. Table 5.8 (Appendix 5A.2) provides a full list of all the föhn "hits" for Methods 3A, 3B and 3C.

Of all the methods used to detect föhn in the lee of South Georgia, Method 3C detects the highest total number of modelled föhn events, with 307 events declared (see Table 5.6). Of these 307 events, only 86 of them are "hits" and the other 221 events are "false positives". Overall, Method 3C has a hit rate of 54.1%. Method 3B performs the least adequately within Method 3, with a hit rate of 47.8% of events. Method 3B declares 248 events in total, but only 76 of these are "hits". Method 3A performs the best of all the methods within Method 3. Method 3A detects 152 events, 103 of which are "hits", and therefore has a hit rate of 64.8%. Since Method 3 also detects events with a duration lasting more than 6 hours, the hit rates of Methods 3A, 3B and 3C increase to 78.0%, 57.6% and 65.2% respectively when this is accounted for. Of the three methods, Method 3A performs the best. As with Method 1, Method 3 somewhat accurately identifies the observed föhn climatology.

Method	Total number of events detected	"Hit"	"False Positive"	"False Negative"	Hit Rate
AWS (surface observations, Chapter 3)					
	159	/	/	/	/
Method 3 (upstream Froude number)					
Method 3A $_{ff}$	152	103	49	56	64.8%
Method 3B $_{u\ (zonal)}$	248	76	172	83	47.8%
Method 3C $_{U_T}$	307	86	221	73	54.1%

Table 5.5 – *The number of föhn events detected in the WRF model using Method 3 compared to the AWS föhn climatology. See Table 5.2 for a description of "hit", "false positive" and "false negative".*

5.6.4 Summary of Modelled Föhn Climatologies

Since each of the methods were introduced, described, and evaluated separately, Table 5.6 summarises the modelled föhn climatologies for all 3 methods. Overall, 9 different methods were tested to deduce the best possible method for detecting observed föhn conditions with the WRF model.

Method	Total number of events detected	"Hit"	"False Positive"	"False Negative"	Hit Rate
AWS (surface observations, Chapter 3)					
	159	/	/	/	/
Method 1 (surface observations)					
Method 1A King Edward Point	73	49	24	110	30.8%
Method 1B Reduced thresholds	163	103	60	56	64.8%
Method 1C Hestesletten	296	59	237	100	37.1%
Method 2 (isentropic drawdown)					
Method 2A Transect A	143	55	88	104	34.6%
Method 2B Transect B	209	120	89	39	75.5%
Method 2C Transect C	209	55	154	104	34.6%
Method 3 (upstream Froude number)					
Method 3A ff	152	103	49	56	64.8%
Method 3B u (zonal)	248	76	172	83	47.8%
Method 3C U_T	307	86	221	73	54.1%

Table 5.6 – *The number of föhn events detected in the WRF model for each of the 9 methods employed, compared to the AWS föhn climatology. See section 5.6.1 for Method 1, section 5.6.2 for Method 2, and section 5.6.3 for Method 3. See Table 5.2 for a description of "hit", "false positive" and "false negative".*

Of all 9 methods for föhn detection presented here, Method 2B has the greatest skill at generating a high ratio of "hits" to "false positives/negatives". Of the 159 föhn events observed in the surface AWS observations at King Edward Point, 75.5% of these events are found to occur in the model using Method 2B. Methods 1B and 3A have the joint second highest hit rate of all methods, and declare 64.8% of observed events each. With a hit rate of just 30.8% (49 events), Method 1A captured the fewest number of observed föhn events despite being the most comparable to the original traditional method used to identify events in the AWS observations. Interestingly, Methods 1C and 3C detected nearly twice as many modelled föhn events compared to observed föhn events (resulting in a large number of "false positives" for both methods), indicating that föhn frequency may be more common outside of King Edward Cove. As previously suggested, an array of island-wide observations would be required to accurately characterise the frequency of föhn across South Georgia.

Table 5.8 (see Appendix 5A.2) presents a list of all the 159 föhn events which were observed in the AWS at King Edward Point between June 2011 and February 2013, arranged by the change in temperature (i.e. the difference between maximum measured temperature and the temperature at föhn onset). Table 5.8 also highlights how each of the 9 methods performed at detecting the observed events by showing whether they were identified by the method or not. In all three methods (which overall encompasses 9 different methods) just one single föhn event is not declared as a "hit" from the AWS climatology (indicated in Table 5.8 by red hatching). Therefore, while Table 5.8 highlights that each of the methods is detecting a different set and number of events, 99% of the 159 events found in the observations were reproduced (in some shape or form) in the WRF model. Of all the 159 events, there are only 7 observed föhn events which are captured by all 9 methods (indicated in Table 5.8 by green hatching). Method 2B identifies 8 unique events which are not detected by any of the 8 other methods. Methods 1B and 3A both identify 4 events which are not detected by any of the other methods, while the rest of the methods do not detect any unique events. In terms of föhn intensity, Method 2B detects the highest number of the top 50 most intense events ($\Delta T \geq 7.7^{o}C$), with a hit rate of 86%. This suggests that Method 2B generally identifies events which have the largest impact on föhn-driven temperatures (i.e. intense föhn events) at King Edward Point. In contrast, Methods 2A, 3B and 3C all detect a larger percentage (38%, 54%, and 50%, respectively) of the bottom 50

most intense events ($\Delta T \leq 5.0^{o}C$) compared to the top 50 most intense events (26%, 32%, and 48% respectively). Therefore, these methods generally identify the events which have the least impact on the föhn-driven temperatures (i.e. weak föhn events) at King Edward Point. It is also important to note that there is no significant seasonal variability in the total number of föhn events detected in each of the three identification methods. Over the 21 month climatological simulation, there is an even distribution of the number of events detected through the year for each of the 9 methods. The frequency of föhn occurrence in any particular season is not statistically different to the annual frequency for any of the methods. Therefore, WRF is not creating an artificial bias to the föhn events which are declared as "hits".

Cleary, high-resolution simulations with the WRF model can be used to explore the föhn climatology of South Georgia further. It is clear that each of the 9 methods presented in this section are capable of detecting an assortment of the observed föhn events. Unsurprisingly, there is not much agreement between the different methods; they detect a mixture of strong and weak föhn events, with some methods performing substantially better than others (see Table 5.6, and Table 5.8, Appendix 5A.2). Therefore, based on the results presented in this section, 40 of the strongest modelled föhn events detected by Method 1B, Method 2B and Method 3A (120 modelled events in total) have been selected for a composite analysis of föhn features across the three methods. The 40 strongest modelled events from Method 1B, Method 2B and Method 3A were chosen as these methods have the highest föhn hit rates. Of the 120 strongest modelled events selected by all three methods, 52 of these are declared "hits" when compared to the AWS föhn climatology. See Table 5.8 (Appendix 5A.2) for a list of these 52 events (indicated in Table 5.8 by stars). The results of this are presented in the next section.

5.6.5 Composite Analysis of Föhn Features across Methods

Mean composite anomalies of the significant surface and near-surface features across many strong föhn events as detected by Method 1B, Method 2B and Method 3A are now presented (Figure 5.15, Figure 5.16, and Figure 5.17). For all 3 methods, only the strongest modelled 40 events are considered, due to their strong characteristics and features. These are the events which produced the highest modelled absolute temperature rise at King Edward Point (Method 1B), the events which had the largest

drop in modelled isentrope height (Z_3, Method 2B), and the events which had the largest modelled upstream Froude numbers (Method 3A).

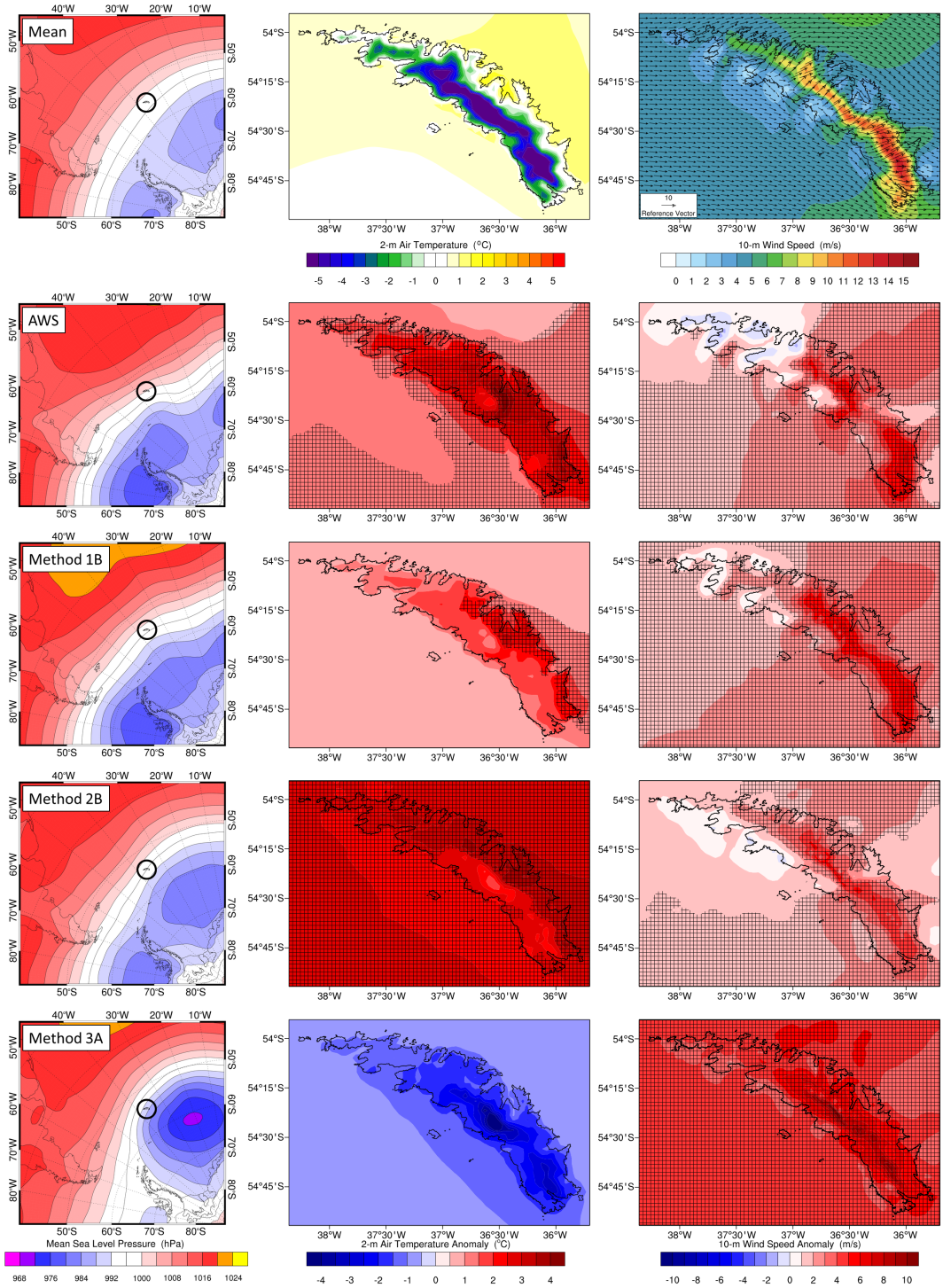

Figure 5.15 – *Mean sea level pressure (left, from ERA-Interim reanalysis), mean modelled 2-m air temperature anomaly (middle), and mean modelled 10-m wind speed anomaly (right) across 40 of the strongest events as detected by the AWS, Method 1B, Method 2B and Method 3A föhn climatologies. Anomalies are expressed from the climatological (June 2011 – February 2013) mean (top). Hatching indicates anomalies are statistically significant at the 95% confidence level. South Georgia is circled in black.*

From Figure 5.15, it can be seen that each of the three methods produces substantially different spatial characteristics of the modelled leeside warming, as well as large differences in the associated synoptic scale mean sea level pressure patterns, during their respective 40 strongest events. This is a result of each of the three identification methods looking at different föhn characteristics and dynamics, and therefore capturing a different set of events. Mean sea level pressure composite analyses in Chapter 3 (section 3.3.3, Figure 3.12) showed that strong föhn events detected in the AWS record were associated with a strengthening of the South Atlantic high pressure system. Similar synoptic patterns for the 40 strongest AWS and Method 1B events can also be observed in Figure 5.15. The föhn composite mean sea level pressure field derived using Method 1B exhibits a strong zonal flow over South Georgia. This upstream air is likely to be *polar maritime* in origin (Mansfield & Glassey, 1957), originating over the Bellingshausen Sea before tracking through the Drake Passage and past Patagonia and the Falkland Islands. This is a similar pattern for the 40 strongest events based on surface AWS observations, and is unsurprising given that the same föhn indicator (surface observations) is used. As such, both methods indicate that their respective intense events are generated by a strengthening of the Argentine Basin high pressure system, and a deepening of the Bellingshausen/South Pacific low pressure system (Figure 5.15). During these conditions, both methods for föhn detection indicate an island-wide warming. It appears that warm air advection (from the north) may be a significant contributor to this spatial pattern of warming. Some of the events recorded by both of these methods may not be (wholly) due to a föhn effect. This is further discussed in section 5.6.6. Despite this, the warming pattern is asymmetrical, which is most noticeable along the north-eastern coastline for both methods, particularly over Greene Peninsula and Nordenskjöld glacier (see Figure 6.3), and this is an expected consequence of the föhn effect (Figure 5.15). Therefore, the clear cross-barrier gradient in the anomalous temperature pattern (Figure 5.16(a)) can be attributed to the föhn effect. It is also unsurprising that the upstream vertical profiles for the AWS method and Method 1 are also similar (Figure 5.17). Therefore, it appears that Method 1 is detecting a similar sample of föhn events as the AWS climatology during the June 2011 – February 2013 period (see Table 5.8, Appendix 5A.2), despite an overall low hit rate.

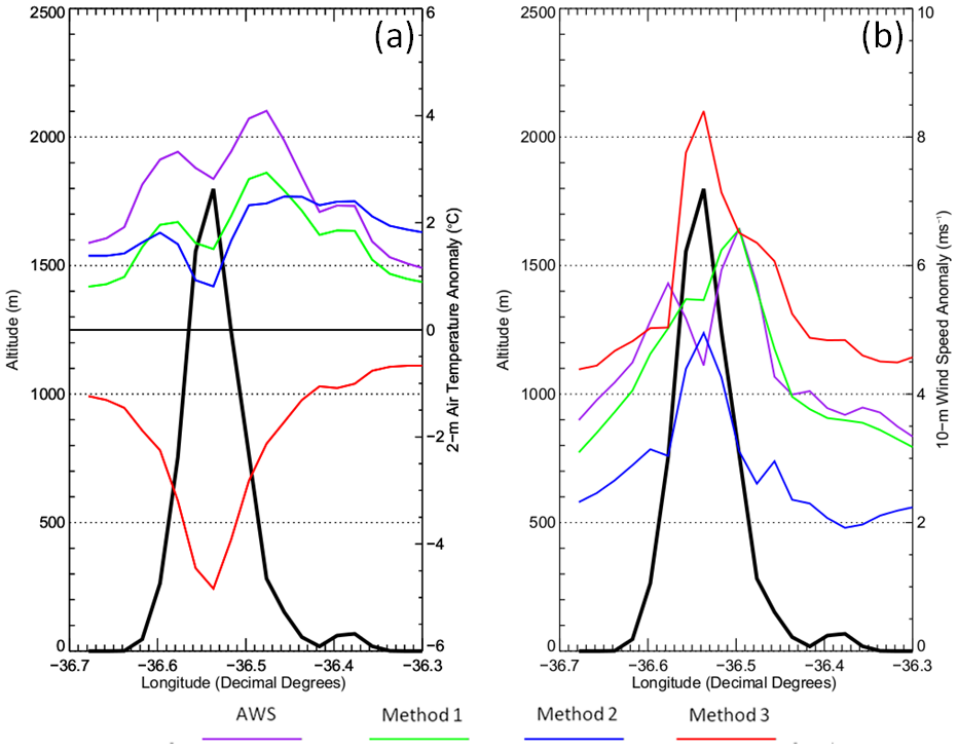

Figure 5.16 – *Horizontal cross-sections of panel (a) 2-m air temperature anomalies from climatological (June 2011 – February 2013) mean, panel (b) 10-m wind speed anomaly from climatological mean. Black solid line – topography cross-section, purple solid line – AWS föhn anomaly, green solid line – Method 1B föhn anomaly, blue solid line – Method 2B föhn anomaly, red solid line – Method 3A föhn anomaly. See Figure 5.5 for geographic reference of cross-section through South Georgia.*

Method 2B also indicates a significant island-wide warming and this is spatially consistent with the AWS pattern (Figure 5.15). This pattern is also asymmetrical, with the warmest temperature anomalies over Neumayer and Nordenskjöld glaciers, Thatcher and Barff Peninsulas, and towards the south end of South Georgia. This is consistent with what we would expect from the föhn effect. Unlike Method 1B and the AWS classification system, which detect events based upon surface föhn-like signatures, Method 2B detects events that are directly related to föhn dynamics. Therefore, it is a valid assumption that the leeside warming signal seen with the events of Method 2B (Figure 5.15 and Figure 5.16(a)) is solely due to the föhn effect. This leeside surface warming (of ~+3°C) is also statistically significantly at the 95% confidence level when compared to the mean climatological (June 2011 – February 2013) 2-m air temperature. The surface warming experienced on the south-western slopes in Method 2B is not statistically significant. The mean wind speed anomalies for the 40 strongest modelled events declared by the AWS classification methods and Methods 1B and 2B, are also spatially and qualitatively consistent with each other

(Figure 5.15). During intense föhn occasions, there is flow deceleration around the northern tip of South Georgia, and this occurs on both the northeast and southwest coastlines. However, this feature is not statistically-significantly different from the climatological mean in any of the methods. There is also flow acceleration over the Allardyce and Salvesen Ranges, particularly over Mount Paget and Mount Paterson. Figure 5.16(b) shows that the föhn events of Method 2B are characterised by lower wind speeds over the main mountain chain, compared to the AWS system and Method 1B. There is also a clear cross-barrier gradient in the anomalous temperature pattern (Figure 5.16(a)). Since the mean sea level pressure field for the intense events declared by Method 2B is more perpendicular to the island (Figure 5.15) than Method 1B, it is unsurprising that the upstream profiles indicate that the air is colder below 5km (Figure 5.17).

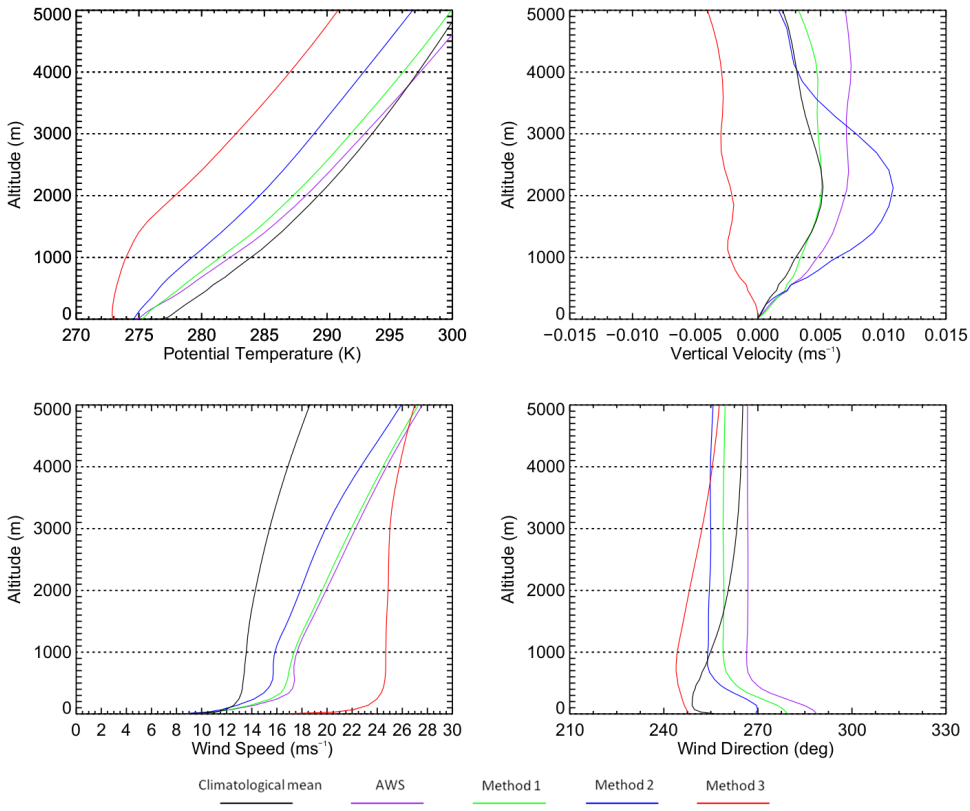

Figure 5.17 – *Upstream vertical profiles of mean potential temperature, vertical velocity, wind speed, and wind direction upstream of South Georgia for each of the föhn detection methods. The vertical profiles are taken from the intermediate (2.7km) WRF model domain, ~140km upstream (-54.492°S, -38.833°W) of South Georgia.*

In comparison to the previous methods, Method 3C shows remarkably different synoptic and anomalous patterns in the near-surface meteorology across South Georgia (Figure 5.15). With a low pressure system situated to the southeast of South

Georgia, the upstream air flow is the most perpendicular to the island. The upstream profiles (Figure 5.17) and composite charts (Figure 5.15) strongly suggest that cold air advection from the Antarctic continent is a cause of these spatial features. Figure 5.15 and Figure 5.16(a) both indicate (weak) lee-side warming, so the föhn effect is likely to be occurring. However, the surface temperature anomaly transect (Figure 5.16(a)) is very different for this case compared to the other methods. This is unsurprising since the upstream air is likely to have originated from the Antarctic continent, and therefore, is the coldest, least oceanic and most unstable air mass which influences the climate of South Georgia (Mansfield & Glassey, 1957). Therefore, this cold air mass has been warmed from below (steepening the lapse rate) making the air more unstable in the lowest layers as it approaches the island. This is seen in Figure 5.17, which indicates that the approaching airflow is less stably-stratified below 1km (the air is unstable below 400m) for Method 3C than it is for the other methods. This cold continental air mass has also previously been associated with unstable conditions and continuous precipitation over King Edward Point in the past (Mansfield & Glassey, 1957). Therefore, this method appears to detect strong wind events, rather than events associated with warming on the lee of South Georgia. Over the central Allardyce and Salvesen Ranges, wind speeds are $>10 ms^{-1}$ stronger than they are for the climatological (June 2011 – February 2013) mean, and these wind speed anomalies are also much greater than the other methods (Figure 5.15 and 5.16). Therefore, it appears that Method 3C is selecting conditions that should be conductive to föhn (i.e. strong flow across the mountains), but these conditions do not appear to be causing strong warming in the lee of the island. In spite of this, the föhn effect (albeit muted) is somewhat observed in the temperature anomalies (Figure 5.16); the temperature anomalies in lee of the island are $\sim+0.5^{o}C$ greater than on the windward side of South Georgia. However, the temperature anomalies associated with the detected föhn events with Method 3C are not statistically significant (Figure 5.15). It may be that this is a poor sample of all föhn events detected by Method 3C, and that the leeside warming signal is more prominent with upstream Froude numbers closer to unity.

5.6.6 Rapid Warming Events versus Föhn Warming Events

Although Method 1B displays anomalous temperature, wind speed and sea level pressure patterns that are spatially coherent with those of the AWS classification method (Figure 5.15), a major limitation of both these methods is that there is no

assurance that the surface warming observed in the observations and in the model is solely due to the föhn effect. In Chapter 3 a simple föhn classification method was developed that could be used with the limited *in situ* observations available. When applied to high-resolution model simulations of events in Chapter 4, it was found that Case C (section 4.5) could be defined as an instance of a (weak) rapid warming event caused by warm-air advection rather than a föhn event. Likewise, in Chapter 3, having explored the synoptic conditions responsible for strong föhn events, it was also found that the strongest events (by temperature change) may be instances of warm air advection from the north-northwest. To explore this further, mean composites of the near-surface conditions during 6 randomly selected strong and weak events (by overall temperature change from the surface AWS observations) are shown in Figure 5.18.

In this very small sub-sample of all föhn events recorded in the surface AWS observations, Figure 5.18 confirms that in some instances warm-air advection contributes to the warming signal detected at the surface (either in the surface AWS observations or in the WRF model). Island-wide warming is particularly noticeable in Figure 5.18(a), and to a lesser extent in Figure 5.18(c), despite both having been classified as a föhn events in Chapter 3. Both of these events are marked by strong northerly air flow, and therefore, the warming experienced at King Edward Point cannot solely be a result of a westerly föhn event. Any föhn warming may be due to flow over minor topographic features (rather than the main mountain chain), however, it appears that warm-air advection may be the main driver of temperature change over these periods. Similarly, the WRF model indicates that during very weak instances of föhn (i.e. when the surface AWS observations at King Edward Point measured a change in temperature of ~2/3^{o}C, thus meeting the föhn criteria) there is also a discernible föhn signal across the climatological leeside of South Georgia. This is the case for Figure 5.18(d). In these three instances (Figure 5.18(a), (c) and (d)), the föhn-like signal detected in the AWS observations is not supported by the large-scale conditions in the model. These events do not appear to be föhn driven. Despite this, the events shown in Figure 5.18(b) and (f) do appear to be a result of westerly cross-barrier flow resulting in leeside föhn warming, particularly over Thatcher and Barff Peninsulas.

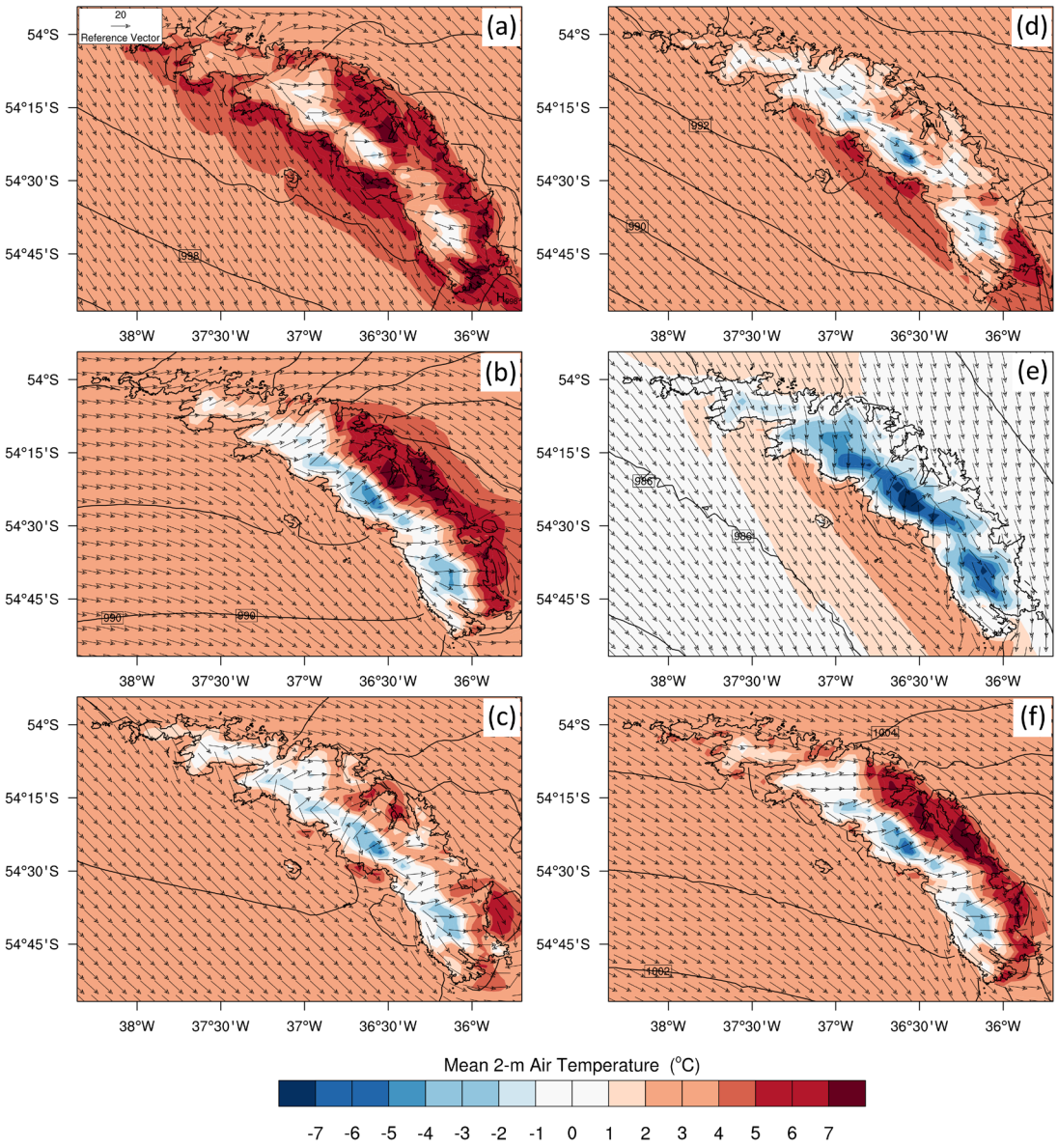

Figure 5.18 – *Mean 2-m air temperature, sea level pressure, and wind vectors during 3 strong (left) and 3 weak (right) föhn events. All 6 events were detected in the surface AWS observations and Method 1B in the WRF model. They were randomly selected from 40 strong and 40 weak (by temperature change) föhn events.*

It is also important to note that this research only considers föhn events which occur on the northeast side of island, which have been generated from strong westerly winds crossing the mountains of South Georgia. An important finding from here is that föhn can also be generated on the south-western coastline through strong northerly and easterly winds, shown in Figure 5.18(d) and Figure 5.18(e). Even though föhn was detected at King Edward Point AWS observations during these events, the surface warming signal is clearly not a result of the föhn effect. In these cases, föhn warming is occurring on the southwest coastline. The author is unaware of this having been

documented or measured before. Unfortunately, it is beyond the scope of this study to explore occasions of föhn on the southwest side of South Georgia since there are no observations available. As previously suggested in section 5.5, further long-term surface observations on the island would be a massive advantage for future research exploring topographic modification of incident airflow and föhn events on South Georgia.

Therefore, in summary, a major weakness of the AWS classification method is that there are an unknown number of events in the AWS catalogue and in the Method 1 catalogue that have been classified as föhn where the surface warming signal is clearly not a result of (or not solely a result of) the föhn warming process. Rather, the warming is primarily advective in these are instances (i.e. strong or weak rapid warming events). Without more observations, it is impossible to adjust the current AWS föhn identification method to detect föhn events more precisely. Instead of using a system which looks at surface föhn-like signatures, the previous results have shown that the model can be used to accurately identify föhn conditions over the entire island by looking at föhn dynamics. Therefore, using the WRF model to develop a more rigorous method which ensures that the surface warming signal is a result of the föhn effect is necessary.

5.6.7 Discussion

Three different methods for identifying and detecting individual föhn events were developed. This was undertaken to deduce the best method for föhn detection using high-resolution model data in the absence of island-wide *in situ* meteorological observations. In comparison to AWS observations from King Edward Point, during the period June 2011 – February 2013, WRF generally produces too few föhn events which are generally too weak. There is not much agreement between the different methods (Figure 5.15), as each method classifies a different number and set of föhn events (Table 5.8, Appendix 5A.2). This is because the flow characteristics and dynamics that are used to define the methods are based upon different precursor conditions for föhn occurrence on South Georgia. Describing the systematic behaviour of föhn events at South Georgia is inherently difficult. Thus creating a classification system to discriminate model föhn conditions from non-föhn conditions is also problematic. It seems that when events are detected in the surface AWS observations

but not in the model ("false negatives"), the WRF model is primarily missing the local response specifically at King Edward Point. There does not appear to be any problem with the model capturing the large-scale setup leading to, and conductive of, föhn. Overall, Method 2 (isentropic drawdown) is the most efficient and reliable method of identifying and detecting föhn flow on South Georgia with the high-resolution WRF output. The reasons for this are now given.

Unsurprisingly, Method 1 is in relatively good agreement with the AWS observations, since they are based on the same system (i.e. detection based upon near-surface meteorological characteristics). In Chapter 3, it was shown that warm air advection may dominate those events which were found to have very rapid increases in 2-m air temperature. This is an inherent problem with Method 1; it does not guarantee that the events declared are a result of the föhn effect. During times of intense föhn as detected by the AWS classification method, South Georgia experiences island-wide warming, and does not appear to have the characteristically asymmetrical pattern of the föhn effect (see Figure 5.18). Therefore, one can assume that Method 1 also detects such occasions. Similarly, in Chapter 4, it was also shown that some weak föhn events declared (i.e. those with small changes in temperature during the event of ~2-3^{o}C) may not be föhn events either due to the lack of descending, potentially warmer air from aloft. Therefore, Method 1 cannot guarantee that the events declared are solely due to the föhn effect.

The results indicate that Method 3 performs the least accurately. Although high upstream Froude numbers indicate stronger flow perpendicular to the mountain chain, they do not necessarily indicate that surface warming is occurring in the lee of South Georgia. This method appears to detect conditions that may lead to strong wind events (such as Case B in Chapter 3) rather than intense, warm, and dry föhn events in the lee of the island. Upstream profiles reveal that the structure and dynamics of the air in Method 3 are very different, as the air being advected over the island is derived from the Weddell Sea and Antarctic Peninsula. All profiles and plots for Method 3 are qualitatively dissimilar to the other methods of föhn detection. Therefore, Method 3 is the least useful as a föhn indicator, but a good indicator of strong wind events.

Method 2 gives confidence that, dynamically, föhn warming and drying is occurring (somewhere) on the lee of South Georgia. As such, it is a reasonable assumption that

the drawdown of air from aloft is the major driver for föhn warming and drying. This has been identified elsewhere and is a common characteristic of strong flow-over conditions (e.g. Elvidge *et al*., 2014a; 2014b; Grosvenor *et al*., 2014). As with the other methods, Method 2 does not guarantee that all the föhn events observed in the AWS at King Edward Point are also found in the WRF model, and it might also declare events that are not observed in the surface AWS observations. Despite this, it is the only method which can confirm cross-barrier descent of air from aloft, and dynamic arguments would suggest that this air has been adiabatically warmed. Therefore, this method should neither detect very weak föhn events, rapid warming events caused by warm air advection, nor strong wind events with no associated surface warming. The temperature anomalies of the strongest events are qualitatively similar to those of Method 1 and the AWS temperature anomalies. Therefore, the spatial pattern of föhn is captured by this method. This method removes any misclassified events from Method 1 and ensures that any events which are detected are a result of cross-barrier isentropic drawdown.

5.6.8 The Composite Föhn Event

Since Method 2B gives confidence that, dynamically, föhn warming and drying is occurring (somewhere) on the northeast coast of South Georgia (as a consequence of detecting considerable leeside isentropic drawdown), the föhn events detected by this method will be used to investigate the role they have on the near-surface energy and mass balances of north- and south-facing glaciers on South Georgia (see Chapter 6). This will subsequently give an insight into the role föhn warming has on asymmetrical glacial retreat. Due to various limitations and inconsistencies, the other methods for föhn detection on South Georgia are not considered any further. Presented in Figure 5.19 is the composite of the 209 föhn events detected between June 2011 and February 2013 by Method 2B.

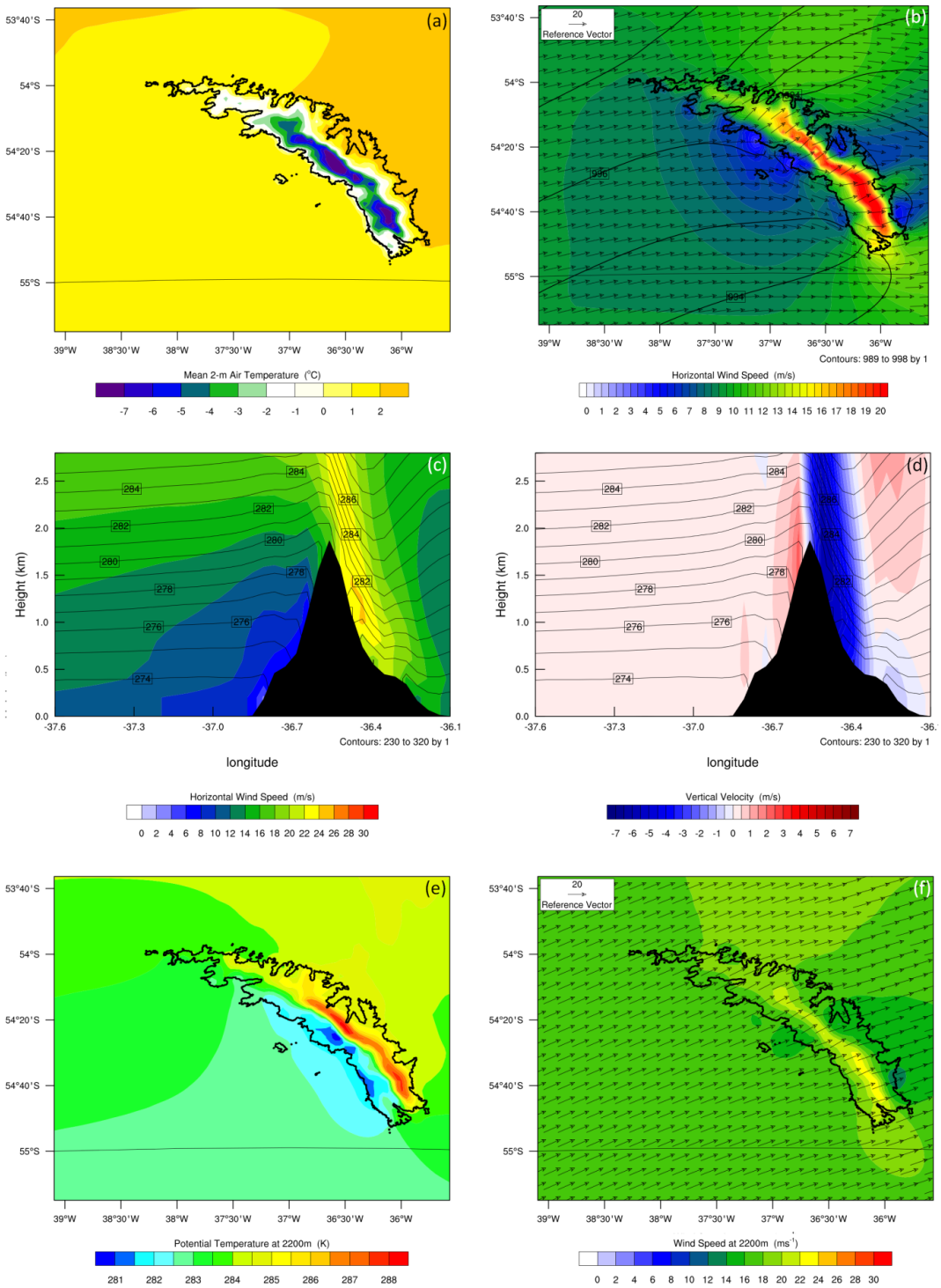

Figure 5.19 – *Mean conditions for the 209 events detected by Method 2B. Panel (a) mean 2-m air temperature. Panel (b) mean sea level pressure (hPa, black contours) and mean 10-m wind speed (filled contours). Panel (c) vertical cross-sections of mean potential temperature (K, black contours) and mean wind speed (ms^{-1}, filled contours) through line (b) in Figure 5.12. Panel (d) vertical cross-section of mean potential temperature (K, black contours) and mean vertical velocity (ms^{-1}, filled contours) through line (b) in Figure 5.12. Panel (e) mean potential temperature at 2200m. Panel (f) mean wind speed and wind vectors at 2200m.*

The mean sea level pressure pattern during these events shows a strong cross-barrier pressure gradient that drives strong winds (>15ms^{-1}) across the South Georgia mountain barrier (Figure 5.19(b)). This results in a clear asymmetrical warming across South Georgia (Figure 5.19(a)). The impact of these föhn events on the regional climate of South Georgia is explored further in Chapter 6. The warmest temperatures are generally on the northeast of the South Georgia, where the wind speeds are also stronger (>20ms^{-1}) over the Salvesen mountains. The warmest location on South Georgia during these föhn conditions is on Hestesletten glacial plain, where the mean temperature is 3.9ºC. This area of warmer temperatures also extends over much of Thatcher Peninsula and Moraine Fjord. At 2200m (just above mountain height, Figure 5.19(e)) the core of high potential temperature (~287K) runs parallel with the axis of the mountain chain, and also illustrates the extent of isentropic drawdown across South Georgia during föhn flow. As with the previous case studies (see Chapter 4), there is evidence of deceleration of the upstream incident flow (≤6ms^{-1}), along with flow splitting around the island (Figure 5.19(b)). There are also two noticeable lee wake regions (≤6ms^{-1}) which extend tens of kilometres downstream of South Georgia (also see Hosking *et al*., 2015; Vosper, 2015). These wake regions are over Greene Peninsula and Nordenskjöld glacier, and the second in the vicinity of Gold Harbour and Iris Bay. The mean dynamics of these 209 events are also discernible. The horizontal cross-sections through South Georgia (Figure 5.19(c) and (d)) show large amplitude wave disturbances in the lee of the island, along with particularly high vertical wind speeds (~7ms^{-1}) directed down the lee slopes underneath a region of tightly-packed isentropes. The mean change in height of the 2200m isentrope upstream of South Georgia (along transect B, Figure 5.12) for all 209 events and the climatological (June 2011 – February 2013) mean is -1311.1m and -383.9m respectively. The difference in the mean value is highly statistically-significantly different ($p < 0.01$). The maximum change in height of the 2200m isentrope over the mountains during föhn flow was -2166m. Clearly, the contribution of isentropic drawdown to the föhn warming effect over South Georgia is significant. This makes Method 2B a very good indicator of föhn conditions in the lee of South Georgia with high-resolution WRF simulations.

5.7 Conclusion

This study presents a new climatological analysis of the regional climate of South Georgia using high-resolution atmospheric simulations with the WRF model. Although the meteorological record of South Georgia dates back to 1905, it only informs us about the climate at a single location on this topographically-complex and climatologically-diverse island. As such, the research presented in this chapter demonstrates the wealth of regional climate information available for South Georgia from a high-resolution atmospheric simulation and just one meteorological station. The high-resolution simulations presented show that the climate of South Georgia is cool, wet and windy, and substantially affected by predominantly westerly circulations. The regional climate of South Georgia is strongly modified by the island's significant orographic divide. The southwest side of South Georgia is wetter, colder, more humid and windier, than the north-eastern side (primarily due to the föhn effect), while the north end of South Georgia is warmer and drier, than the south end (primarily due to exposure, aspect and slope orientation). As such, the wealth of regional climate information available from this high-resolution simulation is exceptional and unique. The regional climate maps add to the 150 years of limited information pertaining to South Georgia's climate and weather (e.g. Mansfield & Glassey, 1957; Hayward, 1983; Richards & Tickell, 1968). Ideally, future simulations of the climate and weather of South Georgia would require very high horizontal resolutions (~1km) over the entire island. The significant flow modification of South Georgia (see e.g. Figure 5.7) suggests that improvements in the representation of topography (e.g. through higher horizontal resolution) are required to further improve results. Improvements gained in modelled variability may justify the increased computational cost of those simulations.

The regional climate of South Georgia was explored further by investigating the climatology of föhn events across the island. As expected, the föhn effect is most likely to be experienced in the immediate lee of the island's major peaks, especially in more exposed, low-lying, seasonally snow-covered regions of the island (e.g. Hestesletten). It has long been known that incoming air-masses onto the island are subsequently topographically modified (Mansfield & Glassey, 1957; Wells *et al*., 2008; Hosking *et al*., 2015), but never has the föhn effect been explored in any great detail nor identified at a regional scale on South Georgia. Given the results of Figure 5.10, Figure 5.15,

and Figure 5.19, it is unsurprising that föhn was measured over 130 years ago at Royal Bay (von Danckelman, 1884). Occasions of föhn events being generated through northerly air flow have also been identified from the climatological model simulations. It remains unknown how frequent, intense and persistent these events are on the western and south-western coast of South Georgia. Similarly, it remains unknown how the föhn climatology at other locations on the northeast coastline (e.g. at Hestesletten and Royal Bay) compare to the climatology of föhn events at King Edward Point. Clearly, there is need for more meteorological observations across the island to examine this further. In particular, a new network of island-wide AWS observations, both placed upstream and downstream of the island's main mountain chain (see Figure 5.10), would confirm whether any sudden warming, drying and increased wind speed events observed at King Edward Point are isolated to King Edward Cove and/or are similarly occurring at multiple locations along the northeast coastline. Such measurements would vastly improve our understanding of the regional climate of South Georgia, and would further aid in model verification.

It is clear from the results presented in this chapter that föhn events frequently manifest dramatic changes in humidity, wind speed and temperature, and it is changes in these parameters that serve as useful indicators for föhn diagnosis in surface AWS observations at King Edward Point. However, distinguishing between föhn and other atmosphere phenomena for the entire northeast coast of South Georgia is difficult with limited island-wide measurements. Therefore, three different methods for detecting individual föhn events were developed using high-resolution WRF model output, with the key aim of deducing the best method for island-wide föhn identification. The three methods were based on the impact of the föhn warming process at the surface (Method 1), the characteristic drop in isentrope height in the lee of the island (Method 2), and the dynamics of the approaching upstream airflow (Method 3). It was found that each of the föhn climatologies were vastly different since each method was based on different precursor föhn conditions. Within each of the föhn methods, Method 1B (64.8%), Method 2B (75.5%), and Method 3A (64.8%) were found to be the best methods for identification due to their high hit rates and spatial characteristics. Of these three, Method 2B was found to be the best method for island-wide föhn identification. This is because the reasonable match between the model and the observations, as well as the ability of Method 2B to sufficiently declare föhn events,

gives confidence that the development and identification of föhn in the WRF model is realistic. Consequently, using all periods declared by Method 2B to be föhn between June 2011 and February 2013, the next chapter will explore the implication of föhn warming and drying on the surface energy and mass balances of glaciers on South Georgia, and what role they play in the asymmetrical pattern of glacial retreat.

Appendix 5A.1 – WRF and AWS Validation (June 2011 – February 2013)

			2-m Air Temperature (°C)	2-m Relative Humidity (%)	10-m Wind Speed (ms^{-1})	10-m Wind Direction (°)	Sea Level Pressure (hPa)
Annual		AWS Mean (St. Dev.)	2.4 (4.5)	70.4 (15.2)	8.4 (6.7)	304	996.9 (12.5)
		WRF Mean (St. Dev.)	1.5 (2.9)	72.5 (17.4)	7.7 (5.6)	295	996.4 (12.4)
		r^2	0.71	0.42	0.36	0.44	0.99
Season	**Austral Summer (DJF)**	AWS Mean (St. Dev.)	5.6 (3.6)	66.9 (15.1)	9.7 (6.8)	303	993.3 (9.9)
		WRF Mean (St. Dev.)	4.1 (2.6)	66.4 (17.5)	8.0 (4.9)	305	994.7 (9.5)
		r^2	0.66	0.48	0.43	0.09	0.99
	Austral Autumn (MAM)	AWS Mean (St. Dev.)	2.2 (3.5)	74.3 (14.4)	6.4 (6.1)	306	999.2 (12.9)
		WRF Mean (St. Dev.)	2.2 (2.4)	77.3 (16.8)	6.3 (4.6)	305	998.4 (12.8)
		r^2	0.60	0.40	0.38	0.07	0.99
	Austral Winter (JJA)	AWS Mean (St. Dev.)	-0.8 (3.5)	73.4 (14.0)	7.5 (6.5)	303	997.5 (13.0)
		WRF Mean (St. Dev.)	-0.4 (2.4)	75.2 (16.6)	7.2 (4.9)	298	997.1 (12.9)
		r^2	0.68	0.40	0.39	0.03	0.99
	Austral Spring (SON)	AWS Mean (St. Dev.)	2.7 (4.2)	68.6 (15.7)	8.9 (6.8)	306	998.8 (13.3)
		WRF Mean (St. Dev.)	1.0 (2.7)	71.0 (17.3)	7.6 (5.1)	305	998.2 (13.2)
		r^2	0.64	0.33	0.42	0.04	0.99

Table 5.7 – *A table summary of annual and seasonal means, and standard deviations, for 2-m air temperature, 2-m relative humidity, 10-m wind speed, 10-m wind direction, and sea level pressure for the surface AWS observations and WRF model output (innermost 0.9km domain). All values are derived from the hourly instantaneous values from the model and the observations at King Edward Point (June 2011 – February 2013).*

Appendix 5A.2 – Modelled Föhn "Hits"

Föhn Case #	Year	Month	Start Day	Temp. Change (°C)	Method 1A	Method 1B	Method 1C	Method 2A	Method 2B	Method 2C	Method 3A	Method 3B	Method 3C
795	2012	February	3	16.4	✓	✓*	✓		✓*		✓		
768	2011	November	12	14.8	✓	✓*	✓	✓	✓	✓	✓		✓
790	2012	January	26	13.4	✓	✓*	✓	✓	✓	✓	✓		
818	2012	April	12	12.6					✓*		✓	✓	✓
761	2011	November	2	12.5	✓	✓*	✓		✓	✓	✓		
862	2012	October	6	12.1		✓*			✓		✓		✓
746	2011	August	24	12.0	✓	✓	✓		✓	✓	✓		✓
864	2012	October	11	11.8		✓*			✓		✓		
750	2011	September	15	11.6		✓*			✓*	✓	✓		✓
754	2011	October	12	11.5				✓	✓	✓	✓	✓	✓
780	2011	December	16	11.5	✓	✓*	✓		✓	✓	✓		
781	2011	December	19	11.1	✓	✓*	✓		✓	✓			
859	2012	September	15	10.9		✓*							✓
779	2011	December	12	10.4		✓*		✓	✓*	✓	✓		✓
821	2012	May	2	10.4	✓	✓*	✓		✓*				
769	2011	November	15	10.4	✓	✓*	✓	✓	✓		✓		
763	2011	November	4	10.2		✓*			✓				
797	2012	February	11	10.2					✓				
822	2012	May	3	10.1		✓*			✓	✓	✓		✓
854	2012	August	23	10.1		✓*	✓		✓	✓	✓		
739	2011	July	15	10.0				✓	✓	✓	✓		
880	2013	February	4	9.7					✓				
884	2013	February	13	9.5	✓	✓	✓				✓*	✓	✓
848	2012	August	3	9.4		✓*	✓	✓	✓		✓*		✓
736	2011	July	12	9.4	✓	✓	✓		✓			✓	✓
785	2012	January	11	9.4	✓	✓*	✓	✓	✓	✓	✓	✓	✓
792	2012	January	30	9.3	✓	✓	✓		✓		✓	✓	✓
886	2013	February	16	9.3	✓	✓	✓		✓	✓	✓	✓	✓
762	2011	November	3	9.2		✓		✓	✓	✓	✓		
755	2011	October	17	9.0		✓			✓*				
861	2012	September	30	9.0		✓							
872	2012	November	30	9.0		✓				✓			
782	2011	December	22	8.9					✓	✓			

Föhn Case #	Year	Month	Start Day	Temp. Change (°C)	Method 1A	Method 1B	Method 1C	Method 2A	Method 2B	Method 2C	Method 3A	Method 3B	Method 3C
812	2012	March	23	8.9	✓	✓	✓	✓	✓	✓	✓	✓	✓
849	2012	August	9	8.9	✓	✓	✓		✓		✓	✓	
835	2012	June	17	8.9		✓	✓		✓		✓	✓	✓
799	2012	February	15	8.7		✓	✓		✓	✓	✓*		
774	2011	November	28	8.7		✓*	✓	✓	✓	✓		✓	✓
804	2012	March	5	8.6		✓			✓		✓		
883	2013	February	12	8.6							✓	✓	✓
834	2012	June	9	8.6	✓	✓	✓	✓	✓	✓	✓		✓
731	2011	June	19	8.5	✓	✓	✓				✓	✓	✓
744	2011	August	10	8.4		✓	✓		✓		✓		✓
767	2011	November	9	8.4					✓			✓	
800	2012	February	18	8.3	✓	✓	✓		✓		✓		
803	2012	March	3	8.2		✓			✓				
805	2012	March	5	8.2		✓					✓		✓
791	2012	January	29	8.1	✓	✓	✓	✓	✓	✓	✓	✓	✓
756	2011	October	19	7.9	✓	✓	✓		✓				
802	2012	March	1	7.7	✓	✓	✓		✓		✓	✓	
857	2012	September	6	7.7	✓	✓	✓	✓	✓	✓	✓	✓	✓
866	2012	October	28	7.7		✓		✓	✓	✓	✓	✓	
851	2012	August	20	7.6	✓	✓	✓	✓	✓		✓	✓	✓
770	2011	November	16	7.6	✓	✓	✓	✓	✓		✓	✓	✓
777	2011	December	8	7.5				✓	✓	✓	✓		✓
801	2012	February	20	7.5		✓		✓	✓*	✓	✓*		
751	2011	October	7	7.5				✓	✓	✓	✓	✓	✓
855	2012	August	30	7.4	✓	✓	✓	✓	✓*	✓			
823	2012	May	3	7.4				✓	✓	✓	✓	✓	✓
811	2012	March	20	7.3		✓		✓	✓	✓	✓		
876	2013	January	20	7.3				✓	✓	✓		✓	✓
749	2011	September	7	7.3		✓	✓	✓	✓		✓		
819	2012	April	18	7.3							✓	✓	✓
747	2011	August	28	7.2	✓	✓	✓		✓		✓		
757	2011	October	19	7.2							✓		
881	2013	February	5	7.2	✓	✓	✓	✓	✓	✓			
870	2012	November	22	7.1		✓			✓*	✓	✓	✓	✓
847	2012	July	30	7.0	✓	✓	✓	✓	✓	✓	✓*	✓	✓

Föhn Case #	Year	Month	Start Day	Temp. Change (°C)	Method 1A	Method 1B	Method 1C	Method 2A	Method 2B	Method 2C	Method 3A	Method 3B	Method 3C
879	2013	February	3	7.0				✓	✓*			✓	
796	2012	February	5	6.9		✓		✓	✓	✓	✓	✓	✓
771	2011	November	22	6.8		✓			✓		✓	✓	✓
867	2012	October	31	6.7		✓			✓*				
743	2011	August	9	6.7	✓	✓	✓	✓	✓			✓	✓
766	2011	November	8	6.6								✓	✓
783	2011	December	29	6.6	✓	✓	✓	✓	✓		✓		
798	2012	February	13	6.6	✓	✓	✓		✓*	✓	✓	✓	✓
748	2011	September	6	6.5	✓	✓	✓	✓	✓				
874	2012	December	20	6.5								✓	✓
794	2012	February	2	6.5		✓			✓		✓		
773	2011	November	27	6.4					✓				
831	2012	June	3	6.4		✓					✓	✓	✓
832	2012	June	5	6.4	✓	✓	✓		✓		✓		✓
732	2011	June	21	6.4	✓	✓	✓	✓	✓	✓	✓		
882	2013	February	5	6.4	✓	✓	✓		✓	✓	✓	✓	✓
786	2012	January	19	6.3	✓	✓	✓				✓		
825	2012	May	17	6.3		✓					✓	✓	✓
816	2012	April	8	6.2								✓	✓
837	2012	June	22	6.2		✓	✓						✓
839	2012	June	26	6.2	✓	✓	✓		✓		✓		✓
758	2011	October	21	6.2	✓	✓	✓		✓*	✓	✓		
807	2012	March	10	6.1					✓*		✓		
760	2011	October	30	6.1				✓	✓*		✓		✓
852	2012	August	21	6.1							✓	✓	✓
873	2012	December	7	6.1					✓	✓	✓		
826	2012	May	21	6.0		✓			✓		✓	✓	✓
842	2012	July	5	6.0							✓		
734	2011	July	6	5.9		✓	✓					✓	✓
733	2011	June	30	5.9	✓	✓	✓					✓	✓
845	2012	July	24	5.8	✓	✓	✓		✓	✓	✓	✓	✓
885	2013	February	13	5.8				✓	✓	✓	✓	✓	✓
824	2012	May	12	5.8		✓						✓	✓
868	2012	November	10	5.7					✓*		✓	✓	✓
778	2011	December	10	5.6	✓	✓	✓						✓

Föhn Case #	Year	Month	Start Day	Temp. Change (°C)	Method 1A	Method 1B	Method 1C	Method 2A	Method 2B	Method 2C	Method 3A	Method 3B	Method 3C
813	2012	March	27	5.6					✓				
875	2013	January	9	5.4					✓	✓	✓	✓	✓
740	2011	July	21	5.2					✓			✓	✓
869	2012	November	22	5.2							✓	✓	✓
730	2011	June	11	5.1		✓			✓*				
742	2011	August	3	5.0	✓	✓	✓	✓	✓	✓	✓	✓	✓
753	2011	October	10	5.0								✓	✓
827	2012	May	22	4.9					✓		✓	✓	
820	2012	April	20	4.8		✓						✓	✓
729	2011	June	8	4.8	✓	✓	✓		✓		✓	✓	✓
745	2011	August	12	4.8	✓	✓	✓	✓	✓		✓*	✓	✓
836	2012	June	21	4.8				✓	✓*	✓			
806	2012	March	6	4.7				✓	✓*	✓	✓		✓
789	2012	January	23	4.7		✓		✓	✓	✓	✓		
764	2011	November	7	4.6					✓				
809	2012	March	17	4.6		✓						✓	✓
871	2012	November	24	4.6		✓					✓		
877	2013	January	23	4.6									
793	2012	January	31	4.5		✓			✓		✓		
865	2012	October	13	4.5					✓	✓	✓*		
741	2011	July	22	4.2		✓		✓	✓		✓	✓	✓
815	2012	March	29	4.1		✓		✓	✓	✓	✓*	✓	✓
840	2012	June	27	4.1	✓	✓	✓	✓	✓		✓*	✓	✓
863	2012	October	7	4.1					✓		✓		
833	2012	June	9	4.0							✓		
843	2012	July	12	3.9				✓	✓		✓	✓	✓
878	2013	February	2	3.9					✓				
784	2012	January	4	3.7				✓	✓		✓		✓
817	2012	April	9	3.7				✓	✓	✓	✓	✓	
814	2012	March	27	3.7		✓			✓*				
772	2011	November	26	3.6					✓				
759	2011	October	27	3.6		✓							
810	2012	March	18	3.6		✓		✓	✓		✓		
788	2012	January	21	3.5		✓			✓		✓		
850	2012	August	14	3.5	✓	✓	✓				✓	✓	✓

Föhn Case #	Year	Month	Start Day	Temp. Change (°C)	Method 1A	Method 1B	Method 1C	Method 2A	Method 2B	Method 2C	Method 3A	Method 3B	Method 3C
858	2012	September	13	3.5	✓	✓	✓	✓	✓		✓*	✓	✓
728	2011	June	5	3.4		✓	✓			✓		✓	
829	2012	May	25	3.4					✓*				✓
853	2012	August	22	3.4								✓	✓
752	2011	October	9	3.3				✓		✓		✓	✓
776	2011	December	7	3.3		✓							
735	2011	July	9	3.3					✓			✓	✓
808	2012	March	13	3.3				✓	✓		✓	✓	✓
737	2011	July	13	3.2					✓				
830	2012	June	2	3.1		✓					✓	✓	✓
738	2011	July	14	2.8		✓							
828	2012	May	24	2.8		✓		✓	✓		✓	✓	
846	2012	July	26	2.8							✓*		
775	2011	December	6	2.8		✓			✓	✓		✓	✓
787	2012	January	20	2.7					✓		✓		
860	2012	September	18	2.6				✓	✓			✓	✓
765	2011	November	8	2.6								✓	✓
838	2012	June	23	2.4		✓			✓*		✓	✓	
856	2012	September	3	2.3	✓	✓	✓	✓	✓	✓	✓	✓	✓
841	2012	July	3	2.0				✓	✓		✓	✓	✓
844	2012	July	15	2.0				✓	✓	✓		✓	✓
Total number of "hits"					**49**	**103**	**59**	**55**	**120**	**55**	**103**	**76**	**86**

Table 5.8 – *A list of all 159 föhn events which were observed in the surface AWS observations at King Edward Point, ranked by total observed temperature change (i.e. the difference between maximum temperature and the temperature at föhn onset). Those that are declared a "hit" by each of the 9 methods are indicated by a tick mark (✓). Green hatching highlights those events (7 in total) which were declared by all 9 methods, while red hatching highlights the 1 event which was not declared by any of the 9 methods. Those that are indicated by a star (*) are observed föhn events which are also in the modelled top 40 strongest events for Method 1B, Method 2B and Method 3A (see section 5.6.5).*

Chapter Six: The Impact of Föhn on the Regional Climate of South Georgia

6.1 Introduction

South Georgia is currently undergoing drastic changes in the climate and glacial systems. The melt and retreat of glaciers on both sides of the island has been a cause of concern (Gordon & Timmis, 1992; Gordon *et al*., 2008; Cook *et al*., 2010). The fluctuations of such glaciers are also of wider global interest in view of significant contribution from melting of small glaciers and ice caps to observed sea level rise (Church *et al*., 2013). There have been signs of rapid ice-mass change across the island since the 1950s, with the most dramatic increases in the last decade (see section 1.5.2 and section 6.2). Using archival photography and imagery, it has been shown that the largest and fastest rates of retreat are taking place along the northeast coastline of South Georgia, while the glaciers on the southwest side of the island have been retreating more slowly (Cook *et al*., 2010). The asymmetry of the retreat is thought to be driven by larger-scale atmospheric changes. The position of South Georgia, firmly embedded in the circumpolar westerlies, implies that circulation changes may affect the island's climate in the same way as the Antarctic Peninsula (Marshall *et al*., 2006; Orr *et al*., 2008) through an enhancement of the leeside föhn warming effect (see section 1.6.3).

South Georgia could be described as the bellwether of climate change for the subantarctic islands. This is because temperatures on South Georgia are near 0^{o}C for most of the year, so even a small increase in average temperatures can lead to a large increase in glacial melt. We have already seen that föhn at King Edward Point can push the surface and air temperature above freezing throughout the year (Chapter 3). As glacier mass balances respond rapidly to slight variations in precipitation and temperature, föhn winds can have large and pronounced consequences for the island's mountain hydrology. Increased glacial melt caused by föhn warming will also impact the delicate terrestrial and marine ecosystems of South Georgia (Cook *et al*., 2010). The shelf waters around South Georgia show properties that are markedly different from the open ocean waters beyond (Brandon *et al*., 2000; Meredith *et al*., 2005), indicating that local atmospheric processes are important in dictating shelf water characteristics around the island. Since many of the floral and faunal species on South

Georgia and in the surrounding sea waters are at their thermal tolerance limits (Hogg *et al.,* 2011; Barnes *et al*., 2010) drastic changes in environmental conditions may have severe and irreversible impacts across the island's biodiversity (see e.g. Thorpe *et al*., 2002; Whitehouse *et al*., 2008; Barnes *et al*., 2010; Hogg *et al*., 2011; Morley *et al*., 2014; SGHT, 2014; among many others). Glaciers respond sensitively to fluctuations in air and surface temperature, humidity, precipitation, cloudiness and incoming solar radiation; all of which can be effected by the föhn warming process. Therefore, changes in the frequency or intensity of föhn winds may have contributed to the recent observed period of glacial retreat.

Observations of high-elevation meteorological conditions, glacier mass balance, and glacier run-off are almost non-existent across South Georgia, leading to uncertainty regarding the potential impacts of ongoing glacier recession on the ecology of the island. Since there are no long-term *in situ* glaciological measurements from South Georgia, the Weather Research and Forecasting (WRF) model output can provide information with spatial and temporal coverage that would otherwise not be possible from observations alone. Therefore, the aim of this chapter is to explore the impact of the föhn effect on the regional climate of South Georgia, in particular to understand the different impacts that föhn events have on the near-surface conditions between north- and south-facing glaciers, and to investigate the cause of the recent observed asymmetrical retreat of glaciers. The spatial and temporal variability of the surface mass balance of glaciers on South Georgia is also explored, and this is related to changes in the local climate of the island. In order to quantify the role of föhn winds in the asymmetrical pattern of climate change on the island, the aims of the work described in this chapter are as follows:

- Creation of a glacier catchment map of South Georgia, using a high-resolution Digital Elevation Model dataset
- Exploration of the impact of föhn on the regional climate of South Georgia, with a particular focus on temperature, and the surface energy and mass balance components
- Calculation of the surface energy and surface mass balance, using WRF model output as proxy accumulation and ablation estimates, for 14 glaciers on South Georgia

- Quantifying the link between föhn winds and the observed asymmetrical glacial retreat

This study offers the first systematic attempt to investigate the contribution of föhn winds to mass balance on South Georgia, and also delivers a useful basic insight into how föhn and glaciers interact. The results of this chapter also fill a significant gap in the literature on glacier-climate relations on South Georgia, by providing modelling estimates of surface energy and mass balances, as well as ablation rates, for 14 glacier basins on South Georgia.

The chapter begins with a brief history of glacier retreat and advance, before providing a detailed description of the methodologies adopted in this chapter, including creating a watershed map for South Georgia and the energy and mass balance calculations. Following this, the impact of föhn is investigated. WRF model data is used to demonstrate the strong influence of föhn events on the near-surface meteorology, the surface energy balance and the surface mass balance of the island's glaciers. Finally, a conclusion with perspectives for future work is provided.

6.2 A Brief History of Glacier Retreat and Advance on South Georgia

As with many previous environmental observations on South Georgia, measurements of glacier fluctuations have been sporadic. Photographs and maps dating back to 1882 have previously been used to explore glacier fluctuations (Gregory, 1915). In the 1970s, Cumberland East Bay was photographed by helicopters from HMS *Endurance*, while annual visiting expeditions have also provided useful observations. Satellite images using Landsat have been available since the 1970s, and have been used in more recent years to look at glacial changes on South Georgia (see e.g. Cook *et al*., 2010). However, such datasets are single observations, and often there are large time intervals between observations, meaning that many fluctuations may have passed unobserved. As a consequence of this, it is impossible to assign specific dates for maxima and minima for all glaciers on the island. Previous glaciological research has shown a complex pattern of glacial advance and retreat over time. Geomorphological evidence from South Georgia generally indicates a period of advance throughout the Holocene, with glaciers on the island reaching an extensive maximum approximately 2200 years before present (Clapperton & Sugden, 1988; Clapperton *et al*., 1989a; Hodgson *et al*.,

2014). During this period, evidence suggests that a glacier covered a portion of the Thatcher Peninsula which discharged into King Edward Cove (Timmis, 1986). It is thought there was also a general period of advance during the late 19th century, which was quickly followed by a period of recession (Smith, 1960). The early 20th century, when extensive exploration of the island began, was characterised by a complex period of advance and retreat. Studies indicate significantly different responses during this period between valley, tidewater, sea-terminating and corrie/cirque glaciers (Hogg *et al*., 1982; Hayward, 1983; Timmis, 1986; Gordon & Timmis, 1992). Since the 1950s, there has been an island-wide retreat of glaciers (Cook *et al*., 2010). As previously summarised in section 1.5.2, the largest retreats have all taken place along the north-eastern coast (i.e. north-facing glaciers), where retreat rates have accelerated to an average of 60 metres per year, but those on the southwest coast (i.e. south-facing glaciers) have been retreating more slowly since the 1950s (Hogg *et al*., 1982; Gordon & Timmis, 1992; Gordon *et al*., 2008; Cook *et al*., 2010). Although this pattern of change is broadly comparable with atmospheric warming, such generalisations mask the important differences between glaciers. The rapidity and asymmetry of the retreat suggests that local factors may be important.

6.3 Methodology

6.3.1 A New Inventory of South Georgia's Glacier Basins

An extensive and detailed inventory of the glaciers on South Georgia, resolving individual glaciers and allowing an accurate estimate of total glacierized areas, is essential for the investigation of the island's glacier surface energy and mass balances. Therefore, in order to investigate the differences in the modelled near-surface meteorology between north- and south-facing glaciers, a watershed map of South Georgia had to first be created to define, separate and identify major glacier catchment areas. This watershed map was subsequently applied over the WRF model grid to delineate glacier basins in the model. The author is unaware of any existing catchment map or glacier basin dataset for South Georgia.

6.3.1.1 Creating a Glacier Basin Inventory for South Georgia

ArcMap 9, part of the ArcGIS suite, was used to conduct the analysis, which involved delineating the boundary of a drainage area (i.e. creating a watershed polygon) based on a high-resolution Digital Elevation Model (DEM) of South Georgia (Figure 6.1(b)). The DEM was created from the same model topography dataset which was used to improve the topographical representation of South Georgia in the WRF model (see Chapter 2, section 2.3.1.1). The original data was generated using the 90 m resolution Shuttle Radar Topography Mission (SRTM, Jarvis *et al.*, 2008). The SRTM DEM depicts the land surface, and does not penetrate beneath ice/snow to observe the subsurface structure. The steps for generating a catchment map for South Georgia are detailed below and are also summarised in Figure 6.1. The method described below is typically used for hydrological purposes (e.g. Ahmadi *et al*., 2014), but it has similarly been used to automate delineation of glacier drainage basins (see Bliss *et al*., 2013; Cook *et al*., 2014).

The first step was to fill sinks (depressions in elevation) in the DEM topographic dataset. A sink is usually an incorrect elevation value lower than the elevation values of its surroundings. The sinks must be filled otherwise water that flows into them cannot flow out, and this may result in an erroneous flow direction grid. To ensure proper drainage mapping, an ArcGIS function was employed to fill all the sinks in the input DEM and create a depressionless DEM. This step provides the desired input for the flow direction algorithms; it identifies all sinks in the DEM and raises their elevation to the level of the lowest pour point around their edge. Following this, the direction of flow down a slope and the flow accumulation was calculated (Figure 6.1(c)). The direction of flow determines the ultimate destination of the water flowing across the surface of the landscape. It assigns a flow direction to each grid cell in the catchment such that each grid cell flows to only one neighbouring grid cell with the steepest slope. The flow accumulation determines the number of upstream cells that flow into it. For instance, areas of very high values are likely perennial streams or rivers, while areas with lower values may be intermittent streams, rills or brooks. The output from this step provides a hydrological layer, showing all hypothetical fluvial courses along the topographic surface (Figure 6.1(d)).

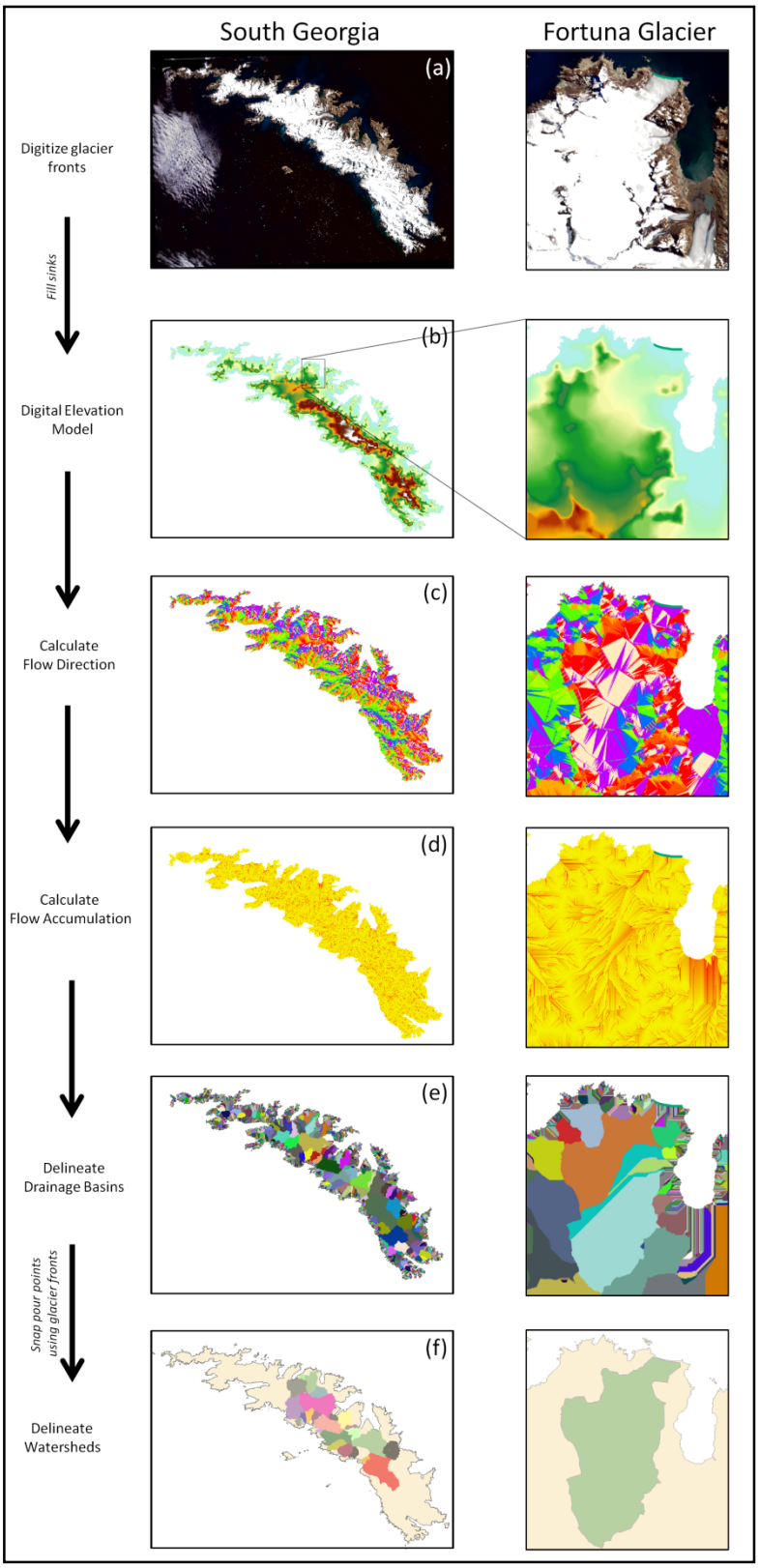

Figure 6.1 – *Schematic detailing the creation of the glacier catchment map of South Georgia (left), focusing on Fortuna glacier as an example watershed (right). The final glacier catchment map can be seen in Figure 6.2.*

Following this, a pour line was used to define the outlet of the watershed. Normally, fluvial watershed analyses use the lowest point on the coastline (e.g. where the river exists the catchment) as the pour point. Instead of using a pour point here, a line denoting the glacier ice front was defined, which forces the algorithm to include the whole surrounding glacier catchment. This method is similar to that employed by Bliss *et al*. (2013) and Cook *et al*. (2014). Defining the location of the pour line can be subjective. However, the glacier fronts for South Georgia's marine-terminating glacier fronts are well documented. The most recent observations of glacier fronts (see Cook *et al*., 2010, and The South Georgia Geographic Information System, www.sggis.gov.gs) were used to visually determine glacier tongues and pour lines (Figure 6.1(a)). For the north- and south-facing glaciers the most recent observations of glacier fronts dated from 2003 – 2008, and from 2003 – 2006, respectively. Therefore, the pour lines (and subsequent watershed boundaries) are all based on a relatively consistent time period. Other, more automated and more rigorous methods exist, but are beyond the scope of this project. Having selected pour lines, the cell with the highest flow accumulation into that line within a specified distance was selected. This ensures that the point is the lowest point along the boundary of a watershed. Now that a hypothetical river (or glacier) mouth exists, the entire watershed was delineated using the flow direction calculations (Figure 6.1(e)). The contributing area of each grid cell was taken as itself, plus the upslope neighbours that drain in to it. This was evaluated recursively starting from the catchment outlet and moving back inside the catchment. This provides a watershed polygon which delineates the boundary of a drainage area (Figure 6.1(f)).

6.3.1.2 The Glacier Basin Inventory

Glacier catchments, watersheds and drainage divides were calculated for 29 glaciers on South Georgia. All 29 glaciers were either fully or partly within the predefined 0.9km innermost (-54.0739°S – -54.5014°S, -36.9771°W – -36.2868°W) domain of the WRF model. They include 11 north-facing glaciers, and 18 south-facing glaciers. Unfortunately, it was beyond the scope of this study to conduct a watershed analysis for all glaciers on South Georgia. The resulting glacier catchment map is shown in Figure 6.2.

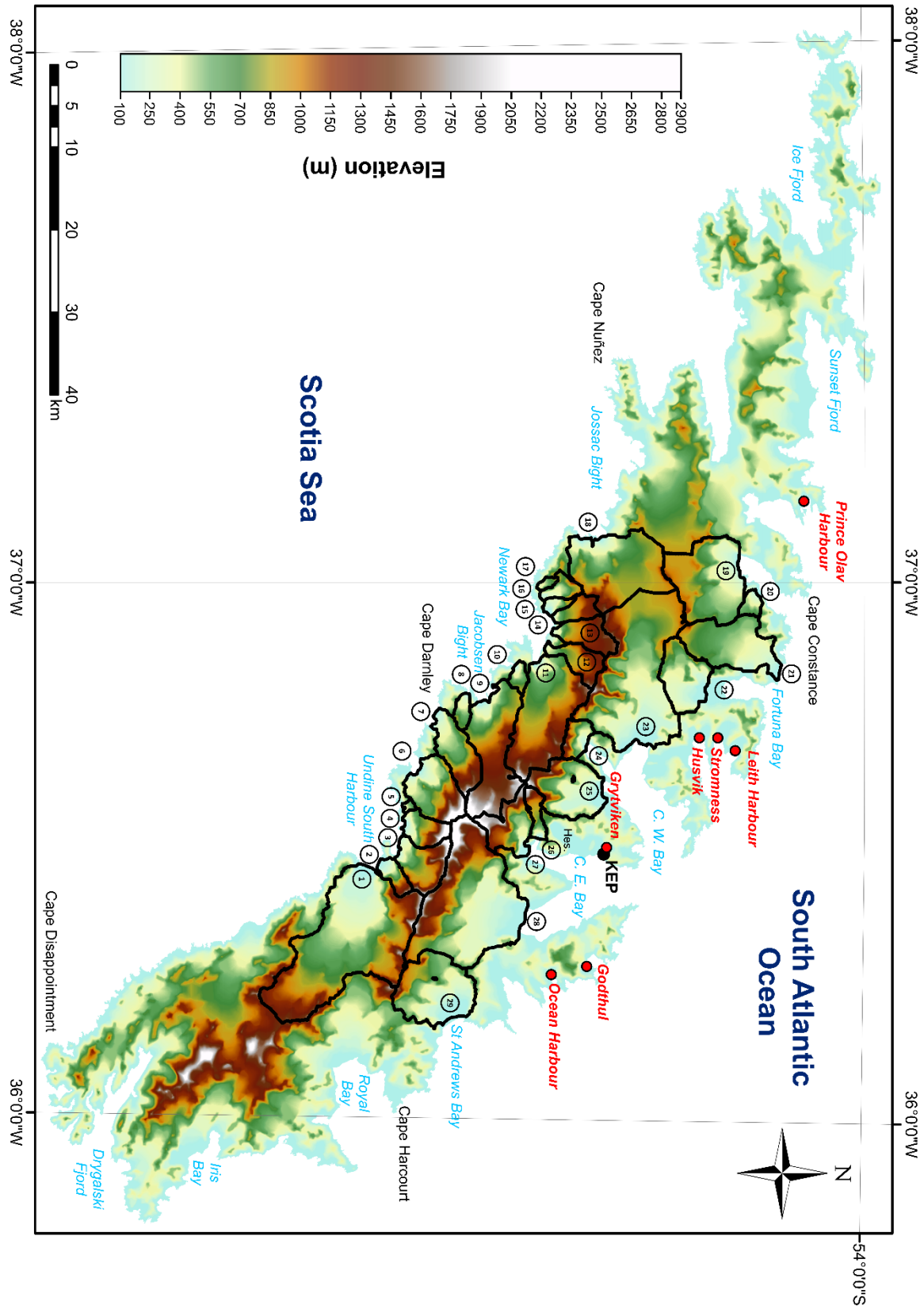

Figure 6.2 – *The glacier catchment map for South Georgia. Watersheds 1 to 18 are defined as south-facing glaciers, while watersheds 19 to 29 are defined as north-facing glaciers (see Table 6.1).*

The 29 glacier watersheds (along with tributary glaciers) are as follows:

		Glacier (& Tributary Glacier) Name	Area (km^2)	Watershed Length (km)
South-facing Glaciers	1	Brøgger glacier (& Spenceley glacier)	186.7 km^2	73.5 km
	2	Brøgger 2 glacier	10.5 km^2	15.0 km
	3	Reusch glacier	30.7 km^2	25.9 km
	4	Undine South Harbour 1 glacier	18.1 km^2	18.6 km
	5	Undine South Harbour 2 glacier	1.6 km^2	5.9 km
	6	Helland glacier	40.7 km^2	27.2 km
	7	Henningsen glacier	33.8 km^2	30.5 km
	8	Bary glacier	6.9 km^2	11.4 km
	9	Christophersen glacier	74.5 km^2	55.1 km
	10	Eclipse glacier	6.1 km^2	10.8 km
	11	Kjerulf glacier	89.0 km^2	47.4 km
	12	Christensen glacier	19.0 km^2	23.6 km
	13	Lancing glacier	21.9 km^2	22.7 km
	14	Newark Bay 1 glacier	12.1 km^2	18.0 km
	15	Newark Bay 2 glacier	5.3 km^2	11.3 km
	16	Newark Bay 3 glacier	9.8 km^2	15.3 km
	17	Sandefjord glacier	2.5 km^2	6.9 km
	18	Jewell/Keilhau glacier	85.1 km^2	45.1 km
North-facing Glaciers	19	Crean glacier	77.1 km^2	49.5 km
	20	Antarctic Bay 1 glacier	6.4 km^2	10.8 km
	21	Fortuna (& Fortuna 2 glacier)	57.9 km^2	41.0 km
	22	König glacier	38.4 km^2	27.4 km
	23	Neumayer glacier	158.0 km^2	69.2 km
	24	Geikie glacier	13.2 km^2	16.0 km
	25	Lyell glacier	49.8 km^2	42.6 km
	26	Hamberg glacier	10.3 km^2	18.0 km
	27	Harker glacier (& Tyrrell glacier)	31.6 km^2	33.5 km
	28	Nordenskjöld glacier (& Paget glacier)	151.9 km^2	61.0 km
	29	Heaney/Buxton/Cook glacier	65.2 km^2	37.6 km

Table 6.1 – *The 29 glaciers in South Georgia's glacier basin inventory, including total areas (km^2) and watershed lengths (km).*

It is difficult to evaluate the error of the underlying DEM without expending considerable effort to create independent outlines from high-resolution satellite imagery. The vertical accuracy (contour heights) of the DEM is between ±7m for flatter areas (e.g. glaciers) and ±25m on steep mountain sides and summits (British Antarctic Survey, 2004). Therefore, lacking detailed information for a more rigorous approach, here it is assumed a 5% error for the total area of the inventory (as with Paul & Andreassen, 2009; Bolch *et al*., 2010; Bliss *et al*., 2013). For the 29 glaciers, the

inventory includes 1314.1 ± 65.7 km^2 of ice (see Table 6.1). This constitutes 37.2 ± 1.9% of the total area of the island (3528 km^2). Glacier sizes range from 1.6 km^2 (Undine South Harbour 2 glacier) to 186.7 km^2 (Brøgger glacier). The five largest glaciers in the inventory (> 80 km^2) have a combined area of 670.7 km^2; 51.0% of the total area of glaciers in the inventory and 19.0% of the total area of South Georgia. Altitudes of all glaciers in the inventory range from 0m to 2934m m above sea level.

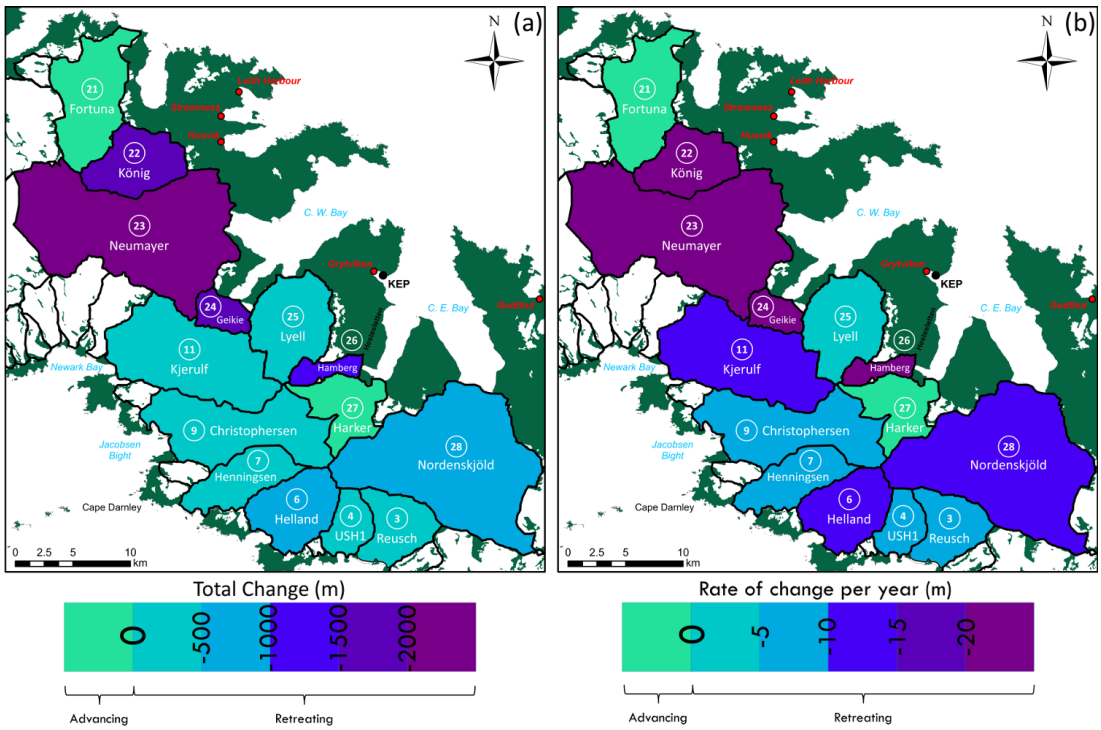

Figure 6.3 – *Glacier catchment map over the region of interest (approximately the innermost WRF domain), coloured by total length of retreat or advance (panel (a)) and rate of change per year (panel (b)). Data on rates of retreat originally from Cook et al. (2010) (see Appendix 6A.1). Hereafter, Undine South Harbour 1 will be referred to as USH1. Kjerulf, Christophersen, Henningsen, Helland, USH1 and Reusch are south-facing glaciers. Fortuna, König, Neumayer, Geikie, Lyell, Hamberg, Harker and Nordenskjöld are north-facing glaciers. The outlines of the 29 glaciers are shown by black solid lines. For the areas that are not coloured by length/rate of retreat/advance, permanent snow and ice is shown in white and land that is bare rock or vegetated in summer is shown in green.*

Within the innermost domain of the WRF model, 14 glacier catchments have been selected for further investigation (Figure 6.3). These 14 glaciers were chosen as their catchments fall fully within the 0.9km WRF grid, they are amongst the largest glacier catchments, and each of the glaciers has undergone variable rates of retreat since the 1950s. The 14 glaciers have a combined area of 797.9 km^2; 60.7% of the total area of

glaciers in the inventory and 22.6% of the total area of South Georgia. The total change and the rate of change per year for each of the glaciers is given in Appendix 6A.1 (also see Figure 1.5, Figure 6.3, and Cook *et al*., 2010). Of the 14 glaciers chosen in this study, 2 north-facing glaciers (Fortuna and Harker) have advanced in the last 50 years, while the 12 remaining have all retreated (Figure 6.3(a)). Of the 103 marine-terminating glaciers investigated by Cook *et al*. (2010), Neumayer glacier has retreated the most, with -2299.4 metres of retreat observed since 1938. König glacier has the highest rate of retreat per year, at -36.9 metres of retreat per year (Figure 6.3(b)). It should also be noted that all glaciers apart from König and Lyell are marine-terminating glaciers. Up until ~1958, König glacier had been marine-terminating, but has since drastically retreated (Cook *et al*., 2010). König glacier now ends in a proglacial lake which drains into Antarctic Bay. In addition to König glacier, Lyell glacier terminates partly on land and partly in a calving ice front in Cumberland West Bay. Previous observations during field expeditions have shown that the Lyell glacier terminates with stepped moraine deposits, rock avalanche debris and steep icefalls (Gordon *et al*., 1978; Gordon & Birnie, 1986; Gordon & Timmis, 1992). By far the largest glaciers investigated here are Neumayer (158.0 km^2) and Nordenskjöld (151.9 km^2), both of which range from the highest peaks of South Georgia down to sea level. The smallest glacier in this study is Hamberg (10.3 km^2). See Appendix 6A.2 for a comparison of the total areas of each glacier catchment as calculated from the original DEM dataset and the WRF model grid cell areas. Since the differences between the true catchment areas and the WRF model catchment areas are small, it can be assumed that all of the glacier watersheds are adequately resolved within the model. However, it is also important to recognise even a small difference in the areas of the accumulation and ablation zones in the model will have consequences on the calculated surface mass balance of South Georgia (see section 6.6 for further discussion).

6.3.2 Calculating the Surface Energy Balance

To determine the amount of energy available for melt over the glaciers of South Georgia, the surface energy and mass balances must be calculated. The components of the surface energy balance (i.e. the radiation and turbulent fluxes) ultimately impact the surface snow and ice through effecting accumulation, ablation, sublimation and

evaporation. Therefore, the ablation processes (melt and evaporation) depend crucially on the surface energy balance. In order to calculate the energy balance, it is necessary to use WRF as proxy observations for turbulent heat fluxes and solar and longwave radiation. The surface energy and surface mass balances were calculated for one season; September 2011 – August 2012. The innermost domain of the nested model setup (at a spatial resolution of 0.9km) is used (see Figure 5.1(b)) for these calculations. Although not shown, the glaciers of South Georgia are not sufficiently resolved in the intermediate domain (2.7km resolution), which was previously used to explore the regional climate of South Georgia. Therefore, the high-resolution domain is required to explore individual glacier basins. The surface energy and mass balances were calculated over grid cells which are permanent snow and ice in the WRF model (see Figure 5.1(c)).

Neither the temperature nor the phase of a glacier surface will change, unless there is a net gain or loss of energy at the glacier surface (Oerlemans, 2001; King *et al*., 2008). Therefore, glacier melting is determined by the energy balance at the glacier surface. If the surface of a glacier is heated (through net gain in energy) to the freezing point, any subsequent gain in energy at the surface will cause melting. The temperature at the surface of a melting glacier cannot exceed 0^{o}C. If there is a net loss of energy at the surface, the glacier surface will cool. The energy balance at the surface of a glacier is computed by considering all of the inputs and outputs of energy at the surface, and is defined as the sum of all energy fluxes at the surface. Conservation of energy requires close of the energy balance and this is expressed mathematically as:

$$Q_M = (L\uparrow + L\downarrow) + (S\uparrow + S\downarrow) + Q_L + Q_S + Q_G = 0$$

or,

$$Q_M = Q_N + Q_L + Q_S + Q_G = 0$$

Where:

Q_M = energy available for heating and melting (residual)
Q_N = net radiation, sum of incoming and outgoing solar and terrestrial radiation
Q_L = latent heat flux (latent heat of evaporation and sublimation)
Q_S = sensible heat flux
Q_G = ground heat flux

$S\downarrow$ = incoming/down-welling solar radiation

$S\uparrow$ = outgoing/up-welling solar radiation

$L\downarrow$ = incoming/down-welling longwave radiation

$L\uparrow$ = outgoing/up-welling longwave solar radiation

All fluxes are stated in Wm^{-2}. Here, the positive inward sign convention for all terms is used. All fluxes and that deliver energy to the surface are defined as positive, whereas fluxes away from the surface are negative. Ground heat flux (Q_G) is positive upward (towards the surface) and negative downward (into the ground). Sensible (Q_S) and latent heat (Q_L) fluxes are also referred to as turbulent heat fluxes. If Q_M is positive, then the energy available first goes into heating the surface, and then into melting when the temperature of the surface is 0^oC. If Q_M is negative, then the surface of the glacier cools and melting is zero.

6.3.3 Calculating the Surface Mass Balance

The change in mass of a glacier is known as the surface mass balance. It is a key quantity for this study as it characterises mass exchanged between glaciers and the wider hydrological system, and quantifies the link between the föhn effect and annual melting. The mass balance is defined as the difference between all accumulation and ablation on a glacier (Oerlemans, 2001). Accumulation includes all processes that add mass (i.e. frozen precipitation), and ablation includes all processes that cause reductions in mass of a glacier (i.e. melting, evaporation). Mass additions (accumulation) to the ice mass are positive. Mass losses (ablation) to the ice mass are negative. The units of mass balance are in metres water equivalent (m w.e.) over a specified time period (e.g. 1 day, 1 year, season etc.). The following equations are used to calculate the surface mass balance at a single point on a glacier surface:

$$Melt = \frac{Q_M}{l_f \times \rho}$$

$$Evaporation = \frac{Q_L}{l_v \times \rho}$$

$$Ablation = (Melt + Evaporation)$$

$$Accumulation = \frac{Frozen\ Precipitation}{1000}$$

$$Surface\ Mass\ Balance = Accumulation - Ablation$$

Where:

l_f = Latent heat of fusion (taken as 334×10^3 Jkg^{-1})

ρ = Density of water (taken as 1000 kgm^{-3})

l_v = Latent heat of vaporization (taken as 2.5×10^6 Jkg^{-1})

The total mass balance for the entire surface of the glacier is the sum of all mass balances over all grid cells within the glacier catchment. The residual from the energy budget (Q_M) can be used to either increase the surface temperature of a glacier, or to melt the glacier. As explained earlier, when the surface temperature is below the melting point, Q_M either heats or cools the surface, depending on the sign. If the surface skin temperature is at the melting point (= 0^oC), then the melt rate and evaporation rate is calculated using the net surface energy flux available for melt (Q_M). In all other times when the surface skin temperature is < 0^oC, then the melt rate is set to zero. The energy balance is calculated at each model output time (i.e. every hour). Melt and evaporation rates are then summed over the period of interest (e.g. 1 day, 1 year, season etc.) to give total melt and evaporation over the specified period. Frozen precipitation includes all snow, ice, hail and graupel accumulation fields in WRF. The surface mass balance calculations assume that all melt water runs off of the glacier surface. There are no assumptions regarding (thus effectively ignoring) the direction of melt water into the glacier (e.g. through percolation and/or throughflow), nor the possibility of surface melt being stored in the glacier. Similarly, the calculations do not account for liquid precipitation accumulation (via freezing on the glacier surface).

6.4 A Regional Climatology of the Surface Energy Balance Components

In Chapter 5 (section 5.4), a regional climatology of the near-surface meteorology of South Georgia using the high-resolution WRF model output was presented. To complement this, presented in this section is a brief regional climatology of the surface albedo and of the key components of the surface energy balance across South Georgia. Figure 6.4 shows annual and seasonal horizontal cross-sections through South Georgia for these components. Figure 6.5 and Figure 6.6 also show annual mean and seasonal (austral summer, autumn, winter and spring) computed energy balance components, for the June 2011 – February 2013 period. Since there are few equivalent detailed *in*

situ measurements, the maps presented here provide the only base to study the intra-annual variation and the distribution of energy balance components across South Georgia.

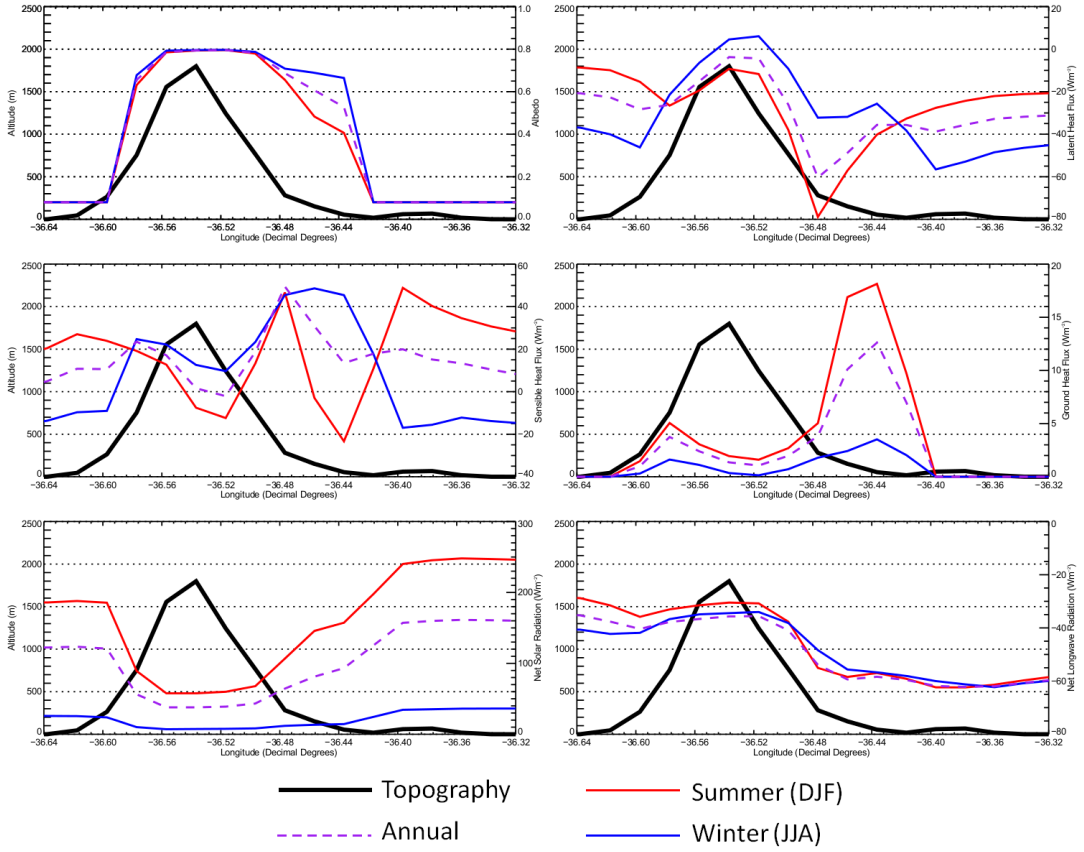

Figure 6.4 – *Horizontal cross-sections of panel (a) surface albedo, panel (b) latent heat flux (Wm^{-2}), panel (c) sensible heat flux (Wm^{-2}), panel (d) ground heat flux (Wm^{-2}), panel (e) net solar radiation (Wm^{-2}), and panel (f) net longwave radiation (Wm^{-2}). Black solid line – topography cross-section, purple dashed like – annual mean, red solid line – austral summer (DJF) mean, blue solid line – austral winter (JJA) mean. See Figure 5.5 for geographic reference of cross-section through South Georgia.*

6.4.1 Surface Albedo

The surface albedo is defined as the fraction of incident solar radiation reflected by the surface. The surface reflectance (albedo) is dependent upon the material properties of the surface (e.g. morphology, thermal and physical properties), the properties of the incoming solar radiation (e.g. the solar zenith angle), and the atmospheric conditions (e.g. cloud cover, cloud type and distribution). Typical albedo values for non-melting snow-covered surfaces are high (0.80 – 0.95) (Armstrong & Brown, 2008).

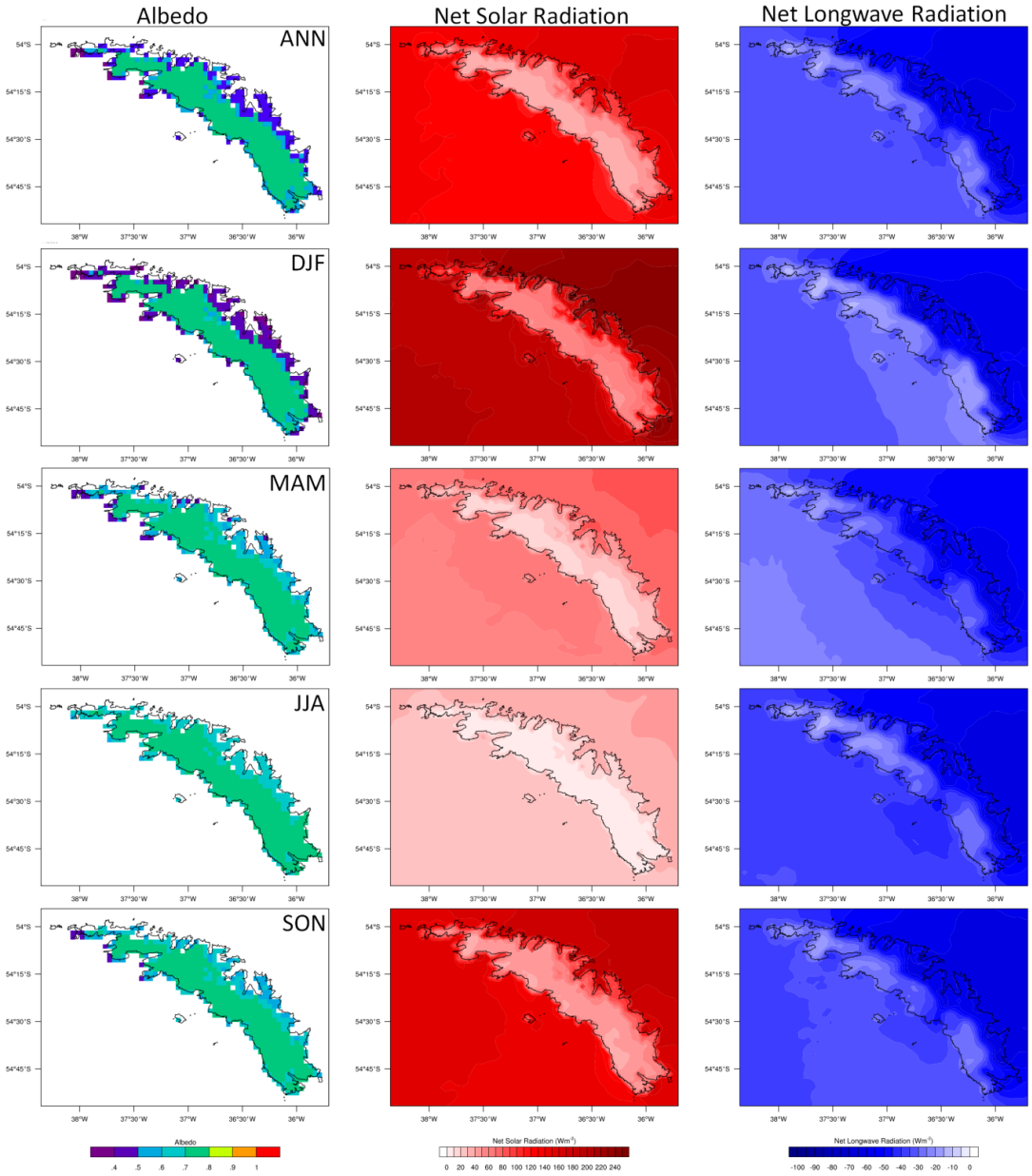

Figure 6.5 – *Mean (annual, summer (DJF), autumn (MAM), winter (JJA), and spring (SON)) maps of surface albedo (left), net solar radiation (S↓ + S↑, middle), and net longwave radiation (L↓ + L↑, right), for the period June 2011 – February 2013.*

The surface albedo of South Georgia shows large spatial variations across the island as well as strong seasonality (Figure 6.5). The largest signals in variability are along the fringes of the island, where these areas are most exposed to the prevailing maritimal conditions of the Southern Ocean, and are only seasonally covered in snow. Many of these areas are defined as barren or sparsely vegetated (see Figure 5.1(c)) and the land surface is exposed for several months a year. These areas of seasonal snow cover will have a lower mean albedo than areas permanently covered in snow and ice

due to the different thermal and physical properties of barren ground and snow and ice. Snow, particularly fresh snow, has a very high albedo as a large proportion of the incoming solar radiation is reflected, while barren ground has a much lower surface reflectance (Armstrong & Brown, 2008). The mean austral summer and winter albedo at King Edward Point is 0.41 (σ of all hourly summer values = 0.06) and 0.69 (σ of all hourly winter values = 0.04), respectively. Surface albedo has in the past been measured at King Edward Point (Shanklin, 1985). In the period 1973 – 1981, the mean austral summer and winter albedo at King Edward Point was 0.23 (σ = 0.03) and 0.76 (σ = 0.08) respectively. Although these measurements were taken over 30 years ago, they suggest that WRF is underestimating the annual variation in surface albedo. The likely cause of the modelled bias in albedo is due to the oversimplification of land surface type at King Edward Point, compared to the complexity of it in reality (see section 2.3.1.1). Albedo shows negligible seasonality in the interior (and across the majority) of the island. The high albedo in the interior of the island (i.e. 0.7 – 0.8) is unsurprising, given the fact that over 50% of the island is permanently covered in snow and ice. As the regional maps of precipitation accumulation have shown (Figure 5.8), these areas are continually refreshed with new snow accumulation. Changes to the albedo of glaciers are most noticeable at their termini. Since the southwest side of the island is steeper and more heavily glaciated compared to the more sheltered north-eastern side of the island, there is also a perennial cross-barrier albedo gradient (Figure 6.4). Figure 6.4 also shows that there is a much lower seasonal variation in albedo on the south-western side of South Georgia. This is unsurprising since the southwest coastline is more heavily glaciated (as well as being colder, see Figure 5.5) with higher snow accumulation (Figure 5.8) than the northeast coastline, thus sustaining higher surface reflectance throughout the year.

6.4.2 Net Solar and Longwave Radiation

There are large seasonal and regional variations in the net solar and longwave radiation energy balance terms (Figure 6.5). There is also a clear cross-barrier gradient of these components throughout the year (Figure 6.4) and these gradients for both net radiation components extend many kilometres (over 20km) into the wake of South Georgia. This is a result of relatively cloudless conditions in the (climatological) lee of the island, which contrasts with the relatively cloudy conditions on the windward side of

the island. This an artefact of having a maritime climate and a significant orographic divide, which results in orographic uplift (hence increased cloudiness) on the upwind slopes and the föhn effect (hence decreased cloud cover) on the downwind side of the island during intense westerly winds.

The seasonality of net solar radiation is largely driven by the azimuth and elevation of the Sun (Figure 6.5). As a result of this, net solar radiation is generally highest during austral spring and summer (September through February) across the island. Throughout the year, net solar radiation is generally reduced on the south-western slopes due to increased cloud cover. Increased cloud cover on the upwind slopes results in increased cloud albedo and cloud absorption of radiation, thus reducing incoming solar radiation. Since net solar radiation is also determined by surface albedo, this radiation term also shows large seasonal variations around the fringes of the South Georgia (i.e. in areas which are seasonally snow-covered).

Figure 6.5 shows that outgoing longwave radiation exceeds incoming longwave radiation throughout the year, though there are noticeable areas where the net longwave radiation is near-zero. This is most noticeable at the north end of South Georgia, where much of the island is covered by low cloud and fog throughout the year. Richards & Tickell (1968) found that Bird Island was covered by cloud up to 90% per annum, compared to just 70% per year at King Edward Point. The variation in net longwave radiation is also comparatively less at the north end of South Georgia.

6.4.3 Latent and Sensible Heat Fluxes

As with net solar and longwave radiation, the turbulent heat fluxes also exhibit clear seasonality and regional-scale differences (Figure 6.4 and Figure 6.6). As a consequence of the cross-barrier climatic divide, the latent, sensible and ground heat fluxes are generally greater in the lee of South Georgia (similarly shown by Hosking *et al*., 2015). The annual mean maps of the turbulent heat fluxes (Figure 6.6) show a large positive sensible heat flux (typically ~50 Wm^{-2}) and negative latent heat flux (typically ~-40 Wm^{-2}) pattern on the northeast coast of South Georgia. This can be attributed to the predominance of descending föhn air on this side of the island, which is both warm and dry.

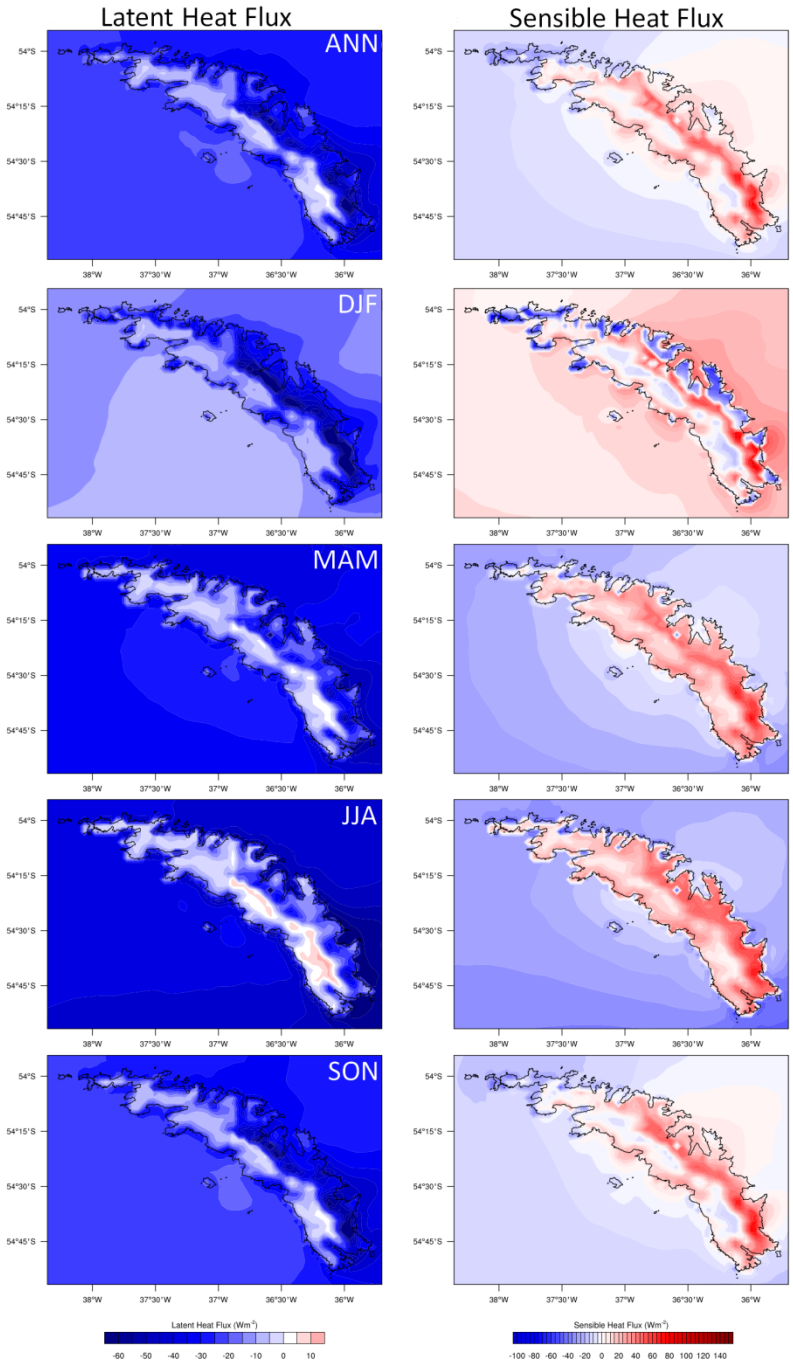

Figure 6.6 – *Mean (annual, summer (DJF), autumn (MAM), winter (JJA), and spring (SON)) maps of latent heat flux (Q_L, left) and sensible heat flux (Q_S, right), for the period June 2011 – February 2013.*

In austral summer, there is a strong net negative latent and sensible heat flux which is pronounced on the northeast side of the island, and along the fringes and most exposed areas of South Georgia. The large net negative sensible heat flux in summer (~-50 Wm^{-2}) is likely due to strong surface heating by solar radiation on the low-albedo surfaces, which drives convection. Warming, and therefore evaporation, is highest in

these barren and sparsely vegetated areas of the island in this season. This contrasts the large positive sensible heat flux in austral winter (~50 Wm^{-2}). Latent heat flux also becomes less negative in winter, and becomes positive around the middle section of South Georgia, where the mountains are at their highest. This positive flux is drives condensation onto the surface at high altitude, and this is also similarly reflected by the higher frozen precipitation totals across the central part of South Georgia, as shown in section 5.4.4, in this season.

6.4.4 Summary

In summary, it is clear that the surface energy balance of the island is strongly modified and controlled by the significant orographic divide. The cold climate of South Georgia is reflected by the island's high albedo and the negative (and near-zero) latent heat fluxes along the central spine of the island throughout the year. The predominance of strong westerly wind speeds (Figure 5.7) and the subsequent downslope föhn winds which dominate the climate of the island result in the large turbulent heat fluxes in the lee of the mountains. The dominance of the föhn effect (i.e. the descent of dry air which has been adiabatically warmed, effectively reducing leeside convection and cloud formation) also accounts for the spatial and annual differences in the net longwave and solar radiation terms. Since there are very few measurements of fluxes for validation, it is clear that WRF can be used as a proxy for observations and that the modelled results are consistent with what we would expect from our current limited understanding of the regional pattern of the surface energy balance of South Georgia (see e.g. Smith, 1960; Richards & Tickell, 1968; Hogg *et al*., 1982; Shanklin, 1985).

6.5 What Impact Do Föhn Events Have On...

In Chapter 5 (section 5.4) and above, the regional climate of South Georgia was explored in detail using the coarse-resolution (2.7km horizontal resolution) WRF model output. This next section explores the impact of föhn flow (and the associated leeside surface warming, drying and increased wind speeds) on the regional climate and on the glaciers of South Georgia using the high-resolution (0.9km spatial resolution) model output for the September 2011 – August 2012 period. Following

this, the annual surface energy balance and annual net mass balance components for each of the 14 glaciers are calculated.

6.5.1 ...the Regional Climate of South Georgia?

The impact of föhn on the near-surface meteorology of South Georgia is striking. Figure 6.7 shows the near-surface air temperature, surface temperature, relative humidity and 10-m wind speed anomalies (from the annual mean) for all föhn events from the WRF model (as detected using the criteria given in section 5.6.2) over the innermost (0.9km resolution) WRF domain. Immediately apparent is the asymmetry of the anomalous temperature (Figure 6.7(a)) and relative humidity (Figure 6.7(b)) patterns, with clear cross-barrier gradients, showing that föhn episodes act to warm and dry the north-eastern slopes, relative to the annual mean. During föhn flow, the near-surface temperature over the north-facing glaciers warms at low elevations (reaching +2^{o}C) and cools by -1.5^{o}C at high elevations. This results in a steepening of the north-facing surface glacier lapse rates over the lee of the island. This is in direct response to föhn flow over South Georgia and the associated leeside warming effect. In contrast, the near-surface temperature over the south-facing glaciers cools at low elevations (typically -0.6^{o}C), and also cools more at high elevations (typically -2^{o}C). The föhn warming and drying is also felt for tens of kilometres downstream of the island as revealed by the WRF model output from the intermediate domain (section 5.6.5, also see Bannister & King, 2015). It is interesting to note that the warm pattern terminates over Fortuna glacier, which marks the northern end of the Allardyce Range. The 0^{o}C anomaly contour closely follows the 600 – 800m elevation contours. Although the decrease in relative humidity (~-20%) is statistically significant downstream of the island, the positive 2-m air temperature anomaly is only significant over a small portion of Greene Peninsula and Nordenskjöld glacier.

Unsurprisingly, during föhn flow, wind speeds are significantly stronger across South Georgia (Figure 6.7(d)). Over the main ridge of the island, wind speed anomalies exceed +10ms^{-1}, reaching a maximum of +15.2ms^{-1} in the vicinity of Mount Paget. The surface temperature anomalies (Figure 6.7(c)) reveal that during föhn conditions, the majority of the surface of the island warms below 1500m, and counter-intuitively, the windward slopes and south-facing glaciers appear to warm (~0.4 – 1.2^{o}C) greater

than the leeward slopes and north-facing glaciers (~0.2 – 0.6ºC). However, the surface temperature anomalies over the island are not statistically significant at the 95% confidence level.

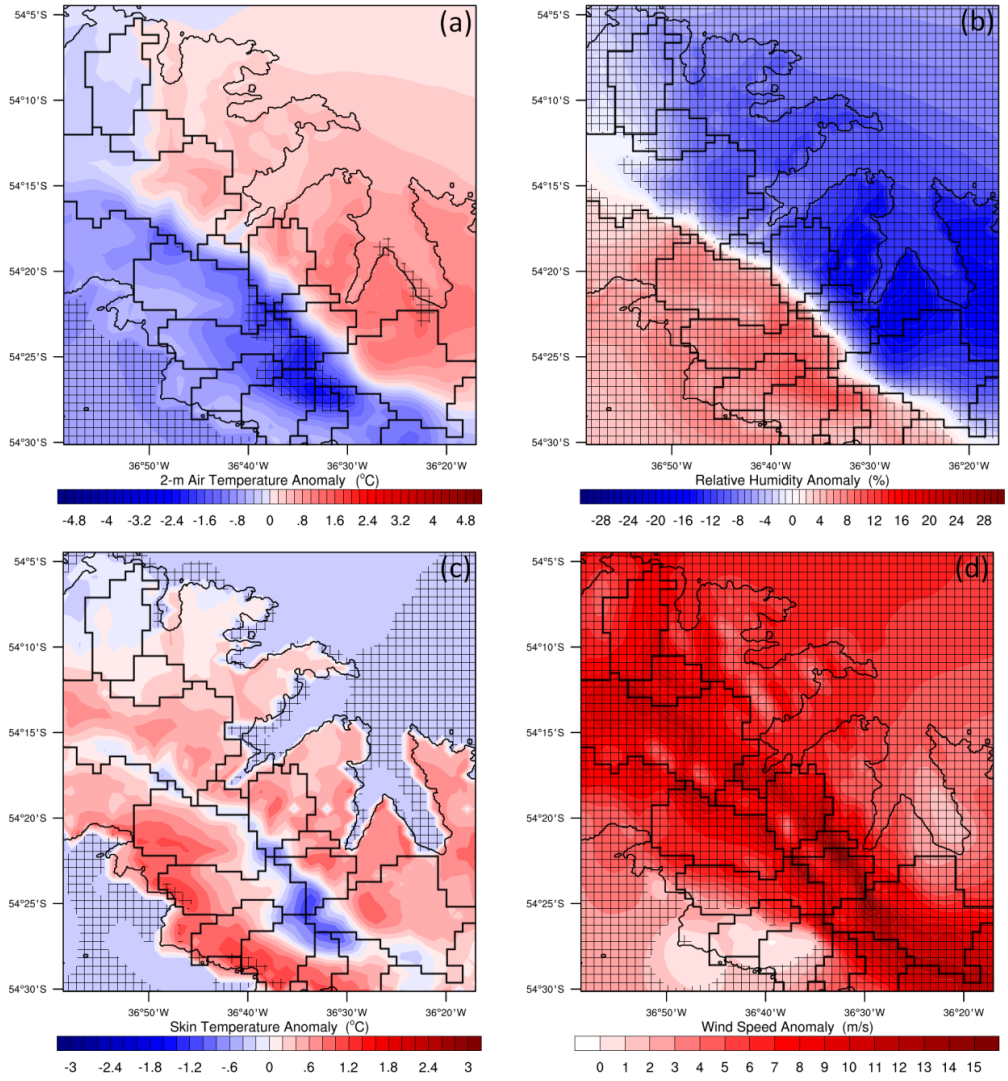

Figure 6.7 – *Panel (a) 2-m temperature föhn anomaly, panel (b) 2-m relative humidity föhn anomaly, panel (c) surface skin temperature föhn anomaly, and panel (d) 10-m wind speed föhn anomaly. All anomalies are expressed from the annual (September 2011 – August 2012) mean. Hatching indicates anomalies are statistically significant at the 95% ($p \leq 0.05$) confidence level. The 14 glacier catchments are also plotted.*

During these föhn times, King Edward Point is 0.8ºC warmer, 12.3% drier and 4.1ms^{-1} windier than on average. As was previously discussed in section 5.5, Figure 6.7 also further confirms that the föhn effect is experienced over a substantial area in the lee of South Georgia. Again, this information is vital for planning placements of automatic weather stations (AWS) and other meteorological observations to research föhn flow

in the future. It is clear that föhn is responsible for the asymmetrical pattern in the climate and weather of South Georgia. The impact of föhn flow on the weather is expressed by anomalously warm temperatures, dry surface conditions, and strong winds across the lee of South Georgia. Due to the warmth and dryness associated with these winds, one would expect föhn flow to also lead to asymmetrical melting and sublimation of snow and ice across South Georgia. This will now be explored in greater detail.

6.5.2 ...the Number of Zero Degree Days?

One metric which can be used to explore the impact of föhn on the glaciers of South Georgia is by quantifying the annual frequency of 0°C days opposed to the equivalent frequency of 0°C days during föhn events. Since the model output is every hour, a 0°C hour is defined when the surface temperature of an individual grid cell in the model ≥ 0°C. The number of 0°C hours is then converted into 0°C days. For comparison, the number of 0°C days was calculated for one year (September 2011 – August 2012) and for an equivalent föhn year (effectively assuming that föhn is occurring throughout):

$$Annual\ number\ of\ 0^oC\ days = \frac{Number\ of\ hours\ TSK\ \geq 0^oC}{24}$$

$$Equivalent\ number\ of\ annual\ föhn\ 0^oC\ days = \frac{Number\ of\ hours\ during\ föhn\ TSK\ \geq 0^oC}{24} \times \frac{365}{\left(\frac{Total\ number\ of\ föhn\ hours}{24}\right)}$$

Where:

TSK = surface skin temperature

As detected using the criteria given in section 5.6.2, there were a total number of 2894 föhn hours, which is roughly equivalent to 121 days, between September 2011 and August 2012. The number of 0°C days for September 2011 – August 2012 and the equivalent number of föhn 0°C days is presented in Figure 6.8.

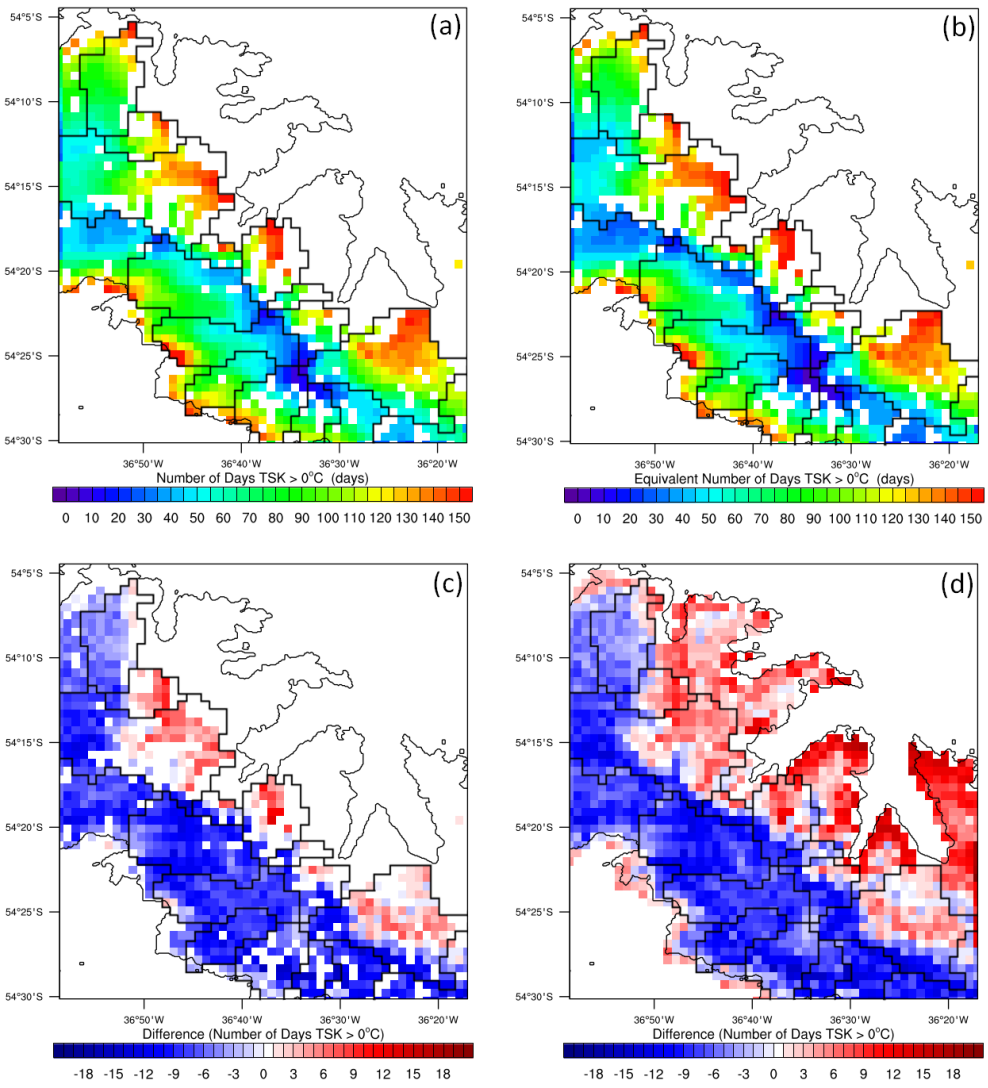

Figure 6.8 – *Panel (a) the number of days during September 2011 – August 2012 when the surface temperature ≥0°C. Panel (b) the equivalent number of annual föhn 0°C days. Panel (c) the difference in the number of 0°C degree days between (a) and (b). Non-permanent snow and ice grid cells are masked in panels (a) through (c). Panel (d) as panel (c), but for all land grid cells. The catchment areas for all 14 glaciers are also plotted.*

Over one year, it is clear that the number of 0°C days is negatively correlated with elevation (Figure 6.8(a)). There are generally fewer than 30 0°C days over 1500m, while there are greater than 130 0°C days at the termini of the glaciers across the island (Figure 6.8(a)). Since the northeast of South Georgia is generally less steep, and the north-facing glaciers are wider and more gently sloping and at lower elevation compared to the south-facing glaciers, it is unsurprising that the frequency of 0°C days is much higher over these glaciers. The spatial pattern in 0°C days also strongly corresponds with the mean annual 2-m air temperature (Figure 5.5), which previously

showed warmer air temperatures over the low-lying areas of northeast South Georgia. During the September 2011 – August 2012 period, the greatest total number of 0°C days occurred at the termini of Lyell glacier (157 0°C days), while the fewest total number of 0°C days occurred in the basin of Helland glacier (5 0°C days) near to Mount Paget.

The equivalent föhn annual number of 0°C days clearly shows an enhancement of the annual spatial pattern (Figure 6.8(b)), with more 0°C days at lower elevations (particularly along the northeast coast) and fewer 0°C days at high elevation. The greatest total number of equivalent föhn 0°C days also occurs at the termini of Lyell glacier (168 0°C days), while the fewest total number of equivalent föhn 0°C days also occurs in the mountains of Helland glacier (3 0°C days).

The difference between the annual and equivalent föhn annual number of 0°C days clearly shows the impact and asymmetry of surface föhn warming on the northeast coastline of South Georgia (Figure 6.8(c)). Föhn winds result in ~10 more 0°C days across large areas of the north-facing glaciers, and this is particularly noticeable over König, Neumayer, Lyell, and Nordenskjöld glaciers. On average, föhn increases melt days by ~5.5% at low elevation on the northeast side of South Georgia. At the termini of Lyell glaciers, föhn leads to 6.8% more 0°C days. Figure 6.8(c) also shows that there are fewer 0°C days at high elevation and across all the south-facing glaciers. On average, föhn decreases melt days by ~3.1% at low elevation on the southwest side of South Georgia. Figure 6.8(d) also shows the difference for all land grid-cells in the WRF model to further highlight the asymmetry of 0°C days across the island of South Georgia due to the föhn effect. Therefore, the impact of föhn on surface temperature is apparent. The fraction of time that the ice surface is at or above 0°C during all föhn conditions clearly shows an asymmetrical pattern across South Georgia, with an increase in the fraction over the northeast of the island and a decrease in the fraction over the southwest of the island. Therefore, based on the assumption that glacial melt occurs when the surface skin temperature reaches 0°C, then the föhn effect experienced across South Georgia does have the potential to lead to asymmetrical melt. As with Figure 6.7, the spatial pattern of 0°C days gives another indication that föhn is (at least partly) responsible for the observed pattern of asymmetrical climate and glacial retreat.

6.5.3 ...the Surface Energy Balance?

To better understand the intra-annual evolution of snow and ice on South Georgia, the monthly means of the surface albedo, air and surface temperature, and the key components of the surface energy balance were calculated for each of the 14 glaciers using WRF model output data. These are presented in Appendix 6A.3.

Since South Georgia has a subantarctic climate and is characterised usually by low temperatures, one would expect melt to generally occur during the austral summer months. This is evidenced by the (albeit small) decrease in albedo across all 14 glaciers in this season (Appendix 6A.3). The extent to which the mean albedo decreases varies between north- and south-facing glaciers. The mean summer albedo for north-facing glaciers is 0.76, which compares to a mean albedo of 0.78 for the 6 south-facing glaciers. Across the majority of glaciers, albedo reaches a minimum in November, followed by a second minimum in February. The minimum albedo in November across all glaciers is closely connected with maximum air and skin temperatures, while the second minimum in February may be an artefact of increased liquid precipitation during austral summer across South Georgia (see Figure 5.8). As expected, surface albedo for all 14 glaciers is highest during the winter months. This annual cycle is similarly reflected in the 2-m air temperature and surface skin temperature timeseries. In the summer, the air temperature exceeds 0^{o}C over the majority of the north-facing glaciers (excluding Neumayer, Harker and Nordenskjöld glaciers), but remains below freezing for south-facing glaciers. However, during the summer, the surface temperature follows the air temperature closely on south-facing glaciers. This drives a negative (or near zero) sensible heat flux in summer, which in contrast, remains high and positive for north-facing glaciers throughout the year. Net solar radiation also dominates the radiation budget in summer, which results in positive values of net radiation for all glaciers. The cross-barrier gradient in net solar radiation is also noticeable, whereby it is higher for north-facing glaciers due to the generally clear and cloudless conditions in the lee of the mountains. In winter, the reduced incoming solar radiation means that net longwave radiation determines the radiative budget. During the winter the decreasing longwave radiation reflects the cooling atmosphere and glacier surface. Sensible heat transfer from the atmosphere to the cooler glacier surface chiefly balances the negative longwave radiation budget. As a result, the net radiation

in winter for all glaciers is negative (or near zero). As previously highlighted, the sensible heat flux remains high and positive throughout the year for north-facing glaciers, and rarely falls below 30 Wm^{-2}, as the air temperature is warmer than the glacier surface. This contrasts the negative latent heat flux (which denotes mass loss by evaporation and sublimation) in summer, and the very small positive flux (condensation) in winter. For the south-facing glaciers, both turbulent heat fluxes are less extreme, and the sensible heat flux becomes negative (or near zero) in summer. In spring, increasing amounts of solar radiation heat the atmosphere and snow surface, as seen from the synchronously increasing surface energy balance across all 14 glaciers. In summary, the intra-annual variations of the energy balance magnitude terms are considerable.

The seasonal and annual net values of the surface energy balance are given in Table 6.2. The annual mean values are given in Table 6.3.

	Glacier	Summer Net Q_M, DJF (Wm^{-2})	Autumn Net Q_M, MAM (Wm^{-2})	Winter Net Q_M, JJA (Wm^{-2})	Spring Net Q_M, SON (Wm^{-2})	Annual Net Q_M, (Wm^{-2})
North-facing	**Fortuna**	104.4	1.5	-18.0	28.5	**116.5**
	König	114.8	-16.5	-34.2	27.1	**91.1**
	Neumayer	87.3	-25.0	-35.6	18.6	**45.4**
	Geikie	46.6	-50.5	-50.8	-9.3	**-64.1**
	Lyell	44.9	-52.9	-62.0	-2.0	**-72.2**
	Hamberg	19.7	-58.5	-53.0	-19.1	**-111.0**
	Harker	18.8	-57.2	-55.0	-17.9	**-111.5**
	Nordenskjöld	55.5	-46.0	-56.0	-5.0	**-51.5**
South-facing	**Kjerulf**	75.2	-23.9	-24.7	19.8	**46.4**
	Christophersen	71.5	-24.6	-25.4	19.4	**40.7**
	Henningsen	100.6	-15.2	-25.0	31.2	**91.5**
	Helland	92.2	-21.9	-32.5	22.7	**60.6**
	USH1	48.5	-27.2	-31.4	7.7	**-2.3**
	Reusch	52.3	-28.6	-31.8	9.0	**0.9**

Table 6.2 – *Seasonal and annual net surface energy flux (Q_M) for each of the 14 glaciers, September 2011 – August 2012.*

In the September 2011 – August 2012 period, the net surface energy balance components across the majority of South Georgia's glaciers do not balance. The annual net surface energy flux (Q_M, residual) is shown in Table 6.2. Interestingly, Undine South Harbour 1 and Reusch glacier are close to balance (-2.3 Wm^{-2} and 0.9

Wm^{-2}, respectively) while glaciers such as Fortuna (116.5 Wm^{-2}) and Henningsen (91.5 Wm^{-2}) have a large positive surface energy balance. Both neighbouring Harker (-111.5 Wm^{-2}) and Hamberg (-111.0 Wm^{-2}) glaciers have large negative surface energy balance. The nonlinear behaviour of the surface energy balance means that substantial ablation can still occur even though the annual net surface energy balance is <0 Wm^{-2}. It is also interesting to note that Q_M generally decreases between Fortuna (the northernmost north-facing glacier) and Nordenskjöld glacier (the southernmost north-facing glacier) (Table 6.2 and Table 6.3). For the southernmost north-facing glaciers, the turbulent fluxes of sensible and latent heat tend to offset each other, and net negative radiation (Q_N) becomes dominant, which overall drives a negative annual surface energy balance. This appears to be a result of glacier location and the fact that these glaciers in particular (i.e. Lyell, Harker, Hamberg and Nordenskjöld glaciers) are impacted by föhn warming and drying more so than the northernmost north-facing glaciers (i.e. Fortune and König glaciers) (see Figure 6.7, which shows greater leeside warming and drying over Nordenskjöld glacier than Fortuna glacier).

	Glacier	Mean Albedo	Mean Air Temp. (°C)	Mean Skin Temp. (°C)	Mean Q_L (Wm^{-2})	Mean Q_S (Wm^{-2})	Mean Q_G (Wm^{-2})	Mean SW_{net} (Wm^{-2})	Mean LW_{net} (Wm^{-2})	Mean Q_M (Wm^{-2})
North-facing	**Fortuna**	0.78	-2.6	-4.0	-12.2	28.5	2.6	36.3	-45.5	**9.7**
	König	0.77	-1.9	-4.0	-25.2	42.6	2.7	41.5	-54.0	**7.6**
	Neumayer	0.78	-2.9	-4.8	-26.3	35.4	2.7	38.1	-46.2	**3.8**
	Geikie	0.78	-3.2	-5.0	-37.6	34.4	2.4	35.6	-40.1	**-5.3**
	Lyell	0.77	-1.9	-4.5	-44.3	48.4	2.8	39.9	-52.8	**-6.0**
	Hamberg	0.78	-3.6	-6.0	-42.8	47.5	2.3	38.3	-54.4	**-9.2**
	Harker	0.78	-5.3	-7.3	-34.3	35.1	1.9	37.8	-49.7	**-9.3**
	Nordenskjöld	0.78	-3.2	-5.7	-36.1	44.1	2.5	39.2	-54.0	**-4.3**
South-facing	**Kjerulf**	0.79	-5.4	-6.6	-5.6	8.9	2.0	30.8	-32.3	**3.9**
	Christophersen	0.79	-5.8	-7.1	-5.6	9.7	2.0	30.4	-33.0	**3.4**
	Henningsen	0.78	-3.9	-5.6	-12.0	20.4	2.4	30.8	-34.0	**7.6**
	Helland	0.78	-4.2	-6.4	-20.6	30.2	2.2	33.7	-40.5	**5.1**
	USH1	0.79	-6.5	-8.4	-17.5	26.6	1.6	35.3	-46.2	**-0.2**
	Reusch	0.79	-6.1	-7.9	-14.0	21.2	1.8	34.0	-43.0	**0.1**

Table 6.3 – *Annual mean albedo, temperatures and surface energy balance components for each of the 14 glaciers, September 2011 – August 2012.*

To further uncover the impact of föhn across South Georgia, Figure 6.9 shows the sensible heat flux, latent heat flux, and incoming solar and longwave radiation anomalies (from the annual mean) for all föhn events from the WRF model over the innermost (0.9km resolution) WRF domain.

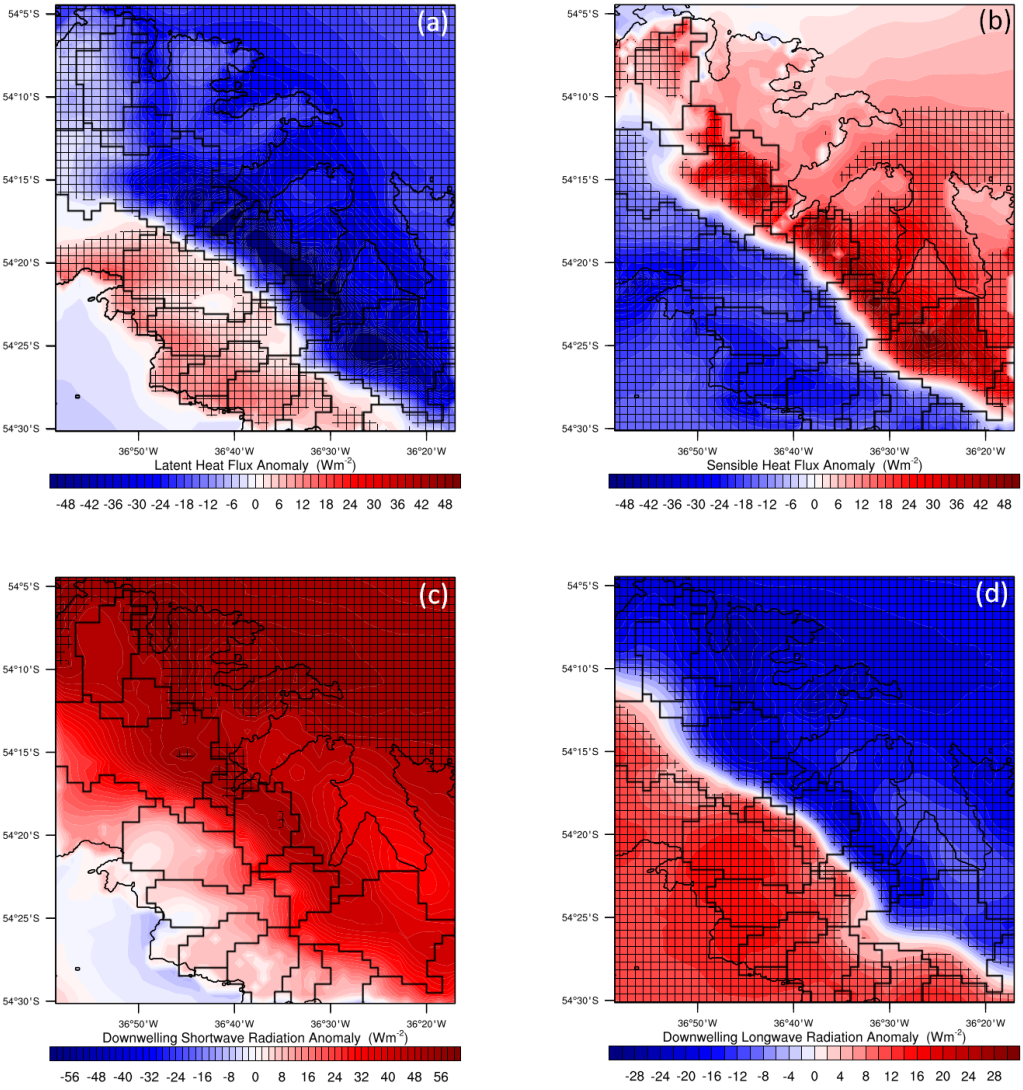

Figure 6.9 – *Panel (a) latent heat flux föhn anomaly, panel (b) sensible heat flux föhn anomaly, panel (c) incoming solar radiation föhn anomaly, and panel (d) incoming longwave föhn anomaly. All anomalies are expressed from the annual (September 2011 – August 2012) mean. Hatching indicates anomalies are statistically significant at the 95% ($p \leq 0.05$) confidence level. The 14 glacier catchments are also plotted.*

The impact of föhn on the surface energy balance is clear. The negative and positive latent and sensible heat flux anomalies (respectively) are a direct consequence of leeside surface warming and drying (as previously seen in Figure 6.7). The föhn effect acts to increase evaporation of water from the surface and thus increase the flux of

latent heat flowing from the surface to the atmosphere (< -20 Wm^{-2}, Figure 6.9(a)), and the warming increases the flux of sensible heat from the atmosphere to the surface on the leeside of South Georgia (> +15 Wm^{-2}, Figure 6.9(b)), particularly over the north-facing glaciers. The strong positive incoming solar radiation anomaly in the lee also indicates clear conditions and this is similarly reflected in the negative incoming longwave radiation anomalies (Figure 6.9(c) and (d)). The solar radiation anomalies on the southwest side of the mountains and upstream of South Georgia are near-zero or negative, generally indicating cloudier conditions. This is also reflected in the positive longwave radiation anomalies across the southwest side of South Georgia.

Despite these rather striking asymmetrical anomalies in the individual components, when the net surface energy balance (Q_M) across the island is calculated, the model indicates that the energy available for warming/melt over north-facing glaciers decreases during föhn (Figure 6.10). Over the north-facing glaciers, föhn flow causes surface warming and drying (Figure 6.7), and is associated with reduced cloud cover. Therefore, the sensible heat flux becomes more positive (i.e. heat is flowing from the atmosphere to the surface), and the latent heat flux becomes more negative (i.e. moisture transport into the atmosphere) (Figure 6.9). The net turbulent flux tends to become more positive, especially at low elevations, and this is primarily driven by a more positive sensible heat flux in response to föhn acting to warm the surface. Additionally, Q_N is also more strongly negative relative to the annual mean, indicating an energy deficit with more energy leaving the surface of north-facing glaciers than going into them. This, overall, drives a net negative surface energy balance during föhn for the majority of the north-facing glaciers (Figure 6.10). In contrast, on the southwest side of South Georgia, föhn causes near-surface cooling (Figure 6.7) which is also accompanied by an enhancement of cloud cover. Therefore, the sensible heat flux becomes more negative, and the latent heat flux becomes more positive (Figure 6.9). This causes the net turbulent fluxes to become more negative or near-zero across all elevations (when compared to the annual mean), which is unsurprising since föhn acts to cool the south-facing glaciers. Additionally, Q_N becomes more positive during föhn, resulting in an energy gain, which subsequently drives a positive surface energy balance (Figure 6.10). Therefore, the south-facing glaciers have a basin-wide positive

net surface energy balance, while the north-facing glaciers generally have a basin-wide negative net surface energy balance, during föhn conditions.

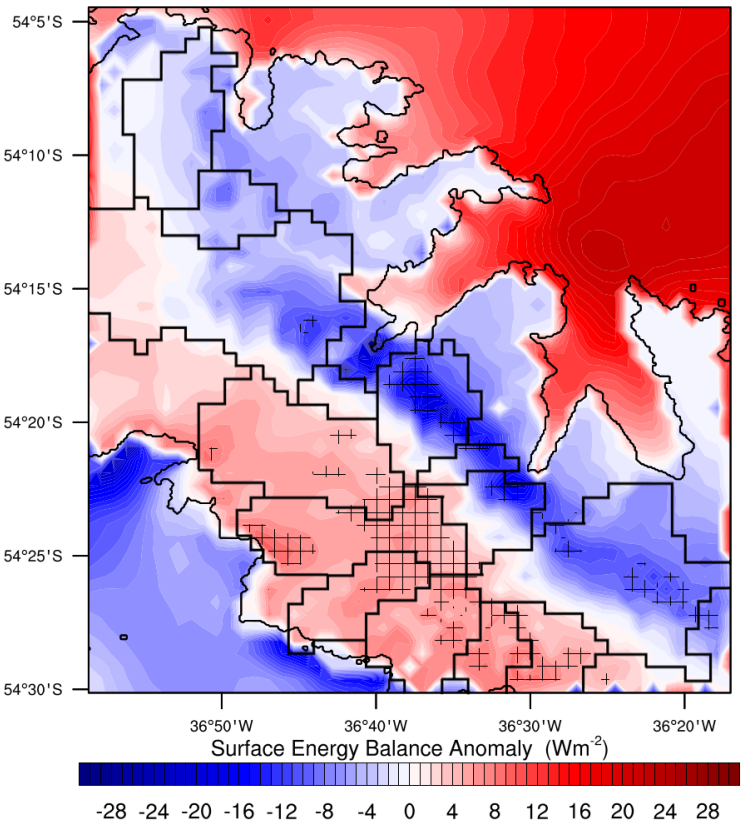

Figure 6.10 – *Surface energy balance anomaly (expressed from the annual mean). Hatching indicates anomalies are statistically significant at the 95% ($p \leq 0.05$) confidence level. The 14 glacier catchments are also plotted.*

Despite this, much of the impact of föhn on the net surface energy flux (Figure 6.10) is not statistically significant at the 95% confidence level. The WRF model calculations for the ground, latent and sensible heat fluxes are dependent on the chosen parameterisation of boundary layer, turbulence and surface processes, as well as near-surface temperature and humidity. Therefore, the model results for the surface energy balance are very sensitive to the way in which the model is configured. In the case studies presented in Chapter 4 and the validation of WRF and the surface AWS observations in Chapter 5 (section 5.3) it was shown that relative humidity is especially poorly reproduced at King Edward Point. Rapid evaporation is driven by the very low humidity of föhn winds that descend the mountains onto the northeast coastline of South Georgia. If relative humidity and/or temperature is poorly reproduced in the WRF model, then so is water vapour content, and thus the ability of

föhn winds to evaporate water from the surface of South Georgia's glaciers. Without further observations and sensitivity simulations with the WRF model, the true surface energy balance of the glaciers of South Georgia remains largely ambiguous. The reliability of the calculated surface energy balance is discussed in section 6.6.

6.5.4 ... the Surface Mass Balance?

Figure 6.11 shows the annual and seasonal net mass balance, along with the annual and seasonal net precipitation accumulation and net water equivalent ablation, across the island for the September 2011 – August 2012 period. Figure 6.11 shows that accumulation and ablation happen in clearly distinguished seasons on South Georgia. Ablation occurs throughout the year at low elevations, but substantial ablation (>0.5 m w.e.) begins in October on South Georgia, and ends by April. Accumulation occurs throughout the year (as previously seen at a regional scale in Figure 5.8), with heavy precipitation over the highest mountains of the island. Net annual precipitation accumulation at Mount Paget is 16.0 m w.e (Figure 6.11). In winter, snowfall makes a positive contribution to the mass balance, and ablation across the entire island is reduced to less than 0.1 m w.e. In summer, ablation acts to balance accumulation, and a visible equilibrium line spanning a wide altitudinal range can be seen across the island. The maritime climate of South Georgia also leads to strong altitudinal glacier mass balance gradients. Over one year, there is net loss of mass at glacier termini, and net gain at glacier heads. Since the north-facing glaciers are generally wider and less steep than the south-facing glaciers, an asymmetrical annual surface mass balance develops (Figure 6.11).

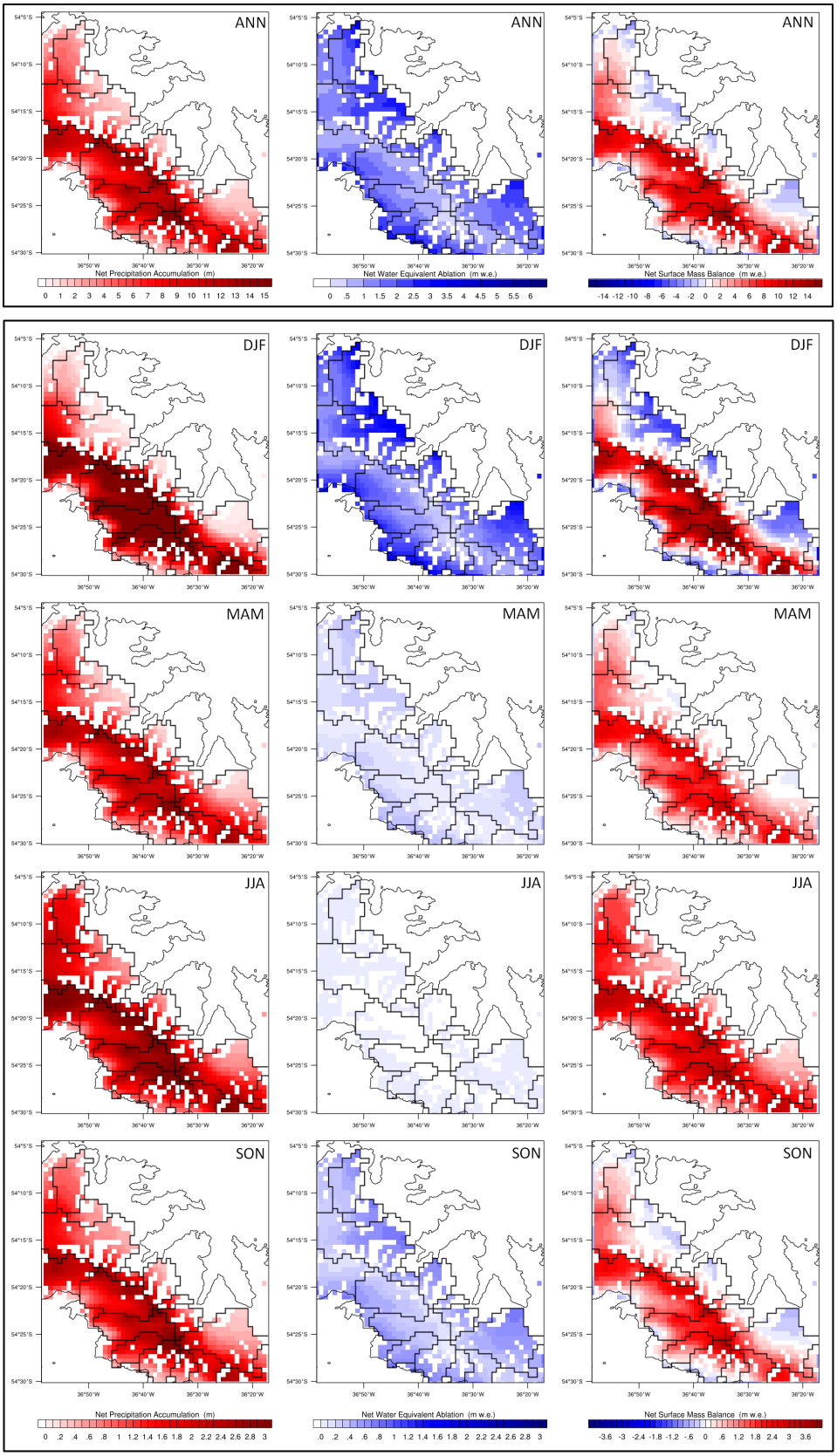

Figure 6.11 – *Annual and seasonal net precipitation accumulation (left), net water equivalent ablation (middle), and net surface mass balance (right) across South Georgia, for the September 2011 – August 2012 period.*

Since the mass balance of South Georgia depends on accumulation and ablation, it can be directly influenced by the föhn effect via above freezing temperatures over glacier surfaces, thus promoting surface ablation. Figure 6.8 has already shown that during föhn, the number of 0ºC days increases over the northeast side of South Georgia. As a consequence of this, föhn conditions ought to increase surface melt over the north-facing glaciers of the island. Therefore, the change in mass of glaciers can be considered as an indicator of climatic variation as a consequence of the föhn warming process. The cumulative föhn precipitation accumulation, water equivalent ablation, and net surface mass balance across the island of South Georgia is shown in Figure 6.12.

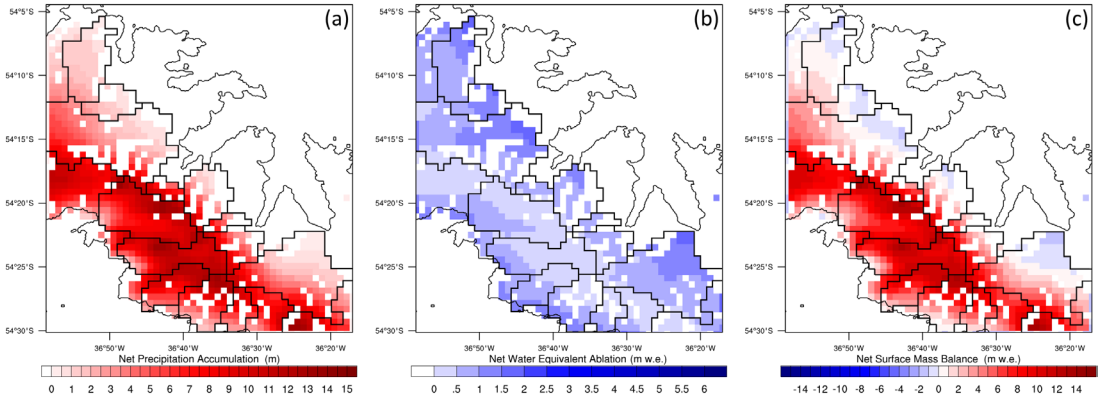

Figure 6.12 – *Net precipitation accumulation (panel (a)), net water equivalent ablation (panel (b)), and net surface mass balance (panel (c)) across South Georgia during modelled föhn times (2894 hours) between September 2011 and August 2012.*

Immediately apparent is that the pattern of accumulation, ablation and net surface mass balance are similar to the annual net values in Figure 6.11. However, during föhn flow, the asymmetry of the net values is much more pronounced. During föhn, heavy precipitation (>5 m w.e.) occurs on the southwest side of South Georgia, and this is associated with the thermodynamics of föhn flow over the island (see section 1.6.2.1). Net precipitation on the northeast of South Georgia decreases with increasing distance from the main mountain chain. Over the north-facing glaciers, especially at their termini, there is a clear band of net negative surface mass balances (~-2 m w.e.), and ablation reaches 3 m w.e. at the termini of the north-facing glaciers (Figure 6.12(b) and (c)). There are no net negative mass balance grid cells over any of the south-facing glaciers of South Georgia during föhn (Figure 6.12(c)). This emphasises that net mass loss only occurs at the termini of the north-facing glaciers during föhn flow.

The annual and föhn net surface mass balance for each glacier basin was calculated, and are shown in Table 6.4. For comparison, an annual equivalent föhn net surface mass balance was calculated, whereby:

$$Equivalent\ Annual\ Surface\ Mass\ Balance\ for\ Föhn = Föhn\ Net\ Surface\ Mass\ Balance \times \frac{365}{\left(\frac{Number\ of\ föhn\ hours}{24}\right)}$$

	Glacier	Annual Net Surface Mass Balance (m w.e.)	Equivalent Föhn Net Surface Mass Balance (m w.e.)	Difference (±m w.e.)
North-facing	**Fortuna**	2.0 m w.e.	1.5 m w.e.	-0.5 m w.e.
	König	1.0 m w.e.	1.2 m w.e.	+0.2 m w.e.
	Neumayer	3.1 m w.e.	8.8 m w.e.	+5.7 m w.e.
	Geikie	6.9 m w.e.	22.4 m w.e.	+15.5 m w.e.
	Lyell	2.9 m w.e.	9.7 m w.e.	+6.8 m w.e.
	Hamberg	4.8 m w.e.	13.3 m w.e.	+8.5 m w.e.
	Harker	6.7 m w.e.	17.9 m w.e.	+11.2 m w.e.
	Nordenskjöld	3.5 m w.e.	10.0 m w.e.	+6.5 m w.e.
South-facing	**Kjerulf**	8.3 m w.e.	26.3 m w.e.	+18.0 m w.e.
	Christophersen	9.0 m w.e.	28.5 m w.e.	+19.5 m w.e.
	Henningsen	6.1 m w.e.	28.5 m w.e.	+22.4 m w.e.
	Helland	5.3 m w.e.	17.6 m w.e.	+11.5 m w.e.
	USH1	6.7 m w.e.	20.6 m w.e.	+13.9 m w.e.
	Reusch	6.7 m w.e.	20.6 m w.e.	+13.9 m w.e.

Table 6.4 – *The annual net and equivalent annual föhn net surface mass balance for each glacier. Values are presented as water equivalent melt accumulated over a year.*

The aggregate annual net mass balance for South Georgia's glaciers appears to have been positive during the September 2011 – August 2012 period (Table 6.4). The mean annual net mass balance for all north- and south-facing glaciers is 3.9 m w.e per year and 7.0 m w.e. per year ($p < 0.05$) respectively. Therefore, the south-facing glaciers have a much larger surface mass balance compared to the north-facing glaciers. One would expect König (1.0 m w.e.) and Geikie (6.9 m w.e.) glaciers to have near-zero annual surface mass balances since they are land-terminating glaciers. Net ablation for land-terminating glaciers is usually less compared to marine-terminating glaciers, since ablation is limited to surface melting, basal melting and sublimation (Oerlemans, 2001). The large surface mass balance values are indicative of mass gain, and therefore, glacier advance in the September 2011 – August 2012 period. While these

values could be balanced by calving for the marine-terminating glaciers, it appears that these values are unrealistically large, especially given reservations regarding the reliability of the surface energy balance results. These results disagree with recent observations that the majority of glaciers are retreating, and that the glaciers on the northeast coast (north-facing glaciers) are retreating at a faster rate that the glaciers on the southwest coast (south-facing glaciers) (Cook *et al*., 2010).

The difference between the equivalent föhn and the annual net surface mass balance show that during a föhn year, föhn flow adds mass to the surface of 13 of the glaciers (i.e. there is an increase in the area of the accumulation zone). Surprisingly, the north-facing glaciers have a larger surface mass balance during föhn compared to the net annual surface mass balance, though this positive difference is somewhat smaller than it is for the south-facing glaciers. The mean difference in the net surface mass balance for all north- and south-facing glaciers is +6.7 m w.e. and +16.5 m w.e. respectively. It is interesting to note that Fortuna is the only glacier to have a smaller surface mass balance during föhn. This indicates that during föhn, föhn flow removes mass from Fortuna (thus increasing the area of the glacier's ablation zone). To explore the impact of föhn on the individual surface mass balance components further, equivalent annual föhn net precipitation, water equivalent ablation and surface mass balance anomalies (from the annual net, Figure 6.11) are presented in Figure 6.13.

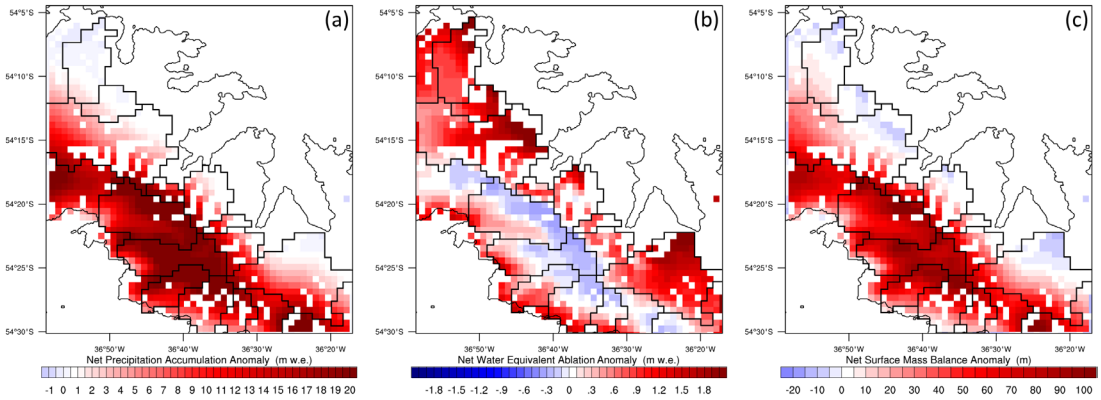

Figure 6.13 – *Equivalent annual föhn net precipitation accumulation anomaly (panel (a)), equivalent annual föhn net water equivalent ablation anomaly (panel (b)), and equivalent annual föhn net surface mass balance anomaly (panel (c)). Equivalent annual föhn anomalies are expressed from the annual net (Figure 6.11).*

Over all of the south-facing glaciers, there is a clear increase in the volume of precipitation (> +10 m w.e.) during föhn conditions (Figure 6.13(a)). There is reduced

ablation at high elevation (~-0.3 m w.e.), which is consistent with the colder and more humid anomalies over these glaciers (Figure 6.7(a) and (c)). Ablation over the southwest side of the island generally increases with proximity to the coastline. As a consequence of these anomalies, there is a clear positive basin-wide surface mass balance anomaly for all 6 south-facing glaciers (Table 6.4, Figure 6.13(c)). There are no negative grid cells of surface mass balance anomaly over any of the south-facing glaciers in Figure 6.13(c)). The north-facing glaciers show a different pattern in the surface mass balance component anomalies. Over the north-facing glaciers, precipitation accumulation is positively correlated with elevation; there is increased precipitation at high elevation (between +1 and +10 m w.e.), and this positive anomaly decreases with decreasing elevation. Since föhn ought to reduce the amount of precipitation in the lee of South Georgia, the positive anomaly over the north-facing glacier heads may be a result of the smoothed terrain in the model and/or poor physical parameterisation (see section 6.6.3). For 5 of the 8 north-facing glaciers, the precipitation anomalies at low elevation/close to their termini are approximately equal to the annual accumulation rates seen in Figure 6.11. However, for Fortuna (reaching -0.19 m w.e.), König (reaching -0.01 m w.e.) and Nordenskjöld (reaching -0.01 m w.e.) glaciers, the precipitation anomalies during föhn conditions are negative at their termini. Ablation rates are also increased across all of the north-facing glaciers; from their peaks down to their termini. This is particularly enhanced over the more gently-sloping glaciers (e.g. Nordenskjöld and Fortuna glaciers), which reach +2.7 m w.e ablation. Overall, this pattern of accumulation and ablation drives basin-wide positive surface mass balances (Table 6.4). Despite this, the surface mass balance anomaly is clearly negative at low elevation (~-13 m w.e.). This pattern emphasises that föhn does lead to asymmetrical mass loss, and this is enhanced over the low-lying, less steep northeast glaciers.

In summary, the specific surface mass balances for each of the glaciers indicates that 13 of the glaciers advances through volume gain during föhn over the September 2011 – August 2012 period. Föhn enhances this through precipitation gain in the accumulation zones of the glaciers. There is no evidence of island-wide mass or volume loss. Although the basin-wide mass balance results do not indicate asymmetrical glacial retreat during this period (see section 6.6 for further discussion),

the results do clearly highlight that there is an asymmetrical pattern of the surface mass balance; mass loss only occurs at the termini of north-facing glaciers during föhn flow. Therefore, the results do support the hypothesis that warm föhn winds do enhance melt over the north-facing glaciers. Consequently, the föhn warming process is at least partly responsible for an asymmetrical pattern in the net surface mass balance across South Georgia. It is important to note that any discrepancy in the area of the ablation and/or accumulation zones is going to give unrealistic surface mass balance results, while the absolute value of net accumulation and ablation are easily masked by errors in the modelled precipitation and melt. Unfortunately, there are absolutely no recent island-wide surface observations of accumulation or ablation to verify the modelled estimates. Therefore, the reliability of these results will now be discussed in greater detail in the following section.

6.6 Discussion

There can be little doubt that a föhn-mass balance link exists, and that it is the geometric configuration of each glacier, and their link to the past climate, which drives current accumulation and ablation rates on South Georgia. Clearly, the response of the glaciers on South Georgia can be related to the direct effects of föhn warming. Based upon these results, an enhancement of the föhn warming process (either in frequency or in intensity) would lead to further asymmetrical changes in the regional climate of South Georgia. However, the model results presented here give unrealistically large net surface mass balances. The model results also indicate an increase in the surface mass balance over 13 out of 14 glacier basins studied, including 7 of the 8 north-facing basins (Table 6.4). Therefore, the surface mass balance results do not appear to support the original hypothesis that föhn events are responsible for asymmetrical *basin-wide* glacial retreat. Despite this, the föhn effect is clearly responsible for the *asymmetrical* regional pattern of the climate of South Georgia. There is a very clear signal in the near-surface meteorology of South Georgia, and this is consistent throughout the results. Föhn acts to warm and dry the northeast coast (Figure 6.7), along with causing positive sensible heat fluxes and negative latent heat fluxes (Figure 6.9) which direct heart towards the surface and drives evaporation over north-facing glaciers. Föhn is also responsible for an increase/decrease in 0^{o}C days over northeast/southwest South Georgia (Figure 6.8). However, when the surface mass balance for each glacier basin

is calculated, the signal related to the föhn effect becomes more ambiguous. Despite the large positive surface mass balance results, it does not mean the original hypothesis is wrong. A problem arises when calculating the surface mass balance largely because the input (precipitation) to glaciers and output (ablation) from glaciers are both large numbers (e.g. Figure 6.11) while the differences between them (net mass balance) are small, often an order of magnitude less. Therefore, the absolute values of net mass balance for individual glacier basins are easily masked by errors in the modelled variables. The reliability of these modelled estimates will now be discussed in greater detail.

6.6.1 A Brief Climatological Summary of September 2011 – August 2012

We have previously seen that South Georgia's climate exhibits inherent inter-annual variability (see e.g. Figure 1.4 and Figure 3.10). In order to put the meteorological conditions at King Edward Point and the island-wide surface mass balance estimates of the September 2011 – August 2012 period into a longer-term context, a brief climatological summary of the period is provided. The temperature of the September 2011 – August 2012 period was warmer (2.87°C, $\sigma = 4.5$) than the September through August 2003 – 2012 mean (2.63°C, $\sigma = 3.4$). An independent-samples t-test was conducted to compare these means; there is a significant difference in the mean September 2011 – August 2012 period at King Edward Point ($p < 0.01$) compared to the 10 year mean. The near-surface air temperature at King Edward Point was above average throughout all seasons, except austral autumn which was 0.7°C cooler than average. The austral spring season was 0.8°C above average; the greatest of all four seasons. In the 10 year record of temperature at King Edward Point, this September – August period was the fourth warmest. Using monthly mean temperatures dating back to 1905 from the Grytviken and King Edward Point sites, this September – August period was also the fourth warmest on record, and 1.0°C warmer than the average. It is important to note that although the four warmest September – August periods were all in the 21st century, there is a large amount of missing data in the 1980s and 1990s (see section 2.2). The maximum temperature reached during this period was 19.0°C (which occurred during a föhn event), while the minimum temperature reached was -9.4°C. Unsurprisingly, the temperature distribution at King Edward Point is also positively skewed, with large warm anomalies being more common than large cold

anomalies. The skew in the observed daily mean temperatures between September 2011 and August 2012 is 0.07 (standard error = 0.13). This compares to the 10 year (September – August) daily mean of 0.04 (standard error = 0.04). This skew in the temperature data is expected since föhn dominates the weather at King Edward Point, which thus frequently results in temperatures rising above the mean. Wind speed was also above average (9.16ms^{-1}, σ = 6.7) at King Edward Point compared to the longer-term mean (8.88ms^{-1}, σ = 6.7). The maximum wind speed recorded in the AWS observations (39.0ms^{-1}) did not occur during a föhn event. Unfortunately, precipitation measurements at King Edward Point are only available since February 2010, and as such, there are not enough observations available to compare against a longer time period. In summary, therefore, the September 2011 – August 2012 period at King Edward Point was one of the warmest and windiest on record. As such, we might expect the WRF model to have produced larger positive föhn ablation anomalies (see Figure 6.12) along the north-eastern side of the island during this particularly warm period. Since this is not the case, errors in the model which likely influence the accuracy and reliability of these modelled surface mass balance estimates will now be discussed.

6.6.2 The Role of Temperature Errors in South Georgia's Surface Mass Balance

One of the major causes of the unrealistically large positive net surface mass balance estimates is likely an artefact of the negative bias in the modelled 2-m air temperature (see Chapter 4 and Figure 5.2). It has already been established that the WRF model exhibits a clear negative cold bias throughout the year, along with less variability in air temperature, at King Edward Point (section 5.3). In comparison to the observed skew (0.07) in the daily mean air temperatures at King Edward Point, the modelled skew in the daily mean temperatures is just 0.01 (standard error = 0.13) during this period. As such, the model simulates less frequent large warm anomalies compared to the observations. This negative temperature bias, as a consequence, has the potential to primarily translate into reduced rates of evaporation and melt (ablation) across South Georgia's glaciers.

The modelled temperature distribution with height also has potential to directly influence accumulation across South Georgia. In particular, the modelled elevation of

the zero-degree isotherm for individual basins affects both the precipitation phase (liquid or solid) and the sign of the sensible heat flux (i.e. energy gain via condensation or energy loss via evaporation or sublimation) at the surface of a glacier. Since the hypsometries of all 14 glaciers intersect this isotherm (not shown), it is imperative that the WRF model correctly simulates the elevation of the zero-degree isotherm. Since it has been shown that there is a cold bias at King Edward Point, this may correspond to an island-wide reduction in the height of the zero-degree isotherm compared to reality. This has further important repercussions on the surface mass balance via the modelled equilibrium line altitude. The equilibrium line marks the position where, over a period of one year, accumulation of precipitation is exactly balance by ablation (Oerlemans, 2001). Therefore, there is a close connection between the equilibrium line altitude and local climate; particularly winter precipitation (accumulation) and summer air temperatures (ablation) (Ohmura *et al*., 1992; Braithwaite, 2008). The equilibrium line altitude is sensitive to perturbations in either of these two variables, and the line will rise in elevation in response to decreasing accumulation and/or increasing frequency of positive air temperatures, and vice versa. As such, if the height of the accumulation and ablation zones is unrealistic (which can either be caused by a bias in the air temperature and/or an incorrect representation of topography in the WRF model), then it alters the liquid-frozen precipitation ratio at the elevation of the equilibrium line altitude. Clearly, misrepresenting high-elevation temperatures can greatly affect precipitation timing and magnitude. Furthermore, this misrepresentation can feedback into precipitation accumulation from the alteration of the model's albedo, slope aspect and surface energy balance.

As such, one of the leading errors in the estimated surface energy and mass balances for South Georgia's glaciers can be attributed to the negative 2-m air temperature bias in WRF, which in turn affects the equilibrium line altitude and the zero-degree isotherm height, and hence the accumulation and ablation rates across the island's glaciers. The bias in temperature can be attributed to the representation of the South Georgia's surface energy balance and the errors which emanate from the chosen model physics, planetary boundary layer and dynamics schemes (see section 6.6.4). The WRF model physics are complex, and determining optimal parameters which

substantially reduce the air temperature bias for South Georgia is still in need of future research (see section 4.7.7).

6.6.3 The Role of Precipitation Errors in South Georgia's Surface Mass Balance

For an accurate representation of South Georgia's surface mass balance, it is also important that precipitation over the island is simulated correctly. However, it has previously been shown that the regional topography strongly controls accumulated solid and liquid precipitation (Figure 5.8). The calculated surface mass balances for individual glacier basins is sensitive to the magnitude of snow accumulation, and therefore, it is problematic if the modelled precipitation accumulates in the wrong catchments. Errors in the magnitude of precipitation accumulation are exacerbated by any incorrect representation of individual glacier catchments (e.g. in extent and/or morphology) and topography in the WRF model. Any small discrepancy in the area of the ablation and/or accumulation zones is going to give unrealistic surface mass balance results. If precipitation accumulation over the island of South Georgia is not accurately captured and/or the size and area of individual glacier catchments are incorrectly represented, then precipitation will accumulate in the wrong catchment, subsequently giving unrealistic individual net surface mass balances.

Modelled precipitation accumulation is dependent upon the individual pre-selected WRF parameterisations and microphysics schemes, and precipitation biases in mountainous regions with the WRF model have previously been well documented (see e.g. Heikkilä *et al*., 2010; Argüeso *et al*., 2012; Chubb *et al*., 2012; Duethmann *et al*., 2013). For instance, Heikkilä *et al*. (2010) found significant biases in precipitation accumulation with WRF over Norway, especially at high elevation. Overall, WRF simulated too small precipitation accumulation across the mountains of Norway, and that too much precipitation accumulated in the lee of the mountains. This was attributed to the model not accurately capturing orographic uplift at the spatial resolution of the model (10km), as well as uncertainties in the precipitation field in the forcing (ERA-40) data. The WRF model has also been tested across numerous other mountain ranges where good mass balance data (e.g. precipitation and/or ablation measurements), along with high spatial and temporal resolution temperature and humidity observations, exists (see e.g. Caldwell *et al*., 2009; Favier *et al*., 2009;

Maussion *et al*., 2014; Schaefer *et al*., 2014). Such studies have been met with mixed success; Schaefer *et al*. (2014) found that the WRF model accurately reproduced the surface mass balance over the Southern Patagonia Icefield, Maussion *et al*. (2014) overall found that the modelled precipitation was also close to their observations made over the Himalayas, while both Caldwell *et al*. (2009) and Favier *et al*. (2009) found strong over-predictions of precipitation at high elevations resulting in unrealistic surface mass balances.

Unfortunately, precipitation accumulation measurements from South Georgia are severely (temporally and spatially) lacking (Pepper, 1954; Mansfield & Glassey, 1957; Shanklin *et al*., 2009), even more so over the island's glaciers (e.g. Smith, 1960; Hogg *et al*., 1982; Hayward, 1983; Clapperton *et al*., 1989a). To get a full appreciation of accumulation rates across South Georgia, future observational campaigns and long-term monitoring is required. This will also aid in future model validation, which will help determine whether or not the modelled precipitation accumulation over South Georgia is unrealistic. Since the analyses in Chapter 4 and Chapter 5 show that the model underestimates 2-m relative humidity at King Edward Point (see e.g. section 5.3), unrealistic precipitation rates may be related to the modelled moisture over this region. Unrealistic precipitation accumulations could be because most of the physics parameterisations in WRF were originally developed for a coarser resolution. At high-resolutions there is less topographic smoothing (i.e. higher elevations are preserved) which has the potential to increase orographic effects, thus making it possible for higher precipitation amounts to exist. Previous dynamical downscaling studies have similarly shown that positive precipitation biases in WRF are either inherited from the driving reanalysis dataset or contributed by WRF itself due to the physics parameterisations (see e.g. Janowiak *et al*., 1998; Caldwell *et al*., 2009; Hahn & Mass, 2009; Jin & Wen, 2012). Determining whether using alternative physics schemes would produce a more accurate description of the surface mass balance is challenging. Most likely, the potential errors in precipitation accumulation in the model are from a combination of sources, including the boundary conditions, the choice of physics and dynamic parameters, and the characterisation of the land surface and glacier areas. The only way to explore this further is through very high-resolution model simulations,

along with an intensive meteorological observational programme, across South Georgia.

6.6.4 The Role of Energy Flux Errors in South Georgia's Surface Mass Balance

It is clear that many of the issues surrounding biases in temperature (which in turn influences the zones of accumulation and ablation), relative humidity, precipitation and the amount of energy available for melt and evaporation, stem from the physics schemes, the downscaling methodology and the parameter estimations. Arguably therefore, the main uncertainty with the calculated surface mass balances is a consequence of the model's errors and biases in the representation of the surface energy fluxes (particularly net longwave and shortwave radiation). By comparing measurements of the surface energy balance with observations on the Larsen C Ice Shelf (Antarctic Peninsula), King *et al*. (2015) found that the WRF model had significant positive biases in the net solar radiation, together with a corresponding (but smaller) negative bias in net longwave radiation. This resulted in an excessive amount of energy available for heating and melting the surface when compared to observations. Biases in modelled solar and longwave radiation were subsequently related to the model simulating too little cloud cover (or clouds that were too optically thin). Generally, the WRF model does not resolve clouds appropriately (especially at high southern latitudes), meaning that incoming solar and longwave radiation are incorrectly modelled. This can have a major impact on the surface energy balance calculations, and thus upon the modelled temperature, humidity and precipitation fields, which in turn also controls the surface mass balance for individual glacier basins. This has also been documented before with other WRF modelling studies in similarly glaciated and mountainous regions. Studies by Solomon *et al*. (2009), Wilson *et al*. (2012), Bromwich *et al*. (2013), Schaefer *et al*. (2013), Valkonen *et al.* (2013) and Aas *et al*. (2015) have all shown how biases in solar and longwave radiation are related to the parameterisation of cloud microphysics with the WRF model, typically resulting in considerable biases in the near-surface meteorology on seasonal and shorter time scales. Consequently, these studies have illustrated that deficiencies in how the WRF model parameterises cloud processes can be attributed to biases in the modelled surface energy balance. It is clear, therefore, that the cause of biases in the modelled surface energy balance for South Georgia's glaciers, as well as the associated

topographical uncertainties with glacier geometries, should be evaluated carefully before interpreting the modelled surface mass balance estimates.

6.6.5 Summary

In summary, the results of the annual net and equivalent föhn surface mass balance provide the very first basic insight into the surface energy fluxes of the glaciers of South Georgia. While the results do not support the hypothesis that the north-facing glaciers are retreating at a faster rate because of the föhn effect, it should be noted that the absolute values of the modelled melt rates may be significantly biased and should be interpreted with caution. Given the original hypothesis of this work, the results appear to underestimate surface heating and melting during this period (and during föhn conditions) over the glaciers of South Georgia. The unrealistically large positive net surface mass balances are likely an artefact of the modelled temperature and humidity fields and/or as a result of an inadequate parameterisation of cloud microphysical processes. Since the model underrepresents temperature and relative humidity at King Edward Point (see Chapter 4 and Chapter 5) we can assume that, regionally, WRF also underrepresents the energy available for heating and melting the ice surface during föhn conditions. Despite this, the föhn effect is clearly responsible for the asymmetrical regional pattern of the climate of South Georgia. A surface signal is apparent over the north-facing glaciers, and this is significantly different to the conditions of the south-facing glaciers (i.e. mass loss occurs at the termini of north-facing glaciers during periods of föhn). However, the absolute extent to which föhn events cause surface melt remains uncertain. The only way this can be successfully answered is through observational programmes across South Georgia, as well as extended very high-resolution simulations (to fully replicate glacier geometries in the model) testing the modelled mass balance to the sensitivity of the microphysics schemes. There is a clear need for future improvements in the way we model the regional climate of South Georgia.

6.7 Conclusion

The results from this chapter present a new insight of the seasonal thermal and energy regimes of glaciers on the island of South Georgia. Understanding the energy and mass balance of glaciers on South Georgia is essential to understand the sensitivity of

glaciers to Southern Hemisphere atmospheric circulation changes, and to understand how glaciers respond to the föhn warming process. The model simulations provide a detailed description of the spatial distribution of the impacts, which show marked variations over very short distances. By defining the outlines for numerous individual ice masses on South Georgia, the new inventory of glacier basins has provided a means for glacier-by-glacier mass balance exploration across the island. This work adds to the limited body of research that highlights the vulnerability of the ecology, hydrology and climatology of South Georgia and the surrounding area to climate change.

The results from this chapter further show that there is a clear and significant divide between the climates of the north-eastern and the south-western sides of South Georgia, and that topographic modification is responsible for these spatial patterns. Though a narrow mountain range, the difference in climate across South Georgia is maintained by the effect of the high mountains on the atmosphere. Since föhn flow is so frequent, these events have an important role to play in shaping the asymmetrical pattern of the regional climate of South Georgia. The impact of föhn flow on weather is expressed by anomalously warm temperatures, dry surface conditions, and strong winds across the lee of South Georgia. These results also give new insights into meteorological and hydrological conditions of South Georgia and their controls on the surface glacier energy and mass balances. Aggregate mass balances of South Georgia's glaciers appear to have been positive during the September 2011 – August 2012 season (Table 6.4), with south-facing glaciers appearing to thicken the most. Positive mass balances would appear to be driving a cumulative island-wide glacial advance during this period. These rates exhibit large cross-barrier variations. It is beyond the scope of this study to explore whether this is a true positive trend, or a systematic bias within the WRF model's representation of accumulation and ablation rates. The uncertainty of the calculated energy and mass balance depends critically on the quality of the WRF model output (see e.g. Bromwich *et al*., 2013; Valkonen *et al*., 2013; King *et al*., 2015). Although the results presented here provide useful information on the spatial pattern of the surface energy balance, the absolute values of ablation should be interpreted with caution. To obtain a full appreciation of the surface mass balance across South Georgia, and how precipitation and ablation respond to the föhn warming process, additional *in situ* surface observations along with high-

resolution atmospheric model simulations (for periods longer than 10 years) are required.

Fundamentally, the results from this chapter have shown that the föhn effect has a very important and significant impact on the regional climate of South Georgia. What is clear is that the föhn effect does lead to an asymmetrical pattern in the regional climate of South Georgia, which subsequently controls the asymmetrical pattern of accumulation and ablation. During föhn, ablation is enhanced over the northeast side of South Georgia resulting in net negative surface mass balances at the termini of the north-facing glaciers. Föhn events thus remove mass from the termini of these glaciers (most notably Fortuna glacier), even though the basin-wide aggregate föhn mass balances indicate mass gain. In addition to this, Figure 6.8 shows an increase in the fraction of time that each grid point is $\geq 0^{o}$C for all north-facing glaciers during föhn conditions. This indicates increased melt potential during föhn, since these results are not sensitive to the biases in the WRF surface energy balance components. There a clear asymmetrical signal as a consequence of the föhn effect in the model results, supporting the hypothesis that föhn is (at least partly) responsible for the observed asymmetrical pattern of climate and glacial retreat. Since the mountains of South Georgia act as substantial barriers against the prevailing westerly winds, an asymmetrical regional climate develops. Therefore, the results of this chapter support the idea that an enhancement of the föhn warming process through stronger surface westerlies could drive more intense melt over the north-facing glaciers. Although the calculated net surface mass balance results do not agree with the observations of Cook *et al*. (2005), calculating melt rates and surface energy balances over many seasons and years will give a clearer picture as to why the north-facing glaciers are retreating faster than the south-facing glaciers. The results presented in this chapter imply that regional island-wide atmospheric warming is the cause of island-wide glacial retreat, while the föhn warming process, which we now know occurs approximately 30% of the time over South Georgia, enhances surface warming over the north-facing glaciers.

The glaciers of South Georgia do matter, and they have global importance. They stop the slow creep of invasive species from one catchment basin to another (Cook *et al*., 2010, SGHT, 2014). A retreating glacier on South Georgia does not just impact the island within its own catchment, but the ecology of the entire island. The continued

retreat of glaciers has potential to open up new areas of colonisation on South Georgia. This will have consequences on the breeding populations of ground- and burrow-nesting sea birds. The glaciers of South Georgia also have wider global important and interest, due to the significant contribution from melt of glaciers across the world to observed sea level rise (Church *et al*., 2013). As a consequence, the retreat of glaciers on South Georgia presents a real risk. Environmental changes will result in more habitable conditions on the island, thus providing better habitats for invasive species. The status of these glaciers is important for environmental management of South Georgia, and this work provides a better understanding of the pattern of glacier change on South Georgia.

Appendix 6A.1 – Rate of Glacial Retreat and Advance

	Glacier	Total Change (m)	Rate of Change (m per year)	Period of Available Data
North-facing	Fortuna	64.5 m	1.3 myr^{-1}	50 years
	König	-1846.1 m	-36.9 myr^{-1}	50 years
	Neumayer	-2299.4 m	-32.8 myr^{-1}	70 years
	Geikie	-1646.8 m	-32.9 myr^{-1}	50 years
	Lyell	-67.2 m	-1.3 myr^{-1}	51 years
	Hamberg	-1293.7 m	-25.4 myr^{-1}	51 years
	Harker	37.5 m	0.7 myr^{-1}	51 years
	Nordenskjöld	-746.4 m	-10.7 myr^{-1}	70 years
South-facing	Kjerulf	-495.0 m	-11.0 myr^{-1}	45 years
	Christophersen	-390.6 m	-8.7 myr^{-1}	45 years
	Henningsen	-321.7 m	-6.7 myr^{-1}	48 years
	Helland	-714.5 m	-14.9 myr^{-1}	48 years
	USH1	-351.3 m	-7.3 myr^{-1}	48 years
	Reusch	-465.0 m	-9.9 myr^{-1}	47 years

Table 6.5 – *The total change and the rate of change per year for each of the 14 glaciers. This data is originally from Cook et al. (2010).*

Appendix 6A.2 – DEM and WRF Model Glacier Areas

	Glacier	Catchment Map Area (km^2)	WRF Model Area (km^2)	Difference (km^2)
North-facing	Fortuna	57.90 km^2	63.18 km^2	5.28 km^2
	König	38.40 km^2	38.07 km^2	-0.33 km^2
	Neumayer	158.00 km^2	162.81 km^2	4.81 km^2
	Geikie	13.20 km^2	13.77 km^2	0.57 km^2
	Lyell	49.80 km^2	49.41 km^2	-0.39 km^2
	Hamberg	10.30 km^2	11.34 km^2	1.04 km^2
	Harker	31.60 km^2	33.21 km^2	1.61 km^2
	Nordenskjöld	151.90 km^2	154.71 km^2	2.81 km^2
South-facing	Kjerulf	89.00 km^2	90.72 km^2	1.72 km^2
	Christophersen	74.50 km^2	75.33 km^2	0.83 km^2
	Henningsen	33.80 km^2	34.02 km^2	0.22 km^2
	Helland	40.70 km^2	40.50 km^2	-0.2 km^2
	USH1	18.10 km^2	17.82 km^2	-0.28 km^2
	Reusch	30.70 km^2	29.97 km^2	-0.73 km^2

Table 6.6 – *Comparison between the surface area for each north- and south-facing glacier using the DEM catchment map and the areas from the innermost WRF model domain (horizontal grid spacing of 0.9km).*

Appendix 6A.3 - Mean Monthly Glacier Surface Energy Balance Components

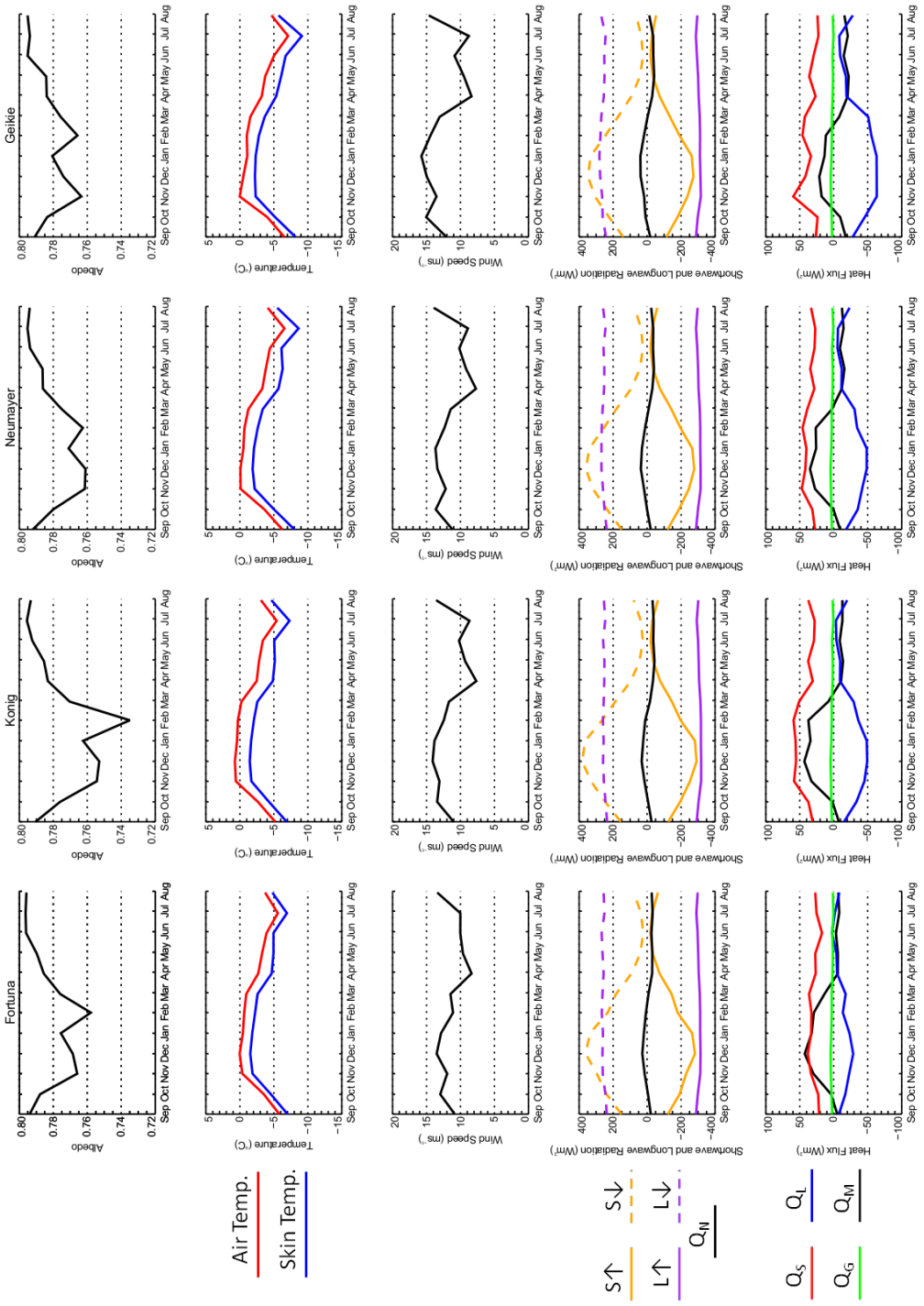

Figure 6.14 – *Mean monthly near-surface meteorology and surface energy balance components over the period 2011 – 2013 for Fortuna, König, Neumayer and Geikie glaciers.*

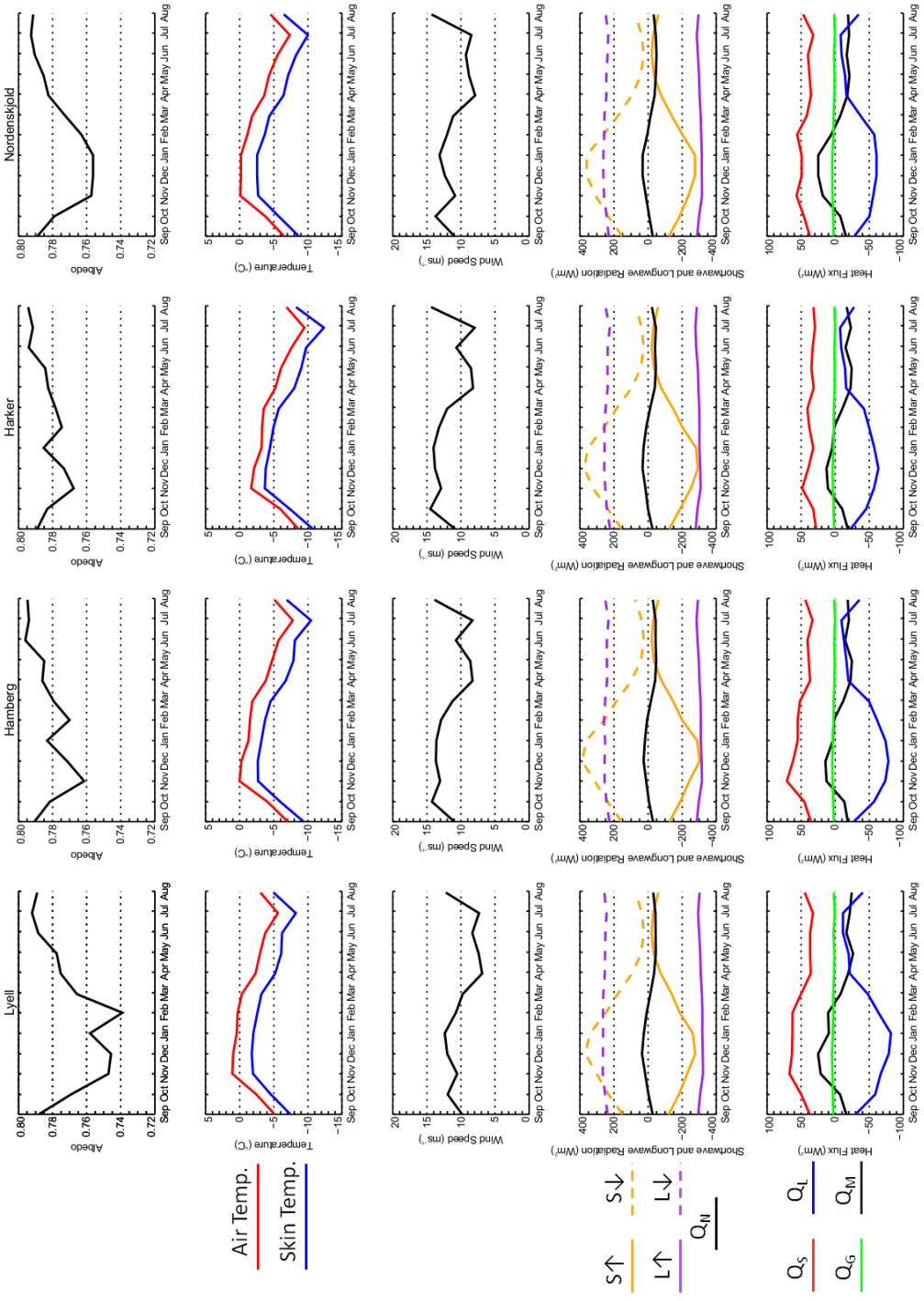

Figure 6.15 – *Mean monthly near-surface meteorology and surface energy balance components over the period 2011 – 2013 for Lyell, Hamberg, Harker and Nordenskjöld glaciers.*

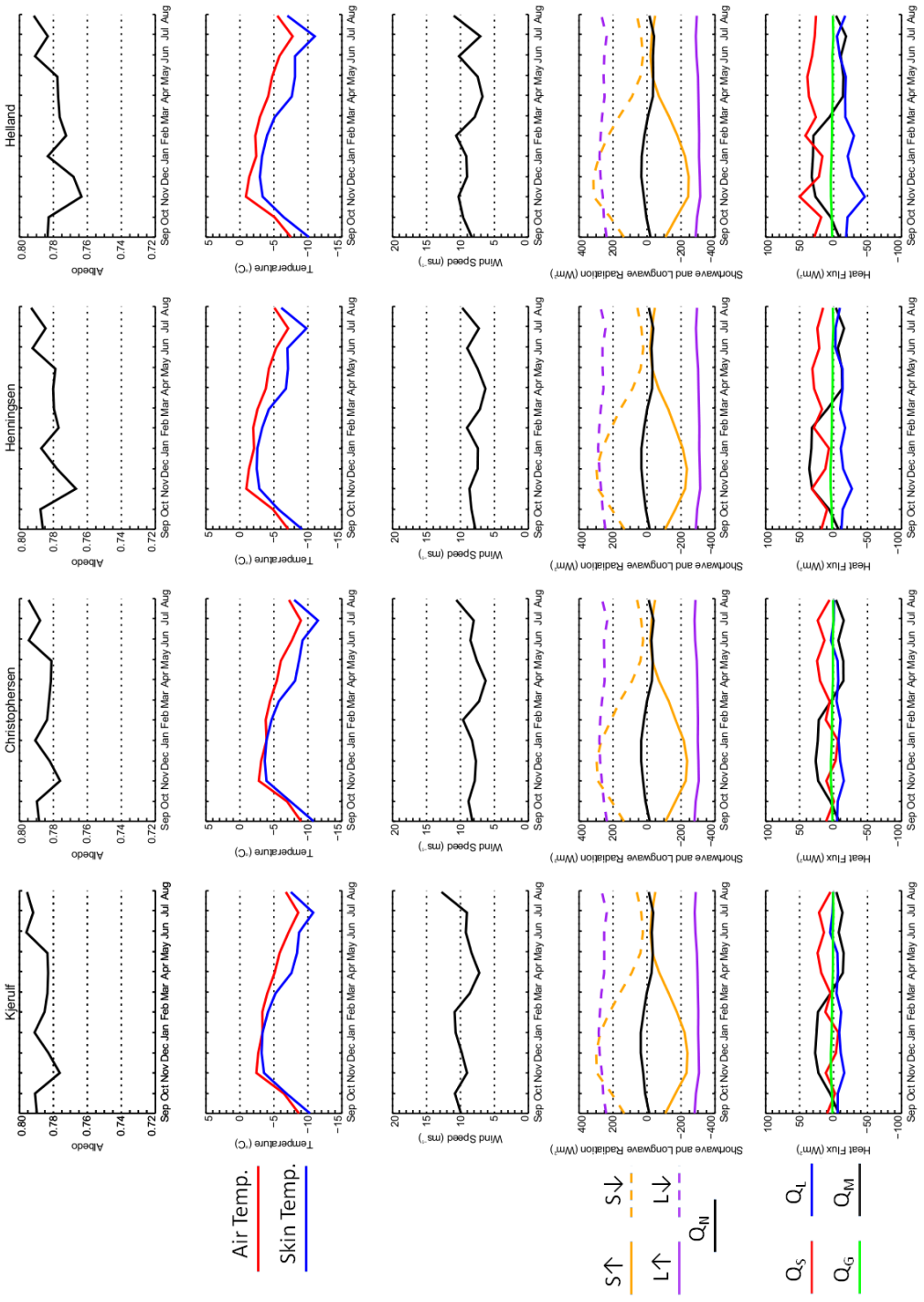

Figure 6.16 – *Mean monthly near-surface meteorology and surface energy balance components over the period 2011 – 2013 for Kjerulf, Christophersen, Henningsen and Helland glaciers.*

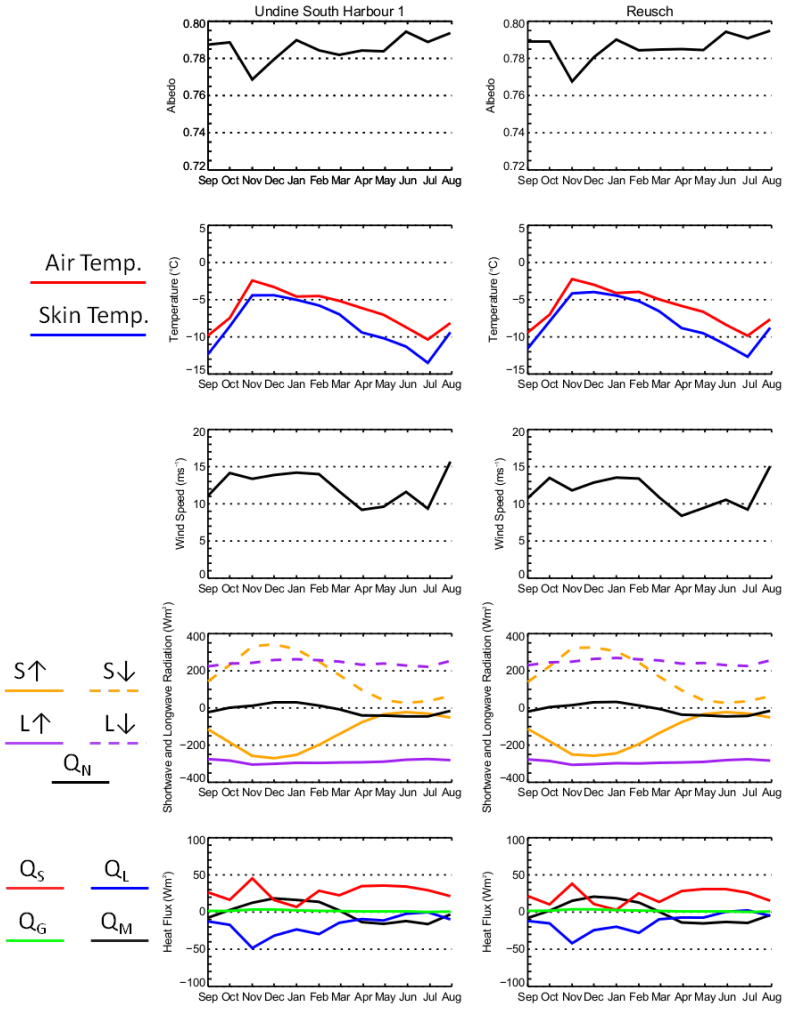

Figure 6.17 – *Mean monthly near-surface meteorology and surface energy balance components over the period 2011 – 2013 for Undine South Harbour 1 and Reusch glaciers.*

Chapter Seven: Conclusions

7.1 Introduction

The research presented in this thesis was motivated by the hypothesis that the recent asymmetrical glacial retreat on South Georgia's north-eastern coast is a consequence of the föhn warming process. Therefore, this research set out to explore the climatology of föhn events on South Georgia, how they control the regional climate, and whether they are responsible for the observed asymmetrical glacial retreat on the island. No previous studies had addressed these topics. Understanding the dynamics responsible for föhn events, the large-scale circulation patterns that support their development, and their impacts on the glaciology of South Georgia, are clearly of high interdisciplinary importance and interest. Therefore, this research aimed to answer the following questions:

- *How frequent are föhn events and what synoptic conditions are associated with föhn at King Edward Point?*
- *Can we accurately simulate weak and strong föhn flow using a state-of-the-art atmospheric model?*
- *How does the orography of the island control the regional climate of South Georgia, what is the best method for detecting föhn in the model, and how well does the model capture föhn events?*
- *What impact do föhn winds have on the regional climate of South Georgia and, in particular, on the surface mass and energy balance of its glaciers?*

The results presented in this thesis uncover a new insight into föhn events at King Edward Point, and the regional climate of South Georgia. Firstly, a unique climatology of föhn events was presented in Chapter 3. In Chapter 4, high-resolution atmospheric model simulations were presented for four different weak and strong föhn case studies. Sensitivity tests conducted as part of this chapter included varying the horizontal, vertical and topographical resolution, as well as the physics and planetary boundary layer schemes. The model simulations were verified against surface automatic weather station (AWS) observations at King Edward Point, and when possible, radiosonde and

lidar measurements from a field campaign in January 2013. These results then informed the selection of the best model set up for a regional climate study using a very high-resolution 21 month Weather Research and Forecasting (WRF) model simulation. The results of this study were then presented in Chapter 5. In Chapter 6, model output from the 21 month run was used to determine the impact of föhn on surface energy and mass balances for 14 glaciers on South Georgia. A summary of the results is now presented, and the questions first posed in Chapter 1 are revisited here. A synthesis of the findings is given in section 7.3. In section 7.4 future useful extensions to the project are proposed, and final remarks are made in section 7.5.

7.2 Summary of Findings

7.2.1 Chapter Three: A Climatology of Föhn Events at King Edward Point

The first objective of this thesis was to conduct a climatological analysis of föhn events on South Georgia, since the characteristics and frequency of events on the island had never been quantified. A technique for föhn identification using surface AWS observations, which has been used extensively across many other geographical regions (see Conrad, 1936; Osmond, 1941; Obenland, 1956; Inaba *et al*., 2002; Speirs *et al*., 2013; and many others), was used to identify föhn events which occurred at King Edward Point, during January 2003 – December 2012. Föhn events were distinguished by abrupt and sudden temperature, relative humidity and wind speed changes, and a surface wind from the direction of the main mountain range.

Analysis of the föhn climatology shows that föhn winds play a significant and important role in the overall wind and temperature regime of King Edward Point. Föhn events occur frequently at King Edward Point. Between January 2003 and December 2012, 874 föhn events were identified from the surface AWS observations. This corresponds to one event occurring approximately every four days. They have an average duration of 29 hours and 49 minutes (σ = 27.7), but ranged from as short as 40 minutes to longer than 3 days. In austral winter, föhn events can raise the near-surface air temperature above freezing. The average maximum temperature reached by all 874 events is 8.9ºC. There are occasional very intense föhn events, which are associated with anomalously extreme temperatures (reaching 23.5ºC), wind speeds (exceeding 40ms^{-1}) and relative humidities (lower than 10%). There is negligible

seasonal variation in the frequency of föhn days at King Edward Point, but there is evidence of a seasonal cycle in the intensity of föhn events. It was found that föhn events tend to be longer, with more intense temperature, relative humidity and wind speed changes during austral summer months, in comparison to those events which occur during austral winter months. It was also found that the occurrence and characteristics of föhn are strongly correlated to the large scale atmospheric circulation. Strong föhn events tend to occur when there is a large area of high pressure in the Argentine Basin of the South Atlantic Ocean, and a low pressure system located in the Weddell Sea. These features are absent during weak and non-föhn episodes. There is no significant relationship between föhn frequency or duration and the Southern Annular Mode (SAM) index.

It is important to note that the föhn climatology presented in this chapter is specific to King Edward Point, and the results do not identify föhn conditions that may occur elsewhere on the island. Therefore, the methodology used in this chapter is limited by the length of the AWS observations available at King Edward Point (10 years) as well as only having data from a single location on South Georgia. Using only AWS observations, it is not certain how many of the 874 events catalogued are true föhn events and which events are artefacts of other meteorological phenomenon, such as warm air advection (i.e. rapid warming events). In addition to this, given the relatively short length of the record analysed, no long-term assertions can be made on whether föhn events are becoming more frequent or intense at King Edward Point. In section 7.4 suggestions of how future additional meteorological observations across the island of South Georgia could help improve our understanding of the intra- and inter-annual variations in föhn frequency and intensity are made. Despite these shortcomings, the methods presented in this chapter could be applied to other short and discontinuous meteorological records to give the first fundamental insight into the climatology of föhn events, in similarly isolated locations. This chapter, therefore, successfully answers *how frequent are föhn events and what synoptic conditions are associated with föhn at King Edward Point?*

7.2.2 Chapter Four: High-resolution Weather Research and Forecasting (WRF) Simulations of Föhn Events at King Edward Point

Owing to the lack of meteorological observations across South Georgia, high-resolution atmospheric modelling over the island is needed as a proxy for observations. Atmospheric model simulations can be used to explore the characteristics, features and dynamics of South Georgia's föhn events more extensively, both spatially and temporally. Therefore, having constructed a catalogue for föhn events at King Edward Point using surface AWS observations, four representative events of varying intensities were selected for further investigation. These föhn case studies were simulated using a state-of-the-art atmospheric model (the WRF model), and the model output was validated against surface AWS observations from King Edward Point. For one of these cases (Case 1, 5 February 2013) additional atmospheric measurements (upper air radiosonde launches and lidar measurements) were also available, and this allowed a more comprehensive validation.

By validating the WRF model with available meteorological observations, Chapter 4 shows that the model can produce an accurate simulation of föhn flow. The observed flow structure and föhn dynamics in the model during each of the events is similar to that observed; near-surface wind speed and wind direction at King Edward Point are particularly well captured. However, the overall intensity of each of the events is somewhat underestimated, and this is especially true for the response in 2-m air temperature (typically 3 – 5^{o}C too cool) and relative humidity (typically 20% too dry). At a resolution of 3.3km, the mean root-mean-square errors for temperature, relative humidity and wind speed across the four case studies were 4.5^{o}C, 19.1% and 6.1ms^{-1}, respectively. Errors in these modelled meteorological variables are consistent throughout the case studies and the sensitivity simulations, highlighting that this appears to be a systematic error within WRF itself. The results from this chapter show that the agreement between the WRF model and the surface AWS observations is improved when the horizontal resolutions is better than 3.3km. The results clearly demonstrate the important role of horizontal resolution in simulating the meteorological conditions at King Edward Point. Since the four föhn case studies are better captured in domains with higher horizontal resolution (0.9km resolution), this implies that the horizontal resolution of the model is a key constraint for capturing

sufficient small-scale detail of the föhn flow at King Edward Point. However, even at high-resolution, reservations regarding the accuracy of the vertical structure of föhn flow, as well as the muted response to föhn warming and drying, should also be taken into consideration. It should be reiterated that although the WRF model and the surface AWS observations are in good agreement, there are inherent limitations in both datasets. Given the complex nature of the terrain and topography around King Edward Point, it would be naive to expect WRF to validate perfectly against the single point limited observations which are available.

From these results, the best model setup which gave the most realistic interpretation of föhn flow at King Edward Point was deduced. The various sensitivity simulations highlight that the relatively large biases in the modelled meteorological fields are exacerbated by the unresolved topography of South Georgia at 3.3km resolution. As such, these biases, particularly in 2-m air temperature and 10-m wind speed, are substantially reduced by increasing the horizontal and vertical resolution of the model, along with utilising high-resolution topographical and land surface type data sets, as well as by using a planetary boundary layer scheme that explicitly considers the effects of non-resolved topography. The results indicate that the model is largely insensitive to the choice of planetary boundary layer parameterisation, the microphysics scheme, the longwave and shortwave radiation scheme, and the land surface scheme. This suitable model configuration was subsequently used for the climatological simulation in Chapter 5.

The results from this chapter also extend our understanding of föhn dynamics over South Georgia, and the January 2013 field campaign provided invaluable observations on the structure of föhn at King Edward Point. The research presented in this chapter clarifies that the föhn mechanism is responsible for frequent and strong warm downslope winds at King Edward Point, and across the northeast side of South Georgia. Since South Georgia features narrow valleys and complex topography, föhn flow appears to be controlled by process acting on multiple scales; ranging from local processes (local pressure gradients), to mesoscale (valley winds, flow splitting), and synoptic (large-scale pressure gradients, mountain waves) scales. The features identified in this chapter are shown to be robust across many föhn events. These föhn dynamics, characteristics and processes are also prevalent elsewhere, and have been

identified by studies looking at föhn in the McMurdo Dry Valleys of Antarctica (Speirs *et al*., 2010; Steinhoff *et al*., 2013), the Alps (Zängl, 2003; Drobinski *et al*., 2007), as well as over the Antarctic Peninsula (Elvidge *et al*., 2014a; Elvidge *et al*., 2014b; Grosvenor *et al*., 2014). This chapter also demonstrates that rapid warming events not due to föhn warming may also have been inherently (mis-)classified as föhn in the AWS climatology. Therefore, regional climate modelling appears to be the best method for studying föhn processes in the absence of *in situ* surface meteorological observations. These model-based results provide a wealth of detail about orographic wind regimes across South Georgia, where few observations exist, and also illustrate that the dynamics of flow over South Georgia is complex and needs future investigation.

Therefore, this chapter successfully shows that we can *accurately simulate weak and strong föhn flow using a state-of-the-art atmospheric model*, and have confidence that the modelled dynamics and characteristics of the föhn flow are realistic.

7.2.3 Chapter Five: Exploring the Regional and Föhn Climatology of South Georgia with the Weather Research and Forecasting (WRF) Model

Beyond qualitative descriptions of the weather and climate of South Georgia (see e.g. Mansfield & Glassey, 1957; Richards & Tickell, 1968; Hayward, 1983), and the patchy, short and discontinuous surface meteorological measurements made at Bird Island, Grytviken and King Edward Point, surprisingly little is known about the regional climate of South Georgia. Having determined the optimal WRF model setup in Chapter 4, results of a 21 month climatological simulation (1 June 2011 – 1 March 2013) were presented in this chapter. Temperature, precipitation, wind and humidity conditions discussed in this chapter offer insights into the regional climate of South Georgia. The regional climate maps of the island, which are unique datasets, show that the climate of South Georgia is predominantly modified by the high mountain chain which divides the island in two. The southwest side of South Georgia is wetter, colder, more humid and windier, than the northeast side (primarily due to the föhn effect), while the northern end of South Georgia is warmer, less windy and drier, than the southern end (primarily due to exposure, aspect and slope orientation).

In addition to exploring the regional climate of South Georgia, three different methods for föhn detection using the model output were also described, tested and analysed in this chapter. As previously noted, regional climate modelling is the best method for studying föhn processes as it appears that the surface AWS observations used alone can misclassify rapid warming events (primarily caused by warm air advection) as föhn warming events. Therefore, one of the aims of this chapter was to deduce the best method for detecting the occurrence of föhn flow from non-föhn flow using the WRF model. Unlike the method presented in Chapter 3, this method had to identify the occurrence of föhn flow conditions over the entire island, and not just at King Edward Point. Three different model-based föhn detection methods were developed using: (1) model surface data, (2) leeside isentropic drawdown, and (3) upstream Froude number, as indicators for föhn events across South Georgia. The climatology of föhn events detected by each of the three methods was also compared to the climatology of AWS föhn events. Compared to the observations, WRF generally produces too few föhn events. Depending on the method, of the 159 events detected in the AWS observations, between 49 and 120 events are detected in the model. The events that are simulated are generally weaker than those observed, which is consistent with the negative temperature bias found in the case studies of Chapter 4, and there is also poor agreement between the modelled föhn climatologies for each of the three methods. This lack of agreement is attributed to the fact that each of the methods is defined by a different precursor condition for föhn occurrence on South Georgia, and therefore, each method classifies a different number and set of föhn events. The results from this chapter further confirm that instances of weak and strong rapid warming events are included in the AWS föhn climatology. Therefore, using model output may be a more reliable way of identifying föhn conditions across the island of South Georgia. As such, the final föhn identification method (Method 2B) selected ensures that flow over and leeside warming is solely a response to the föhn effect. This method captures 75.5% of all föhn events as detected by the surface AWS observations between June 2011 and February 2013. Between June 2011 and February 2013, this method indicates that föhn flow is occurring over South Georgia for 33% of the total time. This is consistent with the observational results of föhn frequency at King Edward Point from Chapter 3. This method does not detect very weak föhn events, rapid warming events caused by warm air advection, or strong wind events without an

associated leeside surface warming, thus avoiding what appears to be a major weakness with the AWS classification method. The composite fields of key meteorological variables during föhn are also shown, and the large-scale föhn features first identified in Chapter 4 are again prominent in these composites. The simulations reveal that föhn warming is also experienced on the southwest side of the island during strong northerly/easterly winds; a phenomenon that has never been recorded.

In this chapter, the regional climate of South Georgia is explored, and a robust method for föhn detection using WRF model data is deduced and is shown to effectively separate föhn from non-föhn conditions. This chapter therefore answers: *how does the orography of the island control the regional climate of South Georgia, what is the best method for detecting föhn in the model, and how well does the model capture föhn events?*

7.2.4 Chapter Six: The Impact of Föhn on the Regional Climate of South Georgia

The aim of this chapter was to quantify spatial and temporal variability of the surface mass balance of glaciers on South Georgia, and to relate this to changes in local climate and regional atmospheric circulation. This chapter reviews the general characteristics of the glacier mass balance of South Georgia in relation to the background of ongoing climate and glacial changes on the island. Using the 21 month simulation from Chapter 4, the WRF model data is used to demonstrate the strong influence of föhn events on the near-surface meteorology, the surface energy balance and the surface mass balance of the island's glaciers. Since föhn events are so frequent in the lee of South Georgia, and because they are typically associated with large temperature increases and humidity decreases, they might be expected to have a large impact on glacial melt across the island. In this chapter, the extended model simulation of Chapter 5 was used to demonstrate the impact of föhn on the regional climate and the surface energy and mass balance of South Georgia.

Previously, little was known about the spatial distribution and pattern of turbulent heat fluxes and net solar and longwave radiation across South Georgia (Smith, 1960; Richards & Tickell, 1968; Hogg *et al*., 1982; Shanklin, 1985). In this chapter, unique regional maps of these key energy balance components are presented. These maps revealed the seasonal variation of these components, and highlighted that the turbulent

heat fluxes are larger along the lee coast of South Georgia, and the predominance of westerly winds (which produces air that is dry from adiabatic descent on the north-eastern coastline) also accounts for the spatial differences in the net longwave and solar radiation terms. As with the regional climate of the island, the spatial pattern and intra-annual variability of the surface energy balance components is strongly modified and controlled by the high mountain chain.

The impact of föhn on the regional climate, the surface energy balance, and the surface mass balance of South Georgia was also explored in detail. Föhn acts to warm and dry the north-facing glaciers and the northeast coast of South Georgia through large positive sensible heat fluxes and negative latent heat fluxes (reaching 40 Wm^{-2} and -50 Wm^{-2}, respectively). This acts to transfer heat to the surface, and moisture to the atmosphere. Because föhn air is dry from adiabatic descent, föhn events are also associated with reduced incoming longwave radiation and increased incoming solar radiation (an indication of reduced cloud cover) on the northeast side of South Georgia. The fraction of time that the ice surface is at or above 0°C during all föhn conditions clearly shows an asymmetrical pattern across South Georgia, with an increase in the fraction over the northeast of the island and a decrease in the fraction over the southwest of the island. Due to the warmth and dryness associated with these winds, one would expect föhn flow to lead to asymmetrical melting and sublimation of snow and ice across South Georgia.

The aggregate mass balances suggest mass gain across all of South Georgia during the September 2011 – August 2012 period, and during all occasions of föhn (as previously detected by Method 2B in Chapter 5). This does not agree with recent observations of island-wide glacial retreat (Gordon *et al*., 2008; Cook *et al*., 2010). Unfortunately, it is beyond the scope of this study to explore whether this is an actual trend in the island's mass balance, an inter-annual variation in the island's mass balance, a bias in the model's representation of the surface energy balance components, and/or an error in the model's precipitation and ablation rates. Despite this, the results clearly show that although the *basin-wide* modelled estimates for the surface mass balance remain positive during föhn, there is a clear *asymmetrical* pattern of change in accumulation and ablation. During föhn, there is energy available for heating and melting the surface of north-facing glaciers on South Georgia. This supports the view that föhn is at least

partly responsible for the asymmetrical retreat of glaciers, via enhanced surface ablation at the termini of north-facing glaciers.

This work has shown that föhn does have implications for the surface energy and mass balance of the glaciers of South Georgia. The effect of mass loss and gain may have implications on future glacial retreat and advance. Future climatic changes will affect the magnitudes and balance of these processes through changes in regional climate and weather. Therefore, we can expect that a strengthening of the circumpolar westerlies in this region of the Southern Ocean will lead to increased föhn warming activity on South Georgia via enhanced flow over the main mountain chain; a process which has already been found to be responsible for recent warming trends on the leeside of the Antarctic Peninsula (see e.g. Marshall *et al*., 2006; Orr *et al*., 2008; Elvidge *et al*., 2014a; 2014b). Consequently, increasing frequencies of föhn events will lead to increased leeside surface mass loss. Overall, the results from this chapter find that the föhn warming process is a major influence of the regional climate of South Georgia. The surface mass balance estimates presented here provide an exceptional base to study the intra-annual variation and the distribution of energy balance components, and the resulting accumulation and ablation rates on South Georgia. Although there are likely to be limitations in the model representation of the surface energy balance components, it is for future research to provide accurate accumulation and ablation values through observational studies to further our understanding and knowledge of the regional climate of South Georgia.

The results support the hypothesis that westerly föhn events are associated with leeside warming extending to near-surface levels, and that mass loss occurs on the northeast glaciers. However, the confidence in the absolute values of the surface mass balance is linked to the quality of the model output. By creating a unique glacier catchment map of South Georgia, and by exploring how individual glacier basins respond to the föhn warming process, Chapter 6 partially answers w*hat impact do föhn winds have on the regional climate of South Georgia and, in particular, on the surface mass and energy balance of its glaciers?* The results strongly imply that regional island-wide atmospheric warming is the cause of basin-wide glacial retreat, while the föhn warming process enhances asymmetrical surface warming and thus ablation, over the north-facing glaciers. The glaciers of South Georgia are an early detection system for

significant climate change, and therefore, recommended avenues for future work which will help fully answer this question are given in section 7.4.

7.3 Synthesis

It has been over 130 years since the föhn effect was first measured and observed on the northeast coast of the island (von Danckelman, 1884), yet this study is the first to comprehensively examine the physical characteristics and features of föhn events experienced across South Georgia. Similarly, the lack of *in situ* observations has greatly restricted our knowledge of the regional climate of the island. This research has substantially filled gaps in our understanding of the weather and climate of South Georgia.

This study has advanced our understanding of the föhn effect of South Georgia, and its potential to induce climatically-important warming and glacial melt. We now know that föhn events are an inherent characteristic of the climate of South Georgia. The majority of the island remains cool, moist and windy throughout the year, but during occasions of strong westerly flow over South Georgia, föhn warming and drying is experienced on the north-eastern slopes. The results have shown that föhn events are very frequent on South Georgia, and that they play a significant and important role in shaping the regional climate of South Georgia. Föhn events do not just occur within King Edward Cove itself but across the entire Cumberland Bay region and beyond. During northerly and north-easterly flow, föhn warming is also experienced on the southwest side of South Georgia. Föhn events at King Edward Point occur throughout the year, and largely determine the weather experienced there. Not only do föhn winds cause surface warming and drying, but they are also often characterised, marked and occur alongside a föhn gap, mountain wave activity and orographically-induced clouds. Since föhn flow is synoptically driven, the results have shown that föhn events are linked to the large-scale Southern Hemisphere circulation pattern. There is evidence that both the thermodynamic and the dynamic mechanism are responsible for föhn warming on South Georgia, and this is similar to the conclusions of Elvidge *et al*. (2014a) and Elvidge & Renfrew (2015) who looked at föhn dynamics over the Antarctic Peninsula. We now know that the asymmetry of the South Georgia's regional climate is a result of the interaction between the island's topography and the

prevailing westerly winds, resulting in the föhn warming process. This asymmetry extends beyond the near-surface meteorology of South Georgia, and the föhn warming process also impacts the island's surface accumulation and ablation rates. This also leads to an asymmetrical pattern in the surface energy and mass balances of glaciers on South Georgia. We now know that the föhn effect is an important cause of ablation at the termini of north-facing glaciers, and that föhn events are at least partly responsible for the recent observed asymmetrical glacial retreat on South Georgia. We can be sure that föhn warming acts on regional scales, and that they are an important driver of inter-annual and intra-annual climate variability on the island of South Georgia.

This research has filled some of the gaps in our knowledge and understanding of the climate of South Georgia, which were originally set out at the beginning of this thesis. In doing so, new questions on the climate of South Georgia and the dynamics of föhn flow have emerged.

7.4 Recommendations for Future Research

This research has revealed numerous useful avenues for future related work. A number of issues emerged in this research primarily related to the lack of observational data, and this warrants considerable further investigation of the climate of South Georgia. The most important questions that require answering to further understand the full mechanisms and local impacts of the föhn effect, their role in controlling the regional climate, how they are linked with large-scale atmospheric and oceanic systems, and their effect on the future ecology and glaciology of South Georgia are discussed in detail below.

How frequent and intense are föhn events elsewhere on South Georgia?

The current limited surface observations are not sufficient to assess the frequency and the extent to which föhn is experienced elsewhere across South Georgia. In Chapter 5, föhn events on the south-western slopes of South Georgia driven by northerly air flow were also found to occur. It remains unknown how frequent, intense and persistent these events are on the south-western coast of South Georgia. This is an obvious avenue for further investigation. Therefore, an expanded observational

program on South Georgia would tremendously aid meteorological studies. The results of this research strongly suggest that further observations are required both upstream and downstream of the main mountain range. Additional surface observations should be made downwind of the island's mountains (e.g. in the vicinity of Hestesletten glacial plain, roughly 3km south of King Edward Point), and at St. Andrews Bay and Royal Bay, as well as at Husvik, Stromness, Godthul or Leith Harbour whaling stations. The regional analysis of the climate of South Georgia (presented in Chapters 5 and 6) showed that these areas may also frequently experience föhn events. Additional observations made upwind of the island's mountains (e.g. near Larvik, Cape Darnley, Undine South Harbour or Annenkov Island) would also be of great use. Additional upwind observations would provide a greater understanding of the climate of South Georgia as well as the information on the characteristics of the incident airflow before it is topographically modified by the Allardyce and Salvesen mountain ranges.

How has föhn frequency and intensity changed since the beginning of the meteorological record on South Georgia?

Confidence in the conclusions drawn from this climatological work is limited by the short length of time considered. A similar, more comprehensive, climatological study considering a longer time period would be useful in furthering the understanding of föhn frequency. Changes in föhn frequency and intensity can be investigated by future *in situ* observations and as the length of the current meteorological record continues to grow. The episodic nature of föhn events at King Edward Point suggests the importance of intra-seasonal variability. Due to the current limitation of hourly near-surface observations only being available at King Edward Point since 2003, longer high-resolution model hindcasts using forcing data since 1979 (ERA-Interim), and even as far back as 1900 (ERA-20C), could be used to explore föhn frequency. Since the results presented in this thesis give us confidence that Method 2B detects occasions which are dynamically connected to the föhn warming process (see Chapter 5), and that such occasions also produce warm leeside anomalies and increased ablation rates (see Chapter 6) across the northeast coast of the island, then Method 2B could be utilised to see how modelled föhn events have changed in the last century. The model simulations could also be verified against the meteorological data that is available

since 1905 to further uncover the impact of föhn on the climate of South Georgia. Although the temporal resolution of the long-term monitoring from Grytviken and King Edward Point is discontinuous, model simulations and observed daily means since 1905 could be explored to link daily minimum and maximum temperatures to föhn events. In the same manner, the impact of föhn frequency on monthly mean temperatures (i.e. do more föhn events equate to anomalously warm months?) could be examined further, and this could be achieved by both longer meteorological observations and climatological model simulations.

Given the results presented throughout this thesis, an increase in the frequency or the intensity of föhn events would be related to synoptic forcings, and that any change in the frequency or the intensity of föhn events could have large and significant impacts on the surface energy and mass balance of the island. This is because the surface and air temperatures across South Georgia are near 0^{o}C throughout the entire year. As such, even a small increase in the frequency or the intensity of föhn events could lead to a large increase in melt. The results presented in this thesis suggest that the strong events are determined by strong perpendicular flow over South Georgia. Strong winds over the Southern Ocean under a changing climate undeniably have the potential to produce more frequent and more intense föhn events. Therefore, understanding whether föhn events are becoming more frequent and/or intense has interdisciplinary importance if we are to understand future environmental changes on South Georgia. Clearly, future model simulations along with more extensive observational programmes are required to provide further insight in to the climate of South Georgia.

How do föhn features, characteristics, and dynamics vary across South Georgia?

Although the model simulations of föhn events have uncovered new insights into föhn features across South Georgia, the exact mechanism for föhn at King Edward Point, and elsewhere on the island, is unclear. Additional AWS units, a limited field campaign with vertical wind profiling, along with model output, would advance our knowledge on the mechanism and structure of föhn flow immensely. Combined observational-modelling studies are commonplace for the Alps, and have led to great advances in our understanding of föhn mechanics. Likewise, the structure and dynamics of lee-side warming during föhn events over the Antarctic Peninsula has

recently been investigated in detail (Elvidge *et al*., 2014a; Elvidge *et al*., 2014b; Grosvenor *et al*., 2014), and similar research could, without difficulty, be done over South Georgia. Additional surface observations could uncover pressure-driven channelling through some of the major gaps in the Allardyce and Salvesen mountain ranges. In the same vein, the role of mountain waves leading to adiabatic warming and the föhn effect needs further attention. Gap flows need further investigation to understand whether there is a positive relationship between adjusted pressure differences along gaps and near-surface wind speeds. Similarly, recent studies (Alexander *et al*., 2009; Alexander & Grimsdell, 2013; Jiang *et al*., 2014; Vosper, 2015) have shown that isolated mountainous islands in the Southern Ocean can be intense sources of gravity waves that can have climatologically-significant effects on atmospheric circulation. This, too, is an area which needs further investigation since mountain wave activity was observed in the case studies presented in Chapter 4. The frequent observations of *Altocumulus lenticularis* and Kelvin-Helmholtz clouds over Cumberland East Bay support the need for this research. Similarly, future high-resolution model simulations will prove useful in furthering the understanding of the sensitivity of melt rates to upwind and synoptic conditions (i.e. the type of föhn event and the spatial extent of föhn warming). The ultimate aim of this would be to forecast the amplitude of leeside warming and glacial ablation rates given the upwind flow conditions.

What role do atmospheric teleconnections, the synoptic scale meteorology, oceanic circulation and sea ice concentration have on föhn events?

Though it appears that the warmest föhn events are associated with a high pressure system in the South Atlantic due to warm air advection from the north, föhn events of different intensities occur over a wide range of ambient wind directions, and there are no specific synoptic-scale patterns responsible for föhn events. Though this was touched upon in Chapter 3, many questions still remain. The variety of synoptic-scale patterns resulting in föhn events perhaps explains the tenuous connections between the SAM index and föhn, and this needs further investigation. The relationship between other teleconnection patterns and föhn frequency and intensity could also be explored further. Föhn frequency on northeast South Georgia is likely to be effected by the phase of the El Niño-Southern Oscillation (ENSO), particularly the Southern

Oscillation index (SOI), and the semi-annual oscillation (SAO) via synoptic cyclone track variability, zonal wind variability and sea surface temperature anomalies (Meehl, 1991, van Loon *et al*., 1993; Hurrell & van Loon, 1994; Simmonds & Jones, 1998; Kwok & Comiso, 2002a; 2002b; Yuan, 2004; van den Broeke 1998a; 1998b; 2000a; 2000b; 2000c). In particular, the relatively long periodicity of ENSO and its decadal variability may be linked to the inter-annual variability of South Georgia's climate, while the SAOs role in intra-annual activity of storms and their tracks may also be of importance. The correlation statistics for seasonally averaged föhn days and air temperatures against different phases could be tested. This could also be linked with the synoptic circulation (i.e. mean sea level pressure differences) over this region during different phases, and how this coincides with föhn at King Edward Point. Therefore, this a clear area for future work; to link South Georgia's regional climate variability and changes to the variety of teleconnection effects on temperature, pressure, wind speed, precipitation and sea ice extent anomalies in this area of the Southern Ocean. A more detailed analysis of the effect of these combined signals on South Georgia's föhn wind regime is warranted as the length of meteorological records grow, and as a greater number of strong positive and negative phases are observed.

Besides atmospheric teleconnections, other factors influencing synoptic activity in the Scotia Sea region, such as the Antarctic circumpolar current, the position of the Antarctic Convergence zone, and annual sea ice concentrations, may also contribute to föhn variability and intensity. It is important to understand the intricate relationships between the atmosphere, the ocean and the sea ice in this sector of the Southern Ocean, especially as South Georgia and the surrounding waters are one of the most biologically-diverse regions in the world. Through coupled atmosphere-ocean-ice-glacier modelling, it would be possible to explore how the atmosphere determines the ocean and sea ice conditions, and vice versa, and how these conditions feedback into the asymmetrical warming of South Georgia's climate and the stability of the island's glaciers. Carefully targeted field observations could also be utilised to capture natural (e.g. seasonal and inter-annual) variability in the system to test the sensitivities of the models to changes in the forcing.

What improvements could be made to atmospheric simulations of föhn events?

Improved atmospheric model simulations, especially higher horizontal and vertical resolution and more realistic boundary layer processes, will also aid in the understanding of the meteorology within King Edward Cove, and elsewhere on the island. Based upon the results found here, future model simulations would need to properly resolve King Edward Cove in order to significantly improve the simulation of föhn events at King Edward Point. Short test simulations with very fine grid spacing (i.e. <500m) with different physics parameterisations and schemes is an obvious candidate for future work. However, achieving such high-resolution simulations is difficult without violating Courant–Friedrichs–Lewy (CFL) criteria (see section 2.3.1.2). Further testing is clearly necessary. Improved model output would complement additional *in situ* observations, thus helping us to understand and account for the spatial variations of föhn in this area.

How will more frequent and more intense föhn impact the ecology of the island?

There is a clear need for research to focus on how the ecological dynamics are related to the regional climate of South Georgia. South Georgia is a highly diverse island which is poorly studied, and yet uniquely threatened by climate change (Hogg *et al*., 2011; Murphy *et al*., 2012, SGHT, 2014). South Georgia is on the Polar Front, and as such is climatologically and ecologically very sensitive to any changes. There must be future work to understand how föhn events on a warming island could impact numbers of rare and endemic species, as well as how warmer conditions will result in the spread of foreign floral and faunal species.

How do glaciers on South Georgia change on intra-annual timescales, and how far have the glaciers on the island retreated or advanced in the last decade?

The last time the glacier fronts were digitized for many of the 14 glaciers examined in Chapter 6 was in 2008 (Cook *et al*., 2010). As such, we do not have any estimates for the total change and rate of change of retreat or advance for the last 7 years. Therefore, effort should be made to quantify changes in the location of South Georgia's ice fronts in the last decade using available aerial photography and satellite observations (e.g. Shuttle Radar Topography Mission data, laser altimetry, and Landsat images). In

addition to this, while it is known that glaciers are retreating over inter-annual time periods (Gordon & Timmis, 1992; Gordon *et al*., 2008; Cook *et al*., 2010), we do not know of intra-annual variations in advance and retreat. In particular, it remains unclear and unknown why Fortuna and Harker glaciers have advanced, and why neighbouring Harker and Hamberg glaciers have experienced such different rates of change, in the last 50 years. Clearly, this is still an avenue for future research. Further work could examine how synoptic-scale changes bring about changes in air-mass frequency and what impact this has on the surface lapse rates of the island's glaciers. Lapse rates derived from longer time series (either from model output or from meteorological stations) should be studied more in order to study spatial and seasonal patterns across South Georgia. Over longer temporal periods, model simulations may be useful in determining seasonal mass balances and adjustments of the size or volume of glaciers, especially if total precipitation and ablation can also be measured *in situ*. Along with this data, more detailed measurements of winter and summer ablation, precipitation and runoff on glaciers are necessary for proper annual surface mass balances. An improved understanding of how climate, glaciers and föhn flow are related is possible and could be further clarified if nearby AWSs were placed across the island of South Georgia. Near-surface and surface observations over the glaciers of South Georgia would also be useful in verifying model simulations of surface lapse rates, equilibrium line altitudes, the surface energy balance components, and rates of precipitation accumulation and ablation. Therefore, there is a clear need for a sensitivity study using the WRF model (i.e. testing the microphysics schemes), as well as future surface observations across the island of South Georgia. Very high-resolution (0.1km resolution) WRF simulations across the island would allow for the most accurate representation of slope, aspect, land cover and melt within elevation zones. Such simulations would generate the most accurate representation of topographic controls on the climate and weather of South Georgia.

What is the volumetric contribution of South Georgia's melting glaciers to global sea level rise?

The new glacier basin inventory for 29 of South Georgia's glaciers has many possible uses, and this dataset is a major advance over what was previously available. In particular, this new dataset allows area measurements to be made, improving the

possibilities for interpreting glacier changes on South Georgia. Glaciological characteristics, such as geometry, slope and altitudes can now be calculated from the dataset, thus providing a new resource for glacier morphological analyses. Similarly, the improved area estimates and area-altitude distributions will lead to more accurate large-scale mass-balance assessments (of the past) and projections (for the future). To further improve the separation of adjacent glaciers and increase the accuracy of estimated hypsometries (e.g. glacier extent, area, and geometry) better Digital Elevation Models (DEMs) are needed. Similarly, further improvements to the inventory could be made by digitizing a consistent set of outlines from satellite imagery, while old observations of glacier fronts (some of which date back to the 1950s) could be used to create a time series of watershed changes through time.

In addition to this, the total ice volume covering South Georgia expressed as the sea level equivalent could also be estimated using volume-area scaling (see e.g. Bliss *et al*., 2013). However, a prerequisite for exploring the contribution of South Georgia's melting glaciers to global sea level rise is the definition of outlines and basins for each individual glacier. While effort was made in Chapter 6 to create an inventory of 29 glacier basins across South Georgia, a complete inventory of all the island's glaciers is still required. Therefore, a comprehensive inventory, using a consistent technique, is necessary to incorporate all glacier systems across the island. This should be undertaken since the glaciers of South Georgia, which predominately terminate on or near the coast, could contribute to global sea level rise. Relative to the island's area, its contribution to sea level change could rival much larger polar ice sheets of Antarctica and Greenland. However, the total volume of water locked up in South Georgia's glaciers is yet to be measured. Global sea level rise is of concern due to the great societal impact in terms of the rate and timing of sea level rise and the inundation of coastal properties and infrastructure. An effort should be made, therefore, to understand the volume, velocity and iceberg calving rates across South Georgia, and how fluctuations in sea surface and air temperature influence glacier elevation and the acceleration in the rate of ice loss. Similarly, additional ice thickness measurements from South Georgia are required to better estimate the total ice volume and validate the volume-area scaling results.

Ultimately, this new glacier basin inventory and any future improvements can be used to further our understanding of glacier change in this region, and it can also offer a resource for continued glacier monitoring. The inventory of South Georgia's glaciers is an important resource for future mass balance studies.

7.5 The Future of South Georgia

Since this research began, the volume of relevant literature has expanded. There have already been advancements in our understanding and knowledge of flow over South Georgia (see e.g. Hosking *et al*., 2015), and on the island's regional and local (King Edward Point) climate (see e.g. Bannister & King, 2015), as well as new studies into the physical drivers of the ecological variability observed on the island (see e.g. Young *et al*., 2014), the glacial history of South Georgia (see e.g. Hodgson *et al*., 2014), and recent marine and terrestrial ecological changes (see e.g. SGHT, 2014). Clearly, South Georgia has very recently become of great interest across all areas of Earth system science. In the coming decades, we should expect further alterations in the climate, glaciology and ecology of this delicate island. The overall warming of the surface ocean, alterations in precipitation and ice melt, as well as changes in species biodiversity across the island will all impact South Georgia profusely. The waters surrounding the island are particularly sensitive to the effects of warming and changes in patterns of atmosphere and ocean circulation (Murphy *et al*., 2012). Changes that alter the physical properties of the water (such as salinity, ocean stratification and turbidity) will in turn influence the marine ecosystem, with effects that could extend considerable distances offshore from South Georgia (Dierssen *et al*., 2002). Such impacts could result in changes to whole communities and an alteration of food-web structure surrounding the island. This, therefore, has the potential to effect key spawning sites of fish, invertebrates, mammals (both marine and terrestrial) and birds. Many of these large-scale and regional scale geophysical changes can be linked to changes in wind forcing, in particular the intensification and poleward shift of the circumpolar westerly winds (Thompson *et al*., 2000; Thompson & Wallace, 2002). The most recent assessment from the Intergovernmental Panel on Climate Change has concluded that the westerly winds will continue to strengthen and shift poleward in the next century (Kirtman *et al*., 2013). Large-scale atmospheric warming along with

stronger westerly winds inducing more frequent and/or intense föhn flow will undoubtedly influence the future of South Georgia.

It is vital that we continue to investigate local and regional climate mechanisms in order to make predictions on appropriate local scales. South Georgia has entered a period of significant change, driven by regional climate warming. The most critical challenge before us is to understand the small-scale meteorological processes responsible for asymmetrical island-wide change, and the link with synoptic-scale climate change. This research provides the groundwork for such understanding. The environmental challenges South Georgia currently faces, and the possibilities for the future, must drive our curiosities during a time of such rapid and radical climate change.

"*There is nothing like looking, if you want to find something.*
You certainly usually find something, if you look,
but it is not always quite the something you were after."
– J. R. R. Tolkien

References

Aas, K. S., Berntsen, T. K., Boike, J., Etzelmüller, B., Kristjánsson, J. E., Maturilli, M., Schuler, T. V., Stordal, F., & Westermann, S. (2015). A Comparison between Simulated and Observed Surface Energy Balance at the Svalbard Archipelago. *Journal of Applied Meteorology and Climatology*, 54, 1102–1119.

Ahmadi, H., Das, A., Pourtaheri, M., Komaki, C. B., & Khairy, H. (2014). Redefining the watershed line and stream networks via digital resources and topographic map using GIS and remote sensing (case study: the Neka River's watershed). *Natural Hazards*, 72(2), 711-722.

Alexander, M. J., & Grimsdell, A. W. (2013). Seasonal cycle of orographic gravity wave occurrence above small islands in the Southern Hemisphere: Implications for effects on the general circulation. *Journal of Geophysical Research: Atmospheres*, 118(20), 11-589.

Alexander, M. J., Eckermann, S. D., Broutman, D., & Ma, J. (2009). Momentum flux estimates for South Georgia Island mountain waves in the stratosphere observed via satellite. *Geophysical Research Letters*, 36(12), L12186.

Allison, I. F., & Keage, P. L. (1986). Recent changes in the glaciers of Heard Island. *Polar Record*, 23(144), 255-271.

Andersson, E. (2007). Data assimilation in the polar regions. *ECMWF News Letter*, 112**,** 10-15.

Aniya, M. (1999). Recent glacier variations of the Hielos Patagónicos, South America, and their contribution to sea-level change. *Arctic, Antarctic, and Alpine Research*, 31(2), 165-173.

Aniya, M., Sato, H., Naruse, R., Skvarca, P., & Casassa, G. (1997). Recent glacier variations in the Southern Patagonia Icefield, South America. *Arctic, Antarctic, and Alpine Research,* 29(1), 1-12.

Arblaster, J. M., & Meehl, G. A. (2006). Contributions of external forcings to southern annular mode trends. *Journal of Climate*, 19(12), 2896-2905.

Argüeso, D., Hidalgo-Muñoz, J. M., Gámiz-Fortis, S. R., Esteban-Parra, M. J., & Castro-Díez, Y. (2012). High-resolution projections of mean and extreme precipitation over Spain using the WRF model (2070–2099 versus 1970–1999). *Journal of Geophysical Research*, 117, D12108.

Armstrong, R. L., & Brown, R. (2008). Introduction. In: R. L. Armstrong & E. Brun (Eds.), *Snow and Climate: Physical Processes, Surface Energy Exchange and Modelling* (pp. 1-11). Cambridge: Cambridge University Press.

Arntz, W. E., Gutt, J., & Klages, M. (1997). Antarctic marine biodiversity: an overview. *Antarctic Communities: Species, Structure and Survival*, 3-14.

Bannister, D., & King, J. C. (2015). The impact of föhn on the regional climate of South Georgia. *Weather*, Accepted.

Barnes, D. K. A. (2008). A benthic richness hotspot in the Southern Ocean: slope and shelf cryptic benthos of Shag Rocks. *Antarctic Science*, 20(3), 263-270.

Barnes, D. K. A., Linse, K., Waller, C., Morely, S., Enderlein, P., Fraser, K. P. P., & Brown, M. (2006). Shallow benthic fauna communities of South Georgia Island. *Polar Biology*, 29(3), 223-228.

Barnes, D. K. A., Peck, L. S., & Morley, S. A. (2010). Ecological relevance of laboratory determined temperature limits: colonization potential, biogeography and resilience of Antarctic invertebrates to environmental change. *Global Change Biology*, 16(11), 3164-3169.

Barry, R. G. (2008). *Mountain Weather and Climate*. Cambridge: Cambridge University Press.

Black, A., Parker, G., Rexel-Huber, K., & Sommer, R.J. (2013). Kerguelen petrel (*Lugensa brevirostris*), a 'new' breeding species for South Georgia. *Antarctic Science,* 25, 69-70.

Bliss, A., Hock, R., & Cogley, J. G. (2013). A new inventory of mountain glaciers and ice caps for the Antarctic periphery. *Annals of Glaciology*, 54(63), 191-199.

Bolch, T., Menounos, B., & Wheate, R. (2010). Landsat-based inventory of glaciers in western Canada, 1985–2005. *Remote Sensing of Environment*, 114(1), 127-137.

Boyd, I., Arnould, J., Barton, T., & Croxall, J. (1994). Foraging behaviour of Antarctic fur seals during periods of contrasting prey abundance. *Journal of Animal Ecology*, 63(3), 703-713.

Bracegirdle, T. J., & Marshall, G. J. (2012). The reliability of Antarctic tropospheric pressure and temperature in the 756 latest global reanalyses. *Journal of Climate*, 25, 7138-7146.

Brahmananda Rao, V., Do Carmo, A., & Franchito, S. H. (2003). Interannual variations of storm tracks in the Southern Hemisphere and their connections with the Antarctic Oscillation. *International Journal of Climatology*, 23(12), 1537-1545.

Braithwaite, R. J. (2008). Temperature and precipitation climate at the equilibrium-line altitude of glaciers expressed by the degree-day factor for melting snow. *Journal of Glaciology*, 54(186), 437-444.

Brandon, M. A., Murphy, E. J., Trathan, P. N., & Bone, D. G. (2000). Physical oceanographic conditions to the northwest of the sub-Antarctic Island of South Georgia. *Journal of Geophysical Research: Oceans (1978–2012)*, 105(C10), 23983-23996.

Braun, M., Simões, J. C., Vogt, S., Bremer, U. F., Blindow, N., Pfender, M., Saurer, H., Aquino, F. E., & Ferron, F. A. (2001). An improved topographic database for King George Island: compilation, application and outlook. *Antarctic Science*, 13(01), 41-52.

Brinkmann, W. (1971). What is a foehn? *Weather*, 26(6), 230-240.

Brinkmann, W. (1973). *A climatological study of strong downslope winds in the Boulder area*. Ph.D. thesis: National Center for Atmospheric Research.

Brinkmann, W. (1974). Strong downslope winds at Boulder, Colorado. *Monthly Weather Review*, 102(8), 592-602.

British Antarctic Survey. (2004). *South Georgia, 1:200 000 scale map*. BAS (Misc. 12A). Cambridge: British Antarctic Survey.

Bromwich D. H., Nicolas J. P., & Monaghan A. J. (2011). An assessment of precipitation changes over Antarctica and the Southern Ocean since 1989 in contemporary global reanalyses. *Journal of Climate,* 24, 4189-4209.

Bromwich, D. H., Otieno, F. O., Hines, K. M., Manning, K. W., & Shilo, E. (2013). Comprehensive evaluation of polar weather research and forecasting model performance in the Antarctic. *Journal of Geophysical Research*, 118(2), 274-292.

Budd, G.M. (2000). Changes in Heard Island glaciers, King Penguins and Fur Seals since 1947. *Papers and Proceedings of the Royal Society of Tasmania*, 133(2), 47-60.

Cai, W., & Watterson, I. G. (2002). Modes of interannual variability of the Southern Hemisphere circulation simulated by the CSIRO climate model. *Journal of Climate*, 15(10), 1159-1174.

Caldwell, P., Chin, H. N. S., Bader, D. C., & Bala, G. (2009). Evaluation of a WRF dynamical downscaling simulation over California. *Climatic Change*, 95(3-4), 499-521.

Carril, A. F., Menéndez, C. G., & Navarra, A. (2005). Climate response associated with the Southern Annular Mode in the surroundings of Antarctic Peninsula: A multimodel ensemble analysis. *Geophysical Research Letters*, 32(16), L16713.

Chen, F., & Dudhia, J. (2001). Coupling an advanced land surface-hydrology model with the Penn State-NCAR MM5 modeling system. Part I: Model implementation and sensitivity. *Monthly Weather Review*, 129(4), 569-585.

Cheng, W. Y., & Steenburgh, W. J. (2005). Evaluation of surface sensible weather forecasts by the WRF and the Eta models over the western United States. *Weather and Forecasting*, 20(5), 812-821.

Chou, M. D., & Suarez, M. J. (1999). A solar radiation parameterization for atmospheric studies. *NASA Technical Memo*, 104606, 40.

Chubb, T., Morrison, A., Caine, S., Siems, S., & Manton, M. (2012). Case studies of orographic precipitation in the Brindabella Ranges: model evaluation and prospects for cloud seeding. *Australian Meteorological & Oceanographic Journal*, 62(4), 305-321.

Church, J.A., Clark, P.U., Cazenave, A., Gregory, J. M., Jevrejeva, S., Levermann, A., Merrifield, M. A., Milne, G. A., Nerem, R. S., Nunn, P. D., Payne, A. J., Pfeffer, W. T., Stammer D., & Unnikrishnan, A. S. (2013). Sea Level Change. In: T. F. Stocker, D. Qin, G.-K. Plattner, M. Tignor, S.K. Allen, J. Boschung, A. Nauels, Y. Xia, V. Bex, & P.M. Midgley (Eds), *Climate Change 2013: The Physical Science Basis. Contribution of Working Group I to the Fifth Assessment Report of the Intergovernmental Panel on Climate Change* (pp. 1137-1216). Cambridge: Cambridge University Press.

Clapperton, C. M., & Sugden, D. E. (1988). Holocene glacier fluctuations in South America and Antarctica. *Quaternary Science Reviews*, 7(2), 185-198.

Clapperton, C. M., Sugden, D. E., & Pelto, M. (1989a). Relationship of land terminating and fjord glaciers to Holocene climatic change, South Georgia, Antarctica. *Glaciology and Quaternary Geology*, 6, 57-75.

Clapperton, C. M., Sugden, D. E., Birnie, J., & Wilson, M. J. (1989b). Late-glacial and Holocene glacier fluctuations and environmental change on South Georgia, Southern Ocean. *Quaternary Research*, 31(2), 210-228.

Clark, T. L., & Peltier, W. R. (1977). On the evolution and stability of finite-amplitude mountain waves. *Journal of the Atmospheric Sciences*, 34(11), 1715-1730.

Clarke, A.C., Croxall, J. P., Poncet, S., Martin, A. R., & Burton, R. (2012). Important Bird Areas: South Georgia. *British Birds,* 105, 118-144.

Comiso, J. (2010). *Polar Oceans from Space*. New York: Springer.

Comiso, J. C. (2000). Variability and trends in Antarctic surface temperatures from in situ and satellite infrared measurements. *Journal of Climate*, 13(10), 1674-1696.

Condron, A., Bigg, G. R., & Renfrew, I. A. (2006). Polar mesoscale cyclones in the northeast Atlantic: Comparing climatologies from ERA-40 and satellite imagery. *Monthly Weather Review*, 134(5), 1518-1533.

Conrad, V. (1936). Die klimatologischen Elemente und ihre Abhängigkeit von terrestrischen Einflüssen. In: W. Köppen & R. Geiger (Eds.), *Klimatologie*. Borntraeger.

Convey, P., Key, R. S., Key, R. J. D., Belchier, M., & Waller, C. L. (2011). Recent range expansions in non-native predatory beetles on sub-Antarctic South Georgia. *Polar Biology*, 34(4), 597-602.

Cook, A. J., Fox, A., Vaughan, D., & Ferrigno, J. (2005). Retreating glacier fronts on the Antarctic Peninsula over the past half-century. *Science*, 308(5721), 541-544.

Cook, A. J., Poncet, S., Cooper, A. P. R., Herbert, D., & Christie, D. (2010). Glacier retreat on South Georgia and implications for the spread of rats. *Antarctic Science*, 22(03), 255-263.

Cook, A. J., Vaughan, D. G., Luckman, A. J., & Murray, T. (2014). A new Antarctic Peninsula glacier basin inventory and observed area changes since the 1940s. *Antarctic Science*, 26(06), 614-624.

Cook, A. W., & Topil, A. G. (1952). Some examples of chinooks east of the mountains in Colorado. *Bulletin of the American Meteorological Society*, 33(2), 42-47.

Corby, G. A. (1957). A preliminary study of atmospheric waves using radiosonde data. *Quarterly Journal of the Royal Meteorological Society*, 83(355), 49-60.

Corby, G. A., & Wallington, C. E. (1956). Airflow over mountains: The lee-wave amplitude. *Quarterly Journal of the Royal Meteorological Society*, 82(353), 266-274.

Cornes, R., & Jones, P. (2013). How well does the ERA-Interim reanalysis replicate trends in extremes of surface temperature across Europe? *Journal of Geophysical Research-Atmospheres*, 118, 10262-10276.

Costa, D. P., Huckstadt, L. A., Crocker, D. E., Mcdonald, B. I., Goebel, M. E., & Fedak, M. A. (2010). Approaches to studying climatic change and its role on the habitat selection of Antarctic pinnipeds. *Integrative and Comparative Biology*, 50(6), 1018-1030.

Craig, H., & Gordon, J. E. (1990). Summer weather at Royal Bay, South Georgia, 1882–83 and 1981–82. *Polar Record*, 26(158), 187-194.

Croxall, J., Mccann, T., Prince, P., & Rothery, P. (1988). Reproductive performance of seabirds and seals at South Georgia and Signy Island, South Orkney Islands, 1976-1987: implications for Southern Ocean monitoring studies. *Antarctic Ocean and Resources Variability*, 4, 261-285.

Croxall, J., Reid, K., & Prince, P. (1999). Diet, provisioning and productivity responses of marine predators to differences in availability of Antarctic krill. *Marine Ecology Progress Series*, 177, 115-131.

De Broyer, C., & Danis, B. (2010). *SCAR-MarBIN: The Antarctic Marine Biodiversity Information Network*. Retrieved 30 January 2012, from http://www.scarmarbin.be/

de Meij, A., & Vinuesa, J. F. (2014). Impact of SRTM and Corine Land Cover data on meteorological parameters using WRF. *Atmospheric Research*, 143, 351-370.

Deb, P., Orr, A., Hosking, J. S., Phillips, T., Turner, J., Bannister, D., Pope, J., & Colwell, S. (2015). An assessment of the Polar Weather Research and Forecast (WRF) model representation of near-surface meteorological variables over West Antarctica. *Journal of Geophysical Research,* Submitted.

Dee, D. P., Uppala, S. M., Simmons, A. J., Berrisford, P., Poli, P., Kobayashi, S., Andrae, U., Balmaseda, M. A., Balsamo, G., Bauer, P., Bechtold, P., Beljaars, A. C. M., van de Berg, L., Bidlot, J., Bormann, N., Delsol, C., Dragani, R., Fuentes, M., Geer, A. J, Haimberfer, L., Healy, S. B, Hersbach, H., Hólm, E. V, Isaksen, L., Kållberg, P., Köhler, M., Matricard, M., McNally, A. P., Monge-Sanz, B. M., Morcrette, J. J., Park, B. K., Peubey, C., de Rosnay, P., Tavolato, C., Thépaut, J. N., & Vitart, F. (2011). The ERA-interim reanalysis: configuration and performance of the data assimilation system. *Quarterly Journal of the Royal Meteorological Society*, 137, 553–597.

Dierssen, H. M., Smith, R. C., & Vernet, M. (2002). Glacial meltwater dynamics in coastal waters west of the Antarctic Peninsula. *Proceedings of the National Academy of Sciences*, 99(4), 1790-1795.

Drechsel, S., & Mayr, G. J. (2008). Objective forecasting of foehn winds for a subgrid-scale alpine valley. *Weather and Forecasting*, 23(2), 205-218.

Drobinski, P., Dabas, A. M., Haeberli, C., & Flamant, P. H. (2001). On the small-scale dynamics of flow splitting in the Rhine Valley during a shallow foehn event. *Boundary-layer Meteorology*, 99(2), 277-296.

Dudhia, J. (1989). Numerical study of convection observed during the winter monsoon experiment using a mesoscale two-dimensional model. *Journal of the Atmospheric Sciences*, 46(20), 3077-3107.

Duethmann, D., Zimmer, J., Gafurov, A., Güntner, A., Kriegel, D., Merz, B., & Vorogushyn, S. (2013). Evaluation of areal precipitation estimates based on downscaled reanalysis and station data by hydrological modelling. *Hydrology and Earth System Sciences*, 17(7), 2415-2434.

Durran, D. R. (1990). Mountain waves and downslope winds. *Meteorological Monographs*, 23, 59-81.

Durran, D. R. (2003). Lee waves and mountain waves. *The Encyclopaedia of the Atmospheric Sciences*, 1161-1169.

Eliassen, A., & Palm, E. (1960). Wave energy transfer in stationary gravity waves. *Geofysiske Publikasjoner*, 22(3), 1-15.

Elvidge, A. D., & Renfrew, I. A. (2015). The causes of foehn warming in the lee of mountains. *Bulletin of the American Meteorological Society*.

Elvidge, A. D., Renfrew, I. A., King, J. C., Orr, A., & Lachlan-Cope, T. A. (2014a). Foehn warming distributions in nonlinear and linear flow regimes: A focus on the Antarctic Peninsula. *Quarterly Journal of the Royal Meteorological Society*.

Elvidge, A. D., Renfrew, I. A., King, J. C., Orr, A., Lachlan-Cope, T. A., Weeks, M., & Gray, S. L. (2014b). Foehn jets over the Larsen C Ice Shelf, Antarctica. *Quarterly Journal of the Royal Meteorological Society*.

Favier, V., Falvey, M., Rabatel, A., Praderio, E., & López, D. (2009). Interpreting discrepancies between discharge and precipitation in high-altitude area of Chile's Norte Chico region (26–32° S). *Water Resources Research*, 45(2), W02424.

Ficker, H. V. (1931). Warum steigt der Föhn in die Täler herab. *Meteorologische Zeitschrift*, 48, 227-229.

Forcada, J., & Trathan, P. N. (2009). Penguin responses to climate change in the Southern Ocean. *Global Change Biology*, 15, 1618–1630.

Frenot, Y., Chown, S. L., Whinam, J., Selkirk, P. M., Convey, P., Skotnicki, M., & Bergstrom, D. M. (2005). Biological invasions in the Antarctic: extent, impacts and implications. *Biological reviews*, 80(1), 45-72.

Frenot, Y., Gloaguen, J.-C., & Tréhen, P. (1997). Climate change in Kerguelen Islands and colonization of recently deglaciated areas by *Poa kerguelensis* and *P. annua*. In: B. Battaglia, J. Valencia, & D. W. H. Walton (Eds.), *Antarctic Communities, Species, Structure and Survival* (pp. 358-366). Cambridge: Cambridge University Press.

Frenot, Y., Gloaguen, J.-C., Picot, G., Bougère, J., & Benjamin, D. (1993). *Azorella selago* Hook. used to estimate glacier fluctuations and climatic history in the Kerguelen Islands over the last two centuries. *Oecologia*, 95, 140-144.

Frey, K. (1957). Zur diagnose des foehns. *Meteorologische Rundschau*, 10(6), 181-185.

Fritts, D. C., & Alexander, M. J. (2003). Gravity wave dynamics and effects in the middle atmosphere. *Reviews of Geophysics*, 41(1), 1003.

Fyfe, J., Boer, G., & Flato, G. (1999). Arctic and Antarctic oscillations and their projected changes under global warming. *Geophysical Research Letters*, 26(11), 1601-1604.

Gaffin, D. M. (2002). Unexpected Warming Induced by Foehn Winds in the Lee of the Smoky Mountains. *Weather and Forecasting*, 17(4), 907-915.

Gaffin, D. M. (2007). Foehn winds that produced large temperature differences near the southern Appalachian Mountains. *Weather and Forecasting*, 22(1), 145-159.

Gaffin, D. M. (2009). On High Winds and Foehn Warming Associated with Mountain-Wave Events in the Western Foothills of the Southern Appalachian Mountains. *Weather and Forecasting*, 24(1), 53-75.

Garnier, B. J., & Ohmura, A. (1968). A method of calculating the direct shortwave radiation income of slopes. *Journal of Applied Meteorology*, 7(5), 796-800.

Gillett, N. P., & Thompson, D. W. J. (2003). Simulation of recent Southern Hemisphere climate change. *Science*, 302(5643), 273.

Gillett, N., Kell, T., & Jones, P. (2006). Regional climate impacts of the Southern Annular Mode. *Geophysical Research Letters*, 33, 1–4.

Gohm, A., & Mayr, G. J. (2004). Hydraulic aspects of föhn winds in an Alpine valley. *Quarterly Journal of the Royal Meteorological Society*, 130(597), 449-480.

Gohm, A., Zängl, G., & Mayr, G. J. (2004). South foehn in the Wipp Valley on 24 October 1999 (MAP IOP 10), Verification of high-resolution numerical simulations with observations. *Monthly Weather Review*, 132(1), 78-102.

Gómez-Navarro, J. J., Raible, C. C., & Dierer, S. (2015). Sensitivity of the WRF model to PBL parametrizations and nesting techniques: evaluation of surface wind over complex terrain. *Geoscientific Model Development Discussions*, 8, 5437-5479.

Gonçalves-Ageitos, M., Barrera-Escoda, A., Baldasano, J. M., & Cunillera, J. (2015). Modelling wind resources in climate change scenarios in complex terrains. *Renewable Energy*, 76, 670-678.

Gong, D., & Wang, S. (1999). Definition of Antarctic Oscillation Index. *Geophysical Research Letters*, 26(4), 459-462.

Gordon, J. E., & Birnie, R. V. (1986). Production and transfer of subaerially generated rock debris and resulting landforms on South Georgia – An introductory perspective. *British Antarctic Survey Bulletin*, 72, 25-46.

Gordon, J. E., & Timmis, R. J. (1992). Glacier fluctuations on South Georgia during the 1970s and early 1980s. *Antarctic Science*, 4(2), 215-226.

Gordon, J. E., Birnie, R. V., & Timmis, R. (1978). A major rockfall and debris slide on the Lyell Glacier, South Georgia. *Arctic and Alpine Research*, 10(1), 49-60.

Gordon, J. E., Haynes, V. M., & Hubbard, A. (2008). Recent glacier changes and climate trends on South Georgia. *Global and Planetary Change*, 60(1-2), 72-84.

Gregory, J. W. (1915). The physiography of South Georgia as shown by Mr Ferguson's photographs. Geological observations in South Georgia. *Transactions of the Royal Society of Edinburgh*, 50(23), 814-816.

Griffiths, H. J., Barnes, D. K. A., & Linse, K. (2009). Towards a generalized biogeography of the Southern Ocean benthos. *Journal of Biogeography*, 36(1), 162-177.

Grosvenor, D. P., King, J. C., Choularton, T. W., & Lachlan-Cope, T. (2014). Downslope föhn winds over the Antarctic Peninsula and their effect on the Larsen ice shelves. *Atmospheric Chemistry and Physics*, 14(18), 9481-9509.

Hahn, R. S., & Mass, C. F. (2009). The impact of positive-definite moisture advection and low-level moisture flux bias over orography. *Monthly Weather Review*, 137(9), 3055-3071.

Hall, A., & Visbeck, M. (2002). Synchronous Variability in the Southern Hemisphere Atmosphere, Sea Ice, and Ocean Resulting from the Annular Mode. *Journal of Climate*, 15(21), 3043-3057.

Hann, J. F. (1866). Zur Frage über den Ursprung des Föhns. *Zeit. Osterreich Ges. Met*, 1, 257-263.

Hartmann, D. L., & Lo, F. (1998). Wave-driven zonal flow vacillation in the Southern Hemisphere. *Journal of the Atmospheric Sciences*, 55(8), 1303-1315.

Hayward, R. J. C. (1983). Glacier fluctuations in South Georgia, 1883–1974. *British Antarctic Survey Bulletin*, 52, 47-61.

Headland, R. K. (1982). The German station of the first International Polar Year, 1882–83, at South Georgia, Falkland Islands Dependencies. *Polar Record*, 21(132), 287-292.

Headland, R. K. (1992). *The Island of South Georgia*. Cambridge: Cambridge University Press.

Hegerl, G. C., Zwiers, F. W., Braconnot, P., Gillett, N. P., Luo, Y., Marengo Orsini, J. A., Nicholls, N., Penner, J. E., & Stott, P. A. (2007). Understanding and Attributing Climate Change. In: S. Solomon, D. Qin, M. Manning, Z. Chen, M. Marquis, K. B. Averyt, M. Tignor, & H. L. Miller (Eds.), *Climate Change 2007: The Physical Science Basis. Contribution of Working Group I to the Fourth Assessment Report of the Intergovernmental Panel on Climate Change* (pp. 663-745). Cambridge: Cambridge University Press.

Heikkilä, U., Sandvik, A., & Sorteberg, A. (2011). Dynamical downscaling of ERA-40 in complex terrain using the WRF regional climate model. *Climate Dynamics*, 37(7-8), 1551-1564.

Hodgson, D. A., Graham, A. G., Griffiths, H. J., Roberts, S. J., Cofaigh, C. Ó., Bentley, M. J., & Evans, D. J. (2014). Glacial history of sub-Antarctic South Georgia based on the submarine geomorphology of its fjords. *Quaternary Science Reviews*, 89, 129-147.

Hofmann, E., Klinck, J., Locarnini, R., Fach, B., & Murphy, E. (1998). Krill Transport in the Scotia Sea and Environs. *Antarctic Science*, 10(4), 406-415.

Hogg, I. G. G., Paren, J. G., & Timmis, R. J. (1982). Summer heat and ice balances on Hodges Glacier, South Georgia, Falkland Islands Dependencies. *Journal of Glaciology*, 28, 221-238.

Hogg, O. T., Barnes, D. K. A., & Griffiths, H. J. (2011). Highly Diverse, Poorly Studied and Uniquely Threatened by Climate Change: An Assessment of Marine Biodiversity on South Georgia's Continental Shelf. *PLOS ONE*, 6(5), E19795.

Hoinka, K. P. (1985a). Observation of the airflow over the alps during a foehn event. *Quarterly Journal of the Royal Meteorological Society*, 111(467), 199-224.

Hoinka, K. P. (1985b). What is a Foehn Clearance? *Bulletin of the American Meteorological Society*, 66(9), 1123-1132.

Hoinka, K., & Rösler, F. (1987). The surface layer on the leeside of the Alps during Foehn. *Meteorology and Atmospheric Physics*, 37(4), 245-258.

Hong, S. Y., & Lim, J. O. J. (2006). The WRF single-moment 6-class microphysics scheme (WSM6). *Asia-Pacific Journal of Atmospheric Sciences*, 42(2), 129-151.

Hong, S. Y., Dudhia, J., & Chen, S. H. (2004). A revised approach to ice microphysical processes for the bulk parameterization of clouds and precipitation. *Monthly Weather Review*, 132(1), 103-120.

Hong, S. Y., Noh, Y., & Dudhia, J. (2006). A new vertical diffusion package with an explicit treatment of entrainment processes. *Monthly Weather Review*, 134(9), 2318-2341.

Hosking, J. S., Bannister, D., Orr, A., King, J., Young, E., & Phillips, T. (2015). Orographic disturbances of surface winds over the shelf waters adjacent to South Georgia. *Atmospheric Science Letters*, 16(1), 50-55.

Houghton, D. D., & Kasahara, A. (1968). Nonlinear shallow fluid flow over an isolated ridge. *Communications on Pure and Applied Mathematics*, 21(1), 1-23.

Houze, R. A. (2012). Orographic effects on precipitating clouds. *Reviews of Geophysics*, 50(1), RG1001.

Hunt, J. C. R., Olafsson, H., & Bougeault, P. (2001). Coriolis effects on orographic and mesoscale flows. *Quarterly Journal of the Royal Meteorological Society*, 127(572), 601-633.

Hurrell, J. W., & van Loon, H. (1994). A modulation of the atmospheric annual cycle in the Southern Hemisphere. *Tellus A*, 46(3), 325-338.

Hydrographic Office (2009). *The Antarctic pilot: Comprising the coasts of Antarctica and all islands southward of the usual route of vessels*. Somerset: Hydrographer of the Navy.

Inaba, H., Kawamura, R., Kayahara, T., & Ueda, H. (2002). Extraordinary Persistence of Foehn Observed in the Hokuriku District of Japan in the 1999 Summer. *Journal of the Meteorological Society of Japan*, 80(4), 579-594.

Janjić, Z. I. (1994). The step-mountain eta coordinate model: Further developments of the convection, viscous sublayer and turbulence closure schemes. *Monthly Weather Review*, 122, 927-945.

Janowiak, J. E., Gruber, A., Kondragunta, C. R., Livezey, R. E., & Huffman, G. J. (1998). A comparison of the NCEP-NCAR reanalysis precipitation and the GPCP rain gauge-satellite combined dataset with observational error considerations. *Journal of Climate*, 11(11), 2960-2979.

Jarvis, A., Reuter, H. I., Nelson, A., & Guevara, E. (2008). *Hole-filled SRTM for the globe Version 4. Available from the CGIAR-CSI SRTM 90 m database.* Retrieved 17 January 2012, from http://srtm.csi.cgiar.org.

Jaubert, G., & Stein, J. (2003). Multiscale and unsteady aspects of a deep foehn event during MAP. *Quarterly Journal of the Royal Meteorological Society*, 129(588), 755-776.

Jiang, Q., Reinecke, A., & Doyle, J. D. (2014). Orographic Wave Drag over the Southern Ocean: A Linear Theory Perspective. *Journal of the Atmospheric Sciences*, 71(11), 4235-4252.

Jiménez, P. A., & Dudhia, J. (2012). Improving the representation of resolved and unresolved topographic effects on surface wind in the WRF model. *Journal of Applied Meteorology and Climatology*, 51(2), 300-316.

Jin, J., & Wen, L. (2012). Evaluation of snowmelt simulation in the Weather Research and Forecasting model. *Journal of Geophysical Research: Atmospheres (1984–2012)*, 117(D10).

Jones, J. M., & Widmann, M. (2003). Instrument-and tree-ring-based estimates of the Antarctic Oscillation. *Journal of Climate*, 16(21), 3511-3524.

Jones, J. M., & Widmann, M. (2004). Early peak in Antarctic oscillation index. *Nature*, 432(7015), 290-291.

Jones, J. M., Fogt, R. L., Widmann, M., Marshall, G. J., Jones, P. D., & Visbeck, M. (2009). Historical SAM Variability. Part I: Century-Length Seasonal Reconstructions*. *Journal of Climate*, 22(20), 5319-5345.

Kain, J. S. (2004). The Kain-Fritsch convective parameterization: an update. *Journal of Applied Meteorology*, 43(1), 170-181.

Karpechko, A. Y., Gillett, N. P., Marshall, G. J., & Screen, J. A. (2009). Climate impacts of the southern annular mode simulated by the CMIP3 models. *Journal of Climate*, 22(13), 3751-3768.

Kejna, M. (2008). Topoclimatic conditions in the vicinity of the Arctowski Station (King George Island, Antarctica) during the summer season of 2006/2007. *Polish Polar Research*, 29(2), 95-116.

Kiernan, K., & McConnell, A. (1999). Geomorphology of the Sub-Antarctic Australian Territory of Heard Island-McDonald Island. *Australian Geographer*, 30(2), 159-195.

Kiernan, K., & McConnell, A. (2002). Glacier retreat and melt-lake expansion at Stephenson Glacier, Heard Island World Heritage Area. *Polar Record*, 38(207), 297-308.

King, J. C. (1994). Recent climate variability in the vicinity of the Antarctic Peninsula. *International Journal of Climatology*, 14(4), 357-369.

King, J. C., Pomeroy, J. W., Gray, D. M., Fierz, C., Fohn, P. M. B., Harding, R. J., Jordan, R. E., Martin, E., & Pluss, C. (2008). Snow-atmosphere energy and mass balance. In: R. L. Armstrong, & E. Brun (Eds.), *Snow and Climate: Physical Processes, Surface Energy Exchange and Modeling* (pp. 70-124). Cambridge: Cambridge University Press.

King, J. C., Gadian, A., Kirchgaessner, A., Kuipers Munneke, P., Lachlan-Cope, T. A., Orr, A., Reijmer, C., van den Broeke, M. R., van Wessem, J. M., &

Weeks, M. (2015). Validation of the summertime surface energy budget of Larsen C Ice Shelf (Antarctica) as represented in three high-resolution atmospheric models. *Journal of Geophysical Research*, 120, 1335–1347.

Kirtman, B., Power, S. B., Adedoyin, J. A., Boer, G. J., Bojariu, R., Camilloni, I., Doblas-Reyes, F. J., Fiore, A. M., Kimoto, M., Meehl, G. A., Prather, M., Sarr, A., Schär, C., Sutton, R., van Oldenborgh, G. J., Vecchi G., & Wang, H. J. (2013). Near-term Climate Change: Projections and Predictability. In: T. F. Stocker, D. Qin, G.-K. Plattner, M. Tignor, S. K. Allen, J. Boschung, A. Nauels, Y. Xia, V. Bex, & P. M. Midgley (Eds), *Climate Change 2013: The Physical Science Basis. Contribution of Working Group I to the Fifth Assessment Report of the Intergovernmental Panel on Climate Change* (pp. 953-1028). Cambridge: Cambridge University Press.

Klemp, J. B., & Lilly, D. R. (1975). The dynamics of wave-induced downslope winds. *Journal of the Atmospheric Sciences*, 32(2), 320-339.

Klemp, J. B., Dudhia, J., & Hassiotis, A. D. (2008). An upper gravity-wave absorbing layer for NWP applications. *Monthly Weather Review*, 136(10), 3987-4004.

Kruszewski, G. (2000). Inwersje temperatury powietrza. In: A. A. Marsz, & A. Styszyńska (Eds.), *Główne cechy klimatu rejonu Polskiej Stacji Antarktycznej im Arctowskiego* (pp. 105-113). Gdynia: Wyższa Szkoła Morska.

Kuhn, M. (1989). *Föhnstudien*. Wiss. Buchges.

Kuipers Munneke, P., van den Broeke, M. R., King, J. C., Gray, T., & Reijmer, C. H. (2012). Near-surface climate and surgace budget of Larsen C ice shelf, Antarctic Peninsula. *The Cryosphere*, 6(2), 353-363.

Kushner, P. J., Held, I. M., & Delworth, T. L. (2001). Southern Hemisphere atmospheric circulation response to global warming. *Journal of Climate*, 14(10), 2238-2249.

Kwok, R., & Comiso, J. (2002a). Spatial patterns of variability in Antarctic surface temperature- Connections to the Southern Hemisphere Annular Mode and the Southern Oscillation. *Geophysical Research Letters*, 29(14), 50-51.

Kwok, R., & Comiso, J. (2002b). Southern Ocean climate and sea ice anomalies associated with the Southern Oscillation. *Journal of Climate*, 15(5), 487-501.

Lee, J., Shin, H. H., Hong, S. Y., Jiménez, P. A., Dudhia, J., & Hong, J. (2015). Impacts of subgrid-scale orography parameterization on simulated surface layer wind and monsoonal precipitation in the high-resolution WRF model. *Journal of Geophysical Research: Atmospheres*, 120(2), 644-653.

Lefebvre, W., Goosse, H., Timmermann, R., & Fichefet, T. (2004). Influence of the Southern Annular Mode on the sea ice–ocean system. *Journal of Geophysical Research: Oceans (1978–2012)*, 109, C09005.

Limpasuvan, V., & Hartmann, D. L. (1999). Eddies and the annular modes of climate variability. *Geophysical Research Letters*, 26(20), 3133-3136.

Lin, Y. L., Farley, R. D., & Orville, H. D. (1983). Bulk parameterization of the snow field in a cloud model. *Journal of Climate and Applied Meteorology*, 22(6), 1065-1092.

Liu, J., Curry, J. A., & Martinson, D. G. (2004). Interpretation of recent Antarctic sea ice variability. *Geophysical Research Letters*, 31(2), L02205.

Lockwood, J. G. (1962). Occurrence of föhn winds in the British Isles. *Meteorological Magazine*, 91, 57-65.

Loewe, F. (1950). Foehn Effects Near the Balleny Islands, Antarctica. *Weather*, 5(4), 152-154.

Long, R. R. (1953). Some aspects of the flow of stratified fluids: A theoretical investigation. *Tellus*, 5(1), 42-58.

Longley, R. W. (1967). The frequency of winter chinooks in Alberta. *Atmosphere*, 5(4), 4-16.

Lothon, M., Druilhet, A., Bénech, B., Campistron, B., Bernard, S., & Said, F. (2003). Experimental study of five föhn events during the Mesoscale Alpine Programme: From synoptic scale to turbulence. *Quarterly Journal of the Royal Meteorological Society*, 129(592), 2171-2193.

Lubin, D., Wittenmyer, R. A., Bromwich, D. H., & Marshall, G. J. (2008). Antarctic Peninsula mesoscale cyclone variability and climatic impacts influenced by the SAM. *Geophysical Research Letters*, 35(2), L02808.

Luckman, A., Elvidge, A., Jansen, D., Kulessa, B., Kuipers Munneke, P., King, J., & Barrand, N. E. (2014). Surface melt and ponding on Larsen C Ice Shelf and the impact of foehn winds. *Antarctic Science*, 26(06), 625-635.

Mansfield, A. W., & Glassey, S. D. (1957). Notes on weather analysis in the Falkland Islands Dependencies, Antarctica. *Falkland Islands Dependencies Survey Science Reports*, *No. 16*. Cambridge: The British Antarctic Survey.

Manuel, P., & Keighton, S. (2003). Anticipating damaging foehn windstorms east of the central Appalachians. In: *10th Conference on Mesoscale Processes*. Chicago: American Meteorological Society.

Marshall, G. J. (2003). Trends in the Southern Annular Mode from observations and reanalyses. *Journal of Climate*, 16(24), 4134-4143.

Marshall, G. J., Lagun, V., & Lachlan-Cope, T. A. (2002). Changes in Antarctic Peninsula tropospheric temperatures from 1956 to 1999: a synthesis of observations and reanalysis data. *International Journal of Climatology*, 22(3), 291-310.

Marshall, G. J., Orr, A., van Lipzig, N. P. M., & King, J. C. (2006). The impact of a changing Southern Hemisphere Annular Mode on Antarctic Peninsula summer temperatures. *Journal of Climate*, 19(20), 5388-5404.

Marshall, G. J., Stott, P. A., Turner, J., Connolley, W. M., King, J. C., & Lachlan-Cope, T. A. (2004). Causes of exceptional atmospheric circulation changes in the Southern Hemisphere. *Geophysical Research Letters*, 31(14), L14205.

Maussion, F., Scherer, D., Mölg, T., Collier, E., Curio, J., & Finkelnburg, R. (2014). Precipitation Seasonality and Variability over the Tibetan Plateau as Resolved by the High Asia Reanalysis*. *Journal of Climate*, 27(5), 1910-1927.

McGowan, H. A., & Sturman, A. P. (1996). Regional and local scale characteristics of foehn wind events over the south island of New Zealand. *Meteorology and Atmospheric Physics*, 58(1-4), 151-164.

McIntosh, E., & Walton, D. W. H. (2000). *Environmental management plan for South Georgia*. Cambridge: The British Antarctic Survey.

Meehl, G. A. (1991). A re-examination of the mechanism of the semiannual cycle in the Southern Hemisphere. *Journal of Climate*, 4, 911-926.

Meredith, M. P., & King, J. C. (2005). Rapid climate change in the ocean west of the Antarctic Peninsula during the second half of the 20th century. *Geophysical Research Letters*, 32(19), L19604.

Meredith, M. P., Brandon, M. A., Murphy, E. J., Trathan, P. N., Thorpe, S. E., Bone, D. G., Chemyshkov, P. P., & Sushin, V. A. (2005). Variability in hydrographic conditions to the east and northwest of South Georgia, 1996–2001. *Journal of Marine Systems*, 53(1), 143-167.

Meredith, M. P., Murphy, E. J., Hawker, E. J., King, J. C., & Wallace, M. I. (2008). On the interannual variability of ocean temperatures around South Georgia, Southern Ocean: Forcing by El Niño/Southern Oscillation and the southern annular mode. *Deep Sea Research Part II: Topical Studies in Oceanography*, 55(18-19), 2007-2022.

Mignone, B. K., Gnanadesikan, A., Sarmiento, J. L., & Slater, R. D. (2006). Central role of Southern Hemisphere winds and eddies in modulating the oceanic uptake of anthropogenic carbon. *Geophysical Research Letters*, 33(1), L01604.

Mlawer, E. J., Taubman, S. J., Brown, P. D., Iacono, M. J., & Clough, S. A. (1997). Radiative transfer for inhomogeneous atmospheres: RRTM, a validated

correlated-k model for the longwave. *Journal of Geophysical Research: Atmospheres*, 102(D14), 16663-16682.

Mo, K. C. (2000). Relationships between low-frequency variability in the Southern Hemisphere and sea surface temperature anomalies. *Journal of Climate*, 13(20), 3599-3610.

Montes-Hugo, M., Doney, S. C., Ducklow, H. W., Fraser, W., Martinson, D., Stammerjohn, S. E., & Schofield, O. (2009). Recent changes in phytoplankton communities associated with rapid regional climate change along the western Antarctic Peninsula. *Science*, 323(5920), 1470-1473.

Moore, G. W. K., & Renfrew, I. A. (2005). Tip jets and barrier winds: A QuikSCAT climatology of high wind speed events around Greenland. *Journal of Climate*, 18(18), 3713-3725.

Morley, S. A., Belchier, M., Sands, C., Barnes, D. K. A., & Peck, L. S. (2014). Geographic isolation and physiological mechanisms underpinning species distributions at the range limit hotspot of South Georgia. *Reviews in Fish Biology and Fisheries*, 24(2), 485-492.

Murphy, E. J., Cavanagh, R. D., Hofmann, E. E., Hill, S. L., Constable, A. J., Costa, D. P., Pinkerton, M. H., Johnston, N. M., Trathan, P. N., Klinck, J. M., Wolf-Gladrow, D. A., Daly, K. L., Maury, O., & Doney, S. C. (2012). Developing integrated models of Southern Ocean food webs: Including ecological complexity, accounting for uncertainty and the importance of scale. *Progress in Oceanography*, 102, 74-92.

Murphy, E. J., Hofmann, E. E., Watkins, J. L., Johnston, N. M., Piñones, A., Ballerini, T., Hill, S. L., Trathan, P. N., Tarling, G. A., Cavanagh, R. A., Young, E. F., Thorpe, S., & Fretwell, P. (2013). Comparison of the structure and function of Southern Ocean regional ecosystems: the Antarctic Peninsula and South Georgia. *Journal of Marine Systems*, 109, 22-42.

Murphy, E. J., Trathan, P. N., Watkins, J. L., Reid, K., Meredith, M. P., Forcada, J., Thorpe, S. E., Johnston, N. M., & Rothery, P. (2007). Climatically driven

fluctuations in Southern Ocean ecosystems. *Proceedings of the Royal Society of London B: Biological Sciences,* 274(1629), 3057-3067.

Murphy, E. J., Watkins, J., Reid, K., Trathan, P., Everson, I., Croxall, J., Priddle, J., Brandon, M., Brierley, A., & Hofmann, E. (1998). Interannual variability of the South Georgia marine ecosystem: biological and physical sources of variation in the abundance of krill. *Fisheries Oceanography*, 7(3-4), 381-390.

Nakanishi, M. (2001). Improvement of the Mellor-Yamada turbulence closure model based on large-eddy simulation data. *Boundary-layer Meteorology*, 99, 349-378.

Nakanishi, M., & Niino, H. (2004). An improved Mellor-Yamada level-3 model with condensation physics: Its design and verification. *Boundary-layer Meteorology*, 112, 1-31.

Nakanishi, M., & Niino, H. (2006). An improved Mellor–Yamada level-3 model: Its numerical stability and application to a regional prediction of advection fog. *Boundary-layer Meteorology*, 119(2), 397-407.

National Ice & Snow Data Center. (2014). *Monthly Archive: September 2014*. Retrieved 1 December 2014, from http://nsidc.org/arcticseaicenews/2014/09/

Nicholls, J. (1973). The airflow over mountains. *World Meteorological Organization Technical Note no.172*. Switzerland: World Meteorological Organization.

Nicolas, J. P., & Bromwich, D. H. (2011). Precipitation changes in high southern latitudes from global reanalyses: A cautionary tale. *Surveys in Geophysics*, 32(4-5).

Nkemdirim, L. C., & Leggat, K. (1978). The effect of chinook weather on urban heat islands and air pollution. *Water, Air, & Soil Pollution*, 9(1), 53-67.

Norte, F. A. (1988). *Características del viento Zonda en la Región de Cuyo-Argentina*. Ph.D. thesis: University of Buenos Aires.

Oard, M. J. (1993). A Method for Predicting Chinook Winds East of the Montana Rockies. *Weather and Forecasting*, 8(2), 166-180.

Obenland, E. (1956). Untersuchungen zur Föhnstatistik des Oberallgäus. *Berichte des Deutschen Wetterdienstes*, 23.

Oerlemans, J. (2001). *Glaciers and Climate Change*. Tokyo: Balkema Publishers.

Ohmura, A., Kasser, P., & Funk, M. (1992). Climate at the equilibrium line of glaciers. *Journal of Glaciology*, 38(130), 397-411.

Ólafsson, H., & Bougeault, P. (1997). The effect of rotation and surface friction on orographic drag. *Journal of the Atmospheric Sciences*, 54(1), 193-210.

Orr, A., Bracegirdle, T. J., Hosking, J. S., Jung, T., Haigh, J. D., Phillips, T., & Feng, W. (2012). Possible dynamical mechanisms for Southern Hemisphere climate change due to the ozone hole. *Journal of the Atmospheric Sciences*, 69(10), 2917-2932.

Orr, A., Cresswell, D., Marshall, G., Hunt, J., Sommeria, J., Wang, C., & Light, M. (2004). A 'low-level' explanation for the recent large warming trend over the western Antarctic Peninsula involving blocked winds and changes in zonal circulation. *Geophysical Research Letters*, 31, L06204.

Orr, A., Marshall, G., Hunt, J. C. R., Sommeria, J., Wang, C., van Lipzig, N., Cresswell, D., & King, J. C. (2008). Characteristics of airflow over the Antarctic Peninsula and its response to recent strengthening of westerly circumpolar winds. *Journal of the Atmospheric Sciences*, 65, 1396-1413.

Orr, A., Phillips, T., Webster, S., Elvidge, A., Weeks, M., Hosking, S. J., & Turner, J. (2014). Met Office Unified Model high resolution simulations of a strong wind event in Antarctica. *Quarterly Journal of the Royal Meteorological Society*, 140, 2287-2297.

Orr, J. C., Fabry, V. J., Aumont, O., Bopp, L., Doney, S. C., Feely, R. A., Gnanadesikan, A., Gruber, N., Ishida, A., & Joos, F. (2005). Anthropogenic ocean acidification over the twenty-first century and its impact on calcifying organisms. *Nature*, 437(7059), 681-686.

Osmond, H. L. (1941). The chinook wind east of the Canadian Rockies. *Canadian Journal of Research*, 19(4), 57-66.

Paul, F., & Andreassen, L. M. (2009). A new glacier inventory for the Svartisen region, Norway, from Landsat ETM+ data: challenges and change assessment. *Journal of Glaciology*, 55(192), 607-618.

Peck, L. S. (2002). Ecophysiology of Antarctic marine ectotherms: limits to life. *Polar Biology*, 25(1), 31-40.

Peltier, W. R., & Clark, T. L. (1979). The evolution and stability of finite-amplitude mountain waves. Part II: Surface wave drag and severe downslope windstorms. *Journal of the Atmospheric Sciences*, 36(8), 1498-1529.

Pepper, J. (1954). *The meteorology of the Falkland Islands and Dependencies, 1944-1950*. London: Crown Agents for Oversea Governments and Administrations.

Plavcan, D., Mayr, G. J., & Zeileis, A. (2014). Automatic and probabilistic foehn diagnosis with a statistical mixture model. *Journal of Applied Meteorology and Climatology,* 53, 652-659.

Polvani, L. M., & Kushner, P. J. (2002). Tropospheric response to stratospheric perturbations in a relatively simple general circulation model. *Geophysical Research Letters*, 29(7), 1114.

Poncet, S. (2000). *Feasibility of rat eradication at South Georgia: a desk study report*. Cambridge: The British Antarctic Survey.

Randel, W. J., & Wu, F. (1999). Cooling of the Arctic and Antarctic polar stratospheres due to ozone depletion. *Journal of Climate*, 12(5), 1467-1479.

Raupach, M., & Finnigan, J. (1997). The influence of topography on meteorogical variables and surface-atmosphere interactions. *Journal of Hydrology*, 190(3-4), 182-213.

Richards, P., & Tickell, W. (1968). Comparison between the weather at Bird Island and King Edward Point, South Georgia. *British Antarctic Survey Bulletin*, 15, 63-69.

Richardson, J., Wood, A. G., Neil, A., Nowacek, D., & Moore, M. (2012). Changes in distribution, relative abundance, and species composition of large whales around South Georgia from opportunistic sightings: 1992 to 2011. *Endangered Species Research*, 19(2), 149-156.

Richner, H., & Hächler, P. (2008). Understanding and forecasting alpine foehn-what do we know about it today. In: *13th Mountain Meteorological Conference, Whistler, British Columbia, Canada*.

Richner, H., & Hächler, P. (2013). Understanding and forecasting Alpine foehn. In: F. Chow, S. De Wekker, B. Snyder (Eds.), *Mountain Weather Research and Forecasting* (pp. 219-260). Netherlands: Springer.

Rignot, E., Rivera, A., & Casassa, G. (2003). Contribution of the Patagonia Icefields of South America to sea level rise. *Science*, 302(5644), 434-437.

Rivera, A., & Casassa, G. (2004). Ice elevation, areal, and frontal changes of glaciers from National Park Torres del Paine, Southern Patagonia Icefield. *Arctic, Antarctic, and Alpine Research*, 36(4), 379-389.

Rogers, E., Black, T., Ferrier, B., Lin, Y., Parrish, D., & DiMego, G. (2001). Changes to the NCEP Meso Eta Analysis and Forecast System: Increase in resolution, new cloud microphysics, modified precipitation assimilation, modified 3DVAR analysis. *NWS Technical Procedures Bulletin*, 488, 15.

Rogers, J. C., & van Loon, H. (1982). Spatial variability of sea level pressure and 500 mb height anomalies over the Southern Hemisphere. *Monthly Weather Review*, 110(10), 1375-1392.

Roscoe, H., Marshall, G., & King, J. C. (2006). Low potential for stratospheric dynamical change to be implicated in the large winter warming in the central Antarctic Peninsula. *Quarterly Journal of the Royal Meteorological Society*, 132(616), 803-820.

Rosqvist, G. C., & Schuber, P. (2003). Millennial-scale climate changes on South Georgia, Southern Ocean. *Quaternary Research*, 59(3), 470-475.

Roux, A., Calcagno, J., & Bremec, C. (2002). Macrobenthic assemblages of demersal fishing grounds off the South Georgia Islands. *Archive of Fishery and Marine Research*, 49(3), 231-241.

Ruddell, A. (2001). Our subantarctic glaciers: why are they retreating? *Australian Antarctic Magazine*, 2, 6-7.

Russell, J. L., Dixon, K. W., Gnanadesikan, A., Stouffer, R. J., & Toggweiler, J. R. (2006). The Southern Hemisphere Westerlies in a Warming World: Propping Open the Door to the Deep Ocean. *Journal of Climate*, 19(24), 6382-6390.

Schaefer, M., Machguth, H., Falvey, M., & Casassa, G. (2013). Modeling past and future surface mass balance of the Northern Patagonia Icefield. *Journal of Geophysical Research: Earth Surface*, 118(2), 571-588.

Schaefer, M., Machguth, H., Falvey, M., Casassa, G., & Rignot, E. (2014). Quantifying mass balance processes on the Southern Patagonia Icefield. *The Cryosphere Discussions*, 8, 3117-3139.

Schneider, D. P., Steig, E. J., van Ommen, T. D., Dixon, D. A., Mayewski, P. A., Jones, J. M., & Bitz, C. M. (2006). Antarctic temperatures over the past two centuries from ice cores. *Geophysical Research Letters*, 33(16), L16707.

Schofield, O., Ducklow, H. W., Martinson, D. G., Meredith, M. P., Moline, M. A., & Fraser, W. R. (2010). How do polar marine ecosystems respond to rapid climate change? *Science*, 328(5985), 1520-1523.

Schuetz, J., & Steinhauser, F. (1955) Neue foehnuntersuchungen aus dem Sonnenblick. *Archives for Meteorology, Geophysics and Bioclimatology Series B*, 6(3), 207-224.

Schweitzer, H. (1952). Versuch einer Erklärung des Föhns als Luftströmung mit überkritischer Geschwindigkeit. *Archives for Meteorology, Geophysics and Bioclimatology*, *Series A*, 5(3), 350-371.

Scorer, R. S., & Klieforth, H. (1959). Theory of mountain waves of large amplitude. *Quarterly Journal of the Royal Meteorological Society*, 85(364), 131-143.

Scorer, R.S. (1978). *Environmental Aerodynamics*. Chichester: Wiley & Sons.

Scott, J., & Poncet, S. (2003). *South Georgia Environmental Mapping Technical Report no. EBS03/1*. Stanley: South Georgia Environmental Baseline Survey South Georgia Surveys.

Screen, J. A., Gillett, N. P., Stevens, D. P., Marshall, G. J., & Roscoe, H. K. (2009). The role of eddies in the Southern Ocean temperature response to the Southern Annular Mode. *Journal of Climate*, 22(3), 806-818.

Screen, J. A., & Simmonds, I. (2011). Erroneous arctic temperature trends in the ERA-40 reanalysis: A closer look. *Journal of Climate*, 24, 2620-2627.

Seibert, P. (1990). South foehn studies since the ALPEX experiment. *Meteorology and Atmospheric Physics*, 43(1-4), 91-103.

Seibert, P. (2005). Hann's thermodynamic foehn theory and its presentation in meteorological textbooks in the course of time. From Beaufort to Bjerknes and Beyond. *Algorismus*, 52, 169-180.

Sen Gupta, A., & England, M. H. (2006). Coupled ocean-atmosphere-ice response to variations in the Southern Annular Mode. *Journal of Climate*, 19(18), 4457-4486.

Sertel, E., Robock, A., & Ormeci, C. (2010). Impacts of land cover data quality on regional climate simulations. *International Journal of Climatology*, 30, 1942–1953.

Shanklin, J. (1985). *Measurements of solar and terrestrial radiation at King Edward Point, South Georgia, 1973-81*. Cambridge: The British Antarctic Survey.

Shanklin, J., Moore, C., & Colwell, S. (2009). Meteorological observing and climate in the British Antarctic Territory and South Georgia: Part 1. *Weather*, 64(5), 127-134.

Sharples, J. J. (2009). An overview of mountain meteorological effects relevant to fire behaviour and bushfire risk. *International Journal of Wildland Fire*, 18, 737-754.

Sharples, J. J., Mills, G. A., McRae, R. H., & Weber, R. O. (2010). Foehn-like winds and elevated fire danger conditions in southeastern Australia. *Journal of Applied Meteorology and Climatology*, 49(6), 1067-1095.

Shindell, D. T., & Schmidt, G. A. (2004). Southern Hemisphere climate response to ozone changes and greenhouse gas increases. *Geophysical Research Letters*, 31(18), L18209.

Simmonds, I., & Jones, D. A. (1998). The mean structure and temporal variability of the semiannual oscillation in the southern extratropics. *International Journal of Climatology*, 18, 473 - 504.

Simmonds, I., & King, J. C. (2004). Global and hemispheric climate variations affecting the Southern Ocean. *Antarctic Science*, 16(04), 401-413.

Simmons, A. J., Poli, P., Dee, D., Berrisford, P., Hersbach, H., Kobayashi, S., & Peubey, C. (2014). Estimating low-frequency variability and trends in atmospheric temperature using ERA-Interim. *Quarterly Journal of the Royal Meteorological Society*, 140, 329-353.

Simmons, A. J., Uppala, S., Dee, D., & Kobayashi, S. (2007). ERA- Interim: New ECMWF reanalysis products from 836 1989 onwards. *ECMWF News Letter*, 110, 25-35.

Simões, J. C., Dani, N., Bremer, U. F., Aquino, F. E., & Arigony-Neto, J. (2004). Small cirque glaciers retreat on Keller Peninsula, Admiralty Bay, King George Island, Antarctica. *Pesquisa Antártica Brasileira*, 4, 49-56.

Skamarock, W. C., & Klemp, J. B. (2008). A time-split nonhydrostatic atmospheric model for weather research and forecasting applications. *Journal of Computational Physics*, 227(7), 3465-3485.

Skamarock, W. C., Klemp, J. B., Dudhia, J., Gill, D. O., Barker, M., Duda, K. G., & Powers, J. G. (2008). A description of the Advanced Research WRF Version 3. *NCAR Technical Report*, 1–113.

Smirnova, T. G., Brown, J. M., Benjamin, S. G., & Kim, D. (2000). Parameterization of cold-season processes in the MAPS land-surface scheme. *Journal of Geophysical Research: Atmospheres*, 105(D3), 4077-4086.

Smith, J. (1960). Glacier problems in South Georgia. *Journal of Glaciology*, 3(28), 707-714.

Smith, R. B. (1979). The influence of mountains on the atmosphere. *Advances in Geophysics*, 21, 87-230.

Solomon, A., Morrison, H., Persson, O., Shupe, M. D., & Bao, J. W. (2009). Investigation of microphysical parameterizations of snow and ice in Arctic clouds during M-PACE through model-observation comparisons. *Monthly Weather Review*, 137(9), 3110-3128.

Son, S. W., Polvani, L. M., Waugh, D. W., Akiyoshi, H., Garcia, R., Kinnison, D., Pawnson, S., Rozanov, E., Shepherd, T. G., & Shibata, K. (2008). The impact of stratospheric ozone recovery on the Southern Hemisphere westerly jet. *Science*, 320(5882), 1486-1489.

South Georgia Heritage Trust (SGHT). (2014). *Environmental Impact Assessment for the eradication of rodents from the island of South Georgia*. Retrieved 1 October 2014, from http://www.sght.org/newsletters-and-publications

Speirs, J. C., McGowan, H. A., Steinhoff, D. F., & Bromwich, D. H. (2013). Regional climate variability driven by foehn winds in the McMurdo Dry Valleys, Antarctica. *International Journal of Climatology*, 33(4), 945-958.

Speirs, J. C., Steinhoff, D. F., McGowan, H. A., Bromwich, D. H., & Monaghan, A. J. (2010). Foehn Winds in the McMurdo Dry Valleys, Antarctica: The Origin of Extreme Warming Events. *Journal of Climate*, 23(13), 3577-3598.

Stauffer, D. R., & Seaman, N. L. (1994). Multiscale four-dimensional data assimilation. *Journal of Applied Meteorology*, 33(3), 416-434.

Steinacker, R. (2006). Alpiner Föhn–eine neue Strophe zu einem alten Lied. *Promet*, 32(1-2), 3-10.

Steinhoff, D. F., Bromwich, D. H., & Monaghan, A. (2013). Dynamics of the foehn mechanism in the McMurdo Dry Valleys of Antarctica from Polar WRF. *Quarterly Journal of the Royal Meteorological Society*, 139(675), 1615-1631.

Steinhoff, D. F., Bromwich, D. H., Speirs, J. C., McGowan, H. A., & Monaghan, A. J. (2014). Austral summer foehn winds over the McMurdo dry valleys of Antarctica from Polar WRF. *Quarterly Journal of the Royal Meteorological Society*, 140(683), 1825-1837.

Stensrud, D. J. (2007). *Parameterization schemes: keys to understanding numerical weather prediction models*. Cambridge: Cambridge University Press.

Stone, D. A., & Fyfe, J. C. (2005). The effect of ocean mixing parameterisation on the enhanced CO2 response of the Southern Hemisphere mid-latitude jet. *Geophysical Research Letters*, 32, L06811.

Sukoriansky, S., Galperin, B., & Perov, V. (2006). A quasi-normal scale elimination model of turbulence and its application to stably stratified flows. *Nonlinear Processes in Geophysics*, 13(1), 9-22.

Takane, Y., & Kusaka, H. (2011). Formation mechanisms of the extreme high surface air temperature of 40.9 C observed in the Tokyo metropolitan area: Considerations of dynamic foehn and foehnlike wind. *Journal of Applied Meteorology and Climatology*, 50(9), 1827-1841.

Tao, Z., Santanello, J. A., Chin, M., Zhou, S., Tan, Q., Kemp, E. M., and Peters-Lidard, C. D. (2013). Effect of land cover on atmospheric processes and air quality over the continental United States – a NASA Unified WRF (NU-WRF) model study. *Atmospheric Chemistry and Physics*, 13, 6207-6226.

Thomas, E. R., Marshall, G. J., & Mcconnell, J. R. (2008). A doubling in snow accumulation in the western Antarctic Peninsula since 1850. *Geophysics Research Letters*, 35, L01706.

Thompson, D. W. J., & Solomon, S. (2002). Interpretation of recent Southern Hemisphere climate change. *Science*, 296(5569), 895-899.

Thompson, D. W. J., & Wallace, J. M. (2000). Annular Modes in the Extratropical Circulation. Part I: Month-to-Month Variability. *Journal of Climate*, 13(5), 1000-1016.

Thompson, D. W. J., Wallace, J. M., & Hegerl, G. C. (2000). Annular modes in the extratropical circulation. Part II: Trends. *Journal of Climate*, 13(5), 1018-1036.

Thorpe, S. E., Heywood, K. J., Brandon, M. A., & Stevens, D. P. (2002). Variability of the southern Antarctic Circumpolar Current front north of South Georgia. *Journal of Marine Systems*, 37(1), 87-105.

Tickell, W. (1962). Ornithological investigations at South Georgia, 1960-62. *Polar Record*, 11(72), 282-83.

Tickell, W., & Cordall, P. (1960). South Georgia Biological Expedition, 1958-59. *Polar Record*, 10(65), 145-46.

Tickell, W., Pinder, R., & Clagg, H. B. (1965). Biological studies on Bird Island, South Georgia, 1962–64. *Polar Record*, 12(80), 601-602.

Timmis, R. J. (1986). *Glacier changes in South Georgia and their relationship to climatic trends.* Ph.D. thesis: University of East Anglia.

Trathan P.N., Duant, F., & Murphy, E. J. (1996). *South Georgia: An Ecological Atlas.* Cambridge: The British Antarctic Survey.

Trathan, P. N., Forcada, J., & Murphy, E. J. (2007). Environmental forcing and Southern Ocean marine predator populations: effects of climate change and variability. *Philosophical Transactions of the Royal Society B: Biological Sciences*, 362(1488), 2351-2365.

Trathan, P. N., Ratcliffe, N., & Masden, E. A. (2012). Ecological drivers of change at South Georgia: the krill surplus, or climate variability. *Ecography*, 35, 983-993.

Trivelpiece, W. Z., Hinke, J. T., Miller, A. K., Reiss, C. S., Trivelpiece, S. G., & Watters, G. M. (2011). Variability in krill biomass links harvesting and climate warming to penguin population changes in Antarctica. *Proceedings of the National Academy of Sciences*, 108(18), 7625.

Turner, B. (1961). South Georgia. *Oondoona*, 9-20.

Ungeheuer, H. (1952). Zur Statistik des Föhns im Voralpengebiet. *Deutscher Wetterdienst in der US-Zone*, 38, 117-120.

Ustrnul, Z. (1992). Influence of foehn winds on air temperature and humidity in the Polish Carpathians. *Theoretical and Applied Climatology*, 45(1), 43-47.

Valkonen, T., Vihma, T., Johansson, M. M., & Launiainen, J. (2014). Atmosphere–sea ice interaction in early summer in the Antarctic: evaluation and challenges of a regional atmospheric model. *Quarterly Journal of the Royal Meteorological Society*, 140(682), 1536-1551.

Valkonen, T., Vihma, T., Kirkwood, S., & Johansson, M. M. (2010). Fine-scale model simulation of gravity waves generated by Basen nunatak in Antarctica. *Tellus*, 62, 319-332.

van den Broeke, M. R. (1998a). The semi-annual oscillation and Antarctic climate. Part 1: Influence on near surface temperatures (1957–79). *Antarctic Science*, 10(2), 175-183.

van den Broeke, M. R. (1998b). The semi-annual oscillation and Antarctic climate. Part 2: recent changes. *Antarctic Science*, 10(2), 184-191.

van den Broeke, M. R. (2000a). The semi-annual oscillation and Antarctic climate. Part 3: The role of near-surface wind speed and cloudiness. *International Journal of Climatology*, 20(2), 117-130.

van den Broeke, M. R. (2000b). The semi-annual oscillation and Antarctic climate. Part 4: A note on sea ice cover in the Amundsen and Bellingshausen Seas. *International Journal of Climatology*, 20(4), 455-462.

van den Broeke, M. R. (2000c). The semiannual oscillation and Antarctic climate, part 5: impact on the annual temperature cycle as derived from NCEP/NCAR re-analysis. *Climate Dynamics*, 16(5), 369-377.

van Lipzig, N. P., Marshall, G. J., Orr, A., & King, J. C. (2008). The relationship between the Southern Hemisphere Annular Mode and Antarctic Peninsula summer temperatures: Analysis of a high-resolution model climatology. *Journal of climate*, 21(8), 1649-1668.

van Loon, H., Kidson, J.W., & Mullan, A. B. (1993). Decadal variation of the annual cycle in the Australian dataset. *Journal of Climate*, 6, 1227-1231.

Vaughan, D. G., Marshall, G. J., Connolley, W. M., Parkinson, C., Mulvaney, R., Hodgson, D. A., King, J. C., Pudsey, C. J., & Turner, J. (2003). Recent rapid regional climate warming on the Antarctic Peninsula. *Climatic Change*, 60(3), 243-274.

Vergeiner, J. (2004). *South foehn studies and a new foehn classification scheme in the Wipp and Inn valley*. Ph.D. thesis: Innsbruck University.

von Danckelman, A. (1884). Vorlâufiger Bericht über die Ergebnisse der meteorologischen Beobachtungen der deutschen Polarstationen. *Meteorologische Zeitschrif,* 144-155.

Vosper, S. B. (2015). Mountain waves and wakes generated by South Georgia: implications for drag parametrization. *Quarterly Journal of the Royal Meteorological Society*.

Walker, G. (1928). World weather. *Quarterly Journal of the Royal Meteorological Society*, 54(226), 79-87.

Wallington, C. E. (1960). An Introduction to Lee Waves in the Atmosphere. *Weather*, 15(8), 269-276.

Watterson, I. (2000). Southern midlatitude zonal wind vacillation and its interaction with the ocean in GCM simulations. *Journal of Climate*, 13(3), 562-578.

Weber, R. O., & Prévôt, A. S. (2002). Climatology of ozone transport from the free troposphere into the boundary layer south of the Alps during North Foehn. *Journal of Geophysical Research: Atmospheres (1984–2012)*, 107(D3), ACH-4.

Wells, H., Vosper, S. B., Ross, A. N., Brown, A. R., & Webster, S. (2008). Wind direction effects on orographic drag. *Quarterly Journal of the Royal Meteorological Society*, 134(632), 689-701.

Whitehouse, M., Meredith, M., Rothery, P., Atkinson, A., Ward, P., & Korb, R. (2008). Rapid warming of the ocean around South Georgia, Southern Ocean, during the 20th century: forcings, characteristics and implications for lower trophic levels. *Deep Sea Research Part I: Oceanographic Research Papers*, 55(10), 1218-1228.

Whiteman, C. D. (2000). *Mountain Meteorology: Fundamentals and Applications*. Oxford: Oxford University Press.

Wilson, A. B., Bromwich, D. H., & Hines, K. M. (2012). Evaluation of Polar WRF forecasts on the Arctic System Reanalysis domain: 2. Atmospheric hydrologic cycle. *Journal of Geophysical Research: Atmospheres*, 117(D4).

World Meteorological Organization. (1992*). International Meteorological Vocabulary* (second edition). Switzerland: World Meteorological Organization.

Yin, J. H. (2005). A consistent poleward shift of the storm tracks in simulations of 21st century climate. *Geophysical Research Letters*, 32(18), L18701.

Young, E. F., Rock, J., Meredith, M. P., Belchier, M., Murphy, E. J., & Carvalho, G. R. (2012). Physical and behavioural influences on larval fish retention: contrasting patterns in two Antarctic fishes. *Marine Ecology: Progress Series,* 465, 201–204.

Young, E. F., Thorpe, S. E., Banglawala, N., & Murphy, E. J. (2014). Variability in transport pathways on and around the South Georgia shelf, Southern Ocean: implications for recruitment and retention. *Journal of Geophysical Research: Oceans,* 119(1), 241–252.

Yuan, X. (2004). ENSO-related impacts on Antarctic sea ice: a synthesis of phenomenon and mechanisms. *Antarctic Science*, 16(04), 415-425.

Zängl, G. (2002). Idealized numerical simulations of shallow föhn. *Quarterly Journal of the Royal Meteorological Society*, 128(580), 431-450.

Zängl, G. (2003). Deep and shallow south foehn in the region of Innsbruck: Typical features and semi-idelized numerical simulations. *Meteorology and Atmospheric Physics*, 83(3-4), 237-261.

Zängl, G., Chimani, B., & Häberli, C. (2004). Numerical simulations of the foehn in the Rhine Valley on 24 October 1999 (MAP IOP 10). *Monthly Weather Review*, 132(1), 368-389.